



N° d'ordre NNT : xxx

THÈSE DE DOCTORAT DE L'UNIVERSITÉ DE LYON
opérée au sein de
l'Université Claude Bernard Lyon 1

École Doctorale ED52
Physique et Astrophysique de Lyon

Spécialité de doctorat :
Discipline : Physique médicale

Soutenue publiquement le 14/12/2018, par :
Mattia Fontana

Tests and characterization of gamma cameras for medical applications

Test et caractérisation de caméras gamma pour les applications médicales

Devant le jury composé de :

Llosá Gabriela, Professeur associée, IFIC - Institut de Fisica Corpuscular, Paterna, Espagne
Rapportrice

Thirolf Peter, Professeur associé, Fakultät für Physik der LMU München - Lehrstuhl für Experimentalphysik - Medizinische Physik, Garching, Allemagne
Rapporteur

Augier Corinne, Professeur, IPNL - Institut de Physique Nucléaire de Lyon, France
Examinateuse

Cerello Piergiorgio, INFN - Istituto Nazionale di Fisica Nucleare, sezione di Torino, Italie
Examinateur

Morel Christian, Professeur, CPPM - Centre de Physique de Particules de Marseille - Aix-Marseille Université, Marseille, France
Examinateur

Rafecas Magdalena, Professeur, Institut für Medizintechnik - Universität zu Lübeck, Allemagne
Examinateuse

Létang Jean Michel, maître de conférences, CREATIS - Centre de Recherche en Acquisition et Traitement de l'Image pour la Santé, Lyon, France
Co-directeur de thèse

Testa Étienne, maître de conférences, IPNL - Institut de Physique Nucléaire de Lyon, France
Directeur de thèse

Dauvergne Denis, Directeur de Recherche CNRS, LPSC - Laboratoire de Physique Subatomique et de Cosmologie de Grenoble, France
Invité

Tests and characterization of gamma cameras for medical applications

PhD Candidate

MATTIA FONTANA

Thesis directors

ÉTIENNE TESTA and JEAN MICHEL LÉTANG

Université Claude Bernard
Lyon 1
Physics department
Doctoral school ED52:
Physics and Astrophysics

Defended on December the 14th
2018

Abstract

The application of nuclear and particle physics techniques in the field of medical diagnosis and pathology treatment is nowadays well-established in the clinical routine. In particular, several medical imaging techniques are based on the exploitation of elementary particles (Positron Emission Tomography (PET), Single Photon Emission Computed Tomography (SPECT), Computed Tomography (CT) scans, etc.), as well as treatment methods, mainly concerning cancer, which causes about 9 millions deaths per year all over the world.

In this context, ion beam therapy is a promising technique in cancer treatment because of the ion defined range and favorable dose delivery features with respect to standard photon radiotherapy. Strict and precise treatment planning and monitoring are now key points for the method developments and full exploitation. In particular, with the aim of optimizing the ion treatment effectiveness, the ion range monitoring is mandatory: different solutions have been explored, but an online treatment check is still a challenge. The ion beam treatment monitoring is mainly performed by means of secondary charged or neutral particles. In this context, the detection of the Prompt-Gammas (PGs) emitted during treatments has proven its potential in the ion range control in real time. Since the first evidence of the existing correlation between the emitted gamma profile fall-off and the Bragg peak position, several groups are involved in research activities in order to develop and optimize instruments and methods with the aim of improving this monitoring technique. Among the others, collimated and Compton cameras are being studied and optimized for this application. The same detectors can also be employed in nuclear medicine for the detection of the radioactive elements decay products.

A collaboration of 4 laboratories in France, called *Contrôle en Ligne de l'hadronthérapie par Rayonnements Secondaires* (CLaRyS), is involved in the parallel development of two composite detectors for ion beam monitoring and nuclear medicine applications, and this thesis is carried out within this collaboration with the detectors clinical trial as final aim.

The development project started a few years ago and is now at the final stage. The two cameras have been designed according to simulation studies, and the different components are now under tests. The collimated camera is composed of a multi-slit tungsten mechanical collimator, set in front of an absorber composed of 30 Bismuth Germanium Oxide - $\text{Bi}_{12}\text{GeO}_{20}$ (BGO) blocks, for a total size of $210 \times 175 \times 30 \text{ mm}^3$; each block presents a streaked structure with a 8×8 pseudo-pixel matrix and the signal is read-out by 4 photomultipliers. A $\sim 3 \text{ ns}$ time resolution can be achieved on average for the prompt-gamma detection. The same absorber is part of the Compton camera, in addition to a scatterer section composed of 7 Double-sided Silicon Strip Detectors (DSSDs) $96 \times 96 \times 2 \text{ mm}^3$ each.

With the collimated camera, the parallel emitted photons are selected by the collimator and a mono-dimensional emission profile can be reconstructed. The Compton camera has a more efficient detection technique, thanks to the absence of a mechanical collimation system, and could potentially lead to 3D information via the reconstruction of the Compton cones. These features make it suitable for the application in nuclear medicine, in particular as an alternative to the present SPECT collimated cameras, allowing for accurate and efficient image reconstructions with the usage of high energy gamma sources, which should reduce image

blurring effects due to attenuation in the patient and the total released dose with respect to the present clinical routine.

Concerning the monitoring of ion beam therapy treatments, an additional detector component is needed to temporally and spatially tag the incoming beam ions and help rejecting the relevant background (mostly due to neutrons) which strongly affects the prompt-gamma yield. A scintillating fiber tagging hodoscope, which can be coupled to both collimated and Compton camera, is under development: it is composed of 2 perpendicular planes of 128 scintillating fibers, read-out from both sides by 8 64-channel photomultipliers by Hamamatsu.

The thesis work consists in the critical evaluation, characterization and tuning of the different components, together with the associated electronics, and of the complete detectors on beam. In parallel, simulation studies can improve the detection technique and optimize the detector structure, as well as pave the way for further applications.

After a general introduction devoted to expose the thesis context in chapter 1, an overview of the instrumental and technical state of the art of the gamma cameras is given in chapter 2. Chapter 3 focuses on the two cameras developed by the CLaRyS collaboration; the camera components are described in details, and all the characterization measurements performed during the three years of my PhD thesis are explained. Chapters 4 and 5 present the simulation studies I performed with the aim of investigating the potential of the developed detectors for the application on ion beam therapy monitoring and nuclear medicine, respectively. The entire chapter 6 is dedicated to the description of the tests performed on proton beams for the detector characterization measurements. The final chapter 7 is used to summarize and discuss all the results obtained in this thesis work; furthermore, the perspectives of the project are fixed on a time-line for the next future, and new research directions emerging from the obtained results are proposed.

Contents

Prologue	1
1 Context	3
1.1 Ion beam therapy	5
1.1.1 Physics of ion beam therapy	6
1.1.1.1 Charged particle interactions in matter	8
1.1.2 Biological effects of ion beam therapy	16
1.1.3 Accelerators and beam delivery	20
1.1.3.1 Accelerators for ion beam therapy	20
1.1.3.2 Beam time structure	23
1.1.3.3 Beam delivery systems	24
1.1.4 Treatment planning	28
1.1.5 Ion beam therapy uncertainties and treatment monitoring	32
1.1.5.1 Ion radiography and tomography	37
1.1.5.2 Positron Emission Tomography	40
1.1.5.3 Prompt-gamma detection	48
1.1.5.4 Interaction Vertex Imaging	49
1.1.5.5 Other techniques	49
1.2 Nuclear medicine	53
1.2.1 Radiotracers	53
1.2.2 Positron Emission Tomography	59
1.2.3 Single Photon Emission Computed Tomography	64
1.2.4 Theranostics	66
2 Prompt gamma detection	69
2.1 Photon detection	70
2.1.1 Photon interactions in matter	70
2.2 Ion range monitoring with prompt-gamma radiation	78
2.3 Prompt-Gamma (PG) emission during particle therapy	78
2.4 Gamma cameras state of the art	78
3 CLaRyS prototypes	81
3.1 CLaRyS gamma camera components	82
3.1.1 Scatterer	83
3.1.1.1 Scatterer Front-End card	86
3.1.1.2 Scatterer thermal regulated box	87
3.1.2 Collimator	88
3.1.3 Absorber	88
3.1.3.1 Absorber Front-End and read-out cards	90
3.1.3.2 Absorber mechanical support	93
3.1.4 Beam tagging hodoscope	94
3.1.4.1 Hodoscope Front-End card	95
3.1.4.2 Hodoscope mechanical support	98
3.1.4.3 Small hodoscope prototypes	98
3.1.5 Camera acquisition system	100
3.1.6 Camera acquisition, monitoring and slow control software	102

3.1.7	Camera integration and mechanical support	104
3.1.8	Data analysis and image reconstruction	106
3.2	Camera component characterization and development status	107
3.2.1	Scatterer silicon layer characterization	107
3.2.2	Absorber Bismuth Germanium Oxide - $\text{Bi}_{12}\text{GeO}_{20}$ (BGO) blocks characterization	109
3.2.2.1	Space and energy calibration and characterization	111
3.2.2.2	Qualitative test of spatial reconstruction accuracy	112
3.2.2.3	Pixel identification and energy calibration algorithm	112
3.2.2.4	Time response characterization method	113
3.2.2.5	Results: Photo-Multiplier (PM) gain equalization	115
3.2.2.6	Results: block spatial precision	116
3.2.2.7	Pixel identification	121
3.2.2.8	Pixel energy calibration	121
3.2.2.9	Time characterization	126
3.2.2.10	Results for the 30 blocks	126
3.2.3	Hodoscope PMs characterization	130
3.2.4	Hodoscope fiber test with electron source	133
3.3	Summary and perspectives	137
3.3.1	Silicon scatterer	137
3.3.2	BGO absorber	138
3.3.2.1	Absorber upgrade	139
3.3.3	Scintillating fiber hodoscope	139
3.3.3.1	Hodoscope upgrade	140
3.3.4	Acquisition and software	141
3.4	Conclusions	141
4	Compton camera application for ion beam therapy monitoring	145
4.1	Introduction	146
4.2	Material and methods	148
4.2.1	Simulation setup	148
4.2.2	Beam structure	151
4.2.2.1	Beam structure measurements at HIT	151
4.2.2.2	Beam modeling	151
4.2.3	Compton camera events	152
4.2.4	TOF and energy based data selection	153
4.2.5	Reconstruction algorithms	155
4.2.5.1	Line-cone algorithm	156
4.2.5.2	LM-MLEM algorithm	156
4.2.6	Performance study	157
4.2.6.1	Absolute detection efficiency	157
4.2.6.2	Rate of random coincidences	158
4.2.6.3	Camera precision	158
4.3	Results	159
4.3.1	Absolute detection efficiency	160
4.3.2	Rate of random coincidences	162
4.3.3	Camera precision	163
4.4	Discussion	165

5 Compton camera application in nuclear medicine	171
5.1 Introduction	172
5.2 Material and methods	173
5.2.1 Radioactive sources	173
5.2.2 Compton camera simulation and data analysis	173
5.2.2.1 Simulation settings	173
5.2.2.2 Data collection and analysis	176
5.2.2.3 Compton camera study for SPECT application	176
5.2.3 Anger camera simulation and data analysis	178
5.2.3.1 Simulation settings	178
5.2.3.2 Data analysis	179
5.2.4 Figures of merit for the comparison study	184
5.3 Results: Compton camera study for SPECT application	184
5.3.1 Influence of Compton camera scatterer detector energy resolution	184
5.3.2 Compton camera coincidence study	185
5.3.3 Compton camera design study	186
5.4 Results: Benchmark of Compton camera and Anger camera performance	188
5.5 Summary and discussion	191
6 Beam tests	195
6.1 Hodoscope: december 2017	196
6.2 Hodoscope: may 2018	196
6.3 Collimated camera: september 2018	196
7 Conclusions and discussion	199
Appendices	201
Appendix A Compton camera data format	203
A.1 Introduction	203
A.2 General features	203
A.2.1 Common information	203
A.2.1.1 Front End number	203
A.2.1.2 Pre-trigger and trigger	205
A.2.1.3 Mode number	205
A.3 Physical data format	207
A.3.1 Scatterer detector data format	207
A.3.2 Absorber detector data format	207
A.3.3 Beam hodoscope data format	210
A.4 Slow control, trigger and monitoring data format	210
A.4.1 Communication architecture	210
A.4.2 Transport protocol and processor packets	211
A.4.2.1 Definitions	211
A.4.2.2 Data encoding	212
A.4.2.3 Packets format	212
A.4.2.4 Possible control symbols	213
A.4.3 Transport layer	213
A.4.3.1 Control packet	213
A.4.3.2 Configuration packets	214

Contents

A.4.3.3	Monitoring process (Front End cards → Micro Advanced Telecommunications Computing Architecture (μ -TCA))	215
A.4.3.4	Special command process (μ -TCA → Front End cards)	217
A.4.4	Data packets (Front End card → μ -TCA)	217
A.5	UDP packets format	219
A.6	Data throughput expected in clinical conditions	220
A.6.1	Clinical intensities	220
A.6.1.1	Review: detector and target sizes	220
A.6.2	Coincidence rate	221
A.6.3	Data flow (Front End cards → μ -TCA)	221
A.6.4	Acquisition data flow (μ -TCA → Acquisition PC)	222
A.6.5	Conclusions	223
	List of abbreviations	225
	Bibliography	227

List of Figures

1.1	Treatment planning of lung cancer for the irradiation with x-rays (left) or carbon ions (right) (in Durante et al. 2016).	7
1.2	Relative dose as a function of the particle depth in water for different particle species. For photons, the reported energy in MeV corresponds to MV linac-accelerated electron induced bremmstrahlung. In Paganetti 2012a.	7
1.3	Schematic view of an example of the three main interactions mechanics of protons in matter: Coulomb interaction with atomic electrons (a), Coulomb interactions with atomic nucleus (b), nuclear reactions(c). In Newhauser et al. 2015.	8
1.4	Lateral spread of different ions in water obtained with Geant4 Monte Carlo simulations. The Full Width at Half Maximum (FWHM) of the beam spot distribution is presented as a function of depth in water (A) for beams at different energies and as a function of beam energy (B) after 15 cm range in water. In Durante et al. 2016.	12
1.5	Schematic view of the nuclear reaction between a projectile and a target nucleus. The two steps are defined as “collision” and “de-excitation” processes.	13
1.6	Effects of nuclear interactions (first row) on proton (left column) and carbon ion (right column) beams and resulting dose distributions (bottom row).	14
1.7	Ionizing radiations cause DNA damages in tissues, which are the basis for tumor radiation therapy. On the left side, the scheme presents the possible kind of damages induced by radiations on the cell DNA. The radiation effectiveness in killing cells is then related to the distribution of ionization events, which is all the more dense for high-Linear Energy Transfer (LET) primaries at low energies. The Relative Biological Effectiveness (RBE) is then enhanced for this kind of radiation. On the right side, the RBE is related to the LET for different ion species.	18
1.8	Schematic view of the main components of a cyclotron accelerator. On the left side the magnet is sketched together with the radio-frequency elements (“Dees”), which are also shown on the section depicted on the right side, with the ion source in the center. In Paganetti 2012a.	21
1.9	Comparison of the size of various ion accelerators for hadrontherapy. CABOTO is a cyclinac studied by the TERA Foundation; the superconducting cyclotron, designed by Ion Beam Applications, Belgium (IBA), is under installation in Caen, France, within the ARCHADE project; Heidelberg Ion Therapy Center, Germany (HIT) and Centro Nazionale di Adroterapia Oncologica, Italy (CNAO) are in operation in Heidelberg, Germany and Pavia, Italy, respectively; the SIEMENS synchrotron is installed in Marburg and Shangai. In Amaldi et al. 2010a.	22
1.10	Example of Spread-Out Bragg Peak (SOBP). The target region is highlighted and the discrete pristine peaks composing the SOBP are sketched in red. In Durante et al. 2016.	25
1.11	Schematic view of a fully passive beam delivery system. In Schardt et al. 2010.	26
1.12	Schematic view of a fully active beam delivery system. In particular, here the GSI Helmholtz Centre for Heavy Ion Research, Germany (GSI) raster scanning system is depicted. In Schulz-Ertner et al. 2006.	27

1.13 Schemes of a standard gantry design (left) and of the carbon-ion rotating gantry installed at HIT (right).	28
1.14 Hounsfield look-up table for carbon ion treatment planning, based on the data collected at GSI and reported in Jäkel et al. 2001a. In Rietzel et al. 2007.	30
1.15 Comparison of physical (green solid line) and biological (blue solid line) dose for a 290 MeV ^{12}C ion beam with a 6 cm SOBP for an assumed maximum RBE of 3.0. The RBE varies in the range 2.5–3.5 and an uncertainty band is sketched to represent the biological dose possible variation due to the selection of the RBE value (dashed-red line). In Suit et al. 2010.	30
1.16 Schematic view of the potential benefit due to the depth-dose features of protons as compared to photons (a) and influence of range uncertainties on photon irradiation and proton pristine and spread-out Bragg peaks. In Knopf et al. 2013.	33
1.17 Proton and heavier ion radiography and Computed Tomography (CT) are under study in the last years as promising techniques for optimizing the treatment planning performance in hadrontherapy. A standard detector design is sketched in the left panel, while the first image of an hand phantom is reported in the right one.	38
1.18 Schematic representation of the Positron Emission Tomography (PET) technique principle. In the top figure, a standard real annihilation event is presented, while in the bottom line the principle of conventional and Time-Of-Flight (TOF)-PET are compared. In Vandenberghe et al. 2016.	41
1.19 β^+ activity profiles for various ion beams impinging on a Poly Methyl Metacrylate (PMMA) thick target. The depth-dose profiles are also shown in dashed lines for comparison. In Fiedler et al. 2012.	42
1.20 The application of the PET technique to the monitoring of ion range in particle therapy includes three possible modalities: in-beam, in-room and off-line PET, represented in the scheme in (a). The amount of registered events depends on the created positron emitter half-life, and thus on the implemented modality, as shown by the histogram in (b).	45
1.21 Alternative methods for in-vivo range verification of ion beam therapy include the detection of iono-acoustic waves produced by the localized dose deposited by the energetic ion beams, whose principle is sketched on the left side, and hybrid systems for 3-photon detection, which can be applied to both nuclear medicine diagnostics and hadrontherapy monitoring, as the one sketched on the right side.	51
1.22 The various radioactive decay channels are schematized in (a) for a generic isotope ^{A_Z}X . A more detailed scheme, describing the decay processes and products, is given in (b).	55
1.23 The β^+ decay of ^{18}F creates the stable isotope ^{18}O and a positron, which travels short distance (1-2 mm) before interacting with an electron. The consequent annihilation produces two anticollinear 511 KeV photons (a). The two photons are detected by the PET scanner in time coincidence, and the two points of interaction defines a line of response, then extended to a so-called “tube of response” which accounts for the detector’s elements finite dimensions (b). In Vaquero et al. 2015.	60
1.24 In T. Lewellen et al. 2004.	61

1.25 Schematic view of the information provided by TOF measurement to the PET detection. Without TOF, a flat probability is assigned to the reconstructed Line Of Response (LOR) (blue), while the measurement of the arrival time difference between the two coincident photons is translated into a distance from the LOR midpoint where the probability density function should centered (red). In Vaquero et al. 2015.	63
1.26 In Zeng et al. 2004.	65
2.1 Schematic diagram of the photoelectric effect. A photon with energy $h\nu$ interacts with a K-shell electron, which is ejected as photoelectron with kinetic energy E_K . In Podgorsak 2010.	71
2.2 Schematic view of the Compton scattering principle. Image from https://universe-review.ca/R15-12-QFT10.htm	73
2.3 In Podgorsak 2010	74
2.4 Polar plot of the number of photons (incident from the left side) Compton scattered into a unit solid angle at the scattering angle θ , for the different indicated incident photon energies. In Knoll 2000.	74
2.5 Schematic representation of pari production (a) in the COulomb field of a nucleus and triplet production (b) in the Coulomb field of an orbital electron. In Podgirsak2010.	76
2.6 Cross sections of the photoelectric absorption, Thomson scattering, Compton scattering, pair production (electron-positron pairs), and photonuclear absorption for a copper absorber as a function of the photon energy energy. In Hermanss 2013.	76
2.7 Relative importance of the three major types of photon interaction in matter. The lines show the values of Z and $h\nu$ for which the two neighboring effects are just equal. In Knoll 2000.	77
2.8 In Krimmer et al. 2017.	79
3.1 Schematic view of the two CLaRyS gamma camera prototypes: the multi-collimated camera (a) and the Compton camera (b), both coupled to the beam tagging hodoscope. The ion beam is represented by the red line, and some beam bunches has been highlighted. The detection principle is also sketched for the two detectors: the tungsten collimator select the parallel incoming photons for the multi-slit collimated camera (a), while the Compton cone is reconstructed with the two interactions in scatterer and absorber in the Compton camera (b).	83
3.2 Overview of the scatterer layers, with its working principle (a) and a picture of the detector connected to the Front-End (FE) card in the thermal regulated box (b).	85
3.3 Scatterer silicon layers equipment: final version of the Front-End (FE) card (a) and scheme of the detector integration in the thermal regulated box (b).	88
3.4 Tungsten collimator and its setup in the multi-slit collimated camera. Two identical collimators are available, with $1.5 \times 120 \times 170 \text{ mm}^3$ tungsten slabs and a pitch of 8 mm. The two tungsten multi-slit collimators are placed in front of a 6×5 Bismuth Germanium Oxide - $\text{Bi}_{12}\text{GeO}_{20}$ (BGO) block absorber setup in its mechanical support (see section 3.1.3). Both the single collimator setup (size and pitch) and the two collimators configuration can be easily modified to adapt the system to peculiar applications.	89
3.5 Components of an absorber module and its working principle.	91

3.6 Absorber read-out electronics: FE card (a) and Analog Sampling Module (ASM) board (b).	92
3.7 Details of the temporary absorber acquisition based on the Altera development card.	93
3.8 Absorber front view with the BGO block lines arranged in the mechanical support (a). Scheme of the BGO absorber with its mechanical support (b).	94
3.9 128×128 scintillating fiber hodoscope on its 2-dimensional moving stand.	95
3.10 Details of the scintillating fiber hodoscope setup.	96
3.11 HODOPIC board (a) and scheme of the beam-tagging hodoscope two-dimensional moving stand (b).	97
3.12 Hodoscope small prototypes.	99
3.13 Acquisition system components: Micro Advanced Telecommunications Computing Architecture (μ -TCA) crate (a), Advanced Mezzanine Card (AMC)40 board (b) and Trigger et HORloge (THOR) card (c).	101
3.14 Schematic view of the Compton camera acquisition system. For the multi-collimated camera, the trigger and pre-trigger signals are the same.	102
3.15 Software tools: user interface of the acquisition C++ software (a) and example of the ROOT (Brun et al. 1997) monitoring software visualization for the beam tagging hodoscope 32×32 fiber prototype.	103
3.16 Details of the gamma camera integration and mechanical support.	105
3.17 View of the Compton camera assembly with the beam tagging hodoscope on the developed mechanical supports.	105
3.18 Scheme of the spatial and energy characterization test-bench.	110
3.19 Details about the BGO block time response characterization.	111
3.20 Logic for the event assignment to a single pixel. The dual pseudo-pixel grid is displayed: in white the mid points on the pseudo-pixel edges along rows (middle of lines in vertical direction), in red along columns (middle of lines in horizontal directions). The sign of the outer products detailed in the legend are used to define the column and row (so that the pseudo-pixel) where to assign the reconstructed event.	113
3.21 Reference BGO block raw signals collected with the Wave Catcher acquisition system. The four outputs of the single PMTs are shown together with the sum signal.	114
3.22 Photo-Multiplier (PM) signal amplitude spectra before (a) and after (b) the PM gain equalization.	115
3.23 1D integrated position distribution on the two transverse dimensions before (a) and after (b) the PM gain equalization. In the two sub-figures, left side for the horizontal dimension, right side for the vertical one.	116
3.24 Block energy spectrum before (a) and after (b) the PM gain equalization.	116
3.25 2D reconstructed position map before (a) and after (b) the PM gain equalization.	117
3.26 2D reconstructed position maps during a 2-mm step scan performed with the Cobalt-60 (^{60}Co) source with the line aperture from the left to the right size of the block surface. 4 reference measurements points, the position of the aperture is shown by the semi-transparent yellow band.	118
3.27 2D reconstructed position maps during a 2-mm step scan performed with the ^{60}Co source with the line aperture from the bottom to the top side of the block surface. 4 reference measurements points, the position of the aperture is shown by the semi-transparent yellow band.	119

3.28 2D reconstructed position maps during a 1-mm step scan performed with the ^{60}Co source with the line aperture. 9 reference measurements points, the position of the aperture is shown by the semi-transparent yellow band.	120
3.29 Superposition of the event reconstructed position profiles integrated along the vertical axis for 5 points of the 1-mm step scan performed with the ^{60}Co source with the line aperture. The 5 positions correspond to the two-dimensional maps in Figures 3.28a, 3.28b, 3.28c, 3.28d, and 3.28e.	121
3.30 2D reconstructed position maps during a 1-mm step scan performed with the ^{60}Co source with the point-like aperture. 6 reference measurements points, the relative X position of the aperture is reported in the caption of each figure. In the vertical dimension, the aperture is centered on the center of the pseudo-pixel line.	122
3.31 Superposition of the event reconstructed position profiles integrated along the vertical axis for 6 points of the 1-mm step scan performed with the ^{60}Co source with the point-like aperture. The 6 positions correspond to the two-dimensional maps in Figures 3.30a, 3.30b, 3.30c, 3.30d, 3.30e, and 3.30f.	123
3.32 1D integrated position distributions on the two transverse dimensions with the retrieved position of the pseudo-pixel average center (a). Reconstructed 2D map with the identified pseudo-pixels positions and surfaces.	124
3.33 Auxiliary position map used for the assignment of the reconstructed events to a single pixel. The highlighted points represent the “valleys” between neighboring pixels on their separation borders.	124
3.34 2D map of the reconstructed event assignations to pseudo-pixels.	125
3.35 Single pseudo-pixels (a) and whole block (b) energy spectra with the Sodium-22 (^{22}Na) source before (left) and after (right) the calibration process. The whole block spectra are reported in logarithmic scale. Three non calibrated spectra of pixels in reference positions (border, mid-center and center area) on the block are also reported with the non calibrated spectrum (a normalization factor has been applied for visualization purpose).	127
3.36 Relative number of entries for each pseudo-pixel as a function of the pixel relative position, represented by the row and column numbers (0 to 8 from left to right and bottom to top of the block surface). Figure(a) shows the entries in a selected energy window around 511 keV, Figure(b) in an energy window around 1275 keV. All the entries are normalized to the maximum collected number of entries, corresponding to 511 keV events in the central section of the block.	128
3.37 Distribution of arrival time differences between reference scintillator (a Barium Fluoride (BaF_2) monoblock detector with 1 ns FWHM time resolution) and BGO block.	128
3.38 Test-bench and tools for the characterization measurements performed on the Hamamatsu PMs of the beam tagging hodoscope.	131
3.39 Details of the hodoscope PMs and of the performed characterization measurements.	132
3.40 Two-dimensional response maps of one of the Hamamatsu PMs for the scintillating fiber hodoscope readout, obtained with the irradiation with a blue Light Emitting Diode (LED). The signal amplitude is normalized to the reference PM response.	133

3.41 Two-dimensional response maps of the Hamamatsu PMs for the scintillating fiber hodoscope readout, obtained with the irradiation with a blue LED. The signal amplitude is normalized to the reference PM response and then to each PM maximum detected amplitude.	134
3.42 Cross-talk study on neighboring PM pixels. The experimental results obtained with the irradiation with a blue LED through the plastic fiber mask on a reference PM (right) are compared to the specifications provided by the producer, measured in similar conditions (left). The cross-talk is expressed in % with respect to the irradiated anode, which is represented by the light-blue cell with 100% of the signal.	135
3.43 Comparison of the simulated distribution of energy deposited by electrons from the ^{90}Sr source on a single hodoscope fiber to the experimental signal amplitude distribution from a scintillating fiber irradiated with the ^{90}Sr source.	136
4.1 Scheme of the simulation setup (not at scale): a PMMA cylindrical phantom is set in front of the Compton camera prototype. The Compton camera is composed of a stack of 7 double sided silicon strip detectors (scatterer) and a plane of 100 single BGO blocks. The set distances are realistic for clinical conditions. This geometrical configuration has been used for all the simulations presented in this work.	149
4.2 Time micro-structure measured from a carbon ion beam at 400 MeV/u delivered at HIT (time difference between two crossed-scintillating fibers). The offset between the two fibers is arbitrarily set at 130 ns. The pulses have an extraction period of 150.2 ns and the bunches are 21.5 ns FWHM. On the x axis the time has been measured with a two-scintillating-fiber hodoscope, with 1 ns FWHM time resolution.	151
4.3 Diagram showing the different definitions of coincidences in the Compton camera.	154
4.4 Time of flight spectra of true gamma coincidences (blue) and background events (red) obtained with 10^8 160 MeV independent incident protons.	155
4.5 Scheme of the reconstruction principle for Compton events. For line-cone reconstruction methods, two points are extracted for each event (diamonds in the figure), provided by the intersection between the reconstructed Compton cone and the beam line. The reconstructed image is strictly 1D. For the iterative MLEM algorithm, each algorithm iteration adds constraints to the reconstructed cone surfaces, leading to a 3D image.	156
4.6 Compton camera efficiency as a function of the gamma energy for the different kind of possible events (see section 4.2.3).	160
4.7 Absolute Compton camera efficiency as a function of the gamma source position for different gamma energies, in the range between 300 keV to 6 MeV. The left side shows the camera efficiency with no detection energy threshold. In the right side, detection energy thresholds are applied to reproduce a realistic scenario (lower limit of 50 keV for the scatterer, 100 keV for the absorber). These values can change for the final configuration, according to the detector energy resolutions achieved.	161
4.8 Ratio between coincidence events with more than 90% of the primary photon energy absorbed in the detector layer and all detected coincidences for 4 source positions: center of the camera, 40, 100, 300 mm from the center.	162

4.9	Coincidences yield for protons (left) and carbon ions (right) as a function of the beam intensity. The intensity is reported as number of incident particles per bunch. The filled markers correspond to the collected data without time-of-flight discrimination, while this cut is applied to the data reported with empty markers. Moreover, the yields are given before and after the profile reconstruction with the line-cone algorithm.	163
4.10	Data processing comparison for the same proton simulation with the line cone algorithm (left column) and the LM-MLEM algorithm (right column). The first row gives the reconstructed reference profile for 10^{10} incident protons. The second row shows the Non-Uniform Rational Basis Splines (NURBS) curve (blue) obtained after the normalization to a 10^8 incident protons statistics and the profile realization with the addition of Poisson statistical fluctuations (red).	164
4.11	Distributions of the falloff position deviation with respect to the falloff position of the high statistics reference profile for 1000 realizations with 10^8 primary protons, obtained with line-cone (a) and MLEM (b) reconstruction. The RMS of these distributions represents the Compton camera precision for the selected statistics.	165
4.12	Line-cone and LM-MLEM reconstruction for a 160 MeV proton beam, 10^8 total incident protons. The beam intensity is 200 proton per bunch. The Compton camera is centered at the expected Bragg peak position, $y = +50$ mm. The time-of-flight event selection is applied on the collected data set. 20 iterations are performed for the MLEM reconstruction. Figure (a) represents the MLEM reconstructed 2D image in the plane (x, y), parallel to the camera entrance surface. The position $x = 0$ mm corresponds to the center of the PMMA phantom and the y direction corresponds to the beam axis, with the target entrance at $y = -100$ mm and the target end at $y = +100$ mm. In figure (b) the 1D profile along the y axis is sketched. The profile fall-off is located at $y = +50$ mm. Figure (c) shows the profile obtained by means of the line-cone algorithm for the same time-of-flight selected data.	166
4.13	Line-cone and LM-MLEM reconstruction for a 160 MeV proton beam, 10^8 total incident protons. The beam intensity is 1 proton per bunch. The Compton camera is centered at the expected Bragg peak position, $y = +50$ mm. The time-of-flight event selection is applied on the collected data set. 20 iterations are performed for the MLEM reconstruction. Figure (a) represents the MLEM reconstructed 2D image in the plane (x, y), parallel to the camera entrance surface. The position $x = 0$ mm corresponds to the center of the PMMA phantom and the y direction corresponds to the beam axis, with the target entrance at $y = -100$ mm and the target end at $y = +100$ mm. In figure (b) the 1D profile along the y axis is sketched. The profile fall-off is located at $y = +50$ mm. Figure (c) shows the profile obtained by means of the line-cone algorithm for the same time-of-flight selected data.	167
4.14	Fall-off retrieval precision (FRP) for two different reconstruction algorithms: line-cone and LM-MLEM. The precision is shown as a function of the total number of incident protons, in the range 1×10^8 to 5×10^9	168
5.1	Sketch of the simulated geometry of the two systems: Anger camera (left) and Compton camera (right), in 3 dimensions (top line) and side projection (bottom line).	174

5.2	Radial event distribution normalized by the circular surface corresponding to each bin for 4 representative source energies, with the linear fit performed for background rejection. The total number of simulated primaries for each data set is 10^8	180
5.3	Comparison between expected entries in the central collimator hole (blue dashed curve) calculated according to pure geometrical factors and detector interaction cross section and simulated detected entries after background rejection (red solid curve) with null spatial resolution (ideal detector) to avoid resolution effects and lower energy threshold set to 80 keV.	181
5.4	Normalized radial distribution with background rejection (red solid lines) compared to normalized radial distribution for infinite density collimator (blue dashed lines).	182
5.5	Normalized radial distribution with no event selection (red solid lines) compared to normalized radial distribution for full collimator (green dashed lines). Both curves are normalized to the maximum of the raw radial distribution.	183
5.6	Compton camera-reconstructed radial distribution standard deviation as a function of the source energy. Two energy resolution values are set to the silicon detectors ($\sigma_E = 2$ keV - red dots solid line - and $\sigma_E = 4$ keV - blue dots dashed line), the Doppler broadening effect has been removed (green horizontal triangles dashed line) and the scatterer material has been changed with Cadmium Telluride (CdTe) solid state detectors (black vertical triangles dashed line), for a fixed energy resolution of $\sigma_E = 2$ keV.	185
5.7	(a): number of true (green) and random (red) coincidences as a function of the source activity in the range 1-500 MBq, for the reference energy of 555 keV. (b): Percentage of random coincidences as a function of the source energy, with a fixed source activity of 200 MBq. Compton camera parameters: time resolution FWHM of 20 ns for silicon detectors, 3 ns for BGO and a coincidence window of 40 ns. The source branching ratio has been set to 100% for all sources for simplicity in the comparison of results.	186
5.8	Results of the Compton camera event composition study: the absolute Compton camera efficiency (before reconstruction) is shown without any event selection (a) and with the selection of event with single interaction in the scatterer section.187	
5.9	Results of the Compton camera design study: reconstructed events efficiency (left) and standard deviation of the radial event distribution (right) as a function of the primary gamma energies for four reference energies and seven scatterer stack configurations, with reduced number of scatterer layers.	188
5.10	Overlap of the normalized radial distributions for 4 selected source energies.	189
5.11	Detection efficiency as a function of the source energy. Source activity = 200 MBq, Compton camera silicon detector $\sigma_E = 2$ keV. Note the factor 10 scale difference for the vertical axes.	189
5.12	Standard deviation of the radial event distributions as a function of the source energy. Source activity = 200 MBq, Compton camera silicon detector $\sigma_E = 2$ keV.190	
5.13	Signal-to-background ratio as a function of the source energy. Source activity = 200 MBq, Compton camera silicon detector $\sigma_E = 2$ keV.	190
6.1	Layout of the Nice MEDICYC facility. In Mandrillon et al. 1992	196
6.2	197
6.3	197
6.4	197
6.5	198

6.6	198
6.7	198
A.1	Data acquisition logic: pre-trigger and trigger generation and readout process.	206
A.2	Scatterer detector data format.	208
A.3	Absorber detector data format.	209
A.4	Beam hodoscope data format.	210
A.5	Architecture of communication between DAQ cards and μ -TCA.	211

List of Tables

1.1 Orders of magnitude of main time structure parameters for some accelerators used in clinics. Reproduce from Krimmer et al. 2017.	24
1.2 Estimated magnitude of range uncertainties separated for the various sources, and potential benefit provided by Monte Carlo simulations. The estimates are based on data in (Bednarz et al. 2010; Bischel et al. 1992; Chvetsov et al. 2010; Espa�a et al. 2010; ICRU 1980b; Kumazaki et al. 2007; Matsuji et al. 1998; Paganetti et al. 2000; J. B. Robertson et al. 1975; Sawakuchi et al. 2008; Schaffner et al. 1998; Uri et al. 1986; Wouters et al. 1996). Table reproduced from Durante et al. 2016.	36
1.3 Proton-nuclear reaction channels and relative positron emitters produced in human tissues. Table reproduced from Espa�a et al. 2011b.	40
1.4 Commonly-used radioisotopes for the clinical imaging and therapy routine. Table adapted from Ruth 2009.	58
3.1 Comparison of the block energy resolutions at the two reference energies of 511 keV and 1275 keV before and after the calibration process.	125
3.2 Calibration and characterization results for the whole set of tested Bismuth Germanium Oxide - Bi ₁₂ GeO ₂₀ (BGO) blocks.	129
4.1 Estimations of reachable resolutions with the detectors. Those resolutions are applied during the simulations.	150
4.2 Hadronic models used in the Geant4 simulations.	150
4.3 Description of the two beam structures studied: the Ion Beam Applications, Belgium (IBA) cyclotron C230 for protons and the synchrotron installed at the Heidelberg Ion Therapy Center, Germany (HIT) center in Germany for carbon ions. The macro-structure of the synchrotron, at the second time scale, is not considered here. The beam structures are applied to the simulation data.	152
5.1 Radioactive sources used in the comparison study. Decay mode list: EC for electron capture, β^- for electron emission, β^+ for positron emission, IT for isomeric transition. Half-life expressed in days (d), hours (h) or minutes (m). Data extracted using the National Nuclear Data Center On-Line Data Service from the Evaluated Nuclear Structure Data File database, file revised as of (2017-05-17) (Bhat 1992).	174
A.1 Front End number associated to each Front End card.	204
A.2 Packet with an even byte number cargo.	212
A.3 Packet with an odd byte number cargo.	212
A.4 Control symbol definition.	213
A.5 Control symbol definition.	214
A.6 Definition of the acknowledgement packet.	214
A.7 Writing register packet.	215
A.8 Reading register packet.	215
A.9 Two special registers(Micro Advanced Telecommunications Computing Architecture (μ -TCA) → Front End cards)	216
A.10 Measurement packet (Front End cards → μ -TCA)	216

List of Tables

A.11 Monitoring packet	216
A.12 Monitoring messages.	217
A.13 Special command packets	217
A.14 Special commands examples	218
A.15 Control symbol for pre-trigger, trigger and physical data.	218
A.16 Pre-trigger packet	219
A.17 Trigger packet	219
A.18 Physical data packet	219
A.19 Coincidence and single rate as a function of the beam intensity. The BGO single rate corresponds to the pre-trigger rate.	221
A.20 Data flux between Front-End (FE) cards and μ -TCA.	222
A.21 Data flow between μ -TCA and acquisition PC.	222
A.22 Acquisition format of the Compton camera data.	224

Prologue

1

Context

Contents

1.1 Ion beam therapy	5
1.1.1 Physics of ion beam therapy	6
1.1.2 Biological effects of ion beam therapy	16
1.1.3 Accelerators and beam delivery	20
1.1.4 Treatment planning	28
1.1.5 Ion beam therapy uncertainties and treatment monitoring	32
1.2 Nuclear medicine	53
1.2.1 Radiotracers	53
1.2.2 Positron Emission Tomography	59
1.2.3 Single Photon Emission Computed Tomography	64
1.2.4 Theranostics	66

1 Context

The application of physics concepts and techniques to the field of health-care is nowadays well-established in the clinical routine. Even if physical techniques have been used in medicine from the earliest time (Duck 2014), the discipline today known as “medical physics” emerged and grown in the past century thanks to the increasing knowledge and use of ionizing radiations both for diagnosis and disease treatment. In the late 19th century, the x-ray discovery by Röntgen, the radioactivity discovery by Henri Becquerel, and the radium and radioactive isotopes studies by Pierre and Marie Curie paved the way to the whole medical physics practice of the next century, where x-ray imaging and radiotherapy were soon established. Only three weeks after the discovery of the x-rays, Robert Jones and Oliver Lodge imaged with x-rays a boy’s hand (Cantor 1988), officially starting the diagnostic application of such a radiation. Following the first successes, more attention was given to radio-protection and dosimetry studies, and the investigations focused on new ways to use radioactive tracers for imaging purpose; this finally led to the birth of nuclear medicine, with the clinical use of the radioisotope Indium-131 (¹³¹In) in 1939 (Kereiakes 1987). Nuclear medicine rapidly gained importance in the diagnosis clinical panorama, also thanks to the introduction of new detectors, such as the Anger camera introduced in the ’60s, and new imaging techniques, such as the detection of photons from positron annihilation (Positron Emission Tomography (PET)). Moreover, several alternative methods were proposed or implemented for diagnosis (Magnetic Resonance Imaging (MRI), ultrasounds, etc.). In parallel, x-rays were soon employed also for tumor treatment: already in 1896, Emil Grubbe irradiated a woman with breast cancer (Evans 1951), and in the same year in Lyon a patient with a stomach cancer has been treated by Victor Despeignes (Despeignes 1896; Foray 2016). One year later, a skin tumor was successfully irradiated in Vienna using x-rays. Thanks to the invention of the klystron, and, later, of the so-called “magnetron”, by the Varian brothers with William Webster Hansen, the radiotherapy could spread and become a clinical reality; more refined treatment techniques were then introduced with the development of commercial particle accelerators after World War 2 (Keevil 2012).

At present days, the medical physics progress strongly relies on technological development and computer science, which already revolutionized several fields of science. In particular, cancer research is now a key area for technical and technological development, concerning both diagnosis and treatment (Webb 2009). Cancer continues to be one of the major issues in the medical scenario: it is at present the second cause of death worldwide, but it is expected to surpass heart diseases and become the main killer in the next tens of years (Jemal et al. 2010; Thun et al. 2010). The last two decades saw important improvements in radiotherapy techniques and machines, with more precise dose planning and delivery, which enhanced the patient survival and strongly reduced the impact of radiations on healthy tissues. This was possible also thanks to refined imaging technologies, allowing for an accurate tumor volume definition, as well as for image-guided treatments. In this scenario, ion beam therapy, already proposed in the middle of the past century, is rapidly spreading thanks to novel beam delivery technologies, able to relatively reduce the treatment costs and allowing for a commercial diffusion of this treatment method (which is still very limited with respect to standard radiotherapy). Notwithstanding the remarkable steps forward disclosed in the last years, there is still wide room for improvements in this field, which mainly requires strong imaging basis in order to fully profit of the treatment technique potential.

The work presented in this document has been carried out in this context and mainly deals with the development of gamma imaging detectors to be applied in the field of quality assurance for ion beam treatment. Furthermore, the same detectors have been applied to the nuclear

medicine field in simulation, with the aim of assessing its possible clinical implementation for a future development of the nuclear medicine clinical routine.

In the following sections, a general overview of the two main domains concerned in this thesis work is given.

1.1 Ion beam therapy

Radiation treatment is an essential component of the tumor therapy, being the second most applied and successful kind of therapy after surgery (Schardt et al. 2010). The majority of patients with localized malignant tumors are treated with radiations (Baskar et al. 2012; Durante et al. 2009; Moding et al. 2013), applied in several fractions in different days in order to reduce the damages to normal tissues (Bentzen 2006). The most of the patients treated with radiotherapy techniques receives standard photon treatments, with x-rays coming from linear electron accelerators; a small percentage undergoes specialized gamma treatments like gamma knife irradiations, again using x-ray beams from linear electron accelerators, or brachytherapy. About 1 % of the radiotherapy patients are irradiated with charged particle beams, with the so-called ion beam therapy (Durante et al. 2016).

Ion beam therapy, or “hadrontherapy”, is a cancer radiation treatment method based on light ion beams instead of photons. It was first proposed by Wilson in 1946 in a famous seminal paper (R. R. Wilson 1946); the author was asked by its director Ernest Lawrence to clarify the stopping process of protons in matter. Thanks to measurements at the Berkeley cyclotron, he highlighted the physical principles and the possible benefits driven by the implementation of such a kind of radiation in clinical treatments, with particular focus on the simple case of protons and some considerations about heavier ions, like alpha particles and carbon ions. At that time, the accelerator technologies were still under development after the invention of the cyclotron by Ernest O. Lawrence in 1930, which allowed to increase the range of charged particles in matter, in particular in cells and human tissues, and the treatment-required beam energy was about to be reached. Pioneering studies of the biomedical applications of accelerated hadron beams were performed by Cornelius Tobias in 1948 (Blakely et al. 2009) in Berkeley (USA), and the first patients have been treated almost ten years later in the same laboratory by Lawrence and Tobias (Tobias et al. 1958, 1955) with protons and, later on, with He ions (Halperin 2006). New accelerators in four continents were used to continue the quest started in Berkeley, and the experience was extended to carbon ion beams from 1994 in Japan (Heavy Ion Medical Accelerator in Chiba, Japan (HIMAC)), and Germany (Heidelberg - Heidelberg Ion Therapy Center, Germany (HIT)).

Nowadays clinical adapted machines are well-established on the market, making ion beam therapy emerging as a wide-spread technique in the every-day cancer treatment routine all over the world. Starting from the early 2000's, many new treatment centers have been designed and built, mainly in Europe and Japan. An intense research effort has been dedicated to this field in the last decades; in addition to considerable improvements achieved in the accelerator technologies, new and refined imaging techniques allowed for important enhancement in the treatment planning, also supported by the continuous development of computer science and the growth of calculation power. In parallel, the biological implications of ion irradiation has been deeply investigated (Brahme 2004; Friedrich et al. 2012; Tobias et al. 1982).

Moreover, since more and more patients are treated every year with this technique, more clinical data are at present available for further study and the connection between physicists and physicians is strongly progressing both in the research field and in treatment practice. Several advancements are expected in the next years, following the extensive research work carried out by several groups in the world. In the following paragraph, the basic physical principles and features of this treatment method are explained, and advantages and drawbacks with respect to standard radiotherapy techniques are analyzed. After that, the need for ion range verification is discussed and detailed in order to reach the main topic for this thesis: the prompt-gamma detection.

1.1.1 Physics of ion beam therapy

The physics rationale of ion beam therapy is extensively described in all its peculiar aspects in several review, such as Belkić 2010; Bichsel 2013; Durante et al. 2016; Lomax 2009; Newhauser et al. 2015; NuPECC 2014; Schardt et al. 2010. In the following, the physical basis of this tumor treatment technique is highlighted.

Charged nuclear particle beams at relatively high energy show a characteristic depth-dose distribution in matter which makes them suitable for the application in cancer treatment as a valid alternative to standard photon therapy (x-ray or megavolt beams), bringing several advantages to the patient side. The peculiar energy deposition profile (“Bragg curve”) is named for Sir William Henri Bragg, who investigated the slowing-down process of α particles in air (Bragg et al. 1904, 1905). Low-energy (x-rays) and high-energy photons traversing the patient body deposit their energy by interacting with the target atomic electrons (mainly by Compton interaction), with the deposited dose decreasing at increasing depth after a build-up region (mainly due to forward scattered Compton electrons). Even if the entrance surface (the skin for a patient) can be spared thanks to this build-up region, with a dose peak shift of a few centimeters, a high relative dose is delivered to the tissues along the whole beam path. In order to maximize the tumor volume-to-healthy tissue dose ratio, a standard photon treatment always foresees several irradiation fields from different entrance points and angles (see Figure 1.1, left). This energy deposit behavior is common to all neutral particles, as shown in the first two boxes in Figure 1.2 where the depth-dose profiles of photons at various energies and neutrons in water are presented. In contrast to neutral particles, the energy deposited per track unit increases for increasing depth for the charged ones: in the remaining four boxes of Figure 1.2 the depth-dose profile in water is shown for electrons, pions, protons and neon ions; it is characterized by an entrance low relative dose *plateau* and by a narrow high deposited dose peak at the end of the range (in the last few millimeters), called “Bragg peak”. The high-dose peak is sharper the more massive is the particle, as clear from Figure 1.2, where the different species are sorted by increasing mass. As for protons and heavier ions, their clinical interest for the treatment of deep-seated tumors appears clearly from the above considerations: a nuclear particle beam is able to deliver a reduced dose to the healthy tissues surrounding the target volume, where the dose is concentrated. This allows for the treatment of tumor volumes close to Organs At Risk (OAR), also with limited irradiation angles with respect to photons, as shown in the right part of Figure 1.1, where the planning for a carbon ion treatment of a lung cancer with only three irradiation fields is depicted.

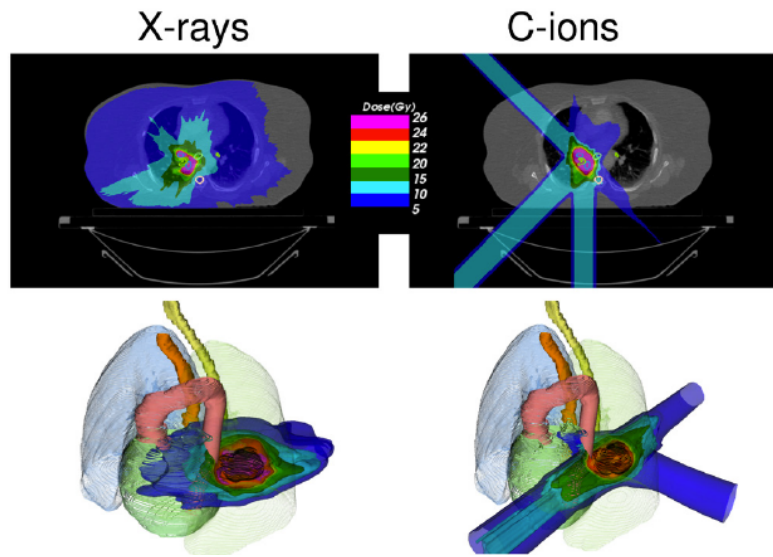


Figure 1.1: Treatment planning of lung cancer for the irradiation with x-rays (left) or carbon ions (right) (in Durante et al. 2016).

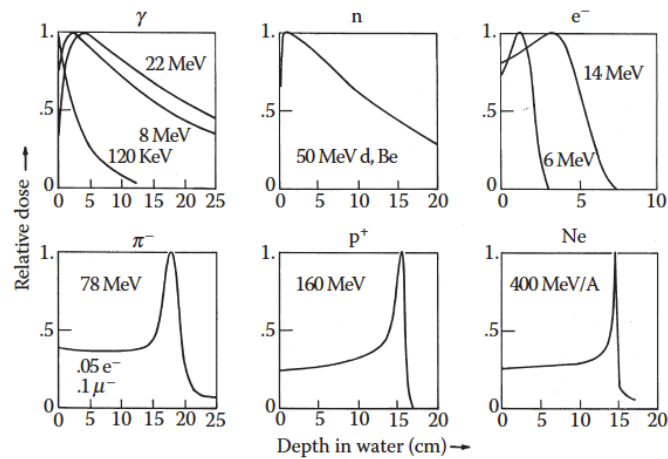


Figure 1.2: Relative dose as a function of the particle depth in water for different particle species. For photons, the reported energy in MeV corresponds to MV linac-accelerated electron induced bremmstrahlung. In Paganetti 2012a.

1.1.1.1 Charged particle interactions in matter

The nuclear charged particle interactions in matter can be described by three main mechanisms: Electromagnetic (EM) inelastic interaction with the atomic electrons, EM elastic interactions with the atomic nuclei, and nuclear reactions. In addition to the listed interactions, also Bremsstrahlung is theoretically possible, but its effect is negligible at ion energies of clinical interest. The EM inelastic interactions with atomic electrons cause an energy loss which is generally approximated with a Continuous Slowing Down Approach (CSDA) for simplicity, assuming a mono-dimensional quasi-linear ion path and an average, continuous energy loss rate. The mass difference between electrons and ions (as an example, the proton mass is 1832 times greater than that of an electron), justifies the quasi-linear approximation, while the significant cross-section for small energy transfer allows one to consider a continuous decelerating force. The elastic repulsion caused by an atomic nucleus is able to deflect the projectile ion, with an angle which depends on the target-projectile relative mass. The inelastic nuclear reactions are less frequent, but reduce the intensity of the primary beam (the primary particle is destroyed or deflected at large angle), and cause the emission of secondary nuclear fragments. A schematic view of the three main interaction mechanisms described is given in Figure 1.3 for the example case of protons, while in the following the effects of these interactions are detailed.

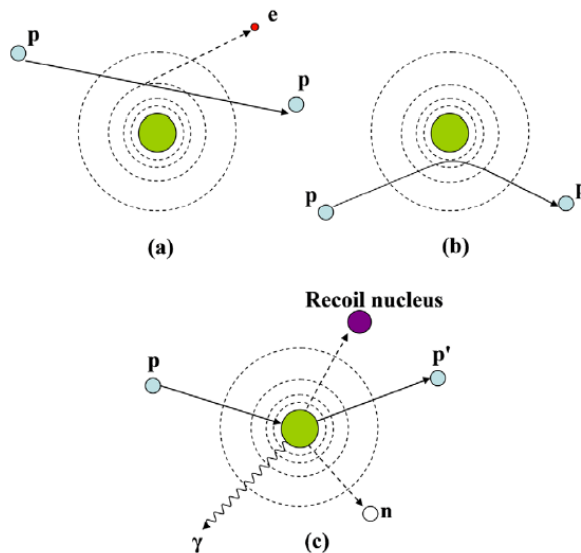


Figure 1.3: Schematic view of an example of the three main interactions mechanics of protons in matter: Coulomb interaction with atomic electrons (a), Coulomb interactions with atomic nucleus (b), nuclear reactions(c). In Newhauser et al. 2015.

EM interactions with target atomic electrons At the primary particle velocities of clinical interest, the ion energy loss rate is dominated by inelastic collisions with the target atomic electrons and is well described by the formula attributed to Bethe (Bethe 1930) and Bloch (Bloch 1933), often referred as Bethe-Bloch formula, reported in equation 1.1 in its form independent of the mass density. This expression is also known as mass stopping power.

$$\frac{S}{\rho} = -\frac{dE}{\rho dx} = 4\pi N_A r_e^2 m_e c^2 \frac{z^2}{\beta^2 A} \left[\ln \frac{2m_e c^2 \beta^2 \gamma^2}{I} - \beta^2 - \frac{\delta}{2} - \frac{C}{Z} \right] \quad (1.1)$$

where N_A is the Avogadro's number ($6.022 \times 10^{23} \text{ mol}^{-1}$), r_e is the classical electron radius expressed in equation 1.2 with $\epsilon_0 = 8.854 \times 10^{-12} \text{ F/m}$ the permittivity of the vacuum, $m_e c^2 = 511 \text{ keV}$ the mass energy of the electron, $e = 1.6 \times 10^{-19} \text{ C}$ the electron charge and c the speed of light,

$$r_e = \frac{1}{4\pi\epsilon_0} \frac{e^2}{m_e c^2} = 2.181 \times 10^{-15} \text{ m} \quad (1.2)$$

z is the charge of the projectile, Z and A are the atomic number and mass of the target material, respectively, $\beta = v/c$ is the projectile velocity, $\gamma = (1 - \beta^2)^{-1/2}$, I is the mean excitation potential of the target material. The last two terms represent corrections for high energies (δ density effect correction term) and low energies (C shell correction term) incident ions. By observing equation 1.1, it clearly emerges how the energy loss rate is proportional to the square of charge and inverse velocity of the projectile. The target material composition also plays a major role. As the logarithmic term varies slowly with the target properties, and since Z/A is also almost constant, it turns that the linear energy loss rate is proportional to the electron density, and thus to the atomic density (to be noticed, for clinical applications, that the density in a patient can vary by almost three orders of magnitude, ranging from the air cavity in the lungs to the most dense bones). As already mentioned, the energy loss increases for decreasing ion energy due to the $1/\beta^2$ dependence at high velocities (when the projectile velocity is much larger than its orbital electron velocities, and therefore remains fully stripped), and the maximum energy-loss rate, corresponding to the Bragg peak depth, is reached at the projectile velocity expresses as

$$v_p = z^{2/3} v_0 \quad (1.3)$$

where $v_0 = e^2/\hbar$ is the Bohr velocity ($\beta = 1/137$). For velocity values below v_p , corresponding to the average orbital velocity in the Thomas-Fermi atomic model, the ion captures electrons and its charge decreases, as well as the stopping force. However, the residual range is small (a few tens micrometers), and therefore the Bragg peak is assimilated to the end of the ion path. Note that, at very small velocities, atomic elastic collisions become important in the slowing down process.

The energy loss rate equation directly leads to the definition of the ion beam range in matter (if we neglect nuclear interactions which cause a modification of the projectile nature), which is the integral over the incident energy of the energy loss per track unit, reported in equation 1.4. This formulation assumes a 1D ion trajectory with negligible lateral scattering (mentioned above and discussed below) and uses the CSDA.

$$R(E) = \int_0^E \left(\frac{dE'}{dx} \right)^{-1} dE' \quad (1.4)$$

where E is the ion beam incident energy. To be noticed that the range is not a deterministic value, but it is intended as an average value and defined for the whole beam, not for single incident particles, which are affected by statistical fluctuations in the energy loss, leading to the so-called “range straggling” (described by different theoretical models, such as the ones in Bohr 1915; Landau 1944; Vavilov 1957, and detailed below). The integration of the Bethe-Bloch is often a hard task, but, as realized by Bragg and Kleeman (Bragg et al. 1905), the range dependence on the incident particle energy can be practically expressed with an analytic approach as the power law in equation 1.5. This approximation directly derives from studies on alpha particles which anticipated the formulation of equation 1.1.

$$R(E) = \alpha E^p \quad (1.5)$$

where E is again the ion beam initial energy, the constant α depends on the target material and the constant p is related to the projectile energy (or velocity). The proton range can be easily scaled to other ions at the same energy per nucleon in the same material with a factor M/z^2 , where M is the ion mass. The range of ions with the same specific energy scales from water to other homogeneous material with a factor A/Z^2 .

Range straggling The ion range predicted by equations 1.4 or 1.5 is an average value, calculated by considering a smooth and continuous energy loss process and neglecting the individual ion behavior. The actual range suffers from statistical fluctuations in the projectile energy loss that broaden the Bragg peak, in the so-called “range straggling”. In general, the longitudinal beam straggling can be described by an asymmetric distribution (Vavilov 1957), which is approximated to a Gaussian in the limit of many collisions, leading to the expression of the relative straggling in equation 1.6:

$$\frac{\sigma_R}{R} = (M^{-\frac{1}{2}})\phi \frac{E}{Mc^2} \quad (1.6)$$

The ratio of the straggling width σ_R and mean range R is then all the more reduced as the ion mass (M) increases, with ϕ a slowly varying function which depends on the target material (Rossi 1952) and E the ion energy. According to equation 1.6, it is interesting to notice how the relative straggling for carbon ions is about 3.5 times smaller with respect to protons (e.g. 7 mm and 25 mm at 18 cm of average range for carbon ions and protons, respectively - see Durante et al. 2016). In addition to energy loss fluctuations, range straggling contributions also come from the beam initial energy distribution: the actual beam is not perfectly mono-energetic, and the energy distribution width is determined by the accelerator and the beam optics elements. This contribution has to be added (quadratic sum) to the range straggling estimate. Figures 1.6c and 1.6d show the depth-dose profiles of proton and carbon ion mono-energetic beams, respectively, at different energies in water. The effect of range straggling is clearly visible in the broadening of the Bragg peak, which is more significant for protons with respect to carbon ions, and increases for increasing range in matter.

EM interactions with target nuclei In addition to the energy loss process considered till here, which shapes the beam in the longitudinal direction (range variations), the actual delivered dose also depends on the lateral beam profile, which derives from the size and angular divergence of the incident beam and is mainly governed, at the target level, by elastic Coulomb scattering with atomic nuclei and

by secondary particles produced by nuclear fragmentation. In case an ion passes close to a target atomic nucleus, it is elastically scattered by the repulsive electromagnetic force: the projectile loses a negligible amount of energy, so that this kind of interaction can be neglected when calculating the energy loss rate described above, but the change in its trajectory must be estimated for range and dose predictions. Starting from the single scattering model by Rutherford (Rutherford 1911), and moving to the calculation of the statistical distribution function for the scattering angle at a certain penetration depth given by Bothe 1921, a complete theory allowing for the calculation of the scattering angle probability in case of Multiple Coulomb Scattering (MCS) has been proposed by Molière (Molière 1948) (confirmed to provide good predictions thanks to a large set of proton beam spread data - see Gottschalk et al. 1993). More practical formulas were then derived afterwards (see Gottschalk 2010; Highland 1975; Lewis 1950). The Molière formulation has been then simplified for analytic calculations towards a Gaussian approximation. The Gaussian standard deviation (σ_θ) expression in equation 1.7 is given by the characteristics MCS angle θ (Highland 1975)

$$\sigma_\theta = \frac{14.1 \text{ MeV}}{\beta pc} Z_p \sqrt{\frac{L}{L_{\text{rad}}}} \left[1 + 0.038 \ln\left(\frac{L}{L_{\text{rad}}}\right) \right] \quad (1.7)$$

where β , p and Z_p are respectively the projectile velocity, momentum and charge, c is the speed of light, L is the material thickness and L_{rad} is the radiation length (reported for common materials in Tsai 1974) expressed in equation 1.8.

$$L_{\text{rad}} = \frac{716.4}{Z(Z+1)\ln\left(\frac{287}{\sqrt{Z}}\right)} \text{ g/cm}^3 \quad (1.8)$$

with Z the atomic number of the material. Even if the Gaussian approach is not always accurate to describe the lateral beam spread (mainly at large angles), the Molière MCS description allows to retrieve the main parameters contributing to this effect: in particular, heavier particles have narrower lateral beam spread, and the scattering effect increases at increasing ion range (but is inversely proportional to the beam energy) and for high-Z materials. A more precise model of the lateral beam spread should involve nuclear reactions and the produced secondary particles, but an analytic approach is difficult and Monte Carlo based calculations are necessary, but still time consuming. The empirical parameterizations are still strongly based on experimental data: as an example, measurements of the lateral beam spread in a water column for different beam energies (ranges) are reported in Pedroni et al. 2005. In Figure 1.4 the lateral spread of different ions in water is plotted as a function of range for various beam energies (A) and as a function of beam energy (B) after 15 cm range in water.

In addition to the electromagnetic interactions with electrons and nuclei which mainly govern the stopping process, primary ions impinging on a target also undergo nuclear reactions with the target nuclei which may cause the disintegration of the projectile and the target nucleus or a partial fragmentation. In general, nuclear reactions induce modifications in the beam composition and cause variations in the longitudinal and lateral beam structure which must be taken into account for the delivered physical and biological dose estimate. Moreover, this kind of reactions leads to the production of secondary particles, such as secondary protons, neutrons, hydrogen and helium isotopes and other ions (mainly with heavy ion irradiation), and gammas. In the high velocity regime (when the relative velocity in the nuclei center of mass is much larger than the nucleon Fermi velocity), the nuclear interactions occurring between

Nuclear reactions

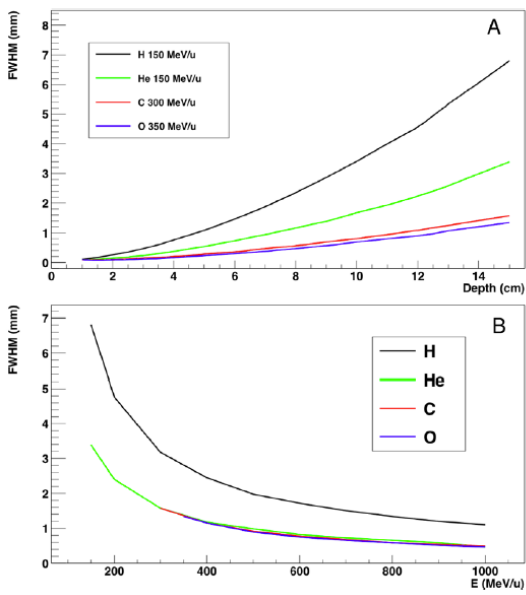


Figure 1.4: Lateral spread of different ions in water obtained with Geant4 Monte Carlo simulations. The Full Width at Half Maximum (FWHM) of the beam spot distribution is presented as a function of depth in water (A) for beams at different energies and as a function of beam energy (B) after 15 cm range in water. In Durante et al. 2016.

projectile ions and target nuclei can be described by a two-step process. At the “collision” stage, depending on the distance between projectile and target centers (impact parameter b), a variable number of nucleons is involved in the interaction and composes the reaction zone generally defined as “fireball”. The so-called “spectator” nucleons are almost not affected and create projectile-like and target-like fragments (“fragmentation” process), often in excited states. After the collision, the excited fireball and fragments decay through the emission of secondary light particles, in the so-called “de-excitation” process, and the lighter fragments continue their path through the target. A schematic view of a typical nuclear reaction is given in Figure 1.5. Several models have been proposed to describe the nuclear interactions in its two steps. The Intra-nuclear Cascade (INC) model has been originally proposed by Serber and Heisenberg (Serber 1947), and later implemented in the sixties (Bertini et al. 1974), and is used to describe the collision stage. It is based on a series of two-body interactions between the incident particle and the target nucleons, which are considered quasi-free. For each nuclear interaction, the code models the complete outcome, and all produced particles are tracked until they are below a given energy threshold, in a process called “intra-nuclear cascade”. Other candidates are the Quantum Molecular Dynamics (QMD), which describes each nucleon as a gaussian wave packet, and all nucleons are included in the collision, and the Boltzmann-Master-Equation (BME), which is a sophisticated model describing the thermalization of composite nuclei for low energy projectiles. The de-excitation stage can involve the so-called “evaporation” (Weisskopf 1937), where light fragments are emitted from the excited nuclei, “fission” of the excited nuclei in two fragments (for high-Z nuclei which can be only found in implants), “Fermi-breakup” of light nuclei which disassembles in smaller fragments (Fermi 1950) and gamma emission to dissipate the residual energy. The majority of the complete models for nucleus-nucleus reactions includes the previously described ones (often in simplified versions) optimized in order to minimize the calculation time) and is a variant of the so-called “abrasion-ablation” model (Hüfner et al. 1975), generally used in therapy

are you sure?
what do you mean
by therapy?

DONE

transport codes. The abrasion phase describes the collision and the ablation one models the de-excitation stage; to be noticed that the ablation description is generally more adapted to peripheral collisions (high b), where the fragments are excited after the collision and decay to the ground state by emitting light particles and gamma rays.

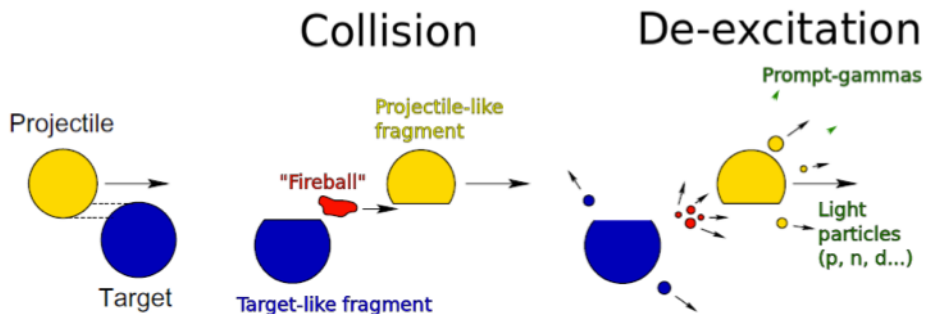


Figure 1.5: Schematic view of the nuclear reaction between a projectile and a target nucleus. The two steps are defined as “collision” and “de-excitation” processes.

Two main effects of fragmentation processes are relevant to ion beam therapy. First, the described nuclear reactions cause a loss of primary beam particles; this effect is all the more important for increasing penetration depth. It is clear that peripheral collisions (high b) lead to smaller loss of primaries with respect to central collisions (small b), where projectile and target are most likely completely destroyed. Figures 1.6a and 1.6b (top panel) show the primary particle fluence loss in a proton and carbon ion beam, respectively, as a function of the depth in water. In the entrance region before the falloff the fluence loss is caused by nuclear reactions, while close to the Bragg peak the fluence falloff is mainly due to stopping of primary particles with zero residual energy. In addition, the range straggling effect is visible. Concerning carbon ion beams, as reported in Durante et al. 2016, during a standard treatment only 50% of the primary ions reach the Bragg peak region for ~ 20 cm range, while the others undergo fragmentation processes and are lost. Second, lower-mass and Z fragments result from the nuclear interactions in case of irradiation with ions heavier than protons (with proton beams, only secondary protons and neutrons are produced). The projectile velocity determines the velocity of the secondary fragments, which can travel with longer ranges with respect to the primaries due to their reduced mass and charge (remember the range scaling factor M/z^2): this produces a tail in the dose distribution (for ions heavier than protons). The features of this tail have been deeply studied for different primary ions species (^{10}B , ^{12}C , ^{14}N , ^{16}O , ^{20}Ne), and shell-structure effects have been verified with a non-direct relationship between proton number Z and tails extension (Schall et al. 1996). Figure 1.6d (and Figure 1.6b, bottom panel) shows the effects of nuclear reactions on the Bragg curves related to carbon ion beams at different energies stopping in water, measured in a water column (Schardt et al. 2008). With increasing primary energy and, consequently, beam penetration depth, the ratio between Bragg peak and entrance plateau dose is reduced by the decreased number of primary ions (this effect is also visible for proton beams in Figure 1.6c), while the tail after the Bragg peak is wider due to the increased number of lower-Z fragments traveling with longer range. In addition to this, the energy loss stochastic fluctuations are clearly visible in the broadening of the Bragg peak, as already described.

I would avoid this sentence. If there is a nuclear reaction with a change of nuclei nature, the incident particle is lost
DONE

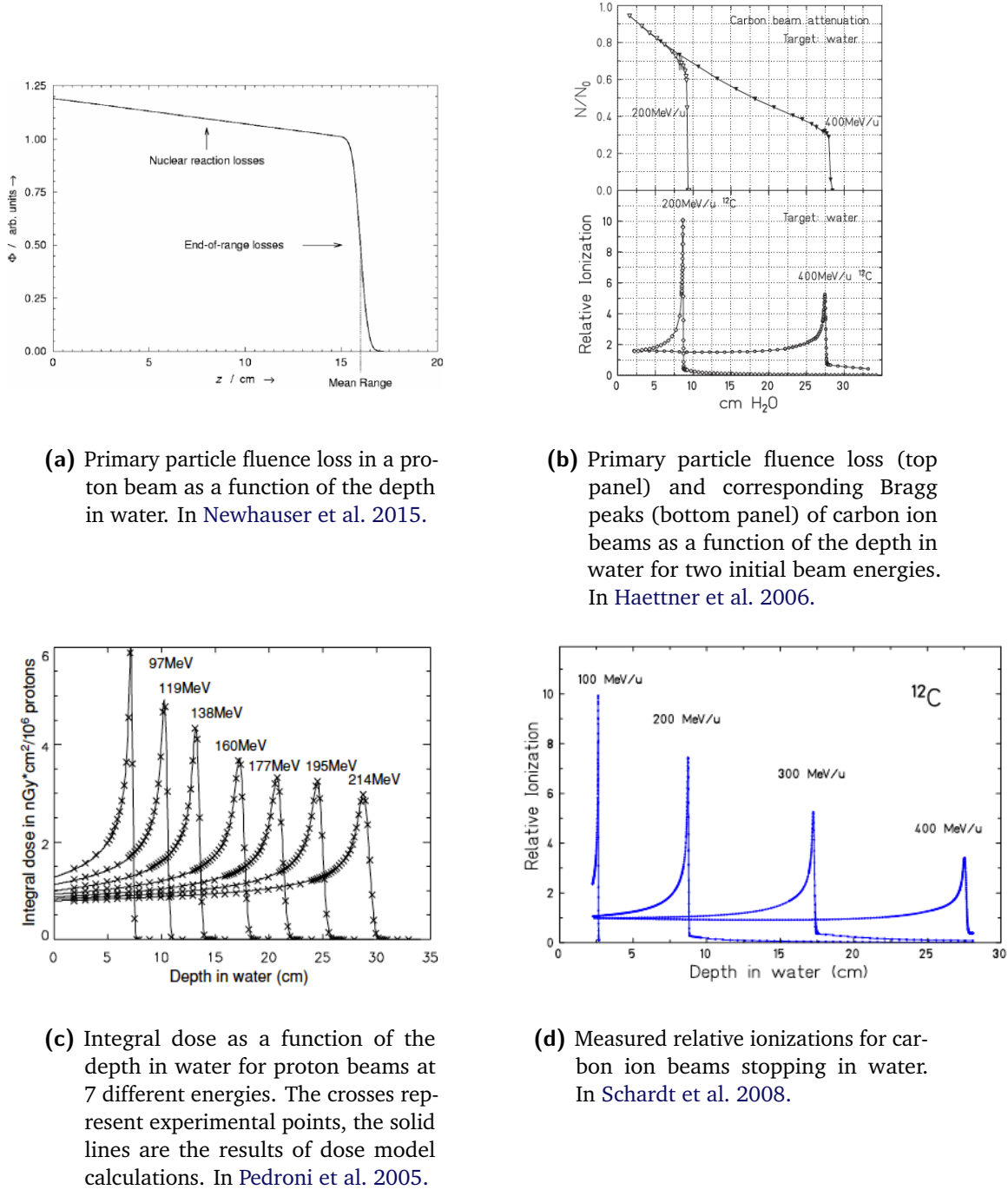


Figure 1.6: Effects of nuclear interactions (first row) on proton (left column) and carbon ion (right column) beams and resulting dose distributions (bottom row).

Well, proton is the best. Carbon ions is a kind of compromise between fragmentation and RBE
(not fully true)
DONE

1.1 Ion beam therapy

Fragmentation processes have been deeply studied in nuclear physics and experimental data are available for many ion species at various energy (Friedländer et al. 1982). Dedicated studies for applications in radiotherapy started at Princeton (MacCabee et al. 1974) with oxygen beams and were carried out for many years at the Bevalac in Berkeley (Llacer et al. 1990, 1984b; Schimmerling et al. 1989, 1983), mainly with the neon beams used, at that time, for patient treatments. Analog studies were conducted later at the HIMAC facility (Matsufuji et al. 2003, 2005) and at GSI Helmholtz Centre for Heavy Ion Research, Germany (GSI) (Golovkov et al. 1997; Schall et al. 1996): several ion species have been compared and carbon has been identified as the one offering the best fragmentation conditions. In addition, the positron-emitting fragments (^{10}C and ^{11}C) can be used for online range monitoring with PET techniques (see section 1.1.5.2). Results concerning the build-up characteristics of secondary fragments, also based on carbon ion irradiation of water targets, are published in Haettner et al. 2006 and Haettner et al. 2013; in these works, 200 and 400 MeV/u ions have been used to investigate energy spectra and yields of the produced fragments at different angles and various depths along the beam path. A similar analysis has been carried out with 95 MeV/u carbon ion beam irradiation data collected at Grand Accelerateur National d'Ions Lourds, Caen, France (GANIL): in this case, Poly Methyl Metacrylate (PMMA) thick targets (5, 10, 15, 20 and 25 mm) have been used (Braunn 2010; Braunn et al. 2011). The obtained results have been compared to simulated data produced with fragmentation models implemented in Geant4 and mentioned in previous paragraphs, such as the Binary Intra-nuclear Cascade (BIC) (based on the INC) and the QMD models, showing that model improvements were still needed to reproduce the experimental data. Indeed, detailed information about fragmentation can be retrieved via Monte Carlo simulations and used to evaluate the impact on the delivered dose. As an example, in Wroe et al. 2005 the authors studied in simulation the impact of nuclear reactions in the dose delivered with proton beams in different targets, like water, tissue equivalent plastic, and International Commission on Radiological Protection (ICRP) muscle, bone and adipose. Simulations published in (Grassberger et al. 2011) of 160 MeV protons in water allowed to estimate the dose contributions given by primary particles (between 90% and more than 99% of the total depending on the range), with the remaining fraction of dose mainly connected to secondary protons and α particles: negligible dose is given by heavier fragments. A more intense dose contribution from heavier fragments is expected for carbon ion irradiation, but an accurate Monte Carlo simulation of these processes is still a challenge.

The dose deposition in the distribution tail beyond you mean that the tail regions represents 36% of the total simulation: in Francis et al. 2014, for example, the deposite energy?
been estimated in 36% of the total in the tail region
DONE

As mentioned, in addition to charged fragments, nuclear interactions also produce gammas, mainly originating from atomic de-excitation processes (prompt-gammas) or from the annihilation of positrons emitted by beta-emitter fragments (^{10}C , ^{11}C , ^{13}N , ^{14}O , ^{15}O), and neutrons there are also PG, which can induce the emission of further gammas. All the secondary particles which are absorbed by the target contribute to the total dispensed dose, while the others (with the exception of neutrons), escaping the target volume, can be exploited for non-invasive measurements of beam and target features. In particular, different techniques have been proposed and tested to measure secondary protons and gamma rays (both prompt-gammas and positron-annihilation gammas) with the aim of retrieving information about the ion range and obtain an online treatment verification. A detailed discussion about this topic will be given in section 1.1.5.

Focusing on neutrons, which are produced in large quantities and over a wide energy range,

1 Context

due to elastic scattering in the target?

they cannot be expDONEring since they are not correlated with the ion path in matter (M. Testa et al. 2010). The neutron signal can be used to retrieve dosimetric information in vivo, as reported in Carnicer et al. 2014: the research group at the Centre Antoine Lacassagne, Nice, France (CAL) studied the secondary radiation in the proton ocular treatment room as a function of the beam modulation, with a large volume ionization chamber. A strong correlation was found between the secondary ambient dose equivalent per proton dose and proton dose rate, which enables in vivo dosimetric verification independently from the beam monitoring system. In any case, neutrons must be modeled with care in order to evaluate the safety measures to be implemented in treatment centers (Newhauser et al. 2002), as well as the implications in the delivered dose and secondary cancer probability (Newhauser et al. 2011). The dose contribution caused by secondary neutrons strongly depends on the beam delivery system (see section 1.1.3 for the description of the beam delivery systems), as demonstrated in Gottschalk 2006. In particular, passive elements used for beam shaping have been identified as one of the main sources of secondary neutrons contributing to the total delivered dose to the patient (Yan et al. 2002), so that in modern facilities deflecting elements are set after the passive modules in order to limit the neutron flux towards the target. It is interesting to notice that the amount of produced neutrons and resulting dose is comparable for protons and carbon ion irradiation, even if the neutron yield is higher for carbon ions: this is due to the different beam intensities used in clinics for the two species, with more than a factor 20 in favour of protons. Finally, if compared to photon standard radiotherapy at high acceleration voltage (about 25 MV), the neutron dose associated to ion beam therapy treatments results to be smaller, as demonstrated in recent studies (U. Schneider et al. 2015).

Mention the order of magnitude of the energy deposited by neutrons with carbon ion beams (Gunzert-Marx)? I think it is <3% of the total biological dose.

In the following see
ment modality.

DONE

1.1.2 Biological effects of ion beam therapy

In addition to the already presented physical differences between photon radiation therapy and ion beam therapy treatments, a fundamental aspect to be addressed is the biological effect of such radiations. In the following, the main biological implications of radiation therapy are summarized with the aim of highlighting the favorable contribution given by charged particles with respect to photons and, at the same time, discuss some controversial points (Paganetti et al. 2013).

Not only. There are more and more evidence that other targets are involved in cell response, e.g. mitochondria and membrane

DONE

which lead to cellular and molecular effects. The effectiveness of ionizing radiation in curing cancer is based on the consequences produced by these ionizations, which can affect the double-helical DNA macro-molecules inducing various kinds of damages. In most of the cases, localized damages, also called strand breaks, can be repaired with cellular reparation processes. In case DNA breaks are in close proximity they can originate the so-called Double-Strand Breaks (DSBs), both with direct ionizations or indirect process (such as δ -electron energy deposition). Figure 1.7a shows a schematic view of the different kinds of DNA damages induced by radiations, together with their effects in case of successful or unsuccessful reparation mechanisms. DSBs are generally harder to be repaired and lead to cellular dysfunction and loss of genetic material, resulting in cell death or in the loss of reproductive capacity. It appears clear from this simplified presentation that not only the total absorbed

and reactive chemical species

DONE

dose, but also the ionization event distribution plays a major role in the determination of the radiation effectiveness (Belli et al. 1992). The absorbed dose is defined in ICRU 1980a, 1998 as

$$D = \frac{d\bar{\epsilon}}{dm} \quad (1.9)$$

where $d\bar{\epsilon}$ is the mean energy imparted by ionizing radiation to matter of mass dm . To be precise, the imparted energy must also be defined: in the same ICRU reports we find that

$$\epsilon = R_{in} - R_{out} + \sum Q \quad (1.10)$$

well, they are around Compton or photo-electric interactions...

with R_{in} and DONE ring or leaving the volume, respectively, $\sum Q$ the sum of all changes of the rest mass energy of nuclei and elementary particles in any nuclear transformations occurred in the volume due to the ionizing radiation. As mentioned, for the same absorbed dose, the ability of killing tumor cells is linked to the nature of the delivered radiations via the ionization event distribution. It is useful here to introduce the concept of Linear Energy Transfer (LET) = defined as the amount of energy deposited by a particle per track unit, directly related to the number of ionization per unit distance. In general, photons, x-rays and γ -rays are referred to as low-LET radiation, while the larger stopping power of protons and ions make them a high-LET kind of radiation. For low-LET radiation, the distribution of the caused lesions is approximately random, while it is more closely related to the particle track for high-LET primaries (Lobrich et al. 1996) causing a clustering effect in radiation damage which has been verified to be effective for cell killing (Holley et al. 1996; Rydberg 1996). This is due to the nature of interactions of photons and ions in matter, already detailed in the previous section. Photons transfer energy to the cells by photo-electric or Compton interactions, with rather low cross-sections which determine a small number of ionization events and freed electrons per incident photon within the cell volume. Such freed electrons can further create secondary electrons along their path, but many photons are required to deposit the prescribed dose, and given the random spatial distribution of the photons in the irradiating beam, the resulting ionization distribution is almost homogeneous. The physical interactions of ions determine a completely different distribution of the deposited energy, localized along the ion path. The dose imparted in the radial direction is governed by a large amount of low energy electrons (Auger electrons) emitted in ion-atom interactions (also a limited amount of high-energy δ electrons are created), which are scattered by the medium atoms (electrons and nucleus) and cause secondary ionizations. The cross-section of these ionizations exhibits a maximum at about 100 eV, corresponding to a mean free path of a few nm. Given the DNA molecule size, this effect leads to a high probability of creating DSBs or correlated single-strand breaks. Cell survival studies (Blakely et al. 1984; Tobias et al. 1982) verified these theoretical considerations showing that heavy charged particles have an increased biological effectiveness compared to x-rays. These data are generally analyzed with a parameterization of the cell survival curve through a Linear-Quadratic (LQ) model (Hall et al. 2012)

Linear
Energy
Transfer

cluster
DONE

$$S(D) = \exp(-\alpha D - \beta D^2) \quad (1.11)$$

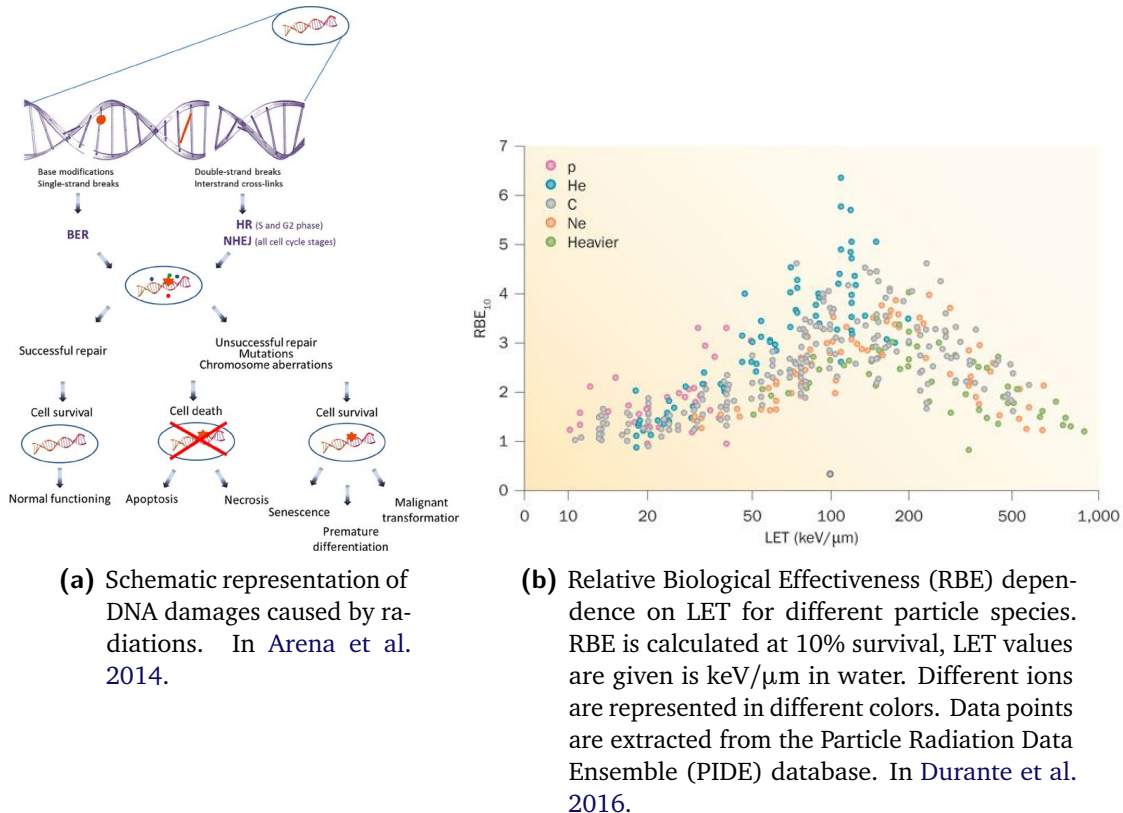


Figure 1.7: Ionizing radiations cause DNA damages in tissues, which are the basis for tumor radiation therapy. On the left side, the scheme presents the possible kind of damages induced by radiations on the cell DNA. The radiation effectiveness in killing cells is then related to the distribution of ionization events, which is all the more dense for high-LET primaries at low energies. The RBE is then enhanced for this kind of radiation. On the right side, the RBE is related to the LET for different ion species.

where S is the survival fraction, D is the absorbed dose and α and β are parameters which are experimentally determined, or obtained via radio-biological models (see section 1.1.4). The α/β ratio is linked to the radio-sensitivity of cells: the smaller it is, the larger the DNA repair capability will be. This is the rationale for fractionation in radiation therapy. Indeed, the total dose planned for the treatment of malignant cells is delivered in fractions along several days, because split doses have the advantage to spare normal tissues, with low α/β ratio, more than tumors, showing higher α/β ratio.

why however?

Given the complex scenario presented till here, it is physical absorbed dose is not sufficient to describe the effect of the delivered radiation treatment, and weighting factors based on radiation protection data have been introduced to account for both the biological properties of ions and the response of different tissues. However, in order to transfer the experience from photon data to ion irradiation and to create a common evaluation parameter, the more powerful and versatile concept of RBE has been introduced. The RBE is defined as the ratio between the photon and ion doses necessary to produce the same biological effect (isoeffective dose):

$$\text{RBE} = \frac{D_{\text{photon}}}{D_{\text{ion}}} \Big|_{\text{iso}} \quad (1.12)$$

where D_{photon} and D_{ion} are the absorbed dose for photon and ion irradiation. Notwithstanding the apparently simple definition, RBE results to be a very complex quantity, but for the moment the only one really used in clinics. It depends on several physical and biological parameters, such as LET, dose, dose rate, fractionation scheme, particle type, target biological features (radiosensitivity, oxygen concentration, etc.) (Durante et al. 2009). As a result, the RBE value changes along the primary ion path in matter, and is very difficult to be accurately predicted at the treatment planning stage. As an example, the dependence on LET is shown in Figure 1.7b. Although an accurate prediction is difficult to be obtained, the overall evolution of the RBE as a function of LET demonstrate a further advantageous feature of ions with respect to photons. From very low LET to approximately 100-200 keV/ μm , the RBE increases: an overkilling effect determines then a drop at very high LET values. Thus, RBE is higher for low energetic high-LET particles, which cause larger ionization density as their velocity decrease. This effect means that in the Bragg peak region the biological effectiveness of such radiations is more pronounced with respect to the plateau entrance area, where healthy tissues are spared. The RBE enhancement for increasing LET is at present neglected in proton therapy, and a constant value of 1.1 is implemented in the clinical routine. This point is deeply discussed in the last years, and many simulation results and models have been produced to verify or propose modification to this usage (Giantsoudi et al. 2013; Giovannini et al. 2016; Guan et al. 2015; Jones 2015; McNamara et al. 2015; Sethi et al. 2014). Anyway, it is verified that a significant increase in RBE with respect to photons can only be achieved with heavier ions, as also shown by the experimental data reported in Figure 1.7b. For this reason, clinical trials have been conducted at the Lawrence Berkeley Laboratory starting from 1975 on different ion species such as He, Ne, N, O, C, Si, Ar (Castro 1995). Very heavy ions have the advantage of providing very-high LET (and so RBE) in the Bragg peak region, useful to overcome cell killing capability limitation due, for example, to cell oxygenation effects (discussed in the following) (Blakely et al. 1984). On the other side, heavy ions also show very high LET in the entrance region, which is not desirable. These results led to the implementation of carbon ion therapy, together with proton therapy, as a good comprise between radio-biological enhanced effectiveness in the target region (carbon-ion RBE ranges between 3 and 4 in the Bragg peak - see Wilkens et al. 2008) and limited LET in the entrance plateau. As outlined in previous lines, a further parameter to account for in the evaluation of the biological effects of radiations is the cell oxygen status. If compared to healthy tissues, tumor masses can grow in size producing malignant cells, and tumor core generally show lower oxygen levels. Even if the reason is not completely explained, hypoxic conditions cause an increased cell radio-resistance, probably linked to the reduction of indirect DNA damages induced by radicals. This effect is quantified via the Oxygen Enhancement Ratio (OER),

$$\text{OER} = \frac{D_{\text{hypoxic}}}{D_{\text{aerobic}}} \quad (1.13)$$

reactive chemical species
DONE

Oxygen Enhancement Ratio

with D_{hypoxic} and D_{aerobic} the absorbed dose for normal and reduced oxygen level resulting in the same clinical effect. Its value is about 3 for conventional radiation (Schardt et al. 2010), while it is reduced for ion irradiation due to the increased RBE, making them fundamental for curing tumors with hypoxic regions.

Only some of the biological aspects have been cited here, and all their clinical implications should be ideally taken into account for an accurate treatment planning. This is the reason why some of the points discussed here will be further addressed in section 1.1.4.

1.1.3 Accelerators and beam delivery

The goal of ion beam therapy is to treat deep-seated tumors with a conform dose distribution. Different ion species, hadrons and charged particles in general have been and are under study for the clinical application (neutrons, charged pions, antiprotons, helium ions - i.e. alpha particles -, heavier ions like lithium, oxygen, up to silicon ions), but only two are at present implemented for the patient treatments: protons and fully stripped carbon ions (Degiovanni et al. 2015). The ability of treating any kind of tumor at any depth in human body relies on the possibility of providing the employed particles enough energy to obtain a range of about 25 cm in soft tissues. The ions employed in treatment must be then accelerated to about 60-70% of the speed of light ($\beta = 0.6\text{-}0.7$, see Durante et al. 2016) via different acceleration techniques and machines. This translates into maximum energy values of the order of 200-250 MeV and 4500 MeV (i.e. 375 MeV/u) for protons and carbon ions, respectively (Braccini 2010). In order to achieve the desired ion energy, sizable accelerators are needed and different solutions have been explored; at present, cyclotrons and synchrotrons are clinically implemented and available on the market. In the following, after a brief historical introduction, we sketch the main characteristics of the accelerators used in clinics, and we highlight the main features which are reflected in the treatment delivery. In addition to this, the beam delivery systems are described. Moreover, an overview of the main directions followed for the future acceleration and beam delivery techniques upgrade is provided.

1.1.3.1 Accelerators for ion beam therapy

Cyclotrons The way towards the possible application of ion beams in therapy (proposed only later by Wilson - see R. R. Wilson 1946) was opened by the invention of the cyclotron by Ernest Orlando Lawrence in 1929 (Lawrence et al. 1932), which added a magnetic field to the recently proposed linear accelerator (Wideröe 1928). A cyclotron is composed of two hollow electrodes with a frequency-alternating voltage applied between them, which accelerates the charged particles at each revolution. The circular trajectory is obtained thanks to a fixed vertical magnetic field. A scheme of the main components of a cyclotron is sketched in Figure 1.8.

Nuclear physics saw a paramount development thanks to this invention, but also in the medical field the impact was remarkable. Already in 1935, Lawrence produced the first cyclotron-originated radionuclides, then used for radiotracing, diagnosis and treatment. The first cyclotron-based treatment was performed with fast neutrons (i.e. with kinetic energies between a few MeV and a few tens of MeV) in 1938, following a paper by Gordon Locher who underlined the therapeutic potentialities of neutrons (Locher 1936); the neutrons were produced by bombarding a beryllium target with cyclotron-accelerated deuterons (Stone et al. 1940). The unfavorable depth-dose distribution of neutrons and the difficulties linked to their collimation finally led to abandon the neutron treatments in 1948 (Stone 1948) and move towards proton-beam treatments in the 50's: neutrons were revised in 1965 by Catterall in London (Catterall et al. 1971) and are still used today in Boron Neutron Capture Therapy (BNCT) techniques (Barth et al. 2005; Nedunchezhian et al. 2016). As already mentioned in section 1.1, the first proton therapy treatment was conducted by Cornelius Tobias, and John Lawrence with the Lawrence cyclotron in 1954 (Tobias et al. 1958, 1955). Between 1954 and 1974, more than 100 patients were treated in Berkeley with cyclotron-accelerated protons. In parallel, in 1957 the first tumor was irradiated with protons at the Uppsala cyclotron in Swe-

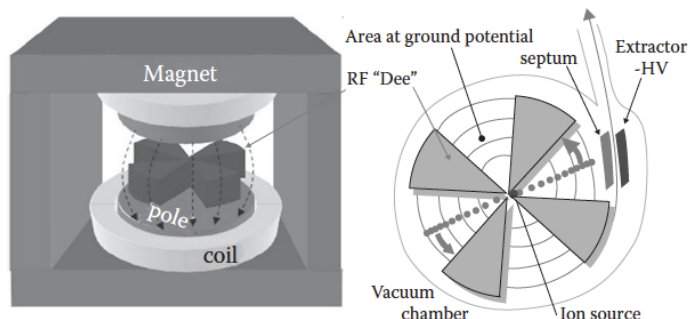


Figure 1.8: Schematic view of the main components of a cyclotron accelerator. On the left side the magnet is sketched together with the radio-frequency elements (“Dees”), which are also shown on the section depicted on the right side, with the ion source in the center. In Paganetti 2012a.

den (B. Larsson 1962), and an intensive proton therapy program, leaded by Robert Wilson, was started in Harvard with a new-built cyclotron (R. Wilson 2004). Following these first experiences, new physics laboratories decided to set up proton beams for therapy (USSR, Japan, Switzerland), until the creation of the first hospital-based center, built at the Clatterbridge Oncology Center in the United Kingdom, which started operating in 1989 with a 62.5 MeV cyclotron. This historical overview shows how the cyclotron technology has soon spread all over the world, not only in research centers, but also for therapy purpose. The present cyclotron machines, which are now commercially available by different providers, still rely on the same accelerating principle as the first Lawrence system, but the technology has greatly advanced. In particular, the vertical magnetic fields in charge of bending the particles on a spiral trajectory has been improved, giving the beam the desired transverse compactness. Moreover, the beam extraction efficiency has been improved, and multiple extractions are now possible to supply different transport lines. Moreover, synchrocyclotrons are a solution compatible with hadrontherapy applications. Based on the cyclotron accelerating principle, a synchrocyclotron presents a variable frequency for the alternating voltage which is used to compensate for relativistic effects when the accelerated ions approach the speed of light. Such a solution has the advantage of allowing for the creation of more compact systems with high magnetic fields, and is at present exploited for commercial accelerators by the main providers. In addition to cyclotrons and synchrocyclotrons, other accelerating machines initially developed for fundamental research have been translated to medical applications and are nowadays knowing a large diffusion: the synchrotrons. While the cyclotron present a fixed-value magnetic field, so that the radius of the beam trajectory increases during the acceleration process, in the synchrotron the trajectory radius is kept constant thanks to the variation of the bending magnetic field. The boost is provided by radio-frequency cavities, based on the same principle as the one composing linear accelerators: the radio-frequency increases to follow the particle revolution speed, and this acceleration principle allows to overcome the cyclotron energy limitation, as well as to obtain beam at different energies by tuning the extraction process. The invention is based on the independent ideas of Vladimir Veksler (Veksler 1944) and Ed-

Synchrotrons

win McMillan (McMillan 1945): the latter both coined the name of the machine in its letter, and constructed the first electron synchrotron in 1945 in Berkeley. Some years later, the first proton synchrotron was designed in 1952 by Sir Marcus Oliphant, who already published a preliminary sketch of the machine in 1943 (Oliphant 1943). As for the cyclotron case, several years have been required to see the construction of the first hospital-based hadrontherapy facility using a synchrotron. The first center was built at Loma Linda University in California, were a 7-m-diameter synchrotron constructed by Fermilab was installed and started treating patients in 1990. The center has been a pioneer in the field also for the presence of three 10-m-diameter rotating gantries. After the clinical studies performed at the University of Tsukuba, in Japan, between 1983 and 2000, with the treatment of about 700 patients with synchrotron proton beams, a second hospital-based center was built and equipped with an Hitachi synchrotron and two rotating gantries. Since the first use of synchrotrons for treatment purpose, several improvements have been achieved in the accelerator technology to better adapt its features to the hadrontherapy needs. In particular, the beam size can be now reduced with strong focusing optics, and the beam energy can be varied on a single spill basis (1-2 s).  present, all the hadrontherapy facilities in operation are based on circular accelerators (cyclotrons and synchrotrons): proton beams are produced with both the solutions, while only synchrotron-produced carbon-ion beams are used. In Figure 1.9 the size of different accelerators design is compared (CABOTO is still at the design stage, the Ion Beam Applications, Belgium (IBA) superconducting carbon cyclotron is under design in France, while HIT, Centro Nazionale di Adroterapia Oncologica, Italy (CNAO) and the SIEMENS accelerator are at present in operation).

No
DO
NE

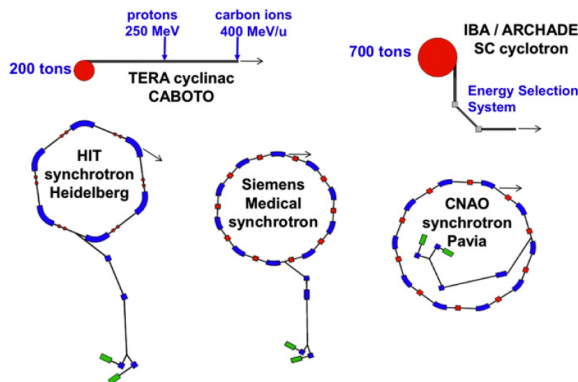


Figure 1.9: Comparison of the size of various ion accelerators for hadrontherapy. CABOTO is a cyclinac studied by the TERA Foundation; the superconducting cyclotron, designed by IBA, is under installation in Caen, France, within the ARCHADE project; HIT and CNAO are in operation in Heidelberg, Germany and Pavia, Italy, respectively; the SIEMENS synchrotron is installed in Marburg and Shanghai. In Amaldi et al. 2010a.

not yet!

DONE

Novel acceleration approaches In the last years, novel approaches have been proposed to improve the present accelerators and beam features, mainly for what concerns the beam quality and the machine size and cost. It is worth to mention the Fixed Field Alternating Gradient (FFAG) accelerator, which combines the fixed magnetic field and variable radio-frequency with separated sector magnets (Sheehy 2017). This approach allows for the production of higher intensity beams with respect to

synchrocyclotrons, and for the variation of the extracted beam energy at high repetition rate. Some designs have been proposed for hadrontherapy applications in the last decade (Antoine et al. 2009; Peach et al. 2010), but the present machine size still limits its spread in treatment centers. Furthermore, linear acceleration approach has been proposed since 1991 in both “all-linac” (Hamm et al. 1991; Lennox 1991) and “cyclinac” (Amaldi 2009) solutions. In addition to the compactness, the main advantage of linacs is the possibility to continuously vary the output beam energy on a pulse to pulse basis; in addition to this, there is neither the need for complex injection or extraction systems, such the ones used in synchrotrons, nor the need of an energy passive modulation technique as the one used in cyclotrons (see section 1.1.3.3). An extended description of linear accelerators for hadrontherapy is given in Amaldi et al. 2009. Following the first successful prototypes tested by the TERA Foundation and the Italian Istituto Nazionale di Fisica Nucleare, Italy (INFN) in the last twenty years (Amaldi et al. 2004; Ronsivalle et al. 2011), the Conseil Européen pour la Recherche Nucléaire, Geneva, Switzerland (CERN) spin-off company Advanced Oncotherapy (A.D.A.M.) is proposing a commercial solution called Linac for Image Guided HadronTherapy (LIGHT). A further solution can be given by the Dielectric Wall Accelerator (DWA) (Caporaso et al. 2009), where the acceleration tube is made of High Gradient Insulator disks alternated with conducting elements. A laser pulse is used to activate the switching units connected to these conducting modules. Very interesting thanks to a reduced size, this acceleration scheme still suffers beam focusing issues; moreover, it presents very short pulses which force a very precise selection of the number of ion per pulses at the source level. Finally, the electric field needed for reducing the machine size till 2-2.5 m is of the order of 100 MV/m; this challenging value has not been achieved yet, even if a prototype is under study at the Lawrence Livermore National Laboratory, USA (LLNL), with promising results (Hettler et al. 2013; Zografos et al. 2013). Another attractive technique is the so-called “laser driven” acceleration, based on the use of short and powerful laser pulses irradiating a thin target, with the generation of a plasma field (Tajima et al. 2009). The electrons emerging from this plasma are able to induce a strong electric field which accelerates the protons (or ions). Again, this solution would allow for the creation of very compact systems, with relatively simple and light beam optics, but some issues are still under study to be solved; in particular, the accelerated beam has an almost continuous energy spectrum which forces to implement energy modulation solutions to be adapted to treatment purposes.

1.1.3.2 Beam time structure

A particle beam can be described by a set of quantifying parameters which relates to single particle properties or to a collection of particles. In addition to the beam energy (which should be defined as an energy spectrum), beam current (which describes the beam intensity as the flux of particles per time unit) and emittance (transverse size and momentum), it is worth to describe in details what is defined as time structure. A basic distinction is made between continuous beams and bunched beams. Whenever particles are accelerated by means of radio-frequency varying fields, the accelerating machine output is a bunched beam, composed of bunches with fixed time length. Concerning the acceleration systems employed to produce clinical beams, synchrotron and cyclotrons (or synchro-cyclotrons) present strongly different time structures. In order to give an overall description of the typical time features of synchrotron- and cyclotron-produced beams, it is possible to distinguish between micro- and macro-structure. The macro-structure describes cycles of several radio-frequency periods, while the micro-structure gives the details of the particle time distribution within the same radio-frequency period. By comparing the two cited kinds of accelerators, it is possible

for
DO
NE

not sure
DONE

1 Context

Surprised by these duty cycles

DONE

Cyclotron-produced beams as continuous, with a macro-structure characterized by sub-millisecond periods (depending on the specific machine) and approximately 10% duty cycle (fraction of period with active ion delivery). In contrast, synchrotrons produce pulses which are separated in periods of several seconds, so that during the irradiation the active beam time is limited (10^{-3} average duty cycle). Each accelerator pulse (for both cyclotrons and synchrotrons), corresponding to one Radio-Frequency (RF) period, contains several micro-bunches, creating the micro-structure. For cyclotrons, micro-bunches duration is in the ns scale, while a synchrotron micro-bunch can last several tens of ns. The period separating micro-bunches varies in the range of tens of ns for cyclotrons till hundreds of ns for synchrotron beams.

Table 1.1 shows the orders of magnitude for the beam time structure for some particle accelerators used in the clinical routine. The differences between synchrotrons, cyclotrons and synchro-cyclotrons are evident. In addition, the beam typical intensity is reported.

Table 1.1: Orders of magnitude of main time structure parameters for some accelerators used in clinics. Reproduce from Krimmer et al. 2017.

	Synchrotron	Cyclotron C230 IBA	Cyclotron Varian	Synchro- cyclotron S2C2 IBA
	^{12}C	Protons		
Typical intensity (ions/s)	10^7	10^9	10^{10}	$10^8 - 10^{10}$
Macrostruct.	Period (s)	1-10	/	10^{-3}
	Duty cycle	10^{-1}	10^{-1}	10^{-3}
	Bunch width	20-50	1-2	0.5
Microstruct.	Period (ns)	100-200	10	14
	Ions/bunch	2-5	200-500	2-200
				4000

An accurate knowledge of the beam time structure is of utmost importance for the optimization of the interface to the beam delivery systems (see section 1.1.3.3), for the treatment planning, as well as for treatment monitoring purpose. The design of detectors able to exploit the emission of secondary particles to retrieve beam range and dose information must account for the beam time structure in order to evaluate the best solution to deal with signal background, counting rate and read-out channel occupancy. This topic will be further discussed in section 1.1.5 where the sources of uncertainties affecting ion beam therapy treatment are described and the detection monitoring solutions are presented. In particular, for the specific case of Prompt-Gamma (PG) detection (one of the main topic of this thesis work), a complete overview is given in chapter 2.

1.1.3.3 Beam delivery systems

Once accelerated, the high-energetic ions must be delivered to the patient in order to be conform to the treatment specification, focusing the provided dose on the Planned Target Volume (PTV). As described and detailed in section 1.1.1, the beam range can be varied by modulating the primary particle energy with the aim of covering the whole tumor volume. The Bragg

curve obtained with a monoenergetic beam is called “pristine Bragg curve”, and can be used to irradiate a section of the target volume at a given depth. The superposition of several pristine Bragg curve is necessary to deliver the prescribed dose to the tumor, which has been previously modeled in three dimensions. In particular, the beam energy spectrum has to be spread in order to increase the axial dimension of the peak region, in the so-called Spread-Out Bragg Peak (SOBP). At the same time, the beam fluence must be adapted to avoid over-irradiation of the entrance region. An example of SOBP is given in Figure 1.10. Note that the distal spot has a significantly higher fluence than proximal ones, since there is no contribution of higher energy particles. This will have an influence on the sensitivity of the method used to control the position of the distal part of the SOBP, as discussed in section 1.1.5.

It is true for a single field treatment. It may not be the case with several fields

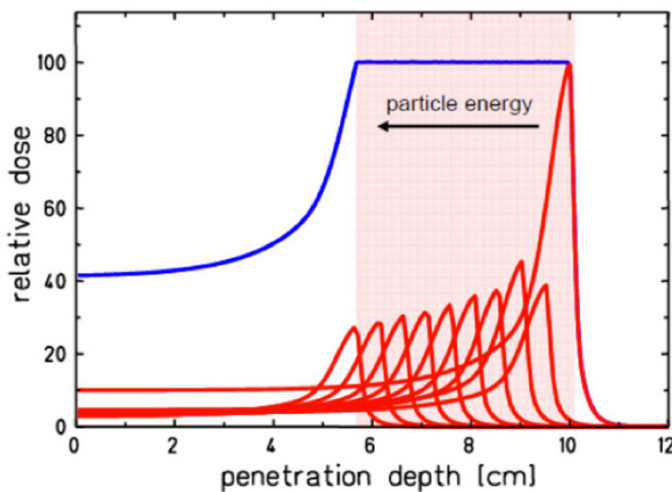


Figure 1.10: Example of SOBP. The target region is highlighted and the discrete pristine peaks composing the SOBP are sketched in red. In Durante et al. 2016.

All the described tasks are in charge of the beam delivery system, which must be optimized to interface with the accelerator and to the patient by transporting the beam to the treatment area and adjusting its features to obtain the desired dose distribution. The delivery systems implemented in clinics are based on two main strategies: passive beam modulation and active scanning. For an extensive presentation of this topic, refer to Gottschalk et al. 2008. The technique must be chosen according to the accelerator machine: it is important to remind that cyclotrons provide fixed energy beams with pulses separated by tens of nanoseconds, while in a conventional synchrotron the energy can be varied cycle by cycle, with short pulses generally separated by 1-2 s dead-time (see section 1.1.3.2).

The passive beam delivery approach generally applies to cyclotron-produced beams, and its principle is sketched in Figure 1.11. The beam extracted from the accelerator is fixed in size and energy, and is first broadened by scattering devices. Afterwards, a range modulator (generally a rotating wheel) is used to spread out the mono-energetic Bragg peak with the aim of covering the whole target thickness. The wheel periodically inserts material of varying thickness into the beam line, resulting in a range modulation with the desired features. The obtained SOBP can be shifted as a whole thanks to the addition of range shifters of fixed thickness. After the energy (range) adaptation, the beam is shaped according to the PTV definition with collimators (often multi-leaf) and compensators, which are specific to each patient and irradiation port.

Passive beam shaping

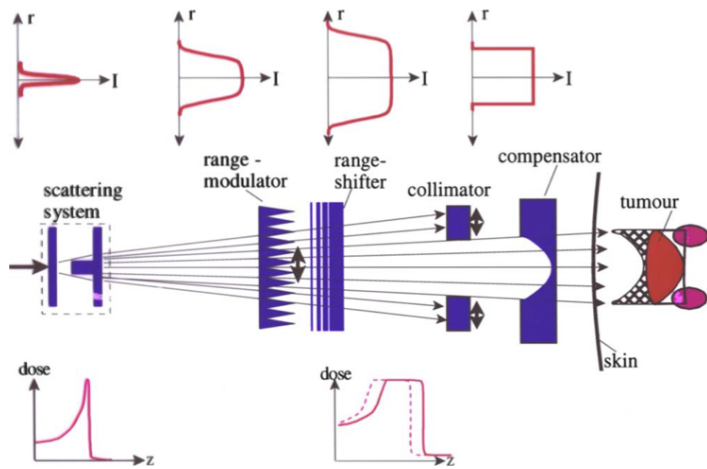


Figure 1.11: Schematic view of a fully passive beam delivery system. In Schardt et al. 2010.

The passive beam delivery technique presents **two** main disadvantages with respect to the active delivery described in the following. First, the structure of the created SOBP is fixed and the depth-dose can only be tailored to the distal end of the target volume and not to the proximal end, given the fact that the SOBP can only be shifted towards the entrance region. This feature automatically leads to a considerable dose given to normal tissues outside the target volume, in particular in the proximal part, as illustrated by the hatched region in Figure 1.11. Second, the amount of material inserted in the beam line causes nuclear interactions which lead to the creation of secondary high-LET fragments (mainly neutrons), affecting the dose delivered to the entrance region. Third, each collimator/compensator are specifically designed for each patient irradiation port, which leads to complex and costly manufacturing for such devices. The main asset of passive beam delivery is that the whole target volume is irradiated at once, which leads to shorter irradiation times. This last point is quite important for the irradiation of large PTVs.

Active beam scanning When the beam is produced with a synchrotron, the possibility to switch the energy from pulse to pulse makes feasible an active target scanning and beam range adaptation. Active beam delivery is also possible with cyclotron-accelerated beams, but the beam energy is modulated with degrading passive elements, and a spectrometer is needed for energy selection, at the cost of an important intensity reduction. The active beam delivery systems exploit the electrical charge of the accelerated particles to deflect the beam laterally through magnets and perform a scan of the defined treatment field. A schematic view of an example of active delivery system is provided in Figure 1.12. The target volume is divided into iso-energetic layers which are irradiated sequentially by deflecting the beam with dipoles in order to fully cover a grid of pre-defined voxels.

Even if this approach is demanding from the accelerator performance point of view, it brings several advantages with respect to a passive one: there is no need for patient specific equipment like collimators and compensators, and any volume can be in principle covered with a conformal dose; the dose can be adapted on a single voxel basis; the material in the beam line close to the patient is minimized so that the production of secondary particles is strongly reduced. With such a delivery system, the term Intensity-Modulated Particle Therapy (IMPT)

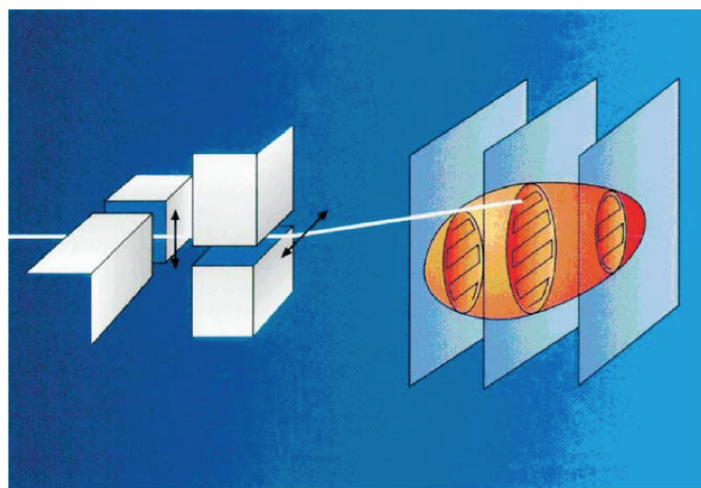


Figure 1.12: Schematic view of a fully active beam delivery system. In particular, here the GSI raster scanning system is depicted. In Schulz-Ertner et al. 2006.

has been introduced, in analogy to the Intensity-Modulated RadioTherapy (IMRT) techniques applied in standard photon radiotherapy. Indeed, the IMRT exploits multi-leaf collimators to tailor the beam to the target, so that it results to be similar to ion passive delivery systems. In photon therapy, the beam modulation on a single spot basis is possible with cyber-knife machines (Srivastava et al. 2015). The first so-called “spot-scanning” system was introduced at National Institute of Radiological Sciences, Japan (NIRS), already in the early 80’s (Kanai et al. 1983). This first experience was soon followed by a pilot project of spot-scanning at Paul Scherrer Institut, Villigen, Switzerland (PSI) (Pedroni et al. 1995) and by the realization of a fully 3D scanning beam system at GSI, where the “raster-scan” technique is implemented (Haberer et al. 1993) (with the beam moved from one voxel to the next one with no interruptions, and all points in an iso-energy slice connected together in a dense grid). Nowadays, various companies are offering commercial scanning beam system solutions, so that a rapid spread of this convenient technique is foreseen for the next years. The counterpart of the active scanning system is a relatively slow delivery of a given dose in a large tumor volume, which can be more rapidly covered by passive delivery approaches.

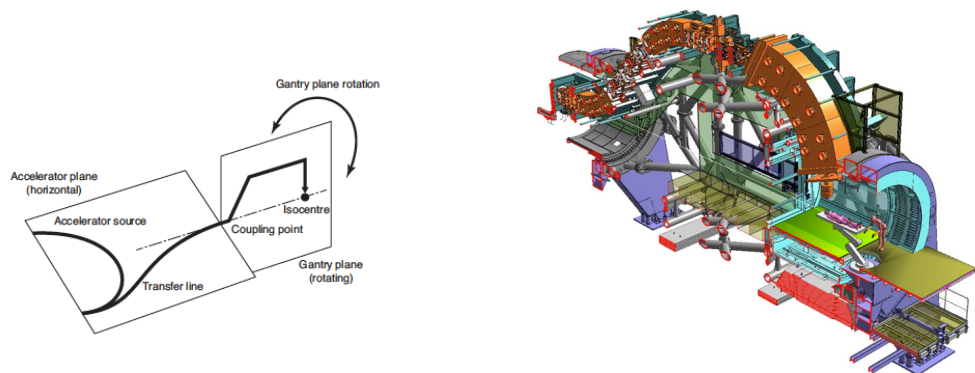
Give some orders of magnitude (a few tens of s / 2 min?)

We described till here static beam configurations, with a fixed irradiation position. In the clinical routine, in order to further improve the target volume-to-healthy tissue dose ratio, various beam penetration angles can be foreseen, similarly to standard photon therapy (even if a reduced number of different angles is required). In addition to this, deep-seated tumors close to OAR can require specific irradiation angles to be treated with the desired safety margins. In order to achieve this goal, two approaches are possible: rotate the patient or rotate the beam line. Even if the patient rotation solution has been explored in the past, several reasons are in favor of a fixed supine position, with only horizontal rotations allowed: the supine position is in compliance with the pre-treatment imaging (Computed Tomography (CT) scan) used for treatment planning (see section 1.1.4); a patient rotation necessarily leads to organ motion which is undesired; the supine position is more reproducible in the different treatment fractions. As a consequence, rotating gantries have been developed to allow for the beam line displacement. The electron linacs employed in conventional radiotherapy are generally mounted on gantries which can rotate 360 degrees around the patient couch to select the

Rotating-gantries

optimum beam direction. Likewise, in hadrontherapy, rotating gantries solutions have been designed for both protons and heavier ions. In contrast to the compact gantries used in standard radiotherapy, the high beam magnetic rigidity (defined as the product of the bending radius and the required magnetic field strength, equal to the ratio of momentum to charge of the particles) is a constraint on the size of these structures for proton therapy, and, much more, for heavier ion therapy. In general, the beam is first deflected away from the extraction axis, and then bent back to the patient direction with several dipoles. Moreover, quadrupoles are used to optimize the beam focusing before the treatment room. A scheme of a standard gantry design is given in Figure 1.13a. As already mentioned in section 1.1.3.1, the first gantry for protons was installed at the Loma Linda University Medical Center in 1990, followed in 1996 by the first one in Europe at PSI in 1996, which also included an upstream scanning system ([Pedroni et al. 1995](#)). At present most of proton therapy centers are equipped with at

are you sure? least one rotating gantry, generally with passive beam delivery systems. The huge dimensions imposed by the carbon ion beam rigidity (three times bigger rigidity for 5000 MeV carbon ions with respect to 200 MeV protons) limited the implementation of such a technology in carbon therapy centers, while different technical solutions have been explored. As an example, at HIMAC, in a single treatment room the beam can be delivered to the patient via an horizontal and a vertical line, for the sequential treatment from different angles. The first rotating gantry system for heavy ions was installed at HIT and is now in operation: the diameter is of 13 m, for a total weight of about 700 tons (see Figure 1.13b).



(a) Schematic design of a rotating gantry installed in a particle therapy center.
In [Owen et al. 2014](#).

(b) Scheme of the HIT ion rotating gantry.
In [Schardt et al. 2010](#).

Figure 1.13: Schemes of a standard gantry design (left) and of the carbon-ion rotating gantry installed at HIT (right).

Intense research efforts are dedicated to improve the gantry technology, mainly directed towards the implementation of more compact systems equipped with superconducting magnets. A first superconducting carbon ion gantry has been recently installed at NIRS, and is approximately half size with respect to the German one ([Iwata et al. 2013](#)).

1.1.4 Treatment planning

Given the available accelerator and beam delivery system, the best possible treatment features are elaborated by the treatment planning process, which combines the clinical information about the patient with the physical and biological aspects of particle therapy. The treatment

planning is always patient and disease-specific, and is based on imaging techniques aiming to provide the physicians with the data necessary to delineate the target volume and the surrounding OAR. The minimal approach is represented by a pre-treatment x-ray CT scan, providing quantitative information about the anatomical structures via photon attenuation images. As briefly outlined in the previous paragraph, it is important to record the pre-treatment images in the same conditions (patient position, fixation structures, etc.) later applied in the treatment itself. Complementary imaging devices, such as MRI and PET (Levy 2007), are often used in combination with CT to improve the target definition quality, mainly in case of proximity with OAR. In addition to the target delineation, the physicians are also in charge of the therapy prescription, which includes the total dose to be delivered to the PTV, the dose limits for the surrounding tissues, and the fraction planning. All the listed information are the input for the Treatment-Planning System (TPS), which makes the connection between the prescribed dose distribution and the beam acceleration and delivery devices. The physicists and clinicians use the TPS to define all the treatment beam-specific features such that the clinical prescription is satisfied at the maximum extent. The software output details the beam entrance ports to be used (in terms of gantry positions, if a gantry is available), the beam ranges and intensities, the irradiation scheme in terms of dose-per-voxel, and, more generally, the expected dose distribution in the patient, which allows to quantify the Tumor Control Probability (TCP) and the probability of complications to the normal tissues. As the whole planning process is based on x-ray CT scans, providing photon beam attenuation images, a relationship between the CT values and ion Relative Stopping Power (RSP) is needed. The CT values are expressed in Hounsfield Units (HU), defined as

Treatment-Planning System

From Hounsfield units to relative stopping power

$$\text{CT value}(\vec{x}) = 1000 \times \frac{\mu(\vec{x}) - \mu_w}{\mu_w} \quad (1.14)$$

where \vec{x} is the considered location, $\mu(\vec{x})$ the x-ray absorption coefficient in tissue, μ_w the one in water as reference. Water is always used as reference medium, in particular through the concept of Water-Equivalent Path Length (WEPL). There is not a functional relationship between the two quantities, and systematic studies have been carried out at PSI for protons (Schaffner et al. 1998; U. Schneider et al. 1996). For carbon ions, similar investigations have been performed at NIRS (Kanematsu et al. 2003; Matsufuji et al. 1998) and GSI (Jäkel et al. 2001a; Rietzel et al. 2007), and experimental verification has been obtained via measurements on animal tissues. In Figure 1.14 the data of a look-up table for the conversion of HU into carbon ion WEPL are plotted in the HU range of relevant biological tissues.

The conversion factors are tabulated and implemented in the main TPSs, but several studies are still ongoing in order to optimize the calibration accuracy (as an example, see Inaniwa et al. 2018). As highlighted in several research works, this is one of the main sources of uncertainty affecting proton and carbon ion range prediction and, so, treatment precision. Possible investigated solutions to reduce systematic uncertainties in the RSP determination related to the Hounsfield unit conversion are represented by proton Computed Tomography (pCT) and dual energy x-ray CT (Yang et al. 2010). Further details will be given in section 1.1.5. In addition to the beam range determination, the TPS software must also deal with biological dose calculations. Indeed, as highlighted in section 1.1.2, charged particles differ from photons in their radiobiological properties and effects. Notwithstanding the 10-20% RBE variations verified for protons with varying LET along the path in the patient tissues, a practical constant value of 1.1 is generally used in clinics (ICRU 2007; Paganetti et al. 2002). This value corresponds to the average RBE at mid SOBP overall dose levels. In the distal section of the Bragg peak,

Biological dose modeling

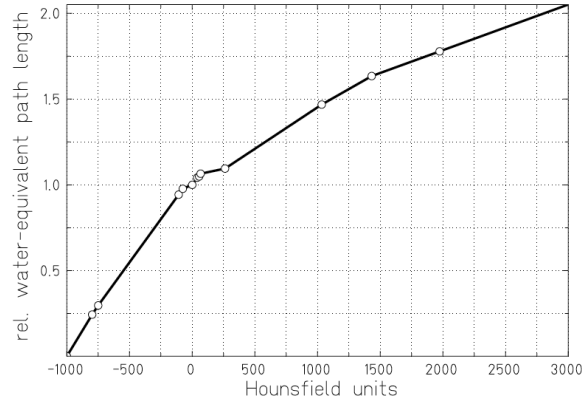


Figure 1.14: Hounsfield look-up table for carbon ion treatment planning, based on the data collected at GSI and reported in Jäkel et al. 2001a. In Rietzel et al. 2007.

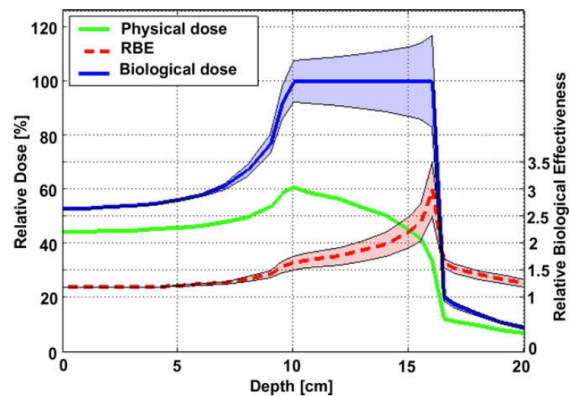


Figure 1.15: Comparison of physical (green solid line) and biological (blue solid line) dose for a 290 MeV ^{12}C ion beam with a 6 cm SOBP for an assumed maximum RBE of 3.0. The RBE varies in the range 2.5–3.5 and an uncertainty band is sketched to represent the biological dose possible variation due to the selection of the RBE value (dashed-red line). In Suit et al. 2010.

what is the RBE model used?

an higher RBE has been verified; this effect slightly affects the dose profile fall-off in proton-therapy and is not modeled in the present planning systems. As mentioned in section 1.1.2, several studies are ongoing in the last years with the aim of optimizing the biological models and applying a variable proton RBE in clinics, and the topic is still open to discussion in the expert community (Lühr et al. 2018; Paganetti 2014; Paganetti et al. 2013; Unkelbach et al. 2018; Willers et al. 2018). A different approach must be applied to heavy ions (carbon ions in particular), given the much stronger dependence of their RBE on the various parameters listed in section 1.1.2. Focusing on carbon ions, treatment plans are generally optimized using the so-called RBE-weighted dose, calculated according to verified models based on experimental data. In Figure 1.15, the physical and biological doses absorbed during a carbon ion beam irradiation with a SOBP are compared and the RBE variation along the beam path is also reported, together with the estimated uncertainties which also affect the RBE-weighted dose evaluation. For this purpose, two main models are nowadays implemented in clinical practice. On one side, the Japanese centers use a model developed at NIRS, based on in vitro cell killing experiments on human salivary glands and neutron irradiation experience gathered at HIMAC, as well as on the application of the LQ model (Matsufuji et al. 2007). Recently, a modified Microdosimetric Kinetic Model (MKM) has been introduced in order to optimize the plans to active scanning with ion beams (Inaniwa et al. 2015). On the other side, a specific biophysical model has been developed in Germany at GSI, called Local Effect Model (LEM), and it is now used in the clinical centers in Germany, Italy and China. Its main idea is to transfer known cell-survival data for photons to ions, assuming that the difference in biological efficiency arises only from a different pattern of local dose deposition along the primary beam (Jäkel et al. 2001b; Krämer et al. 2000). The two models have been verified to give comparable results, in agreement with the measured RBE, with in-vitro experiments on mice cells (Uzawa et al. 2009), while different predictions are obtained when different treatment schemes on different tissues are studied (Fossati et al. 2012; Steinsträter et al. 2012). Besides, the NanOx model (described in Cunha et al. 2017) is being developed in order to overcome conceptual inconsistencies of the LEM and MKM. The model is able to predict cell survival with good agreement to experimental data, and its parameters are under study for optimization (Monini et al. 2018). The definition of a common effective dose prediction method is ongoing: this will allow for comparative studies of clinical results and for an improved collaboration of the few ion treatment centers operating all over the world. These biological models are mainly applied for the planning of active scanning treatments, for which the target volume is previously divided into slices: the dose is then optimized for iso-range slices. In contrast, for passive beam delivery systems, the plan optimization is generally reduced to the study and production of the patient-specific beam modulators. In the future, biology-guided forms of particle therapy can be foreseen; the RBE variations, instead of being an issue for which corrections are needed to the treatment planning, could be used to the treatment effectiveness advantage. Focusing on the possible direction of improvements in the future of treatment planning, the research efforts are concentrated in the last years also on another fundamental topic: the treatment of moving organs. It is clear that the well-defined ion range and narrow dose peak make ion treatments potentially more sensitive to inter- and intra-fractional organ motion, as highlighted in Bert et al. 2008; Engelsman et al. 2013; Phillips et al. 1992 and Thörnqvist et al. 2013, as an example. Concerning the organ displacement between following fractions, it can be corrected by more frequent imaging scans, ideally a new one before every treatment fraction, in order to adapt the treatment planning to weight variations, target size modifications and similar anatomical effects. The organ movement caused by the respiratory cycle requires more complex strategies to be taken into account for the treatment plan and delivery. The respiratory motion patterns are generally complex and not regular, involving translational and rotational displacements.

You talk here
about proton
beams?

address some of
the flaws

These models are
used for carbon
ion beams for
which only active
beam delivery is
used

Treatment of
moving organs

Several strategies to mitigate the effect of organ motion are being investigated, some of them directly coming from the experience gathered in IMRT. As well summarized in Schardt et al. 2010, among these strategies it is worth to mention rescanning of repainting techniques, based on the average effect of several irradiations with reduced beam fluence on the same iso-range slices; gating techniques, which aim to correlate the irradiation active time to a continuous monitoring of the respiration cycle; tracking, which requires a 3D compensation of the target motion in real-time, particularly adapted for scanning techniques. A further step will be the real time monitoring of moving organs by means of external markers linked to biomechanical modelling of internal organs (Manescu et al. 2013). Some of the cited techniques, or combinations of them, are being tested and are now at the validation stage, but there is still wide room for improvements towards the application of 4D treatment planning (Bert et al. 2017; Graeff et al. 2013). Further information about this topic can be found in a recent review by Kubiak (Kubiak 2016). Range predictions, biological modeling and organ motion are only some of the sources of uncertainties affecting the planning and delivery of ion therapy treatment, detailed in section 1.1.5; for this reason, safety margins are applied in clinics for the definition of the irradiation target volume and the quantification of the planned dose. In the actual clinical routine, the PTV is a geometrical extension of the so-called Clinical Target Volume (CTV) and is delineated in order to account for treatment uncertainties. Safety margins are also applied in standard x-ray therapy (McKenzie et al. 2000), where under- or over-shooting errors have limited effects with respect to ion beam therapy. As highlighted in Albertini et al. 2011, the application of safety margins is useful to improve the treatment plan robustness in case low dose gradients are applied, while the effect results marginal for highly modulated IMPT. At present, in order to account for the overall effects of all sources of uncertainties in the range prediction (MCS, beam energy straggling, imaging tools accuracy and calibration, biological effects, patient positioning and organ motions), margins up to $3.5\% + 3\text{ mm}$ can be applied around the CTV (Paganetti 2012b), mainly based on Monte Carlo or analytical dose calculations which result in clinically compatible predictions.

Safety margins

In the following paragraph, the uncertainties related to ion therapy treatment are discussed in details, with particular care devoted to possible clinical solutions.

1.1.5 Ion beam therapy uncertainties and treatment monitoring

Heavy charged particles are suitable for cancer radiation therapy given the better achievable dose conformity and the reduced energy deposit in tissues surrounding the target with respect to standard photon treatment techniques. These advantageous features directly derive from the nature of ion interactions in matter, described in section 1.1.1, which determines a peculiar depth dose profile characterized by a finite range and a energy deposit (dose) peak (Bragg peak). In order to accurately predict the ion range and, more generally, the dose distribution delivered during a clinical treatment, all the possible ion interactions in matter must be considered. This prediction is associated with considerable uncertainties due to imaging precision, patient setup, anatomical variations and motions, beam delivery system accuracy, dose calculation approximations and biological considerations (Paganetti 2012b). Ideally speaking, a perfect knowledge of the beam and target structure and perfect evaluation of all the parameters involved in the dose determination would result in the optimal way to treat a deep-seated tumor, with a reduced dose delivered to the surrounding healthy tissue (even close to OAR) with limited fields of irradiation, and a dose accurately concentrated to the tumor volume. The actual clinical routine must face limitations in beam production and control as well as in

important?

patient composition evaluation, which causes the need for approximated treatment planning and the setup of treatment safety margins (see section 1.1.4), limiting the full exploitation of this treatment technique potential. In this section, an overview of the different sources of uncertainties affecting ion therapy treatments is given, and the solutions, already implemented or under study, are presented, with particular attention focused on ion range monitoring techniques, main topic for this thesis. All the mentioned sources of uncertainties associated to hadrontherapy treatment converge in a considerable spread in the beam effective range with respect to the predicted one. Treatment planning systems are able to accurately model range straggling and MCS broadening along the beam path in water (Hong et al. 1996), but the prediction accuracy has limitations when translated to patients. As highlighted in Schlegel et al. 2008, a precise determination of the primary ion penetration depth is essential in order to rely on particle therapy treatments, much more than for standard photon treatments. The reason is schematically presented in Figure 1.16.

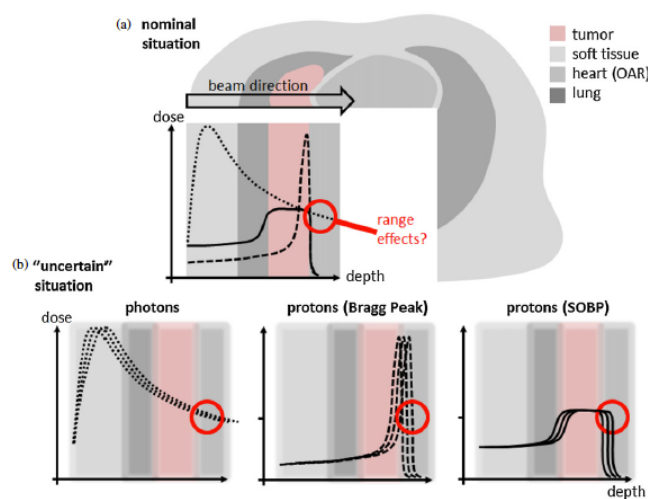


Figure 1.16: Schematic view of the potential benefit due to the depth-dose features of protons as compared to photons (a) and influence of range uncertainties on photon irradiation and proton pristine and spread-out Bragg peaks. In Knopf et al. 2013.

In the top panel of Figure 1.16 the ideal treatment configuration is shown, with the pristine Bragg peak located at the distal limit of the PTV (dashed line) and the SOBP covering the whole tumor volume (solid line); the two proton irradiation methods are compared to the photon dose profile (dotted line), which releases the maximum of the dose in the entrance region and it is not capable of sparing the tissues surrounding the tumor volume, before and beyond the tumor in the beam direction. In the bottom line of the same figure, the effect of range uncertainties are represented: from left to right, in case of photon dose profile shifts, the modification in the dose delivered to healthy tissues is relatively limited, the main effect being a shift in the dose maximum in the entrance region; for a monoenergetic Bragg peak, a shift in the peak position can result in both an under-irradiation of malignant tissues and a dose maximum located in soft healthy tissues; the same effect is present for the SOBP, with the only advantage of a reduced under-irradiation of the tumor region. It is clear from this simple case how the extremely sharp dose gradient provided by heavy charged particles must be accurately controlled in order to fully profit of its beneficial effect in treating cancer. As mentioned, an exact range calculation is extremely difficult to be obtained in human tissues. As described in section 1.1.4, the treatment planning is at present based on a pre-treatment

1 Context

CT scan which is generally acquired only before the first treatment fraction. The CT image accuracy is indeed the first source of uncertainty in range calculation . The limitations in the imaging precision (mainly due to image noise - see Chvetsov et al. 2010) and the reconstruction artifacts (which can be relevant in presence of metal implants as verified in Jäkel et al. 2007; Newhauser et al. 2007) already affect the reference data set. Small but not negligible effects are also related to the CT resolution (España et al. 2011a). The obtained CT data must be then converted from x-ray attenuation values (HU) related to water to relative ion stopping power (see section 1.1.4). The conversion is based on calibration curves (U. Schneider et al. 1996; W. Schneider et al. 2000), generally obtained with CT scans of tissue phantom materials with known density and elemental composition. These curves are affected by uncertainties, to be added to the fact that the actual conversion is dependent on the material composition: same x-ray attenuation values can correspond to different relative stopping powers, or vice versa. In addition to this, the conversion may depend on the specific CT scanner, as shown in Ainsley et al. 2014. Several studies have highlighted the magnitude of such uncertainties, which varies, for example, in the range 1-2% from soft tissues to bones for protons (Schaffner 1998), which is translated in range possible discrepancies of 1-3 mm. Specific studies have also been conducted on animal fresh tissues in order to otpimize the CT calibration for carbon ion treatments (Rietzel et al. 2007). In total, uncertainties of the order of 3% are generally considered to take into account the described imaging limitations (Moyers et al. 2001). It has been proven that dual-energy CT can improve material composition information (Bazalova et al. 2008; Hünemohr et al. 2014; Wohlfahrt et al. 2018; Yang et al. 2010) and the resulting range uncertainties can be reduced, in particular for carbon ion therapy (Hünemohr et al. 2014). A possible solution to further reduce the errors related to the HU values conversion is the implementation of direct density measurements techniques, where the treatment beam is also used for imaging purposes giving direct access to stopping power data. This possibility was discussed since the late sixties (Koehler 1968), and the technological advancements (mainly in data acquisition systems and detection techniques) recently allowed to obtain promising results in the last years. In addition to the advantageous removal of the data conversion stage, the so-called ion radiography brings other benefits to the treatment side, with the possibility of performing position verification with fast scans just before the treatment delivery (U. Schneider et al. n.d.), as well as on the patient side, given the reduced dose necessary for a complete scan with respect to standard x-ray CT (U. Schneider et al. n.d.). Further details about this imaging technique are given in the dedicated section 1.1.5.1. Till here the uncertainties directly coming from the treatment planning process have been described, and can be considered as systematic errors, reproduced unchanged for every delivered fraction of the treatment. Conversely, stochastic uncertainties emerge at the treatment delivery level and affect the planned range with random variations. The majority of treatment planning system operating in clinics are based on analytical calculations relying on WEPL data, not able to account for complex geometries. In presence of tissue inhomogeneities , MCS causes what is generally referred to as a degradation in the distal fall-off of Bragg peaks (Urie et al. 1986), in particular in proximity of high-density gradients. Accurate modeling of MCS is then strictly required for correct range predictions (Schuemann et al. 2014). The patient anatomical configuration plays a major role not only on a single fraction basis, but also in different fractions. Conventional fractionation schemes foresee treatments which can last for several weeks; the patient anatomical characteristics can experience significant changes, such as tumor mass reduction, weight loss or gain (Albertini et al. 2008), modifications in the filling of internal cavities. It is clear that such variations introduce further shifts in the predicted ion range, which can be different from fraction to fraction. Moreover, in different fractions, slight differences in the delivered ion energy are possible, with small but not negligible effects. Moving on but

MCS range degradation

Patient anatomy changes

always referring to static anatomy issues, the patient setup in the treatment room is another source of uncertainty which can cause discrepancies between the planned and the delivered dose distribution, as shown for example in Fattori et al. 2014. Furthermore, in particular for the treatment of tumors in the thorax, organ motion is an important source of dose delivery errors. Focusing on lung cancers, which are already difficult to be precisely targeted due to the low lung density (3 times lower than water), the respiratory motions are hard to be modeled and cause an overall blurring of the dose distribution and severe local range variations due to the high-density gradient between dense tumor tissues and low-density lung tissue. Important research efforts are devoted to the optimization of the treatment of moving organs, as explained in section 1.1.4. In particular, for active scanning delivery techniques, potentially powerful if synchronized with the movements of the target areas, an interplay effect involving beam and organ motion can affect the dose homogeneity and must be minimized (Dowdell et al. 2013; Grassberger et al. 2015). To conclude the list of source of uncertainties affecting ion beam therapy treatment planning and delivery, it is worth to mention the contribution of biological effects. For protons, a generic constant RBE value is generally used in clinics to relate proton dose to photon dose, while it has been verified how the biological effectiveness varies along the beam path, in particular at varying LET. In SOBP, the increasing LET at decreasing primary residual energy is compensated by a reduction of the proton fluence, in order to obtain an homogeneous dose distribution. The increase in LET causes an increase in the RBE which is not considered and results in a shift in the biologically effective range, estimated in \sim 1-2 mm (Paganetti et al. 2000; J. B. Robertson et al. 1975; Wouters et al. 1996). Heavier ion therapy planning systems already account for RBE variations to prescribe a conformal dose distribution, but the prediction process is not error-free. Moreover, the dose distribution delivered with heavy ion irradiation is also characterized by the peculiar tail beyond the Bragg peak caused by the nuclear interaction fragments; a correct prediction of the nuclear interaction channel becomes significant, and it is at present not accurate enough to point the beam towards critical structures and fully profit of the narrow dose peak. The optimization of treatment planning system is focused, in the last years, on Monte Carlo-based dose plans, which can reduce the listed uncertainties, and rely on the continuous progress of physical and biological modeling. A complete overview about this topic is given in Paganetti 2012b for the case of protons. In table 1.2, originally presented in Paganetti 2012b and here reported with the modifications which can be found in Durante et al. 2016, the sources of uncertainties in the proton range are reported with an estimate of their relative contribution with and without the application of Monte Carlo optimization techniques.

Organ motion
dose blurring

Biological ef-
fects

As mentioned in section 1.1.4, the current approach to deal with range uncertainties directly comes from standard x-ray radiation therapy and involves the setting of margins around the target volume. The margins are generally determined analytically and result to be larger in the distal end of the target volume to account for range shifts, while smaller margins are applied laterally to include beam penumbra uncertainties. The field arrangement is another applied mitigation of the problem (Lomax et al. 2001), in particular in proximity of OAR. For example, lateral fields can be used instead of distal ones. Notwithstanding the several solutions used, *in-vivo* verification of the delivered range is still a pressing desire in the clinical community. Standard imaging devices are commonly used to monitor photon therapy treatments, where the delivered beam is not stopped in the patient. On the contrary, ion beams do not exit the patient body, so that monitoring techniques can only be based on secondary radiation or indirect measurements. An exception is represented by implanted devices, proposed for the dose and range measurements, briefly discussed in section 1.1.5.5. As highlighted in Parodi 2015, the monitoring should be ideally in three-dimensions on-line, time-resolved and in

Table 1.2: Estimated magnitude of range uncertainties separated for the various sources, and potential benefit provided by Monte Carlo simulations. The estimates are based on data in (Bednarz et al. 2010; Bischel et al. 1992; Chvetsov et al. 2010; España et al. 2010; ICRU 1980b; Kumazaki et al. 2007; Matsufuji et al. 1998; Paganetti et al. 2000; J. B. Robertson et al. 1975; Sawakuchi et al. 2008; Schaffner et al. 1998; Uriel et al. 1986; Wouters et al. 1996). Table reproduced from Durante et al. 2016.

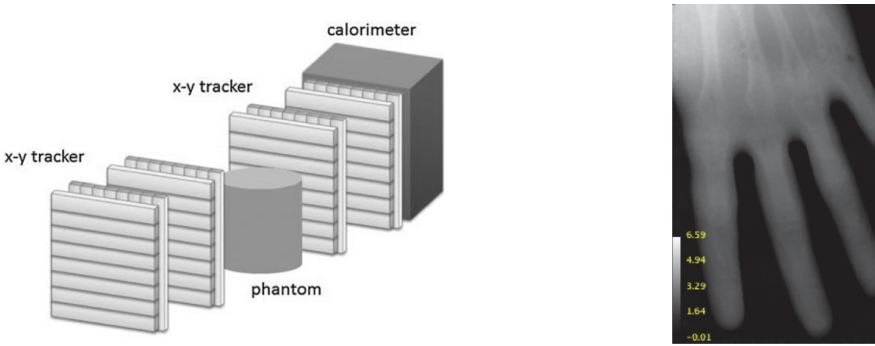
Source of range uncertainty in the patient	Range uncertainty w/o Monte Carlo (%) or mm)	Range uncertainty with Monte Carlo (%) or mm)
<u>Independent of dose calculation:</u>		
Measurement uncertainty in water for commissioning	± 0.3 mm	± 0.3 mm
Compensator design	± 0.2 mm	± 0.2 mm
Beam reproducibility	± 0.2 mm	± 0.2 mm
Patient setup	± 0.7 mm	± 0.7 mm
<u>Dose calculation:</u>		
Biology	+ ~ 0.8%	+ ~ 0.8%
CT images and calibration	± 0.5%	± 0.5%
CT conversion to tissue (excluding I-values)	± 0.5%	± 0.2%
CT grid size	± 0.3%	± 0.3%
Mean excitation energy (I-values) in tissues	± 1.5%	± 1.5%
Range degradation: complex in-homogeneities	- 0.7%	± 0.1%
Range degradation: local lateral in-homogeneities	± 2.5%	± 0.1%
<u>Total</u> (excluding biology and lateral in-homogeneities)	2.7% ± 1.2 mm	2.4% ± 1.2 mm
<u>Total</u> (excluding biology)	4.6% ± 1.2 mm	2.4% ± 1.2 mm

real-time, in order to allow for a prompt detection of severe deviations between prescribed and delivered dose, and eventually for the interruption of the beam delivery. A number of different approaches have been proposed in the last years, and significant research efforts are dedicated to this specific point by several groups all over the world. In particular, nuclear reactions products are deeply investigated as a source of information about the beam range. The developed techniques have to be adapted to the present clinical routine, so that the beam features (clinical intensity, time structure, size) and treatment plan characteristics (kind of beam delivery, spot size, irradiation intensity per spot, etc.) must be considered. In the following sections, after a paragraph devoted to charged particle CT, the main techniques implemented for ion range monitoring purpose or at present under study are described, and the current available or future instrumentation is presented. In chapter 2, the attention will be focused on the detection of PGs, central topic of this thesis, and a detailed overview of the state of the art of this particular monitoring techniques is provided.

1.1.5.1 Ion radiography and tomography

Given the considerable contribution of x-ray HUs conversion to ion stopping power to the treatment planning uncertainties, the best solution to overcome this limitation relies in avoiding this conversion step. This can be obtained by directly using high-energy ions to perform patient imaging scan. After the original proposal delineated in the Cormack seminal paper in 1963 (Cormack 1963), the first studies with protons date back to 1968 (Koehler 1968), and at the beginning of the seventies the feasibility of this techniques to obtain high contrast images was demonstrated (Cookson 1974; Cormack et al. 1976; Steward et al. 1973). After the first pioneering studies, the developments were almost abandoned in favor of other imaging techniques, in particular x-ray based, providing better spatial resolution with simpler machines (Kramer et al. 1977). As a consequence of the present widespread of hadrontherapy and the multiplication of treatment centers, several research groups showed a renewed interests in the field, and various development projects are ongoing in Europe and USA with promising results guaranteed by the significant technological advancements occurred in the last years. To date, most of the experimental efforts have been and are being devoted to proton-based imaging (reviewed for example in Bucciantonio et al. 2015; Poludniowski et al. 2015), but pioneering imaging experiments with heavier ions were already carried out in the late seventies and eighties (Chu et al. 1993; Tobias et al. 1977). In recent years, many research groups in Japan and Europe are working on carbon-ion imaging prototypes to be applied in the existing carbon therapy centers. An overview of the ongoing research in the field of proton and ion imaging is given at the end of this section. The radiography technique is based on ion beams applied to the patient at higher energy with respect to the treatment ones, which must traverse the body and can be detected on exit to directly retrieve the residual range. In Figure 1.17a the design of a standard detection system for ion radiography is sketched. The Most Likely Path (MLP) through the patient (phantom) is estimated thanks to two thin tracking detector stages, measuring the primary particle trajectories both entering and exiting the target. The second tracker is followed by a range or energy detector, which measure by complete absorption the residual range or energy of the primary ion. Thanks to the coincidence detection of entrance and exit coordinates and residual energy/range of each primary particle, a density two-dimensional map of the target area can be obtained.

Already said Since all the primary incident particles must completely pass through the target for a residual energy measurements, the beam energy must be higher than the one applied for radiother-



(a) Schematic view of standard ion CT detector design. Each primary incoming particle is tracked before the interaction in the patient and at the exit, and its residual energy is absorbed and measured by a calorimeter. In [Mattiazzo et al. 2015](#).

(b) Proton CT image of an hand phantom. In [Plautz et al. 2014](#).

Figure 1.17: Proton and heavier ion radiography and CT are under study in the last years as promising techniques for optimizing the treatment planning performance in hadrontherapy. A standard detector design is sketched in the left panel, while the first image of an hand phantom is reported in the right one.

apy treatments. In the case of protons, standard clinical accelerators can provide beam at a maximum energy of 230-250 MeV (the projected range of 250 MeV protons in water is ~ 38 cm - see National Institute of Standards and Technology (NIST) tables at [Berger et al. 2018](#)), not enough to pass in all directions through the hip region of a typical adult, and far short of the shoulder-to-shoulder distance through a human male. Such energies are anyway sufficient for scanning the head or the lung region for most patients ([Johnson 2017](#)). The optimal beam conditions for radiography have already been pointed out for protons in one of the first studies about this topic ([Moffett et al. 1975](#)). At that time, small pencil beams were preferred, with low intensity and limited energy spread. In reality, the beam can be also passively spread to cover the whole detector aperture, or a scanning technique can be used as suggested in the original papers. In addition to the first highlighted advantage of this technique, which provides direct access to stopping power data, there are other factors determining its convenience with respect to x-ray imaging. A dosimetric advantage with respect to x-rays has been already proven in 1975 ([Moffett et al. 1975](#)), and a reduction of imaging dose by a factor 10 to 20 has been reported in [U. Schneider et al. n.d.](#). Recent results showed, for equal spatial and density resolution, 50-100 times lower image exposure for protons with respect to x-rays ([U. Schneider et al. 2004](#)). Moreover, the low dose enables one to perform proton imaging scans before each treatment fraction: this is potentially very useful for positioning optimization (the scan is performed under the same geometrical conditions as the treatment) and for the detection of anatomical changes, which cannot be included in the present treatment planning, based on a single CT scan performed before the beginning of the whole treatment cycle. However, it must be considered that ion radiographies are performed in the same treatment room and couch, limiting the patient flow. Moreover, a major limitation of proton radiography techniques is represented by a poor spatial resolution due to MCS, already highlighted in the first publications ([Koehler 1968; Moffett et al. 1975](#)). Several small angle deflections produce uncertainties in the reconstructed trajectories ([Penfold et al. 2009; U. Schneider et al. 2004, n.d.](#)). Heavier ions are less affected by MCS in the

Surprising!

target, so that better spatial resolution with respect to protons can be achieved, but they suffer from substantial nuclear spallation and the projectile and target fragmentation can add background to the final image (Parodi 2014). The helium ions, which already have the advantage of requiring much less energy than carbon ions in order to fully penetrate a phantom, behave more like protons within the phantom, but with significantly reduced scattering and increased spatial resolution. Helium, indeed, appears to be the optimum compromise, even if it is not implemented in clinics for tumor treatments at present. With the increasing diffusion of heavy-ion therapy centers, anyway, we can expect a further development of this field in the next years (Parodi 2014). The described ion transmission imaging method provides two-dimensional information, but it can be extended into 3D with the rotation of the system around the target (or the patient rotation) and the application of tomographic reconstruction. The so-called ion-CT makes use of optimized Filtered Back-Projection (FBP) methods or Algebraic Reconstruction Techniques (ARTs) to obtain 3D patient images by combining various data sets from different angles. At present, ion transmission imaging for both radiography and tomography is not yet clinically implemented, but a number of research groups conducts instrumental development campaigns to produce prototypes to be tested in clinics. Although the basic design is common, with tracker and absorber components, different technological solutions are being explored. The first prototype designed for this purpose, after the first trial conducted at the early stage of this research field, was studied at PSI; it was based on a pair of Multi Wire Proportional Chambers (MWPCs) as tracker, followed by a Sodium Iodide (NaI) 7.5 mm diameter crystal for the energy measurement (U. Schneider et al. n.d.). The detector was later upgraded to overcome rate and size limitations, with the use of scintillating fiber hodoscopes instead of MWPCs and plastic scintillator tiles to substitute the monoblock NaI crystal (Pemler et al. 1999). Similar scintillating-fiber trackers have been used by the OFFSET collaboration for its prototype (Lo Presti et al. 2014), which showed very low efficiency. The same author recently presented a beam monitoring and radiography prototype (QBeRT) with upgraded read-out system, providing enhanced results (Gallo et al. 2016; Lo Presti et al. 2016). The TERA Foundation at CERN has been involved for several years in the development of detectors to be applied in the quality assurance for hadrontherapy. Within the Advanced QUality Assurance (AQUA) project (Amaldi et al. 2010b), proton radiography instruments were developed and tested on clinical beams, starting from 2009. The first prototype, based on Gas Electron Multiplier (GEM) detectors (Sauli 1997) for tracking and plastic scintillator layers for the calorimeter, had an active area of $10 \times 10 \text{ cm}^2$ (Amaldi et al. 2011), then extended to $30 \times 30 \text{ cm}^2$ for the second version of the machine, with similar detection technologies but improved rate acceptance capabilities thanks to new read-out systems (Bucciantonio 2015; Bucciantonio et al. 2013). A complete, wide surface proton CT system has been proposed by an American collaboration of the Northern Illinois University (NIU) and the Fermi National Accelerator Laboratory (FNAL) (Naimuddin et al. 2016). It is based on 0.5 mm diameter scintillating fibers read out by SiPM, for an active area of $24 \times 20 \text{ cm}^2$. Alternative, more expensive designs include silicon-strip detectors for proton tracking, such as the one in development in Italy by the PRIMA collaboration, with eight layers of silicon sensors and a calorimeter composed of a 2×7 array of Cerium-activated yttrium aluminum garnet (YAG:Ce) crystals, $3 \times 3 \text{ cm}^2$ section and 10 cm length each (Scaringella et al. 2013). The experience of a collaboration of the Loma Linda University (LLU) and the University of California and Santa Cruz (UCSC) started with a small prototype with slow acquisition (Sadrozinski et al. 2011), based on doped Cesium Iodide (CsI) crystal to measure the residual range, then extended to a larger one (Johnson et al. 2016), sufficient for a human head scan, which already provided advanced results. The “Phase-II Scanner” is based on two silicon-strip detector modules for the tracking section and five polystyrene-based scintillator segments for the range

?

measurements. In Figure 1.17b a proton CT image of an head phantom obtained with the first generation detector is shown. A similar system has also been studied in simulation by a group in Korea (Lee et al. 2016). The same tracking detectors are used in a Japanese collaboration project; the group developed a slow-acquisition and small aperture prototype and already planned an upgrade to a ten times larger system with increased acquisition rate capabilities (Saraya et al. 2014). The British collaboration Proton Radiotherapy Verification and Dosimetry Application (PRaVDA) tested a first prototype of a proton CT system entirely based on silicon detectors (Taylor et al. 2015, 2016). An alternative and simpler approach has been investigated with a system using a stack of 40 nuclear emulsion plates which records the proton tracks then reconstructed off-beam (Braccini et al. 2010); the results are interesting, even if such a solution is not suitable for real-time imaging. Even if the majority of the research efforts are devoted to proton application of the radiography/tomography technique, some tests have been made also for heavier ions. At NIRS, a combination a fluorescent screen viewed by a Charge-Coupled Device (CCD) camera and rotational range shifters has been investigated (Abe et al. 2002), together with a more conventional system composed of scintillating fibers for tracking and a thick plastic absorber (Shinoda et al. 2006). At HIT, studied setups involved silicon flat panel detector (Telssemeyer et al. 2012) or a range telescope consisting of a stack of parallel plate Ionization Chambers (ICs) with 3 mm thick plastic absorbers, and single beam spot-based radiographies have been performed (Rinaldi et al. 2013). All the listed systems produced promising results (Parodi 2014).

It is surprising that you don't mention "integral measurements" at a spot scale instead of at event-by-event basis

1.1.5.2 Positron Emission Tomography

As explained in section 1.1.1.1, the fragmentation processes involving target nuclei during proton therapy irradiation and both projectile and target nuclei in case of heavier ion beam therapy, can produce radioactive isotopes. In particular, β^+ emitting fragments are of significant interest for range verification purpose. Table 1.3 shows the main reaction channels and relative isotopes produced along a proton beam path in tissue. More details about the most relevant reaction channels and their characteristics (energy threshold, isotope decay constant, maximal kinetic energy of the emitted positrons), can be found in Oelfke et al. 1996. Additional channels and isotopes are produced during carbon ion irradiation, given the possible projectile activation.

Table 1.3: Proton-nuclear reaction channels and relative positron emitters produced in human tissues.
Table reproduced from Espa a et al. 2011b.

Target	Nuclear reaction channel	β^+ isotopes	Half-life
C	$^{12}C(p, pn)^{11}C$, $^{12}C(p, p2n)^{10}C$	^{10}C , ^{11}C	19.29 s, 20.33 min
N	$^{14}N(p, 2p2n)^{11}C$, $^{14}N(p, pn)^{13}N$, $^{14}N(p, n)^{14}O$	^{13}N (^{11}C , ^{14}O)	9.96 min
O	$^{16}O(p, pn)^{15}O$, $^{16}O(p, 3p3n)^{11}C$, $^{16}O(p, 2p2n)^{13}N$, $^{16}O(p, p2n)^{14}O$, $^{16}O(p, 3p4n)^{10}C$	^{14}O , ^{15}O , (^{11}C , ^{13}N)	70.61 s, 122.24 s
P	$^{31}P(p, pn)^{30}P$	^{30}P	2.50 min
Ca	$^{40}Ca(p, 2pn)^{38}K$	^{38}K	7.64 min

Figure 1.18 (top) shows the concept of the PET detection technique. The emitted positrons annihilate with human tissue electrons after traveling few mm distances, and 511 keV back-to-back photons are produced and can be detected in coincidence with PET machines. The spatial distribution of the β^+ decay points can be then obtained via the reconstruction of the so-called “lines of response” connecting the two detected photons, and it correlates, even if not directly, to the dose profile. Figure 1.19 shows the one-dimensional β^+ activity profiles along the beam axis for various incident beam types impinging on a PMMA target. The positron

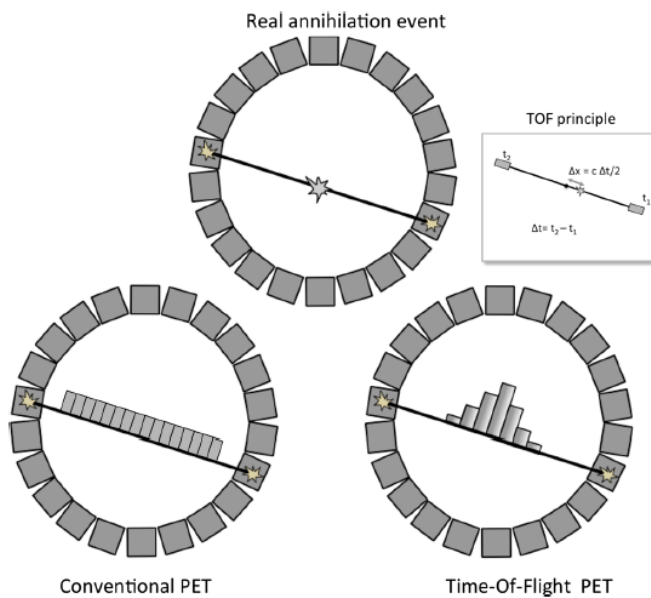


Figure 1.18: Schematic representation of the PET technique principle. In the top figure, a standard real annihilation event is presented, while in the bottom line the principle of conventional and Time-Of-Flight (TOF)-PET are compared. In Vandenberghe et al. 2016.

emitter distribution dependence on the beam nature clearly emerges from these profiles, but a form of indirect correlation with the dose profile distal edge is always verified. In particular, a remarkable difference exists between light ions (protons, ^3He and ^7Li), for which the induced activity is almost only due to target residuals, and heavier ones (^{12}C and ^{16}O), with a considerable contribution also coming from projectile fragmentation sub-products, which

the expected Bragg peak region

concentrate near the end of the range, explaining the activity peak. The investigation of the correlation between delivered dose and β^+ detected activity must face several issues, as highlighted in Parodi 2018, mainly connected to the difficulty to retrieve quantitative information from PET images and to wash-out effects. Long-lived positron emitters, indeed, can be transported away from the production point by blood flow and metabolic processes, affecting the precision of the obtained images. This effect has been deeply studied experimentally at HIMAC with rabbit tissues and Anger-type scintillation cameras (Mizuno et al. 2003; Tomitani et al. 2003), and, more recently, at GSI with ^{12}C beams (Fiedler et al. 2008a). A reduction of a factor up to 1.5 in the precision of the range determination due to wash-out processes is reported, and a correlation between biological half-life and local dose has been verified and used in simulation to improve the quality of PET images. Although several research efforts have been dedicated to improve the precision of the dose recovery from β^+ -emitter distributions (Parodi et al. 2006, 2010, 2007), the only feasible solution for the monitoring of dose delivery is the comparison of measured distributions to simulated ones (Pönisch et al. 2004). These Monte Carlo simulations are based on the planning CT scan, the irradiation scheme, the detector geometry, the imaging procedure; deviations in the delivered dose caused by patient positioning or anatomical modifications can be detected, mainly because they are reflected in changes in the maximum particle range in the target tissues. Thus, the main quality criterion of the PET monitoring method is the precision in the measurement of range shifts with respect to the predicted ones (Fiedler et al. 2010). The accuracy of the reference simulated activity distribution has advanced in the last years, but it is still limited by the lack of underlying cross-

sectional data, the not perfect knowledge of the elemental composition of the patient and the complex prediction of metabolic wash-out processes. Complementary imaging modalities can give fundamental contributions to the simulation predictions: for example, the use of supplemental MRI data has been proposed to better analyze local wash-out effects. In addition to this, the implementation of hybrid PET-CT systems, preferably with dual-energy CT, would improve the conversion of CT information to the material composition needed for the PET simulations (Landry et al. 2013).

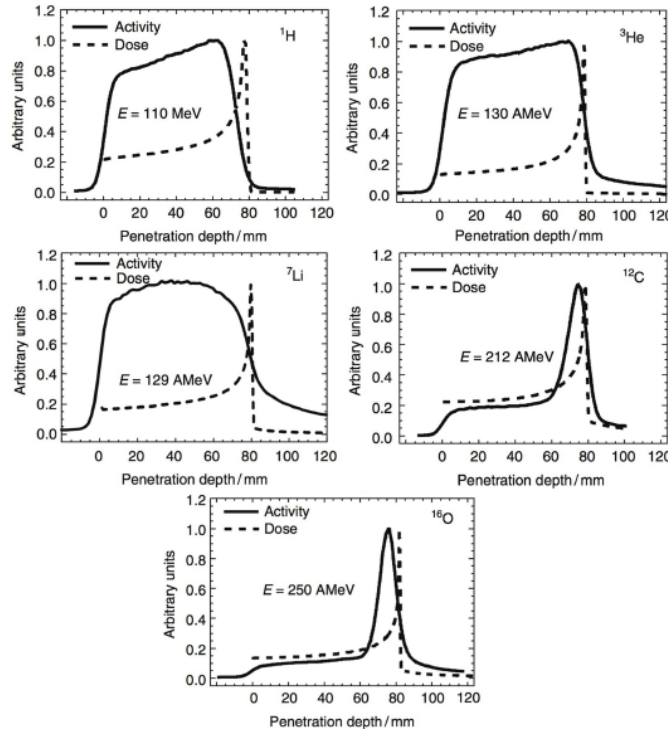


Figure 1.19: β^+ activity profiles for various ion beams impinging on a PMMA thick target. The depth-dose profiles are also shown in dashed lines for comparison. In Fiedler et al. 2012.

The PET data acquisition can be performed following three main strategies:

- In-beam data acquisition: the PET system is integrated in the beam delivery system and the data acquisition is performed during or immediately after irradiation in the treatment room. In synchrotron facilities, a further solution is represented by acquisitions in the time between different spills, while for cyclotrons data-taking during beam extraction has been explored and seems feasible (Kraan et al. 2014). On one hand, this method is advantageous because it allows detecting short-lived isotopes, thus increasing the available statistics, and reducing the effects of biological processes. Moreover, the patient position does not change with respect to the treatment. On the other hand, the integration of PET scanners in the treatment site can be costly and cause limitations on the detector geometry affecting detection efficiency and, consequently, image quality. The scanner should not be directly exposed to the beam in order to avoid damage and activation of active modules and electronics, and at the same time it should allow enough degrees of freedom for the patient table. The need of an opening for the beam portal typically results in the choice of planar dual-head configurations.

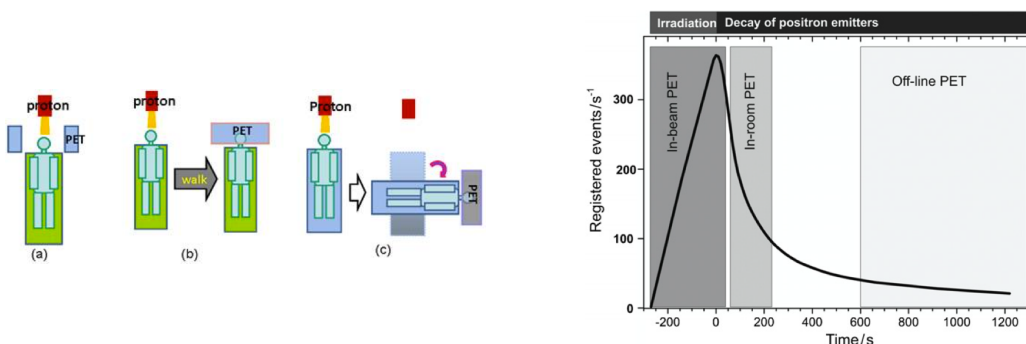
- In-room data acquisition: the installation of commercial full-ring PET scanners in the treatment room, but not directly on the beam line, allows the so-called “in-room” data acquisitions quickly after the end of the treatment irradiation. This solution leads to longer treatment room occupation, because some minutes of imaging time is required to gain enough statistics, but allows one to use commercial machines, less expensive and more efficient than custom integrated scanners designed for in-beam applications. Moreover, patient positioning issues are minimized by the limited movements and signal wash-out is reduced.
- Off-line data acquisition: if the patient has to be transported out of the treatment room for the PET scan, the implemented strategy is classified as “off-line”. The limited cost and treatment occupation time are probably the only advantages of this method, which suffers from relevant signal decay and wash-out processes given the long time between the end of the irradiation and the beginning of the PET scan. Off-line images predominantly show activity from isotopes whose half-life is comparable or longer *then* the transportation and setup time, thus it is mainly restricted to ^{11}C (half-life longer than 20 minutes), produced in relative small amount in proton therapy, more abundant in carbon treatments. The reduced number of available decays requires longer acquisition time with respect to in-beam and in-room solutions, which further enhance the effect of metabolic processes. The patient repositioning issues also contribute to the image quality degradation.

A schematic view of the three PET acquisition modalities is presented in Figure 1.20a. As mentioned in the three data acquisition modality description, the counting statistics is one of the fundamental parameters to be studied for the design of PET monitoring solutions. It can be estimated as the integral of the decay curve shown in Figure 1.20b, where the time intervals corresponding to the three acquisition strategies are separated. The curve is based on measurements performed at GSI during therapeutic irradiation with carbon ions; an in-beam solution has been adopted, with 40 s additional data taking time after the irradiation. The in-room selected window lasts 3 minutes, and for the off-line case, long-time measurements of one patient have been used (Fiedler et al. 2008b). If 100% is assigned to the number of registered true events in the in-beam condition, 50% is estimated for the in-room solution and 58% for the off-line data taking (Shakirin et al. 2011). It is then clear that off-line solutions are severely challenged by the extremely low signal, considerably lower with respect to the standard application of the employed commercial scanners (down to average activity values of few tens of Bq/ml (Bauer et al. 2013)). The scanner geometry is another fundamental parameter to be considered: as mentioned, the chosen data-acquisition strategy determines the scanner design. In-room and off-line solutions can make use of commercial full-ring systems, with a complete field of view. In addition to this, modern combined PET-CT scanners enable an accurate co-registration of treatment and imaging position, so that the unavoidable patient movement due to transportation and repositioning can be partially corrected. The geometrical constraints imposed by in-beam integrated solutions cause reduced efficiency and restricted field-of-view, which are reflected in image artifacts (Crespo et al. 2006), particularly significant in the imaging of large tumor objects. Improvement can be provided by TOF-PET detectors (Crespo et al. 2007; Surti et al. 2011), as discussed below. In Parodi 2015 the author highlights how the first historical attempts to implement PET particle therapy monitoring, described in the following, have not relied on optimized instrumentation for the peculiar application. Anyway, the promising results obtained by several groups encouraged dedicated investigations which are leading to substantial improvements of such a technique in the last

years. In particular, the application of gamma detectors with depth-of-interaction capability, also studied for standard diagnostics applications, has demonstrated its effectiveness in correcting parallax artifacts in the reconstructed images; improvements in data acquisition and synchronization with the accelerator radio-frequency offer the possibility of including the signal detected during the beam-on time for in-beam solutions, thus increasing the counting statistics and reducing the acquisition time; new adapted geometries, such as the Japanese OpenPET system (Tashima et al. 2012; Yamaya et al. 2008), recently finalized in its upgraded version (Yamaya 2017), offer higher-efficiency alternatives to standard dual-head systems. It is worth to dedicate particular attention to the already mentioned TOF-PET, deeply studied in the last years, which already demonstrated improved imaging capabilities with respect to standard scanners. The measurement of the detection time of each of the two photons helps, through the calculation of the arrival time difference, in restricting the emission point along the reconstructed line of response and thus also in rejecting part of accidentals. In standard PET, the three-dimensional reconstruction relies on the superposition of several lines of response and on filtered back-projection algorithms. The time information adds a second dimension to the line of response reconstruction, with the localization of the interaction point in a few cm along the line, depending on the detector time resolution. For example, a coincidence timing resolution of 600 ps FWHM translates to a position uncertainty of 9 cm FWHM. In Figure 1.18 (bottom line), the TOF-PET principle is sketched and compared to the conventional PET detection scheme. The potential benefits of TOF information in PET image reconstruction were already understood since the early stage of its development for diagnosis purpose, and the first TOF-PET systems were built already in the 1980s in the US (Gariod et al. 1982). They were based on Cesium Fluoride (CsF) or Barium Fluoride (BaF_2) scintillators, the best available at the time in terms of time resolution, but their spatial performance and sensitivity were poor with respect to conventional PET scanners. The improvements in scintillating material as well as in Photo-Multiplier (PM) performance and reliability allowed for the first commercial proposal of a TOF-PET scanner only in 2006, by Philips (Surti et al. 2007). The development of TOF-PET machines is strongly connected to their application in diagnosis, and further details will be given in section 1.2.2. As for particle therapy monitoring application, the TOF technique applied to PET can be used to partially reverse the effects caused by non-complete angles of in-beam data collection (Crespo et al. 2006), and in general to improve the image quality. Various groups are developing detector solutions for clinical implementation of such a technique; some of them have already been tested on beam with promising results. They will be described in more details in the following, after a brief historical overview of the PET application in particle therapy quality assurance.

As emerges from the above paragraphs, PET is probably the most extensively studied technique for online beam range verification and is at present the only method clinically implemented (Enghardt et al. 2004). The first published proposal of using PET for range verification in particle therapy dates back to 1975 (Bennett et al. 1975). In the next years, further suggestions were connected to pion (Goodman et al. 1986; Shirato et al. n.d.) and neutron therapy (Vynckier et al. 1989), but the actual clinical implementation was pioneered in the context of heavy ion therapy at Lawrence Berkeley Laboratory (LBL) (Chatterjee et al. 1981; Llacer et al. 1979). The original idea was to verify the correctness of ${}^{20}\text{Ne}$ ion therapy treatment plans by delivering a low dose β^+ emitting ion beam (e.g. ${}^{19}\text{Ne}$) prior to the treatment and measuring its range via PET imaging of the emitted photons; before the regular treatment with stable beams. Pilot experiments were conducted with a planar PET camera based on two blocks of Bismuth Germanium Oxide - $\text{Bi}_{12}\text{GeO}_{20}$ (BGO) crystals, including measurements in a live dog (Llacer et al. 1984a). The experimental data showed interesting results, even

Reference
not adequate



(a) Schematic view of the three PET configurations for the application in ion range monitoring. Form left to right: in-beam, off-line and in-room PET. In Zhu et al. 2013.

(b) PET registered events as a function of time corresponding to the measurement of one field during irradiation and up to 20 minutes after irradiation. The time intervals corresponding to in-beam, in-room, and off-line PET measurements are highlighted. In Shakirin et al. 2011.

Figure 1.20: The application of the PET technique to the monitoring of ion range in particle therapy includes three possible modalities: in-beam, in-room and off-line PET, represented in the scheme in (a). The amount of registered events depends on the created positron emitter half-life, and thus on the implemented modality, as shown by the histogram in (b).

if the use of a passive beam shaping system determined a significant activation of the BGO camera (mainly due to neutrons) and, thus, a substantial noise level. Analog investigations using radioactive ion beams (^{15}O , ^{17}F , ^{19}Ne) were carried out in the nineties at GSI with various PET cameras (Pawelke et al. 1996), and further developments of this technique were obtained at the HIMAC facility (Iseki et al. 2004; Kitagawa et al. 2006), where a dedicated line was set up for radioactive beam based treatments (Kanazawa et al. 2002; Urakabe et al. 2001). The “autoactivation” process (Tobias et al. 1971) described above (i.e. the production of radioactive nuclei in the target by incident beam of stable ions) makes anyway possible the implementation of PET monitoring techniques on standard high-energy beams, and the first clinical implementation of such technique was launched at GSI in 1997, after the tests with radioactive beams mentioned above and fragmentation studies conducted with ^{12}C , ^{16}O , ^{20}Ne beams on a PMMA target (Enghardt et al. 1992). An in-beam PET system was designed and installed into the treatment room and has been employed routinely for monitoring the irradiation of more than 440 patients (mainly suffering from head-and-neck cancer), with data acquisitions performed in the pause of pulsed beam delivery. This experience proved how PET is a valuable tool for particle therapy quality assurance (Enghardt et al. 2004). In parallel to these developments in Germany, an off-line solution was implemented at NIRS with a commercial full-ring volumetric scanner, but it was not used in clinics. As previously explained, notwithstanding the lacking peak structure in the activity profile (cf. Figure 1.19), also proton irradiation therapy can be monitored by PET scanners. Various detailed studies investigated its feasibility and performance in the nineties (Litzenberg et al. 1992, 1999; Oelfke et al. 1996; Paans et al. 1993). Two groups worked in parallel on clinical studies of PET monitoring in proton therapy. In Japan, a dual-head PET scanner has been installed at the National Cancer Center, Kashiwa (Nishio et al. 2006): it is based on high-resolution BGO detector components and integrated in the proton gantry. The measurements are collected immediately after

New paragraph

irradiation (in-room solution), mainly due to the considerable radiation background during the continuous beam delivery and the passive beam shaping. The satisfactory results led to the implementation of a daily PET workflow, which allowed the research group to follow the anatomical changes of the patient during the treatment progress and correct the treatment planning. The test of this method included 48 patients suffering from head-and-neck, liver, lung, prostate and brain tumors (Nishio et al. 2010). In the US, at the Massachusetts General Hospital (MGH), Boston, a pilot clinical study was performed with an off-line solution which made use of a commercial full-ring scanner (Parodi et al. 2007). The PET scan was performed about 20 minutes after proton irradiation. The off-line approach has been deeply studied in the same context in those years, and compared to in-beam PET solutions in cyclotron and synchrotron based scenarios (Knopf et al. 2011; Parodi et al. 2008). The advantage in terms of available statistics for in-beam solutions has been measured: the ratios between the amount of physical decays available for in-beam and off-line detection range from 40% to 60% for cyclotron-based facilities, to 65% to 110% (carbon ions) and 94% to 166% (protons) at synchrotron-based facilities (Parodi et al. 2008). The in-room solution has also been explored at the same institution, with an acquisition time reduced to less than 5 minutes thanks to the higher sensitivity with respect to the off-line modality (Zhu et al. 2011). At HIT, in Germany, both an in-beam (Sommerer et al. 2009), and an off-line solution (Bauer et al. 2013) have been tested, while alternative off-line solutions have been implemented in Japan (Hishikawa et al. 2002) and US (Hsi et al. 2009). With the aim of extending the field of view and thus enhancing the sensitivity of in-beam PET designs, Japanese researchers proposed the already mentioned OpenPET as a new geometrical solution. Its first-generation prototype is composed of two complete rings, with the beam port between the two (Yamaya et al. 2008, 2009) and the possible implementation of an integrated CT. A more efficient geometry has been proposed some years later, consisting of a single-ring which can provide an accessible and observable open space with higher sensitivity and reduced number of detectors compared to the previous generation one (Tashima et al. 2012). The ring is cut at a slant angle in order to be disposed at a certain angle with respect to the beam line, but maintain parallel detector modules orientation. A similar solution was proposed in Crespo et al. 2006, but with a conventional PET ring with an oblique orientation with respect to the beam direction ("slant PET"). A small prototype of single-ring OpenPET was produced, consisting of 4 layers (16×16 array) of Zr-doped GSO scintillators with a size of $2.8 \times 2.8 \times 7.5 \text{ mm}^3$ read out by H8500 Hamamatsu PMs (Tashima et al. 2016), and tested at HIMAC with radioactive ^{11}C beam. The prototype can operate in open and closed mode, the second only adapted for acquisition in beam-off condition, and easily arranged in the two configurations. The tests, performed in the two modes, the spatial resolution and sensitivity were 2.6 mm and 5.1% for the open mode and 2.1 mm and 7.3% for the closed one. A rapid transformation to a closed arrangement is foreseen by the authors immediately after irradiation in order to minimize the decrease of resolution and sensitivity. After these encouraging results, a full-size whole-body version of the single-ring OpenPET has been recently completed (Yamaya 2017). Extensive studies about PET monitoring have been and are being carried out also in Italy. An in-beam prototype consisting of two planar heads made of Lutetium-Yttrium Oxyorthosilicate - $\text{Lu}_{2(1-x)}\text{Y}_{2x}\text{SiO}_5$ (LYSO) crystals (Vecchio et al. 2009), $5 \times 5 \text{ cm}^2$ active area, has been tested at the proton therapy center CATANA, in Catania, equipped with a 62 MeV beam line for ocular tumor treatments (Cirrone et al. 2003). The measurements validated the detector design (Attanasi et al. 2008), which has been called DoPET and also compared to the in-beam system installed at GSI with simultaneous measurements of β^+ activity induced in a PMMA target (Attanasi et al. 2009), showing improved spatial resolution mainly due to the smaller crystals. The field of view of the first prototype was a major issue, so that an extended version with $10 \times 10 \text{ cm}^2$ active area per head has been realized.

and tested by the Italian collaboration at CNAO (Kraan et al. 2015; Rosso et al. 2013) and in Catania (Camarlinghi et al. 2014; Sportelli et al. 2014). The comparison of the results with Monte Carlo simulated data showed good agreement; for treatment-like data taking, the ability of the system to give valuable feedback on particle range on homogeneous targets within 2 minutes after irradiation has been demonstrated, but the data collected during beam-on time were not satisfactory. In the context of PET data taking during beam-on time, several studies have been performed concerning short-lived isotopes, which has to be included in the total activity evaluation in case of in-spill acquisitions. Already mentioned in the DoPET related publications, they have been deeply studied experimentally. Defined as positron emitters with half-life below 19 s, the ones significant for in-vivo PET monitoring have been identified in Dendooven et al. 2015: in particular, the author concludes that the contribution to the β^+ activity given by ^{12}N isotopes in the first tens of seconds after irradiation can potentially lead to real-time range verification of proton therapy with the implementation of optimized knife-edge detectors, providing equal or superior information with respect to PG detection (see section 1.1.5.3 and chapter 2). A proof-of-principle experiment for the detection of such isotopes has been performed at the KVI-CART cyclotron with 90 MeV protons and a PET system based on LYSO crystals coupled to digital Silicon Photo-Multipliers (SiPMs) (Buitenhuis et al. 2017). A range shift of 5 mm could be measured with 3 mm accuracy using the ^{12}N activity profile. Another PET prototype based on SiPMs is the one developed by the Italian Innovative Solutions for Dosimetry in Hadrontherapy (INSIDE) collaboration (Marafini et al. 2015), and described in (Bisogni et al. 2017). The design is based on fast pixelated Lutetium Fine Silicate (LFS) scintillators coupled one-to-one to SiPMs. The readout electronics has been developed to accept the count rate expected from synchrotron beams during the spill phase (Rolo et al. 2013). The whole system also includes a charged particle tracker (“dose profiler”), and its design has been studied for the installation on the CNAO beam line, where it has been tested and is at present in operation. The first characterization tests performed with PMMA and anthropomorphic phantoms demonstrated the capability of the system to operate in both beam-on and -off condition, and the comparison between in-spill and interspill data showed a substantial agreement in terms of distal fall-off. The results were also in agreement with Monte Carlo simulated data. In December 2016, the INSIDE PET was also tested during a patient treatment, and the possibility of online monitoring of proton therapy in clinical conditions has been demonstrated (Ferrero et al. 2018). For carbon ion irradiation, in-spill measurments have not been satisfactory due to the large amount of random coincidences, but at treatment end, or at most 20 s afterwards, the range measurement has been verified to be reliable within 1–2 mm, when comparing both different experimental sessions and data with simulations (Pennazio et al. 2018). Digital photon counters have been the basis for the development of TOF-PET prototypes, attractive solution for improved spatial reconstruction capabilities in both full-ring and dual head solutions. Within the European project ENVISION, two different configurations have been explored for in-beam TOF-PET imaging: one of them relies on LYSO crystal read out by SiPM, and a TOF resolution of 235 ps Coincidence Resolution Time (CRT) FWHM have been obtained (Morrocchi et al. 2012). The alternative solution involved low-cost gas detectors (multigap Resistive Plate Chamber (RPC)), but it was less performing in terms of time resolution (Watts et al. 2013). Another small prototype based on LYSO crystal and digital photo-sensors, presented in (Degenhardt et al. 2012), has been tested for TOF application in clinical conditions at HIT with protons. The acquisitions were performed in the pauses between spills or after irradiation, providing relevant information for a future development of a clinical size detector (Cambraia Lopes et al. 2016).

The *Contrôle en Ligne de l'hadronthérapie par Rayonnements Secondaires* (CLaRyS) collabora-

Dont' mention CLaRyS here

tion, in France, also included in its research project proposal the development of an in-beam PET detector; the advancement of the study is at present limited to the Laboratoire de Physique de Clermont, France (LPC) research group. The prototype, called *Détecteur Pixélisé de Grande Acceptance* (DPGA) (French) or Large Area Pixelized Detector (LAPD) (English), is composed of 240 identical $13 \times 1 \times 315 \text{ mm}^3$ LYSO crystals glued to PMs, assembled in groups of four (“quartets”) with similar gain PMs for the read-out on a custom Front-End (FE) board (Montarou et al. 2016). The system has been first tested in a hospital in Clermont-Ferrand with a PMMA phantom and Fluoro-Deoxy-Glucose (FDG) injected radiotracer (some tenth of MBq of activity), and then with proton beams at HIT, in a reduced-size version. These first tests have been used to validate and characterize the detector, but limited acquisition rate capabilities have been verified with the preliminary VERSABUS Module Eurocard (VME)-based solution. The prototype is now installed at the CAL in Nice, on the 65 MeV line, and the new acquisition system based on Micro Advanced Telecommunications Computing Architecture (μ -TCA) is at the test stage.

PET is at present the only applied solution for ion range monitoring in clinical conditions (Enghardt et al. 2004), and, as described, the research is ongoing to provide real-time control capabilities with improved image quality. Its principle can also be applied to hybrid systems, investigated in the last years and briefly mentioned in section 1.1.5.5, including the detection of β^+ activity in combination with PGs (see section 1.1.5.3 and chapter 2) or additional single photon emission. This implementation will probably imply compromises in the individual technique performance, but their complementary information can open new perspectives for *in vivo* ion range verification.

1.1.5.3 Prompt-gamma detection

An alternative way to access valuable information about the Bragg peak position of both proton and carbon ion beams in human tissue is represented by the detection of high-energy photons promptly emitted as a by-product of nuclear interactions (see section 1.1.1). For many years, this kind of radiation was investigated as a source of background in PET-based monitoring system (Parodi et al. 2005), mainly because the produced photon energy is too high to be detected with standard devices like Single Photon Emission Computed Tomography (SPECT) cameras (Kraan 2015). The idea of using prompt-gamma radiation to obtain a direct and instantaneous verification of the beam stopping position in tissues was first proposed by Stichelbaut and Jongen at the 39th Particle Therapy Co-Operative Group (PTCOG) meeting in 2003 (Stichelbaut et al. 2003). Experimental verification of the correlation between prompt-gamma profiles and Bragg peak position has been presented for protons and carbon ions (Min et al. 2006; É. Testa et al. 2008) few years later, and the method is nowadays deeply studied as a promising solution for online range verification in clinical conditions. The research efforts involve imaging and time or energy resolved techniques, for which several detection solutions are being developed and tested. My thesis project is carried out in this context, so that the chapter 2 of this manuscript is dedicated to the prompt-gamma detection physical principle for range verification and specific attention is devoted to the state of the art of this research field. The details of the detection solution under development by the CLaRyS collaboration, within which this thesis has been conducted, are presented in chapter 3 and chapter 6 (dedicated to the detector beam tests); the simulation results of the clinical application of the Compton camera for proton and carbon ion range verification are illustrated and discussed in chapter 4.

1.1.5.4 Interaction Vertex Imaging

As described in section 1.1.5.1, high-energy traversing ion beams can be used for radiography and tomography purposes in order to increase the accuracy of stopping power measurements for treatment planning. The detection of protons can also be used as a treatment monitoring technique, if secondary protons produced in nuclear collisions are considered. This ion range control modality has been proposed less than a decade ago (Amaldi et al. 2010b; Dauvergne et al. 2009) and is generally referred to as Interaction Vertex Imaging (IVI). The charged particles created during fragmentation processes in the target can be energetic enough to exit the patient and are most likely forward directed; thanks to a detector located downstream from the patient, their trajectories can be then reconstructed and extrapolated back to the production point. The principle is similar to vertex identification problems in fixed target particle physics experiments. The comparison of the obtained distribution with the one simulated at the treatment planning stage provides a means of controlling the ion range. In addition, the amount of emerging charged particles can be, in principle, correlated to the dose. Given the larger amount of protons generated by carbon irradiation with respect to proton ones (Gunzert-Marx et al. 2008), this method is more suitable for carbon ion therapy monitoring. A feasibility study has been presented in Henriet et al. 2012; the authors investigated the possible implementation of such a control in carbon ion therapy with Geant4 simulations. The modeled detector is composed of two pairs of $50 \mu\text{m}$ thick pixelized Complementary Metal Oxide Semiconductor (CMOS) trackers, placed at an angle of 30 degrees with respect to the beam direction, and two methods have been tested, one based on the coincidence of two protons emitted from the same vertex, the second relying on the incident carbon ion trajectory determined by a beam hodoscope in coincidence with single secondary proton detection. The study showed the possibility of achieving millimetric precision on the Bragg peak position in the ideal case of homogeneous targets with pencil beams of 2×10^5 carbon ions. Experimental tests have been conducted at HIT with a similar setup involving hybrid-pixel detector with CMOS read-out, and with higher statistics the accuracy in the beam range monitoring was found to be 1-3 mm (Gwosch et al. 2013). In the experimental studies reported in Agodi et al. 2012 and Piersanti et al. 2014, PMMA targets have been irradiated with mono-energetic carbon-ion beams at different energies, and secondary protons have been measured with systems placed at 60 and 90 degrees with respect to the beam direction; the results have been compared to FLUKA predictions, and reasonable agreement has been verified. The detector developed by the TERA Foundation at CERN (Bucciantonio 2015) has been also proposed as a solution for IVI, but it has never been tested for this purpose. Recently, the method was tested in clinical conditions with measurements performed at HIT; the resolution of the Bragg peak position was found to be about 4-5 mm in an homogeneous PMMA phantom with 10^6 incident carbon ions (Finck et al. 2017). The IVI method could therefore monitor the Bragg peak position with a promising resolution in clinical conditions, but further efforts are needed to improve Monte Carlo predictions of the angular distribution of the fragments, as well as to increase acceptance and efficiency of the employed detectors.

Tracker size of $2 \times 2 \text{ cm}^2$

1.1.5.5 Other techniques

The detection of secondary radiations emerging from the patient body during particle therapy is not the only available channel for measuring the ion stopping position and, more generally, verify the treatment delivery. The dose delivered in photon and electron treatments have been

Point measurements

1 Context

measured in vivo with diodes and thermo-luminescence dosimeters, as reviewed in [Essers et al. 1999](#), and implantable devices with wireless readout have been introduced in standard radiotherapy ([Black et al. 2005](#); [Scarantino et al. 2008](#)) and investigated for proton range verification. The main challenge is the positioning of the detector, which strongly influences the measurement of the steep dose distal fall-off of ion beams, and two solutions have been proposed by the same author to overcome this issue. The residual range of the irradiation beam can be retrieved at each position via its time dependence, which is unique at every point in depth ([Lu 2008b](#)). This method, proposed for passively scattered beams but also applicable to actively scanned ones, has been tested with a small IC, and sub-millimeter precision for the determination of the proton range at a specific position in water has been proven (even if in ideal conditions). The second proposed method relies on the delivery of a pair of complementary fields, with sloped depth dose profiles ([Lu 2008a](#)). The ratio between the two measured distributions can verify the radiological path length. As the previous one, this approach has been experimentally tested, in this case with a commercial implantable dosimeter ([Lu et al. 2010](#)), and dose ratios have been measured with a relative uncertainty of 1-3%. Notwithstanding the valuable obtained results, the applicability of both solutions is strongly limited by the need of implanting devices in the patient, ideally close or within the tumor, which is often not possible. In any case, possible improvements are still being studied recently ([Toltz et al. 2017](#)). An alternative way to measure the range with simple detectors in one dimension is the so-called “range probe” ([Mumot et al. 2010](#); [Watts et al. 2009](#)). This concept relies on the direct measurement of the Bragg peak of single high-energy pencil beams passing through the patient, in a sort of simplified mono-dimensional version of proton radiography discussed in section 1.1.5.1, and can in principle both validate the range in vivo and verify patient positioning errors with low additional dose. MRI imaging has also been considered as a way to observe delivered dose distributions. The application of such a technique is made possible by the changes induced by radiations in tissues, and it has been investigated mainly for spine patients ([Gensheimer et al. 2010](#)), but the accuracy was not sufficient to verify the ion range, but the high spatial resolution achievable with commercial scanners is a good point in favor of further investigations.

MRI imaging

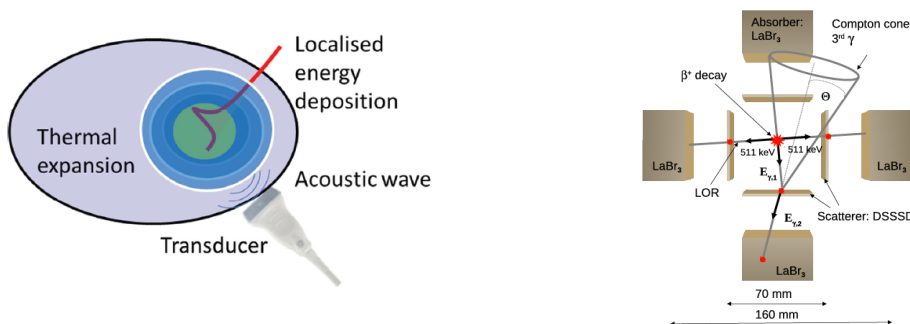
The application of such a technique is made possible by the changes induced by radiations in tissues, and it has been investigated mainly for spine patients ([Gensheimer et al. 2010](#)), but the accuracy was not sufficient to verify the ion range, but the high spatial resolution achievable with commercial scanners is a good point in favor of further investigations.

Acoustic imaging

The improvement of ultrasound imaging techniques determined in the last years a renewed interest on its application to ion range verification. It has been demonstrated that iono-acoustic detectable signals are produced by the localized dose deposition of ion beams ([Tada et al. 1991](#)), which induces local temperature increases and, thus, a pressure wave ([Parodi et al. 2015](#)); these pulses have been already measured in 1995 in a proton therapy treatment ([Hayakawa et al. n.d.](#)). A schematic view of the detection principle is presented in Figure 1.21a. Recently, tests on proton beam have been performed at the CAL, in Nice, with mono-energetic beams in the energy range 145-227 MeV ([Lehrack et al. 2017](#)); as the author stated, the method as been proven to be a cost-effective, fast and accurate way to obtain quality control measurements in proton therapy, with sub-millimeter range determination accuracy (the results have been compared to reference data collected with an IC). However, it has been highlighted how the synchrocyclotron offered ideal condition for the application of iono-acoustic measurements, thanks to the delivered intense and short (microsecond) bunches. Signal-to-Noise Ratio (SNR) is an additional problem at the present development stage, but it has to be pointed out that iono-acoustics offers a method not only to locate the Bragg peak, but also to correlate it with an ultrasound tumor image; the research effort is so clearly justified, and improvements are expected in the next years. To be noticed, anyway, that the iono-acoustics probes can be used only with soft tissues, so that their application, for example in head-and-neck treatment monitoring seems not feasible. In addition to the deeply investigated techniques based on secondary particles generated by nuclear reactions (PET and PGs), there are also photons emitted by Bremsstrahlung ion deceleration.

Bremsstrahlung imaging

The basic principle is explained in Yamaguchi et al. 2012, where the author highlights that the dependence of the bremmstrahlung photon energy spectrum on the incident beam energy provides a method to control the beam range. In particular, secondary electron bremmstrahlung dominates at low ion energies, close to the Bragg peak, and its energy spectrum allows one to retrieve the correlated Bragg peak position. A complete experimental confirmation has been provided with measurements performed in Japan in different centers (HIMAC among them) with carbon ion beams and a Cadmium Telluride (CdTe) detector, involving also background estimates. This technique provides in principle an overall better sensitivity with respect to PG detection and PET, and completely avoids the wash-out effects which affect positron emitter activity measurements, and has been developed in the last years. As secondary electron bremmstrahlung cross section scales as Z^2 , this method is potentially advantageous for carbon ions. In particular, mono-energetic carbon ion beams have been recently imaged with a pinhole gamma camera (Yamaguchi et al. 2018), but the clinical necessary resolution in detecting range shifts has not been achieved yet. In addition, given the low energy of the emitted Bremsstrahlung photons, this technique is intrinsically limited to superficial tumor treatment control.



(a) Schematic view of the basic principle of iono-acoustic waves detection for ion range verification. In Parodi et al. 2015.

(b) Conceptual design of the 3- γ detection system proposed in Lang et al. 2014, composed of multiple Compton camera arms for the detection of correlated PET and de-excitation gammas or PET and prompt photons produced in nuclear interactions during particle therapy treatments. In Lang et al. 2014.

Figure 1.21: Alternative methods for in-vivo range verification of ion beam therapy include the detection of iono-acoustic waves produced by the localized dose deposited by the energetic ion beams, whose principle is sketched on the left side, and hybrid systems for 3-photon detection, which can be applied to both nuclear medicine diagnostics and hadrontherapy monitoring, as the one sketched on the right side.

Also water luminescence effects have been verified during the irradiation with proton pencil beams, and are under investigation as a promising solution for range and field width estimations (Komori et al. 2018). As mentioned, the listed methods have been proposed as alternatives with respect to the more investigated detection of secondary emitted photons, both from positron annihilation and prompt-emission. These two techniques are anyway the most advanced ones, and also hybrid systems are under investigation to obtain a combination of their main advantages and a potential reduction of the identified drawbacks. The so-called “3- γ ” imaging concept has been explored in France and Germany. The French group combined

Water luminescence

Hybrid systems

1 Context

a standard full ring PET scanner with a time projection chamber filled with liquid xenon for the Compton measurement ([Oger et al. 2012](#)), while the German one focused on multiple Compton camera heads for the detection of the three γ s ([Lang et al. 2014](#)). This system, although originally designed for the detection of positron annihilation photons and correlated de-excitation rays for nuclear medicine application, can be adapted to perform combined detection of 511 keV photons from β^+ emission and PGs, as already highlighted in ([Lang et al. 2014](#)). A conceptual detector design for such an applications shown in Figure 1.21b. Another interesting simulation study applying this “whole-gamma imaging” concept in nuclear medicine is reported in ([Yamaya et al. 2017](#)). Further information about hybrid systems can be found in chapter 2 for what concerns the application in ion range verification and in section ?? for the investigation devoted to the nuclear medicine field.

1.2 Nuclear medicine

Nuclear medicine is a medical specialty which makes use of particle physics concepts (in addition to medical, biological and chemical knowledge) and instrumentation to study physiological processes and perform non-invasive diagnostic examinations and disease treatments. More specifically, nuclear medicine groups all the medical techniques which foresee the use of chemical compounds containing a radioactive isotope; this radio-pharmaceutical is given to the patient (or mixed to patient samples, for example blood) orally, by injection or by inhalation, and the isotope decay products are used to deliver a treatment dose, for example to cancerous tissues, or for imaging purpose, in case the emitted particles can exit the body and be detected by radiation detectors. This thesis focuses on the development of gamma detectors, originally designed for the application in particle therapy; the following sections are devoted to delineate the context in which the studied detectors can be applied for diagnostics, and simulation results of such an application are reported in chapter 5.

Some hints about the historical origins of this medical fields have been given in the introduction of this chapter. The use of radioactive isotopes for medical purposes has been investigated since 1920, at the beginning only theoretically, then, since 1940, attempts have been undertaken at imaging radio-nuclide concentration in the human body. The first scan of a radio-nuclide activity in the body was obtained with a very slow planar scanner introduced by Ben Cassen at the beginning of the fifties (Blahd 1996), and less than 10 years later Hal Anger developed the first gamma camera, introducing the approach still followed for the modern detectors (Anger 1958). The Anger scintillation camera is a planar physically collimated detector which produced two-dimensional projection images of the radio-isotope activity without scanning. The Anger camera, if rotated around the patient, can also be used for tomography, with reconstruction algorithms able to reproduce the three-dimensional emission distribution from two-dimensional multiple-angle slices. The method to reconstruct images from projections had been published by Radon in 1917 (Radon 1917), and then applied in CT and nuclear medicine after 1970. Iterative reconstruction methods were also being investigated, but their application started in the eighties when more computer power became available. The tomographic translation of the Anger gamma camera determined the born of SPECT imaging: together with PET, SPECT is still the basis of present diagnostic nuclear medicine. The idea of detecting photon pairs produced by positron annihilation is also attributed to Anger, but the first dedicated PET system was built by Ter-Pogossian and colleagues in the 1970s, and employed for phantom and animal studies (Ter-Pogossian 1983; Ter-Pogossian et al. 1975). Soon afterwards, Phelps, Hoffman and colleagues built the first whole-body PET-scanner (Hoffmann et al. 1976). In the next sections, the physics of radioactive decays is briefly reminded to introduce the detailed discussion of PET and SPECT techniques, including a short historical overview, the presentation of the imaging principle and an overview of state-of-the-art machines.

1.2.1 Radiotracers

Nuclear medicine imaging techniques are based on radio-tracers. A tracer is a chemical compound which transports an unstable isotope (radio-nuclide); this molecule is designed to be involved in specific metabolic processes and, thus, to concentrate in the area to be targeted for imaging purpose. The γ -rays emitted by the radio-nuclide can be measured as a function

of position and time, providing anatomical and metabolic information. In the following, the main physical aspects of radioactive decays are briefly recalled.

As mentioned, a radio-nuclide is an unstable isotope of a chemical element which decays towards a stable atomic configuration and loses energy by emitting radiation in the form of particles and electromagnetic rays. The decay can involve several steps, if the resulting “daughters” are still unstable, and the process continues until a stable nuclide is reached. Some general features of radioactive decay processes can be detailed mathematically without regard to a specific mechanism. In particular, the decay rate of a sample of radioactive nuclides depends on the nuclides population N , according to a decay constant noted as λ , as expressed by equation 1.15.

$$\frac{dN}{dt} = -\lambda N \quad (1.15)$$

On one hand, the decay constant λ is specific of each nuclide, and reflects its degree of instability. The decay rate, on the other hand, is a representation of the sample activity, which is measured in the International System of units (SI) in Bequerel (1 Bq = 1 disintegration per second) and its multiples, even if an older and still used unit is the curie (Ci) (1 Ci = 3.7×10^{10} disintegration per second). The solution of the differential equation in 1.15 gives the number of parent atoms N at any time t , or the activity by multiplying both side by λ :

$$\begin{aligned} N &= N_0 e^{-\lambda t} \\ A &= A_0 e^{-\lambda t} \end{aligned} \quad (1.16)$$

with N_0 and A_0 the original number of parent atoms and the original activity, respectively. Following these first expressions, the physical half-life $T_{1/2}$ of a radioactive nuclide is the time required for the decay of half of the atoms in a sample; its mathematical form is reported in equation 1.17.

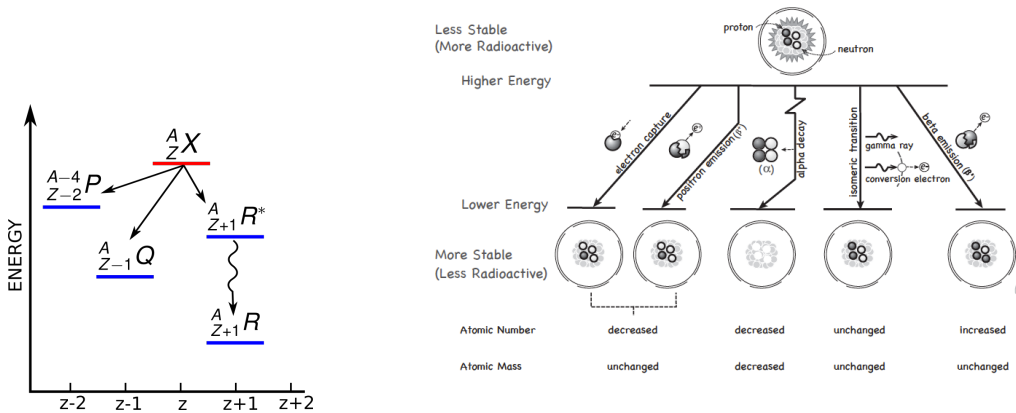
$$T_{1/2} = \frac{\ln 2}{\lambda} = \frac{0.693}{\lambda} \quad (1.17)$$

Several decay modes exist, and they can be divided into three main categories: emission or capture of nucleons (protons and neutrons), emission or capture of β -particles (electron and positrons), emission of photons. In particular, five main decay channels have been identified:

- α -decay;
- electron emission - β^- -decay;
- electron capture;
- positron emission - β^+ -decay;

- isomeric transition.

In Figure 1.22a the decay scheme of a generic nuclide ${}^A_Z X$ is depicted (A is the atomic mass, Z the number of protons); the α -decay produces ${}^{A-4}_{Z-2} P$, electron capture and positron emission equivalently generate ${}^A_{Z-1} Q$, while ${}^A_{Z+1} R$ originates from electron emission and can be created in a metastable configuration ${}^A_{Z+1} R^*$ which then decays to the stable state via isomeric transition with the emission of a photon.



(a) Radioactive decay scheme. In Hendeel et al. 2002

(b) Schematic view of the radioactive decays. In Powsner et al. 2013.

Figure 1.22: The various radioactive decay channels are schematized in (a) for a generic isotope ${}^A_Z X$. A more detailed scheme, describing the decay processes and products, is given in (b).

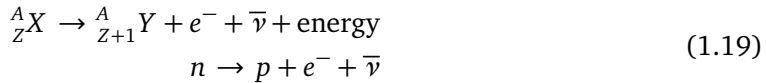
The α -decay is the spontaneous emission of an α particle (i.e. an helium nucleus, consisting of two protons and two neutrons), typically from heavy nuclides ($A > 150$). It was discovered by Marie and Pierre Curie in 1898 (Curie et al. 1898) and first described by Rutherford one year later (Rutherford 1899), who also identified the α particles as helium nuclei, together with Boltwood in 1911 (Boltwood et al. 1911). The decay can be described by equation ???. Often it is followed by the emission of characteristic x-ray or gammas, accompanied by competing processes of internal conversion and Auger electron emission. The produced α particles have energies in the range 2-10 MeV and are not used for imaging purposes, given the very limited range in tissues (about 100 μ m). This characteristic makes such a decay appropriate for therapy, even if the very short decay time is a limiting factor. Only the α -decay of a few high-Z elements is actually used, for example, for tumor irradiation in the so-called “internal radiotherapy” or “brachytherapy” (Dahiya 2016; Suntharalingam et al. 2005).

α -decay



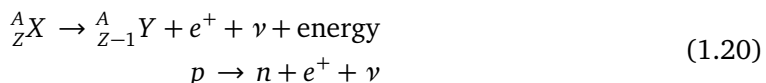
The decay via emission of an electron (β^- - or negatron-decay) can be seen as the conversion of a neutron in a proton-electron pair, as in the generic reaction reported in equation 1.19.

Electron emission



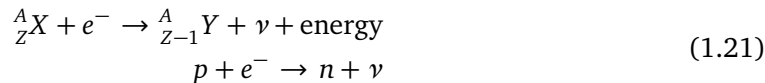
This decay channel pertains to nuclei with a N/Z ratio (with N the number of neutrons) too high for stability and results in nucleus with Z increased by one, N decreased by one and so the same atomic mass A (isobaric transition) but a different chemical element. β^- -decay pathways are characterized by specific maximum energies E_{\max} , but in most of the cases the emitted electron energy is lower than the maximum, with an average value of approximately $1/3 E_{\max}$, and the remaining energy is carried away by the anti-neutrino. This results in poly-energetic energy spectra for the emitted electrons. The difference in the energy released during decay and the one possessed by the emitted electron threatened the energy conservation law for years. In 1930, in a letter, Wolfgang Pauli suggested that a second particle was emitted during the decay, explaining the energy, momentum and angular momentum conservation. The name neutrino was attributed to such a particle by Enrico Fermi. Any possible excess energy in the nucleus after the decay (metastable state) is emitted as gamma rays or internal conversion electrons. As for the α particle case, electrons have limited range in matter, thus release dose to the tissues, and have no diagnostic value (but they are used in brachytherapy), but metastable states deriving from β^- -decays are pure sources of γ -rays and are so employed for imaging. One of the most diffused tracer is a metastable daughter of ^{99}Mo , the ^{99m}Tc ; it decays in stable ^{99}Tc (half life = 6 hours) by emitting a 140 keV photon.

Positron emission On the other side of the “nuclide stability line”, neutron-poor radionuclides (with low N/Z ratio) tend to decay by the emission of a positron (β^+ decay) and to increase the neutron number by one. As shown by equation 1.20, the net result is the conversion of a proton into a neutron with the ejection of a neutrino, in addition to the positron. As in the previous case, the transition is isobaric because the total number of nucleons is unchanged.



The emission of positrons was discovered in 1933 by the Marie Curie daughter Irene Curie and her husband Frederic Joliet, in bombardments of aluminium by α particles (Leone et al. 2010). Even if the reaction principle is similar to β^- -decay, an important difference resides in the behavior of the decay product. Both electron and positron undergo energy deposition processes by excitation and ionization, but if electrons can be captured by atoms (or absorbed in free electron bands) when they come to rest, positron react with their antiparticle (electron) by annihilation. The entire rest mass of the particle pair is converted to energy and emitted as two back-to-back 511 keV photons for conservation laws. The annihilation takes place in a time window of about 1 ns after the β^+ -decay, and within a few millimeter of the decay site (depending on the medium). This kind of reaction is the basis of one of the most diffused nuclear medicine imaging technique, the PET, discussed in section 1.2.2. An example of a positron emitter used in imaging is ^{18}F , with a half-life of 109 minutes. To be noticed that, as for β^- -decay, the daughter nucleus can further emit photons to lower its energetic level, which can be used in combined imaging techniques (three- γ imaging). The N/P ratio of neutron deficient nuclides can also be increased via Electron Capture (EC) reactions ; the nucleus

can capture and orbital electron and convert a proton into a neutron, with the consequent emission of a neutrino. This phenomenon is described by equation 1.21.



Most electrons are captured from the K shell, more uncommon are the capturing processing involving L shell or even shells farther from the nucleus. As a result of the capture, a vacancy is created and filled by an electron from an higher-energy shell. This transition leads to a reduction of the atomic rest energy, and the release of characteristic x-rays and/or Auger electrons. As with other modes of decay, further γ -rays can be emitted if the daughter nucleus is left in an excited state after the capture process. An example of electron capture decay is represented by ${}^{201}\text{Tl}$, which decays to ${}^{201}\text{Hg}$ with the emission of K-x-rays of 69-83 keV (98% abundance) and γ -rays of 135 and 167 keV in 10% total abundance. Many nuclei decay by both electron capture and positron emission , as for example the ${}^{22}\text{Na}$. As mentioned for the previously described decay modes , often the daughter nucleus is formed in an excited state, which is still unstable. The transition towards a condition of stability entails an internal atomic re-arrangement and the emission of γ -rays at characteristic energies. In general, such a transition is almost instantaneous, but some excited states can persist for longer periods, with half-lives which ranges on several orders of magnitude, between 10^{-6} s and hundreds of years. The decay of this kind of nuclei, called metastable or isomeric, is called isomeric transition, and only results in the γ -ray emission with no emission or capture of other particles by the nucleus. A complementary pathway for the energy release is represented by the interaction of the nucleus with an atomic electron; this process is called Internal Conversion (IC), and the involved electron is ejected. This emission is further followed by x-rays and Auger electron emission, so that the atom can resume a stable state. The isomeric transition is described by equation 1.22, where the letter m indicates the metastable state.

Isomeric transition - γ -decay



To be noticed that no radioactive nuclide decays solely by an isomeric transition, which is always preceded by another decay mode. In addition to the already mentioned decay of ${}^{99m}\text{Tc}$, deriving from the previous decay of ${}^{99}\text{Mo}$, also ${}^{60}\text{Co}$ decays in excited ${}^{60}\text{Ni}$ nuclei which then reach the ground energy state by isomeric transition and with the emission of 1.17 and 1.33 MeV photons. In table 1.4 some of the radioisotopes typically used for imaging and therapy are listed with their half-life and common uses.

Although many naturally occurring radioactive nuclides exist , all of those commonly administered to patients in nuclear medicine tracers are produced artificially in order to fit the clinical requirements. Artificial induced radioactivity was introduced by the already mentioned Irene Curie and his husband, who bombarded aluminum targets with α particle (Leone et al. 2010). Nowadays, most radionuclides are produced with cyclotrons, nuclear reactors or radionuclide generators. In general, β^- emitters are produced by bombarding stable nuclei with neutrons from nuclear reactors, while β^+ -decay nuclides are produced with bombardment with protons, helium ions, deuterons or tritons accelerated with cyclotrons (see section 1.1.3.1 for the description of the cyclotron). In other cases, radionuclides are produced as by-products of

Radionuclide production

Table 1.4: Commonly-used radioisotopes for the clinical imaging and therapy routine. Table adapted from Ruth 2009.

Application	Radioisotope	Half-life	Details
Imaging	Technetium-99m	6 h (from ⁹⁹ Mo 66 h)	Used to image the almost all the body, skeleton and heart muscle in particular.
	Cobalt-57	272 d	Used as marker to estimate organ size and for <i>in vitro</i> diagnostic kits.
	Gallium-67	78 h	Used for tumor imaging and localization of inflammatory lesions.
	Indium-111	67 h	Used for specialist diagnostic studies and colon transit studies.
	Iodine-123	13 h	Used for diagnosis of thyroid function.
	Krypton-81m	13 s (from ⁸¹ Rb 4.6 h)	Used in gas status for images of pulmonary ventilation and in general for lung applications.
	Rubidium-82	65 h	Convenient PET agent for myocardial perfusion imaging.
	Thallium-201	73 h	Used for diagnosis of coronary artery disease and other heart studies.
	Carbon-11	20.4 m	
	Nitrogen-13	9.97 m	Positron emitters used in PET for studying brain physiology and pathology.
Therapy	Oxygen-15	2 m	They also have a significant role in cardiology.
	Fluorine-18	110 m	
	Bromine-77	2.4 d	Auger electrons decay mode.
	Palladium-103	17.5 d	Auger electrons decay mode.
	Rhenium-186	90.6 h	β^- -decay mode.
	Astatine-211	7.2 h	α -decay mode.

fission in nuclear reactors, or as decay product of other isotopes produced with one of the listed methods. In the cyclotron-based production, the accelerated ions collide with the target nuclei causing nuclear reactions, presented in section 1.1.1.1. As explained, fragmentation processes can create radioactive nuclei, such as β^+ emitters, employed in PET diagnostics. In general, cyclotron facilities must be in close proximity to the hospital where the produced radionuclides will be administrated because of their short half-life. ¹⁸F, created with this technique as product of nuclear reactions with ¹⁸O, is an exception in this sense, with an half-life of 109 minutes. In nuclear reactors, two techniques are exploited: nuclear fission and neutron activation. The absorption of neutrons from nuclear reactors can induces fission processes in heavy nuclei, which split in lighter (often unstable) ones. Its long half-life makes ²³⁵U the most widely used fissile element; when it absorbs a neutron, the resulting state of ²³⁶U is highly unstable and promptly splits into its fission fragments. For example, ⁹⁹Mo has already been mentioned as the parent nucleus for the production of ^{99m}Tc and derives by the fission of uranium. Another widely used nuclide produced with fission procedure is the ¹³¹I. The creation of the fission fragments is very often accompanied by the emission of secondary neutrons which can be used to create other nuclides by neutron activation. Stable nuclei, indeed, can capture neutrons and produce, in most cases, β^- emitters, as the ³²P or the ⁵⁰Cr. In some cases, the sample activity reached with such a production technique is not sufficient, because stable nuclei are still present among the parent atoms, and so fission mechanisms are preferred. The last mechanism involves radionuclide generators, particularly interesting for short half-life nuclides. In order to solve the supply problem for short-living isotopes, the sample is often prepared with the longer-living parent nuclide (the so-called “generator”), which then decays in the desired one continually providing it. This is for example the case of the most important radio-nuclide used in a variety of application, ^{99m}Tc, result of the decay of ⁹⁹Mo.

Radiotracer features Once produced, the radioactive nuclei must be attached to appropriate substances providing the desired biological properties, for example to be preferentially absorbed in the target region. The final product, ready to be administrated to the patient, is called “radiotracer”. For diagnostics, the selected radioisotope half-life should be short enough so that a considerable part of the decays occurs during the examination time; any radiation released after the end of the examination is a source of useless dose to the patient. The dose delivered after the end of the treatment can be reduced if the biological excretion, guaranteed by the tracer characteristics, is rapid. Always focusing on diagnosis, the optimal decay scheme is the pure γ -decay,

with an isomer as radionuclide; anyway, the amount of produced non-penetrating radiation should be minimized. The exception is represented by β^+ emitters, resulting in the positron annihilation 511 keV photons exploited by PET techniques. In addition to this, the produced photon energy must be considered: nowadays, the majority of scintillation cameras are optimized for energies close to 140 keV (main emission of ^{99m}Tc), which is a compromise among patient attenuation, spatial resolution and detection efficiency. Photons at lower energies are largely attenuated by dose and increase the patient dose without contributing to the image formation. High-energy photons escape the body and deliver a minimal dose to the patient, but the present machines have poor detection efficiency in such an energy range, and the physical collimators are not optimized; both these factors result in image quality degradation. High-energy photons can be used if new detector solutions are explored, like the one presented in chapter 5. For therapy non-penetrating radiation are requested and must be maximized, and correlated photon emission can be in principle used for dosimetric verification, in the so-called theranostics approach (Yordanova et al. 2017). From the biological point of view, “hot spots” (in which the tracer is more concentrated than in other regions) are desired for therapy, while for diagnosis it is possible to profit from both “hot” and “cold spots” in which the tracer is more concentrated than in other regions. Several mechanisms can be implemented in order to concentrate the radiotracer in the target area. Localized administration of the radiotracer in the target region is the first option, while with active transport techniques, the tracer is concentrated into specific organ against concentration gradients thanks to cellular metabolic processes. The glucose metabolism is also exploited, for example for the FDG tracer used in 85% of the PET clinical practice. The tracer size is fundamental in techniques based on the phagocytosis by specialized cells or on traps in specific organs. Very large molecules (20-40 μm diameter) can concentrate in capillaries with smaller diameter. An irregular diffusion through tissue membrane can also be used to identify lesions if specific tracers are employed. Chemotaxis (the movement of a cell in response to chemical stimulus) can also promote the migration and accumulation of radiotracers, for example as part of an overall inflammatory response. Moreover, some radio-pharmaceuticals are produced with specific characteristics which provide them high affinity to bind to receptor sites, for example in tumors. Finally, the blood flux can be used for blood specific studies.

The choice of the radiotracer depends on the specific organ or region of the body to be examined and on the chosen detection technique. As already detailed, on one side PET aims to detect the two back-to-back photons produced by the annihilation of a positron emitted by the radio-isotope and an electron of the patient body. On the other side, SPECT detects single photons, and the spatial localization is given by mechanical collimation systems. In both cases, tomographic reconstruction is foreseen to obtain three-dimensional images.

The physical basis, historical development and present status of these two techniques are detailed in the following sections. In addition, the theranostics approach, aiming to perform combined diseases radiation treatment and diagnosis and/or verification imaging, is also addressed in the last section of this chapter.

1.2.2 Positron Emission Tomography

PET systems rely on the detection of annihilation gamma rays that follow positron decay of the radioisotope injected in the patient and consequent positron annihilation. The gamma rays exiting the patient body are detected in coincidence by scintillating detectors surrounding the

patient, and the distribution of positron emitters is retrieved *in vivo*. Figure 1.23 shows the principle at the basis of PET imaging.

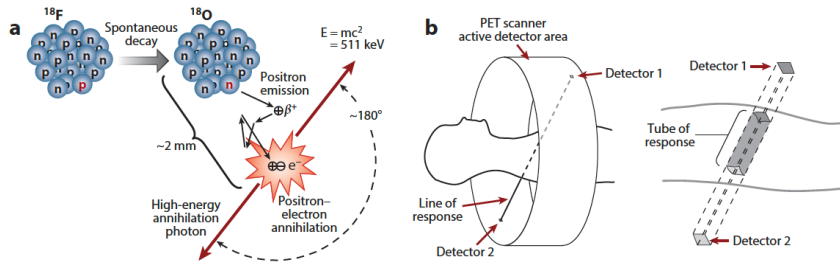
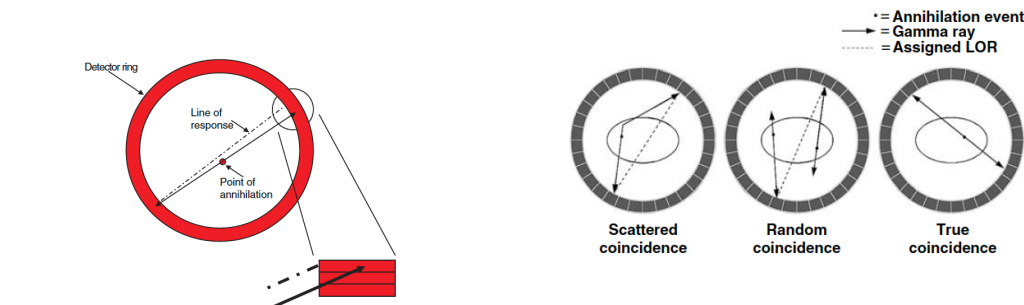


Figure 1.23: The β^+ decay of ¹⁸F creates the stable isotope ¹⁸O and a positron, which travels short distance (1-2 mm) before interacting with an electron. The consequent annihilation produces two anticollinear 511 KeV photons (a). The two photons are detected by the PET scanner in time coincidence, and the two points of interaction defines a line of response, then extended to a so-called “tube of response” which accounts for the detector’s elements finite dimensions (b). In Vaquero et al. 2015.

The two annihilation photons are typically detected with time coincidence windows ranging between 1 and 10 ns, depending on the specific features of the employed scanner. The spatial resolution of PET imaging is intrinsically limited by the fundamental nature of positron annihilation, if we consider that after its creation, the positron can travel a few millimeters and follow a tortuous path through the tissue (mainly due to Coulomb scattering with electrons which can occur at large angles given the fact that the rest mass of positron is the same as the one of the electron) before reaching thermal energies and annihilating. In addition to the positron range, also the variation in the momentum of the positron leads to a limitation of the spatial resolution of PET images. Indeed, such a variation results in an angular uncertainty in the direction of the two annihilation photons known as “noncollinearity”. Moreover, significant limitations are linked to the employed detector: the coincidence detector-pair resolution is normally specified as the FWHM of the Point-Spread Function (PSF) obtained from the convolution of the two individual detector PSFs. For a detector composed of small discrete crystals, the interactions are generally assumed to take place at the center of individual crystals, and the resulting FWHM of the coincident detector PSF is one-half the crystal size. A further factor affecting PET imaging resolution is the parallax error, which results from the uncertainty of the Depth Of Interaction (DOI) of the gamma rays in the crystal. Thus, unless the DOI within a crystal can be accurately determined (dedicated designs are needed), an incorrect Line Of Response (LOR) will be assigned to the interaction. A schematic representation of the parallax error is provided in Figure 1.24a. The parallax error is all the more increased when the PET ring diameter is reduced or the thickness of the crystals is increased, as the relative thickness of the detector increases.

Figure 1.24b shows the three kinds of coincidence events that a standard PET accepts:

- true coincidences: gamma rays are detected from a single decay that have not scattered in the patient;



(a) Schematic view of the parallax error. The gamma ray (solid line) interacts in a crystal after penetrating one or more adjacent crystals in the detector ring. The detection electronics, if DOI information is not accessible, will incorrectly assign the LOR (dotted line) based on the front of the interaction crystal.

(b) The three types of coincidence events measured in a PET scanner.

Figure 1.24: In T. Lewellen et al. 2004.

- scattered events: one or both gamma rays scatter within the patient;
- random coincidences: two separate decays result in the detection of only one gamma rays from each one and the two events are close enough in time to be in coincidence.

It is clear that increasing the number of true coincidences leads to less noise in the final image and allows one to reconstruct the collected data with high spatial resolution, and the effect of scattered coincidences can be corrected at the reconstruction stage, as well as the attenuation effect in the patient. The random coincidences are hardly treated, but their number can be reduced by decreasing the injected radiotracer activity.

The origin of the PET imaging modality dates back to the beginning of the 50s, when a simple brain probe was used to localize brain tumors by detecting photon coincidences with 2 opposing Sodium Iodide doped with Thallium (NaI(Tl)) detectors at the MGH (Sweet 1951). In the same year, a similar approach was published on *Science* by a second research group (Wrenn et al. 1951). The development of reconstruction techniques for tomographic imaging started in the early 1960s (Kuhl et al. 1963), and in parallel to the first clinical trial for x-ray computed tomography the MGH physics group developed the FBP technique (Chesler 1971). The first ring tomograph was built in 1973 by Robertson of Brookhaven National Laboratory (BNL), and it was composed of 32 detectors disposed in a circular array (J. S. Robertson et al. 1972). One year later, the PETT I (Positron Emission Transaxial Tomography) tomograph prototype was built at the Washington University by Michael E. Phelps: such a prototype was then upgraded until a human-size system, called PET III, which included extended reconstruction not limited to the transaxial plane. The system consisted of an hexagonal array with 48 NaI(Tl) detectors, and of a gantry allowing for a 60-degree rotation. With this system, the first human PET images using the FBP algorithm were produced (Hoffmann et al. 1976), marking the beginning of modern PET development. Following the PET III development, the first commercial

PET scanner, named ECAT II (Emission Computed Axial Tomograph), was designed and put on the market; it was composed of 96 NaI(Tl) crystals, and it had a dedicated computer. The transition to commercial systems continued in the following years, and it boosted the establishment of worldwide PET research programs. Another fundamental step in the development of the PET technology was the discovery of BGO scintillator. The first scanners were all based on NaI(Tl), difficult to manufacture because of its hygroscopic nature, and with a low density, thus limited efficiency in detecting 511 keV gamma rays. The luminescence features of BGO were first studied by Weber at the University of California (Weber et al. 1973), and Nester and Huang characterized the BGO scintillation properties in 1975 (Nestor et al. 1975). These studies leaded to the first design and construction of a BGO-based PET scanner in 1978, and right after to the commercialization of the NeuroECAT, the first commercial machine to use BGO as scintillating material. Hundreds of BGO-based tomographs have been produced since the first introduction. The availability of commercial valuable PET scanners was only one of the factor determining the spread of this imaging technique: in parallel, the development of optimized radiotracers was the second key point. Since the beginning of the PET experience and until the second half of the 1970s, the images were obtained mainly using ^{11}C -glucose, ^{15}O -water and ^{13}N -ammonia for blood flow, ^{15}O -oxygen for oxygen utilization, and ^{18}F fluoride for bone scans. In addition, successful molecular imaging probe was derived from the ^{14}C -deoxyglucose. The synthesis of ^{18}F -tagged deoxyglucose was discussed already at the beginning of the 1970s, and the Brookhaven group (Al Wolf and Joanna Fowler in particular), synthesized the first FDG (Ido et al. n.d.). Refined synthesis methods were developed in the following years, also thanks to the improvements of cyclotron accelerator technology, allowing for a routine basis tracer production. Nowadays, a number of companies provide small cyclotrons with various forms of automated chemistry for producing molecular imaging probes, and FDG is still the most employed one for modern clinical PET imaging. During the 1980s, particular focus was dedicated to the detector side, with the development of the so-called “block detectors”: the new optical multiplexing scheme permitted to use many small scintillator pixels on a small number of PMs, and so provided high granularity (and spatial resolution) with a limited number of read-out channels. Since 1985, the majority of PET tomographs used some form of block detectors, which also allowed for a reduction in the scanner production cost. The introduction of this technology also increased the participation of the major imaging companies in the PET experience: in 1986, Siemens began to distribute PET scanners along with small cyclotrons for the production of radiotracers, and soon after also General Electric (GE) entered the PET market by purchasing the tomograph business from Scanditronix. PET machines and imaging techniques were soon introduced in the clinical routine and approved by the main health-care systems. In the 1980s, research efforts have been also dedicated to the introduction of DOI capabilities in the PET scanners to reduce parallax errors. A combination of NaI(Tl) and BGO crystals has been used by Karp and colleagues (Karp et al. 1987), and the different decay time constants were used to retrieve DOI information. Various techniques have been explored in the following years to develop DOI detection capabilities, such as the introduction of multiple crystal layers in the perpendicular direction (Liu et al. 2001) or the implementation of reflectors to create custom light-sharing patterns (Murayama et al. 1998). Although the research is still active on this topic, it should be considered that the effect of parallax error is small if compared with the overall resolution of the PET scanner itself. Further improvements came with the discovery and first grown of Cerium-doped Lutetium Oxyorthosilicate - $\text{Lu}_{2(1-x)}\text{Ce}_{2x}\text{SiO}_4$ (LSO) crystals, in 1989. BGO is very dense but has only 15% of the light output of NaI(Tl) and relatively slow decay time (300 ns). LSO has a slightly greater density, slightly lower effective atomic number, and 5 times more light output than BGO. Moreover, the decay time is 7.5 times faster than BGO (Melcher et al. 1992). The high

refinement cost initially discouraged the use of LSO for PET, but it soon decreased thanks to the development of cost-effective techniques, so that the first LSO-PET tomograph, microPET, was designed and fabricated in 1997 (Cherry et al. 1997). It was designed for small animals, and commercially reproduced in 30 copies for academic programs and pharmaceutical companies. In February 1999, the first human-size LSO tomograph was delivered to the Max Planck Institute in Germany, while a combination of LSO and NaI(Tl) crystal was used for a PET-SPECT tomograph used in the Free University of Amsterdam since March 2000. In addition to the higher light output of LSO with respect to BGO, leading to better spatial and energy resolution, another major advantage of this scintillator is the fast timing, which translates in lower detector dead time and in the capability to measure the time difference between the arrivals of the two annihilation photons. This TOF measurement provides positioning information which can localize the positron annihilation within a few centimeters along the line of response. A schematic view of the TOF-PET principle is provided in Figure 1.25.

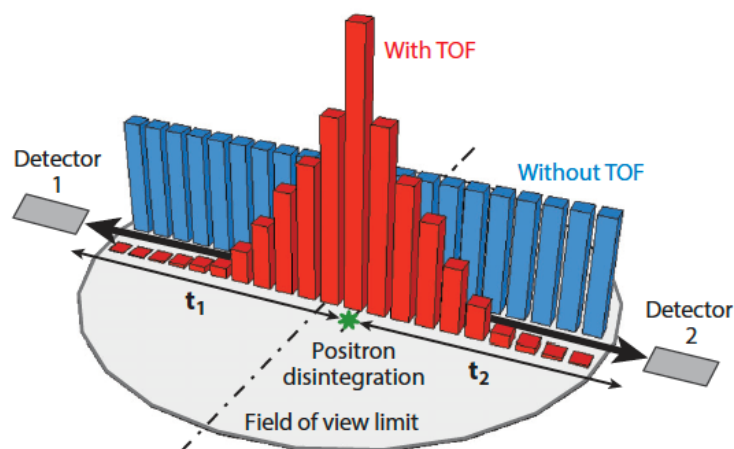


Figure 1.25: Schematic view of the information provided by TOF measurement to the PET detection. Without TOF, a flat probability is assigned to the reconstructed LOR (blue), while the measurement of the arrival time difference between the two coincident photons is translated into a distance from the LOR midpoint where the probability density function should be centered (red). In Vaquero et al. 2015.

This possibility was explored already in the 1980s with fast scintillators (T. K. Lewellen et al. 1988; Ter-Pogossian et al. 1982), such as CsF and BaF₂, which were anyway not adapted to clinical PET application due to a low stopping power. On the other hand, the BGO response was too slow to perform TOF. With the introduction of LSO, it was also recognized that its very good timing resolution (together with the one of the similar scintillator LYSO) could be utilized in the development of TOF-PET systems (Moses et al. 1999), overcoming the limitation of the early designs of the 1980s. In 2005 Siemens presented the results from a prototype that achieved a timing resolution of 1.2 ns, and soon after the first TOF-PET machine was launched by Philips (Philips Gemini TF) (Karp et al. 2008). Based on LYSO crystal, it provided 585 ps system timing resolution. At present, all the main PET vendors offer TOF-PET solutions with hundreds of ps timing resolution. Beyond PET detector designs using conventional PMs, the arrival of SiPMs has led to a great interest in utilizing these new photosensors to achieve im-

proved timing resolution in TOF-PET scanners. Philips recently introduced the Vereos system, which uses digital SiPMs for signal readout from individual LYSO crystals; such a machine provides a system coincidence timing resolution of approximately 310 ps (Miller et al. 2015). In parallel GE developed the SIGNA TOF-PET/MRI system using a detector ring based on analog SiPMs inserted in the magnet bore, thereby allowing simultaneous PET and MR imaging. The reported system coincidence timing resolution of this system is 390–400 ps (Levin et al. 2013). Hence, while scanners with detectors using conventional PMs are pushing closer to 400 ps timing resolution, new SiPM technology indicates that system resolution close to 300 ps is achievable with the lutetium based scintillators. With the rapid improvements of both scintillator and photosensor technology shown by recent results, a TOF resolution below 100 ps seems achievable in the next future (Lecoq 2017; Surti et al. 2016). Recent studies also investigated cost-effective solutions to achieve performance comparable to present commercial systems. In particular, a whole-body PET scanner based on plastic scintillators is being developed in Poland by the Jagiellonian University group. The J-PET is constructed with axially arranged strips of plastic scintillators, aiming to detect the annihilation photons via Compton interaction and read out on both sides by PMs. The position of interaction in the scintillator is determined from the time difference of light signal arriving on each strip end. A Time-Over-Threshold (TOT) technique is used instead of the charge measurement of standard PET systems in order to take advantage of the superior timing properties of plastic scintillators with respect to crystal detectors (LSO and BGO). Preliminary studies showed that it is possible to achieve a coincidence time resolution of about 500 ps FWHM with simple time measurements, coupled to a few millimeters spatial resolution (Niedźwiecki et al. 2017).

1.2.3 Single Photon Emission Computed Tomography

In SPECT tomographic images of the radionuclide distribution in the patient are generated from the emitted gamma photons detected as singles with collimated scintillators. Planar imaging reproduces a two-dimensional projection of the tracer distribution from a single view, while the tomographic image is obtained by the reconstruction of several slices collected from multiple camera positions. Both techniques are used in clinics: planar imaging is less demanding and only requires a single camera head, while multiple camera heads mounted on a rotating gantry are generally used for tomographic imaging, and image reconstruction is required.

Although many innovations have been made since the introduction of the first gamma camera in 1958 by Hal Anger (Anger 1958), today's clinical detectors share many of the essential features of Anger's early designs, and are often called Anger cameras. A standard SPECT gamma camera is composed of an aperture or collimator which mechanically selects photons traveling in specific directions, depending on the collimator configuration. The photons approaching the camera from directions different than those specified by the collimation system are passively absorbed. The gamma photons with the selected direction then encounter a scintillation detectors coupled to photosensors. The related electronics and data acquisition system are generally optimized to impose energy threshold in order to reject undesired photons, such the ones which underwent scattering in the collimator section. A schematic view of the main component of the SPECT camera is given in Figure 1.26a, while a simplified view of the collimation principle is sketched in Figure 1.26b.

The most simple photon passive selection device is the pinhole aperture, but acceptable spatial

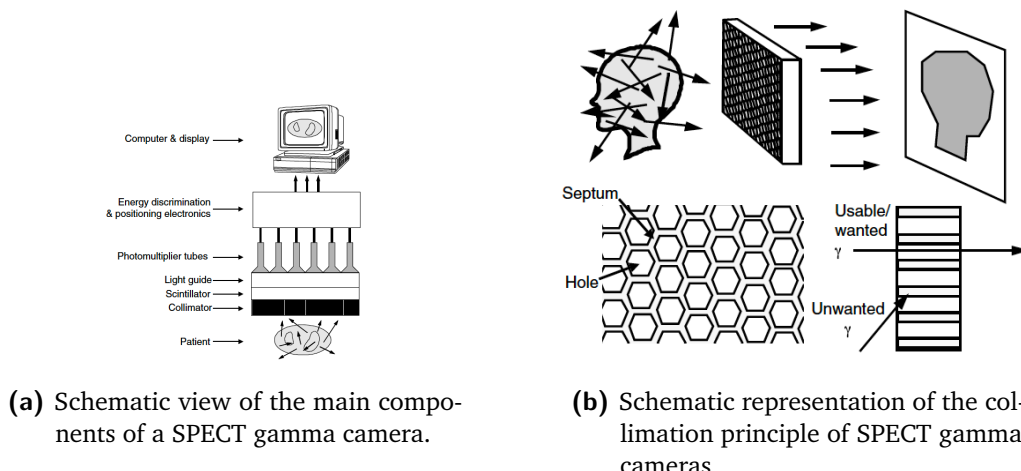


Figure 1.26: In Zeng et al. 2004.

resolution can be only obtained at the expense of the system sensitivity. Improved, but always limited overall sensitivity is provided by the introduction of collimators, composed of array of holes separated by septa. Collimator septa are composed of highly absorbing material with high atomic number and high density. Alloys of lead, tungsten and gold are the most common materials used for this purpose. Various hole shapes (circular, square, triangular or hexagonal) are used in common collimators, but the hexagonal shape is the most diffused because it provides the best efficiency. In addition to parallel hole patterns, also converging and diverging collimators have been developed. Converging collimators magnify an image on a camera face and thus can yield finer resolution and/or higher sensitivity images than those resulting from use of parallel-hole collimators. Converging solutions are adapted to small-size objects with respect to the camera Field Of View (FOV), while the image of large object would result truncated (if part of the object is outside the FOV of the camera) or distorted (because the magnification is dependent on the distance from the collimator). The most spread parallel-hole collimators find routine use in clinics in four configurations: Low Energy High Resolution (LEHR), Low Energy General Purpose (LEGP), Medium Energy General Purpose (MEGP), and High Energy General Purpose (HEGP). Each designation is adapted to a defined gamma energy range, and thus to certain radioisotopes, and is also an indication of the trade-off between resolution and sensitivity which are affected by the septal material, the hole size and length, and the septal thickness. Collimator sensitivity is maximized by the thinnest possible septa, but thin septa can lead to septal penetration which is extremely detrimental to diagnostic performance. The aforementioned trade-off is then a crucial parameter to be considered when designing a SPECT camera, and, together with the employed scintillator and photosensor features, completely determine the overall system performance (Gunter 2004).

The origins of SPECT imaging can be identified with the invention of the Anger scintillation camera in the late 1950s (Anger 1958, 1964); previously, scans were performed by manually positioning a Geiger counter above the organ of interest, but with the Anger camera the entire organ could be scanned at one time. During the 1960s, both longitudinal and transaxial emission tomography were deeply studied. Crandall and Cassen developed a longitudinal tomographic scanner which used a highly focusing collimator placed on a large crystal-matrix detector (Crandall et al. 1966), and in 1969, Anger invented a sophisticated longitudinal tomograph that used a scanning scintillation camera (Anger 1969). Transaxial tomographs were de-

veloped by Kuhl and colleagues between 1963 and 1976, and the final prototype used discrete scintillator arrays (Kuhl et al. 1976). Discrete scintillation detectors have been also used for other scanners in the late 1970s, but the first investigators to explore the possible implementation of an Anger camera for transaxial tomography were Paul Harper and colleagues at the University of Chicago. In the early stages, a rotatable chair was placed in front of a single head fixed Anger camera (Muehllehner et al. 1971). In 1976, Jaszczak and Keyes, independently developed a SPECT system that used an Anger camera mounted on a rotating gantry (Jaszczak et al. 1977; Keyes et al. 1977). In the following years, the first whole-body SPECT system was developed and clinically evaluated in 1978 at the Baylor College of Medicine (Jaszczak et al. 1979). During the late 1970s and the 1980s, both rotating-camera SPECT systems and stationary detector configurations were proposed and developed in Europe and US (S. A. Larsson 1980; W. L. Rogers et al. 1988), and the bases for modern machines were established. The modern cameras, as mentioned, rely on the described designs and have been adapted, in the past years, to new tracers provided by the pharmaceutical industry. SPECT takes advantage of many years of experience and is now a well-established imaging modality in nuclear medicine. Thanks to its cost-effectiveness, such an imaging technique is widely employed in the clinical routine, and all the major medical imaging companies offer a SPECT system, generally in dual-head configuration with rotating gantry. At present, virtually all single-photon imaging in nuclear medicine relies on Anger-type cameras, relatively simple and cost-effective, but limited in sensitivity and energy acceptance given the presence of a mechanical photon selection system. Already in 1974 this limitation was addressed by Todd and Nightingale which proposed the application of Compton imaging method to nuclear medicine (Todd et al. 1974). The Compton detection principle is described in chapter 2. Starting from 1981, Singh and colleagues published a number of seminal papers that described analytical and experimental results for Compton camera composed of a pixelated germanium first detector and a standard Anger camera as second detector (Singh 1983; Singh et al. 1981, 1983). The investigation of such an imaging modality for the application in single photon detection for nuclear medicine continued in the following year and is still today actively explored. In particular, the availability of new high-energy tracers could provide advantages in terms of dose and spatial accuracy, but high-energy photons are hardly collimated with mechanical passive system. The electronic collimation exploited by Compton cameras can be the solution for high-sensitivity and high-resolution SPECT examinations. More details can be found in chapter 5 of this thesis, where the described topic has been addressed with simulation studies. The presented results have been recently published in (Fontana et al. 2017a) and (Fontana et al. 2017b).

1.2.4 Theranostics

The theranostics approach in nuclear medicine couples diagnostic imaging and cancer therapy using the same molecule or at least very similar drugs, given in different dosages. For example, the combination of Iodine-131 (^{131}I) (gamma emitter) and Lutetium-177 (^{177}Lu) (beta emitter), is used for both imaging and therapy. Furthermore, different isotopes of the same elements (for example Iodine-123 (^{123}I), ^{131}I and the newer terbium isotopes - Tb) can also be used for theranostics given the multiple associated emission (beta and gamma, gamma rays at different energies, alpha and gamma) (Alzahrani et al. 2012; Gerard et al. 2002; Muller et al. 2012). During the treatment, theranostics can be applied in monitoring the therapy course and estimating the potential response and eventual toxicity. The safety of high cumulative doses of radioactive agents after multiple repeated cycles is, however, a cause of concern. Anyway, remarkable improvements have been obtained in targeted therapies, which have proven to

be effective with favorable safety profiles (Baum et al. 2012; Kwekkeboom et al. 2008; Strosberg et al. 2017). The diagnostic part of theranostics can be performed with both PET and SPECT machines, depending on the employed radioisotope emissions. Most therapeutic radiopharmaceuticals are labeled with β^- -emitting isotopes, having a tissue penetration of only few millimeters and so adapted to spare the healthy tissues surrounding the tumor. The first theranostic radiopharmaceutical in nuclear medicine history was radioiodine, used for therapy and imaging in thyroid diseases (B. Hertz 2016). Iodine is taken up by the thyroid gland for the production of hormones, vital for the development of the brain, normal growth and metabolic balance. In 19367, Hertz developed the idea of administrating radioactive iodine in patients with thyroid diseases, and few years of preclinical studies at the Massachusetts Institute of Technology (MIT) (where the first cyclotron for medical use had been built) followed this first proposal. In 1941, the first patient was treated with radioiodine (S. Hertz et al. 1942). ^{131}I is to the date the gold standard for certain therapeutical indications, given its low cost and the advantageous combination of β^- and gamma emission. The electron radiation targets the thyroid from the inside, while the organ can be visualized using a gamma camera.

Since its first proposal, the use of theranostic agents has been consistently increasing: the combination of targeted cancer imaging and therapy is a considerable contribution to personalized medicine and may play an important role in the future with the implementation of new chemical agents and the continuous improvement of imaging systems (Yordanova et al. 2017). For the peculiar context of this thesis it is worth to notice that, as for diagnosis SPECT, high-energy gamma emitters can be applied in theranostics, and Compton camera can be implemented for the imaging task. This point is further discussed in chapter 5.

2

Prompt gamma detection

Contents

2.1	Photon detection	70
2.1.1	Photon interactions in matter	70
2.2	Ion range monitoring with prompt-gamma radiation	78
2.3	Prompt-Gamma (PG) emission during particle therapy	78
2.4	Gamma cameras state of the art	78

Ion beam therapy is rapidly emerging as a valuable cancer treatment technique and a superior alternative to photon radiotherapy for specific clinical indications. The narrow dose peak at the end of the ion range allows for targeted delivery of high dose to the tumor while sparing healthy surrounding tissues. However, since such a treatment technique is highly sensitive to dose prediction and delivery uncertainties, online range monitoring solutions are necessary. Over- and under-shooting effects potentially lead to severe damages to healthy tissues and/or treatment inefficiency, and thus have to be controlled in real-time. The research effort in this field mainly focuses on the non-invasive detection of primary by-products of beam-tissue nuclear interactions: photons from electron-positron annihilation and prompt gammas are most extensively studied for this purpose. The research work presented in this thesis focus on the development of gamma cameras for the detection of prompt gamma rays to tackle the challenge of real-time range monitoring during particle therapy treatments. In this chapter, after a brief introduction of the photon interaction channels in matter, the main topic of the thesis will be addressed by discussing the present developed techniques to obtain information about the ion range with prompt gamma ray detection. Finally, the state-of-the-art of gamma detectors employed for this purpose is sketched.

2.1 Photon detection

2.1.1 Photon interactions in matter

In penetrating an absorbing medium, photons may experience various interactions with the atoms of the medium, involving either the nuclei or the orbital electrons. The interactions with nuclei may be direct photon-nucleus collisions or interactions between the photon and the electrostatic field of the nucleus (pair production). On the other hand, the photon-orbital electron interactions can involve either loosely bound electrons (binding energy E_B small in comparison with the photon energy $h\nu$ - $E_B \ll h\nu$) or tightly bound electrons (binding energy comparable to, or slightly smaller than the photon energy - $E_B \lesssim h\nu$). All these processes are characterized by a partial or complete energy transfer of the gamma-ray photon, and two different outcomes are possible:

- Photon disappears (i.e. is completely absorbed) and its energy is transferred to light charged particles (electron and positrons);
- Photon is scattered and two results are possible:
 - the resulting photon has the same energy as the incident photon and no light charged particle is released in the interaction;
 - the resulting scattered photon has a lower energy than the incident photon and the energy excess is transferred to a light charged particle (electron).

We focus here on the interaction channels which play an important role in radiation measurements:

- photoelectric absorption;

- Compton scattering;
- pair production.

In case the photon interacts with an absorber atom and completely disappears by transferring all its energy to the target, the interaction mechanism is called photoelectric absorption. In the interaction an orbital electron is ejected with kinetic energy E_K corresponding to the difference between the incident photon energy $h\nu$ and the electron binding energy E_B , as reported in equation 2.1. The ejected orbital electron is generally referred to as “photoelectron”. A schematic view of the photoelectric absorption mechanism is shown in Figure 2.1.

Photoelectric absorption

$$E_K = h\nu - E_B \quad (2.1)$$

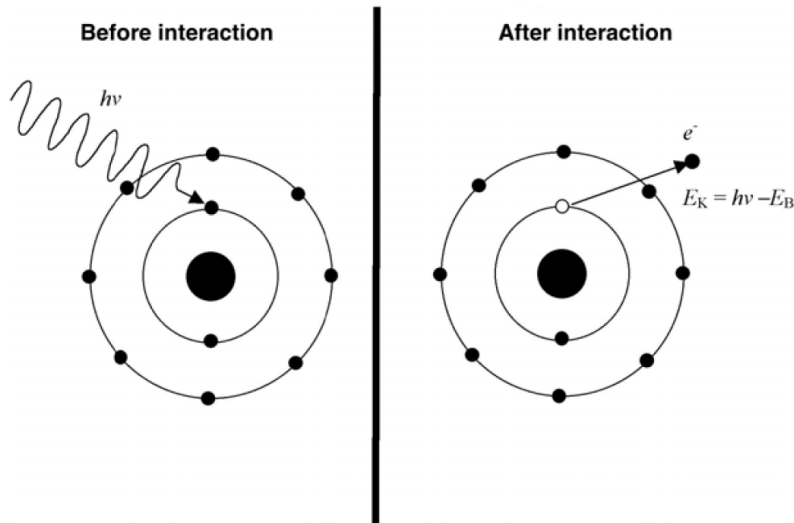


Figure 2.1: Schematic diagram of the photoelectric effect. A photon with energy $h\nu$ interacts with a K-shell electron, which is ejected as photoelectron with kinetic energy E_K . In Podgorsak 2010.

The interaction is with the atom as a whole, and cannot take place with free electrons for conservation of energy and momentum constraints, although the whole photon energy is transferred to an atomic electron in one of the atom bound shells (tightly bound electron). Energy and momentum cannot be conserved simultaneously in a photon-free electron interaction: the momentum conservation requires a third object (the atom) involved in the interaction which must absorb the extra momentum. When the photon energy exceeds the K-shell binding energy of the absorber, about 80% of all photoelectric absorption interactions occur with the K-shell electrons. If the energy transferred to the photoelectron is not below the binding energy threshold, it can be sufficient to raise it to a higher orbit, in a process of excitation. As a result of the photoelectric absorption, in addition to the ejected photoelectron, the absorber atom has a vacancy in one of its bound shells. This vacancy is quickly filled through capture of a free electron of the medium and/or rearrangement of electrons from other shells at higher energy level. Therefore, depending on the involved shells, one or more characteristics x-ray

photons (fluorescent photons) may also be generated. Such photons are generally reabsorbed close to the original atom site through a further photoelectric absorption involving less tightly bound shells. In some fraction of the cases, the emission of an Auger electron may substitute for the characteristic x-ray in carrying away the atomic excitation energy. As the fluorescent photons, Auger electrons are generally reabsorbed very near the site of the original interaction. The photoelectric process is the predominant mode of interaction for gamma rays of relatively low energy, and it is also enhanced for absorber materials of high atomic number Z. Even if a single analytic expression for the probability of photoelectric absorption over all ranges of photon energy E_γ and Z, the probability (σ_{PE}) dependence on these two parameters can be approximated as shown in equation 2.2, where n varies in the range [4,5] depending on the photon energy (4 for relatively low photon energies, 5 in the relativistic region) (Knoll 2000).

$$\sigma_{PE} \propto \frac{Z^n}{E_\gamma^{3.5}} \quad (2.2)$$

In Figure 2.6 the cross section for the photoelectric absorption is compared to the one of the other photon interaction mechanisms for a copper absorber as a function of the photon energy. It exhibits a characteristic sawtooth structure in which the sharp discontinuities arise whenever the photon energy coincides with the binding energy of a particular electron shell. Except for the K shell, all other shells have a fine energy structure which reflect in the cross section curve.

Compton scattering An interaction of a photon of energy $h\nu$ with a loosely bound orbital electron of an absorber is called Compton scattering in honor of Arthur Compton who made the first measurements of photon-“free electron” scattering in 1923 (Compton 1923). Compton earned the Nobel prize for the discovery in 1927. In Compton scattering, the incoming gamma-ray photon is deflected through an angle θ with respect to its original direction, while transferring a portion of its energy to the electron, referred to as “recoil electron”. In theoretical studies of such an interaction mechanism, an assumption is made that the photon interacts with a free and stationary electron. As a result of the interaction, the photon, which had an initial energy $h\nu$, continues traveling in the new direction (angle θ with respect to the incident direction) with reduced energy $h\nu'$, and the recoil electron is ejected from the atom with a kinetic energy E_K and a direction with an angle ϕ with respect to the photon incident direction. A schematic view of the interaction is given in Figure 2.2. The expression that relates the energy transfer and the scattering angle for any given interaction can be derived by writing simultaneous equations for the conservation of energy and momentum. The obtained relationship is presented in equation 2.3, with the notation described above and m_0c^2 the rest-mass energy of the electron (511 keV). From the same calculation the kinetic energy of the recoil electron is also obtained from the expression in equation 2.4.

$$h\nu' = \frac{h\nu}{1 + \frac{h\nu}{m_0c^2}(1 - \cos(\theta))} \quad (2.3)$$

$$E_K = h\nu \frac{\frac{h\nu}{m_0c^2}(1 - \cos(\theta))}{1 + \frac{h\nu}{m_0c^2}(1 - \cos(\theta))} \quad (2.4)$$

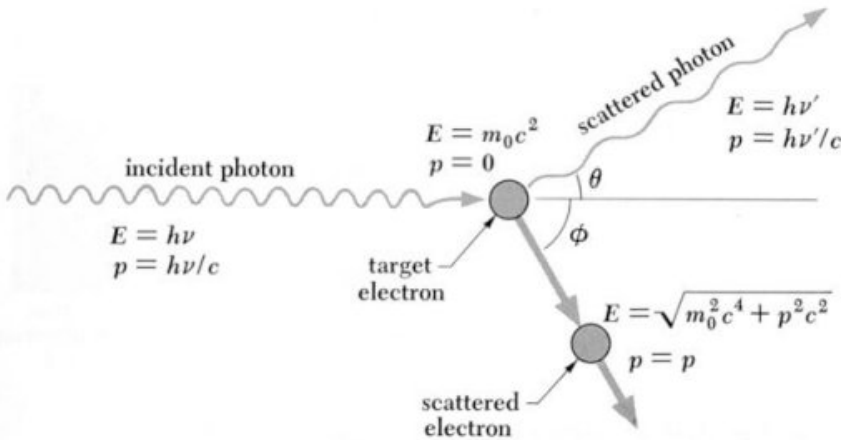


Figure 2.2: Schematic view of the Compton scattering principle. Image from <https://universe-review.ca/R15-12-QFT10.htm>.

From equation 2.3 emerges how small scattering angles correspond to little energy transfers, and the other way around. In particular, for $\theta = 0$, no energy is transferred to the electron and the interaction becomes a classical Thomson scattering. For $\theta > 0$ the energy of the scattered photon saturates at high values of the incident photon energy; the larger is the scattering angle, the lower is the saturation value of $h\nu'$ for $h\nu \lim_{\theta \rightarrow \pi} \infty$. The relationship between the photon energy before and after the interaction is shown in Figure 2.3a for various scattering angles θ between 0° (forward scattering) and π (back-scattering.) The scattering angle θ and the recoil electron angle ϕ are related by equation 2.5.

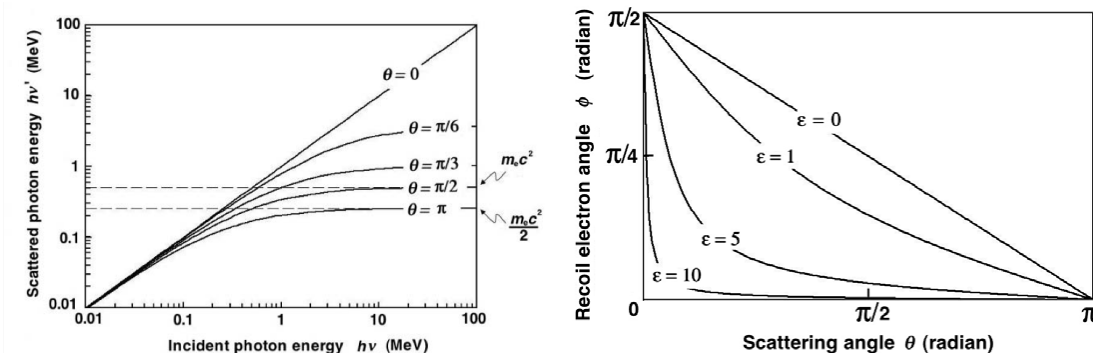
$$\cot(\phi) = \left(1 + \frac{h\nu}{m_0 c^2}\right) \tan\left(\frac{\theta}{2}\right) \quad (2.5)$$

This relationship shows that for a given θ , the higher is the incident photon energy $h\nu$, the smaller is the recoil electron angle ϕ . In Figure 2.3b the scattering and recoil angle dependence is plotted for different values of $\epsilon = h\nu/m_0 c^2$.

The probability of Compton scattering per atom of the absorber depends on the number of electrons available as scattering targets and therefore linearly increases with the atomic number Z. In Figure 2.6 the probability energy dependence is shown for a copper target and compared to the other interaction channels probability. The differential cross section, or angular distribution of scattered gamma rays, is predicted by a formula derived by Oskar Klein and Yoshio Nishina in 1929, and reported in equation 2.6 (Klein et al. 1929).

$$\frac{d\sigma}{d\Omega} = Z r_e \left(\frac{1}{1 + \epsilon(1 - \cos(\theta))} \right)^2 \left(\frac{1 + \cos^2(\theta)}{2} \right) \left(1 + \frac{\epsilon^2(1 - \cos(\theta))^2}{(1 + \cos^2(\theta))[1 + \epsilon(1 - \cos(\theta))]} \right) \quad (2.6)$$

where r_e is the classical electron radius expressed in equation 1.2. The distribution is shown graphically in Figure 2.4 and illustrates the strong tendency for forward scattering at high values of the gamma-ray energy. At low incident photon energies the probability for forward scattering and back-scattering are equal and twice as large as the probability for side scattering. As the incident photon energy increases, the scattering becomes increasingly more forward peaked and back-scattering rapidly diminishes.



(a) Scattered photon energy against the incident photon energy for various Compton scattering angles in the range from 0° to π .

(b) Relationship between the electron recoil electron ϕ and the photon Compton scattering angle θ .

Figure 2.3: In Podgorsak 2010

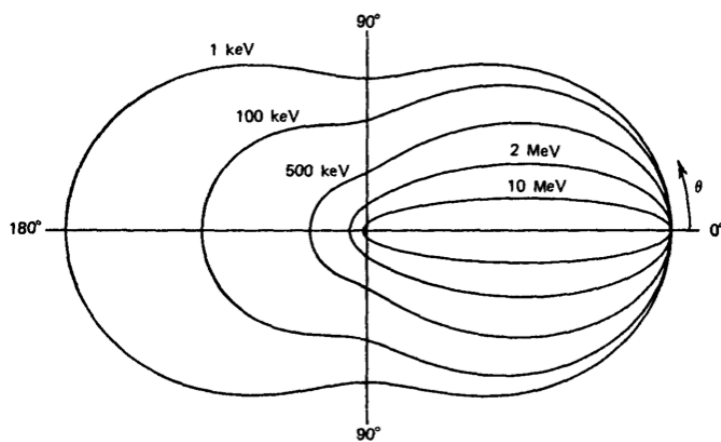


Figure 2.4: Polar plot of the number of photons (incident from the left side) Compton scattered into a unit solid angle at the scattering angle θ , for the different indicated incident photon energies. In Knoll 2000.

As mentioned, the Compton cross section and energy transfer are calculated with the assumption of free electrons, but at very low incident photon energies such an assumption breaks down and the electronic binding energy E_B affects the Compton interaction: the closer is the photon energy $h\nu$ to E_B , the larger is the deviation of the atomic cross section from the one calculated with the Klein-Nishina formula. Various theories have been developed to account for electronic binding energy effects and apply corrections on the Compton atomic cross sections (Bergstrom et al. 1997). It is worth to notice that for a given absorber Z, the binding energy correction is more significant at lower photon energies, and for a given initial energy $h\nu$, the binding energy correction is more significant at higher atomic number Z. The described binding energy effect is also referred to as “Doppler broadening” (DuMond 1928, 1929).

If the photon incident energy exceeds twice the rest-mass energy of an electron $2m_e c^2 = 1.02 \text{ MeV}$, the production of an electron-positron pair in conjunction with a complete absorption of the photon becomes energetically possible. In practice, as shown in Figure 2.6, the probability of such an interaction mechanism, referred to as pair production, remains very low until the gamma-ray energy approaches several MeV and therefore pair production is predominantly confined to high-energy photons. For $h\nu > 2m_e c^2$, energy and charge can be conserved even if pair production occurs in free space, but the conservation of linear momentum requires the Coulomb field of a collision partner (atomic nucleus or orbital electron). The photon, indeed, possesses momentum excess that is not absorbed by the electron-positron pair, and must be absorbed by the collision partner. When such an extra momentum is absorbed by the atomic nucleus, the recoil energy, as a result of the relatively large nuclear mass, is exceedingly small and the effect is described as the standard pair production: the incident gamma-ray disappears and is replaced by an electron-positron pair. When an orbital electron of the atom picks up the extra momentum, the recoil energy may be significant and determine the ejection of the orbital electron; in this case, the photon is absorbed and three particles leaves the interaction site, two electrons and a positron, in the so-called “triplet production”. A schematic representation of these two effects is given in Figure 2.5.

The total kinetic energy transferred to the charged particles is the difference between the photon incident energy and twice the rest-mass energy of the positron-electron pair. In both cases, because the positron will annihilate after slowing down in the absorbing medium, two annihilation photons are normally produced as secondary products of the interaction. No simple expression exists for the probability of pair production per nucleus, but its magnitude varies approximately as the square of the absorber atomic number Z, and it rises sharply with the photon energy.

The relative importance of the three described interaction processes for different absorber materials (Z) and gamma-ray energies ($h\nu$) are illustrated in Figure 2.7. Three areas are defined by the two solid lines in the plot, which indicates the energy/Z values for which the two neighboring effects have equivalent probability.

If we now consider a photon beam interacting with a target, all the mentioned interaction processes removes gamma-ray photons from the beam either by absorption or by scattering away from the beam direction, and can be characterized by a fixed probability of occurrence per unit path length in the absorber. The sum of these probabilities is simply the probability per unit path length that the photon is lost and is referred to as “linear attenuation coefficient” μ . The number of transmitted photons I can be then expressed in terms of the number of

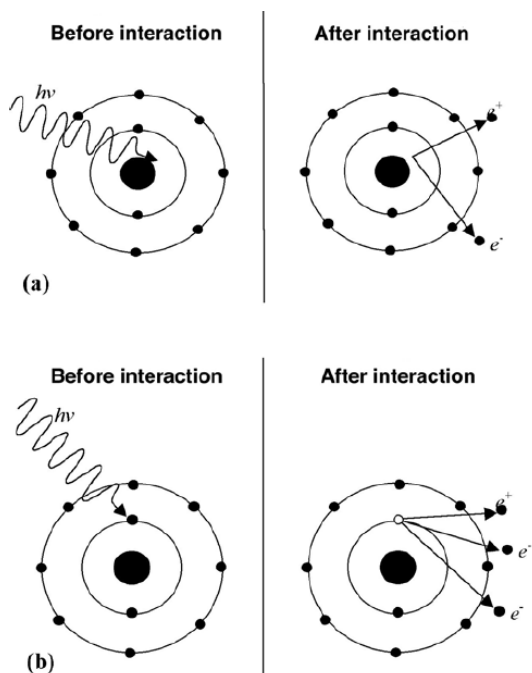


Figure 2.5: Schematic representation of pari production (a) in the COulomb field of a nucleus and triplet production (b) in the Coulomb field of an orbital electron. In [Podgirsak2010](#).

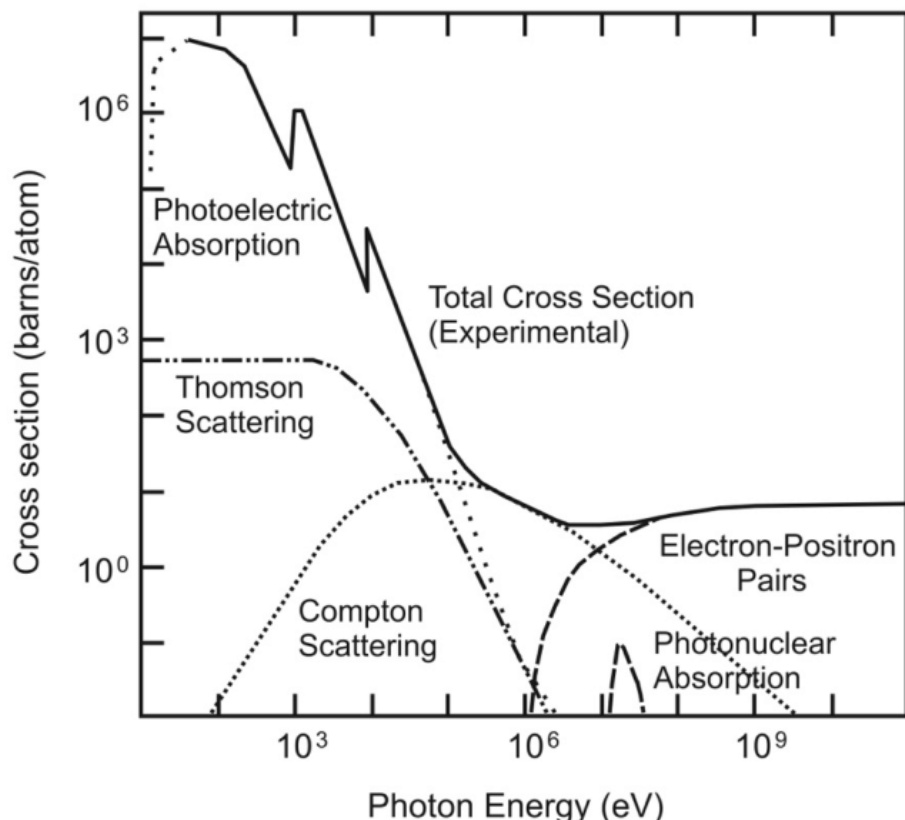


Figure 2.6: Cross sections of the photoelectric absorption, Thomson scattering, Compton scattering, pair production (electron-positron pairs), and photonuclear absorption for a copper absorber as a function of the photon energy energy. In [Hermanns 2013](#).

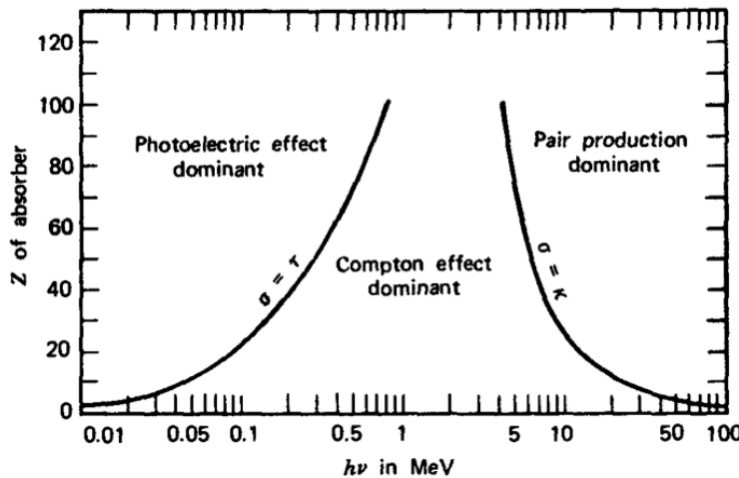


Figure 2.7: Relative importance of the three major types of photon interaction in matter. The lines show the values of Z and $h\nu$ for which the two neighboring effects are just equal. In Knoll 2000.

incident photons in the beam I_0 as a function of the linear attenuation coefficient and the absorber thickness t , as shown by equation 2.7.

$$\frac{I}{I_0} = e^{-\mu t} \quad (2.7)$$

The average distance traveled by a photon of the beam in the absorber before an interaction takes place is called “mean free path” λ , and is the reciprocal of the linear attenuation coefficient. In solids, for common gamma-ray energies, λ can vary in the range between few millimeters to tens of centimeters. A more widely used parameter is the “mass attenuation coefficient” μ_ρ , which normalize the linear attenuation coefficient to the absorber density ρ (equation 2.9).

$$\mu_\rho = \frac{\mu}{\rho} \quad (2.8)$$

If the mass attenuation coefficient is used, the convenient concept of mass thickness is also introduced, corresponding to the product of the absorber thickness t by its density ρ and generally measured in mg/cm^2 . For compound and mixtures, the mass attenuation coefficient is approximated by a summation of a weighted average of its constituent, as expressed in equation ??.

$$\mu_\rho = \sum_i w_i \frac{\mu_i}{\rho} \quad (2.9)$$

with w_i the proportion by weight of the i-th constituent, and μ_i/ρ its mass attenuation coefficient. The attenuation coefficients have specific values for a given photon energy $h\nu$ and absorber atomic number Z, and are tabulated on the National Institute of Standards and Technology (NIST) database according to the calculations in Seltzer 1993.

2.2 Ion range monitoring with prompt-gamma radiation

As introduced in chapter 1, the high ballistic precision of particle therapy is advantageous because it provides high dose selectivity while sparing the healthy tissues surrounding the tumors, but at the same time it makes such a cancer care modality quite sensitive to any source of uncertainty and deviation with respect to the treatment planning: patient mispositioning, organ motion or anatomical between fractions (such as tumor shrinking, weight loss, cavity filling). A reduction of the safety margins presently applied to the Planned Target Volume (PTV) to account for such uncertainties would be only possible with the availability of a real-time range monitoring system. As the primary beam stops inside the patient, the range control should be based on secondary radiations issued from nuclear reactions. In particular, the work presented in this thesis is focused on range monitoring techniques relying on the detection of Prompt-Gamma (PG) rays.

2.3 PG emission during particle therapy

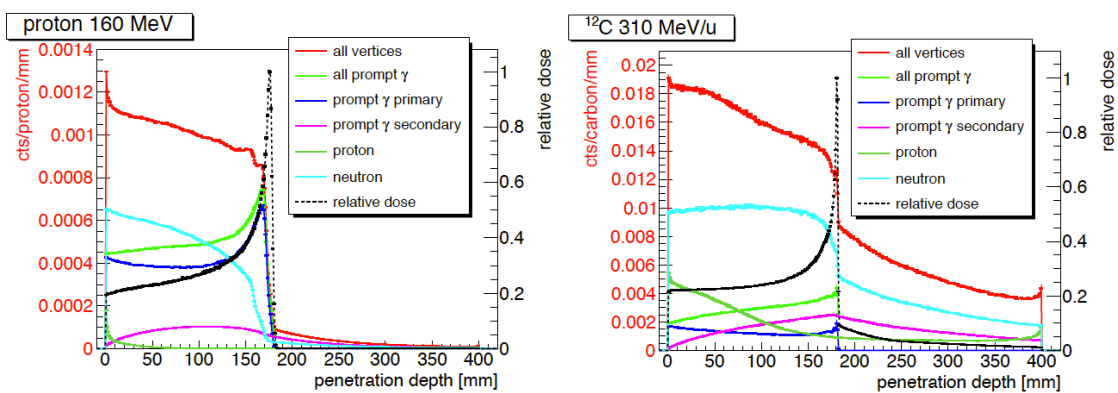
The PG range monitoring techniques rely on the emission of photons due to the de-excitation of excited nuclei within about one nanosecond after the nuclear interaction. The PGs are emitted in the whole solid angle around the patient and in a wide energy range (from some hundreds of keV up to 10 MeV).

Such a prompt radiation has been demonstrated to be correlated to the ion range for both protons and carbon ions. It can be exploited via single photon detection systems to provide a real-time feedback in case of major deviations of the measured range with respect to the planned one, and eventually trigger a treatment emergency stop.

LINE CONE RECONSTRUCTION (Cree et al. 1994), (Basko et al. 1998), (Parra 2000), (Hirashawa et al. 2003), (Maxim et al. 2009)

ITERATIVE RECONSTRUCTION (Schöne et al. 2010), (Zoglauer et al. 2011), (Gillam et al. 2011), (Lojacono et al. 2013), (Mackin et al. 2012)

2.4 Gamma cameras state of the art



(a) Emission vertices of secondary particles emerging from a cylindrical water target (15 cm diameter, 40 cm length) irradiated by a 160 MeV proton beam. An energy lower threshold of 1 MeV has been applied.

(b) Emission vertices of secondary particles emerging from a cylindrical water target (15 cm diameter, 40 cm length) irradiated by a 310 MeV/u carbon ion beam. An energy lower threshold of 1 MeV has been applied.

Figure 2.8: In Krimmer et al. 2017.

3

CLaRyS prototypes

The characterization method and the results presented in section 3.2.2 of this chapter have been published in Fontana et al. 2018.

Contents

3.1 CLaRyS gamma camera components	82
3.1.1 Scatterer	83
3.1.2 Collimator	88
3.1.3 Absorber	88
3.1.4 Beam tagging hodoscope	94
3.1.5 Camera acquisition system	100
3.1.6 Camera acquisition, monitoring and slow control software	102
3.1.7 Camera integration and mechanical support	104
3.1.8 Data analysis and image reconstruction	106
3.2 Camera component characterization and development status	107
3.2.1 Scatterer silicon layer characterization	107
3.2.2 Absorber Bismuth Germanium Oxide - $\text{Bi}_{12}\text{GeO}_{20}$ (BGO) blocks characterization	109
3.2.3 Hodoscope Photo-Multipliers (PMs) characterization	130
3.2.4 Hodoscope fiber test with electron source	133
3.3 Summary and perspectives	137
3.3.1 Silicon scatterer	137
3.3.2 BGO absorber	138
3.3.3 Scintillating fiber hodoscope	139
3.3.4 Acquisition and software	141
3.4 Conclusions	141

Following the highlighted limits of ion beam therapy (see chapter 1), a collaboration of five French research institutions was established in 2010 with the aim of exploring different experimental solutions for the ion range online monitoring. The research group originally involved the Institut de Physique Nucléaire de Lyon, France (IPNL), the Centre de Physique des Particules de Marseille, France (CPPM), the Laboratoire de Physique Subatomique et Corpusculaire, Grenoble, France (LPSC), the Laboratoire de Physique de Clermont, France (LPC) and the Centre de Recherche en Acquisition et Traitement de l’Image pour la Santé, Lyon, France (CREATIS). The collaboration focuses on the investigation of methods and detection solutions for the online monitoring of ion beam range during ion beam therapy treatment, and is so called *Contrôle en Ligne de l’hadronthérapie par Rayonnements Secondaires* (CLaRyS).

The main goal of the created collaboration is the parallel development of three gamma detection systems to be employed for ion range online monitoring purpose in the ion beam therapy field: a Positron Emission Tomography (PET) detector called *Détecteur Pixélisé de Grande Acceptance* (DPGA), a multi-collimated gamma camera and a Compton camera.

The design and development of the PET system is managed by the LPC group, which left the collaboration in 2017, and this detection system is not treated in this thesis work.

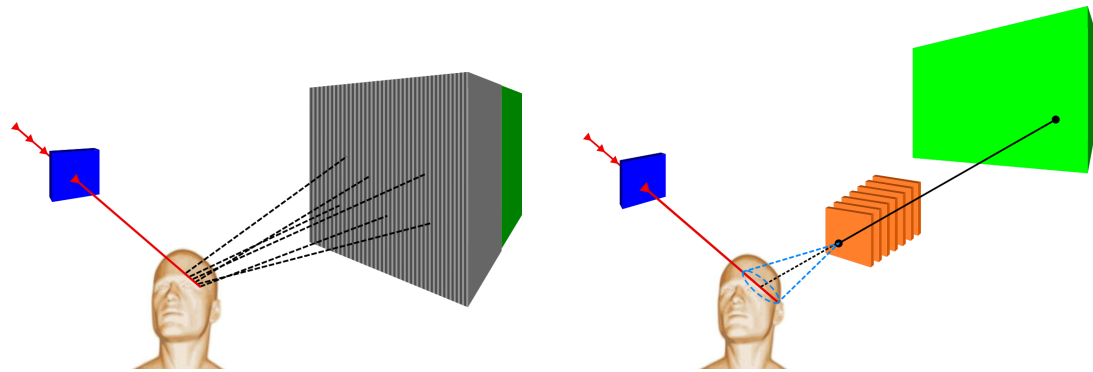
In this chapter the two gamma cameras (multi-collimated and Compton) prototypes are described in details, and the present status of the instrumental development is presented. A complete overview of the detector development carried out in the last years is presented for the sake of completeness, and my personal contributions are listed and detailed in the final section 3.4. In the following, an entire chapter (chapter 6) is dedicated to the tests of the detectors performed on ion beams.

3.1 CLaRyS gamma camera components

The two gamma cameras under development by the CLaRyS collaboration are devoted to the detection of prompt-gamma rays emitted during ion beam treatments (see chapter 2). The design of the two cameras has been optimized by different Monte Carlo simulation studies for what concerns both the detector components and the geometrical setup.

As already mentioned, a Compton camera is usually composed of two detector sections, a scatterer and an absorber: the CLaRyS prototype respects the standard design. In the scatterer, described in section 3.1.1, the prompt-gamma incoming ray is deflected by Compton interaction and the interaction position and energy deposited are stored. The scattered photon reaches then the absorber section, where its energy is ideally totally deposited and stored, again with the interaction position. This configuration is used to provide what is usually defined as “electronic collimation”, but a mechanical collimation is still an option for photon detection and localization. The scatterer section can be replaced by a mechanical collimator, described in section 3.1.2, which selects the parallel incoming photons then absorbed by the same absorber detector (a geometrical setup adaptation is possible to optimize the detection performance and will be discussed in the following). The mechanically collimated system is called multi-collimated camera, due to the collimator multi-slit structure.

As underlined in chapter 2, the prompt-gamma measurements are affected by several sources



(a) Scheme of the multi-collimated camera with the beam tagging hodoscope.

(b) Scheme of the Compton camera with the beam tagging hodoscope.

Figure 3.1: Schematic view of the two CLaRyS gamma camera prototypes: the multi-collimated camera (a) and the Compton camera (b), both coupled to the beam tagging hodoscope. The ion beam is represented by the red line, and some beam bunches have been highlighted. The detection principle is also sketched for the two detectors: the tungsten collimator select the parallel incoming photons for the multi-slit collimated camera (a), while the Compton cone is reconstructed with the two interactions in scatterer and absorber in the Compton camera (b).

of background: in particular, the signals detected by the two cameras can come from secondary particles other than prompt-gammas, like photons from positron annihilation, neutrons and protons (for beam of ions heavier than protons). One of the possible solution for background rejection is the use of Time-Of-Flight (TOF) information (see section ??), requiring a further detection section dedicated to the beam tagging. A beam tagging hodoscope is being developed in parallel and can be coupled to both the gamma cameras for TOF measurements; its description is presented in section 3.1.4.

A schematic view of the two prototypes is given in Figure 3.1.

3.1.1 Scatterer

The scatterer stack is one of the components of the Compton camera prototype. Dedicated to the photon Compton scattering, its design has been studied to fulfill the camera requirements.

The Compton events reconstruction strongly relies on the measurement of the energy deposited by the photon in its Compton interaction, mandatory to properly calculate the Compton scattering angle, which is then the aperture of the resulting Compton cone. The camera accuracy is then strictly dependent on the scatterer energy resolution. At the same time, the camera efficiency is dominated by the balance between Compton interaction and photoelectric absorption probability in the scatterer detector.

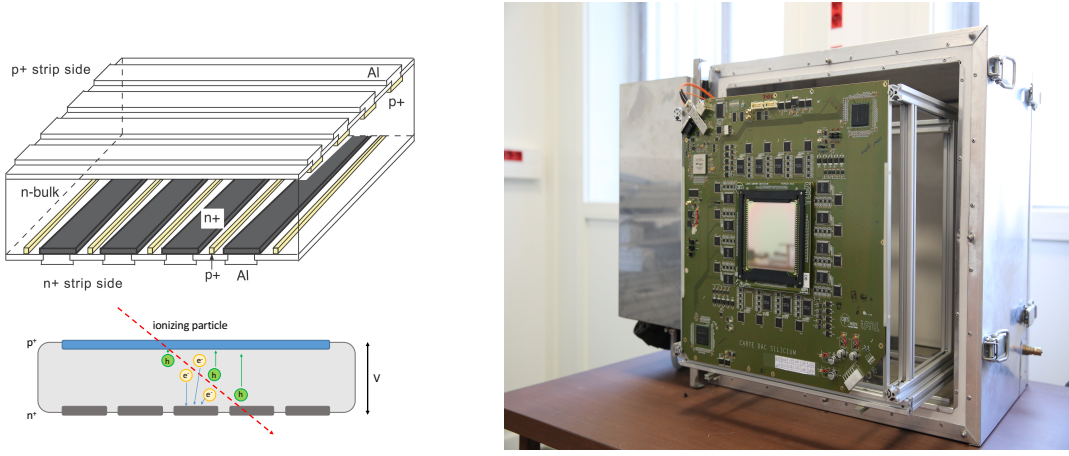
Given the need for at least two interactions for a proper event reconstruction (a Compton scattering in the scatterer section and an ideally complete absorption in the absorber section, described in 3.1.3), the material choice and the geometrical configuration play a fundamental role in the camera operation. The setup must be tuned in order to define the best trade-off

between Compton and photoelectric interaction probability and to optimize, as mentioned, the detector energy resolution.

Given the fact that the Compton interaction probability linearly increases with the material atomic number (Z), while the photoelectric absorption depends on Z^n with n varying between 4 and 5 according to the photon primary energy (Knoll 2000), a low Z material is preferred to optimize the Compton probability with respect to the photoelectric one. Considering now the detector energy resolution, it must be noticed that it is strongly governed by the so-called “Doppler spread”, which affects the relationship between deposited energy and Compton scattering angle. The Compton angle reconstruction formula in equation 2.3 neglects the initial recoil electron state, which is considered unbound. The energy state of the electron adds uncertainty on the reconstructed deposited energy, and so in the Compton angle calculation, with a relatively increasing contributions for decreasing incident photon energy. Given its direct dependence on the recoil electron binding energy, the “Doppler spread” is reduced for low Z materials. For a given material, the effect is larger for large scattering angles and it decreases with increasing energy of the incident photon. Following the described theoretical considerations, silicon detectors are the most coherent choice. This choice was mainly governed by the better energy resolution offered by silicon with respect to other materials (diamond, germanium, Cadmium Zinc Telluride (CdZnTe), scintillators), and it has been verified in simulation, where a silicon scatterer has been compared to competitor materials; the result are included in the Monte Carlo study presented in chapter 5.

Dedicated Monte Carlo simulation studies have been performed in order to define the most suitable geometrical configuration for the Compton camera, including the scatterer stack (Richard 2012). As a trade-off between detection efficiency and total cost, 10 layers were included in the original scatterer design. Concerning the layer size, about $10 \times 10 \text{ cm}^2$ of active area in the transverse plane have been identified as the most convenient choice, also considering the absorber size (see section 3.1.3) and the distances between the detection sections required by the TOF measurements and imposed by the detector rate acceptance in clinical conditions (see appendix A). Moving to the layer thickness, its choice is governed by the definition of the camera operation. The *Contrôle en Ligne de l'hadronthérapie par Rayonnements Secondaires* (CLaRyS) Compton camera does not aim to track the Compton recoil electron, which must be then absorbed inside the same scatterer layer where the Compton interaction took place. This requirement is necessary to well reconstruct the Compton interaction angle, which needs the whole transferred energy as parameter; in addition to this, a recoil electron escaping the involved detection layer can interact in a different layer causing false coincidences which affect the camera efficiency and imaging accuracy. In order to minimize the recoil electron escape probability, relatively thick detectors are needed. On the contrary, thin layers are required to measure precisely the depth of interaction, and thus the scattering angle. A good compromise was obtained with 2 mm thick slabs.

The technological choice of the collaboration was oriented to silicon Double-sided Silicon Strip Detectors (DSSDs), provided by the Norwegian company SINTEF. A schematic view of the detector principle is given in Figure 3.2a. The silicon crystal is doped with negative (n) and positive (p) charge carriers on the two opposite sides, creating diodes which are then reverse biased. A polarization voltage is applied to the two opposite sides of the crystal, and a depletion region with no free charges is created. A ionizing particle interacting in the depletion region generates electron-hole pairs in number proportional to the deposited energy. The generated charges drift towards anode (electrons) and cathode (holes) and are converted



(a) Schematic view of a standard DSSD (from Takeda et al. 2008) and sketch of the signal generation. The actual implantation scheme can slightly differ from the one present on the employed detectors.

(b) Scatterer silicon layer with its Front-End (FE) card in the thermal regulated box (described in section 3.1.1.2).

Figure 3.2: Overview of the scatterer layers, with its working principle (a) and a picture of the detector connected to the Front-End (FE) card in the thermal regulated box (b).

into electrical signals. The read-out is ensured by the implanted strips, which transfer the charges outside the detection region.

Each layer has an active volume of $96 \times 96 \times 2 \text{ mm}^3$, segmented with 64 strips per detection plane. The strip pitch is 1.41 mm, for a strip width of 1.31 mm. The applied bias voltage is nominally -750 V (applied to the p-side while the n-side is set to ground), and it is uniformly shared on the whole surface to obtain a homogeneous depletion region. A guard ring, composed of 23 strips surrounding the read-out ones on the p-side, ensures the desired voltage gradient. The more internal strip of the guard ring on the p-side is connected to the high voltage, while the n-side has a single strip for the guard ring in peripheral position and connected to the ground. The p and n read-out strips are then connected to the Front-End (FE) electronics via bonding cables.

The FE electronics card has been developed by the Institut de Physique Nucléaire de Lyon, France (IPNL) electronics group and is described in details in section 3.1.1.1. The silicon detector is directly plugged on the card, and the mechanical support for the scatterer stack has been studied according to the card size, as shown in Figure 3.2b.

Among the 10 received DSSDs, only 7 fulfilled the requirements imposed by the Compton camera application, mainly in terms of noise level (leakage current); 3 layers have been rejected, so that the final prototype scatterer is composed of 7 silicon planes.

The 7 selected layers have been characterized with a temporary acquisition system in terms of leakage current at different temperatures. The results of these measurements can be found in Ley 2015. The measurements enabled one to verify the producer specifications in terms of bias voltage to be applied for a complete detector depletion, as well as to identify the noisy strips and create a complete characterization database. In addition to this, they highlighted

the need to cool the detectors down with respect to the room temperature (25°C) in order to reduce the leakage current to acceptable levels, and so reducing the total noise level, affecting the detector performance. In order to accomplish the cooling task a thermal regulated box based on cold air pump has been designed and produced. It operates as the scatterer stack mechanical support, and it is described in section 3.1.1.2.

3.1.1.1 Scatterer Front-End card

As mentioned in the previous paragraph, the main requirement for the scatterer detector modules is a very good energy resolution. The desired working performance can be quantified as follows:

- 1 keV Full Width at Half Maximum (FWHM) energy resolution;
- 1.41 mm spatial resolution (corresponding to the strip pitch);
- 15 ns FWHM time resolution.

The scatterer FE card has been developed by the IPNL electronics group in order to achieve this performance. It is composed of two well separated sections, analog and digital, which must be kept separated in the card layout in order to minimize the contribution of the digital noise on the treatment of the analog signals. Moreover, in order to reduce the electronic noise, the analog section must be placed as close as possible to the detector, to minimize the signal path length.

At first, a dedicated Application-Specific Integrated Circuit (ASIC) has been designed and developed to treat the signals directly coming from the DSSD ([Dahoumane et al. 2014](#)). Each ASIC processes 8 detectors channels, so that 8 ASIC per plane are required for the read-out of a complete silicon layer. This section represents the core of the analog stage. The ASIC has been designed and tested to achieve the desired performance in terms of Equivalent Noise Charge (ENC), which must be lower than 118 electrons Root Mean Square (RMS) in order to obtain the 1 keV FWHM energy resolution, signal dynamics and accepted detection rate. The analog raw signal first passes through a Charge Sensitive Amplifier (CSA), which returns an analog amplified signal. This pulse can be further amplified with a Slow Shaper (SHS) based on a Capacitor Resistor - Resistor Capacitor (CR-RC) filter, which filters and shapes the signal in about 1 μ s, or via a fast amplifier (with 15 ns shaping time). The first mode is used for a refined charge (deposited energy) measurement and can be employed for detector tests and characterization, while the second is the standard working one which allows for fast energy and time measurements. The amplified signal finally passes through a discriminator, which gives a digital output. Analog (from CSA or SHS) and digital signals are then sent to the digital stage of the card for the measurement of time, position and energy.

The digital stage is mainly composed of one Analog-to-Digital Converter (ADC) module per ASIC and two Field Programmable Gate Arrays (FPGAs). The analog signal from the ASIC is processed by the ADC, which is a 12-bit module with 8 channels, with a sampling rate of 100 Mega Sample Per Second (Msps). Each ADC returns 16 Low-Voltage Differential Signaling (LVDS) pairs (2 per channel), which are sent to the FPGAs together with two clock signals (two LVDS pairs) and the 8 digital outputs of the ASIC. So, 44 input channels of the FPGA are used

for the acquisition of 8 read-out channels (one ASIC). Two FPGAs Altera Cyclone III ([Altera 2012](#)) are installed on the card to handle the signals coming from the whole detector (128 channels, 64 per detection plane): both of them are equipped with a Time-to-Digital Converter (TDC) for the time measurement.

A third FPGA (Altera StratixII GX ([Altera 2009](#))) is finally installed on the card to handle the processed data collection and the communication with the acquisition system, described in section 3.1.5, via a 3 Gbit/s link.

The ASIC has been developed in three versions, and the cards have been optimized during the development process and produced in its final version (shown in Figure 3.3a) in the Spring 2017. The 7 cards are now available and the development of the FPGA firmware is ongoing.

More details about the card layout, components and operating principle, as well as a description of the tests performed during the development can be found in [Chen 2017](#) and [Dahoumane et al. 2012](#).

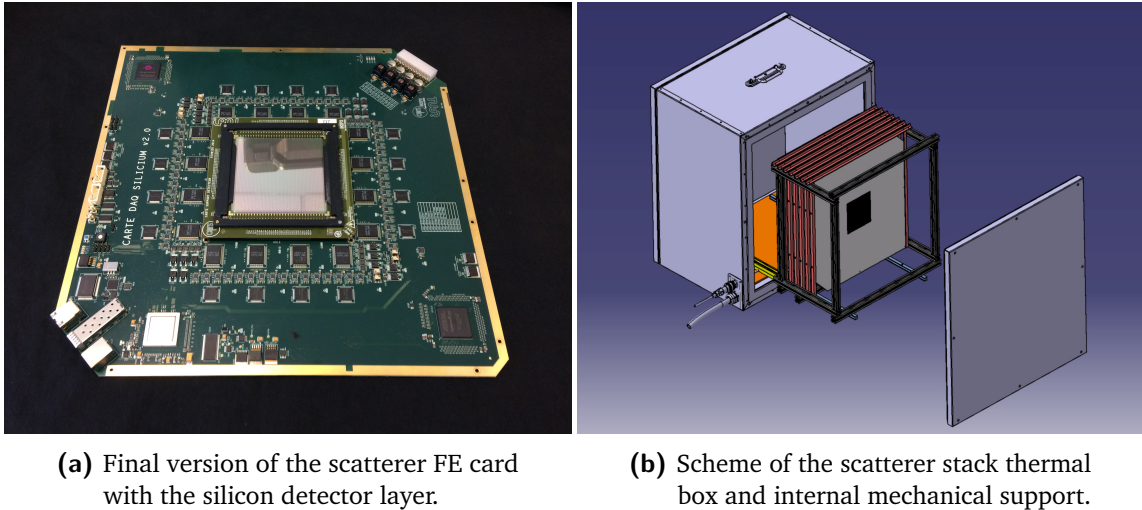
3.1.1.2 Scatterer thermal regulated box

The results of the leakage current tests performed on the silicon detectors showed the need of cooling the detector down to achieve the required performance in terms of noise, which affects the spatial, time and energy resolutions. The leakage current has been studied in temperature cycles in the range -40 - +40 °C, and an overall consistent behavior has been observed both on N and P strips of the detector. The leakage current slightly increases in the range -40 - 0 °C, with values in the range 0 - 8 nA for the analyzed strips, and then drastically increases beyond 0 °C, with peaks of more than 80 nA at +40 °C. The complete description of the performed measurements and the detailed results can be found in [Ley 2015](#).

A cooling system is needed for the silicon detectors operations: it must be able to keep the temperature constant and below, at least, 0 °C, preferably around -20 °C where the leakage current is more stable in case of small temperature variations. The clinical environment limitations must be considered to design such a cooling system (portability, gas, noise level), as well as the material budget and the mechanical integration with the other camera components.

The implemented solution consists in the thermal regulated box shown in Figure 3.2b, together with one of the silicon layers. The size of the box is 490×490×300 mm³, and the structure is composed of 2 mm of aluminum and three insulation layers of 10 mm of silica aerogel Spaceloft® ([Aspen Aerogels 2011](#)), for an equivalent thickness of 2 mm of silicon (0.7% of interaction probability for 1 MeV photons). The cooling is performed via an electric air pump, which is able to keep the temperature inside the box at -20 °C with a 400 W heat evacuation power. The heat power produced by the 7 silicon FE cards in operation must be verified, but the estimate confirms the effectiveness of the thermal box nominal performance. Once card and detector will be fully operational, a test will be performed to check the temperature stability inside the box and possible issues like water condensate/freezing, thermal dilatation, vibrations.

The FE cards and the silicon layers are fixed inside the box via a mechanical support designed and produced by the IPNL mechanics group. The support, which ensures a millimeter position



(a) Final version of the scatterer FE card with the silicon detector layer.

(b) Scheme of the scatterer stack thermal box and internal mechanical support.

Figure 3.3: Scatterer silicon layers equipment: final version of the FE card (a) and scheme of the detector integration in the thermal regulated box (b).

accuracy, is fixed on metal rails which allow to easily handle each detector layer. A scheme of the thermal box and the internal support is shown in Figure 3.3b.

3.1.2 Collimator

The multi-collimated camera is equipped with a multi-slit collimator, with tungsten alloy slabs (97% tungsten, nichel and iron for the remaining components - density 18.5 g/cm^3) of $1.5 \times 120 \times 170 \text{ mm}^3$. Its design has been extensively studied in Monte Carlo simulations (Pinto et al. 2014), and it can be easily adapted to different geometrical configurations of the absorber detector and to various monitoring requirements. In particular, the distance between neighboring slabs can be modified, as well as the number of total slabs, in order to find the best trade-off between detection efficiency and spatial resolution; this depends on the distance patient-collimator, on the required extension of the field of view and on the desired monitoring time. Two identical collimators of $30 \times 14 \times 17 \text{ cm}^3$ have been produced, in order to be able to set several absorber configurations in the transverse direction (extended version along the beam axis or in the perpendicular direction). In Figure 3.4a a picture of the tungsten collimator is presented, while in Figure 3.4b we show a schematic view of a possible multi-collimated camera configuration.

3.1.3 Absorber

The Compton and multi-collimated camera absorber was initially conceived as a very large surface plane composed of 96 BGO blocks recovered from a dismantled PET system HR+ by SIEMENS, documented in (Adam et al. 1997; Brix et al. 1997).

BGO is one of the most used scintillators for gamma detection applications, thanks to a fair energy resolution and an optimal gamma detection efficiency, given the high effective atomic number (75) and high density (7.12 g/cm^3) (Elftmann et al. 2015) which maximize the

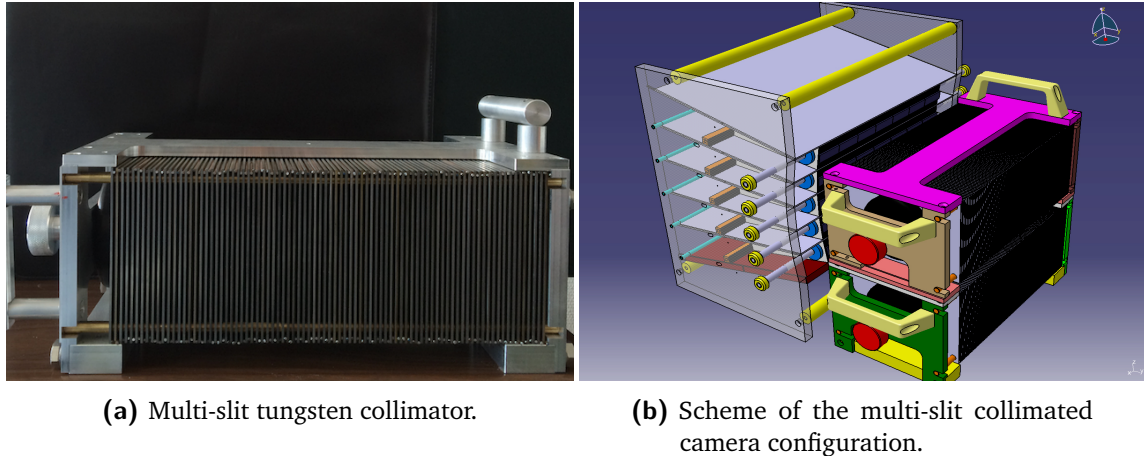


Figure 3.4: Tungsten collimator and its setup in the multi-slit collimated camera. Two identical collimators are available, with $1.5 \times 120 \times 170 \text{ mm}^3$ tungsten slabs and a pitch of 8 mm. The two tungsten multi-slit collimators are placed in front of a 6×5 Bismuth Germanium Oxide - $\text{Bi}_{12}\text{GeO}_{20}$ (BGO) block absorber setup in its mechanical support (see section 3.1.3). Both the single collimator setup (size and pitch) and the two collimators configuration can be easily modified to adapt the system to peculiar applications.

photo-electric probability. Moreover, the absence of internal radioactivity which characterizes other scintillator materials employed in the same field (i.e. Lutetium-Yttrium OxyorthoSilicate - $\text{Lu}_{2(1-x)}\text{Y}_{2x}\text{SiO}_5$ (LYSO), Cerium-doped Lutetium Oxyorthosilicate - $\text{Lu}_{2(1-x)}\text{Ce}_{2x}\text{SiO}_4$ (LSO)), makes it suitable for low noise detectors, required by a Compton camera to reduce the amount of random coincidences, one of the main sources of background for the application in ion beam therapy monitoring (Ortega et al. 2015). As highlighted in (Hueso-González et al. 2015), LYSO and LSO show overall better performances with respect to BGO for what concerns mainly energy and time resolution, due to an about 4 times higher light yield, but the gap is reduced for the detection of gamma rays in the prompt-gamma energy range (especially beyond 1 MeV). The limited cost of BGO with respect to LSO and the comparable performances in the prompt-gamma energy range make it an optimal solution for prompt-gamma camera prototypes, provided fast timing and spectroscopy are not the main requirements.

Each BGO block composing the gamma camera absorber has an area of $3.5 \times 3.8 \text{ cm}^2$, with a thickness of 3.0 cm. The mono-block BGO crystal is streaked in a 8×8 pseudo-pixel matrix; a reflecting material is inserted between the pseudo-pixels to improve the light collection and optimize the spatial information accuracy via pixel separation. The read-out is achieved via four Photo-Multiplier (PM) tubes per block, composing a quartet, coupled to the block back surface. Thanks to the internal streaked structure of the block, the scintillation light is shared between the four PMs depending on the pseudo-pixel where the interaction takes place (in case of multiple interactions more than one pseudo-pixel can be involved). The streaks have a different thickness according to their position in the block: they fully cover the block thickness on the block borders and they progressively shorten towards the block center, with a mono-block structure in the central block section on the entrance face. Note that the crystal dimension and streaked structure were optimized by the manufacturer for the detection of 511 keV photons, therefore it is not a-priori obvious that such blocks could keep their performance above 1 MeV. The reconstruction of the position of interaction is done via Anger logic, i.e. with a center of gravity calculation.

The whole set of recovered blocks was supposed to undergo a “reconditioning” process, including the PM removal, the crystal back surface polishing with diamond-based abrasive tool, the single PMs gain characterization and grouping in quartets with similar gains, the final re-coupling of the PMs and block shielding.

A set of “reconditioned” blocks have been tested with the method described in section 3.2 and their performance have been compared to a set of original blocks. An overall degradation of the detection performance has been verified on all the tested “reconditioned” blocks, which showed lower amplitude output signals probably link to a reduction of the collected scintillation light. Various correction methods have been tested, with unsatisfactory results. According to the outcome of these tests, summarized in [Sandjong et al. 2017](#), the collaboration finally opted to adapt the camera design for the use of original, “non-reconditioned” BGO blocks.

Thirty original blocks are now available to compose the absorber detector. In addition to the already presented features, it must be noticed that the lateral faces of the original blocks, as well as the half of the PM length, are covered with a reflecting material which ensures the complete collection of the scintillation light. This is probably a component which was not well reproduced during the reconditioning process. The whole structure is then protected by a 1 mm thick aluminum foil, which also isolates from external light contamination.

Figure 3.5a shows one BGO block before the coupling to the PM quartet: the streaked structure is clearly visible, as well as the white reflecting material separating the pseudo-pixels and the one surrounding the block lateral sides. As mentioned, the same material also covers part of the photo-multiplier tubes, as shown in picture 3.5b, where the four PMs are glued to the block back surface. The described aluminum cover is visible in Figure 3.5c, while in Figure 3.5d a scheme of a block together with the related PM quartet is given. The spatial reconstruction logic is also reported in the same figure.

3.1.3.1 Absorber Front-End and read-out cards

General design A custom front-end card has been designed and produced by the LPC research group Application et Valorisation des Interactions Rayonnements-Matière (AVIRM) and is used for the read-out of each BGO block. The card is equipped with four voltage modulators which divide the provided high voltage on the four PM tubes. The voltage sent to each PM can be tuned via screw-potentiometers on these modules. A ± 5 V low voltage is applied to the cards as supply for the differential amplifier modules, one per PM. Differential output channels are used to send the PM signals to the read-out card, called Analog Sampling Module (ASM) board, via flat cables. A picture of the FE card is given in Figure 3.6a. To be noticed that four analog output channels have been added on some cards in order to allow laboratory tests with a signal treatment based on standard electronics modules, as described in section 3.2. These outputs retrieve the signal before the differential amplification stage, so that the low voltage supply is not needed for this read-out configuration.

The PM signals amplified by the FE card (differential outputs) are received by the ASM boards. Developed by the LPC AVIRM group, it is based on the VERSABUS Module Eurocard (VME) standard and designed for the application in the *Détecteur Pixélisé de Grande Acceptance* (DPGA) PET system, equipped with LYSO mono-crystals, grouped in quartets and read-out by the same FE card described above. The adaptation to the gamma camera application, so that

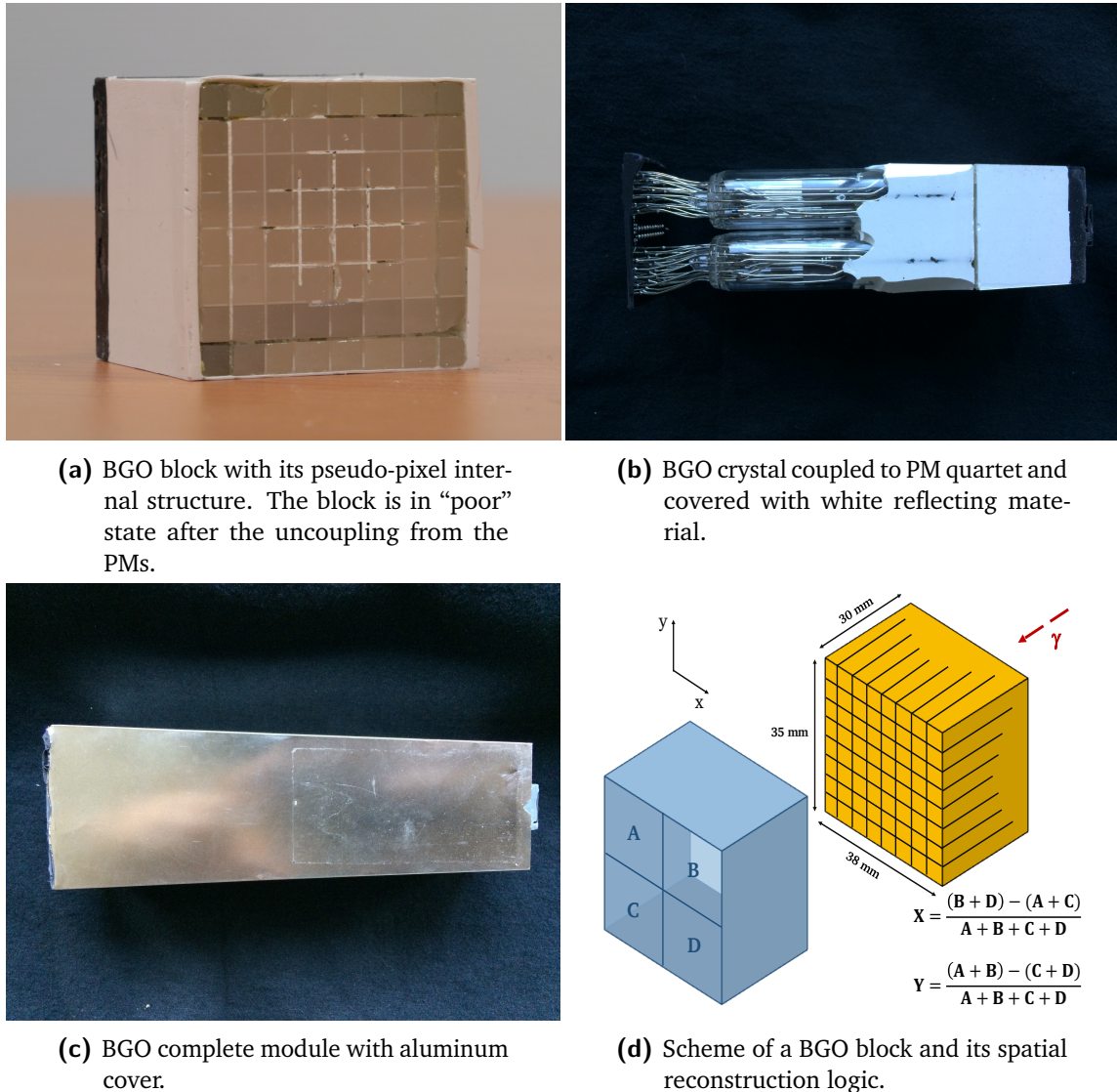
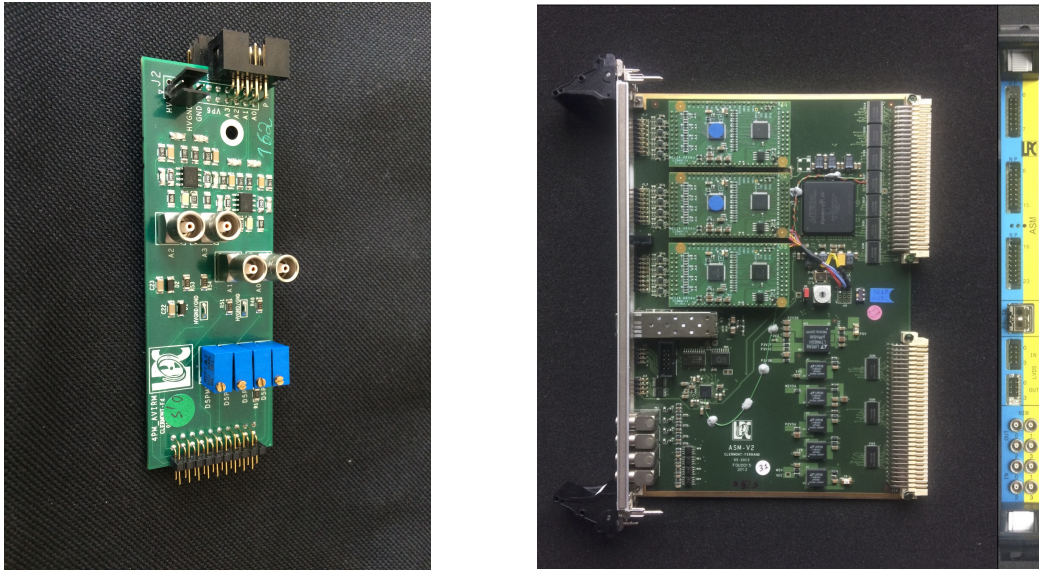


Figure 3.5: Components of an absorber module and its working principle.



(a) FE card of the absorber BGO detectors.
4 analog outputs have been added for test purpose.

(b) ASM board of the absorber BGO detectors. Each board performs the read-out of 6 blocks.

Figure 3.6: Absorber read-out electronics: FE card (a) and ASM board (b).

for the BGO modules signal treatment, involves only the firmware part. Each board has 24 differential inputs and it is so able to read the signals from 6 BGO blocks; a total of 5 boards are then needed for the complete read-out of the gamma camera absorber (30 blocks). The incoming signals are treated by three intermediate cards equipped with a Domino Ring Sampler (DRS4) chip ([Ritt 2009](#)), designed and developed at the Paul Scherrer Institut, Villigen, Switzerland (PSI), with 8 sampling channels at a maximum frequency of 5 Giga Sample Per Second (GspS) (200 ps period) for 1024 samples, and an ADC 12 bit-20 MHz module. The sampling frequency of the DRS4 can be modified to fit with the specific application: in particular, the BGO blocks produce wider signals with respect to the LYSO crystals of the DPGA, therefore the sampling is reduced to 1 GHz for our application. A FPGA Altera Cyclone IV GX ([Altera 2015](#)) receives and handles the digital outputs of the three intermediate cards and is in charge of sending the data to the acquisition system via a 3 Gbit/s optical link. The FPGA also governs the generation of the pre-trigger signal which is sent to an auxiliary board called Trigger et HORloge (THOR) in order to start the acquisition of the gamma cameras, as detailed in section 3.1.5.

Absorber acquisition with development card

During the development of the final camera acquisition system based on the Micro Advanced Telecommunications Computing Architecture (μ -TCA) equipment, which required a dedicated firmware development ad testing process, a temporary acquisition system has been set for the absorber BGO blocks, mainly dedicated to the test and characterization of the ASM boards. It is based on a commercial development card, provided by Terasic (Altera University Program), equipped with an FPGA Altera Cyclone V ([Terasic 2015](#)). The FPGA card can be programmed for the needed tasks, and it is directly connected to an acquisition PC via Ethernet cable. Three High-Speed Mezzanine Card (HSMC) connectors allow for the connection to an expansion board SFP-HSMC ([Terasic 2009](#)), again by Terasic, provided with a second FPGA and with optical fiber input/output connectors for the interface to the ASM boards. A single optical input is configured for this acquisition setup, with the firmware developed by the AVIRM group

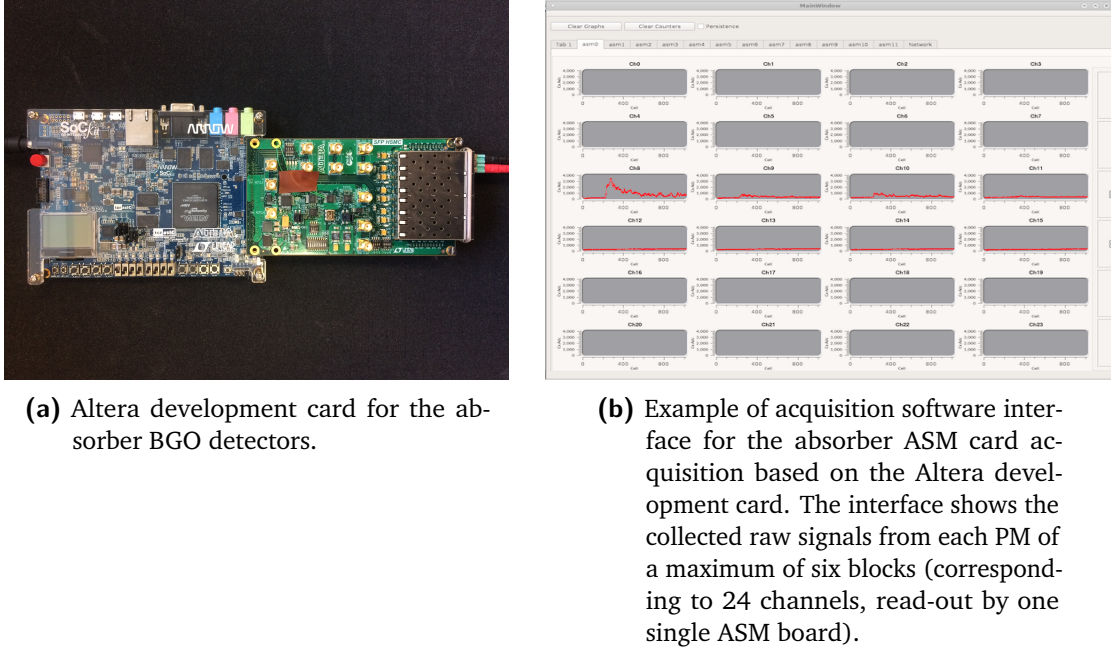
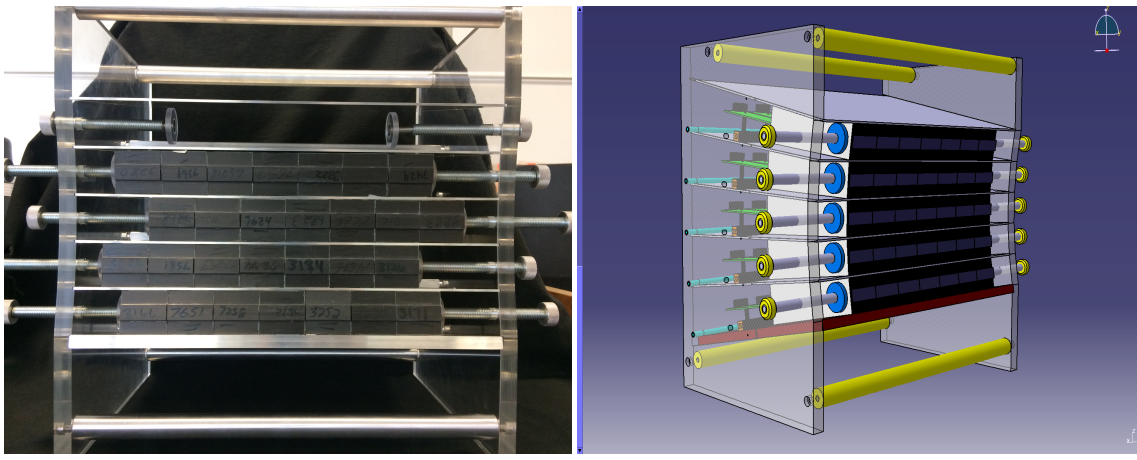


Figure 3.7: Details of the temporary absorber acquisition based on the Altera development card.

in LPC and adapted at the IPNL; one single ASM card can be connected to the board, so that a maximum of 6 BGO blocks can be read-out at the same time. A picture of the development card connected to the mezzanine is given in Figure 3.7a. Figure 3.7b shows an example of the user interface and data visualization of the C++ based acquisition software developed and provided by the AVIRM group.

3.1.3.2 Absorber mechanical support

A first mechanical structure for the absorber detector was initially conceived by the LPC group in order to hold up to 100 modules, foreseen by the original camera design. The reduction of the number of available blocks caused by the “reconditioning” process failure made necessary an adaptation of such a support. The new design has been carried out by the mechanics group of the IPNL in order to be compact and flexible in terms of detection modules setup. Figure 3.8 displays both a picture and a scheme of the absorber configuration with its mechanical support. The two lateral sides are built with Poly Methyl Metacrylate (PMMA) boards connected by metal bars, and the BGO blocks can be arranged in up to 5 rows of variable size, ranging from 3 to 7 blocks. Each block row is supported by a thin metal foil, designed to reduce at minimum the blocks separation and to respect the original ring geometry deriving from the SIEMENS PET system. The blocks composing a row are then laterally pressed via two screws on the two sides of the structure, which can also be used to adapt the relative row position horizontally. On the back side, a metal bar is added to avoid undesired movements, and the FE cards are fixed with plastic pillars. The realized support results to be versatile, compact and adapted to the prototype tests for both the Compton camera (where a squared setup is preferred) and the multi-collimated one (where the collimator geometry must be fit by the absorber geometrical configuration).



(a) Picture of the absorber detector in its mechanical support.

(b) Scheme of the absorber detector with its mechanical support.

Figure 3.8: Absorber front view with the BGO block lines arranged in the mechanical support (a). Scheme of the BGO absorber with its mechanical support (b).

3.1.4 Beam tagging hodoscope

A beam tagging hodoscope is being developed in parallel to the two gamma cameras, mainly for background rejection and reconstruction optimization purposes. As already mentioned, the detection of prompt-gammas (with mechanical or “electronical” collimation), is affected by the presence of other secondary particles produced during the ion beam irradiation, mainly neutrons. This background source can be efficiently identified and reduced by applying TOF selection windows to the data acquisition. The TOF measurements can be performed using the accelerator radio-frequency signal as reference for cyclotron accelerators, while a direct beam detection results to be more accurate for synchrotron based treatments. An auxiliary detector is then needed before the beam interaction in the patient.

The CLaRyS hodoscope prototype is designed to provide space and time information about the incoming primary beam, particle by particle or bunch by bunch, depending on the beam intensity and detector efficiency and rate acceptance which must be characterized. In addition to the already explained use of the time information, a space primary particle tagging can be used to improve the reconstruction accuracy and constraint the possible reconstructed emission vertex in case of analytic reconstruction approach for both the multi-collimated and Compton cameras (see chapter 2).

The detector under development is based on squared 1 mm^2 polystyrene scintillating fibers BCF-12, 140 mm in length, provided by Saint Gobain ([Saint Gobain 2017](#)). A picture of the hodoscope on its mechanical support (detailed in the following) is presented in Figure 3.9. The fibers are arranged into two perpendicular planes for a two-dimensional spatial information: each plane is composed of 128 fibers, for a total active area (for 2D measurements in coincidence) of $128 \times 128\text{ mm}^2$. The active detector surface is completely covered with black tape, which shields from external light. The scintillation light produced in the fibers by a ionizing particle depositing energy is transported to the read-out system via FORETEC optical fibers (1.55 cm diameter, 1 m length), which are connected to the scintillating fibers thanks to a custom mechanical support and to a proper gluing process (see Figure 3.10a). Each scintillat-

ing fiber is read-out on both sides to optimize the detector efficiency and to improve the time resolution, which does not depend on the interaction position along the fiber with this configuration; the total number of read-out channels is then 512. The signal read-out is ensured by 8 multi-anode PMs Hamamatsu H8500 ([Hamamatsu 2006](#)) shown in Figure 3.10c. The optical fibers are connected to the PM anode surfaces through a plastic custom mask, shown in Figure 3.10d. The PMs are equipped with custom black boxes which operate as mechanical support and external light protection (see Figure 3.10a). In order to provide further light isolation, the whole PM boxes are covered with black tape.

The optical fibers are connected to the 8 PMs with a logic aiming to increase the maximum counting rate. 4 PMs are dedicated to the read-out of the horizontal fibers, and 4 to the vertical ones, and the neighboring fibers are connected to different PMs. An active area of $4 \times 4 \text{ mm}^2$ on the two planes is then read-out by all the 8 PMs. Moreover, the two sides of the same scintillating fiber are connected on the same PM. This fiber connection logic also improves the detector robustness; in case of problem on one PM, only 1 mm each 4 mm is lost on a single plane, so that the detection of the beam is still possible on the whole active area.

Each PM is connected to a single custom FE card. The hodoscope FE cards have been developed by the IPNL electronics group: their design is described in section 3.1.4.1. 8 FE cards are then used for the read-out, and the collected data are sent to the acquisition system described in section 3.1.5.

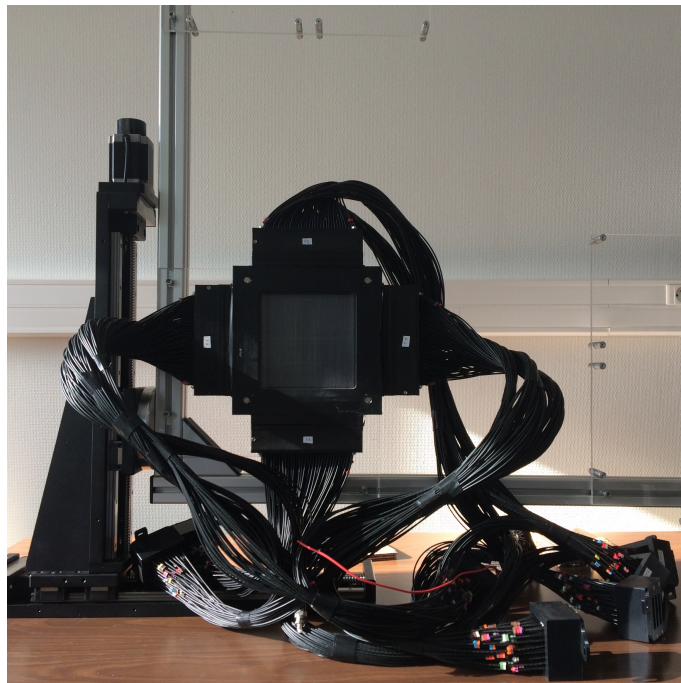


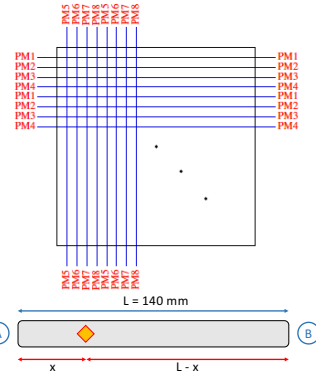
Figure 3.9: 128×128 scintillating fiber hodoscope on its 2-dimensional moving stand.

3.1.4.1 Hodoscope Front-End card

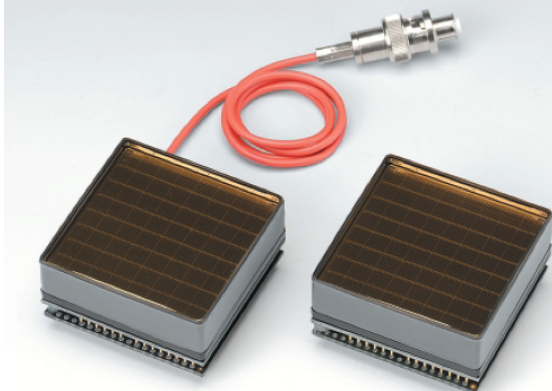
The hodoscope is designed to tag in space and time the incoming beam ions, so that the signal read-out must be optimized to provide accurate time measurements and a high detection rate acceptance, with reduced dead time and detection efficiency close to 100%. In particular, the



(a) Scintillating fiber hodoscope during mounting process.



(b) Scheme of the scintillating fiber connection to the PMs (top) and of the double-sided fiber read-out (bottom).

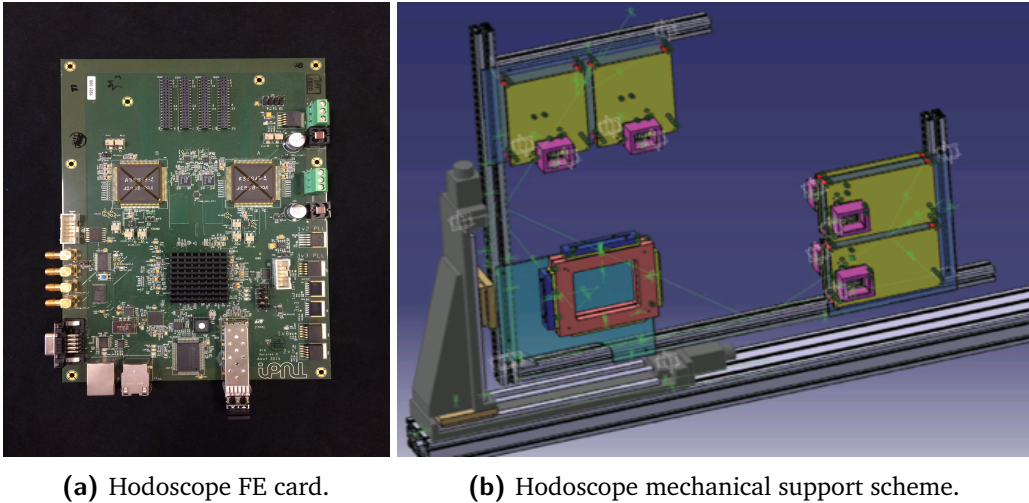


(c) Hodoscope read-out PMs Hamamatsu H8500.



(d) PM plastic mask for optical fiber connection.

Figure 3.10: Details of the scintillating fiber hodoscope setup.



(a) Hodoscope FE card.

(b) Hodoscope mechanical support scheme.

Figure 3.11: HODOPIC board (a) and scheme of the beam-tagging hodoscope two-dimensional moving stand (b).

design requirements include a maximum counting rate acceptance of 10^8 Hz per detection plane, with a time resolution of 1 ns (Krimmer et al. 2014). The hodoscope FE card shown in Figure 3.11a has been developed by the IPNL electronics group to fulfill the listed requirements. The Hamamatsu PM is connected to the 64-channel connector (4 connectors of 16 channels each) and two custom ASICs are dedicated to the data first treatment (32 channels each).

A first version of the FE ASIC has been developed in 2012 by the group Micro-électronique RHône AUvergne (MICRHAU) for the read-out of 8 channels (designed for the 32×32 fiber hodoscope prototype described in section 3.1.4.3). The input part is composed of a current conveyor, and the output one has two sections: a current discriminator and a charge pre-amplifier for the charge measurements in test mode (Deng et al. 2012, 2013). In addition, the ASIC gain can be tuned channel by channel, so that the response of each PM output channel can be fine tuned with respect to the others.

The second version of the ASIC includes all the features of the first version, with the addition of a TDC based on a 160 MHz clock for a more accurate time tagging of the detected events. Moreover, a Delay Locked Loop (DLL) is installed to divide the main clock in 32 intervals: for each event, the DLL state is stored in a 32 bit register and then encoded in a 5-bit Gray decoder. As a result, the TDC has a 6.25 ns dynamics, with a sampling step of 195 ps and a time resolution of 58.8 ps RMS, for a maximum accepted rate of 10^8 Hz (Deng 2012).

The third and final ASIC version, called HODOPIC, is adapted to the big size hodoscope (512 read-out channels), with the extension to 32 channels and with the TDC implemented on the second version. An external ADC is used for the charge measurement in test mode for a single channel, selected via slow control. All the ASIC outputs are sent to a FPGA installed on the card for the actual time measurement and data decoding. The FPGA finally handles the data transmission to the acquisition system, depending on the card version.

A first card has been developed to test the first ASIC version with the 32×32 fiber hodoscope. It is based on a FPGA Altera Cyclone III (Altera 2012) and on 9 ASICs, with a LabVIEW acqui-

sition. A single card is enough for the read-out of the complete small hodoscope prototype. This first setup has been tested on beam at Grand Accelerateur National d'Ions Lourds, Caen, France (GANIL) and Heidelberg Ion Therapy Center, Germany (HIT), and a sub-ns time resolution has been verified, together with the expected 1 mm spatial resolution on the two fiber planes and an efficiency of more than 90% at a 10^6 acquisition rate.

The second prototype of the card, shown in Figure 3.11a, has been adapted to the 512-channel hodoscope described in the previous section and to the gamma camera acquisition system described in 3.1.5: each card has two HODOPIC ASICs, 32 channels each, so that it is designed for the read-out of a single 64-anode PM. 8 cards are then needed for the read-out of the whole hodoscope. This version is based on a FPGA Altera StratixII GX ([Altera 2009](#)), and the connection to the acquisition is ensured by a 3 Gbit/s optical link. 4 digital input-output channels are installed for test and validation purpose, together with an Ethernet port.

Further details about the different card versions and the applied validation tests can be found in [Chen 2017](#).

The hodoscope card firmware has been developed in 2017 and tested in simplified versions on beam, as detailed in chapter 6.

3.1.4.2 Hodoscope mechanical support

The beam tagging hodoscope is set between the beam nozzle and the patient and requires a dedicated mechanical support. In order to profit from the large active area and to be able to remotely control the hodoscope position in the beam transverse plane, the detector is mounted on a 2-dimensional moving table (see the picture in Figure 3.9), which also supports the FE cards. Detector and FE cards are then integral and translate together. A scheme of the moving table is given in Figure 3.11b.

The 2-axis table is provided by Beijing Winner Optical Instruments; it is composed of two motorized linear stages, connected via a right angle bracket. The two stages have a moving range of 30 cm each and the stepper motors have a step resolution of 20 μm . The employed motor controller is a Newport XPS-Q8 ([Newport 2017](#)), equipped with 8 channels for the simultaneous control of a maximum of 8 motors. The movements are steered with an online interface or with a LabVIEW-based program, which will be integrated in the final setup of the slow control software under development with the cameras.

3.1.4.3 Small hodoscope prototypes

Before the production of the large active surface hodoscope prototype described in section 3.1.4, two smaller prototypes have been produced and tested in order to assess the potential of such a kind of detector for the required application. The first and simplest version consisted of one single scintillating fiber per plane, and the readout was performed with two PM tubes directly coupled to the scintillating fibers, without optical fibers. A picture of this prototype is given in Figure 3.12a. This simple version of the detector has been used as a demonstrator of the basic detection principle.

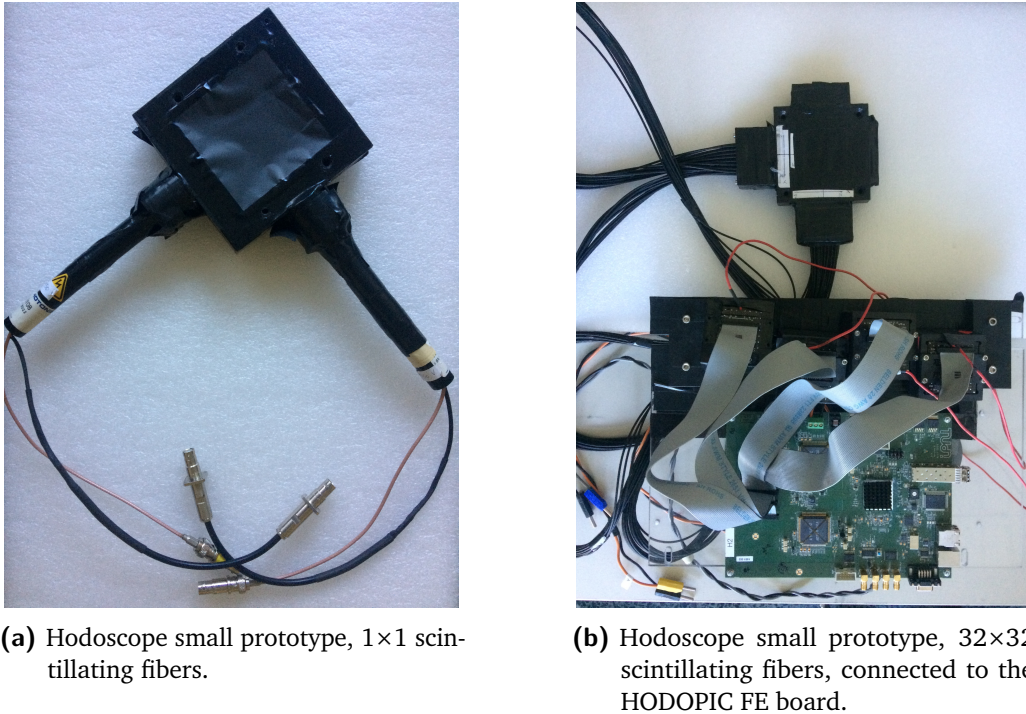


Figure 3.12: Hodoscope small prototypes.

A second small size version of the final detector has been produced with almost the same features as the large area prototype but with simplified read-out logic. It is equipped with two perpendicular planes of 32 1 mm^2 scintillating fibers each (Saint Gobain BCF-10 ([Saint Gobain 2017](#))), with a length of 4 cm and a total active area for a 2D read-out of $32 \times 32 \text{ mm}^2$. As in the big hodoscope, the scintillating fibers are coupled to FORETEC optical fibers which transfer the scintillation light to 4 Hamamatsu H8500 PMs. 16 channels per PM are used, so that 2 PMs are dedicated to the horizontal fibers and 2 to the vertical ones, and the signal read-out is performed on a single side of the scintillating fibers (2 adjacent fibers are read by two different PMs). As the total number of read-out channels is 64, a single FE card is sufficient for the whole detector. In Figure 3.12b the 32×32 -fiber hodoscope prototype is shown together with its FE card; 4 connection cables (16 channels each) are used to couple the PMs to the FE card.

The 32×32 -fiber hodoscope prototype has been tested in 2014 on proton and carbon ion beams (at the GANIL - 75 MeV/u ^{13}C , HIT - protons and carbon ions at various energy, Institut de Physique Nucléaire d'Orsay, France (IPNO) - 25 MeV protons) with the first version of the FE card (see section 3.1.4.1): an efficiency of more than 90% has been retrieved, with a time resolution of 1 ns FWHM (timing measurements performed with respect to the accelerator high frequency signal). Some more details about this beam tests results are given in chapter 6. The final version of the FE card has been also tested with this detector, and the test description and results are presented in chapter 6.

3.1.5 Camera acquisition system

The TOF gamma cameras developed by the CLaRyS collaboration are composed of various detection sections: beam tagging hodoscope and BGO absorber for the multi-slit collimated camera, with the addition of the silicon scatterer stack for the Compton camera. The acquisition system must be able to handle the data flux from the different components, for a total of 20 FE cards (7 for the silicon scatterer, 8 for the hodoscope and 5 for the absorber), select the events according to the chosen trigger logic and create and send the data packets with the right format to the acquisition PC.

The system is based on the μ -TCA standard; originally conceived as an adaptation of the Advanced Telecommunications Computing Architecture (ATCA) systems used in the telecommunication field for high-flux data transfers, it is employed for relatively simpler tasks and adopted in the particle physics domain since less than ten years (Abellan et al. 2013; Cachemiche et al. 2012). A standard μ -TCA crate equipped with a μ -TCA Carrier HUB (MCH) (shown in Figure 3.13a) is used as general purpose support for the Advanced Mezzanine Card (AMC), which is the section adapted for each specific application. An AMC40 has been developed for high energy physics applications, in particular for the Large Hadron Collider beauty (LHCb) experiment at Conseil Européen pour la Recherche Nucléaire, Geneva, Switzerland (CERN), and has been adapted for the gamma camera acquisition system by the CPPM research group (see Figure 3.13b). This card includes a FPGA Altera Stratix V (Altera 2016), 24 optical inputs at 4.8 Gbit/s and 12 at 9.6 Gbit/s, a 1 Gbit/s Ethernet output for the connection to the acquisition PC. In addition to the μ -TCA based components, two intermediate cards in VME format complete the acquisition system. The so-called THOR cards (see Figure 3.13c), developed in VME format at LPC in parallel to the ASM card, are used to generate and share the clock signal (40 MHz) common to the whole electronics cards for synchronization purpose (first card) and to govern the pre-trigger and trigger signals (second card) as explained in the following lines.

For both cameras, the acquisition starts in case the absorber section detects an interaction: the ASM involved card deals with the creation of a pre-trigger signal, which corresponds to the digital output signal and contains a time stamp (see the ASM card description in section 3.1.3.1). The pre-trigger is sent to the THOR card that governs its sending to the AMC40 card. To be noticed that the ASM card should in principle be able to handle both pre-trigger and data packets, but for this first prototype, the THOR card enables one to avoid conflicts in the ASM card signal handling. The acquisition process is easier and safer with the THOR card interaction.

In the multi-slit collimated camera, the pre-trigger signal directly operates as a trigger validating the data collection from absorber and hodoscope. In the Compton camera, the AMC40 receives the pre-trigger from the THOR card and sends it to the scatterer FE cards, which explore their buffer looking for events in the coincidence time window; if a coincidence is found, a trigger signal is generated by the scatterer FE card and sent to the acquisition system, which then starts the data read-out from all the detectors. A simplified graphical overview of the complete acquisition system and logic is given in Figure 3.14.

The AMC40 card makes use of a buffer for each FE card of the three detector sections, where the collected data are stored until the creation of packets of the selected size to be sent to the acquisition PC. The data transfer is achieved via a 1 Gbit/s Ethernet link, and the chosen

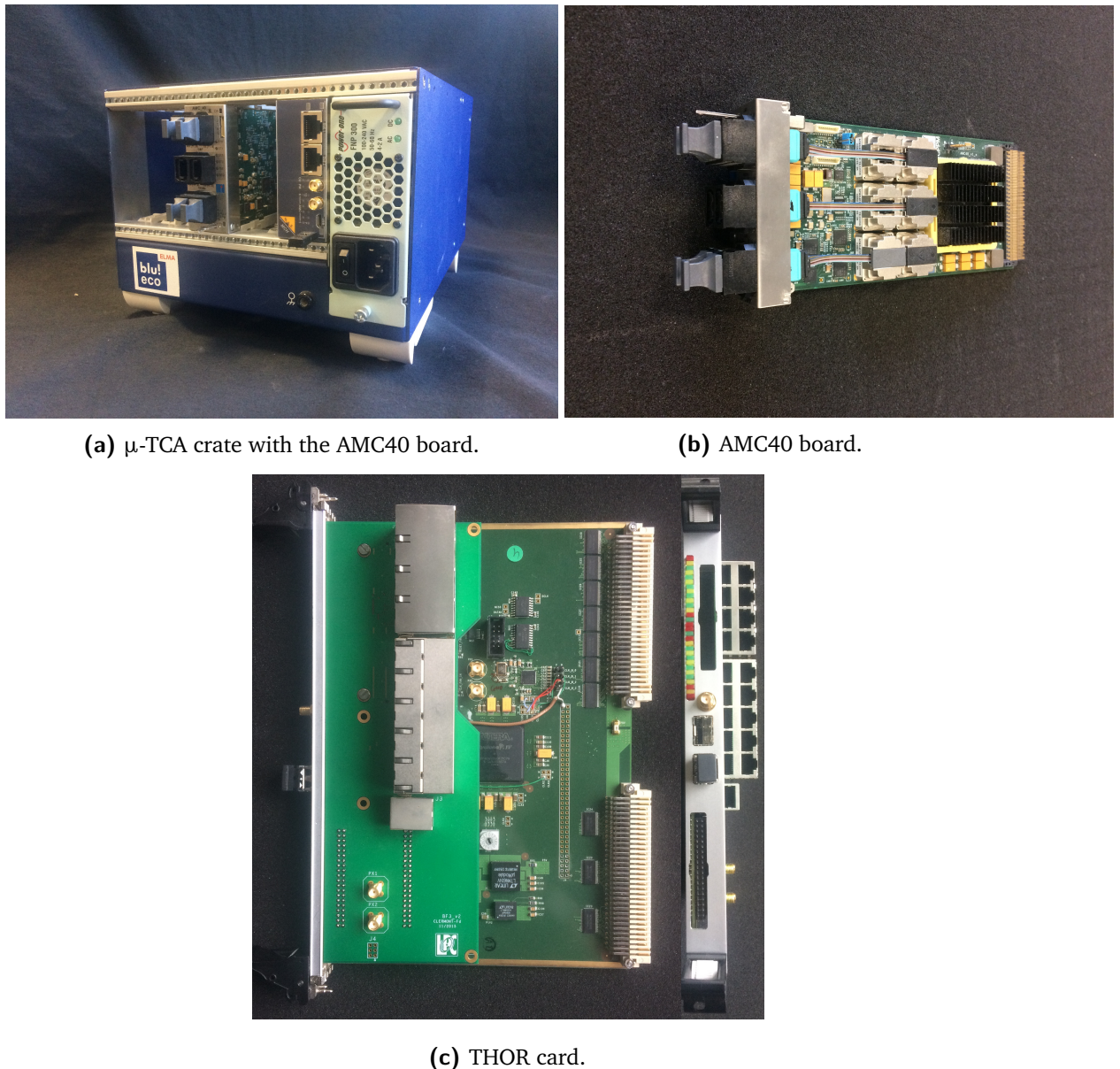


Figure 3.13: Acquisition system components: μ-TCA crate (a), AMC40 board (b) and THOR card (c).

standard is the User Datagram Protocol (UDP). The data format has been fixed at the camera conception stage and slightly modified following the electronics developments; it is deeply described in the appendix A, which also reports the expected data flow obtained in previous simulation studies.

In addition to the already explained functions, the μ -TCA is also in charge of handling the slow control signals for the configuration of the detector FE cards. The chosen format is in this case the Transmission Control Protocol (TCP), which is more reliable and ensures a feedback in case of communication failure. The possible slow control signals are detailed in appendix A.

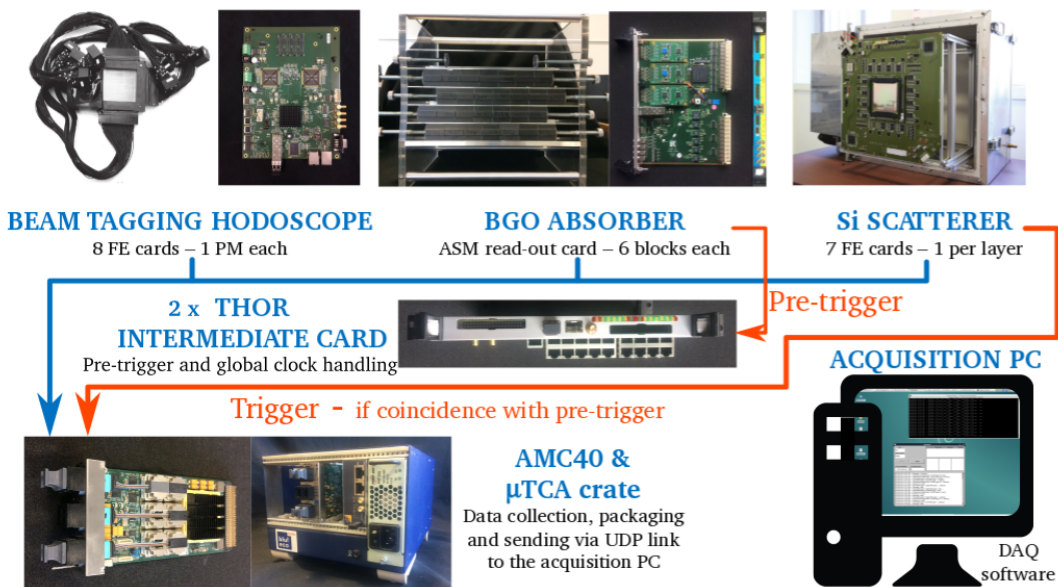


Figure 3.14: Schematic view of the Compton camera acquisition system. For the multi-collimated camera, the trigger and pre-trigger signals are the same.

3.1.6 Camera acquisition, monitoring and slow control software

The UDP data packets sent by the μ -TCA acquisition system via Ethernet link are received by the acquisition PC thanks to a C++ based acquisition software, developed at the IPNL. The software decodes the data packets and builds the events by grouping the data from the two (for the multi-slit collimated camera) or three (for the Compton camera) detection sections according to the time stamp. During the decoding process, the software also verifies the received data format and can highlight problems in the data encoding by the μ -TCA; this feature is used during the test phase to check the functionality of the AMC40 firmware. The reconstructed events are then stored in binary files with the structure presented in appendix A. The data file size can be selected by fixing the number of events stored per run in the acquisition run, knowing that each event can be composed by a slightly variable number of bits, according to the amount of detector modules involved. The file collection corresponding to the same run will be then grouped at the analysis stage. The number of events per file must be tuned taking care of the available Random Access Memory (RAM) (32 Gb), where the data are temporarily stored before the writing process on the hard-disk. In Figure 3.15a the minimal graphical interface developed for the acquisition software is shown.

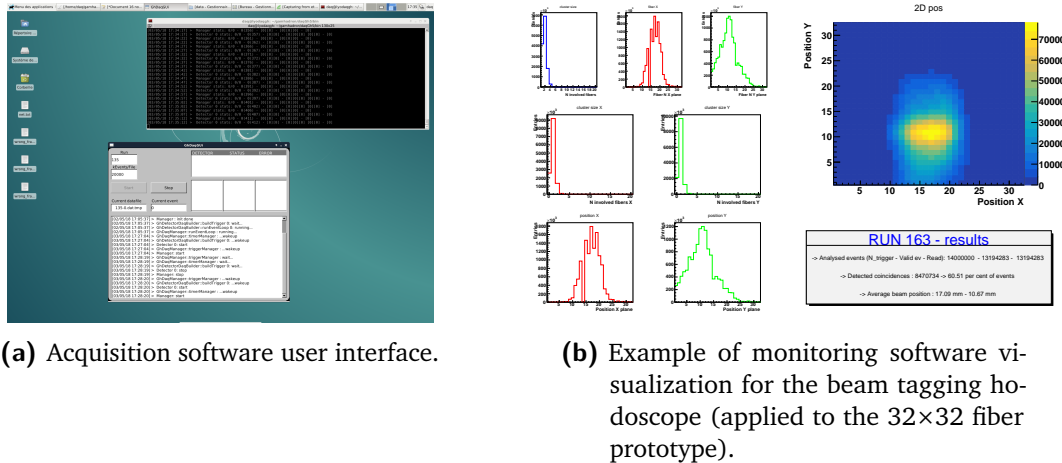


Figure 3.15: Software tools: user interface of the acquisition C++ software (a) and example of the ROOT (Brun et al. 1997) monitoring software visualization for the beam tagging hodoscope 32×32 fiber prototype.

A monitoring software has been developed in order to have a direct real-time feedback on the camera data acquisition. The software can show some information about the ongoing data collection, and it is at present designed to work on a single detector section (hodoscope, scatterer or absorber) or for the coupled acquisition of absorber and hodoscope (collimated camera). It is based on ROOT (Brun et al. 1997) with the following working logic: during the acquisition, it continuously searches for new data files in the storage folder, and analyses in the desired way a selected number of events per file, directly from the binary format. An example of the visualized output for an hodoscope monitoring is shown in Figure 3.15b. This picture corresponds to an acquisition performed during a beam test at the Centre Antoine Lacassagne, Nice, France (CAL), where the 32×32 fiber hodoscope has been tested, together with the monitoring software. More details about the beam tests are given in chapter 6.

As mentioned, the present version of the software is not yet adapted to the monitoring of the whole Compton camera, even if it can handle the three detector components with minor modifications. In addition to this, it is not automatically synchronized with the acquisition software, and not optimized in terms of needed calculation time. In the next future the planned upgrade will slightly modify the working logic by directly connecting the monitoring to the acquisition: the acquisition software will automatically send a selected fraction of events to the monitoring output during the acquisition, so that the search for data files would not be anymore necessary. This will drastically reduce the monitoring dead time and calculation time, achieving an actual online control.

Acquisition and monitoring software has been tested thanks to a data simulator developed in C++, which is able to create data UDP packets with the correct format and send them on the same Ethernet port used for the data collection, simulating a server-client communication.

As mentioned in section 3.1.5, the μ -TCA handles both the data collection and transfer and the slow-control of the whole system, including the configuration of all the electronics cards (discriminator thresholds, channel gains, ASIC reset signals, working mode, etc.) and the read-out of the feedback signals. The development of the slow-control software is ongoing at the IPNL: it is designed in LabVIEW and includes all the needed controls in a single user interface.

A dedicated PC is foreseen for this task, connected to the μ -TCA via TCP protocol. The slow-control software will also govern the high and low voltage suppliers for the detectors and acquisition electronics boards, the scatterer thermal box temperature setup and control, the steering of the 2D positiong table dedicated to the hodoscope, and the steering of the camera moving table, described in the next section. All the listed instruments will be connected to a patch panel, and a local network will be created for the camera equipment.

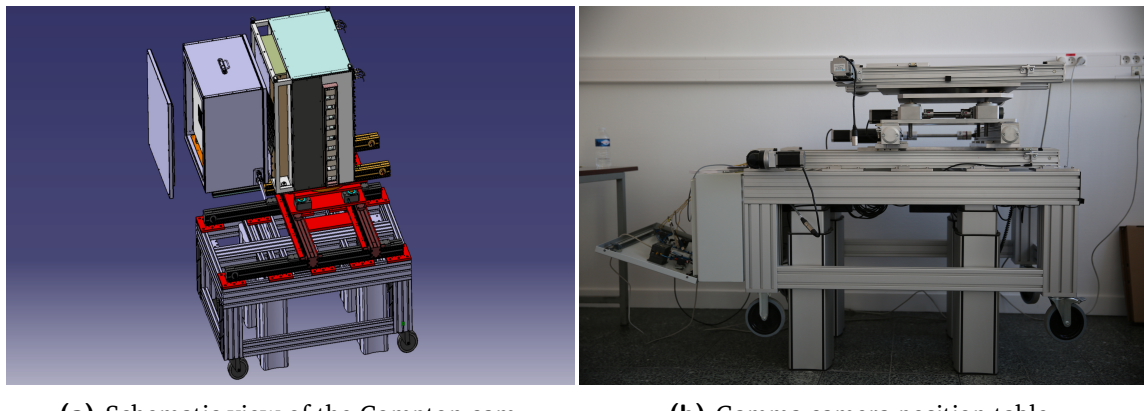
3.1.7 Camera integration and mechanical support

In order to setup the two camera configurations (multi-slit and Compton), the described components, together with the related mechanical supports, must be integrated in an integral system, with the exception of the beam tagging hodoscope which has its own dedicated mechanical support, being placed between the beam nozzle and the target. A general mechanical structure is then needed to support the camera; it is required to be movable, as compact as possible but at the same time robust and large enough to support absorber and scatterer (or collimator), for a total maximum weight of about 100 kg. In addition to this, it should be possible to remotely control the position of the various camera components in order to adapt their position in 3D with respect to the beam line and to the target. The present system is not dedicated to clinical operation. However, it should cope with a versatile use with horizontal beams, including the use with anthropomorphic phantoms at clinical accelerators.

The realized solution is shown in Figure 3.16b. It is composed of two sections: a positioning table on wheels, designed and provided by Rose & Krieger, equipped with 4 telescopic feet, and a 4-axis moving table installed on it, developed by Kinetic System. The wheels allow to first position the camera, and the 4 telescopic feet are used to regulate with 1 mm precision the whole system height, in the range 630 mm - 1280 mm from the ground, to be adapted to the specific beam line. The feet are expected to be able to support a maximum weight of 150 kg. The telescopic feet are not connected to the slow-control but are controlled by a remote controller on the table itself. On the top surface of the table, $1200 \times 750 \text{ mm}^2$, the 4-axis moving table is fixed and allows to adapt the camera position in 3D (distance camera-target, height, direction parallel to the beam line) with a $100 \mu\text{m}$ resolution and a range of 40 cm. In addition to this, a fourth axis allows to adjust the distance between the two detector components in the direction perpendicular to the beam line, in a range of 30 cm (to be noticed that this range is reduced by the size of the scatterer thermal box). The four axes are connected to the positioning table patch panel, which is directly controlled by the slow-control program in LabVIEW. Finally, a further manual control allows to rotate the whole system with respect to the table axis, in a range of ± 10 degrees.

In Figure 3.16a we present the mechanical scheme of the complete positioning table, with the Compton camera installed on it.

In Figure 3.17 we show a view of the three detectors composing the Compton camera, with one scatterer layer installed in the thermal box and the absorber mounted on the positioning table, and the beam tagging hodoscope on the right side on its dedicated mechanical support.



(a) Schematic view of the Compton camera integration on the positioning table.

(b) Gamma camera position table.

Figure 3.16: Details of the gamma camera integration and mechanical support.



Figure 3.17: View of the Compton camera assembly with the beam tagging hodoscope on the developed mechanical supports.

3.1.8 Data analysis and image reconstruction

All the data collected at the detector characterization stage (in standalone working mode) are analyzed via ROOT ([Brun et al. 1997](#)) and Python custom developed codes. Further details are given in section 3.2, where the performed characterization measurement on the three detector section are described. Concerning the data analysis for the complete systems (multi-collimated and Compton camera), automatic ROOT-C++ based programs will be developed in order to achieve an online data treatment for both tests and clinical application purposes. The raw collected data samples must be adapted to the image reconstruction codes, needed to retrieve the final image for both camera configurations.

The multi-collimated camera is designed to provide 1-D information about the prompt-gamma emission distribution along the beam direction: the required data treatment is then relatively simple, and based on the chosen geometrical configuration of collimator and absorber. The detected events are spatially assigned to the BGO block pseudo-pixel where the gamma interaction took place, by means of center of gravity calculation with the four signals provided by the involved block and then with an automatic algorithm developed for test purposes and detailed in section 3.2.2.3. Knowing the block position within the whole absorber setup, the prompt-gamma emission profile can be reconstructed assuming a photon path perpendicular to the absorber entrance face. This simple approach can be refined thanks to the spatial information given by the beam tagging hodoscope. The detected beam position can constrain the reconstructed emission position to a point, so that a 3-D emission profile can be obtained. This solution is being explored but a final, working reconstruction code is still not available.

Concerning the Compton camera, the image reconstruction requires the detection of coincidences in the scatterer and absorber sections: position and deposited energy information in the two detectors allow for the reconstruction of the emission cone via Compton kinematics, as explained in details in chapter 2. The photon emission profile (prompt-gamma for the ion beam therapy application, gamma emitted by the radio-tracer for the nuclear medicine approach) is then obtained via the overlap of several reconstructed cones. As described in chapter 2, analytic and iterative algorithms have been proposed and developed to reconstruct the final image given by a Compton camera, which intrinsically transport a 3-D information. In particular, the image reconstruction of the CLaRyS Compton camera relies on a line-cone analytic algorithm based on back-projection and on the code developed by the CREATIS group for the iterative method ([Hilaire et al. 2014; Lojacono et al. 2013; Maxim 2014](#)).

The analytic line-cone reconstruction is only applicable in ion beam therapy monitoring and is based on the intersection of each reconstructed emission cone with the beam direction information given by the beam tagging hodoscope. This method assumes that the prompt-gammas are generated along the beam path, considered as a straight line, and limits to two points the possible emission position for each detected event. The overlap of several events will then allow for the emission distribution definition in 3-D. The Compton camera performance has been tested for the application in ion beam therapy monitoring, and this reconstruction code has been employed to treat the simulated data: the results are given in chapter 4, where we usually refer to this reconstruction method as “line-cone”.

The iterative algorithm is called List Mode-Maximum Likelihood Expectation Maximization (LM-MLEM) and is able to include in the calculations the space and energy resolution of the involved detectors, leading to the reconstruction of a 3-D image. It requires the definition of

a reconstruction volume, which is divided in a given number of voxels, and the list of coincidence events. Starting from the simple event back-projection, it defines the probability that a given photon detected in the Compton camera has been emitted from the voxels in the defined volume. For every iteration, this probability is re-computed taking into account the results of the previous iteration, converging to the most likely emission distribution. The number of iterations is fixed by the user and must be a trade-off between reconstruction accuracy and calculation time. This method has been used with ion beam therapy monitoring simulated data and compared to the line-cone method (see chapter 4), as well as for the reconstruction of point-like sources simulated for the application of the camera in nuclear medicine, presented in chapter 5. To be noticed that, concerning the reconstruction of prompt-gamma emission distribution in ion beam therapy application, the spatial information about the beam given by the beam tagging hodoscope is still not included in the employed version of the code. An upgrade is under study and is at present at the preliminary test stage.

3.2 Camera component characterization and development status

As detailed in the previous sections, the CLaRyS TOF gamma cameras are equipped with various detector components with very different features. Each part must be separately studied in order to characterize its behavior and allow the final camera integration and operation.

I mostly worked on the beam tagging hodoscope and on the BGO absorber, and in the next paragraphs the performed measurements are described in details. Concerning the scatterer stack, the results achieved before the beginning of my PhD thesis are briefly described for the sake of completeness.

The results presented in this section also introduce the following one (3.3), where all the development steps still needed for a clinical implementation of the cameras are explained.

3.2.1 Scatterer silicon layer characterization

The 7 DSSDs selected for the application in the Compton camera system among the 10 provided by the producer have been characterized in terms of leakage current. The measurements have been performed by colleagues before the beginning of my PhD thesis. The extended description of the employed test-bench, the performed tests and the results are presented in Ley 2015.

The leakage current is an evaluation of the systematic uncertainty expected on each read-out channel, corresponding to a background current detected without an energy deposit in the depletion region. The 7 layers have been tested at the complete depletion voltage of -750 V with a test-bench developed at the IPNL specifically for these measurements. It is composed of a custom electronics card which is used to supply the detector with the depletion voltage and to the current read-out via the connection to a nano-ammeter (Nuclear Instrumentation Module (NIM) module with 0.1 nA resolution). Moreover, temperature variations in the range -40°C - +40°C have been realized with an automatic system, with the detectors and read-out card placed in a temperature programmable chamber Weiss WTL 64 (WeissTechnik 2017). The

temperature variations, the channel selection and the data acquisition are handled by a Raspberry Pi. The temperature step has been fixed to 5°C. Finally, temperature cycles have been carried out in order to study the detector response to rapid temperature variations and the time required to stabilize the leakage current at the working temperature, with temperature steps between -20°C (working temperature) and +25°C (room temperature).

The leakage currents measured at room temperature (+25°C) are homogeneous on all the strips, with some local exceptions. The average detected value is about 20 nA. Concerning the measurements at -40°C, the average value for the n strips is close to 0 nA, while a current of 3-4 nA is still detected on the p strips. On each layer, a maximum of 3 strips show higher leakage current values; this is acceptable for the final application in the Compton camera. Moving from -40°C to +40°C, the leakage currents respect, on average, the expected trend defined by equation 3.1 ([Spieler 1998](#)).

$$I_p(T) \propto T^2 \times e^{-\frac{E}{2k_B T}} \quad (3.1)$$

where $I_p(T)$ is the leakage current as a function of the temperature, T is the temperature in Kelvin, E the silicon energy gap energy in eV, k_B the Boltzmann constant (8.617×10^5 eV K $^{-1}$).

The leakage current is generally stable or is slightly increasing for temperatures below 0°C, with values always below 10 nA. Beyond 0°C, it rapidly increases reaching some tens of nA at 40°C, depending on the specific strip. This observation justifies the need of the described thermal regulated box, which is able to maintain a constant temperature of -20°C during the detector operation, placing them in a minimum and stable leakage current regime.

The application of quick temperature variation steps between -20°C and +25°C allowed to estimate the time required by the detector to re-establish the working regime with minimal leakage current. When moving from -20°C to +25°C, the leakage current increases rapidly up to the values already detected during the slow temperature variations, with a transition time of the order of less than ten minutes. Approximately the same time is required to stabilize the leakage current after the cooling down to -20°C.

In addition to the described leakage current measurements carried out with the 7 10×10 cm 2 DSSDs, a small silicon layer prototype (8×8 strips) has been tested with the first version of the FE card ASIC. The first version of the card allowed for the read-out of 8 channels, so that the 8 p strips have been characterized with this read-out system, while the n strip data have been collected with NIM modules. The data treatment has been performed thanks to VME modules.

The detector has been exposed to Sodium-22 (^{22}Na) and Cobalt-57 (^{57}Co) radioactive sources: the ^{22}Na source, producing two back-to-back 511 keV gammas as a result of the β^+ annihilation, has been used for timing measurements in coincidence with a Lanthanum Bromide (LaBr_3) crystal, while the 122 keV photons of the ^{57}Co source are used to characterize the energy response by photoelectric absorption.

The detected time resolution has been estimated to be in the range 13-23 ns FWHM for the p strips, and between 30 and 80 ns FWHM for the n strips (knowing that the “hole” drift time is about 3-4 times more than the electron one). The energy resolution is between 10 and 20 %

FWHM for the tested strips. This test also allowed to verify the first version of the card and move forward with the development of the second and third version at present available for the final detector.

Thanks to the summarized measurements, a calibration database is available for the 7 silicon layers, which showed overall stable and acceptable performance. The final version of the card must be tested in order to check these results, validate the board behavior and move to the first detector tests on beam. All the details concerning the next development steps are presented in section 3.3.1.

3.2.2 Absorber BGO blocks characterization

The BGO modules composing the Compton and multi-collimated camera absorber have been recovered from a SIEMENS PET system: they have been originally optimized for the detection of 511 keV photons from positron annihilation, and they have to be tested for the new gamma detection system, which must be able to deal with photons in the prompt-gamma energy range, i.e. from about 100 keV to approximately 10 MeV.

Each block must be characterized in terms of spatial and energy response, and the read-out PMs have to be calibrated to obtain a uniform response on the whole block surface (see section 3.1.3 for the detector description). The employed method relies on the work presented in J. G. Rogers et al. 1994 and Tornai et al. 1994 and on the calibration process described in Golnik 2015 and Hueso-González et al. 2015, and has been extended with more refined features.

The measurements are performed with the irradiation by gamma sources, emitting photons at defined energies: in particular, we used 511 keV and 1275 keV photons from a ^{22}Na source, and the two photons emitted by a Cobalt-60 (^{60}Co) source, at energies of 1173 keV and 1332 keV.

The employed ^{22}Na source is a cylindrical source with an active diameter of 4 mm, and an activity of about 400 kBq: it has been placed at a distance of about 5 cm from the block entrance surface, with the center of the source facing the center of the block transverse surface. The ^{60}Co source has been installed in a lead cylindrical container (12 cm radius and 35 cm height), equipped with three different apertures: point-like ($2\times 2\text{ mm}^2$), linear ($2\times 50\text{ mm}^2$) and squared ($50\times 50\text{ mm}^2$). The design of the lead container has been studied in simulation to ensure the proper radiation protection, and produced according to the specifications defined by the IPNL mechanics group. The activity of the ^{60}Co source is about 1.7 MBq, and the square shape has been used to obtain an homogeneous irradiation of the BGO block, with the block set with the center of the entrance surface corresponding to the source position, at a distance of 12 cm.

The signals produced by the four PMs of each block are collected via four analog outputs on the FE card (see Figure 3.6a). The four retrieved signals per event are treated via standard NIM modules in order to be adapted to the acquisition systems and measurement purposes.

Two different acquisition systems have been used for this characterization work. First, the PXIe described in section 3.2.3 with its two flash ADC read-out modules, 8 channels each,

is used for the spatial and energy characterization and calibration of the tested blocks. A scheme of the acquisition setup for this part of the calibration is given in figure 3.18. The raw signals coming from the four PMs are amplified and shaped via NIM modules (quad shaping bipolar amplifiers), which were fine-tuned via a pulse generator in order to adapt the amplification factor of each channel (an amplification factor of about 50 has been applied to the raw signals). The amplified signals are then split in order to be treated for trigger purpose. The trigger for the acquisition is based on the sum of the four signals, and a fixed threshold is applied for background rejection. The employed discriminator provides the logical trigger signal, which is sent to the trigger input of the ADC modules on the PXI. The four amplified signals, conveniently delayed, are sent as inputs to the ADC modules on the PXI, together with the sum signal which is used for experimental verification of the acquisition setup. A LabVIEW-based acquisition software, developed for this particular application at the IPNL, provides real time event visualization together with a partial, on-line spatial reconstruction of the events, and stores them in text files for further analysis. A second threshold can be set at the software level in case particular selections are needed during the acquisition, otherwise the event selection is performed at the analysis stage.

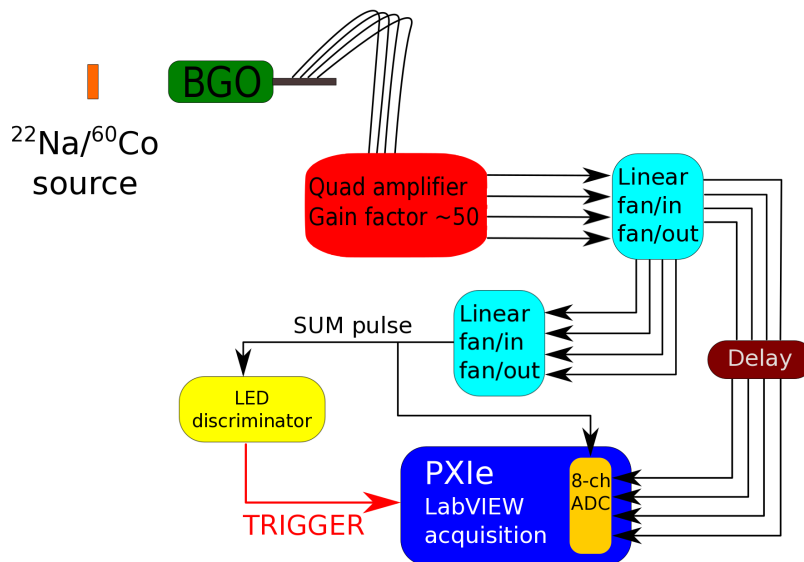


Figure 3.18: Scheme of the spatial and energy characterization test-bench.

Concerning the timing characterization measurements, an eight-channel signal digitizer at 3.2 GS/s has been employed for high time resolution acquisitions. The so-called WaveCatcher, shown in Figure 3.19a, has been developed by the Laboratoire de l'Accélérateur Linéaire, Paris, France (LAL) in Orsay and the Institut de Recherche sur les lois Fondamentales de l'Univers, Paris, France (IRFU) in CEA-Saclay, and its features are detailed in Breton et al. 2014. The digitizer is connected to the acquisition PC via Universal Serial Bus (USB) port, and the data read-out and storage are performed thanks to a custom acquisition software. The measurements are based on the coincidence detection of back-to-back 511 keV photons emitted by a ^{22}Na radioactive source, in order to be able to compare the time response of the tested BGO block to a reference fast timing scintillator. An external trigger is then provided to the WaveCatcher by treating the BGO block and reference scintillator signals with logic coincidence

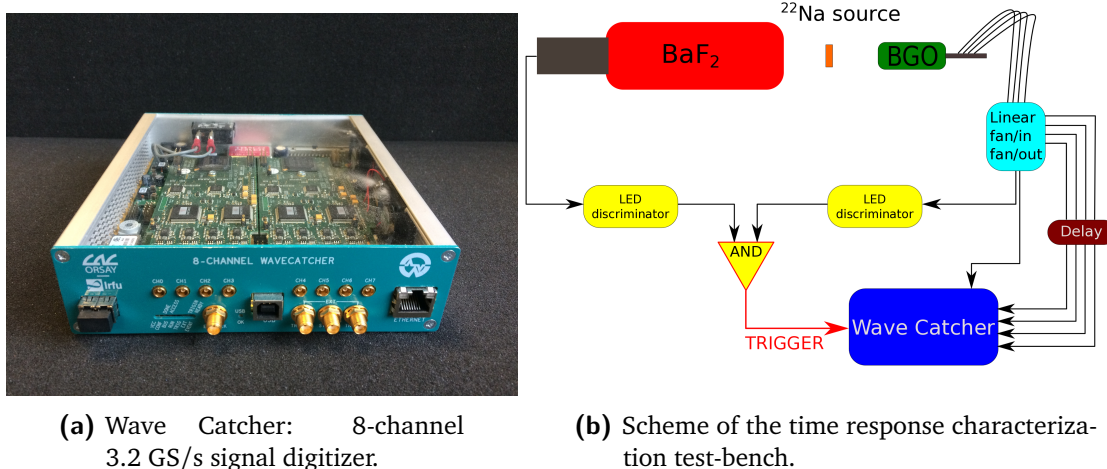


Figure 3.19: Details about the BGO block time response characterization.

NIM modules, after proper discrimination. Further details are given in section 3.2.2.4, while a scheme of the acquisition setup is given in Figure 3.19b.

3.2.2.1 Space and energy calibration and characterization

The space and energy calibration process is mainly divided into three stages:

- PM gain equalization (^{22}Na): the block is irradiated with the ^{22}Na source and the raw ADC distributions for the four PMs are retrieved. The upper-energy falloff in the raw ADC spectra are taken as reference to equalize the distributions. Four energy calibration factors are extracted and used to the data correction; this correction corresponds to the PM gain equalization.
- Pixel identification (^{60}Co): once the calibration factors are extracted thanks to the ^{22}Na irradiation data, the block is exposed to the ^{60}Co source. The collected data are analyzed as in the previous step and calibrated according to the already calculated correction factors. The energy spectrum, the mono-dimensional spatial projections and the flood map are produced. The custom algorithm briefly described in the following section 3.2.2.3 has been developed to identify the pseudo-pixel positions on the flood map. It is applied to the ^{60}Co irradiation data and the pseudo-pixel position map is stored.
- Pixel energy calibration: the ^{22}Na irradiation data are re-analyzed in this last calibration step in order to assign each interaction to a single pseudo-pixel according to the pixel position map obtained with the ^{60}Co data. Then, the energy spectrum of each pixel can be produced and the two identified peaks (corresponding to the two photon energies emitted by the ^{22}Na source - 511 keV and 1275 keV) can be used to equalize the pseudo-pixel response. The sum of all the pixels spectra produces the block energy spectrum. At this stage, the ADC channel values are calibrated to obtain the absorbed energy values in keV.

It is worth noticing that the ^{60}Co irradiation is useful for the pixel identification given the high

energy and narrow energy range of the emitted photons. The equalization factors obtained with the ^{22}Na source irradiation have been verified to be consistent with the ^{60}Co irradiation data, as expected. The whole method results to be robust.

3.2.2.2 Qualitative test of spatial reconstruction accuracy

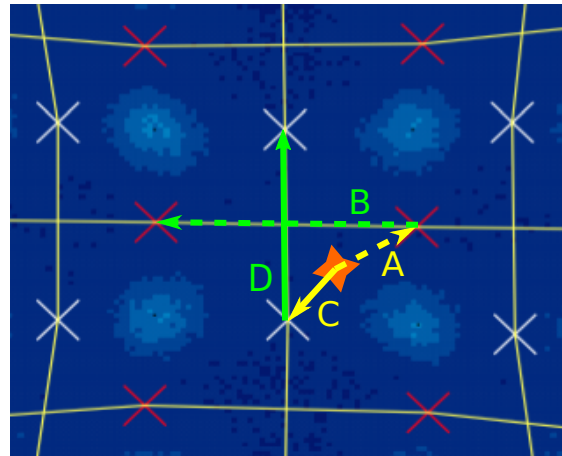
Specific acquisitions have been devoted to the test of the block spatial accuracy potential. The detector is expected to be able to locate the collected interaction on the pseudo-pixel grid, but the possible sub-pixel accuracy can be tested with a collimated source scan of the block surface. The ^{60}Co source has been employed for this purpose, with the linear and point-like aperture. The block has been placed on a moving table with no distance between its entrance surface and the collimator aperture. The whole surface has been irradiated with horizontal and vertical movements of 1 mm and 2 mm per step with the linear collimator aperture. Concerning the point-like aperture test, only part of the block surface has been irradiated for further verification of the spatial accuracy results, with horizontal 1 mm step movements of the table in 1 mm vertically separated lines. The collected data have been calibrated with the factors obtained with the homogeneous ^{22}Na irradiation, as explained in the previous section. We present and qualitatively discuss the results in section 3.2.2.6.

3.2.2.3 Pixel identification and energy calibration algorithm

Subsequent to that gain equalization process, an automatic iterative algorithm has been developed to identify the block pseudo-pixel positions. Integrated mono-dimensional spatial projections are computed along rows and columns of the calibrated flood map in order to derive the peak and valley positions in the distributions with the ROOT (Brun et al. 1997) methods included in the TSpectrum class and simple analytical calculations. With the resulting valley positions, a first rectangular grid of pseudo-pixels is initialized. The projection of each identified pseudo-pixel row (respectively column) is re-analyzed using the same integrated 1-D spatial projections along columns (respectively rows) looking for peaks and valleys as before. A refined grid is then produced, distorted from the initial rectangular one, and this process is iterated until a complete 8×8 pseudo-pixel grid is obtained.

Once the pseudo-pixels grid is fixed, the maximum of each pseudo-pixel region is automatically identified with a bin per bin scan in the defined area and its position defines the pseudo-pixel center relative position in the map.

The event data are then assigned to the pseudo-pixels with the application of the following process, illustrated in Figure 3.20. The dual pseudo-pixel grid is created rows- and columns-wise to get the mid points on the pseudo-pixel edges. The even data assignment is then done by calculating the minimal distance between a column and a row average point with respect to the reconstructed event and then calculating two outer products, between the vector connecting the reconstructed point and closest column (row) average point and the vector connecting this average point to the previous or next one on the same column (row). The sign of the products defines the column (row) where to assign the interaction. Knowing the relative position of the interaction point with respect to the two minimal distance points on row and column, the correct pseudo-pixel is identified. A more simple approach could have been used, using



- ◆ Reconstructed interaction position
- A ⊗ B defines the pseudo-pixel row
- C ⊗ D defines the pseudo-pixel column

Figure 3.20: Logic for the event assignment to a single pixel. The dual pseudo-pixel grid is displayed: in white the mid points on the pseudo-pixel edges along rows (middle of lines in vertical direction), in red along columns (middle of lines in horizontal directions). The sign of the outer products detailed in the legend are used to define the column and row (so that the pseudo-pixel) where to assign the reconstructed event.

the search of the minimal distance between the reconstructed event position and the pseudo-pixels centers, but it proved to be more liable to some assignment discrepancies due to the grid distortions. These distortions are mainly caused by the detection principle that relies on the pseudo-pixel separation via reflecting material, and can be corrected in event post-treatment with the a-priori geometrical knowledge of the block pseudo-pixel structure.

3.2.2.4 Time response characterization method

The test-bench for the time response characterization has been set as shown in Figure 3.19b. A Barium Fluoride (BaF_2) mono-block scintillator, read-out by a single photo-multiplier tube, has been used as reference detector. Its excellent time resolution makes it suitable for relative timing measurements in comparison to the BGO blocks. The reference scintillator and the BGO block under test have been set at arbitrary distances from the ^{22}Na source with the aim of detecting in coincidence the two 511 keV back-to-back photons resulting from the positron annihilation. The four raw signals coming out from the BGO block are summed with a NIM linear fan-in/fan-out module, and the resulting signal is sent to a leading edge discriminator and converted to a logic signal according to a fixed threshold. The single signal emerging from the reference detector passes through a selected threshold and is converted to logic signal. The two digital pulses, 100 ns width, are then sent to a coincidence module to create

the trigger input for the WaveCatcher acquisition system described in section 3.2.2. The four BGO output raw signals, the reference scintillator raw output signal and the sum of the four raw BGO signals are sent to the WaveCatcher for digitization. An example of the collected raw signals from the studied BGO block is shown in Figure 3.21: the 4 output signals of each single PMT are shown together with the resulting sum signal. The four signals exhibit a noisy feature that could be observed using the fast sampling acquisition, with a 80-100 MHz oscillatory behavior. At the present stage we did not infer the sources of this noise, that would be canceled by appropriate lower frequency filtering.

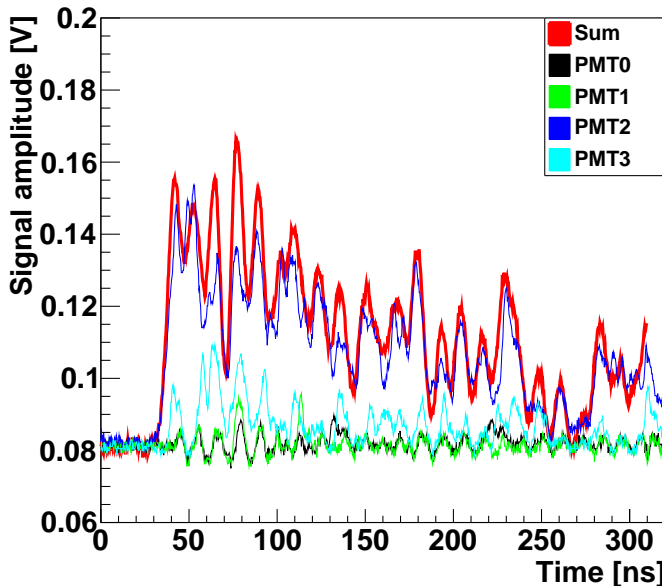


Figure 3.21: Reference BGO block raw signals collected with the Wave Catcher acquisition system.
The four outputs of the single PMTs are shown together with the sum signal.

For each coincidence event, the six collected signals are analyzed with focus on the signal rising edge. The time corresponding to the amplitude maximum and to 20%, 30%, 50% and 80% of the maximum is retrieved for constant fraction discrimination tests. In addition to this, a fixed threshold is used for fixed value discrimination.

Different comparison methods have been tested in order to identify the more robust one for the definition of the time resolution of the blocks. The noisy structure of the single BGO raw signals (see figure 3.21) leads to very variable results depending on the defined threshold, and the more stable results are given by the comparison of the sum of the four BGO signals and the reference scintillator with the arrival time identified by a fixed tuned threshold. With this method, the arrival time of each signal can be defined and the time difference distribution of the two signals can be produced.

The same analysis has been applied to a data set obtained with two identical BaF₂ detectors exposed to the ²²Na source in coincidence. This data set allowed for the definition of the reference scintillator time resolution.

The resulting BGO time resolution is defined as the FWHM of arrival time difference distribution between BGO block and reference scintillator, with the subtraction of the reference scintillator contribution via uncertainties composition calculation.

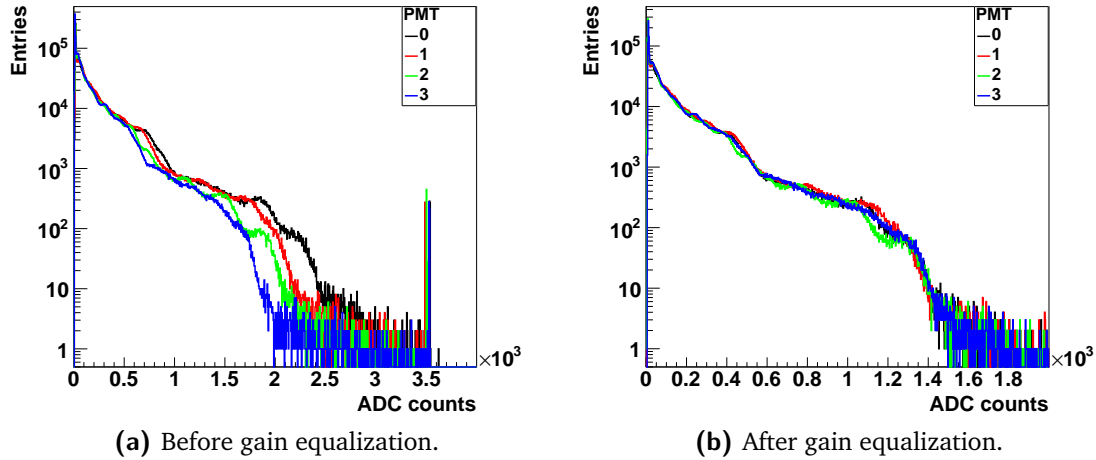


Figure 3.22: PM signal amplitude spectra before (a) and after (b) the PM gain equalization.

3.2.2.5 Results: PM gain equalization

Figures 3.22 and 3.23 show the effect of the PM gain equalization on the ADC count spectra and on the integrated mono-dimensional spatial distributions, while Figures 3.24 and 3.25 show the effect of the PM gain equalization on the block energy spectrum and two-dimensional spatial event distribution. All these results refer to the data collected with the reference BGO block irradiated with the ^{22}Na source.

In particular, Figures 3.22a and 3.22b show the raw and equalized ADC profiles of the four read-out photo-multipliers (the peaks above 3000 ADC counts in Figure 3.22a correspond to the saturation of the NIM linear fan-in/fan-out module used to handle the data read-out; these values are rejected during the equalization stage). Figures 3.23a and 3.23b show the projection on the two axes of the position of interaction reconstructed via Anger logic, before (left) and after (right) the PM gain equalization. Figures 3.24a and 3.24b show the ADC event spectrum, obtained by the sum of the ADC values of the four PMs, before (left) and after (right) the PM gain equalization. Figures 3.25a and 3.25b show the two dimensional event position map (this will be called “flood map” in the following), before (left) and after (right) the PM gain equalization; the interaction position is reconstructed via Anger logic (see Figure 3.5d for details).

As shown by Figures 3.22 to 3.25, the PM gain equalization performed in this first calibration step is mandatory to optimize the spatial and energy response of the tested block. Figure 3.23b highlights the better definition of the pseudo-pixels ensured by the gain equalization: the peak-to-valley ratio is increased, in particular for the most external pixels. The spatial response improvement is also reflected in a better energy response (from about 46 % to 35 % at 511 keV and from approximately 40 % to 30 % at 1275 keV), as shown in Figure 3.24b, where the two energy peaks of the ^{22}Na source are more narrow with respect to the ones obtained with the raw data. The obtained energy response is still not satisfactory, and the next steps of the calibration process are dedicated to the improvement of this result. The flood map in Figure 3.25b shows how the gain equalization and the offset tuning allow to arrange the position map over the whole block surface; the borders are better defined and the pseudo-pixels on the block limits (especially on the corner) are better separated.

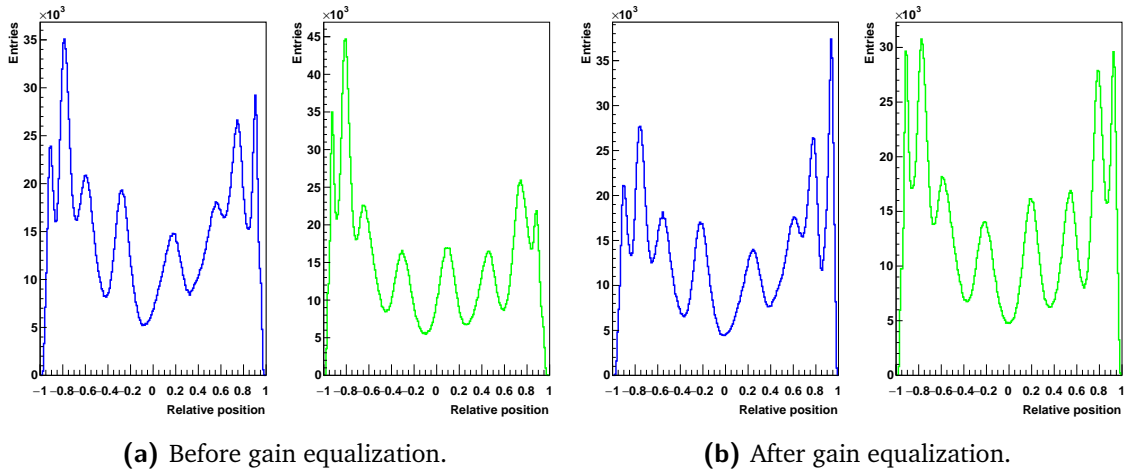


Figure 3.23: 1D integrated position distribution on the two transverse dimensions before (a) and after (b) the PM gain equalization. In the two sub-figures, left side for the horizontal dimension, right side for the vertical one.

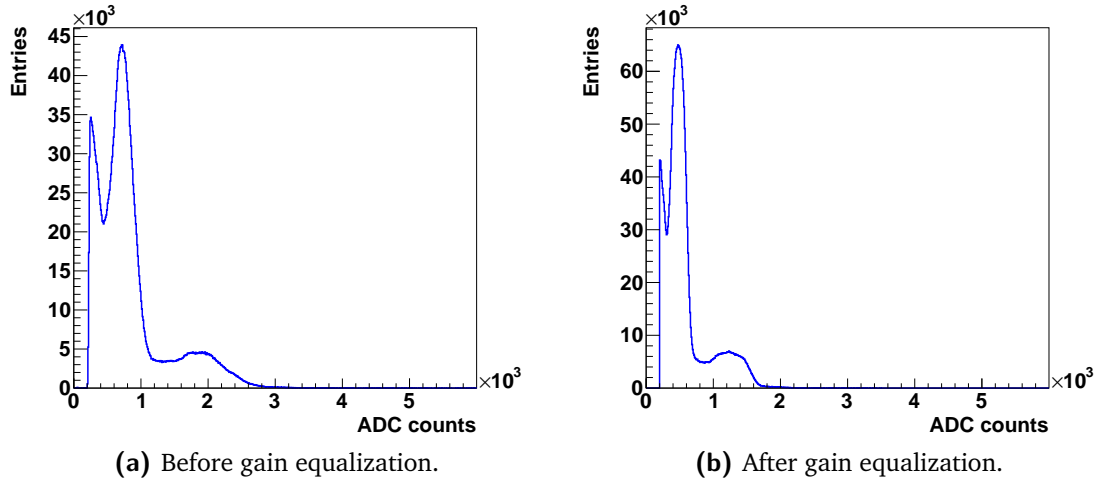


Figure 3.24: Block energy spectrum before (a) and after (b) the PM gain equalization.

3.2.2.6 Results: block spatial precision

Figure 3.26 shows four consecutive steps of the ^{60}Co source collimated irradiation, with a 2-mm step movement from left to right and the linear aperture ($2 \times 50 \text{ mm}^2$) set in vertical position. A qualitative analysis is enough to appreciate the block spatial precision limitation. The presented four points of the scan irradiated a total of three pseudo-pixel columns, moving from the left geometrical border of one column to the center of the next one. As shown by Figure 3.26b and 3.26d, as the collimator aperture position is in front of the center of a pixel column, the whole pseudo-pixel surface is reconstructed: no difference is observed with respect to the same column in Figure 3.25b, obtained with the homogeneous irradiation. In case the aperture faces the border between two pixel columns (Figure 3.26a and 3.26c), the events are shared between the two. This could show a possibility of sub-pixel resolution for integrated measurements, which is anyway not reproducible on a single event basis. The same behavior has been verified with a vertical scan (shown from Figure 3.27a to Figure 3.27d); the

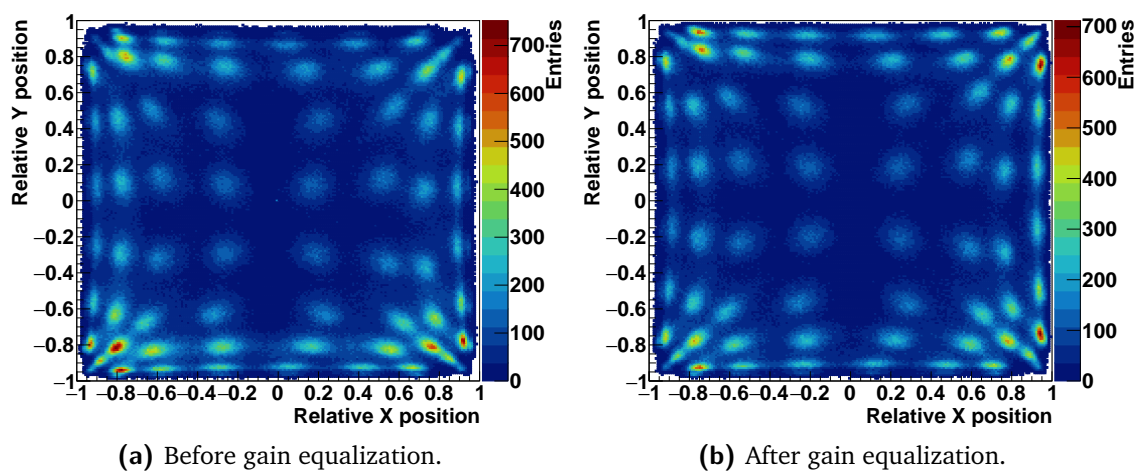


Figure 3.25: 2D reconstructed position map before (a) and after (b) the PM gain equalization.

collimator and table configurations has been kept unchanged, while the block has been turned of 90°. To be noticed that the slit position reported in the presented figures is the geometrical one, while the two-dimensional maps represent the response of the tested block: the spatial reconstruction distortions lead to the mismatch with respect to the real position, which will be corrected at the data treatment stage.

In order to further confirm these results and test the possibility of a sub-pixel resolution, a scan with reduced step size (1 mm) has been performed with the same collimator aperture, and no modifications are visually observed in the spatial distribution of events for the steps centered on the same pseudo-pixel column. As before, when the collimator aperture faces the limit between two pseudo-pixels columns, the events are equally distributed on the two. 9 measurement positions for this 1 mm scan are shown from Figure 3.28a to Figure 3.28i.

Figure 3.29 shows the superposition of the mono-dimensional position profiles integrated along the vertical axis for 5 positions of the 1-mm line-aperture scan: the differences between the distribution peaks related to neighboring positions of the aperture are of the order of 10-20%, and demonstrate how a sub-pixel position accuracy is achievable for integrated measurements, even if it was not evident on the two-dimensional maps.

This result has been also tested with a point-like collimation scan of part of the studied block surface, with 1 mm step movements. The flood maps in Figure 3.30 show 6 reference points of the scan with the point-like aperture, during an horizontal movement from left to right of the table and the center of the aperture vertically centered on one pseudo-pixel line. The reported movement represents the transition from the center of a pseudo-pixel to the right limit of the next one. The aperture physical position is not highlighted on the maps in order to better show the event position distribution.

As for the linear aperture test, the mono-dimensional integrated distributions, reported in Figure 3.31, better show the differences between the various scanned point, approximately in the range 5-20%. As before, these distributions verify how a millimeter accuracy is possible with the integrated analysis of sufficient event statistics.

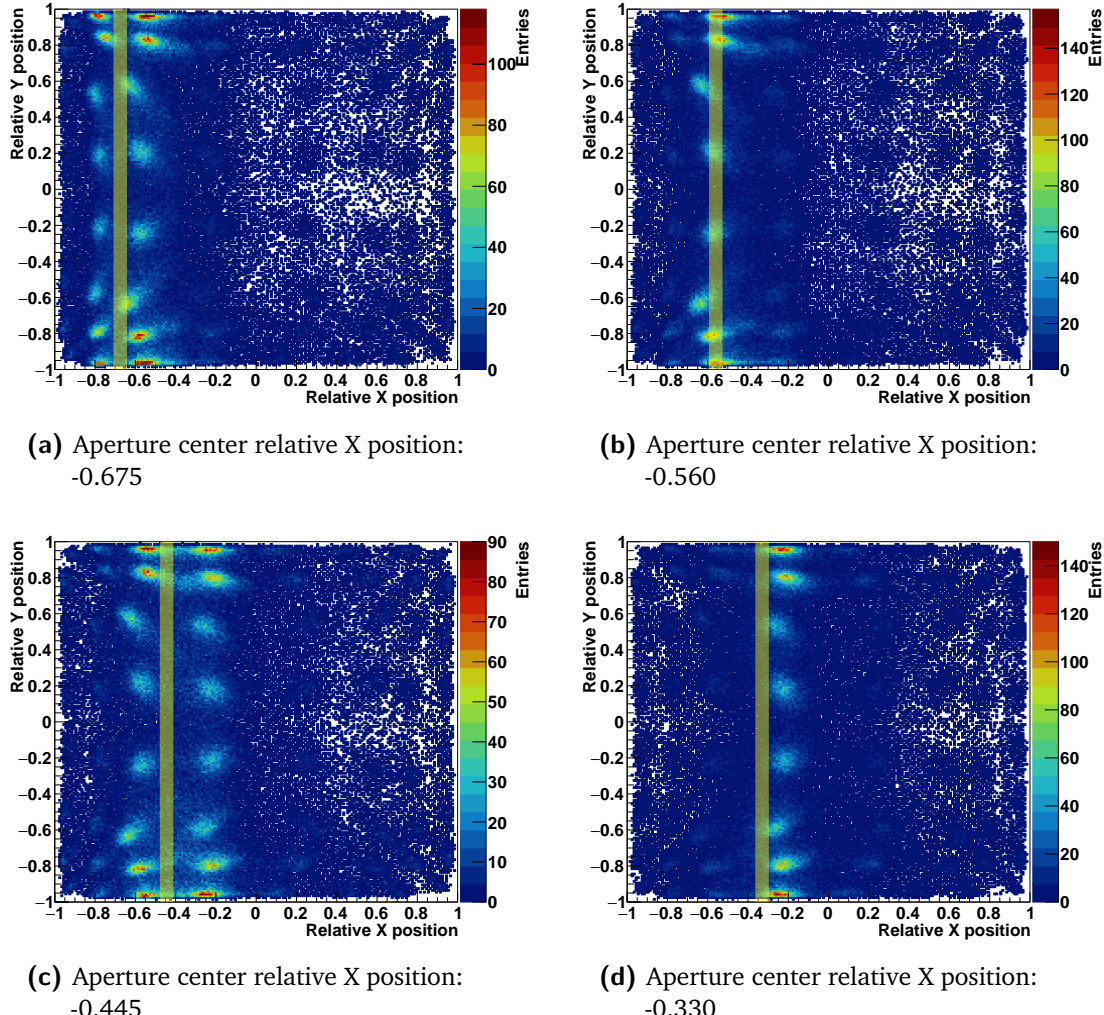


Figure 3.26: 2D reconstructed position maps during a 2-mm step scan performed with the ^{60}Co source with the line aperture from the left to the right size of the block surface. 4 reference measurements points, the position of the aperture is shown by the semi-transparent yellow band.

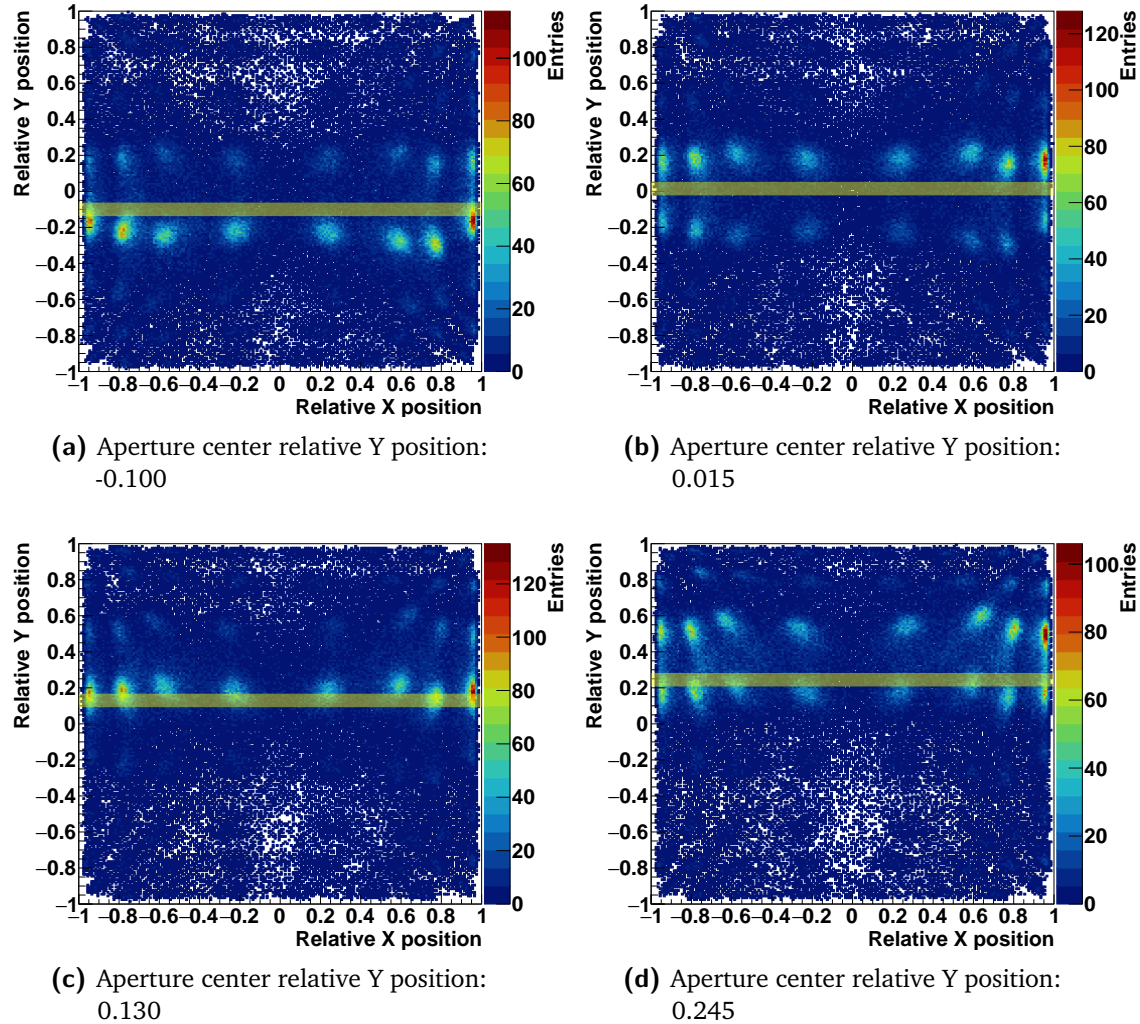


Figure 3.27: 2D reconstructed position maps during a 2-mm step scan performed with the ^{60}Co source with the line aperture from the bottom to the top side of the block surface. 4 reference measurements points, the position of the aperture is shown by the semi-transparent yellow band.

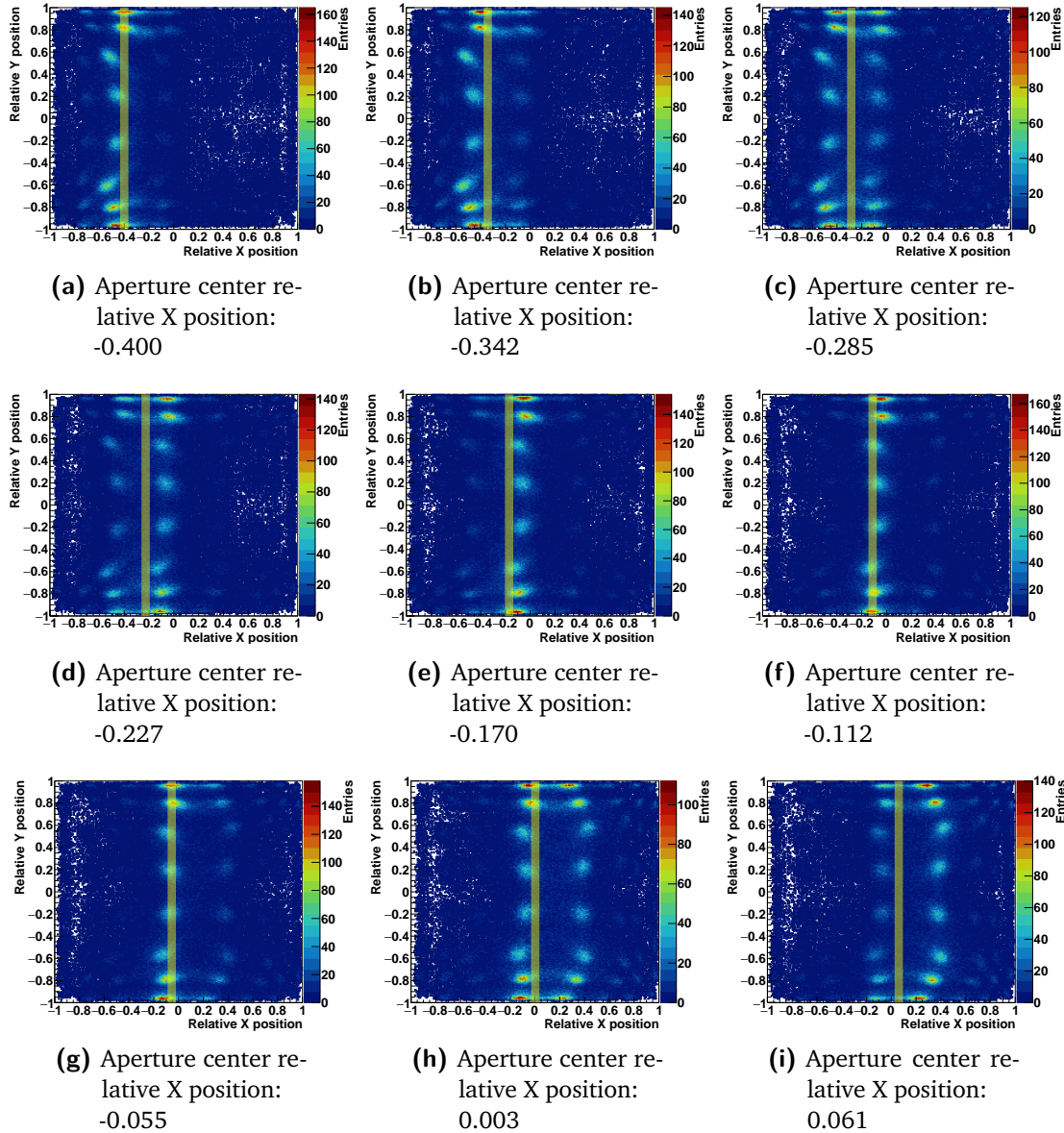


Figure 3.28: 2D reconstructed position maps during a 1-mm step scan performed with the ^{60}Co source with the line aperture. 9 reference measurements points, the position of the aperture is shown by the semi-transparent yellow band.

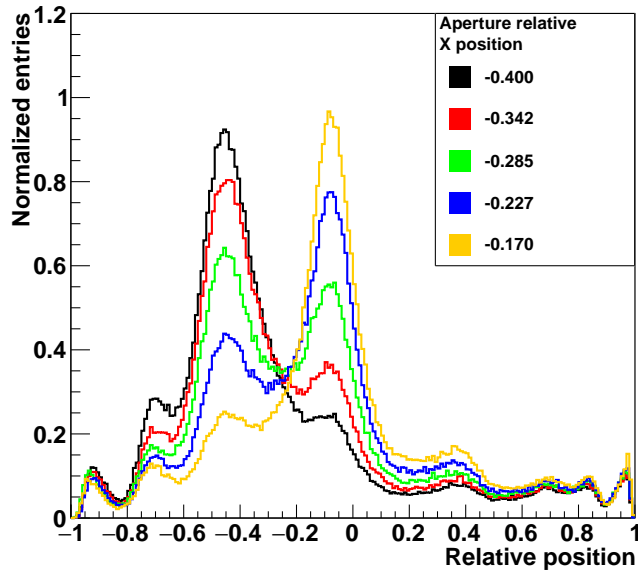


Figure 3.29: Superposition of the event reconstructed position profiles integrated along the vertical axis for 5 points of the 1-mm step scan performed with the ^{60}Co source with the line aperture. The 5 positions correspond to the two-dimensional maps in Figures 3.28a, 3.28b, 3.28c, 3.28d, and 3.28e.

In conclusion, all these sets of data verify that the spatial reconstruction accuracy of the employed blocks is limited to the pseudo-pixel size, and a sub-pixel resolution is not achievable on a single event basis. However, with integrated analysis a millimeter position accuracy can be obtained with both linear and point-like irradiation of the block.

3.2.2.7 Pixel identification

The results of the pixel identification algorithm described in section 3.2.2.3 are shown in Figure 3.32. Figure 3.32a shows the identified average values of the pseudo-pixels positions on the two transverse dimensions. As already detailed in the description section, starting from these average positions, the single pseudo-pixels positions in rows and columns are extracted and the “valleys” between neighboring pseudo-pixels are used to define the grid shown in Figure 3.32b together with the pseudo-pixel center position map.

3.2.2.8 Pixel energy calibration

Once the pseudo-pixel positions and the related grid are defined, each interaction can be assigned to a single pixel. The energy spectrum of each pixel is then separately studied in order to equalize the energy response on a pixel basis.

The assignation method described in section 3.2.2.3 makes use of the dual pseudo-pixel position map shown in Figure 3.33. The position assignment scheme to pseudo-pixels is shown

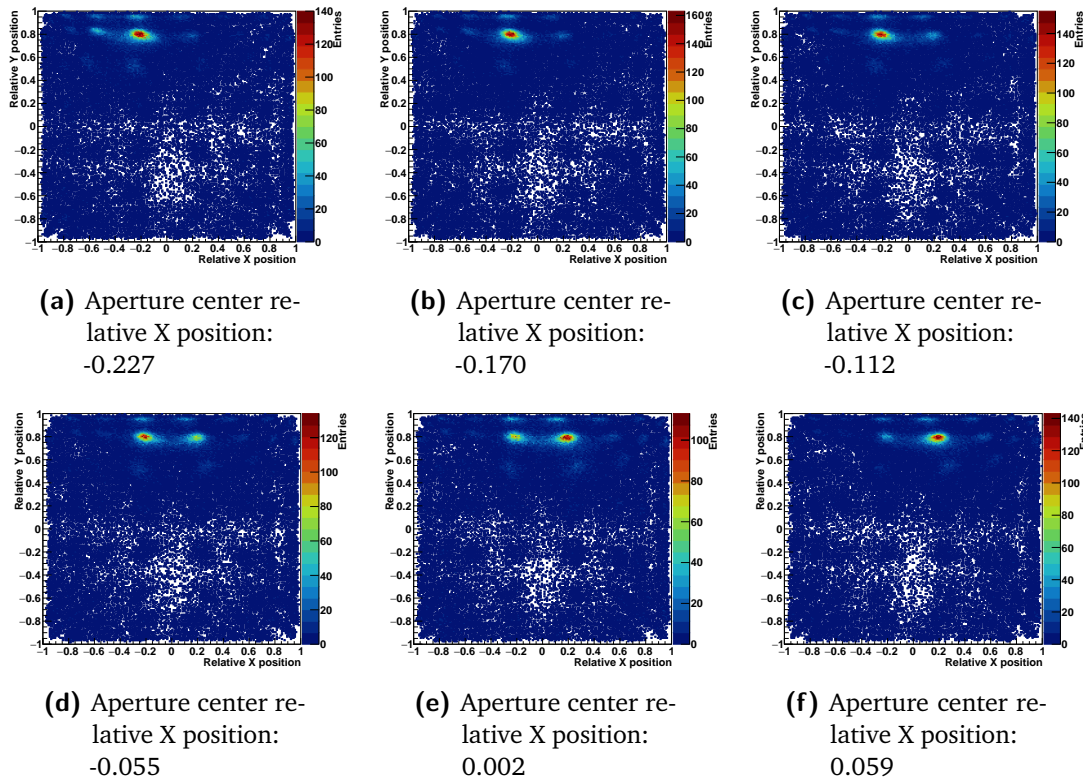


Figure 3.30: 2D reconstructed position maps during a 1-mm step scan performed with the ^{60}Co source with the point-like aperture. 6 reference measurements points, the relative X position of the aperture is reported in the caption of each figure. In the vertical dimension, the aperture is centered on the center of the pseudo-pixel line.

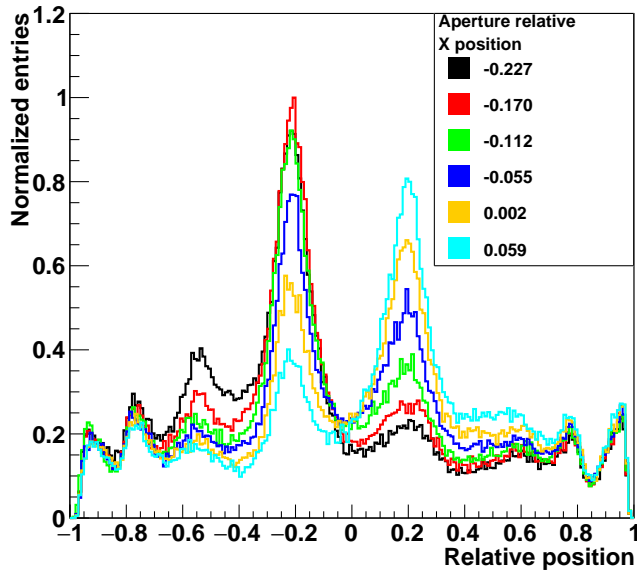


Figure 3.31: Superposition of the event reconstructed position profiles integrated along the vertical axis for 6 points of the 1-mm step scan performed with the ^{60}Co source with the point-like aperture. The 6 positions correspond to the two-dimensional maps in Figures 3.30a, 3.30b, 3.30c, 3.30d, 3.30e, and 3.30f.

in Figure 3.34: a color has been given to each reconstructed point according to the pseudo-pixel region where it has been assigned by the described method. The method robustness is verified by the comparison of this map to the grid in figure 3.32b and 3.33.

In Figure 3.35 the results of the pseudo-pixel energy calibration are shown. Figure 3.35a (left) shows the overlap of the energy spectra for 60 pseudo-pixels before the energy calibration and equalization. The 4 pseudo-pixels on the corners show a very different energy response and are not included in this picture. This is probably due to a non-complete light collection. The different response of each pixel to the two energy peaks is clearly visible. For each spectrum the low energy peak is assigned to 511 keV, and the high energy one to 1275 keV. In this way, the spectra are linearly calibrated and equalized, as shown in Figure 3.35a (right). For the 4 corner pseudo-pixels, the calibration is based only on the 1275 keV peak, while the 511 keV reference peak is substituted by the null ADC value.

Once the single pixel energy responses are equalized and calibrated, the whole block energy spectrum can be derived with the sum of all pixels. In Figure 3.35b (left) the ADC spectrum is shown before the equalization process, while in Figure 3.35b (right) the calibrated energy spectrum is presented. In Figure 3.35b (left) the energy spectra related to three reference positions on the block surface are reported: this makes possible to appreciate the different contributions to the non-calibrated spectrum and the behavior of different block sections. The block peripheral pixels show an overall lower light collection and a lower efficiency in detecting high energy photons (reduced peak integral with respect to the center and mid-center pseudo-pixels). Concerning the central pixels, the slight in-homogeneity is probably due to the streaked structure which guides less than on the borders the scintillation photons.

The two spectra are represented in logarithmic scale in order to better appreciate the calibra-

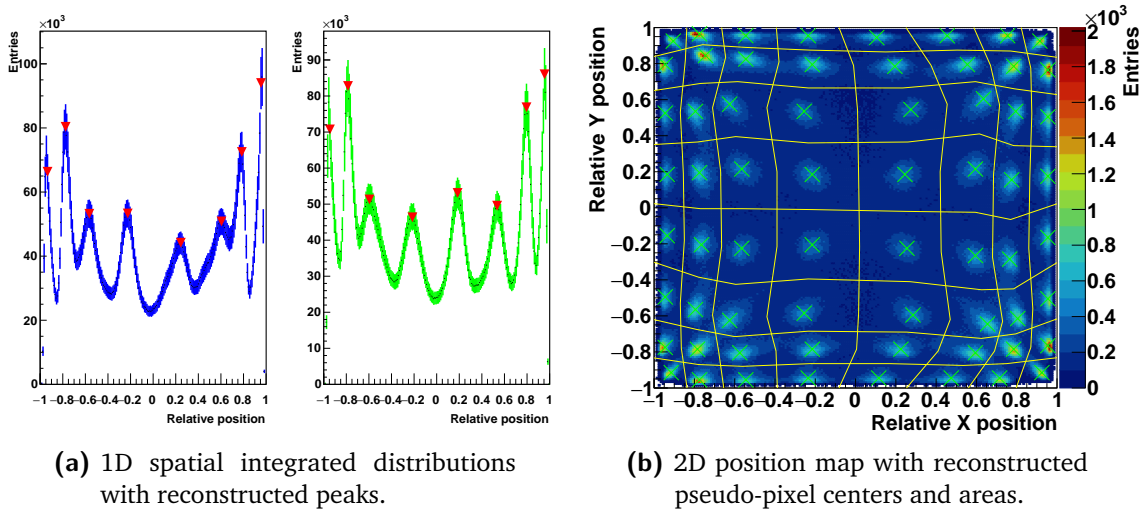


Figure 3.32: 1D integrated position distributions on the two transverse dimensions with the retrieved position of the pseudo-pixel average center (a). Reconstructed 2D map with the identified pseudo-pixels positions and surfaces.

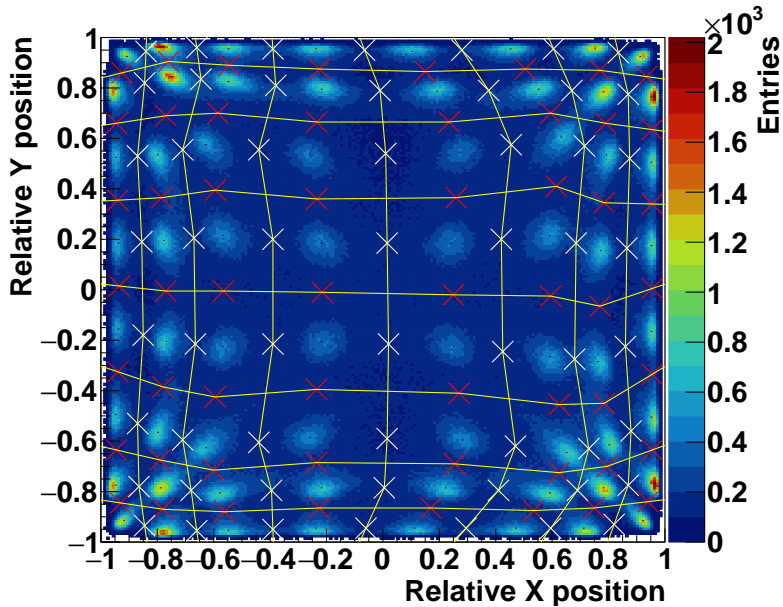


Figure 3.33: Auxiliary position map used for the assignment of the reconstructed events to a single pixel. The highlighted points represent the “valleys” between neighboring pixels on their separation borders.

tion effect: it allows for the optimization of the energy response on the two spectroscopic lines of the ^{22}Na source. At this stage, the energy resolutions of the block can be defined as the FWHM of the two energy peaks.

In Table 3.1, the energy resolutions derived after the calibration process are compared to the raw ones, obtained by the non-calibrated data.

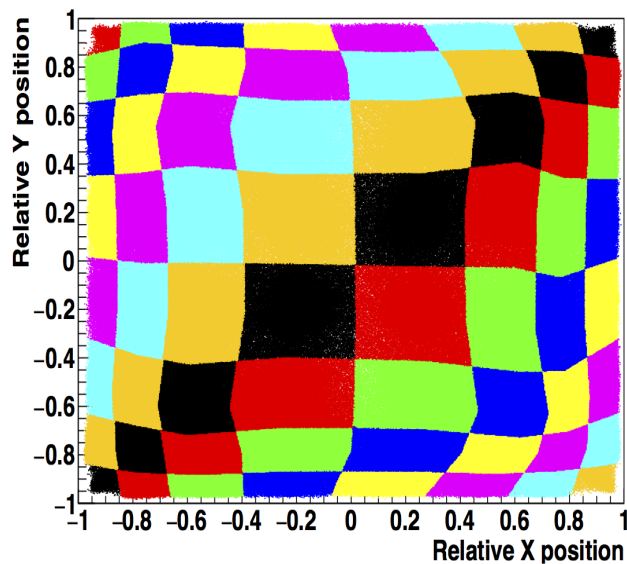


Figure 3.34: 2D map of the reconstructed event assignations to pseudo-pixels.

Table 3.1: Comparison of the block energy resolutions at the two reference energies of 511 keV and 1275 keV before and after the calibration process.

	Energy resolution @ 511 keV FWHM [%]	Energy resolution @ 1275 keV FWHM [%]
Before equalization	46.12	39.43
After equalization	23.03	18.04

The results reported in Table 3.1 show the need for the implemented calibration process, which allows to optimize the BGO block spatial and energy response.

Thanks to the assignment of each reconstructed event to a single pseudo-pixel, the relative efficiency can be evaluated on a single pseudo-pixel basis. The two color maps in Figure 3.36 show the number of events collected by the 64 pseudo-pixels during the ^{22}Na source homogeneous irradiation, with an energy selection performed on the two photon energies emitted by the source (511 keV events in Figure 3.36a and 1275 keV events in Figure 3.36b). The entries are normalized to the maximum number of entries in a pseudo-pixel, detected for a 511 keV energy selection.

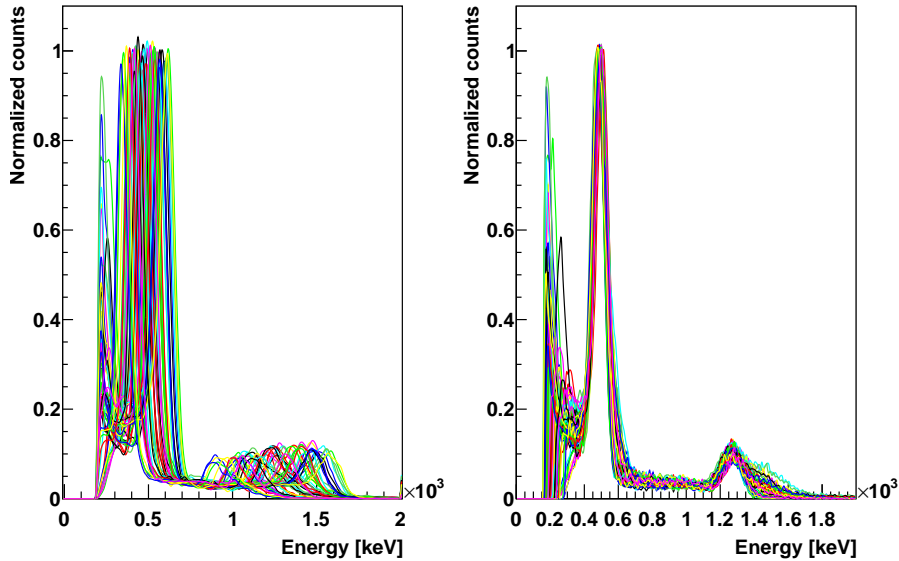
Figures 3.36a and 3.36b show that the expected homogeneous distribution of events over the whole block surface is confirmed for the central pseudo-pixels of central lines (2 to 7), while the block borders present a factor 2-3 lower detection efficiency. In particular, the pseudo-pixels on the 4 corners (line 1 and 8, pseudo-pixels 1 and 8), have an efficiency of a factor between 5 and 6 lower with respect to the center of the block surface. This effect is partially due to geometrical factors, given the fact that the side pseudo-pixels are slightly smaller with respect to the central ones (as also shown by the reconstructed 2D map in Figure 3.32b). In addition to this, the light collection is probably less performing in case of photons interacting on the block borders, causing the loss of events. Moreover, a solid angle effect is also possible given the limited distance between source and tested block (12 cm) with respect to the block size. By comparing the two maps, an overall reduced efficiency for the detection of photons beyond 1 MeV is verified. This is expected given the factor ~ 2 difference in the photopeak efficiency of BGO at 511 keV and 1275 keV ([Saint Gobain 2016](#)). Moreover, the reduced efficiency in the central block area for 1275 keV photons can be related to the photomultiplier tubes round geometry, which determines a dead space in the center of the block back surface ([Uribe et al. 2003](#)). The effect of the dead area is diminished by the light sharing effect at low energy, but it becomes considerable in case of deep-penetrating higher-energy photons. In order to fully understand the relative and absolute efficiency of each block section, an irradiation with a collimated source scanning the whole active area is foreseen. This will allow one to precisely define the detection rate variations on the block active area.

3.2.2.9 Time characterization

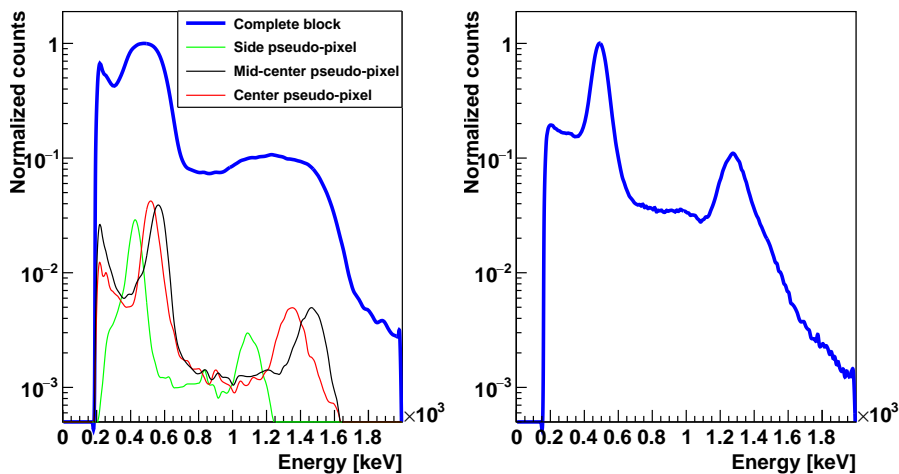
Figure 3.37 shows the distribution of arrival time differences between the reference BaF_2 detector and the tested BGO block. The time resolution is defined as the FWHM of this distribution.

3.2.2.10 Results for the 30 blocks

In Table 3.2 the results obtained for the calibration and characterization of a set of 30 blocks are listed. The characterized blocks show very uniform results, with an average energy resolution of 25% FWHM at 511 keV and 20% FWHM at 1275 keV and an average time resolution of 4.42 ns FWHM tested with coincidences of 511 keV photons. Both the energy and time resolutions are expected to be improved for the detection of photons in the prompt-gamma energy range, in particular above 1 MeV.



(a) Single pixel energy spectrum before (left) and after (right) equalization.



(b) Block energy spectrum before (left) and after (right) pixel response equalization.

Figure 3.35: Single pseudo-pixels (a) and whole block (b) energy spectra with the ^{22}Na source before (left) and after (right) the calibration process. The whole block spectra are reported in logarithmic scale. Three non calibrated spectra of pixels in reference positions (border, mid-center and center area) on the block are also reported with the non calibrated spectrum (a normalization factor has been applied for visualization purpose).

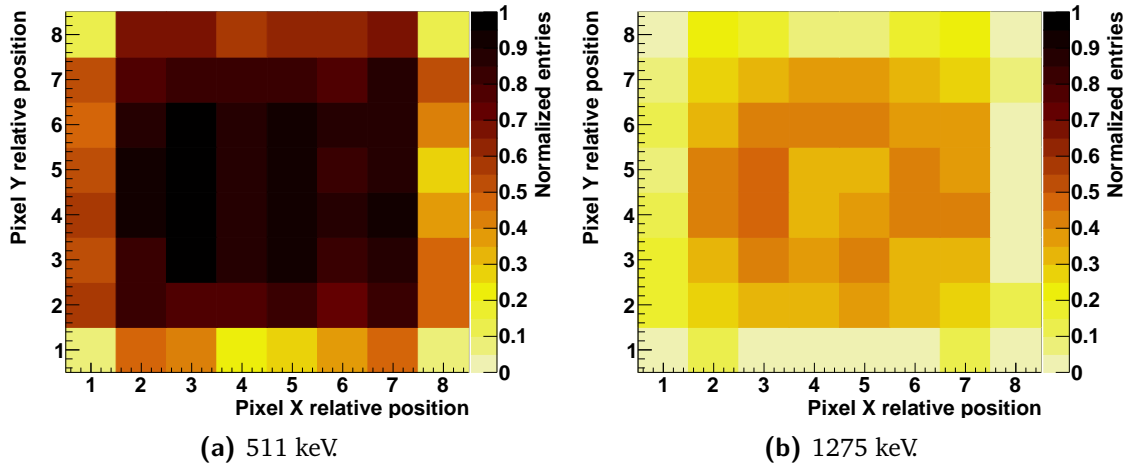


Figure 3.36: Relative number of entries for each pseudo-pixel as a function of the pixel relative position, represented by the row and column numbers (0 to 8 from left to right and bottom to top of the block surface). Figure(a) shows the entries in a selected energy window around 511 keV, Figure(b) in an energy window around 1275 keV. All the entries are normalized to the maximum collected number of entries, corresponding to 511 keV events in the central section of the block.

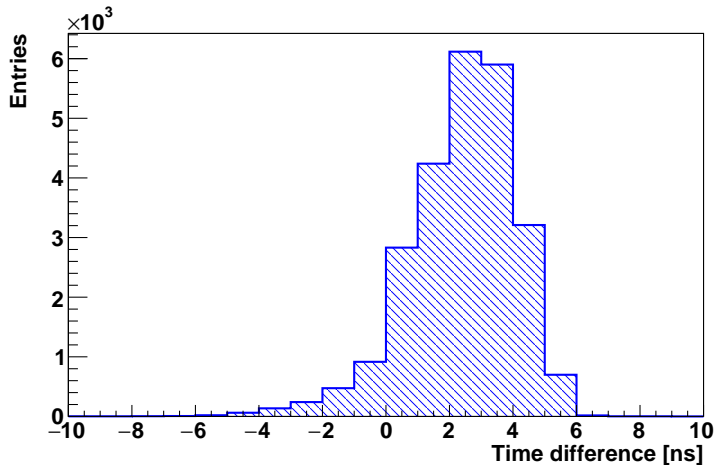


Figure 3.37: Distribution of arrival time differences between reference scintillator (a BaF₂ monoblock detector with 1 ns FWHM time resolution) and BGO block.

Table 3.2: Calibration and characterization results for the whole set of tested BGO blocks.

BGO block ID	Energy resolution @ 511 keV FWHM [%]	Energy resolution @ 1275 keV FWHM [%]	Time resolution FWHM [ns]
Ref. block			
7627	23	18	4.0
3166	27	24	4.4
3171	23	18	4.4
3184	24	20	4.3
3232	24	20	3.6
3280	24	19	4.3
3322	25	20	4.2
3972	25	21	5.2
4368	25	20	5.3
5243	25	19	3.9
7130	24	21	4.9
7218	25	21	2.1
7240	25	20	6.7
7258	26	19	4.9
7369	23	19	4.3
7424	25	21	4.9
7581	26	23	4.1
7586	26	24	4.4
7601	24	19	4.1
7612	23	19	4.1
7624	22	19	3.9
7651	24	20	3.9
7657	24	19	2.7
14676	25	19	5.1
31210	25	21	4.8
3252	problem with PM 0		
3375	1 pseudo-pixel missing		
6823	1 pseudo-pixel missing		
7644	problem with PM 2		
7653	1 pseudo-pixel missing		
21097	problem with PM 2		
Complete set	25 ± 1	20 ± 2	4.5 ± 0.9

The last five blocks in the list of Table 3.2 showed detection problems, due to very low signal level on the read-out PMs or a poor spatial reconstruction accuracy with one missing pseudo-pixel on the two-dimensional map, probably due to crystal aging. The blocks with PMs issues will not be employed in the final absorber configuration, while the other two will be probably placed in the peripheral area in order to keep a wide active detection surface.

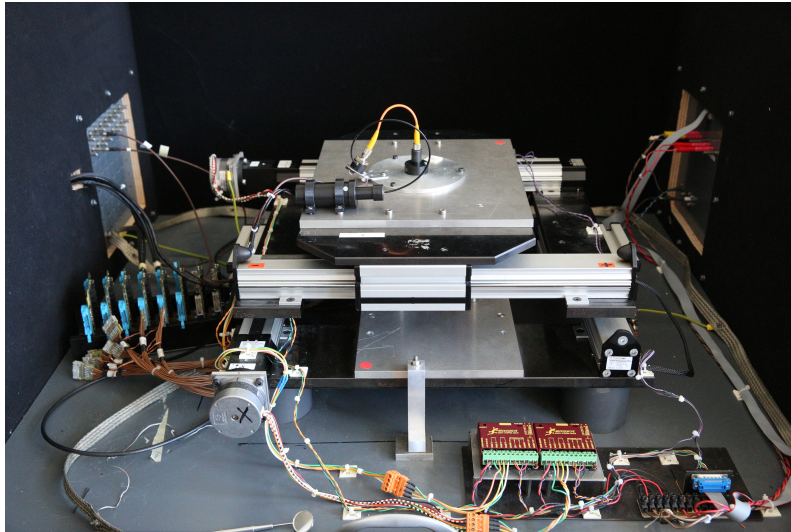
All the characterization measurements and tests described in the previous paragraphs have been performed with temporary acquisition system, because the final camera acquisition was still not optimized for the absorber blocks. The first tests with the final acquisition have been recently performed in order to characterize the BGO block response. In addition, 6 blocks have been tested on beam in a first configuration of multi-collimated cameras, coupled to the beam tagging hodoscope. The results are presented in chapter 6.

3.2.3 Hodoscope PMs characterization

The beam tagging hodoscope read-out is performed via 8 multi-anode PMs, Hamamatsu H8500 ([Hamamatsu 2006](#)), shown in Figure 3.10c. In order to guarantee a uniform response of the whole detector active area, composed of 256 scintillating fibers, the PMs must be previously characterized in terms of gain with a light source of fixed and known wave-length and intensity. The source selected for the measurements is a blue Light Emitting Diode (LED) ([Hewlett-Packard HLMP-CB](#)), installed on the test-bench shown in Figure 3.38a and described in the following. The test-bench has been developed by the LPC AVIRM group (see [Gaglione 2013](#)) and adapted at the IPNL to a different acquisition system.

The goal of the characterization measurements is to trace a gain map of the whole PM surface, with the aim of storing calibration data to be used to both tune the PM working parameters (supply voltage and threshold) and correct the collected data. This is achieved by scanning the PM photo-cathode surface with the LED. The LED is so mounted on a motorized double-axis table, controlled by two G203V stepper modules provided by GeckoDrive Motor Controls ([GeckoDrive 2010](#)). The two axes have a total range of 20 cm each, and the step resolution achieved by the controllers is 20 μm . A metal support is set on the table in order to fix the LED. It produces light pulses synchronized with a pulse generator, which is also used as trigger signal for the acquisition system, as detailed later. The light pulse produced by the LED is split into two pulses with a 45°C mirror: one pulse is sent to the H8500 PM to be tested via optical fiber, in order to obtain a light beam perpendicular to the cathode surface (FWHM beam width estimated in 0.5 mm), the second one is detected by an Hamamatsu R5600 PM ([Hamamatsu 1995](#)), used as reference for the correction of temperature fluctuations. The PM under tests is fixed below the optical fiber output with a plastic support, not connected to the moving table. The whole described system is contained in a black box for external light shielding.

The output signals from the H8500 PM are initially amplified by custom pre-amplification cards: 8 cards are available and have been characterized in terms of amplification gain. Once amplified, the signals of the H8500 PM, together with the output of the reference PM, are sent to the acquisition system composed of a National Instrument PXI Express 1082 ([National Instruments 2010](#)) equipped with two 8-channel flash ADC modules (NI PXI-5105) and a two-channel ultra-fast digitizer (NI PXI-5154). The flash ADC modules have a maximum sampling rate of 60 MHz and are used for the read-out of the H8500 PM signals, while the ultra-fast digitizer, able to sample at a frequency up to 1 GHz, is used for the reference PM.



(a) Overview of the test-bench setup for the Hamamatsu PM characterization.



(b) National Instruments PXIe acquisition system.



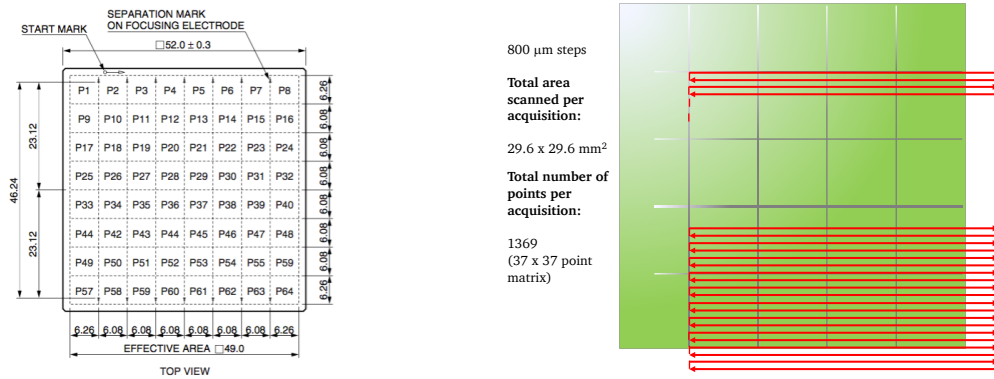
(c) Example of LabVIEW software interface for the Hamamatsu PMs characterization.

Figure 3.38: Test-bench and tools for the characterization measurements performed on the Hamamatsu PMs of the beam tagging hodoscope.

The acquisition and control software is developed with LabVIEW (2009) installed on the PXI; a picture of the software user interface is shown in Figure 3.38c. The PXI receives the signals from the two PMs and is also connected to the table stepper modules, so that the LabVIEW software can handle and synchronize data acquisition and table movements. The table movements can be automatized via LabVIEW macros, where step size, number and direction are stored and then used for the acquisition. The acquisition trigger, as mentioned, is given by the pulse generator which also controls the light pulses of the LED; in this way, a fixed number of pulses per table position can be recorded, and the measurement process is completely automatic. During the acquisition, the LabVIEW software automatically corrects the collected data according to the reference PM signal amplitude and to the pre-amplification card gain.

Given the limited number of flash ADC channels, only 16 PM pixels can be characterized per acquisition; four acquisitions are needed to scan the complete PM surface.

Each performed acquisition is set to scan a matrix of 4×4 PM pixels, and safety margins are arranged on the PM sides in order to ensure a complete surface irradiation. As shown in the



(a) Scheme and quotation of the Hamamatsu H8500 multi-anode PMs.

(b) Scheme of the scan performed for the Hamamatsu PM characterization measurements.

Figure 3.39: Details of the hodoscope PMs and of the performed characterization measurements.

schematic view of the PM in Figure 3.39a, the total PM size is $52 \times 52 \text{ mm}^2$, for an active area of about $49 \times 49 \text{ mm}^2$. The active area of the pixels on the borders is slightly wider than the central ones. In order to optimize the measurement process, a preliminary analysis has been done for the definition of the needed step length, and the details are reported in Coudurier 2015. A trade-off between measurement accuracy, required time and stored data file size has been found with a step of $800 \mu\text{m}$, so that each pixel is scanned with approximately 64 measurement points and the transition between neighboring pixels can be appreciated. A schematic of a table reference movement is presented in Figure 3.39b. To be noticed that for each irradiated point, 100 LED pulses are sent to the detector and the average amplitude value is calculated and collected.

The 8 Hamamatsu PMs have been completely scanned without the optical fiber mask used in the hodoscope and shown in Figure 3.10d, and the results are shown here for one reference PM. Some tests have been also performed with the fiber mask, in order to test the PM response mainly in terms of expected cross-talk between neighboring pixels. A complete result database has been created for calibration purpose.

Figure 3.40a shows the two-dimensional maps of a reference PM response for a complete irradiation, obtained with four separated acquisitions without the plastic fiber mask. Figure 3.40b shows the response of the same PM with the plastic fiber mask fixed on its surface. The reported signal amplitude has been normalized to the reference PM Hamamatsu R5600 for temperature oscillation correction.

In Figure 3.41 the two-dimensional response map for the 8 PMs are shown. In order to obtain a visual uniformity, the amplitude values have been normalized to the maximum value of each PM. We can observe response dis-uniformity on each PM surface, estimated in a factor ranging between 2 and 3. The retrieved response of each pixel will be useful for the calibration of the hodoscope final acquisition chain, in particular for what concerns the electronics FE settings (threshold and gain of each channel). In addition to this, these calibration measurements will allow for a proper data correction at the analysis stage.

The irradiation performed with the fiber plastic mask is also used to study the signal cross-

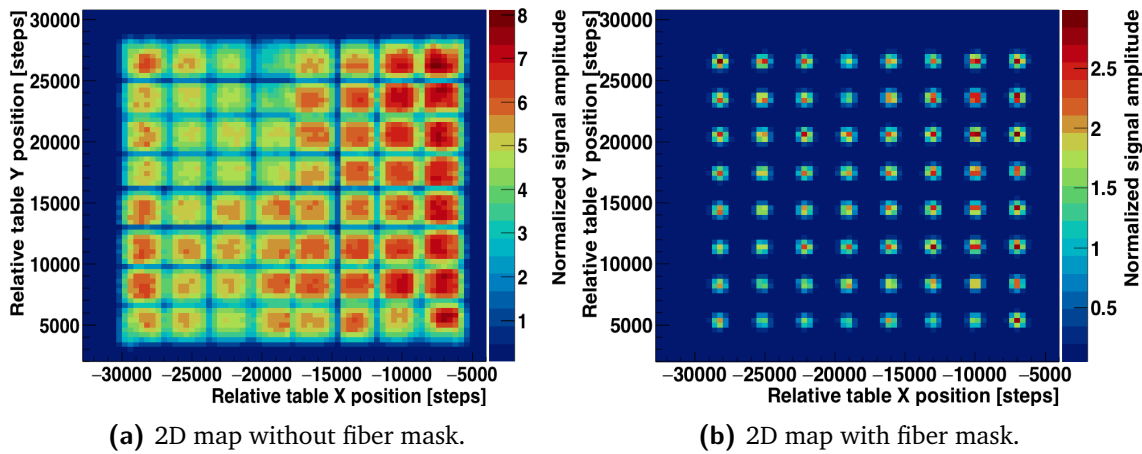


Figure 3.40: Two-dimensional response maps of one of the Hamamatsu PMs for the scintillating fiber hodoscope readout, obtained with the irradiation with a blue LED. The signal amplitude is normalized to the reference PM response.

talk between neighboring pixels, which is expected to be negligible according to the provider specifications, given for similar measurements and shown in Figure 3.42a. The analysis results for one of the studied PMs are shown in Figure 3.42b as reference.

The retrieved cross-talk is more important with respect to the provider specifications (to be noticed that the measurement conditions are slightly different), but always below 3% for the tested anodes. This cross-talk level is negligible and can be easily suppressed by a proper threshold setting.

3.2.4 Hodoscope fiber test with electron source

After the complete characterization of the Hamamatsu multi-anode PMs, they have been installed in the black boxes connected to the optical fibers of the hodoscope prototype, and the complete detection chain has been qualitatively tested to check the scintillating fiber light transmission to the optical fibers and to the read-out PMs. The observations have been performed by directly checking the pre-amplified PM output signal (with the same custom cards mentioned in the previous section) on an oscilloscope. A mechanical intervention has been necessary to fix some of the optical fibers not properly pasted to the plastic mask on the PM surface. In addition to this, a layer of black silicone has been added on the plastic mask surface to improve the light isolation on the only side where it is impossible to place the isolating black tape.

Then the hodoscope prototype has been tested with a beta source (^{90}Sr) for verification, and the obtained signal distributions (retrieved as before with an oscilloscope acquisition after signal pre-amplification) have been compared to simulation study performed by an internship Master 1 student (Vallois 2016). He tested by simulation the irradiation of the whole hodoscope surface with an equivalent ^{90}Sr source to retrieve the deposited energy distribution on the scintillating fibers. This distribution can be compared to the collected signals amplitude distribution obtained with the experimental tests, in order to calibrate the relationship

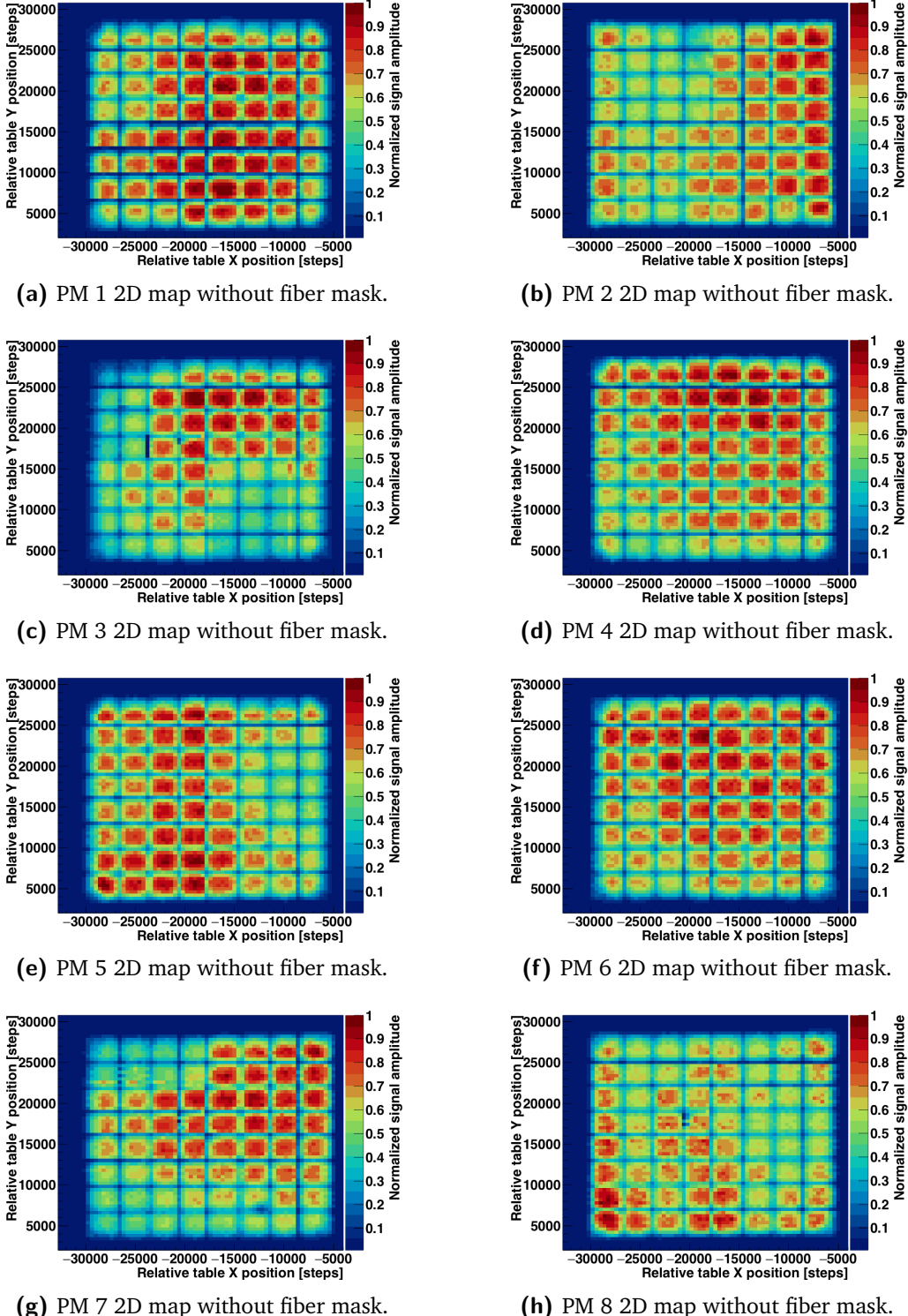
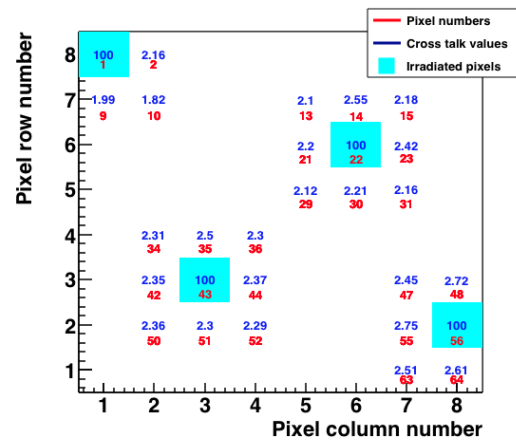
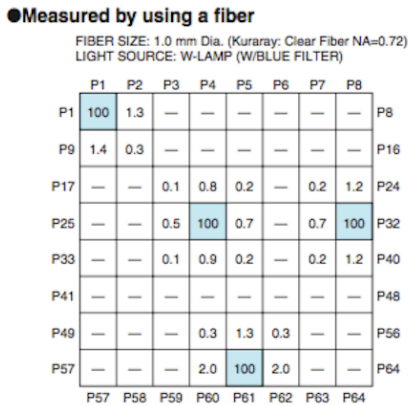


Figure 3.41: Two-dimensional response maps of the Hamamatsu PMs for the scintillating fiber hodoscope readout, obtained with the irradiation with a blue LED. The signal amplitude is normalized to the reference PM response and then to each PM maximum detected amplitude.



(a) Signal cross-talk provided by Hamamatsu for the PM H8500 (Hamamatsu 2006). The measurements have been performed with a 1 mm diameter optical fiber; the irradiated anode is in the light blue box, and the cross-talk on the neighboring ones is expressed in %.

(b) Signal cross-talk on a reference PM measured with a blue LED irradiation through the plastic fiber mask. The irradiated anode is in the light blue box, and the cross-talk on the neighboring ones is expressed in %.

Figure 3.42: Cross-talk study on neighboring PM pixels. The experimental results obtained with the irradiation with a blue LED through the plastic fiber mask on a reference PM (right) are compared to the specifications provided by the producer, measured in similar conditions (left). The cross-talk is expressed in % with respect to the irradiated anode, which is represented by the light-blue cell with 100% of the signal.

signal amplitude-deposited energy. The distance between the source and the fiber was set to 3 mm in the simulation code, to reproduce the gap created by the plastic box of the real source, which was directly on the fiber for the experimental measurements. In Figure 3.43 the results for a reference fiber are shown. The distribution entries have been normalized to the total number of events for visualization purpose.

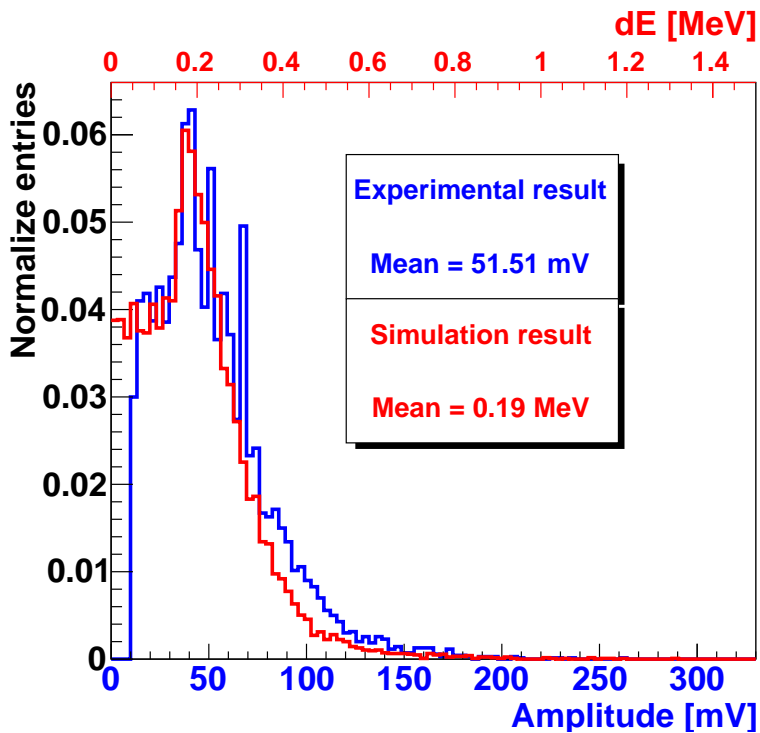


Figure 3.43: Comparison of the simulated distribution of energy deposited by electrons from the ^{90}Sr source on a single hodoscope fiber to the experimental signal amplitude distribution from a scintillating fiber irradiated with the ^{90}Sr source.

The comparison presented in Figure 3.43 can be useful as estimate of the expected signal for a given energy deposited by a ionizing particle (about 50 mV for about 200 keV of energy deposited). Knowing the applied amplification factor (given by the per-amplification card characterization) and the relative gain of each PM pixel, the expected raw signal integral can be estimated.

A complete characterization of the hodoscope acquisition chain will be necessary on proton and carbon beams in order to verify the beam primaries energy deposit on the scintillating fibers and tune the working parameters. In particular, the increased energy deposit expected for proton and carbons with respect to electrons should allow for a reduction of the high voltage applied to the PM. With reduced voltage, the detection rate capability would be improved. All these assumption will be tested on beam in the next future.

A preliminary study of the hodoscope acquisition chain characterization has been performed by developing an automatic parameter scanning system, which has been tested for background characterization. The code is able to loop on each acquisition channel by testing its response to increasing threshold and gain values, in the range allowed by the electronics FE board. This work has been performed with the collaboration of a bachelor internship student, and the results are presented in (Colléaux et al. 2018). Such a method will be applied during tests

with proton and carbon beams to optimize the hodoscope acquisition parameters on a single channel basis.

3.3 Summary and perspectives

The CLaRyS collaboration is developing in parallel two gamma cameras for ion beam therapy monitoring and nuclear medicine applications. At present, the detector components are being tested separately for characterization purposes at the IPNL. I presented in this chapter a complete description of the detector components with the related FE electronics, mechanical support, acquisition system and software tools, together with all the characterization measurements I performed on the various detector sections. In the following, in addition to a short summary of the present status of the instrumental development of each camera component, I list the main tasks to be accomplished for the final integration a complete operation of the whole camera.

3.3.1 Silicon scatterer

Among the 10 DSSD layers provided by the seller, only 7 respected the design requirements and have been selected for the use in the Compton camera prototype. The 7 selected layer have been characterized in terms of leakage current with an acquisition system specifically developed for this purpose. Temperature cycles have been performed in order to precisely define the cooling performance needed to obtained the required noise level. These measurements allow to fix the working temperature to -20°C and lead to the conception and production of a thermal regulated box, working with cold air and so adapted to the clinical use. A modular mechanical support has been fixed inside the camera to sustain the silicon layers with their FE cards. The FE card has been designed and tested at the IPNL, and includes a custom ASIC which has been optimized with three different developed versions. The final version of the whole board has been produced in 7 copies in 2017 and they are now available for the next test stages.

The development of the FE board firmware is at present ongoing at the IPNL, and the first tests of data collection with a temporary acquisition system and injected charges have been performed. A further verification and optimization of the code will be carried out in the next future, and the silicon layers will be tested with their FE cards by the end 2018 with the μ -TCA acquisition system. The present AMC40 firmware performance has never been tested with the scatterer detectors before; some modifications can then be foreseen to optimize the data taking process, for what concerns both the stand-alone test mode and the operation within the complete system.

Moving to the thermal regulated box, its cooling performance has been tested without the detectors, so that a test with the power consumption of the seven operational detectors and boards has still to be performed. Dry air or nitrogen will be tested and used for the final setup. Additionally, the box has to be adapted to arrange the incoming and outgoing cables (power supply and data). Outside the box, a patch-panel will be also realized in order to properly set all the needed connections. The patch panel will be conceived to be integral to the box

and adapted to the camera moving table, where the box will be installed for the final camera integration.

Once the acquisition will be fully operational, laboratory measurements with gamma sources are foreseen to characterize the detector response. Low energy gammas will be employed to test the DSSD energy resolution with full gamma absorption on a single strip basis, on p and n sides, while higher energy gamma irradiation is foreseen to study realistic detection conditions and verify efficiency, time and spatial performance (time resolution, average cluster size as a function of the energy). In addition, we will also infer 3D position capability by comparing p and n signals. Once a full characterization of each channel of the 7 layer will be achieved, tests on beam with prompt-gammas are planned in stand-alone operation and, finally, with the complete Compton camera.

3.3.2 BGO absorber

As mentioned in the detector description section, the original camera design included 96 BGO blocks recovered from a dismantled SIEMENS PET system. The reconditioning process aimed to re-polish the crystal surfaces, tests the PMs with a light source and group them in quartets with compatible gains. As reported, the reconditioned block prototypes tested didn't show the expected improved performance, but on the contrary an overall signal degradation has been observed, probably due to a worsened light collection. Several configurations have been tested with non satisfactory results, so that the present camera is set up with 30 original blocks, which have been deeply studied and characterized at the IPNL, as detailed in section 3.2.2. The calibration and characterization methods developed for the BGO block can be applied to similar detectors and represent an extension of previous studies ([Golnik 2015](#); [Hueso-González et al. 2015](#); [J. G. Rogers et al. 1994](#); [Tornai et al. 1994](#)). Some of the features developed for the characterization tests, as the automatic research of the pseudo-pixel position and the pseudo-pixel assignation algorithm, will be used in the final camera at the data analysis stage, with simple adaptation to the camera acquisition system and data format. The complete set of characterization measurements described in this chapter has been performed with commercial acquisition systems and the required raw data treatment was performed with commercial NIM modules. The ASM read-out boards are at present under test at the IPNL, and their firmware must be optimized for the μ -TCA acquisition. A first, non-optimized version of the complete acquisition chain has been tested, including the pre-trigger logic with the THOR board, the μ -TCA data collection and communication to the acquisition PC, and used for the beam test described in chapter 6.

With a fully operational absorber, test with prompt-gammas (and so on proton and carbon beams) will be performed to test the block behavior in the prompt-gamma energy range, where an overall performance improvement is foreseen (in terms of space, time and energy resolution). Some tests performed at the GANIL in 2014, with an original block and an acquisition similar to the one employed for the characterization tests, showed promising results: in particular, a 2 ns FWHM time resolution was achieved with prompt-gammas (see [Ley 2015](#)). These results have to be confirmed with all the camera BGO blocks. In addition to this, with proton and carbon beams the absorber geometry (in terms of block arrangement in the mechanical support) will be tested to obtain the optimal configuration with the minimization of dead areas between the blocks. To be noticed that different geometrical setup can be foreseen for Compton and multi-collimated camera, and for the peculiar desired measurement (detection

of the all ion range, test of prompt-gamma distribution in the plane parallel to the beam line, etc.).

Concerning the mechanical support, it is finalized and already prepared for the integration on the moving table. As for the scatterer, a patch panel will be realized to arrange all the cables which have to be connected between FE and ASM cards. The 5 needed ASM cards will be placed in a dedicated VME crate, which will be integral to the table. Its setup will be fixed in order to minimize the interference with the table movements.

3.3.2.1 Absorber upgrade

One of the already identified main limitations of the Compton camera for the application in ion beam therapy monitoring at clinical beam intensity is the relevant background due to random coincidences. As already mentioned, the random coincidences can be created by secondary particles different from prompt-gammas, or, less likely, by two prompt-gammas in the same time window. The TOF solution has been verified to be efficient in reducing the first kind of random coincidences, and the background subtraction performance ensured by this method strongly relies on the detector time resolution. An improvement in the camera component time resolution would allow for a reduction of the coincidence window, further increasing the amount of rejected random coincidences. A challenge concerning the absorber, if we keep the actual architecture, would be an improvement of the timing and efficiency (with 3 cm thickness the probability of full absorption is reduced). An additional layer of LYSO would improve the performance; replace PMs by Silicon Photo-Multipliers (SiPMs), replace VME acquisition by on-board or μ -TCA dedicated cards, these would be necessary steps in view of a broader diffusion of a Compton camera for Single Photon Emission Computed Tomography (SPECT) application and Prompt-Gamma (PG) detection.

A possible changement of the absorber architecture has already been considered for a second version of the Compton camera prototype, and involves a commercial detector provided by Damavan Imaging, called Temporal Delta Compton. It is based on a scintillation LYSO or Cerium Bromide (CeBr_3) crystals coupled to very fast Philips DPC3200 Tile sensors (based on SiPMs), with a Single Photon Time Resolution (SPTR) of the order of 100 ps (Brunner et al. 2016). This excellent time resolution allows for a direct measurement of the scintillation light shower development within the crystal, resulting in the possibility to retrieve a 3D spatial information in parallel to a time resolution in the hundred of ps scale. This solution will be further discussed in the future and can be applied for a second prototype of the Compton camera.

3.3.3 Scintillating fiber hodoscope

Three prototypes of scintillating fiber hodoscope are available at the IPNL: 1×1 fiber, 32×32 fibers and the large size version with two planes of 128 fibers. The 1×1 fiber has been studied at the beginning of the development process as proof of concept, and the employed technology has been transferred to the two final prototypes with the required improvements. The increased size of the 128×128 fiber one lead to the addition of the two-side fiber read-out, for efficiency optimization and improved timing performance. All the other features are common

to the two, including the installed multi-anode PMs (Hamamatsu H8500) and the related FE card. The advantage of the 32×32 hodoscope is the possibility to perform a complete read-out of the active surface with a single FE card, so that no synchronization features are required in the card and acquisition firmwares. This is the main reason why the first beam test performed on the hodoscope have been carried out with the small version (see chapter 6 for the description and the results of the beam tests). The FE card firmware is at present at the optimization stage, and the performed test allowed to define the needed improvements, mainly connected to the time measurements capabilities. In addition to this, the synchronization of the 8 cards used for the read-out of the 128×128 fiber prototype still has to be achieved. The first acquisition tests performed during the proton beam exposure allowed to validate the acquisition software and the μ -TCA firmware in a simple version, but additional trigger features must still be added to integrate the hodoscope in the final camera configuration. Concerning the detector performance, the optimization of the working parameters (gain and threshold of each read-out channel) required the development of an automatic measurement system, which will be employed on beam to perform similar characterization in presence of proton induced signals. Finally, the mechanical support is fully operational: the motor steering must be integrated in the slow-control software.

The overall development is at the final stage, and the integration of the 32×32 -fiber hodoscope in a first multi-slit collimated camera configuration has been tested on beam in September 2018, in order to perform preliminary tests of TOF capabilities. The obtained results are shown in chapter ??.

Previous measurements with discrete electronics lead to counting rate capability up to 10^7 counts/s on a single multi-anode PM H8500. However, this count rate capability needs to be more systematically studied with the large hodoscope with the sharing of channels among PMs, as a function of the energy deposit (incident particles), PM bias and detection threshold. A larger size hodoscope may also be envisaged in order to cope with particle therapy irradiation fields. A more general issue concerns the use of additional > 2 mm water equivalent thick material upstream of the patient. A clinical integration of such a hodoscope would require the optimization of the material budget (possibly thinner fibers) and a redesign of the holder.

3.3.3.1 Hodoscope upgrade

As already explained concerning the absorber possible upgrade, the main direction for an improved camera prototype is the optimization of the detector timing capability. The LPSC group in Grenoble is developing high time resolution diamond detectors, which can be considered for a new version of the beam tagging hodoscope. The so-called MoniDiam project aims to develop a diamond based hodoscope prototype with the related fast electronics to enable a time resolution of a few tens of ps. In addition to this, the diamond based detectors are intrinsically affected by a very low noise level and allow to overcome the radiation hardness limitation imposed by the present scintillating fiber prototype, together with further extending the rate capabilities to an expected 100 MHz acquisition rate without splitting the readout channels to several acquisition cards. Some tests of small diamond detector prototypes have already been performed with pulsed beams at the European Synchrotron Radiation Facility, Grenoble, France (ESRF) in Grenoble and with 95 MeV/u carbon beam at the GANIL, with promising results: a polycrystalline detector, $5 \times 5 \times 0.3$ mm³, exposed to the 95 MeV/u GANIL carbon beam, showed a time resolution of 37 ps RMS coupled to an energy resolution of the order

of 7% RMS for 25 MeV of deposited energy (see [Gallin-Martel et al. 2016](#)). Similar measurements performed with diamond crystal with different sizes showed compatible results, with a time resolution between 20 and 90 ps RMS and an energy resolution between 7 and 9 % RMS ([Gallin-Martel, M.-L. et al. 2018](#)). Although sufficiently large area diamonds are not yet available, a mosaic assembly of several diamonds (with a total area of $15 \times 15 \text{ cm}^2$) is expected to be tested in 2019-2020 and is a good candidate for a improved version of the Compton and multi-collimated cameras.

3.3.4 Acquisition and software

The acquisition μ -TCA based system development is managed by the CPPM research group, and frequent tests has been performed at the IPNL to verify and integrate its functionality to the read-out detector cards. As reported in the description, it should be able to receive and treat the trigger signal generated by the absorber for the multi-collimated camera or by the silicon scatterer for Compton one, collect the data flow from all the detectors, group them into UDP packets with the proper format and send them to the acquisition PC. The main tasks (data collection, packet creation and communication to the PC) have been already verified on beam for a single detector and a single FE board, so that now the trigger treatment capabilities and the ability to handle all the detectors components have to be developed in the AMC40 firmware and tested with the final system. Moreover, the μ -TCA must also be able to transfer the slow control signals sent by the LabVIEW software to the selected read-out cards; this feature is still at the debug stage.

Concerning the acquisition software, it has already been tested and validated with a data simulator, with a maximum achieved acquisition rate of about 300 Mb/s, sufficient to manage the data from the complete camera (see appendix A). It will be tested step by step with the increasing number of FE boards involved in the measurements. In parallel, the monitoring software is now available and operational for each single detection section, but an optimized version allowing for an on-line visualization of the whole camera acquisition must still be studied. Finally, the slow control software development is ongoing; all the required working parameters can already be controlled by various pieces of software, which must be integrated in a complete user interface and tested with the μ -TCA for what concerns the FE cards configuration. All the parameters related to the moving table motors (for camera and hodoscope), detector and card low and high voltage, have already been tested and do not require the μ -TCA intervention.

3.4 Conclusions

During the three years of my PhD thesis, the instrumental development of the single detector components, as well as of the two cameras, saw an important advancement, thanks to the synchronized effort of the whole collaboration. In this chapter, the advancements achieved in the last years have been described in details, including, in addition to my personal contributions, results obtained before the beginning of my PhD thesis or in parallel by CLaRyS collaborators.

I personally characterized the hodoscope PMs as described in section 3.2.3, following the preliminary internship work of a master student (Coudurier 2015) and using an instrumental setup already created by a previous PhD student (Gaglione 2013). During the first months of my work, I adapted the acquisition system in order to perform automatic scans of the hodoscope PM surfaces, I acquired data for the whole set of available PMs and I performed the complete data analysis to produce the results presented in the description section. In parallel, I studied in simulation the design of the lead collimator produced to host the ^{60}Co high activity source described in section 3.2.2. The source was originally foreseen to be employed for the characterization of the scatterer silicon layers, so that I optimized the design of the three apertures (point-like, linear and squared) in order to obtain the desired irradiation of the DSSDs layer surfaces. The collimator structure is designed, in collaboration with the radiation protection IPNL expert, to allow the source usage in a “public” area, so that the geometrical configuration is imposed by these constraints. The collimator production has been performed by an external company, and I directly participated in the source positioning inside the collimator, as well as to the radiation tests in its final location. Since the Spring 2016, I focused my efforts on the hodoscope, starting from the 128×128 fiber prototype mounting (I installed the characterized PMs) and testing with a simple acquisition, in order to verify the optical fiber and scintillating fiber connection. I identified the defective channels and participated in the fixing process with the mechanics IPNL group. After that, with the help of a master student, I performed a first characterization of the complete read-out chain for each channel, and compared the results of the irradiation with a beta source to simulation, for a preliminary detector calibration (see section 3.2.4 and Vallois 2016). In the following months I mainly focused on the simulation works presented in chapters 4 and 5, participating in parallel to the electronics development advancements. In particular, I collaborated with the IPNL electronics group to the characterization of the scatterer FE card in terms of electronic noise, by analyzing and discussing the collected data. Since the beginning of 2017, my attention was directed to the absorber components. As described in section 3.1.3, the whole set of original recovered block should have been “reconditioned” in order to be adapted and optimized to the new application in the CLaRyS gamma camera, and I directly worked on the test and characterization of the first reconditioned blocks received by the LPC group. With the help of a master student working for its internship, we developed an acquisition system based on the BGO block acquisition card, commercial NIM modules and the PXI described in section 3.2.3, and we tested several blocks reconditioned with different methods, in comparison to a reference original block. The test results are reported in Sandjong et al. 2017 and were not satisfactory, so that we decided to move to the application of original, “non-reconditioned” blocks, with a reduced size absorber configuration. The acquisition system we developed to characterize the reconditioned blocks has been used to test the original ones, which I completely characterized starting from September 2017. During the characterization process, I optimized, with the participation of a master student, the test method and developed the analysis and performance optimization process described in section 3.2.2 and published in Fontana et al. 2018. Concerning the mechanical supports, I participated in the design and realization of the reduced-size camera absorber support, in the final configuration of the hodoscope moving table, with particular focus on the setup of the patch panel for the cable connections, and to the first cooling tests involving the thermal regulated chamber to be employed with the scatterer layers. Moreover, I worked with IPNL colleagues to develop the LabVIEW based remote control of the camera moving table described in section 3.1.7 and shown in Figure 3.16b, which is still under test. Moving to my contribution to the camera software, I personally developed all the analysis code used to produce the results presented in this chapter, with the exception of the scatterer layer tests. Furthermore, I developed the camera monitoring software described in section 3.1.6, and I

always participated in the optimization of the acquisition software, coded by the IPNL computing group, as well as in the design of the different acquisition card firmwares. Finally, I tested the hodoscope on beam during three tests campaigns, described in details in chapter 6.

The project is now reaching the final stage, where all the performed laboratory test and development studies will be transferred to the multi-collimated and, even most, to the Compton camera, which is foreseen to be tested on beam before the end of 2019. The next two years will be fundamental to estimate the potential of the developed detectors in realistic conditions and to plan the first clinical tests, final goal of the entire project.

4

Compton camera application for ion beam therapy monitoring

The results presented in this chapter have been submitted for publication on the journal *Physics in Medicine and Biology*.

Contents

4.1	Introduction	146
4.2	Material and methods	148
4.2.1	Simulation setup	148
4.2.2	Beam structure	151
4.2.3	Compton camera events	152
4.2.4	TOF and energy based data selection	153
4.2.5	Reconstruction algorithms	155
4.2.6	Performance study	157
4.3	Results	159
4.3.1	Absolute detection efficiency	160
4.3.2	Rate of random coincidences	162
4.3.3	Camera precision	163
4.4	Discussion	165

4.1 Introduction

Ion beam therapy is a cancer treatment technique which is rapidly gaining importance in the global tumor therapy panorama. In addition to the already operational 70 clinical facilities, with more than 175000 patients already treated by the end of 2017, several new centers have been designed and approved for construction worldwide (Particle Therapy Cooperative Group 2017). The favorable feature of this treatment technique is connected to the peculiar energy deposition profile of charged particles as a function of depth in matter. As first observed by Bragg (Bragg et al. 1904), the depth-dose profile of charged particles shows a maximum close to the end of their range in matter; in addition to this, a strong enhancement of the Relative Biological Effectiveness (RBE) is observed for ions heavier than protons in the region of the Bragg peak (Elsässer et al. 2004; Weyrather et al. 1999), which further enhances the dose ratio between target and healthy tissues.

The maximum of the dose is deposited in the Bragg peak region in the patient and must be tuned to cover the target volume (defined via Computed Tomography (CT) scan) and, at the same time, spare the surrounding healthy tissues. Treatment planning and delivery uncertainties limit the tumour targeting capabilities, like uncertainties in the material composition determination, CT units conversion to ion stopping power, patient mis-positioning, organ motion or morphological changes between treatment fractions. These uncertainties force the clinicians to fix relatively large safety margins around the planned treatment volume, up to 3.5% + 3 mm (Paganetti 2012b). Ion-range verification is one of the conditions required for a broader usage of ion beam therapy and for its further development. With the goal of fully exploiting the ion beam therapy dosimetric potential, the monitoring should be in real-time and ideally in 3 dimensions, in order to detect important deviations between the planned and delivered dose to the target volume or to surrounding organs, in particular in case of proximity to Organ At Risk (OAR). This capability would allow for a reduction of the above mentioned safety margins and for a better tumor targeting; in addition to this, it could permit the use of new irradiation fields with OAR downstream with respect to the tumor position (Knopf et al. 2013).

Several range verification techniques have been considered worldwide for twenty years. Most of them rely on the detection of secondary radiation generated during the slowing down process of incident ions, in particular during nuclear reactions. Among these secondary radiations, positron emitters have been deeply studied in order to exploit Positron Emission Tomography (PET) machines for treatment monitoring. The only available and functional range monitoring systems in a clinical center are based on this technique (Enghardt et al. 2004; Yamaya 2018), which is anyway affected by physical and technical limitations (Parodi 2015).

In addition to positron annihilation products, the relaxation of excited nuclei also produces secondary photons in a wide energy range, between some hundreds of keV till about 8-10 MeV. After the first idea proposal published in 2003 (Stichelbaut et al. 2003), these secondary products of particle treatment have been deeply investigated and the correlation of this gamma radiation to the ion depth-dose profile has been confirmed by several research groups, starting from Min et al. 2006 for protons and É. Testa et al. 2008 for carbon ions. The so-called Prompt-Gamma (PG)-rays have the advantage to be emitted almost instantaneously after the beam interaction in the tissue, making them more adapted than PET 511 keV gammas for real-time monitoring. Moreover, as shown in (Robert et al. 2013), the emission rate is compa-

rable or superior to the one of the annihilation gammas for both protons and carbon beams. Consequently, different techniques have been proposed to exploit this signal for treatment monitoring purpose, with the related detection systems. More details on PG monitoring can be found in chapter 2.

Originally designed for astrophysics applications, the potential of Compton cameras for medical imaging has been soon recognized (Todd et al. 1974) and then directly translated to the ion beam therapy monitoring domain. Such a gamma detection system is generally composed of two sections: a scatterer and an absorber. The scatterer is dedicated to the gamma Compton-scattering, and should be designed to optimize the Compton scattering probability in the prompt gamma energy range, while reducing the so-called Doppler broadening effect due to electron binding and motion (Ordonez et al. 1997); in most of the cases, this leads to the choice of a light material (low Z), segmented in several subsections. On the other hand, heavier materials may be used to improve photon detection efficiency (Aldawood et al. 2017; Polf et al. 2015; Solevi et al. 2016)). The absorber finally intends to capture the Compton scattered photons via photoelectric effect and is often composed of segmented high- Z scintillating materials. A slightly different Compton camera configuration can also achieve Compton electron tracking in the scattering detector (Frandes et al. 2010; Yoshihara et al. 2017), which results in additional information for the further reconstruction algorithm. The collected interaction positions and energy depositions in the two detector sections are used to constrain the emission point to the surface of a cone (or to a segment in the cone if the Compton electron track information is retrieved), via Compton kinematics (for an electron initially at rest):

$$\cos \theta = 1 - \frac{m_e c^2 E_1}{E_2(E_1 + E_2)}, \quad (4.1)$$

where $m_e c^2 = 511$ keV, E_1 and E_2 are the energies, respectively, deposited in the scatterer and the absorber. Analytic or iterative algorithms use these cones to create the image of the prompt gamma emission distribution, with intrinsic 3 dimensional capability (Kuchment et al. 2016; McKisson et al. 1994).

Several sources of uncertainty and signal background are connected to the above described detection method. The reported Compton kinematics formula (equation 4.1) assumes valid the relation in equation 4.2:

$$E_0 = E_1 + E_2. \quad (4.2)$$

Since the initial photon energy (E_0) is not known a priori, a complete photon energy absorption is needed for the cone calculation, or at least two photon scattering interactions are required in a single event. An under-estimation of the total initial energy (caused by a photon non-complete absorption in the absorber section or by the Compton electron escape from the scatterer section), leads to a mi-estimation of the Compton angle, so to a Compton cone reconstruction uncertainty. If double scattered photons are selected, the initial photon energy can be calculated analytically so that a complete absorption is not mandatory. In addition to this, the Compton formula considers the Compton scattering electron initially at rest, and its energy configuration creates a blur in the Compton angle reconstruction, resulting in the already cited Doppler broadening effect (Ordonez et al. 1997). Furthermore, the detection principle is based on time coincidences between the two detector sections, therefore the time structure of the incoming particles plays an important role. The final image accuracy suffers from random coincidences generated by two prompt gammas interacting within the same time window or by contamination of secondaries, mainly neutrons and protons. The effect of random coincidences can be reduced by high detector time resolution or background

rejection methods (Draeger et al. 2017). Energy selections can be applied to the collected coincidences (Hilaire et al. 2016; Polf et al. 2009) or the homogeneous neutron background can be reduced via time-of-flight information (M. Testa et al. 2010).

Ortega and colleagues (Ortega et al. 2015) presented a detailed analysis of the noise sources for Compton imaging in proton therapy monitoring, and the clinical application of this method for detecting range shifts was tested for the setup under development in Valencia. The simulation study showed the relative expected rate of prompt gammas and neutrons, and the resulting rate of random coincidences ranging from 19 % to more than 60 % depending on the beam energy and the coincidence time window. This amount of fake events leads to complex reconstruction scenarios, where the identification of a 3 mm range shift is not clear for all cases.

Starting from these results, we propose in this paper to study with Monte Carlo simulations a Compton camera prototype based on semiconductor and scintillator detectors Fontana et al. 2018; Krimmer et al. 2015 developed by the CLaRyS collaboration. The camera performance is studied with respect to the gamma energy in the prompt gamma energy range. Furthermore, the feasibility of its clinical application as depth-dose profile monitor during ion beam therapy clinical treatment is analyzed. After a preliminary study with point-like gamma sources irradiation focused on detector efficiency measurements as a function of the source position and gamma energy, clinical proton and carbon beams impinging on an homogeneous Poly Methyl Metacrylate (PMMA) phantom are simulated to reproduce treatment conditions and analyze the prompt gamma detection resulting scenario. The ratio between true and random coincidences is studied as a function of the beam intensity. Two kinds of reconstruction algorithms, a line-cone analytic method and a Maximum Likelihood Expectation Maximization (MLEM) iterative one, are applied to the collected data in order to compare the imaging results. Finally, the precision with which the dose profile fall-off can be detected with the Compton camera is reported.

4.2 Material and methods

4.2.1 Simulation setup

The monitoring system modeled in this simulation work is a Compton camera prototype under development within the French collaboration CLaRyS. The detectors detailed characteristics can be found in chapter 3.

The scatterer consists of seven parallel planes of silicon detectors (Double-sided Silicon Strip Detectors (DSSDs)), $9 \times 9 \times 0.2 \text{ cm}^3$, with 1 cm distance between the centers of two neighboring planes, while the absorber is composed of an array of 10×10 Bismuth Germanium Oxide - $\text{Bi}_{12}\text{GeO}_{20}$ (BGO) blocks ($3.5 \times 3.5 \times 3.0 \text{ cm}^3$ each) placed behind the silicon layers at a distance which can be tuned according to the requirements.

The silicon detectors have a strip pitch of 1.4 mm, for a total of 64 strips per side (double-sided readout based on electron and hole pairs collection). Regarding the BGO blocks, their entrance surface is streaked in a 8×8 matrix of pseudo-pixels, $4.4 \times 4.4 \text{ mm}^2$ size, and the

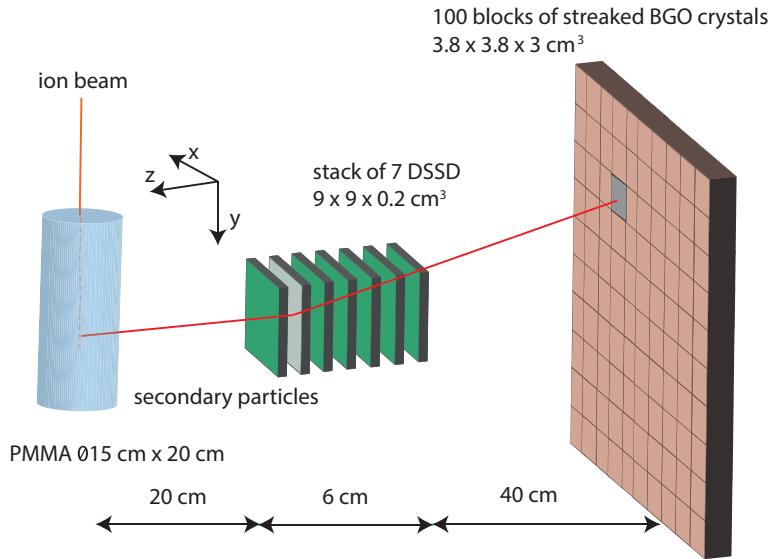


Figure 4.1: Scheme of the simulation setup (not at scale): a PMMA cylindrical phantom is set in front of the Compton camera prototype. The Compton camera is composed of a stack of 7 double sided silicon strip detectors (scatterer) and a plane of 100 single BGO blocks. The set distances are realistic for clinical conditions. This geometrical configuration has been used for all the simulations presented in this work.

readout is performed via 4 photo-multiplier tubes. The position reconstruction is achieved via Anger logic.

A scheme of the simulation setup is given in figure 4.1. The ion beam interacts with a cylindrical PMMA (PolyMethylMethAcrylate) phantom (15 cm diameter and 20 cm length) placed in front of the Compton camera as target. It is placed 20 cm far from the first silicon plane (center-to-center distance) which seems a realistic distance in clinical conditions. The distance between the last silicon layer and the absorber array (center-to-center) is set to 40 cm in order to enable time-of-flight measurements (see section 4.2.4).

The silicon detector strips are not reproduced in the simulation code, and the transverse spatial resolution is set to 0.9 mm Full Width at Half Maximum (FWHM) at the reference energy of 1 MeV, according to preliminary measurements performed on smaller detector prototypes. Concerning the transverse direction (perpendicular to the beam line), the interaction position is set to the center of the involved silicon plane. A mono-block crystal is simulated for the absorber for simplicity. The events are selected to be limited to a single block component based on the interaction localization, and the interaction position is reconstructed via center of gravity calculation if multiple interactions occur within the same block. An uncertainty contribution, randomly extracted by a Gaussian of 5 mm FWHM (corresponding to an overestimation of the geometrical resolution given by the pseudo-pixel matrix, set to reproduce not yet tested experimental conditions), is added to the reconstructed position to mimic the pseudo-pixel-based readout. For what concerns the parallel direction, given the fact that the employed BGO blocks have not depth of interaction reconstruction capabilities, the interaction position is fixed to the center of the mono-block crystal.

The energy resolution of the BGO blocks was estimated in preliminary measurements and is

accordingly set to 20% FWHM at the reference energy of 667 keV (a 137-cesium source has been used for the measurements). The energy resolution of the silicon detector is set to 5 keV (FWHM) according to the design expectations.

The time resolution has been set to 3.0 ns FWHM for the BGO blocks and to 15.0 ns FWHM for the silicon slabs, according to preliminary measurements performed on test detector modules at the Grand Accelerateur National d'Ions Lourds, Caen, France (GANIL) center in France.

The detector resolutions play an important role in the Compton camera performances. The spatial resolution of the absorber influences the position of the apex of the Compton cone as well as its axis orientation. The energy resolution of the scatterer determines the Compton cone aperture angle. The time resolution impacts the coincidence window between the absorber and the scatterer, and therefore the detectors ability to distinguish between true and random coincidences.

The CLaRyS project also includes the development of a beam tagging hodoscope, composed of scintillating fibers read out by multi-channel photomultipliers. This detector is used to synchronize the beam time and space structure to the prompt gamma detection in order to tune the detection window reducing the background contamination. In addition to this, the spatial localization of the impinging beam bunch can be included in the event reconstruction algorithm to add constraints to the obtained solutions (see section 4.2.5). The hodoscope is not included in the simulation, but its spatial and time resolution have to be taken into account for the time-of-flight discrimination (see section 4.2.4) and events reconstruction. They are set to 1 ns and 1 mm FWHM, respectively.

The detector's spatial, energy, and time resolutions are summarized in table 4.1.

Table 4.1: Estimations of reachable resolutions with the detectors. Those resolutions are applied during the simulations.

Resolution (FWHM) at 1 MeV	Scatterer	Absorber	Hodoscope
spatial [mm]	0.9	5	1
energy	5 keV	17 %	/
timing [ns]	15	3	1

The Monte Carlo simulation is performed with the Geant4 toolkit, version 9.6.02. The particle interactions in matter are described in this work by means of the models listed in table 4.2. Additionally, the Doppler broadening and the photon polarization effects are included.

Table 4.2: Hadronic models used in the Geant4 simulations.

Process	Protons	Ions	Neutrons
Electromagnetic			standard _{option3}
Inelastic	G4BinaryCascade	G4QMDReaction (G4IonsShenCrossSection)	G4BinaryCascade + G4NeutronHPInelastic (<19 MeV)
Elastic	G4LElastic	G4LElastic	G4LElastic + G4NeutronHPElastic (<19 MeV)
Fission	/	/	G4LFission + G4NeutronHPFission(<19 MeV)
Capture	/	/	G4LCapture + G4NeutronHPCapture (<19 MeV)
Radioactivedecay	/	G4Radioactivedecay	/

4.2.2 Beam structure

4.2.2.1 Beam structure measurements at HIT

Our group performed a set of measurements to characterize the beam time structure of the synchrotron installed at Heidelberg Ion Therapy Center, Germany (HIT), Germany (Peters et al. 2008). This set of measurements extends the results reported in Peters et al. 2008 and is then used to reproduce a realistic beam in the simulation.

The beam characterization has been performed for 200 MeV/u and 400 MeV/u primary ion energy with a two-fiber hodoscope (basic prototype of the one at present under development) and the spill signal was given by the accelerator. Figure 4.2 shows the results for carbon ions at 400 MeV/u. The pulses have a spill period of 150.2 ns and each bunch is approximately 21.5 ns. The mentioned measurements have shown that the spill phase changes during the extraction: this implies that the HF signal from the synchrotron can not be used to trigger the pulses, so that the use of an additional beam time stamp system like the hodoscope seems required for time-of-flight background rejection purposes.

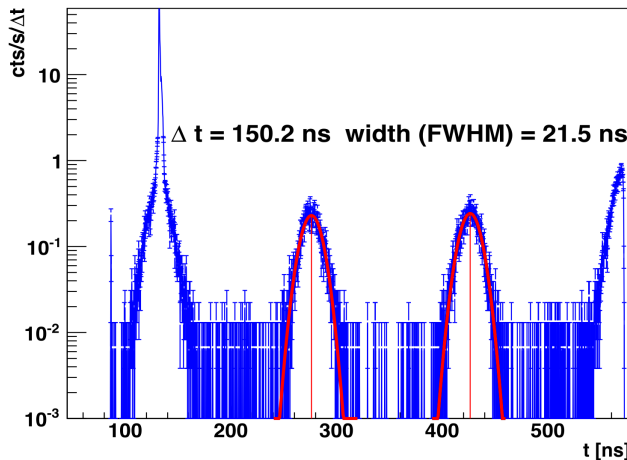


Figure 4.2: Time micro-structure measured from a carbon ion beam at 400 MeV/u delivered at HIT (time difference between two crossed-scintillating fibers). The offset between the two fibers is arbitrarily set at 130 ns. The pulses have an extraction period of 150.2 ns and the bunches are 21.5 ns FWHM. On the x axis the time has been measured with a two-scintillating-fiber hodoscope, with 1 ns FWHM time resolution.

4.2.2.2 Beam modeling

The two main beam particles used in clinics are considered in the simulation: protons and carbon ions. The beam range of interest is 15.2 cm in the PMMA phantom, and the associated energy is 160 MeV for protons and 305 MeV/u for carbon ions.

The beam transverse dimension is modeled with a Gaussian distribution with a standard deviation of 5 mm for protons at 160 MeV and 3.5 mm for carbon ions at 305 MeV/u. The number of incident ions for a spot in pencil beam scanning (PBS) mode is 10^8 for protons (distal spot - upper intensity limit) and 10^5 for carbon ions (average spot intensity) (Grevillot

et al. 2011; Krämer et al. 2000; Smeets et al. 2012). In the simulation, the beam intensity is modeled by an average number of particles per bunch. The exact number of particles in each bunch is given by a random extraction from a Poisson distribution, where the mean value is the selected beam intensity.

The beam time structure is applied at the data analysis stage. Two different time structures have been considered for this study, related to two kinds of accelerators used in clinical practice: the Ion Beam Applications, Belgium (IBA) C230 cyclotron for protons (used in 16 clinical centers worldwide) and the HIT synchrotron for carbon ions. For protons at 160 MeV, the primary particles are grouped in bunches of 2 ns (this value may vary also according to the distance between the cyclotron and the treatment room, and energy spread selection) at a frequency of 106 MHz (9.42 ns) (Roellinghoff et al. 2014). The clinical beam intensity is 3.2 nA which corresponds to about 200 protons per bunch. Concerning the carbon ion beam at 305 MeV/u, the simulated time structure refers to the measurements presented in section 4.2.2.1. We used 30 ns duration bunches at a frequency of 5.9 MHz (170 ns period). The clinical beam intensity for carbon ions is 5×10^7 ions/s during extraction, corresponding to about 9 ions per bunch. The macro-structure (50% duty cycle with [1,5] ns period) is not considered.

The coincidence window (between scatterer and absorber events) is set to 40 ns, centered on each absorber detected interaction. This value is adapted to the detectors time resolutions. At the simulation stage, each interaction in the detector layers is collected with the related local time. The beam time structure is then applied to each single hit, and the selected coincidence window is used to retrieve scatterer-absorber coincidence events.

Table 4.3 summarizes the presented beam time structures and coincidence reconstruction features.

Table 4.3: Description of the two beam structures studied: the IBA cyclotron C230 for protons and the synchrotron installed at the HIT center in Germany for carbon ions. The macro-structure of the synchrotron, at the second time scale, is not considered here. The beam structures are applied to the simulation data.

		Protons	Carbon ions
Clinical features	Facility	IBA Cyclotron C230	Synchrotron at HIT
	Clinical intensity	2×10^{10} p/s	5×10^7 ions/s
	Energy	160 MeV	305 MeV/u
Beam structure	Bunch time [ns]	3.2	30
	Period [ns]	9.4	170
	Primaries/bunch	217	9
Detectors	Coincidence window [ns]	40	40
	Time resolution (FWHM) [ns]	Si: 15 and BGO: 3	

4.2.3 Compton camera events

The Compton detection principle is based on the time coincidence of at least one scatterer and one absorber gamma interaction, where an interaction is defined as an energy deposit in a detector module. As discussed in section 4.2.2, the coincidence reconstruction relies on a

defined time window, fixed according to the detector resolution. In a simulation environment, different kinds of coincidence events can be distinguished and studied:

- real coincidences: created by a single photon first interacting in the scatterer stack and then in the absorber block array;
- quasi-simultaneous interaction of two secondary particles;
- double interaction of the same particle, not a photon (e.g. protons, neutrons).

As described in section ??, the simulation setup selects events with absorber interactions limited to a single BGO block; the employed blocks do not provide depth-of-interaction information, so that the inclusion of events with more than one block involved would degrade the spatial reconstruction accuracy. Concerning the scatterer section, among the real coincidences, three different kinds of events can be identified:

- single Compton interaction in one silicon layer;
- multiple gamma interactions in more than one silicon layers;
- electron escape events.

As mentioned in the introduction, events involving more than one photon interaction in the scatterer layers are advantageous since the total absorption of the detected prompt gamma is not required to reconstruct the Compton cone. However, the actual selection of such kind of events with respect to background interactions in real conditions is hardly achievable.

On the other hand, electron escape events can be in principle identified and exploited. They are characterized by two or more scatterer layers involved: if the first Compton interaction in one layer provide enough energy to the recoil electron, it can escape the silicon plane and be detected by one (or more), following planes. Thus, such events can be identified by the electron tracking, and carry additional information with respect to a Compton interaction with no electron escape. The electron tracking allows to reduce the reconstructed Compton cone to an arc, by the overlap of the cone with the electron tracking plane.

4.2.4 TOF and energy based data selection

In an experiment the collected data are affected by a certain number of the so-called random coincidences, which cannot be experimentally distinguished from true coincidences, from the timing coincidence point of view. The amount of random coincidences depends on the detector time resolutions, the fixed time coincidence window and the beam time structure, the phantom composition and camera prototype setup. In figure 4.3, a schematic view of the different kinds of coincidences is presented.

In addition to this, the prompt gamma measurement is contaminated by other secondary particles (mainly massive and charged particles like protons and neutrons, but also electrons in the low energy regime), produced by the interaction of the primary particles with the pa-

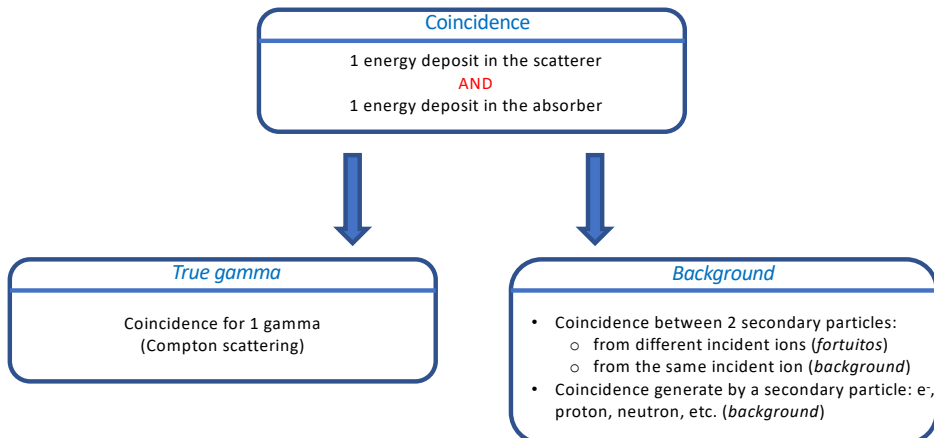


Figure 4.3: Diagram showing the different definitions of coincidences in the Compton camera.

tient/phantom. Ad-hoc filtering methods are applied to reduce the above described contamination.

- Time-Of-Flight: it has been demonstrated that a time-of-flight discrimination is possible and effective in reducing the background generated by massive particles interactions (M. Testa et al. 2010). The massive particles approach the detector at a lower speed with respect to photons. The time information provided by the hodoscope and the absorber can be combined to fix a detection time window and reject all the events outside the window. The time elapsed between the incident particle creation (t_{creation}) and the secondary particle detection in the absorber (t_{absorber}) is considered as the time-of-flight. The particle creation time is modeled according to the beam time structure, as presented in section 4.2.2.2. The detection time in the absorber is calculated with the simulation local time of the hit in the detector layer. The hodoscope time resolution (1 ns FWHM) is applied to the primary particle creation time, with a contribution randomly extracted from a Gaussian with $\sigma = 1/2.35$ ns ($u_{\text{hodoscope}}$). The detection time in the absorber is affected by the absorber time resolution, already included in the simulation code.

In order to define the appropriate time window, the TOF spectra of the collected events resulting from the irradiation of the PMMA target with 10^8 160 MeV protons have been produced for true gamma coincidences and background events, identified in simulation. Only events with single Compton interactions ion the scatterer are included (given the results presented in section 4.3.1). The results are shown in figure 4.4. For this study, no time structure have been applied to the primary protons. The detector resolutions have been included as described above.

$$TOF_{\text{simulation}} = t_{\text{absorber}} - (t_{\text{creation}} + u_{\text{hodoscope}}) \quad (4.3)$$

The time-of-flight spectrum resulting from the simulation shows that the coincidences

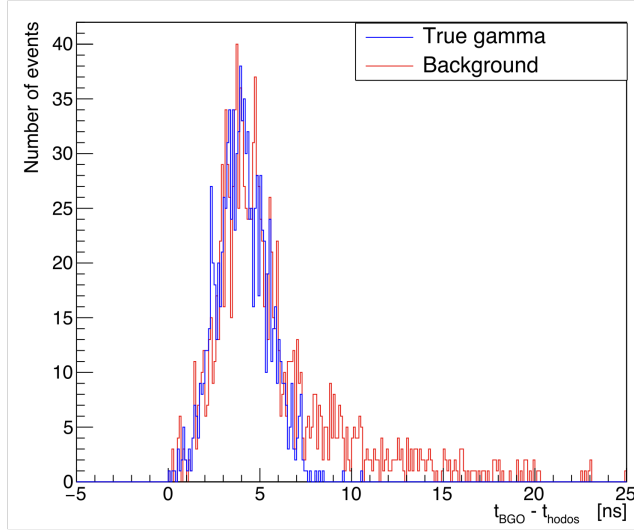


Figure 4.4: Time of flight spectra of true gamma coincidences (blue) and background events (red) obtained with 10^8 160 MeV independent incident protons.

of interest (produced by prompt-gamma rays) are included in a window between 0 and 8 ns. Therefore, all the coincidences with a TOF not included in this time window will be rejected when this selection is applied. The time-of-flight selection method limits the background events affecting the prompt-gamma coincidence measurements, but in the TOF window a comparable amount of true coincidences and background events is anyway expected.

- Energy selection: energy thresholds are defined for the event detection. 50 keV and 100 keV are set as lower threshold for the energy deposited in a single silicon layer and absorber, respectively. For a complete event, a total absorbed energy lower limit is set to 1 MeV. In addition to the effect of background rejection, this selection also reduces the impact of partially absorbed photons and events with Compton electron escape.

Further energy selections, assuming for instance $E_1 + E_2$ equal to one of the strong gamma lines, have been applied by other authors (Draeger et al. 2017). Also, filters checking the possibility of reconstructing a Compton cone could be used. At this stage we did not consider such approaches in order to cope with simple considerations on signal to noise on raw data.

4.2.5 Reconstruction algorithms

Once the coincidences are defined and selected according to the fixed physical cuts, the prompt-gamma emission point has to be reconstructed for each event. This can be done via analytic or iterative algorithms based on the Compton kinematics. Both are presented in the following sections.

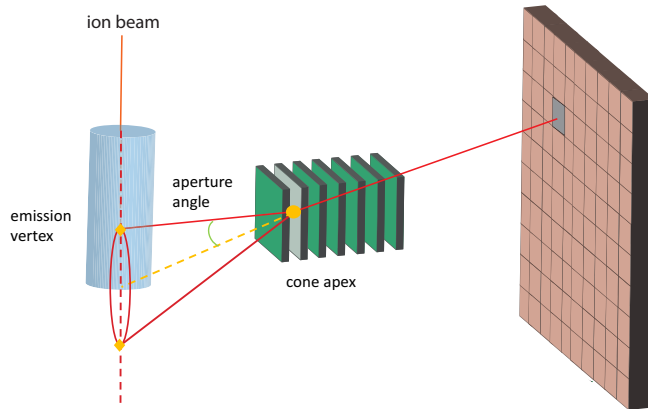


Figure 4.5: Scheme of the reconstruction principle for Compton events. For line-cone reconstruction methods, two points are extracted for each event (diamonds in the figure), provided by the intersection between the reconstructed Compton cone and the beam line. The reconstructed image is strictly 1D. For the iterative MLEM algorithm, each algorithm iteration adds constraints to the reconstructed cone surfaces, leading to a 3D image.

4.2.5.1 Line-cone algorithm

The reconstruction via line-cone algorithm exploits the energy deposit and position information collected by the camera in addition to the beam spatial information provided by the hodoscope. Thanks to the deposited energies in the detectors and the interaction positions, a cone surface is analytically defined via the Compton equation ???. Figure 4.5 shows a sketch of the reconstruction principle. The interaction position in the scatter gives the cone apex and the line connecting the interaction positions in scatterer and absorber gives the cone axis. We assume that the initial energy of the gamma ray is fully absorbed in the absorber. According to previous simulation results, the rate of events fully absorbed in the Compton camera is more than 60 % in the PG energy range. In order to constrain the reconstruction, the beam direction is used to limit the possible solutions (lying on the reconstructed cone surface) to two points (intersection of the beam direction and the reconstructed cone). At this stage we do not consider the lateral beam spread in the target, due to multiple scattering. The set of all the reconstructed points gives the emission source distribution. The final image is the mono-dimensional projection of the prompt gamma emission profile.

4.2.5.2 LM-MLEM algorithm

The iterative methods allow to get a 3D image reconstruction, potentially by taking into account the spatial resolution and the energy resolution of the detectors. Several iterative algorithms have been developed for Compton event reconstruction (Gillam et al. 2011; Huang et al. 2018; Mackin et al. 2012; Schöne et al. 2017, 2010; Taya et al. 2017; Zoglauer et al. 2011).

The List Mode-Maximum Likelihood Expectation Maximization (LM-MLEM) algorithm is a

MLEM version which enables one to reconstruct the image directly from the list of detected events. The features of the LM-MLEM algorithm used for this study are detailed in Hilaire et al. 2014.

4.2.6 Performance study

In this section the parameters studied for the camera performance evaluation are explained. The study is mainly divided into three sections:

- Absolute efficiency: the camera absolute efficiency for gamma detection is studied by means of mono-energetic irradiation with point-like sources;
- Rate of random coincidences: with proton and carbon beams interacting with the PMMA phantom, the rate of random and true detected coincidences is studied as a function of the beam intensity;
- Camera precision: the camera capability of identifying the fall-off of the prompt-gamma emission profile is tested and the two reconstruction methods presented above are compared.

4.2.6.1 Absolute detection efficiency

The absolute efficiency is crucial for the Compton camera performances and for its possible application in treatment monitoring. An efficient monitoring system should be ideally in real time, in order to allow for a treatment adaptation or interruption in case of severe issues detected in the delivered dose profile with respect to the planned treatment. In order to achieve an online detection of such deviations, given the limited prompt gamma emission rate per incident ion (Ortega et al. 2015), a high detection efficiency is required to perform a monitoring on, ideally, a beam spot basis. In addition to this, the absolute detection efficiency directly affects the image reconstruction quality, which is in general increased for increased statistics.

In order to well define the expected camera efficiency, it has been studied with the irradiation from point-like mono-energetic gamma sources. Different energies have been tested to mimic different prompt gamma lines: 300 keV, 500 keV, 1 MeV, 2 MeV, 4 MeV, 6 MeV. No time structure is reproduced for this part for the study. The absolute efficiency in the detection of specific kinds of events detailed in section has been estimated. The results of this preliminary study (see section 4.3.1) determined the choice to limit the next investigations to single Compton interactions in the scatterer.

The absolute efficiency ϵ is therefore defined as:

$$\epsilon = \frac{N\gamma_{\text{coinc}}}{N\gamma_{\text{total}}}, \quad (4.4)$$

with $N\gamma_{\text{coinc}}$ the number of gamma events corresponding to true coincidences of single photon interactions in the scatterer, $N\gamma_{\text{total}}$ the total number of emitted gammas.

The setup is the same as figure 4.1, with the exception of the PMMA phantom which is removed to leave the gamma source in air. The absolute efficiency has been also studied as a function of the point-like source position. It is set in the range -300 mm to $+300$ mm (with the center of the camera transverse section set in the position 0), and moved with variable length steps, up to 1 cm. The movement followed the transverse axis of the camera.

Moreover, the rate of events with almost full primary energy absorption has been studied as a function of the primary gamma energy, with the point-like source set in the center of the camera. The threshold for the energy absorption has been set to 90% of the primary gamma energy. The rate of absorption has been also evaluated for multiple gamma interactions and for electron escape events, for comparison.

4.2.6.2 Rate of random coincidences

As the Compton detection principle relies on time coincidences, in addition to the main importance played by the detectors energy resolutions, the beam intensity and time structure are important parameters to be studied in order to assess the possible clinical implementation of a Compton detection based monitoring of ion beam treatment. The ability of the detection system to distinguish between true and random coincidences, i.e. the resulting signal over noise ratio, strongly depends on the beam time structure. The number of true and random coincidences (where the two cases listed in section 4.2.4 are included in the random coincidences) is studied as a function of the beam intensity, before and after data reconstruction via line-cone algorithm (see section 4.2.5).

The range of intensities is defined in order to cover a wide range of operation: from a very low beam intensity to a realistic clinical particle rate. Therefore, for proton and carbon ions, the lowest beam intensity is set to 0.1 particles per bunch on average, while the upper limit is set to 217 protons or 70 carbon ions per bunch. All the simulations are performed with a total of 10^8 primary protons and 2×10^5 primary carbon ions (see section 4.2.2.2). For the analysis of the results, the coincidence yields are scaled to the number of incident ions and the beam intensity to the average number of ions per bunch.

4.2.6.3 Camera precision

The camera precision is defined as the difference between the predicted PG Fall-Off Position (FOP) (according to the treatment planning) and the detected one. In this study, a reference profile has been defined as the reconstructed emission vertex profile at high statistics (10^{10} incident protons). This Bragg peak position is used as reference and compared to the ones at lower statistics, deduced as described in the following.

For the LM-MLEM reconstruction, the reconstruction volume is set to $20 \times 40 \times 1$ cm³ around the expected FOP with a $100 \times 200 \times 5$ voxel matrix. To be noticed that the two reconstruction methods produce different results: the line-cone method is based on the beam direction information, so that it naturally returns a mono-dimensional image as result, while the LM-MLEM method is able to reconstruct the prompt-gamma emission distribution in three dimensions. A

mono-dimensional projection along the beam direction is used for the falloff identification and for a direct comparison of the line-cone method. The *SmoothKern* method, with the Nadaraya-Watson regression (Nadaraya 1964; Watson 1964), is used to smooth the reference profiles in order to reduce relative statistical fluctuations.

A Region Of Interest (ROI) ranging from $y = 0$ mm to $y = +100$ mm is defined around the expected Bragg peak position, located at $y = +50$ mm in the phantom. The reference reconstructed profiles are modeled in the ROI by a linear combination of Non-Uniform Rational Basis Splines (NURBS) (D. F. Rogers 2001).

The reference data set is normalized in order to obtain lower statistics profiles, in the range 1×10^8 to 5×10^9 . Statistical fluctuations, randomly extracted following a Poisson law, are added to the obtained PG profiles to mimic realistic reconstructed profiles. This method is used to reduce the analysis time.

For each chosen statistics, 1000 PG profiles are generated and a custom minimization method is applied to deduce the minimal shift between the reference profile and the one at lower statistics. The minimization algorithm shifts the reference profile in a 60 mm range, between -30 mm and $+30$ mm with respect to the initial position, with a step of 0.1 mm, and for each position it compares its position to the low statistics profile by calculating the χ^2 as follows:

$$\chi^2 = \sum_{i=1}^{N_{bin}} (y_{\text{sample},i} - y_{\text{NURBS},i})^2, \quad (4.5)$$

where for every bin i y_{sample} is the number of events in the low statistics profile, y_{NURBS} is the number of events for the reference profile NURBS (scaled at the same low statistic). The described approach is robust and allows to avoid artifacts at low statistics.

The global minimum of all the calculated χ^2 is then retrieved and the shift associated to this value is added to the shift distributions. The standard deviation of the distribution resulting of the thousand results gives the precision of the camera for a given number of incident protons.

4.3 Results

The possible implementation of the CLaRyS Compton camera as a monitoring system for ion beam therapy has been investigated. The detection efficiency of the camera has been estimated with point-like gamma sources, and the relative efficiency in detecting various kinds of coincidence events has been studied. Single Compton interaction events in the scatterer has been selected for the following part of the analysis, and the camera absolute efficiency has been estimated with the point-like source set in different positions with respect to the center of the camera. A PMMA cylindrical phantom has been simulated and exposed to proton and carbon beams at increasing intensities for an analysis of the prompt gamma detection environment (background, random coincidence contamination). The camera precision in the identification of the fall-off of the prompt gamma emission profile has been investigated. For this purpose, the comparison of two different reconstruction methods (line-cone analytical reconstruction and MLEM iterative algorithm) is presented. In the following sections we show the obtained results.

4.3.1 Absolute detection efficiency

Figure 4.6 shows the Compton camera efficiency in detecting the kinds of coincidence events described in section 4.2.3, as a function of the gamma energy in the prompt-gamma energy range (between 300 keV and 6 MeV). The results show how the single events, consisting in the coincidence between an energy deposit in a single scatterer layer and in one single absorber block, decreases at increasing energy, in favor of an increase in the number of electron escape events (consisting in one primary photon Compton interaction in one scatterer layer, at least one interaction of the Compton escape electron in a different scatterer layer, and one primary photon interaction in one single absorber block). At the maximum investigated primary gamma energy, the amount of electron escape collected events is more than 35%. Anyway, the single events represent more than 60% of the total amount of collected events in all the explored energy range, so that the results in the following paragraphs are focused on this kind of events (with the other kinds of events rejected at the analysis stage), as first approach for a feasibility study. The amount of multiple events is limited and negligible over the whole energy range.

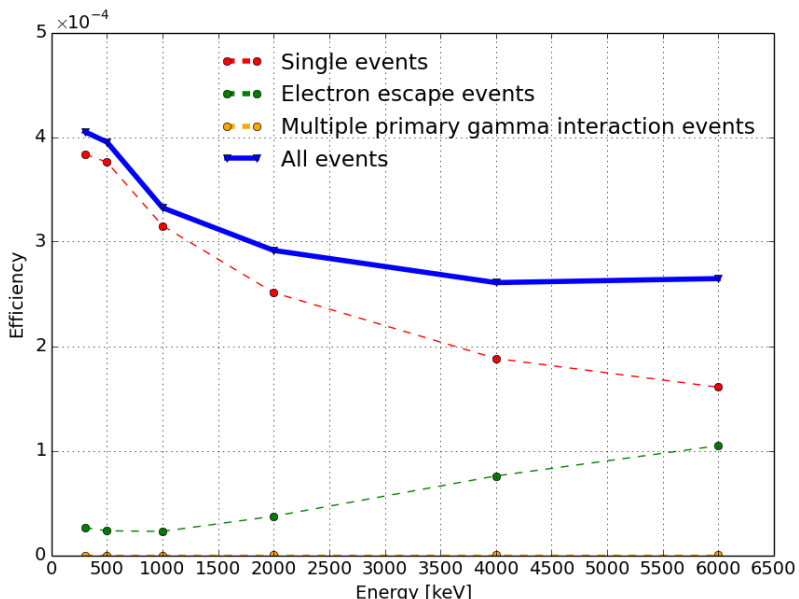


Figure 4.6: Compton camera efficiency as a function of the gamma energy for the different kind of possible events (see section 4.2.3).

Figure 4.7 shows the absolute gamma detection efficiency as a function of the gamma source position with respect to the center of the camera in the transverse plane. On the left side, we show the results achieved with an ideal detector (i.e. without energy detection threshold). On the right side realistic energy thresholds are applied on each detector section.

As expected according to the interaction probability energy dependency, the efficiency is higher for low gamma energies, and it lies in the range 4×10^{-4} at 300 keV and 1.5×10^{-4} at 6 MeV at the center of the camera. Moreover, it can be noticed how the efficiency slightly drops as the point source is shifted away from the camera center: efficiency reductions at 500 keV and 4 MeV are respectively of 25% and 35% with the source at 300 mm distance from the camera center, with respect to the value detected in central position. This effect is more important for high energies, for which the incident gamma is less deflected in the

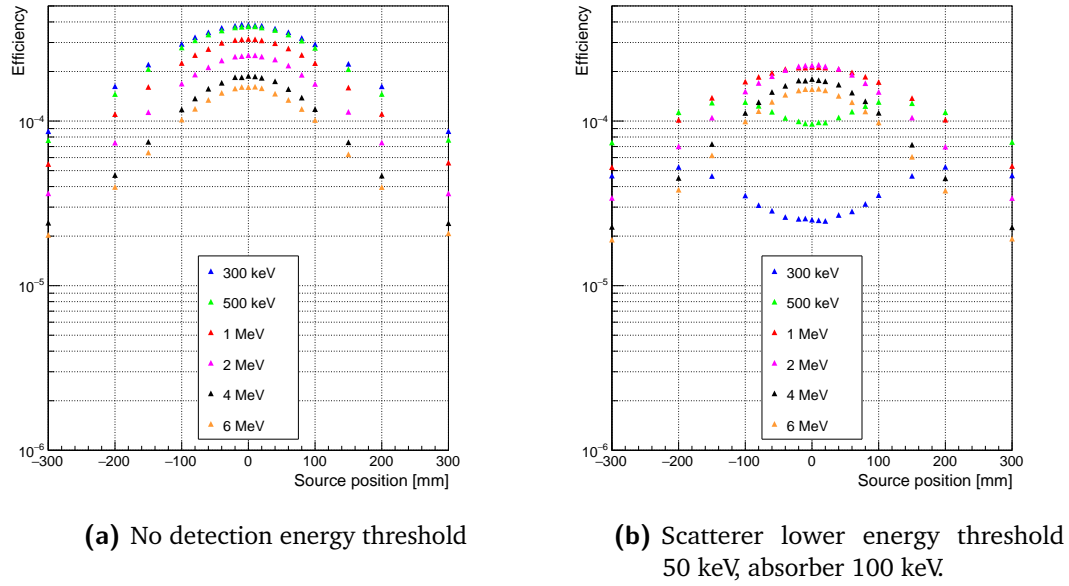


Figure 4.7: Absolute Compton camera efficiency as a function of the gamma source position for different gamma energies, in the range between 300 keV to 6 MeV. The left side shows the camera efficiency with no detection energy threshold. In the right side, detection energy thresholds are applied to reproduce a realistic scenario (lower limit of 50 keV for the scatterer, 100 keV for the absorber). These values can change for the final configuration, according to the detector energy resolutions achieved.

scatterer for the same energy deposited compared to a low energy gamma (see equation ??). Figure 4.7(b) shows the effect of realistic camera detection thresholds as opposed to ideal detection. The gamma detection efficiency drops of a factor ranging from about 1.25 to more than an order of magnitude for the central detection area for energies in the range 300 keV to 2 MeV respectively. The effect is reduced by the distance of the source from the center of the camera. Negligible effects are detected for positions with a distance greater than 200 mm from the center of the camera, and for any distance at energies above 2 MeV, while the efficiency is reduced in the central area of the camera for energies below 4 MeV.

Figure 4.8 shows the rate of events with more than 90% of the primary gamma energy deposited in the detector layers; the source is placed in the center of the camera transverse surface, and no selection are applied on a single detector layer basis. The rate of 90% absorbed events is reported for the different kinds of detected events. As expected, the rate of almost fully absorbed events decreases as the energy increases, in a range between more than 80% and 40% for 300 keV and 6 MeV primary photon energy, respectively. The most of the 90% absorbed events single events, with the electron escape and multiple ones negligible for primary gamma energies above 1 MeV. At lower energy, the Compton recoil electron is often able to exit the scatterer layer were the Compton interaction takes place, but can be lost without further interactions, so that this kind of events is considered as single with an energy absorption below 90%. This can explain the decrease of single almost full absorption at 300 keV. If the electron interacts with a scatterer layer, is more likely to be absorbed at low energy, explaining the increasing electron escape absorbed events below 1 MeV.

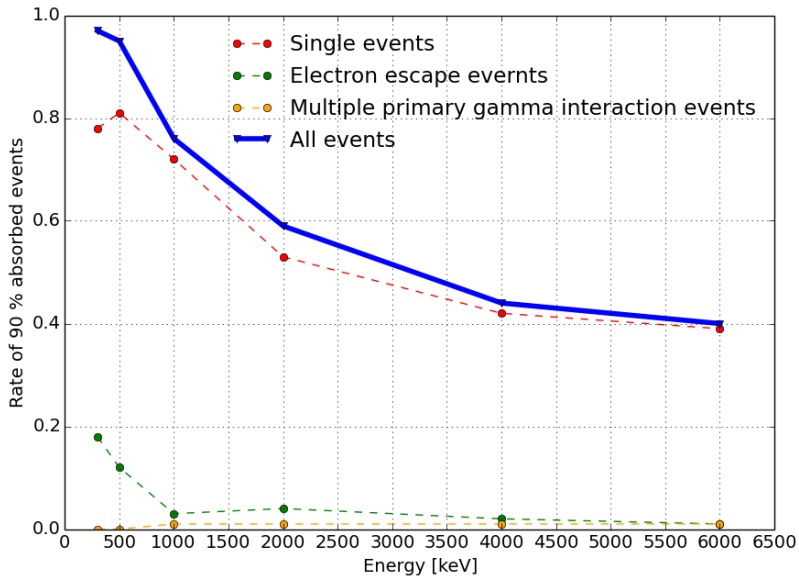


Figure 4.8: Ratio between coincidence events with more than 90% of the primary photon energy absorbed in the detector layer and all detected coincidences for 4 source positions: center of the camera, 40, 100, 300 mm from the center.

4.3.2 Rate of random coincidences

In figure 4.9, the different components of the signal resulting from the PMMA exposure to proton and carbon ion beams are shown as a function of the beam intensity. The true coincidences represent scatterer-absorber time coincidences generated by the same gamma ray (only single events). All the other coincidence types compose the background. The collected data sets are reported with and without the applied time-of-flight discrimination, mainly employed for neutron rejection, as mentioned in section 4.2.4.

In figure 4.9(a) and (b) the amount of true gamma coincidences and background events are reported before and after reconstruction via line-cone algorithm as a function of the beam intensity for proton (a) and carbon ion (b) beams. In addition to this, for each curve realized with the complete collected data set, the related one realized after time-of-flight selection of events is sketched (empty symbols). All the curves have been normalized to the number of incident ions.

The amount of background events (mainly random coincidences) increases with the increasing beam intensity: a factor of about 30 with respect to true gamma events is obtained for proton beams at the intensity of 200 protons per bunch with no event selection, while a factor more than two times higher is reported for carbon ions in the same conditions. The time-of-flight selection can slightly improve the signal -over-noise ratio by reducing the amount of background events. The amount of true gamma events and background events becomes similar at the intensity of about 1 proton per bunch.

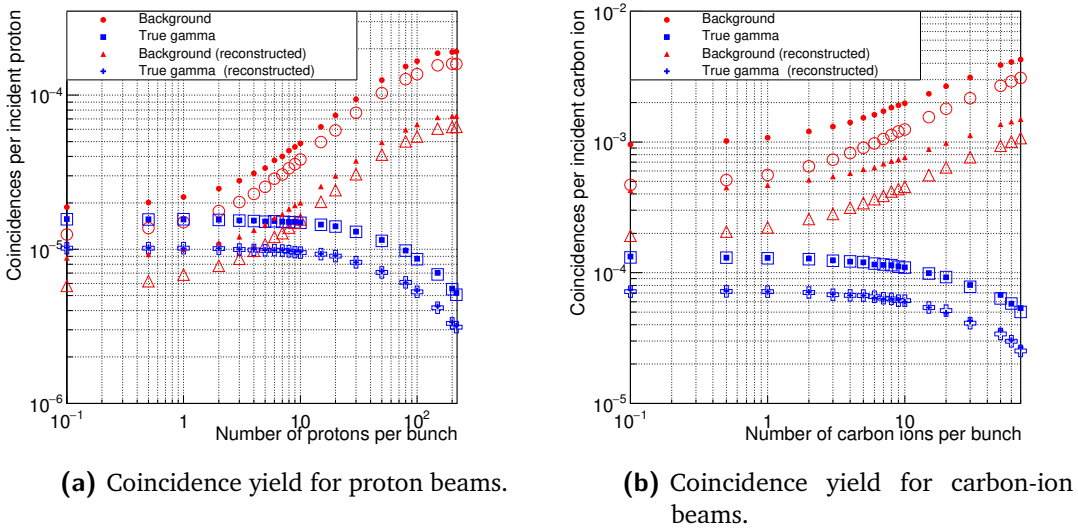


Figure 4.9: Coincidences yield for protons (left) and carbon ions (right) as a function of the beam intensity. The intensity is reported as number of incident particles per bunch. The filled markers correspond to the collected data without time-of-flight discrimination, while this cut is applied to the data reported with empty markers. Moreover, the yields are given before and after the profile reconstruction with the line-cone algorithm.

4.3.3 Camera precision

Given the results presented in the previous section, the camera precision in the fall-off identification is investigated with proton beams at reduced intensities. A single data set has been collected, corresponding to the irradiation of the PMMA phantom with a monoenergetic 160 MeV proton beam, with a reduced intensity of 1 proton per bunch in average. A total of 10^{10} protons has been simulated to define the reference PG profile, and then different low statistics profiles have been produced for the precision estimate as explained in section 4.2.6.3.

The high statistics profile reconstructed via line-cone algorithm is shown in figure 4.10a and via the LM-MLEM reconstruction method in figure 4.10b. A NURBS fit of a low statistics sample (10^8 incident protons) is shown in figures 4.10c for the line cone and 4.10d for the MLEM. The retrieved optimal shift distribution is shown in figure 4.11a and 4.11b for the line-cone and LM-MLEM algorithm respectively, for 10^8 incident protons as well. Figure 4.13 shows the results of the reconstruction of the profile obtained with 10^8 primary protons.

The analysis method described in section 4.2.6.3 is applied to the different PG obtained profiles to retrieve the camera precision in the falloff identification. The results are shown in figure 4.14, where the two reconstruction methods are represented by different markers.

The iterative MLEM reconstruction method enables one to achieve a better precision, with a reduction of about 3 mm of the falloff retrieval accuracy in the whole range of statistics explored. A linear behavior, highlighted by the performed linear fit of the two data sets, is verified with increasing number of primary protons, starting from the single spot scale of about 10^8 primaries, till 5×10^9 protons, which can correspond to the monitoring of a group of spots with the same planned range.

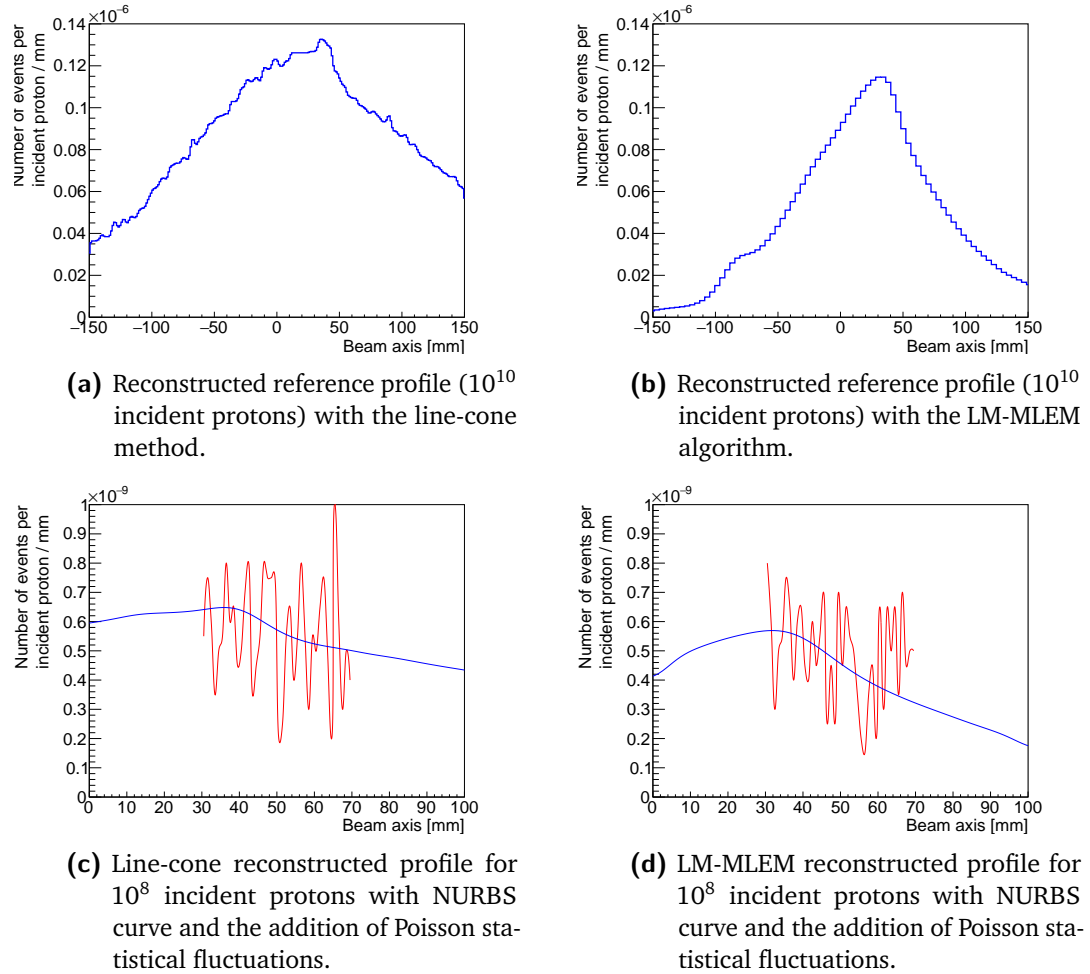


Figure 4.10: Data processing comparison for the same proton simulation with the line cone algorithm (left column) and the LM-MLEM algorithm (right column). The first row gives the reconstructed reference profile for 10^{10} incident protons. The second row shows the NURBS curve (blue) obtained after the normalization to a 10^8 incident protons statistics and the profile realization with the addition of Poisson statistical fluctuations (red).

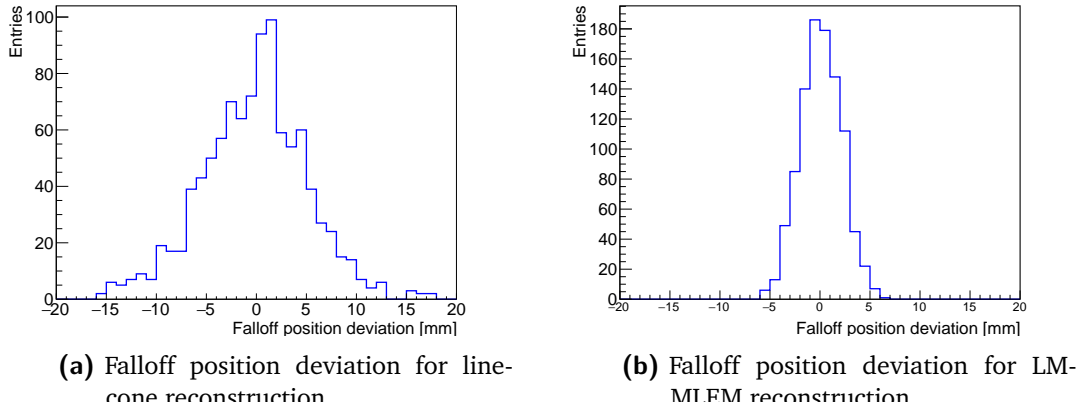


Figure 4.11: Distributions of the falloff position deviation with respect to the falloff position of the high statistics reference profile for 1000 realizations with 10^8 primary protons, obtained with line-cone (a) and MLEM (b) reconstruction. The RMS of these distributions represents the Compton camera precision for the selected statistics.

4.4 Discussion

We studied in this simulation work the performance of the CLaRyS Compton camera prototype and its possible implementation as prompt-gamma detector for ion beam therapy monitoring. The proposed analysis is focused on three main points: absolute gamma detection efficiency, true and random coincidence rate and camera precision in the identification of the prompt-gamma emission profile fall-off.

The absolute gamma detection efficiency has been measured with the detector exposed to gamma sources at six different energies, and the efficiency variation as a function of the source position has been reported. In addition, the composition of the collected events has been studied considering single Compton interactions in the scatterer, Compton recoil electron escape events and multiple primary gamma interaction events. The whole study has been performed with a fixed camera geometry, but different geometrical configurations can change the obtained results. The coincidences composed of one single Compton interaction in one of the scatterer layers and an energy deposit in one single absorber blocks represent the majority of the collected events in whole the explored energy range. for energies above 1 MeV, anyway, the amount of electron escape events become considerable. Such kind of events can be ideally exploited in the reconstruction, and the selection can be based on tracking analysis (if the recoil electron interacts in more than one scatterer layer). In this study, only single events have been selected as first approach for a feasibility study of the Compton camera application in ion range monitoring. In [Fontana et al. 2017b](#) we tested the same prototype with two absorber configurations, showing an absolute efficiency reduction of a factor approximately two when reducing the absorber from a 8×6 block matrix to a 3×3 one. To this efficiency reduction corresponds an increased spatial resolution, probably given by the selection of gamma scattered with small angles. This hypothesis is confirmed by the efficiency variation generated by the applied energy thresholds. Indeed, for low energies, below 2 MeV, the increased efficiency in the central section of the camera active surface - shown in figure 4.7(a) - is linked to the increased relative number of photons approaching the camera with small angles. These photons are more likely undergoing Compton scattering with a reduced energy deposition, which

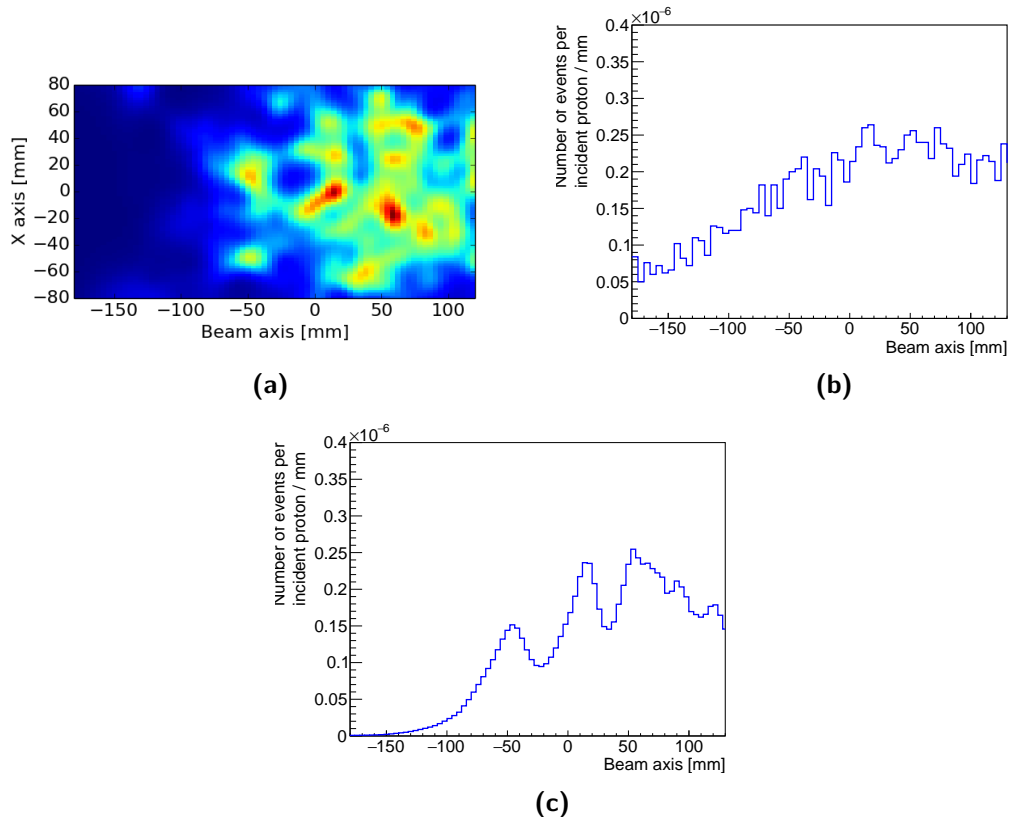


Figure 4.12: Line-cone and LM-MLEM reconstruction for a 160 MeV proton beam, 10^8 total incident protons. The beam intensity is 200 proton per bunch. The Compton camera is centered at the expected Bragg peak position, $y = +50$ mm. The time-of-flight event selection is applied on the collected data set. 20 iterations are performed for the MLEM reconstruction. Figure (a) represents the MLEM reconstructed 2D image in the plane (x, y) , parallel to the camera entrance surface. The position $x = 0$ mm corresponds to the center of the PMMA phantom and the y direction corresponds to the beam axis, with the target entrance at $y = -100$ mm and the target end at $y = +100$ mm. In figure (b) the 1D profile along the y axis is sketched. The profile fall-off is located at $y = +50$ mm. Figure (c) shows the profile obtained by means of the line-cone algorithm for the same time-of-flight selected data.

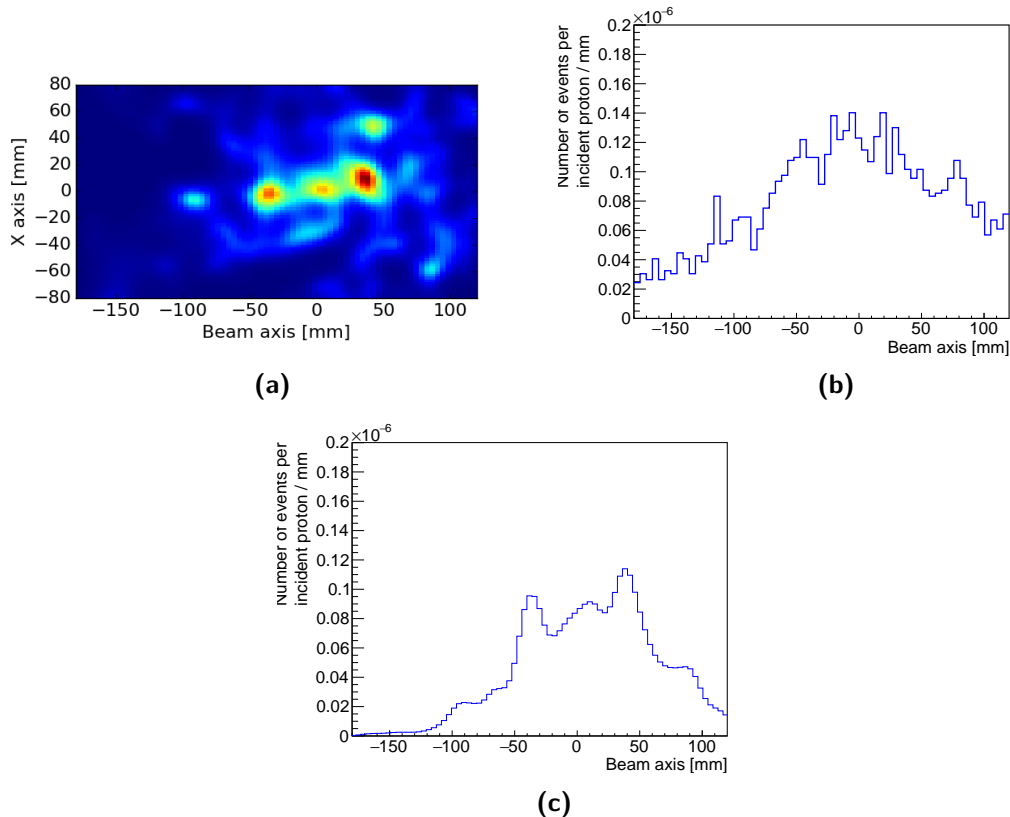


Figure 4.13: Line-cone and LM-MLEM reconstruction for a 160 MeV proton beam, 10^8 total incident protons. The beam intensity is 1 proton per bunch. The Compton camera is centered at the expected Bragg peak position, $y = +50$ mm. The time-of-flight event selection is applied on the collected data set. 20 iterations are performed for the MLEM reconstruction. Figure (a) represents the MLEM reconstructed 2D image in the plane (x, y), parallel to the camera entrance surface. The position $x = 0$ mm corresponds to the center of the PMMA phantom and the y direction corresponds to the beam axis, with the target entrance at $y = -100$ mm and the target end at $y = +100$ mm. In figure (b) the 1D profile along the y axis is sketched. The profile fall-off is located at $y = +50$ mm. Figure (c) shows the profile obtained by means of the line-cone algorithm for the same time-of-flight selected data.

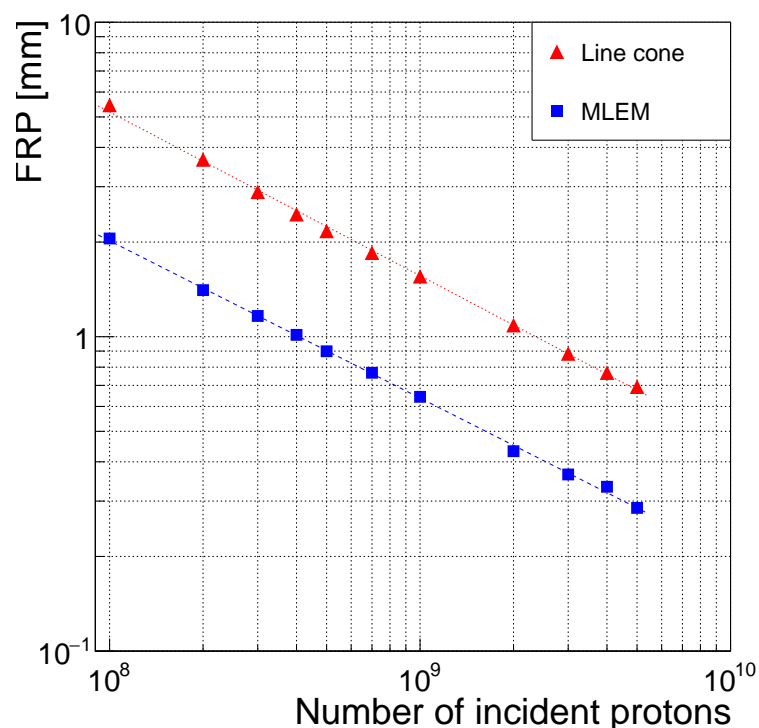


Figure 4.14: Fall-off retrieval precision (FRP) for two different reconstruction algorithms: line-cone and LM-MLEM. The precision is shown as a function of the total number of incident protons, in the range 1×10^8 to 5×10^9 .

is recorded by an ideal detector and rejected by the energy threshold. The effect is all the more important as the primary gamma energy is limited, creating the peculiar energy dependence of the efficiency reduction observed in the results in figure 4.7(b). Therefore, in case the compactness of the detector must be privileged, the efficiency reduction is not dramatic for the Bragg peak monitoring purpose. Moreover, such a compact configuration allows for the implementation of several detector heads, which can be set at different angles and provide additional spatial information, in particular in view of 3D imaging. In case the highest possible efficiency is required, the distance between scatterer and absorber can be modified, knowing that for reduced distances the efficiency is increased because a minimal amount of scattered photons escapes the absorber field of view. On the other hand, a reduction of the inter-detector distance is not recommended for accurate TOF measurements (for fixed target-scatterer distance), given the uncertainty added by the detectors time resolutions. In addition to this, also the spatial resolution is affected by a reduction of the scatterer-absorber distance, given the increased amount of photons scattered with large Compton angles included in the collected events. Indeed, large angle scatterings tend to degrade the spatial resolution. Regarding the dependence of the efficiency on the Compton camera position, an accurate setup with respect to the expected Bragg peak position appears mandatory for the detection optimization.

A further study showed how this effect is mainly due to the cut applied on the scatterer detector. The study of the signal to noise ratio as a function of beam intensity was performed (see figure 4.9). The results show that, at clinical intensities, this ratio is very low. The TOF selection is effective in the case of carbon beams, where a significant proton and neutron contamination is expected. If we consider the case of proton beams, the amount of random and true coincidences is comparable at an intensity of about 1 proton per bunch, so that a clinical intensity reduction should be necessary to fit this configuration. Even if a possible image reconstruction is not excluded by the low signal-over-noise ratio detected at realistic beam intensity, given the fact that the random coincidences are distributed in an homogeneous way in the reconstructed volume, an intensity reduction can be an option in order to obtain more significant data sets. It must be noticed that the need for online check of Bragg peak position is all the more necessary for distal spots, which are in general the first to be treated, so that a beam intensity reduction at the beginning of the treatment can be foreseen in case an accurate monitoring is strictly needed. This would not affect the treatment delivery, nor the planned patient rate in the clinical work-flow; indeed, the spreading of the time duration for few spots is of the order of one second. In the case of carbon ions, the larger amount of secondary neutron produced during the patient treatment seems to require other background rejection methods in order to lead to an advantageous signal-over-background ratio. Note also that online filtering strategies may be used to improve the quality of the date: already in figure 4.9, one can notice that the amount of reconstructed events is about half that of true gamma, which means that partial absorption in the absorber leads to events which cannot be reconstructed via the line-cone method. More refined pre-analysis could be used and have been proposed in Draeger et al. 2017. Note also that the line cone reconstruction used here is quite rough: the two reconstruction points are systematically considered, although further selection may refine the procedure and improve the profile quality (for instance, rejecting points outside the planned treatment volume).

The camera precision has been estimated starting from a reference prompt gamma emission profile obtained at high primary particle statistics (10^{10}), with the random extraction of 1000 data subsets per intensity and applying a robust minimization algorithm to define the shift of the identified profile fall-off with respect to the reference one. The camera precision in the

falloff identification rapidly increases for increasing primary particle statistics. A sufficiently good precision is achieved on a spot basis for proton beams, where the precision is about 2 mm with a MLEM reconstruction: a qualitative monitoring of each spot seems then possible. In order to achieve millimeter precision, some spot grouping methods must be considered. As a general result, the LM-MLEM iterative algorithm, which is now the standard for this kind of image reconstruction, guarantees a better fall-off identification precision over the whole explored intensity range. However, MLEM does not exploit the additional information provided by the knowledge of the beam position in the transverse plane. In future studies, such a priori information should be considered in order to improve the reconstruction rapidity and image quality. At present, given the long calculation time required by the iterative algorithm, the line-cone reconstruction method can still be an option for on-line treatment check, when safety limit can be fixed in order to exclude severe deviation from the treatment planning and an interruption of the dose delivery in real time can be foreseen. Moreover, the Time-Of-Flight (TOF) information can be included in the line-cone reconstruction method in order to constrain the emission on a single point, and improve its accuracy. To be noticed that the presented study is focused on single events: the inclusion of electron escape events can increase the reconstruction accuracy, given the constraint imposed on the reconstructed surface by the electron tracking information. Further study is needed to asses the gain in precision provided by such kind of events.

The Compton detection principle has already proven its potential in detecting prompt gammas for ion beam therapy monitoring purpose, and the CLaRyS Compton camera prototype shows promising results for this application. The detector is now at the final development stage, its components are being tested on beam in clinical facilities and a first beam test with a complete system is foreseen for the next year. New simulation studies are to be carried out to benchmark the Compton camera device to other detection systems, like PET machines or collimated detectors, already used or tested in clinics for ion beam therapy monitoring.

5

Compton camera application in nuclear medicine

Most of the results presented in this chapter have been published in (Fontana et al. 2017a) and (Fontana et al. 2017b).

Contents

5.1	Introduction	172
5.2	Material and methods	173
5.2.1	Radioactive sources	173
5.2.2	Compton camera simulation and data analysis	173
5.2.3	Anger camera simulation and data analysis	178
5.2.4	Figures of merit for the comparison study	184
5.3	Results: Compton camera study for SPECT application	184
5.3.1	Influence of Compton camera scatterer detector energy resolution	184
5.3.2	Compton camera coincidence study	185
5.3.3	Compton camera design study	186
5.4	Results: Benchmark of Compton camera and Anger camera performance	188
5.5	Summary and discussion	191

5.1 Introduction

Single Photon Emission Computed Tomography (SPECT) is one of the most widespread techniques for nuclear medicine diagnostics examinations. In most of the clinical cases, a radio-tracer is injected in the patient and the emitted γ -rays are collected by scintillating detectors coupled to physical collimation systems. This process leads to the reconstruction of a planar transmission image. Such a kind of imaging tool relies on the first idea proposed by Hal Anger ([Anger 1958, 1964](#)), and it is now commercially available in different variants with peculiar features and applications. A complete system is often composed of at least two rotating detection heads, allowing a tomographic data acquisition and the reconstruction of a three-dimensional image of the radio-tracer distribution (see chapter 1 for further details).

The main consequence of the collimation system is a forced trade-off between sensitivity and spatial resolution: The spatial resolution is completely determined by the collimator geometry, and it can only be increased by reducing the collimator hole size, at the expense of a reduction in the detector sensitivity since fewer photons survive the mechanical selection. Moreover, the collimator thickness and septa limit the primary energy acceptance, and the performance of Anger cameras generally downgrades as the energy increases.

In order to overcome this mechanical collimator limitation, it is natural to move towards an “electronic collimation”, where the emitted photons are tracked and the emission point is reconstructed via Compton kinematics, and so to the application of Compton cameras in this field ([Everett et al. 1977; Singh 1983](#)).

L. Han and colleagues ([Han et al. 2008](#)) have performed a simulation work comparing a standard Anger camera and a Compton camera prototype for a fixed source energy of 364 keV (Iodine-131 (^{131}I) gamma ray emission). The expected enhanced detection efficiency associated to the Compton camera with respect to the Anger system was estimated to a factor 20 at the tested energy, while the spatial resolution was compared for equal imaging time.

Starting from the results of Han and colleagues, we tested in simulation the performance of the CLaRyS Compton camera prototype (see chapter 3) for the application in SPECT. The aim of this simulation work consists in extending the aforementioned study to a wide energy range, with simplified analysis methods. The CLaRyS prototype is compared to the Infinia Anger camera delivered by General Electrics Healthcare ([GE Healthcare 2006](#)). The detector performances are compared in terms of efficiency and spatial response with the exposure to mono-energetic point-like radioactive sources at different energies, ranging from 245 keV to 2.614 MeV. The noise components related to the target (patient), such as photon attenuation, photon diffusion, patient movements, are common for both detectors and not considered in this context.

It should be noticed that the Compton detection principle requires coincidences between the two detector sections (scatterer and absorber), so that the random coincidence rate plays a fundamental role in the complete system performance, like in Positron Emission Tomography (PET) machines. The effect of these random coincidences will therefore be investigated. Moreover, a reliable Compton scattering cone reconstruction requires a precise energy resolution for the scatterer section of the detector. The influence of this parameter will be studied. Finally, the Doppler broadening effect will be quantified to give the physical limits of the Compton

imaging technique knowing that silicon corresponds to the lowest Z material available for gamma detection with precise energy resolution. A comparison with a different possible scatterer material is also performed for verification.

All the obtained results are discussed with direct reference to (Han et al. 2008), focusing on the possible advantages offered by the use of a Compton camera (in particular the CLaRyS prototype), which intrinsically introduce the possibility to update the clinical standards in terms of source kinds, energies and activities, examination duration, patient dose, imaging techniques.

5.2 Material and methods

In this section, the sources of gamma rays simulated for the study are presented and discussed and the two simulated systems are described in detail, as well as the proposed analysis techniques. In addition to this, some comments are given about the criteria chosen to represent a relevant comparison between the two investigated detectors.

5.2.1 Radioactive sources

Both simulated systems have been exposed to monochromatic point-like gamma sources in air. The performance of the two cameras has been studied in terms of spatial resolution and detection efficiency as a function of the gamma source energy, related to actual radioemitters, already used in clinical practice or suggested for this kind of application in previous works (Nurdan et al. 2015). The explored energy range was chosen having in mind the possible clinical usage of Compton systems like the one developed by the CLaRyS collaboration, to extend the present field of application of SPECT imaging.

In Table 5.1, the characteristics of the considered radioactive sources are given. Most of the sources do not emit gamma rays at a single energy, but only the ones selected for this study are presented in the table, together with the related branching ratio.

5.2.2 Compton camera simulation and data analysis

5.2.2.1 Simulation settings

The simulation code for the Compton camera was developed with GEometry And Tracking 4 (GEANT4) v.9.6 and the camera design is based on the specifications of the prototype at present under development by the CLaRyS collaboration, detailed in chapter 3. It should be noticed that the real size of the detector components slightly differs from the ones reproduced in simulation, which have been used in the code for simplicity. The geometric setting of the camera has initially been optimized for the application in ion therapy monitoring via prompt-gamma emission (see chapter 4) and has been adapted for SPECT for this study in order to maximize the similarities between the two systems (Compton and Anger camera) in terms

Table 5.1: Radioactive sources used in the comparison study. Decay mode list: EC for electron capture, $\beta-$ for electron emission, $\beta+$ for positron emission, IT for isomeric transition. Half-life expressed in days (d), hours (h) or minutes (m). Data extracted using the National Nuclear Data Center On-Line Data Service from the Evaluated Nuclear Structure Data File database, file revised as of (2017-05-17) (Bhat 1992).

Isotope	Gamma energy [keV]	Branching ratio [%]	Decay mode	Half-life
Indium 111	245	94.1	EC	2.8 d
Iodine 131	364	81.5	$\beta-$	8 d
Yttrium 91m	555	95.0	IT	50 m
Bismuth 212	727	6.7	$\beta-$	60 m
Iodine 132	773	75.6	$\beta-$	2.3 h
Iron 59	1099 - 1292	56.5 - 43.2	$\beta-$	45 d
Zinc 65	1116	50.0	EC / $\beta+$	244 d
Calcium 47	1297	67.0	$\beta-$	4.5 d
Magnesium 28	1342	54.0	$\beta-$	21 h
Sodium 24	1368	100.0	$\beta-$	25 h
Potassium 42	1524	18.1	$\beta-$	12 h
Thallium 208	2614	99.8	$\beta-$	3 m

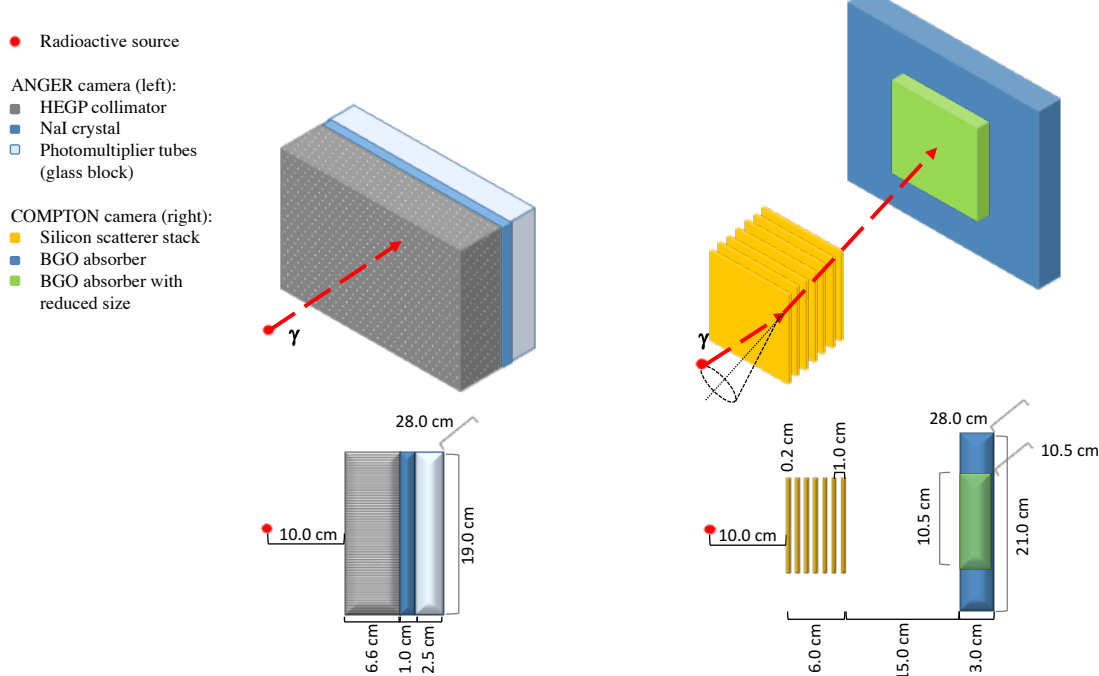


Figure 5.1: Sketch of the simulated geometry of the two systems: Anger camera (left) and Compton camera (right), in 3 dimensions (top line) and side projection (bottom line).

of detector acceptance, as detailed in the following. A SPECT specific optimization would depend on the choice of the particular gamma energy and it has not been studied yet.

The distance between the last silicon plane (center) and the center of the absorber is set to 15 cm (see Figure 5.1). Moreover, the absorber size has been adapted to be as close as possible to the Anger camera detector, maintaining the real Bismuth Germanium Oxide - Bi₁₂GeO₂₀ (BGO) block size. As a result, a matrix of 8×6 blocks has been arranged, for a total surface of 28×21 cm². In the work of Han and colleagues ([Han et al. 2008](#)) a Philips camera was described in GATE as Anger system and the same NaI absorber detector was adapted for the simulation of the Compton system with the introduction of silicon pad detectors as scatterer part. The two geometries compared in this study are slightly different but the common absorber size strategy has been maintained.

The values for energy and spatial resolution of the silicon and BGO detectors used in the simulation were derived from the first tests performed on the detector prototypes (see chapter 3). For the silicon planes, the energy resolution is obtained from the Equivalent Noise Charge (ENC):

$$\sigma_E = W_{Si} \sqrt{ENC^2 + F_{Si} \frac{E_{dep}}{W_{Si}}}, \quad (5.1)$$

where $F_{Si} = 0.115$ is the silicon Fano factor, E_{dep} is the energy released in the detector (in eV) and W_{Si} is the energy required to create an electron-hole pair in silicon (3.6 eV). The ENC strongly affects the detector performance and it will be analyzed in the following.

The spatial resolution was set according to the geometric parameters considering that the employed Double-sided Silicon Strip Detectors (DSSDs) have a total of 64 strips per side, with a pitch of 1.4 mm. The position of each interaction is set in the center of the strip where it is recorded in both detection planes. Charge sharing on neighbor strips can in principle allow for sub-pitch resolution, but according to preliminary characterization measurements the probability of such a kind of events is less than 10%, and will be so neglected. The interaction depth is set as the center of the involved detector slab. The time resolution has been set to 20.0 ns Full Width at Half Maximum (FWHM) based on characterization measurements performed at the Grand Accelerateur National d'Ions Lourds, Caen, France (GANIL) accelerator in France and at the Institut de Physique Nucléaire de Lyon, France (IPNL) (see chapter 3 and [Ley 2015](#)).

The energy and timing resolution in the BGO blocks are set to 21% FWHM and 3.0 ns FWHM respectively, also based on characterization measurements performed with a cesium-137 source (662 keV gamma ray emission) and at the GANIL with prototype blocks. Concerning the spatial resolution, it has been verified that a sub-pixel resolution is not achievable on a single event basis, it is therefore fixed to the size of a single pixel (see chapter 3). Each block surface is streaked with an 8×8 pixel matrix, 4.4 mm side, not reproduced in the simulation code. Each interaction is assigned to the center of the pixel where it is localized at the analysis stage, while the interaction depth is set at the center of the involved block.

5.2.2.2 Data collection and analysis

The radioactive source is placed at 10 cm distance from the first silicon detector, in the center of the scatterer stack transverse surface, and the number of simulated primaries is set to 10^7 gammas per energy step. To speed up the simulation, the primary gammas are emitted in a direction within the acceptance cone defined by the first Compton camera silicon plane. All results are then normalized to the full solid angle.

All the events with at least one interaction in a silicon plane or at least one interaction in a BGO block are stored during the simulation process in two data sets, one per detector section. A small fraction of events presents interactions in more than one scatterer plane (< 1% at 245 keV) and/or in more than one BGO block (~8% at 245 keV). This kind of events leads to ambiguities in the cone reconstruction, because the cone vertex and axis are not univocally defined, and it is not treatable via List Mode-Maximum Likelihood Expectation Maximization (LM-MLEM) reconstruction. Alternative reconstruction algorithms (such as the one included in the Medium-Energy Gamma-ray Astronomy library (MEGAlib) (Zoglauer et al. 2006)) are able to estimate the most likely scenario for multiple interactions, at the expense of larger uncertainties and longer calculation time. The multiple interaction events, representing approximately 8% of the total at 245 keV, are then refused in this study for simplicity. This choice reduces the detection efficiency, so that the value obtained here could be seen as the lower limit for this kind of detection system. Once the two lists of events are built, the time coincidences are defined according to the source activity, the detector geometry and the single detection section time resolution. Finally, the emission points are reconstructed with a LM-MLEM algorithm developed by the Centre de Recherche en Acquisition et Traitement de l'Image pour la Santé, Lyon, France (CREATIS) institute in Lyon (Lojacono et al. 2013). The iterative algorithm reconstructs the Compton cones from the position and energy deposited in the scatterer stack and in the absorber blocks. A reconstruction volume must be defined, as well as a voxel 3 dimensional matrix in this volume. For this study the reconstruction volume has been fixed to $5 \times 5 \times 5 \text{ cm}^3$ around the source, with a matrix of $51 \times 51 \times 51$ voxels, and 15 algorithm iterations: this number is a compromise between reconstruction performance and calculation time.

5.2.2.3 Compton camera study for SPECT application

As already mentioned in the introduction, a critical parameter in the Compton camera performances is the scatterer detector energy resolution. The goal of the instrumental development is to obtain an energy resolution as close to 1 keV (σ_E) as possible. The silicon detectors composing the stack have been tested at various temperatures in order to understand the behavior of the electronic noise and of the leakage current, and the read-out electronics is being developed with the aim to reduce the electronic noise (see chapter 3). The first laboratory tests showed an energy resolution at 25°C of approximately 10-15 keV FWHM with a first read-out card prototype. The new card has been tested with simulated signals and gives a noise level closer to the expectations. No data are yet available to determine the detector energy resolution at different temperatures and with the final card version. In the simulation two different resolutions have been considered in order to verify the influence of this parameter on the final reconstructed image. The two chosen values are $\sigma_E = 2 \text{ keV}$ and $\sigma_E = 4 \text{ keV}$, corresponding to about 5 keV and 9.5 keV FWHM, respectively, both calculated at 200 keV of released energy

using equation 5.1. The influence of Doppler broadening has also been studied by disabling the Doppler effect in the simulation with the energy resolution set to $\sigma_E = 2 \text{ keV}$. Finally, a different possible scatterer material, Cadmium Telluride (CdTe), has been tested at the same resolution in order to verify the expected advantage given by the choice of silicon.

A coincidence study is mandatory to define the source activity to be used in the simulations dedicated to the benchmark with the Anger camera. Timing information is not included in the simulation code and a time structure must be assigned to the simulated primaries at the data analysis stage. A reference time is chosen randomly from an uniform distribution between 0 s and the data acquisition time and assigned to a primary photon. The data acquisition time (T_{DAQ}) is calculated as the expected time needed for the emission of the desired number of primaries ($N_{\text{primaries}}$) according to the source activity A_{source} :

$$T_{\text{DAQ}} = \frac{N_{\text{primaries}}}{A_{\text{source}}}. \quad (5.2)$$

The source activity is not fixed at the simulation stage but only during data analysis afterwards. It can therefore be easily modified to perform a study of the camera performance with different kinds of sources. The scatterer and absorber interaction times are calculated with respect to the reference primary emission and included in the related data sets for the analysis.

Two sets of data are produced as output of this analysis, one for the scatterer and one for the absorber: Each element in the two sets corresponds to an interaction in the detector and includes the 3D interaction position, energy released, time with respect to the total data acquisition time and primary reference index provided by the simulation. The elements in the two data lists are ordered for increasing time. The detectors time resolution specified in section 5.2.2 and a time window set to 20 ns, corresponding to a 3σ acceptance, are then used for the coincidence definition for different source activities. The time of each element in the absorber data set is compared to the time of the elements in the scatterer data set. A coincidence is defined when the scatterer event time is within the time window centered in the absorber event time. Each element is used only once, and the analysis continues until the end of the absorber data list. If the two elements (one from the scatterer data set and one from the absorber one) forming a coincidence have the same reference index, they correspond to interactions of the same primary photons and the coincidence is then a true one. If the reference index is different for the two elements, the coincidence is random. The number of true and random coincidences has been studied as a function of the source activity in a range of clinical interest between 1 MBq and 500 MBq, for a fixed energy value of 555 keV. The variation of the influence of random coincidences as a function of the energy was also investigated at a fixed source activity of 200 MBq.

The scatterer energy resolution and the source activity have been fixed for the benchmark study. The choice of their values is discussed in section 5.3.

Finally, with the same scatterer energy resolution, the design of the Compton camera has been tested for this specific application, in particular for what concerns the number of employed scatterer planes. In addition to the original design configuration with seven DSSDs, additional sets of simulations have been performed at four reference primary gamma energy reducing the number of layers in each set, in order to assess the camera optimal configuration as a func-

tion of the gamma energy. The analysis involved a study of the kind of events detected by the camera, with particular focus on the scatterer section, which can collect both single and multiple interaction (the benchmark study will be then focused on single Compton interactions for simplicity). The efficiency in detecting independent events (with no time structure applied) is estimated and compared in case of inclusion or rejection of multiple interaction events. With the selection of single events, the absolute camera efficiency after reconstruction is then studied for the selected source activity. The results are shown in section 5.3.3 and are expressed according to the figures of merit used for the benchmark study (see section 5.2.4).

5.2.3 Anger camera simulation and data analysis

5.2.3.1 Simulation settings

The Anger camera system is simulated with GEANT4 Application for Tomographic Emission (GATE) v.7.1 and it is based on the General Electrics Healthcare Infinia SPECT system ([GE Healthcare 2006](#)), a commercial clinical camera with parallel hole collimator and Sodium Iodide doped with Thallium (NaI(Tl)) scintillator. A single detection head is simulated in order to obtain a direct performance comparison to the Compton system.

The chosen configuration includes a High Energy General Purpose (HEGP) lead collimator, 6.6 cm thick, with a surface of $28 \times 19 \text{ cm}^2$ (see Figure 5.1). The parallel hole grid is composed of hexagonal shaped holes, 0.2 cm radius, arranged in a quincunx structure, with a septal thickness of 1.8 mm. This collimator is optimized for energies below 364 keV, corresponding to the main gamma emission energy of ^{131}I . The NaI(Tl) crystal is simulated as a single block of $28 \times 19 \times 1 \text{ cm}^3$, in contact with the collimator back surface and read out by photo-multiplier tubes. The photo-multiplier grid is represented with a glass block of 2.5 cm thickness behind the crystal, with the same transverse surface (see Figure 5.1). The spatial and energy resolutions have been set according to the manufacturer specifications. Unless otherwise stated, their values correspond to one standard deviation. A lower detection energy threshold has been set to 80 keV.

The point-like source is placed at 10 cm distance from the collimator surface (the distance chosen in the Infinia data sheet), as for the Compton camera with respect to the first silicon layer, and its transverse position corresponds to the center of the central collimator hole. For each source energy, 10^8 primary photons are simulated in 4π . An event corresponds to single or multiple interaction of a photon (or secondary particle produced by the photon interaction in the collimator) in the NaI(Tl) crystal. All the detected interactions are computed and the gamma interaction position is calculated during the simulation as the center of gravity of the positions of all the hits (energy transfers of secondary electrons), with the deposited energy as weight for the calculation. The deposited energy corresponds to the sum of the energies released during each hit. A set of interaction points and energy deposited is then stored.

5.2.3.2 Data analysis

Four source primary energies have been chosen as references of the studied energy range and are used in the following to show the analysis method and the study results. The low energy range is represented by the Indium-111 (^{111}In) emission at 245 keV, the first energy above the Anger camera construction limit has been set to 555 keV Yttrium-91m (^{91m}Y), while Iron-59 (^{59}Fe) at 1099 keV and Potassium-42 (^{42}K) at 1524 keV have been chosen to represent the medium and high energy range respectively.

Figure 5.2 presents the raw radial event distributions for the four reference energies. Each distribution bin content is normalized according to the surface of the circular region corresponding to each radius. The first distribution bin always corresponds to the radius of the central collimator hole, with the partial inclusion of the surrounding septa. This choice is determined by the detector and collimator geometry and by the source position. It is possible to list three different kinds of events contributing to the radial distributions:

1. photons passing through the collimator holes without interactions,
2. photons traversing the collimator septa without interactions,
3. photons interacting in the collimator septa.

Only the first listed contribution transports true spatial information about the source location, and these photons generate the signal. All other kinds of events contribute to the background, which rapidly increases with the primary photon energy.

A background rejection is performed in order to extract the distribution corresponding to the signal. The complex background contribution cannot be determined analytically, we therefore approximated the background profile as a linear fit to the tail of the radial distribution. The fit limits have been defined as follows:

- the lower limit is calculated as the radial distance where the photon flux on the NaI(Tl) detector is reduced to a fraction $\frac{1}{e}$ by absorption effect in the collimator septa;
- the upper limit has been fixed to the half of the collimator smaller lateral side (95 mm), in order to avoid any kind of geometric effect due the binning choice or the normalization surface selection. The bin size creates artifacts in the radial distribution corresponding to the collimator limits, because three different geometries are involved: the circular surface covered by each distribution bin, the hexagonal shape of the collimator holes and the rectangular collimator geometry.

The estimated background profile is subtracted from the raw distribution and the result is used as reference of the image signal (Figure 5.2).

Three validation tests have been performed in order to check this analysis method.

First, according to the geometry of the collimator and to the mass attenuation coefficient of NaI(Tl) (Hubbell et al. 1987), we evaluated the expected number of entries in the first distribution bin (before normalization), corresponding to the central collimator hole in front

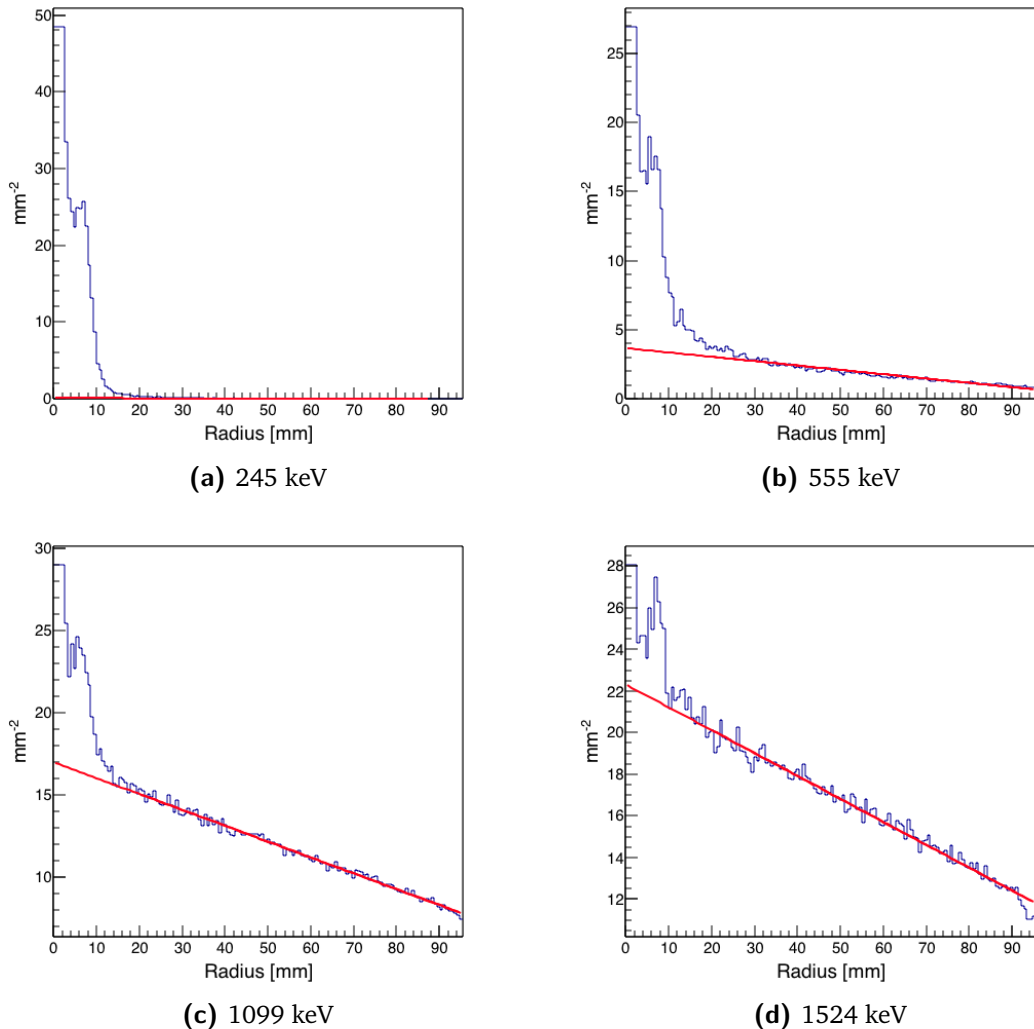


Figure 5.2: Radial event distribution normalized by the circular surface corresponding to each bin for 4 representative source energies, with the linear fit performed for background rejection. The total number of simulated primaries for each data set is 10^8 .

of the source. The calculation is performed with the attenuation law of photons in 1 cm of NaI(Tl). A dedicated set of simulations has been performed equivalent to the ones for the Anger camera described in section 5.2.3.1, but using an ideal detector and a reduced number of photons of 10^7 . No uncertainties are applied on the position of photon interactions to avoid resolution effects and the background is estimated via a linear fit as described above. The obtained entries in the first distribution bin after the fit selection are compared to the ones obtained with the theoretical calculation. In Figure 5.3 the results are shown as a function of the source energy.

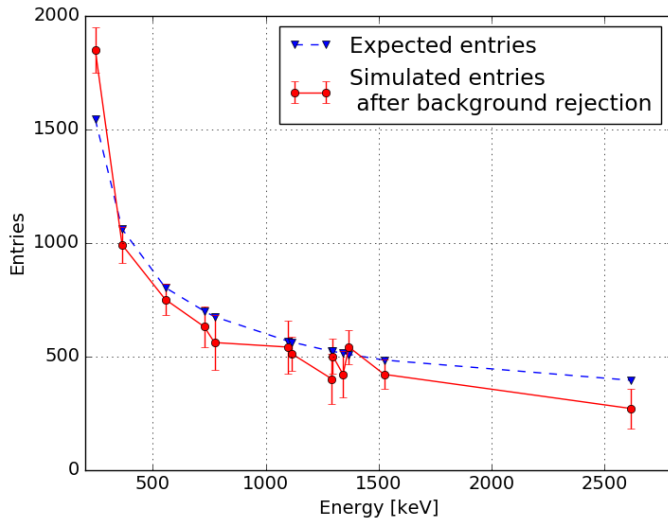


Figure 5.3: Comparison between expected entries in the central collimator hole (blue dashed curve) calculated according to pure geometrical factors and detector interaction cross section and simulated detected entries after background subtraction (red solid curve) with null spatial resolution (ideal detector) to avoid resolution effects and lower energy threshold set to 80 keV.

There is a good agreement between the values calculated with the attenuation law and the simulation data selected with the fit-based background subtraction, and the detected variations from the ideal trend are within the statistical fluctuations. A slight overall effect of under-detection is observed (about 10% on average), while the single value at 245 keV shows an opposite behavior (with a difference of less than 20%). This is related to the chosen fit function.

As a second validation, an additional set of simulations has been performed with the same settings as defined in section 5.2.3.1 but with an infinitely dense collimator. This configuration removes the background contribution given by the photons deflected via Compton interaction on the collimator septa. The raw radial distributions obtained with this set of simulation is compared to the radial distribution “derived” by the simulations with nominal settings after the application of the fit-based background subtraction. The results are shown in Figure 5.4.

It can be noticed that the distribution overall trend is reproduced by the fit-based background subtraction method, the main source of difference being probably the contribution of the scattering in the hole grid surrounding the central one.

The third validation test consisted in a set of simulation with a full lead collimator, with no holes. This configuration allows to estimate the distribution of events traversing the collimator

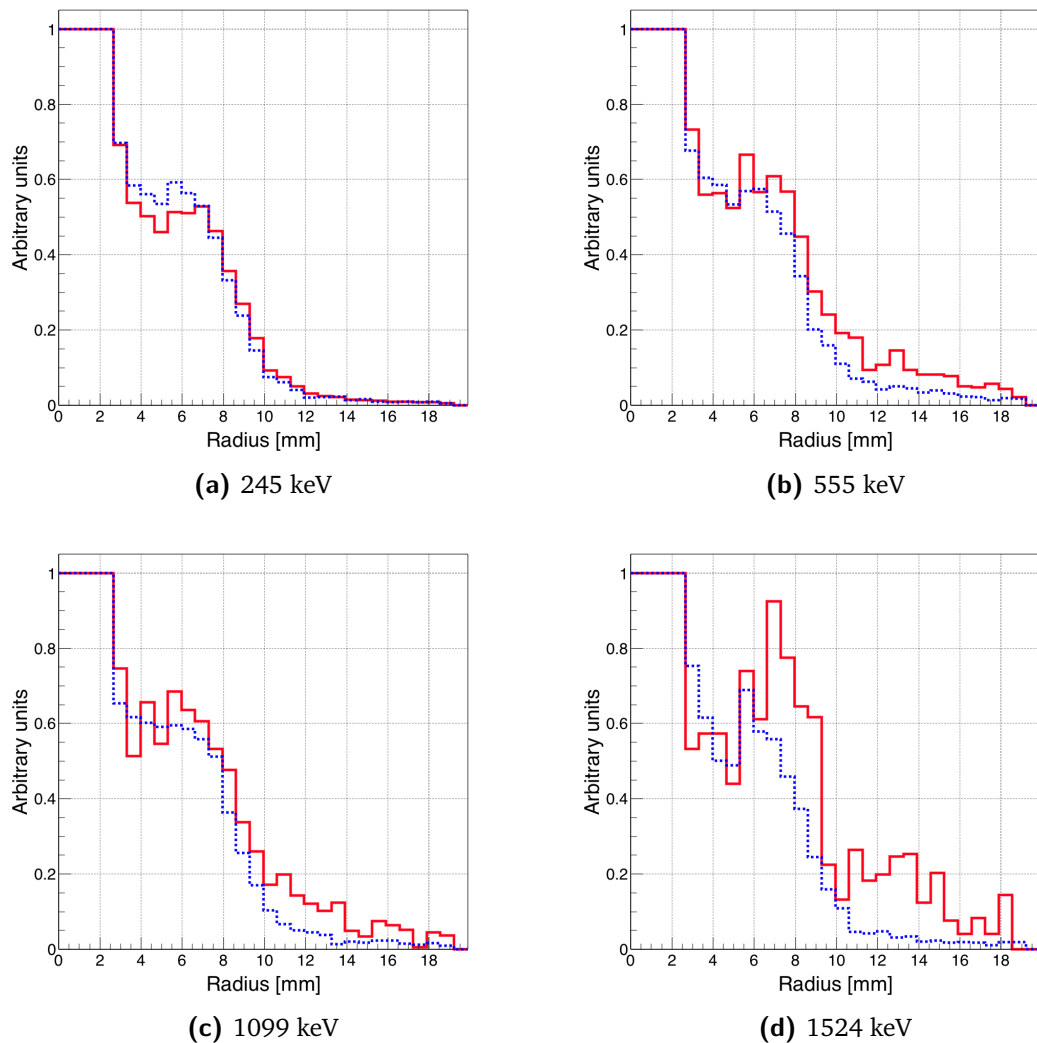


Figure 5.4: Normalized radial distribution with background rejection (red solid lines) compared to normalized radial distribution for infinite density collimator (blue dashed lines).

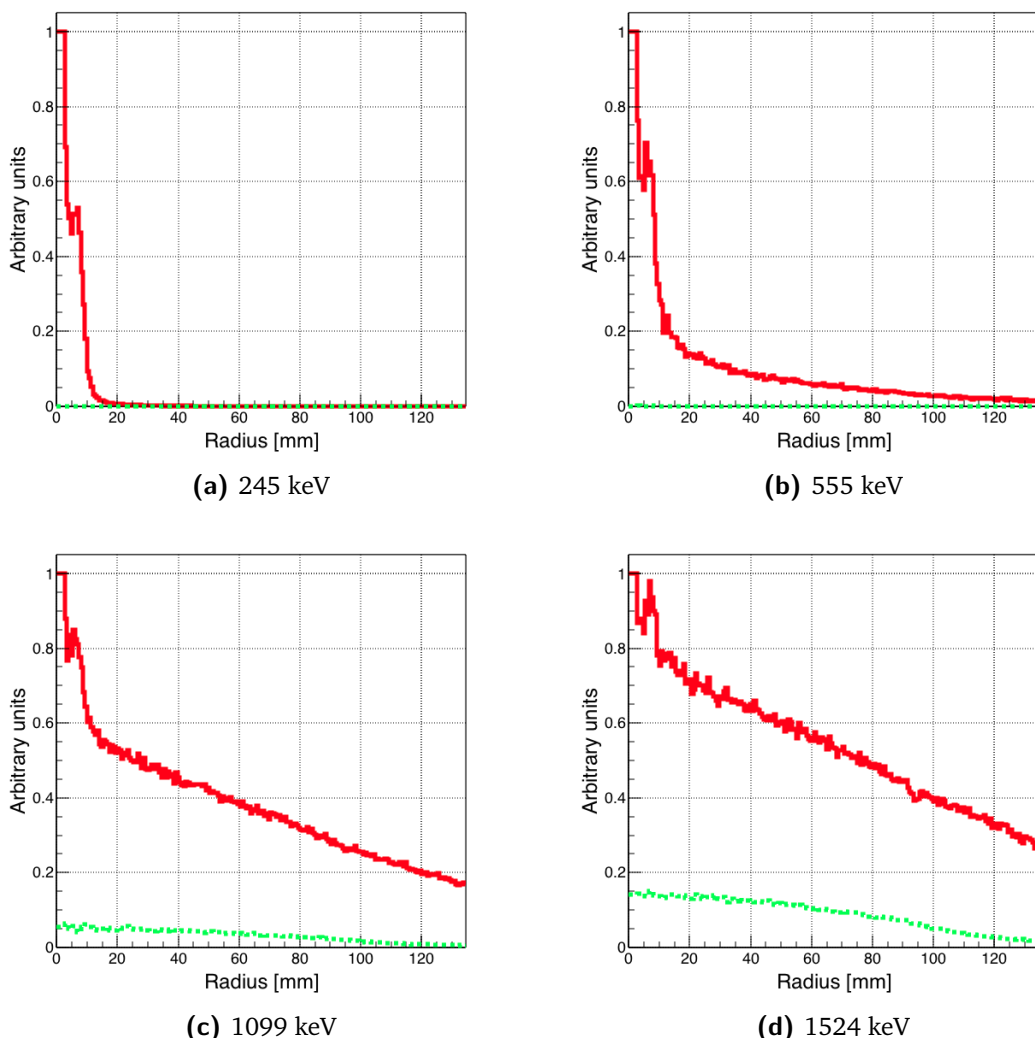


Figure 5.5: Normalized radial distribution with no event selection (red solid lines) compared to normalized radial distribution for full collimator (green dashed lines). Both curves are normalized to the maximum of the raw radial distribution.

with no interaction, with the aim of demonstrating the efficiency of the selection method to remove their contribution to the final image. Figure 5.5 shows the comparison between the raw distributions (no event selection is applied) obtained with the standard configuration and with the full collimator. The amount of photons able to traverse the lead block at low energy (245 and 555 keV) is totally negligible, while at higher energies this kind of events creates an offset which follows the raw event distribution. Anyway, by observing the selection functions obtained by the linear fit in Figure 5.2, the efficiency of the background employed rejection method in removing this contribution results clear.

The linear fit appears to be a robust way to select the signal transporting spatial information from the source and is applied with no modification for the entire energy range, giving to the analysis method the desired consistency.

5.2.4 Figures of merit for the comparison study

The two cameras are studied and compared according to three figures of merit which refer to their main detection parameters: spatial resolution, detection efficiency, and signal-to-background ratio. The definition of these three values must be adapted to the two detectors, keeping in mind their differences: on one side the Anger camera provides a transmission image through a mechanical collimator, with no need for a reconstruction process and with a single detector component; on the other side, the Compton camera relies on event time-coincidences and needs a reconstruction algorithm to obtain the final spatial distribution.

In this study, the imaging process of a point source was simulated. The three figures of merit are therefore evaluated based on the radial event distribution, in order to profit from the radial symmetry of the simulated system.

For the Compton camera, the standard deviation of the radial distribution is used to express the detector spatial resolution, the detection efficiency is defined as the ratio between reconstructed events (via LM-MLEM algorithm) and total simulated primaries, and the signal-to-background ratio corresponds to the ratio between the number of reconstructed events and the total number of coincidences selected before the reconstruction with the coincidence analysis.

For the Anger camera, it is difficult to define the spatial resolution, as shown in (Cecchin et al. 2015). Here, we use the standard deviation of the signal radial distribution in order to be consistent with the Compton camera definition already proposed (the “signal” substantive means entries after background rejection). The detection efficiency is defined as the ratio between the number of signal events and the total number of simulated primaries. Finally, the signal-to-background ratio is evaluated as the ratio between the signal events (the entries in the radial distribution after the fit-based background rejection) and the total number of events recorded by the detector (the entries in the raw radial distribution).

5.3 Results: Compton camera study for SPECT application

The results of the characterization of the CLaRyS Compton camera prototype for the application in SPECT are presented in the following sections, dedicated to the study of the scatterer detector energy resolution and of the Doppler broadening effect, and to the analysis of the rate of random coincidences, respectively.

5.3.1 Influence of Compton camera scatterer detector energy resolution

Figure 5.6 shows the standard deviation of the radial distribution obtained after the LM-MLEM reconstruction (see section 5.2.2.2) as a function of the source energy for the two different analyzed noise levels ($\text{ENC} = 500 \text{ e}^-$, corresponding to $\sigma_E = 2 \text{ keV}$, and $\text{ENC} = 1100 \text{ e}^-$, corresponding to $\sigma_E = 4 \text{ keV}$). The maximum detected difference is about 35%, but the influence of the silicon detectors’ energy resolution rapidly reduces at increasing energy. In the same figure, the results for the simulation without the Doppler broadening for the lowest energy

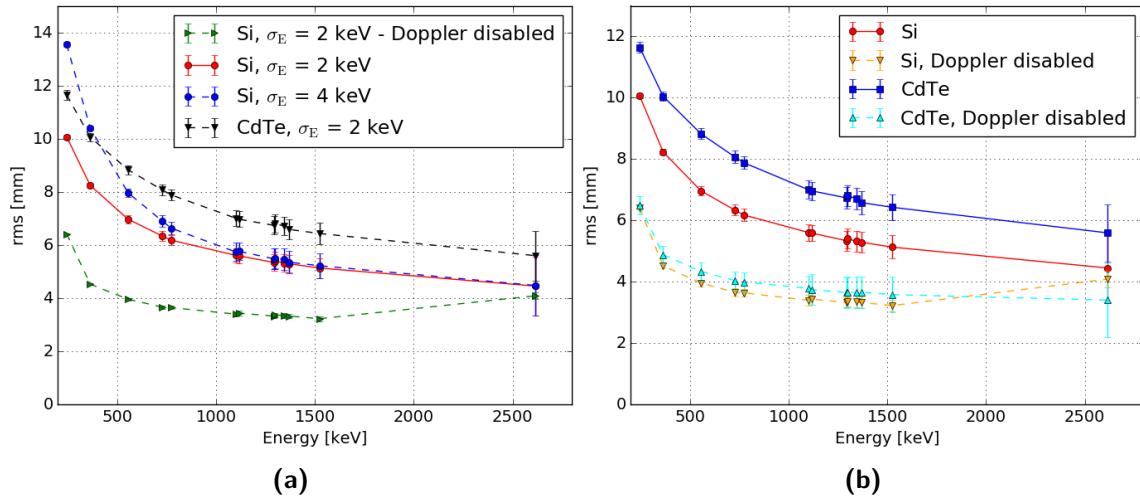


Figure 5.6: Compton camera-reconstructed radial distribution standard deviation as a function of the source energy. Two energy resolution values are set to the silicon detectors ($\sigma_E = 2\text{ keV}$ - red dots solid line - and $\sigma_E = 4\text{ keV}$ - blue dots dashed line), the Doppler broadening effect has been removed (green horizontal triangles dashed line) and the scatterer material has been changed with CdTe solid state detectors (black vertical triangles dashed line), for a fixed energy resolution of $\sigma_E = 2\text{ keV}$.

resolution are shown. It is clear that this parameter has a strong influence for the Compton camera spatial resolution, at least for energies below 2.5 MeV. This result justifies the choice of silicon as scatterer material, because it is the lowest Z available detector and therefore minimizes the Doppler contribution. This is underlined by the black curve corresponding to a CdTe detector, i.e. a higher Z material than silicon (average value of $Z=50$ for CdTe). For this last study, the electronic noise level has been set for CdTe in order to have the same intrinsic resolution as for silicon ($\sigma_E = 2\text{ keV}$ obtained with equation 5.1). Such a resolution for CdTe detectors seems realistic, at least for thin detectors (Alharbi 2018).

For the benchmark with the Anger camera, the ENC value of the Compton camera scatterer components has been fixed to 500 e^- , which corresponds to the expected average level of noise affecting the silicon detectors between -20°C (identified as the ideal working temperature) and 0°C (the silicon detectors are cooled down with a thermal-regulated box, see chapter 3 for a detailed description) and with the final acquisition card (about $2\text{ keV } \sigma_E$). This value has to be experimentally verified.

5.3.2 Compton camera coincidence study

Figure 5.7 (left) shows the numbers of true and random coincidences as a function of the source activity, ranging between 1 and 500 MBq in order to explore the whole range potentially employed in real examinations. The energy is set to 555 keV.

At 200 MBq source activity, the same amount of true and random coincidences is observed at 555 keV gamma energy. With activities above this value, the ratio between true and random coincidences is less than one. In principle the reconstruction LM-MLEM program can partially reject this kind of events and if we consider the expected important increase in detection

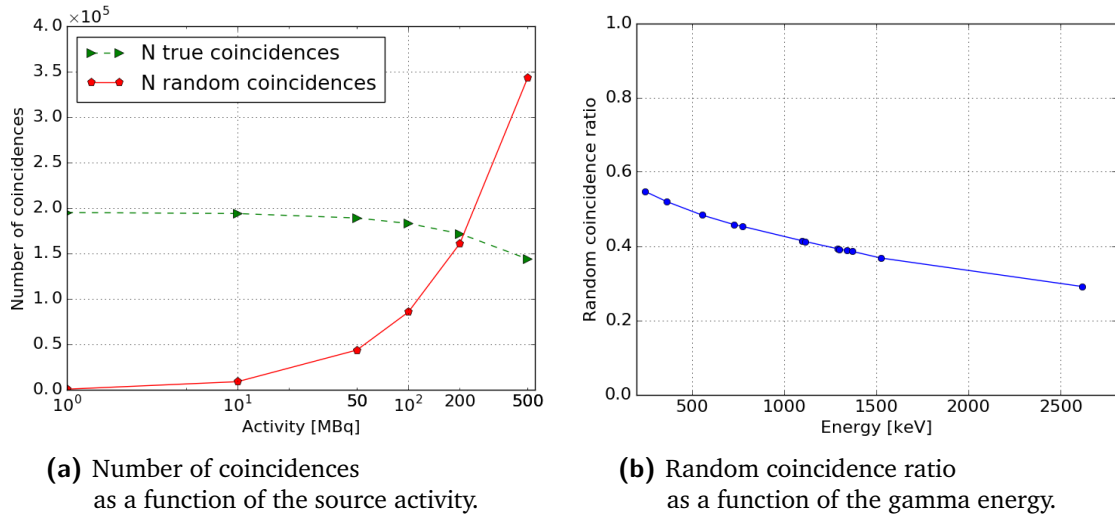


Figure 5.7: (a): number of true (green) and random (red) coincidences as a function of the source activity in the range 1-500 MBq, for the reference energy of 555 keV. (b): Percentage of random coincidences as a function of the source energy, with a fixed source activity of 200 MBq. Compton camera parameters: time resolution FWHM of 20 ns for silicon detectors, 3 ns for BGO and a coincidence window of 40 ns. The source branching ratio has been set to 100% for all sources for simplicity in the comparison of results.

efficiency guaranteed by the “electronic collimation”, it results clearly that it is not worth to employ high activity sources (or that a smaller camera can be considered at the expense of the examination time). Note also that filtering criteria, such as total energy detected or rejection of events that cannot be reconstructed, will certainly help decreasing the fraction of random coincidences. However, the efficiency for the detection of true coincidences clearly decreases with increasing activity, due to the camera occupancy fraction.

For the further analysis and the final detector comparison, the source activity has been then set to 200 MBq, and the number of random coincidences is studied as a function of the source energy. Figure 5.7 (right) shows the ratio of detected random coincidences over the total number of reconstructed coincidences (see Section 5.2.2.2) as a function of energy for a fixed activity of 200 MBq. The ratio decreases for increasing energies, because the product of independent interaction probabilities in two detectors decreases faster than the true coincidence one. Therefore, an increasing reconstruction efficiency with LM-MLEM is verified (see Section 5.4).

5.3.3 Compton camera design study

In order to test the Compton camera design for the application in SPECT, a preliminary investigation has been dedicated to the composition of the events collected by the camera, in particular by the scatterer section. As presented in chapter 4, a primary photon can undergo a single Compton interaction in one scatterer layer and be then, ideally, absorbed in the absorber blocks (single event), or multiple Compton interactions can occur in different scatterer layers before the absorption (multiple event). Finally, the Compton recoil electron can have enough energy to exit the scatterer layer where the Compton interaction took place, and interact in a different layer (electron escape event). The raw efficiency (before reconstruction) of

the Compton camera has been studied with the inclusion or rejection of multiple and electron escape events, as a function of the gamma energy for four reference primary gamma energies and for various scatterer configurations: starting from the original design with seven silicon layers, one layer has been removed for each simulation set, until a minimal scatterer stack composed of only one layer. The results are compared in Figure 5.8a, which shows the camera efficiency with no event selection, and Figure 5.8b, which shows the efficiency with the selection of single events.

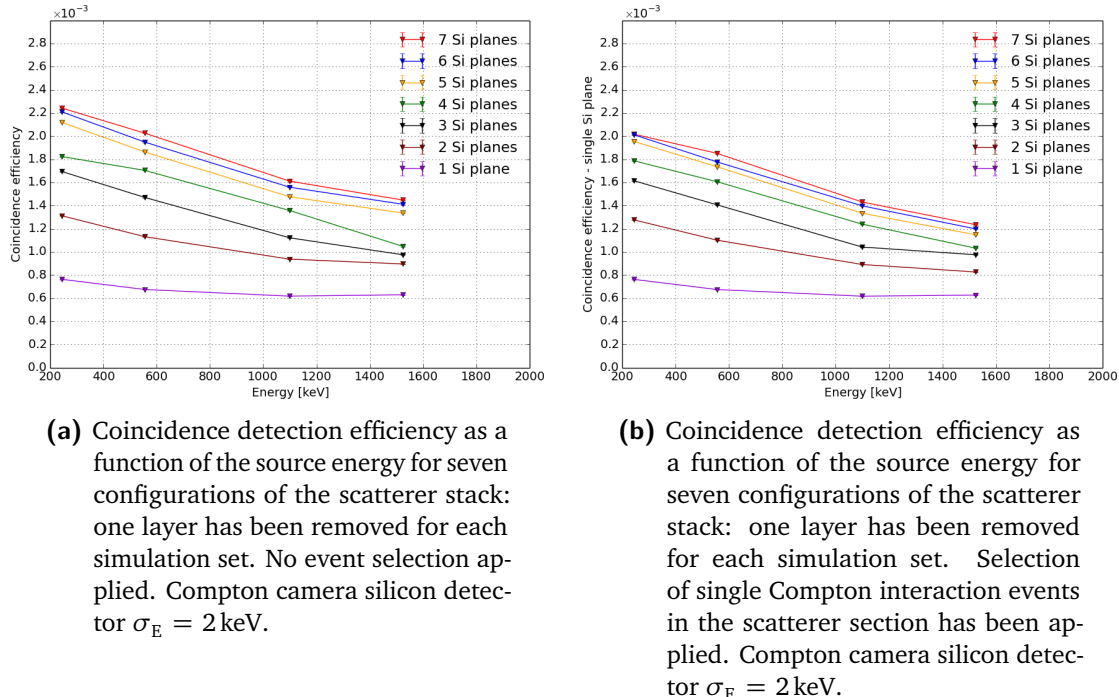
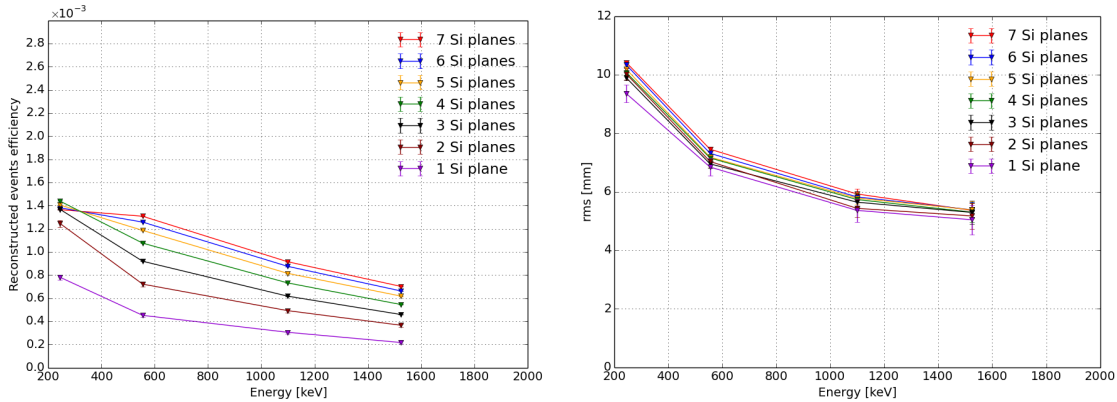


Figure 5.8: Results of the Compton camera event composition study: the absolute Compton camera efficiency (before reconstruction) is shown without any event selection (a) and with the selection of event with single interaction in the scatterer section.

A slight reduction in the overall camera efficiency is verified when selecting single Compton interaction events. The amount of multiple and electron escape events is limited in the explored gamma energy range. This justifies the selection of single events for the benchmark study and the presented Compton camera analysis.

The reconstructed events efficiency for the four reference primary gamma energies is shown in figure 5.9a for the different scatterer configurations. Figure 5.9b shows the results of the same sets of simulations for what concerns the reconstructed event radial distribution Root Mean Square (RMS).

An overall efficiency drop is observed for the scatterer configurations with more than four layers at 245 keV photon energy: this probably reveals an effect of total gamma absorption in the scatterer detector section, in parallel to an increased number of events deflected with large Compton angles which escape the absorber field of view. This effect is not confirmed at increasing gamma energy, already at 555 keV. In this energy range, the expected reduction of the overall efficiency for reduced number of scatterer layers (due to the diminished Compton effect probability) is verified. The radial distribution standard deviation shows minimal variations for the different tested configurations.



(a) Reconstructed efficiency as a function of the source energy for seven configurations of the scatterer stack: one layer has been removed for each simulation set. Selection of single Compton interaction events in the scatterer section has been applied. Source activity = 200 MBq, Compton camera silicon detector $\sigma_E = 2 \text{ keV}$.

(b) Standard deviation of the radial event distributions as a function of the source energy for seven configurations of the scatterer stack: one layer has been removed for each simulation set. Selection of single Compton interaction events in the scatterer section has been applied. Source activity = 200 MBq, Compton camera silicon detector $\sigma_E = 2 \text{ keV}$.

Figure 5.9: Results of the Compton camera design study: reconstructed events efficiency (left) and standard deviation of the radial event distribution (right) as a function of the primary gamma energies for four reference energies and seven scatterer stack configurations, with reduced number of scatterer layers.

At very low gamma energy a scatterer configuration with four silicon scatterer planes appears to be the optimal solution. This is the energy range for which the Compton camera advantages with respect to the commercial Anger cameras are expected to be less remarkable, as explained and verified in the next sessions. At increasing energy, relevant to profit from the Compton camera advantageous features, the original CLaRyS camera design is verified to be the best configuration; this setup has been implemented for the benchmark study.

5.4 Results: Benchmark of Compton camera and Anger camera performance

The analysis methods presented in section 5.2.2.2 and section 5.2.3.2 for the Compton and Anger camera, respectively, have been applied to the simulated data sets of the two cameras at all energies.

The radial distributions for Anger and Compton camera at the different reference source energies and a source activity of 200 MBq are shown in Figure 5.10. The same reference energies selected in section 5.2.3.2 are included here. The radial range is limited to the smaller collimator lateral size (95 mm), according to the fit limits imposed on the Anger camera data (see Section 5.2.3.2). The curves are normalized to 1 for an easier visual comparison.

In Figures 5.11, 5.12, and 5.13, the detection efficiency, the radial distribution standard devi-

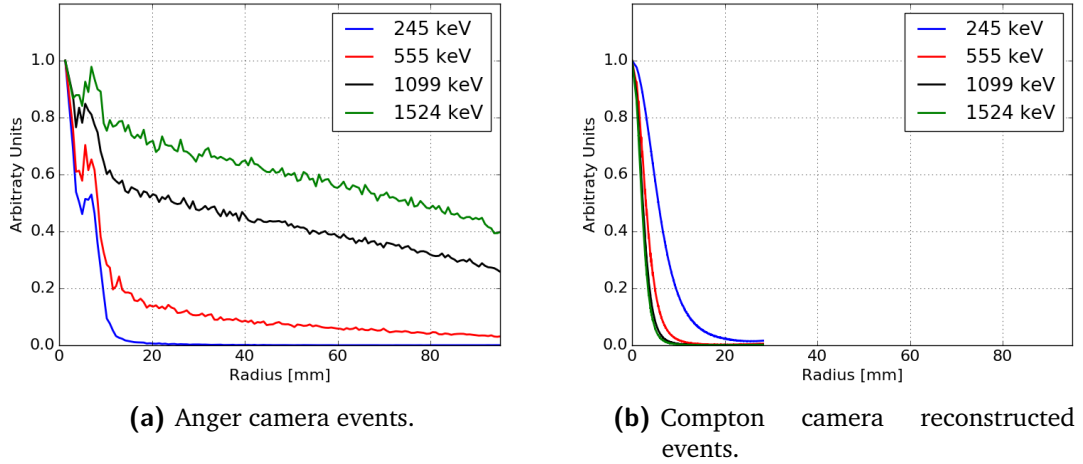


Figure 5.10: Overlap of the normalized radial distributions for 4 selected source energies.

ation and the signal-over-noise ratio are respectively shown as a function of the source energy for the two sets of data. Uncertainties (one standard deviation) are reported for all the values and included in the data points when not visible.

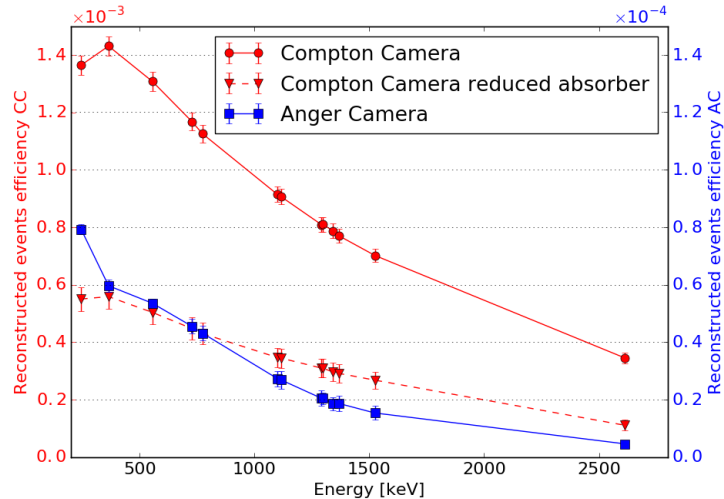


Figure 5.11: Detection efficiency as a function of the source energy. Source activity = 200 MBq, Compton camera silicon detector σ_E = 2 keV. Note the factor 10 scale difference for the vertical axes.

From Figure 5.11 one can point out the advantage provided by the absence of a physical collimation system in terms of detector efficiency. It should be noticed that two different scales are applied to Figure 5.11 in order to show the two plots on the same figure and appreciate the variations with respect to the energy. The detection efficiency of the Compton camera is always more than a factor 20 higher than the one of the Anger camera. Although the images of the Anger and Compton cameras are based on different kinds of spatial information (a line and a cone, respectively), the Compton camera efficiency should allow a substantial reduction of the injected source activity and/or of the acquisition time. The efficiency of both cameras constantly decreases with increasing energy, because of the decreasing photon interaction

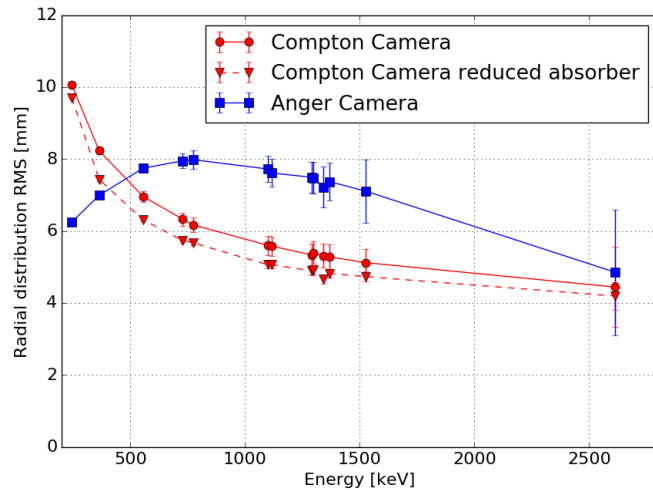


Figure 5.12: Standard deviation of the radial event distributions as a function of the source energy. Source activity = 200 MBq, Compton camera silicon detector $\sigma_E = 2\text{ keV}$.

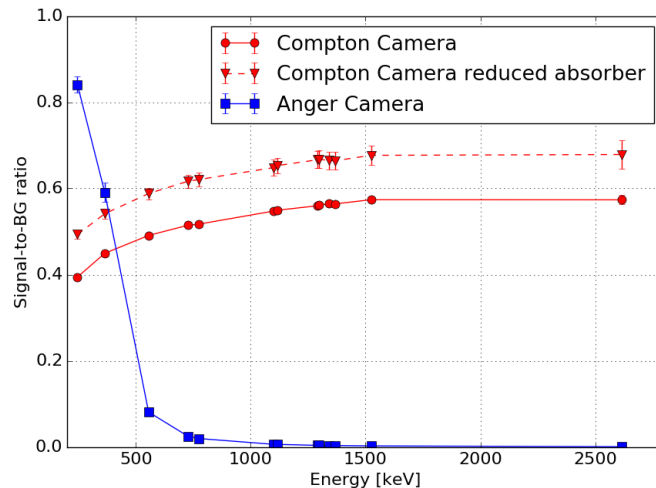


Figure 5.13: Signal-to-background ratio as a function of the source energy. Source activity = 200 MBq, Compton camera silicon detector $\sigma_E = 2\text{ keV}$.

probability. The only exception is found at the lowest considered energy of 245 keV in the Compton camera, due to an increased probability of photon absorption in the scatterer and, additionally, a larger fraction of events with wide Compton scattering angles at low gamma energy.

The standard deviation of the radial distribution, shown in Figure 5.12, confirms the optimization of the chosen collimator for the Anger camera for low energies (below 364 keV). With the ad-hoc background subtraction operated here, which is not realistic for an extended source, the Anger camera outperforms the Compton one in terms of spatial resolution at low energies (by > 3 mm at 245 keV and about 1.3 mm at 364 keV). However, above 500 keV, the Compton camera can provide a better spatial resolution with a difference ranging between a fraction of millimeter up to about 2 mm. For energies above 1.5 MeV, the two curves of standard deviation for the two cameras reach similar values (< 0.5 mm difference at 2614 keV), but Figure 5.13

shows how the background rejection for the Anger camera and the MLEM reconstruction for the Compton system (see Sections 5.2.3.2 and 5.2.2.2) affect this result. Above 364 keV, the selection for the background rejection of the Anger camera data drastically reduces the number of events contributing to the final image (the ratio between selected and detected events approaches zero). With an extreme selection, at very high energy the only events contributing to the final image are the events traversing the central hole of the collimator, resulting in an enhanced spatial resolution (see Figure 5.4d). The signal-to-background ratio of the Compton camera confirms the expectations concerning the reconstruction algorithm performance: if compared to Figure 5.7 (right), the curve in Figure 5.13 shows how the rejected events correspond approximately to the amount of random coincidences.

5.5 Summary and discussion

The Compton camera under development by the CLaRyS collaboration is now at the characterization stage. Originally designed and optimized for the application in ion beam therapy monitoring for the detection of prompt-gamma rays in a wide energy range (between some hundreds of keV until about 10 MeV), it is here studied as SPECT detector in comparison to a commercial system based on the Anger gamma camera design.

The expected significant enhancement in terms of detection efficiency, for comparable imaging performance in terms of spatial accuracy, has been already proven in simulation in (Han et al. 2008) with a silicon-sodium iodide based Compton camera prototype at a single primary energy of 364 keV. A factor 20 efficiency gain has been reported.

First of all, the present simulation study aimed to extend these results by testing the two detectors at increasing primary gamma energies, ranging from 245 keV to 2614 keV. A common analysis method has been defined in order to obtain comparable results, always keeping as reference the final image. The results were directly compared in terms of detection efficiency, spatial resolution (standard deviation of the radial event distribution) and event selection (background rejection for the Anger camera and LM-MLEM algorithm selection for the Compton camera) via the definition of three figures of merit.

A preliminary study has been performed on the simulated Compton camera data in order to fix the main parameters of the camera simulations, namely the energy resolution of the silicon scatterer detectors and the source activity determining the coincidence rate. Two ENC values have been studied, resulting in a maximum difference in spatial resolution of 35% at the lowest energies, rapidly decreasing at increasing primary energy. A value of $\text{ENC} = 500 \text{ e}^-$ has been chosen as the closest to the instrumental development expectations and first tests. The influence of the Doppler broadening on the spatial resolution has been also estimated in a factor $\sim 1/3$ at 500 keV, then reduced up to ~ 0 at 2.5 MeV of primary gamma energy, with fixed energy resolution ($\sigma_E = 2 \text{ keV}$ - $\text{ENC} = 500 \text{ e}^-$) in the silicon detectors. Moving to the coincidence rate analysis, at the reference energy of 555 keV and with detector time resolution set according to first characterization results, the simulated data have been analyzed by reproducing a source activity in the range 1-500 MBq. The result shows the expected increase in the random coincidence rate at increasing source activity, with a ratio between true and random coincidences close to one at 200 MBq. This value has been chosen as clinical reference for the comparison analysis. In addition to this, the geometrical configuration of the scatterer

stack has been studied in order to check alternative setups with reduced number of DSSDs; this study confirmed the choice of seven planes, as well as the choice of selecting events with one single interaction in the scatterer section, implemented for the benchmark analysis.

The results discussed in section 5.4 confirm the conclusion of Han et al. about the advantage given by the usage of a Compton system and show how the gain factor in the detector efficiency is maintained at increasing energy. Concerning the detector spatial resolution, the Compton camera outperforms the Anger system at energies above about 500 keV. The Anger camera spatial resolution can be boosted by aggressive background subtraction in the considered case (point-like source image), at the expense of a drastic signal suppression. However, this approach is not reproducible and exploitable in actual clinical conditions and the obtained results are not comparable to the Compton camera performance at the same energy.

The results of this work clearly show the potential of the Compton camera for the application in nuclear medicine examination, opening new possibilities for the clinical implementation. The studied detector has originally been designed and optimized for another application, and it has only been adapted for SPECT here, but not yet optimized in terms of detector geometry (size, position, and inter-detector distances). For an optimized detector, performance is therefore expected to be improved with respect to the presented results. In future development, the reconstruction LM-MLEM algorithm should be adapted to this application and the reconstruction parameters should be studied to further enhance the final performance, in particular for what concerns random coincidence rejection.

Anyway, these first evidences already allow one to investigate the possible modifications introduced by the clinical set of Compton detection systems. The enhanced detection efficiency in parallel with comparable spatial performances paves the way to the diffused usage of less active sources, or alternatively allows a substantial reduction of examination time: as a result, the dose delivered to the patient would be reduced. On the other side, the possible introduction of sources with higher primary emission energy will reduce the effect of photon attenuation in the patient (not studied in this simulation work), improving by definition the spatial information and further reducing the effective dose delivered to the patient. Simple analytic calculations can show how a photon attenuation of about 66% is foreseen for 364 keV photons in 10 cm of water, while the effect is reduced, for example, to 49 % at photon energy of 1099 keV (Hubbell et al. 1987). Higher energies can be employed also with Anger cameras, at the expense of introducing thicker collimators with reduced holes size, with the result of a reduced efficiency with respect to the analyzed HEGP collimator. Furthermore, a possible implementation of Compton cameras is also foreseen for targeted radionuclide therapy, where the radionuclides used in clinics often have gamma radiation emission at relatively high energy. This signal is difficult to be detected and treated with conventional SPECT cameras, while the Compton detection technique could make it quantitatively exploitable in clinical practice, for both pre- and per- treatment images.

Even though Compton cameras intrinsically lead to 3 dimensional images with a single detector head, the spatial resolution associated to the direction normal to the detector planes has to be more deeply studied, but this feature is an additional point in favor of the introduction of Compton systems in the clinical environment, moving beyond the tomographic concept and towards more compact detector solutions. Several studies are ongoing in order to improve the image reconstruction algorithms and, so, the 3 dimensional imaging performance (Kuchment et al. 2016). Different detection approaches can also, in principle, lead to improved image

quality in 3 dimensions, such as the Compton electron tracking (Kabuki et al. 2007; Sonoda et al. 2015). Moreover, a further enhancement in image reconstruction should be given by the measurement of the photon depth of interaction: the photon is assumed to interact in the center of the detector components for our prototype, while perpendicularly segmented detectors can ensure an improved resolution in the third dimension and a resulting enhanced reconstruction accuracy, also involving better 3 dimensional imaging capabilities.

The advantages of the Compton detection principle are here shown thanks to a first detector prototype, but there is still wide room for improvement.

Once the CLaRyS Compton camera will be completed and characterized, tests in clinical environment are foreseen in the field of medical imaging. The actual potential of such a kind of detector will be then quantified with experimental data.

6

Beam tests

Contents

6.1	Hodoscope: december 2017	196
6.2	Hodoscope: may 2018	196
6.3	Collimated camera: september 2018	196

As described in chapter 3, the components of the CLaRyS gamma cameras are at the final characterization phase, and the efforts of the collaboration are presently mainly focused on the optimization of the acquisition chain, including the electronics boards, the Micro Advanced Telecommunications Computing Architecture (μ -TCA) acquisition system and the associated acquisition, monitoring and slow control software. These tasks foresee several measurements campaigns, and three of them have been performed between the end of 2017 and the date of writing (September 2018), and are presented in this chapter. All the presented beam tests have been carried out at the Centre Antoine Lacassagne, Nice, France (CAL) in Nice with a 65 MeV proton beam. The Nice hadrontherapy platform was the first site in France starting to treat patients in June 1991 with the MEDICYC cyclotron proton beams. The cyclotron was designed to support regular neutron and proton therapy programs, as well as for the production of ^{18}F for Positron Emission Tomography (PET) applications (Mandrillon et al. 1992, 1989). The accelerator is a fixed frequency 25 MHz isochronous cyclotron with a peak voltage of 50kV. Negative hydrogen ions are produced by an external source, axially injected and accelerated to 65 MeV. The extraction is performed by a $60 \times 10^{-6} \text{ g/cm}^2$ carbon stripping foil and the exiting protons are transported down the beam line to the treatment room (Herault et al. 2005), or to the research nozzle used for the presented beam tests. The layout of the MEDICYC facility is shown in Figure 6.1.

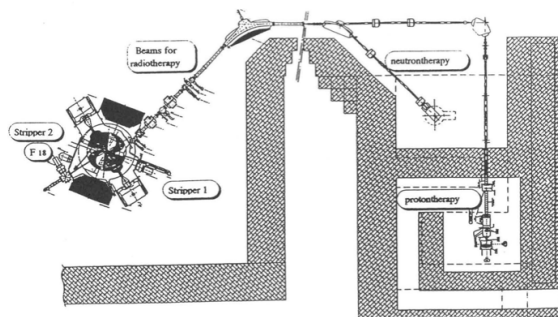


Figure 6.1: Layout of the Nice MEDICYC facility. In Mandrillon et al. 1992.

6.1 Hodoscope: december 2017

6.2 Hodoscope: may 2018

6.3 Collimated camera: september 2018

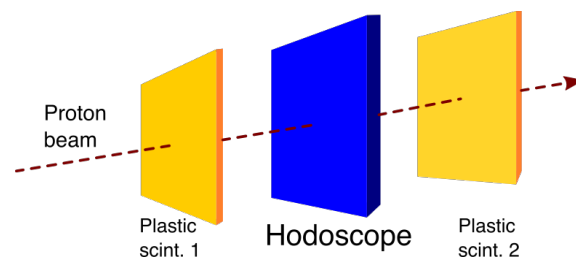


Figure 6.2

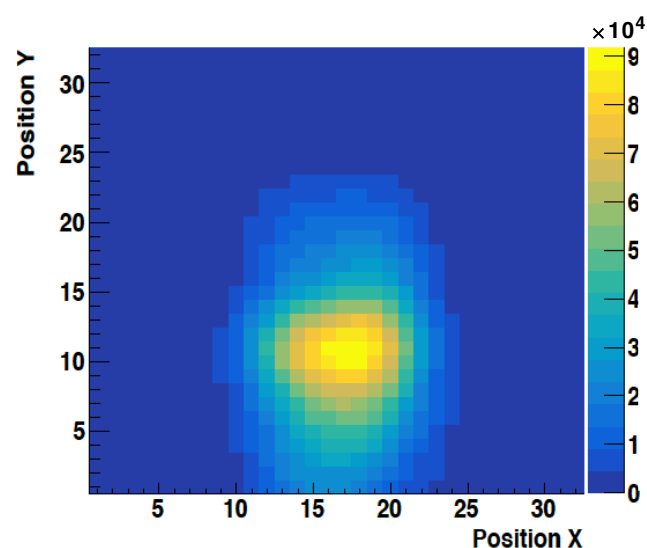


Figure 6.3

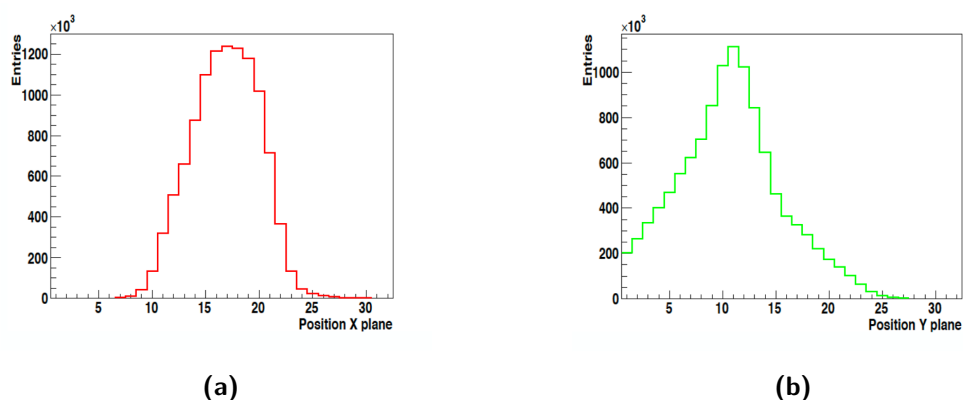


Figure 6.4

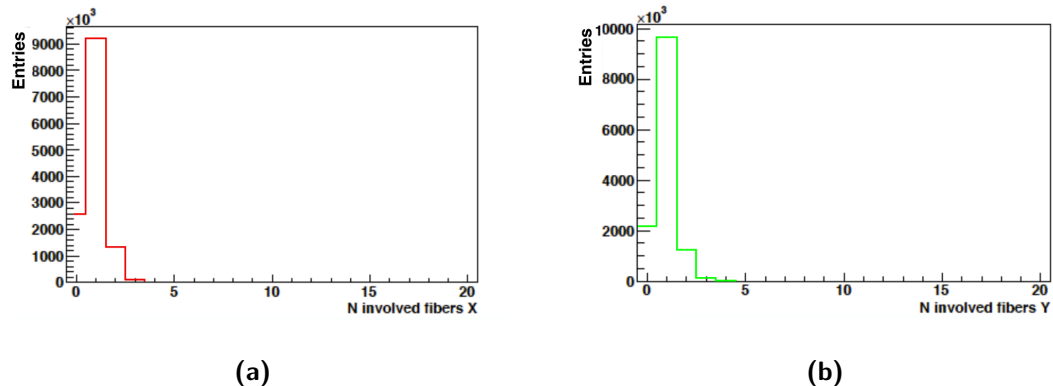


Figure 6.5

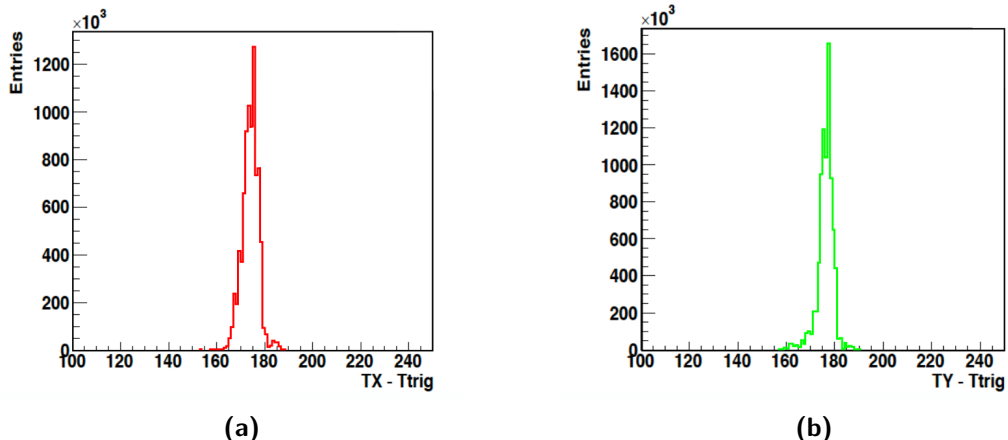


Figure 6.6

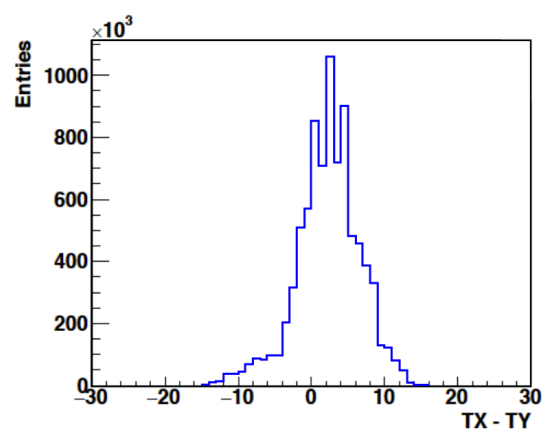


Figure 6.7

7

Conclusions and discussion

Appendices

A

Compton camera data format

A.1 Introduction

This document aims to formalize and fix the Compton camera data format. The structure of the data sent by each detector section (scatterer, absorber and beam hodoscope) to the acquisition card is detailed, as well as the structure of the events sent to the acquisition PC.

A.2 General features

A.2.1 Common information

The detector Front-End (FE) cards are connected to the Micro Advanced Telecommunications Computing Architecture (μ -TCA) via optical links, with a speed of 3.0 Gbit/s. The transfer frequency is 150 MHz.

All the FE card Time-to-Digital Converters (TDCs) share the same synchronized clock, at a 40 MHz frequency, which is sent to the cards through an external link.

Every data packet sent to the μ -TCA by the Front End cards starts with the following information:

- N° Front End (8 bits);
- N° Trigger (24 bits);
- N° Mode (8 bits);
- N° of element in the packet (8 bits).

A.2.1.1 Front End number

The FE number is the identification code of each FE card. A mechanical switch on the card defines the ID which is sent in the data packet header.

In Table A.1 the FE number IDs are listed with the corresponding cards.

Table A.1: Front End number associated to each Front End card.

FE number	FE card
0	All detectors
1	Silicon 1
2	Silicon 2
3	Silicon 3
4	Silicon 4
5	Silicon 5
6	Silicon 6
7	Silicon 7
8	Silicon 8
9	Silicon 9
10	Silicon 10
11	ASM 1
12	ASM 2
13	ASM 3
14	ASM 4
15	ASM 5
16	ASM 6
17	ASM 7
18	ASM 8
19	ASM 9
20	ASM 10
21	ASM 11
22	ASM 12
23	ASM 13
24	ASM 14
25	ASM 15
26	ASM 16
27	Hodoscope 1
28	Hodoscope 2
29	Hodoscope 3
30	Hodoscope 4
31	Hodoscope 5
32	Hodoscope 6
33	Hodoscope 7
34	Hodoscope 8
99	μ -TCA

A.2.1.2 Pre-trigger and trigger

The trigger number identifies each event, where an event is generated every time a coincidence is detected between a Bismuth Germanium Oxide - $\text{Bi}_{12}\text{GeO}_{20}$ (BGO) block and a silicon layer. Once an interaction is detected in a BGO block, the associated Analog Sampling Module (ASM) card generates a pre-trigger signal which is sent to the Trigger et HORlogé (THOR) card. This intermediate card shares the pre-trigger signal with the silicon FE cards; if an interaction with a compatible time stamp is found in one of the silicon layer, a trigger signal is generated and sent to all the silicon FE card, as well as to the ASM and hodoscope cards via the THOR card. The trigger signal validates the event, and each FE card sends the collected data to the μ -TCA system. The trigger number allows for a complete event reconstruction by the event builder on the acquisition PC. In Figure ?? the trigger generation process is sketched.

To be noticed that each FE cards sends the collected data independently from the others.

Trigger and pre-trigger encoding

Pre-trigger and trigger signals are used by all the detectors to select the collected data to be sent to the acquisition system. The data selection and transfer must be as fast as possible in order to minimize the trigger latency and camera dead time. In order to reduce the transmission time, pre-trigger and trigger signals have been encoded on 24 bits.

This same trigger number is sent at the beginning of each data packet and is used by the event builder to associate the interactions collected by the three detector sections. With a 24-bit encoding, the trigger number is reset every $1 \text{ ns} \times 2^{24} = 16,78 \text{ ms}$. This time window is short for the event builder, so that for the physical data it is extended to 32 bits for all the FE cards in order to have a reset every $1 \text{ ns} \times 2^{32} = 4,2 \text{ s}$, which is enough for the reconstruction of the events.

A.2.1.3 Mode number

The Compton camera detector components can work in different mode, according to the application requirements. At least two working modes are possible for every detector section: an “optimal” mode, corresponding to the final camera configuration; a “test” mode, allowing for the collection of more raw information. Every operating mode presents a peculiar data format, so that the data packets size is not fixed. In order to fix the acquisition tuning, the mode number is defined before its beginning.

The operating mode are identified as following:

- N° Mode = 1 : 1st mode for silicon
- N° Mode = 2 : 2nd mode for silicon
- N° Mode = 3 : 3rd mode for silicon

A Compton camera data format

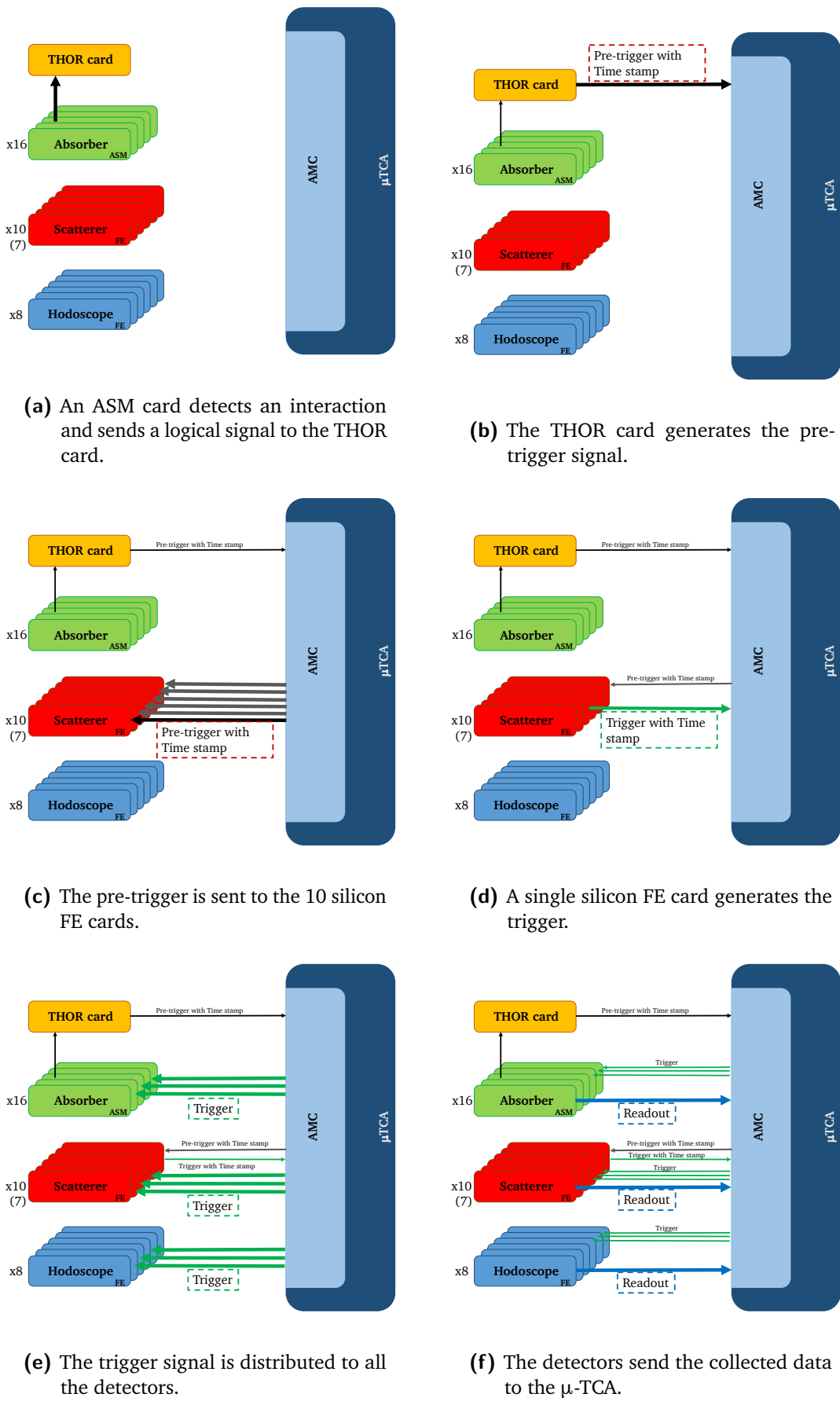


Figure A.1: Data acquisition logic: pre-trigger and trigger generation and readout process.

- N° Mode = 4 : 4th mode for silicon
- N° Mode = 5 : 1st mode for BGO
- N° Mode = 6 : 2nd mode for BGO
- N° Mode = 7 : 1st mode for hodoscope
- N° Mode = 8 : 2nd mode for hodoscope.

A.3 Physical data format

A.3.1 Scatterer detector data format

Four different data formats, corresponding to four working modes, have been defined for the silicon scatterer operation (Figure A.2). For mode 1 and 2, the collected total charge is directly evaluated on the FE card via the slow shaper output and one Application-Specific Integrated Circuit (ASIC), while for mode 3 and 4 the ASIC pre-amplifier output directly sends a sampling of the raw signal. In this last case, the number of samples can be tuned and each sample corresponds to 10 ns. The complete sampling is stored in a dedicated buffer.

Modes 1 and 3

In mode 1 and 3, for each detector strip involved in the interaction, the strip ID, total collected charge and time are stored. The interaction position will be calculated via a center of gravity algorithm at the analysis stage. The raw information about the number of involved strips is useful for the evaluation of the signal dispersion in the detector.

Modes 2 and 4

In mode 2 and 4, the interaction is calculated on the FE card and the number of involved strip is then not stored.

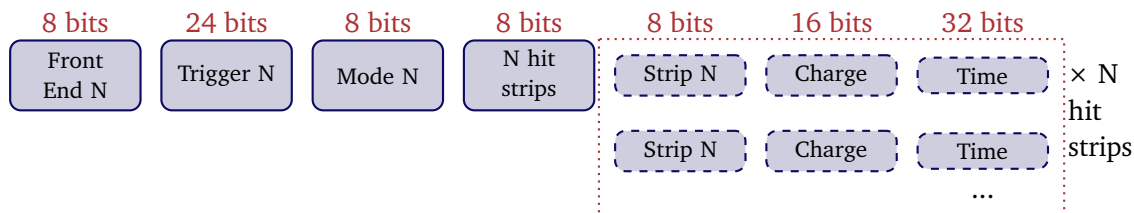
A.3.2 Absorber detector data format

The BGO block readout is performed via the ASM cards. Each card is equipped with 24 input ports (signal Photo-Multiplier (PM)), corresponding to 6 BGO blocks. Two possible working modes have been defined for the BGO absorber: the collected total charge and time are evaluated on the card, or the PM raw signals are sampled and the sampling is sent to the acquisition (Figure A.3). Charge and time are then calculated at the analysis stage. This second operating mode can be useful in the test phase but it determines a low acquisition rate, so that it can be used only at low beam intensity.

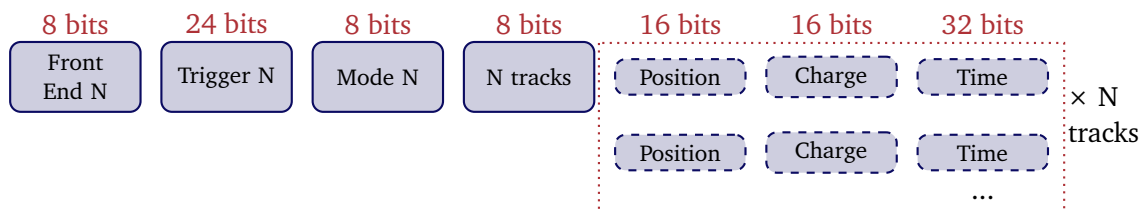
The complete sampling is stored in a dedicated buffer.

A Compton camera data format

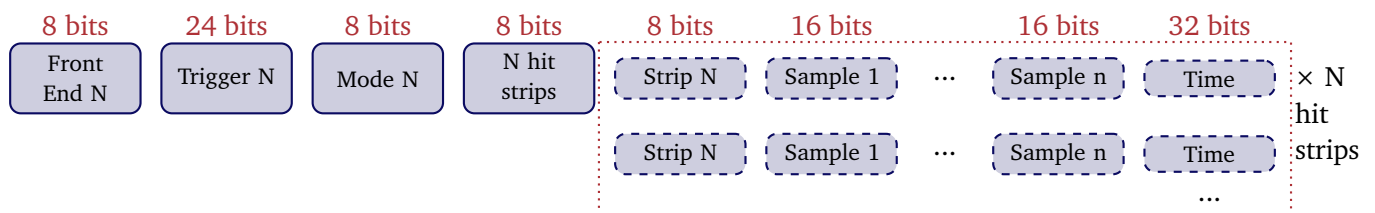
Mode 1



Mode 2



Mode 3



Mode 4

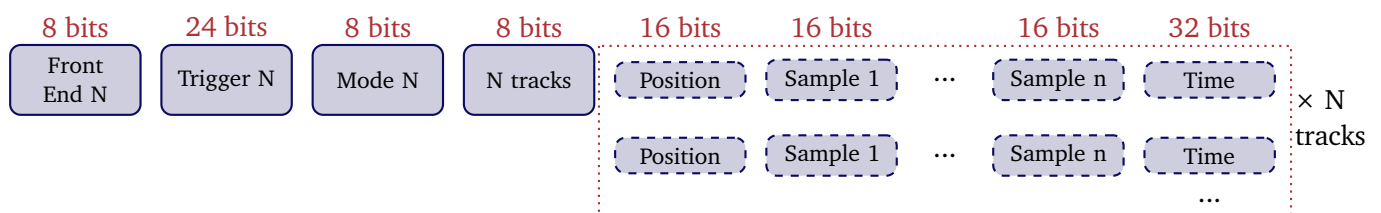
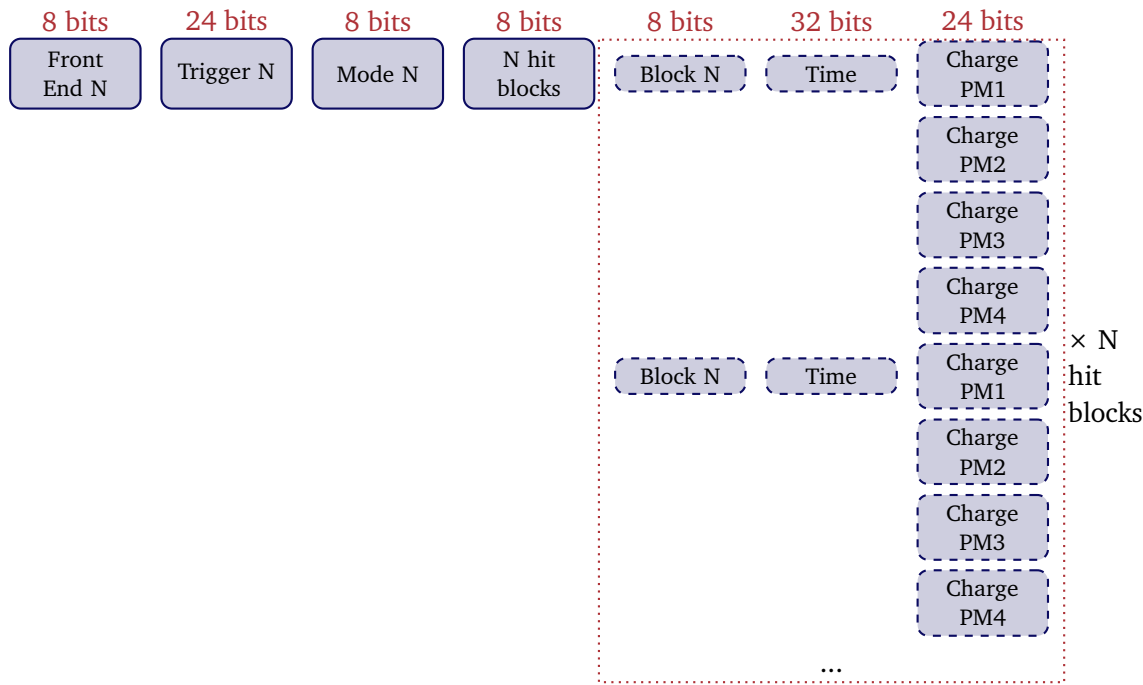
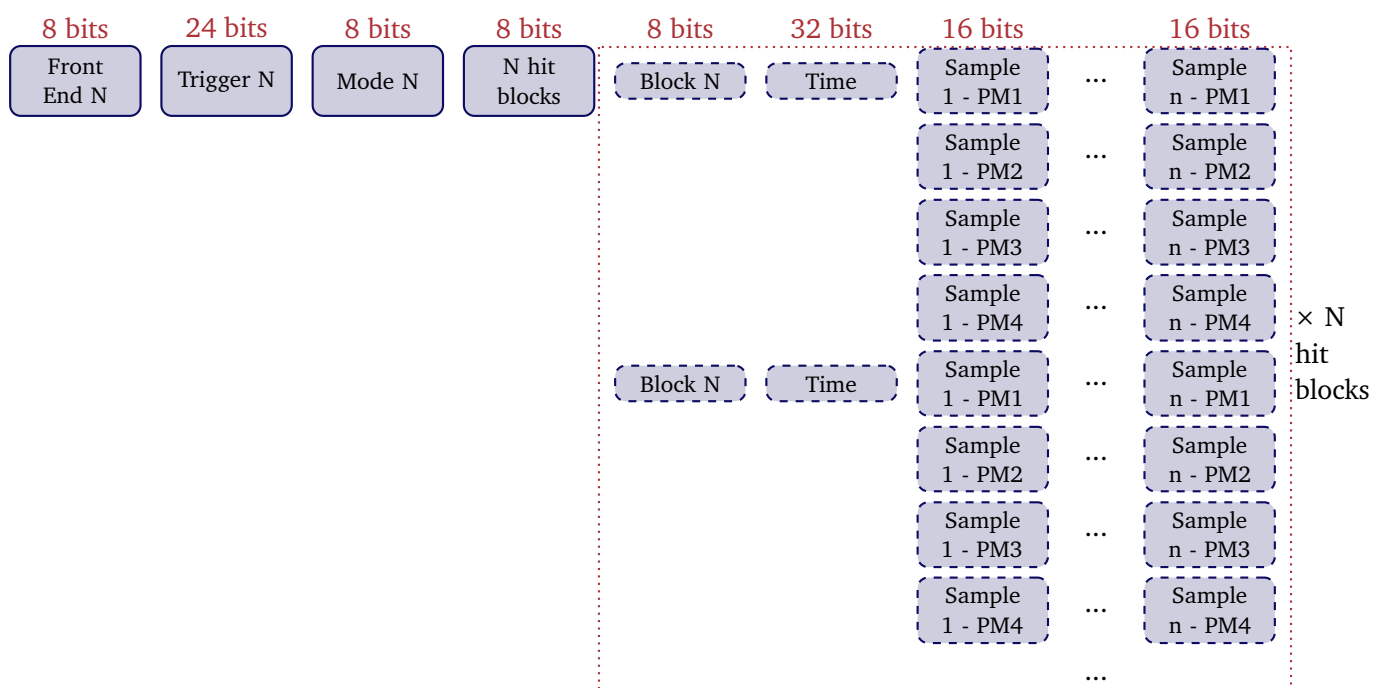


Figure A.2: Scatterer detector data format.

Mode 1

Mode 2

Figure A.3: Absorber detector data format.

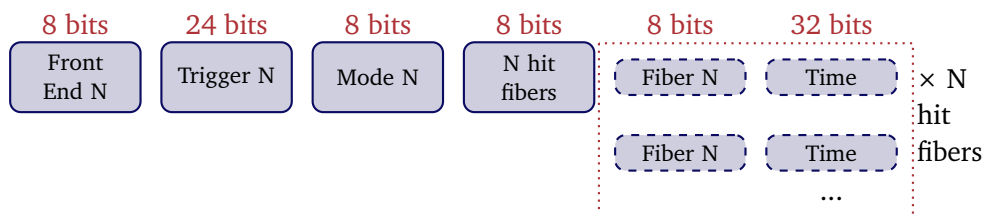
A.3.3 Beam hodoscope data format

The beam tagging hodoscope is composed of two perpendicular planes of 128 scintillating fibers each. Each fiber is read-out on the two sides, for a total of 512 read-out channels. The output signals are send via optical fibers to 8 64-channel PMs H8500 by Hamamatsu. 8 FE cards have been developed for the signal collection, one per PM, and are equipped with two custom ASICs (32 channels each) and one Field Programmable Gate Array (FPGA).

Concerning the “optimal” mode (1st operating mode for the hodoscope), the only collected information are the ID of the involved fibers and the interaction time. The ASICs allow for a minimum time resolution of 10 ns; this means that if two particles interacts in the hodoscope within a 10 ns window, they will be considered as part of a single event.

In test mode, the total collected charge can be calculated. This feature is useful to evaluate the detector aging effect due to radiation exposure. The charge measurement is anyway limited to a single channel per ASIC, so to two channels per PM. The ASIC channel able to measure the charge is identified as “N° Fiber charge 1” and “N° Fiber charge 2”.

Mode 1



Mode 2

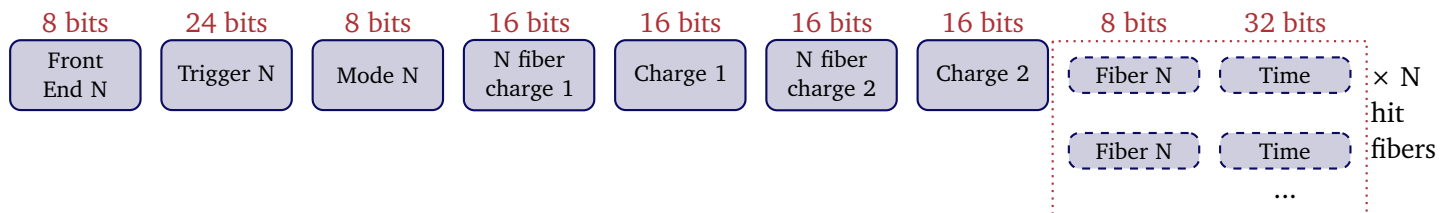


Figure A.4: Beam hodoscope data format.

A.4 Slow control, trigger and monitoring data format

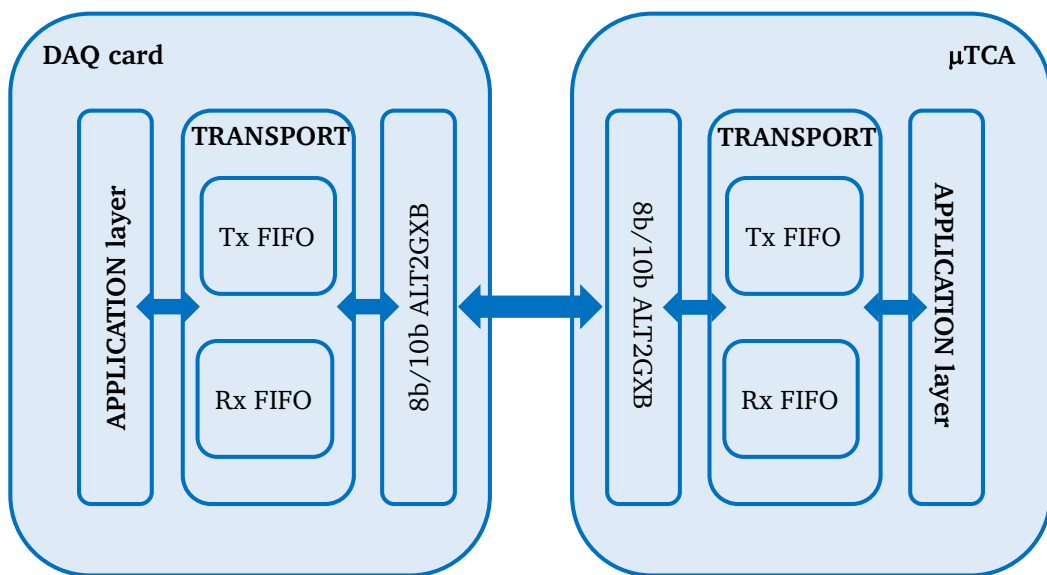
A.4.1 Communication architecture

The Endpoint architecture is composed of three layers:

- application layer

- mac (or transport) layer/processor packet
- physical layer

Figure A.5: Architecture of communication between DAQ cards and μ-TCA.



A.4.2 Transport protocol and processor packets

A.4.2.1 Definitions

It is worth to define some useful terms for the following part of the document:

- byte : 8 bits
- word : 16 bits
- K : control byte
- D : data byte
- cargo : data group
- terminator : packet end

- CRC : cyclic redundancy code

The CRC allows one to detect the transmission errors and the data transfer issues. A specific algorithm must be used, as CRC-16 : $X^{16} + X^{15} + X^2 + 1$. In the present protocol, a “parity pattern of 16 bits” have been used.

The transport layer ensures a proper packets exchange between two terminals via the data encapsulation. The data come from the application layer and are then sent to the physical layer.

A.4.2.2 Data encoding

For the transport layer, the data structure is created via the addition of a packet header, corresponding to a parity bit, of a 16 bit parity pattern and a bit for the end of the packet. The data are 8 bits/10 bits encoded. This standard 8 bits/10 bits encoding ensures sufficient data transitions for clock recovery.

A.4.2.3 Packets format

All the data packets have the same structure. A K byte (control symbol) is followed by the cargo to be sent. The end of the packets changes according to the cargo parity.
If the cargo contains an even number of bytes, the packet ends with K.28.6.

Table A.2: Packet with an even byte number cargo.

Item	Packet beginning	Cargo	Packet end
1	One K byte	0 - N D-bytes	K.28.6

If the cargo contains an odd number of bytes, the packet ends without any control symbol.

Table A.3: Packet with an odd byte number cargo.

Item	Packet beginning	Cargo	Packet end
1	One K byte	0 - N D-bytes	Beginning of a new packet

Remark :

- SYN packet is a special kind of packet starting with K.28.6 and ending with K.28.5. It is only composed of these two bytes (16 bits). It allows the receiver to find the beginning

and the end of the transmitted bytes with the aim to reconstruct the events in parallel. The synchronization speed is 44 Hz (defined by Carlos Abellan).

- In order to optimize the throughput, the control symbol at the beginning of the packet can probably be removed (further study needed).

A.4.2.4 Possible control symbols

In Table A.4, all the possible control symbols are listed (defined by Carlos Abellan).

Table A.4: Control symbol definition.

Item	Name	Control code	Comment
1	K.28.0	0x1C	Acknowledgement
2	K.28.1	0x3C	Ask for writing registers
3	K.28.2	0x5C	Ask for reading registers
4	K.28.3	0x7C	Special command
5	K.28.4	0x9C	Monitoring
6	K.28.5	0xBC	Default synchronization
7	K.28.6	0xDC	IDLE (default) and packet end
8	K.28.7	0xFC	Pre-trigger
9	K.23.7	0xF7	Trigger
10	K.27.7	0xFB	
11	K.29.7	0xFD	
12	K.30.7	0xFE	Physical data

A.4.3 Transport layer

A.4.3.1 Control packet

This kind of packet is used to check the link and for the control/command operations.

- For the link check, two kinds of packets are used: synchronization packet and IDLE packet.
- For the control/command operations, here are some examples: register configuration, FPGA dynamical programming, monitoring, etc.

Control symbol for control :

Acknowledgement packet (Front End cards → μ-TCA)

Table A.5: Control symbol definition.

Item	Name	Control code	Comment
1	K.28.0	0x1C	Acknowledgement
2	K.28.1	0x3C	Ask for writing registers
3	K.28.2	0x5C	Ask for reading registers
4	K.28.3	0x7C	Special command
5	K.28.4	0x9C	Monitoring
6	K.28.5	0xBC	Synchronization
7	K.28.6	0xDC	IDLE (default) and end of packet

This packet is sent by the FE cards and interpreted as an acknowledgement by the μ -TCA. If a part is missing, it is set to zero.

- If 0 = validation
- If 1 = problem detected

Table A.6: Definition of the acknowledgement packet.

Word	1 st byte	2 nd byte							
		7b	6b	5b	4b	3b	2b	1b	0b
1	K.28.0	0	Pb Front End num- ber	Pb with packet begin- ning	Pb with packet end	Pb with CRC	Pb with number of re- ceived words	Pb with parity bit of parity bit of re- ceived words	parity bit of the ac- knowl- edge- ment packet
2		Front End number							

A.4.3.2 Configuration packets

Writing register process (μ -TCA → Front End cards)

The process starts with a packet sent by the μ -TCA asking for the register writing. The receiver (FE card) sends back an acknowledgement packet to finish the process. In Table A.7 the format of this writing register packet is reported.

Reading register process (μ -TCA → Front End cards)

The process starts with a packet sent by the μ -TCA asking for the register reading. The receiver

Table A.7: Writing register packet.

Word	1 st byte	2 nd byte	Comment
1	K.28.1	Front End number + 1 parity bit	N/A
2	2 bytes with the number of words to be written		The length is word-based: max $2^{16} - 1 = 65535$ words
3	Register address		Address where the writing process starts
4..N+3	Data to be written		0000 0000
N+4	CRC composed of the “xor” of all bits in the same position, from word 2 to word (N+3)		

(FE card) sends back the “measure packet” if the command is correct, an acknowledgement packet if it is not.

At the beginning of the slow control, the physical addresses on the FE cards are read at the address 0.

In Table A.8 the format of this reading register packet is reported.

Table A.8: Reading register packet.

Word	1 st byte	2 nd byte	Comment
1	K.28.2	Front End number + 1 parity bit	N/A
2	2 bytes with the number of words to be read		The length is word-based: max $2^{16} - 1 = 65535$ words
3	Address of 1 st data to be read		Address where the reading process starts
4	CRC composed of the “xor” of all bits in the same position, from word 2 to word 3		/

A.4.3.3 Monitoring process (Front End cards → μ-TCA)

In case of issues, for example when the temperature of a card go beyond a fixed threshold, the DAQ card sends a “monitoring” packet to the μ-TCA. There is not a corresponding acknowledgement from the μ-TCA.

A Compton camera data format

Table A.9: Two special registers(μ -TCA → Front End cards)

Register address	Details	Comment
0	Front End number	No writing rights: register in read-only mode. Hard coded on DAQ card.
1	It defines the working modes	Optimal mode, test mode, collimated camera mode, Compton camera mode, individual detector section test. It is possible to write in the register.
2	It defines the detector to test (in single detector test mode)	Scatterer, absorber, hodoscope.
3	BGO number of sampling	For test mode with the BGO blocks signal sampling.
4	Silicon number of sampling	For test mode with the silicon layers signal sampling.

Table A.10: Measurement packet (Front End cards → μ -TCA)

Word	1 st byte	2 nd byte	Comment
1	K.28.1	Front End number + 1 parity bit	
2	2 bytes for the number of data words to send		The length is word-based: max $2^{16} - 1 = 65535$ words
3	Register address		Address where the writing process starts
4..N+3	Read data		0000 0000
N+4	CRC composed of the “xor” of all bits in the same position, from word 2 to word (N+3)		/

Table A.11: Monitoring packet.

Word	1 st byte	2 nd byte	Comment
1	K.28.4.	Front End number + 1 parity bit	Message in Table A.12.
2	15 bits for the message + 1 parity bit		Message in Table A.12.

Table A.12: Monitoring messages.

Item	Message	Bit[15]	...	Bit[7]	Bit[6]	Bit[5]	Bit[4]	Bit[3]	Bit[2]	Bit[1]	Comment
		Message type						Further information			
1	FPGA recon- figura- tion error	0	0	0	0	0	1	0	0	0	N/A
2	Tempe- rature alarm	0	0	0	0	1	0	x	x	x	Bit “x” is 1 if the corresponding detector goes beyond the threshold (0 elsewhere)
3	Busy	0	0	0	1	0	0	0	0	0	Front End is not able to send data
...											

A.4.3.4 Special command process (μ -TCA → Front End cards)

This process is designed to allow the μ -TCA to send special commands to the FE cards.

Table A.13: Special command packets

Word	1 st byte	2 nd byte
1	K.28.3	Front End number + 1 parity bit
2	15 bits for the special command + 1 parity bit	

A register database (containing the operating mode identification) must be fixed and shared between all the detectors.

A.4.4 Data packets (Front End card → μ -TCA)

In the section the packets concerning trigger, pre-trigger and physical data are described. No acknowledgement is demanded for this kind of packets.

Pre-trigger format

This packet is sent to the μ -TCA by the THOR card. The μ -TCA then shares it with all the

Table A.14: Special commands examples

Item	Command name	Bit[15..1] of 2 nd word	Comment
1	System reset	"0000 0000 0001 001"	Acknowledgement packet missing
2	Counter reset	"0000 0000 0001 000"	Acknowledgement packet needed
3	Start run	"0000 0000 0000 100"	Acknowledgement packet needed
4	Stop run	"0000 0000 0000 101"	Acknowledgement packet needed
5	Dynamical FPGA configuration	"0000 0000 0000 010"	Acknowledgement packet needed
6	Veto	"0000 0000 0000 011"	Example: μ -TCA cannot receive the data. Acknowledgement packet needed

Table A.15: Control symbol for pre-trigger, trigger and physical data.

Item	Name	Control code	Comment
1	K.28.7	0xFC	The pre-trigger is generated by the THOR card and sent to the μ -TCA who shares it with the silicon layers cards.
2	K.23.7	0xF7	The trigger is generated by a single silicon layer card and sent to the μ -TCA who shares it with all the FE cards.
5	K.30.7	0xFE	The FE cards send the data.

silicon FE cards.

Table A.16: Pre-trigger packet

Item	1 st byte	2 nd - 4 th bytes
1	K.28.7	24 bits for the trigger number

Trigger format

This packet is sent back to the μ -TCA if a silicon FE card finds an interaction in coincidence after the reception of the pre-trigger packet. The trigger is always sent before the physical data packets. The μ -TCA then sends the trigger packet to all the FE cards (scatterer, absorber, hodoscope).

Table A.17: Trigger packet

Item	1 st byte	2 nd - 4 th bytes
1	K.23.7	24 bits for the trigger number

Physical data packet format

This packet sends the “useful” data to the μ -TCA. The data format (cargo) is defined in chapter 3.

Table A.18: Physical data packet

Item	1 st byte	Cargo	End of packet
1	K.30.7.	From 0 to Nbr-1 words of D characters	K.28.6 or the beginning of a new packet.

A.5 UDP packets format

Once the μ -TCA receives the data from the FE cards, a physical event is generated and stored in dedicated buffers. The buffers are then sent to the acquisition PC via UDP packets. Each detector section has its own UDP socket, and three receiving ports are used for the three data fluxes: 60001 for the hodoscope, 60002 for the absorber, 60003 for the scatterer. The content of the data buffers are sent in order to avoid to divide events in different packets, so that each UDP packet is completely independent from the others and contains complete events. The maximum size of a packet is set to 1500 (UDP data = 1472), or to 9000 for the so called “jumbo frames”, used for high speed acquisitions.

Each UDP packet has a custom defined header, composed of:

- 32 bits: packet number, starting from 0;

- 16 bits: number of data structures in the packet;

The data structures are then in a list one after the other with the already described format.

A.6 Data throughput expected in clinical conditions

A.6.1 Clinical intensities

In clinical standards, the beam maximum intensity is:

- protons : 10^{10} protons/s
- carbon ions : 5×10^7 C ions/s

The Compton camera must be designed in order to be able to handle the whole range of clinical intensities. The design reference is then the maximum intensity, about 3.2 nA (2×10^{10} protons/s) delivered by the cyclotron C230 by IBA. The number of proton delivered per second is higher than the maximum considered rate (10^{10} protons/s).

As shown by the simulation results, the Compton camera can not be used for an online monitoring at the maximum beam intensity for both proton and carbon ion beams. The main limitation comes from the amount of random coincidences detected by the camera for high intensity beams. One possible solution is to deliver a lower intensity beam for the range monitoring before the beginning of the treatment. The results shown here relates to a reduced intensity, corresponding to the one selected via the simulation studies.

A.6.1.1 Review: detector and target sizes

Detectors sizes:

- Silicon scatterer : 7 silicon layers, $9.6 \times 9.6 \times 0.2 \text{ cm}^3$ (first layer 20 cm far from the beam line)
- BGO absorber: BGO block $3.5 \times 3.8 \times 3.0 \text{ cm}^3$ (67.5 cm far from the beam line - center of the block)

Poly Methyl Metacrylate (PMMA) target size: cylindrical shape, diameter 15 cm, 20 cm length along the beam direction.

A.6.2 Coincidence rate

In Table A.19 the coincidence and single (pre-trigger) rates expected for the different detector section are listed according to the beam kind and intensity. These values correspond to the Compton camera, while for the collimated camera a reduced rate is expected for the absorber due to the presence of the physical collimator.

Table A.19: Coincidence and single rate as a function of the beam intensity. The BGO single rate corresponds to the pre-trigger rate.

	Clinical intensity		Reduced intensity		Collimated camera	
	Protons	Carbon ions	Protons	Carbon ions	Protons	Carbon ions
Intensity(ions/s)	2×10^{10}	5×10^7	1×10^8	5×10^6	2×10^{10}	5×10^7
Coincidence rate per incident ion	9×10^{-4}	8×10^{-4}	9×10^{-4}	8×10^{-4}	/	/
Coincidence rate (Hz)	$1,8 \times 10^7$	4×10^4	9×10^4	4×10^3	/	/
Single rate BGO (Hz) - 96 blocks	$7,8 \times 10^7$	$1,4 \times 10^6$	$3,9 \times 10^5$	$1,4 \times 10^5$	/	/
Single rate BGO (Hz) - 1 block	$8,1 \times 10^5$	$1,5 \times 10^4$	4×10^3	$1,5 \times 10^3$	/	/
Single rate BGO (Hz) - 1 ASM card (6 blocks)	$6,5 \times 10^6$	$1,2 \times 10^5$	$3,2 \times 10^4$	$1,2 \times 10^4$	/	/

The application of the Compton camera at clinical intensity seems not feasible. The camera distance with respect to the beam line should be increased to lower the rate to 1×10^5 Hz (which means to put the 1st silicon layer 1 m far from the beam line). For a carbon ion beam at 5×10^7 Hz, the estimated coincidence rate is 4×10^4 Hz, with 1.4×10^6 single rate on the absorber (measurements of coincidence rate on the HIT accelerator adapted to a real camera size with a 40 ns coincidence window, Krimmer ANIMMA 2013). The data flow between the μ -TCA and the acquisition PC corresponds to the coincidence rate, due to the fact that only coincidence events are stored.

A.6.3 Data flow (Front End cards → μ -TCA)

The data format previously described has been used to evaluate the data flow between each FE card and the μ -TCA. The calculation is performed according to the “optimal” mode of each detector. For the BGO, we only consider events where the 4 PMs are involved. For the silicon layers, two cases are considered:

- Case 1 : one single layer with 6 involved strips;
- Case 2 : all the 7 layers involved with 6 hit strips per layer.

A Compton camera data format

Concerning the hodoscope, we considered an event with one hit fiber readout on the two sides.

The 8bits/10bits encoding is included in the calculation.

Table A.20: Data flux between FE cards and μ -TCA.

	Clinical intensity	Reduced intensity		
	<u>Protons</u>	<u>Carbon ions</u>	<u>Protons</u>	<u>Carbon ions</u>
Intensity (ions/s)	2×10^{10}	5×10^7	1×10^8	5×10^6
Pre-trigger flux (Mbits/s)	$2,5 \times 10^3$	47,6	13,3	4,76
Trigger flux (Mbits/s)	612	1,4	3,1	0,1
BGO data flux (Mbits/s) - 96 blocks	$1,7 \times 10^5$	373	873	37,3
BGO data flux (Mbits/s)- 1 block	$1,7 \times 10^3$	3,88	8,73	0,3
BGO data flux (Mbits/s) - 1 carte ASM	$1,4 \times 10^4$	31,1	69,9	3,1
Silicon data flux (Mbits/s) - case 1	$2,3 \times 10^5$	522	$1,2 \times 10^3$	52,2
Silicon data flux (Mbits/s) - case 2	$1,6 \times 10^6$	$3,7 \times 10^3$	$8,2 \times 10^3$	366
Hodoscope data flux (Mbits/s)	$8,1 \times 10^4$	180	404	18

A.6.4 Acquisition data flow (μ -TCA \rightarrow Acquisition PC)

The data flow from the μ -TCA to the acquisition PC is detailed here. The UDP encoding is included in the calculation.

Table A.21: Data flow between μ -TCA and acquisition PC.

	Clinical intensity	Reduced intensity		
	<u>Protons</u>	<u>Carbon ions</u>	<u>Protons</u>	<u>Carbon ions</u>
Intensity (ions/s)	2×10^{10}	5×10^7	1×10^8	5×10^6
Coincidence rate per incident ion	9×10^{-4}	8×10^{-4}	9×10^{-4}	8×10^{-4}
Coincidence rate (Hz)	$1,8 \times 10^7$	4×10^4	9×10^4	4×10^3
Data flow (Mbits/s) - case 1	$2,2 \times 10^4$	46,7	112	5,0
Data flow (Mbits/s) - case 2	6×10^4	133	300	13,3

A.6.5 Conclusions

As already mentioned, the Compton camera application is not feasible at clinical beam intensities.

In order to have an online monitoring of the beam range, a reduced intensity must be foreseen. The main limitation is the rate of random coincidences detected at high intensity, while from the technological point of view no limitations are highlighted by this study. In the collimated camera configuration, where no coincidences are required and the random coincidences limitation is removed, we can then expect to be able to work at real clinical intensity.

Table A.22: Acquisition format of the Compton camera data.

COMPTON CAMERA ACQUISITION DATA FORMAT				
	Description	Size (bytes)	Size (bits)	Details
Beginning of file (10 bytes)	File start ID	2	16	FOFO (hex) fixed ID
	Run number	4	32	Automatically increasing in DAQ software - it can be manually fixed
	Total number of events	4	32	Fixed at the beginning of the acquisition, it defines the file size
Event header (11 bytes) x total number of events	Event start ID	2	16	ABCD (hex) fixed ID
	Event number	4	32	Automatically increasing in μ-TCA data format
	Trigger number	3	24	Automatically increasing in μ-TCA data format
	Number of hits in trigger	2	16	
Data header (7 bytes) x number of hits in trigger	Hit start ID	1	8	EB (hex) fixed ID
	FE number	1	8	see Table A.1
	Trigger number	3	24	repeated from Event Header
	Mode number	1	8	see figure A.4 (7 or 8 for the hodoscope - 7 = optimal, 8 = test)
	Number of involved fibers	1	8	
Hit structure scatterer (7 bytes - mode 1, 9 bytes - mode 2, mode 3 and 4 with signal sampling) x number of involved strips (mode 1 and 3) or tracks (mode 2 and 4)	Strip number	1	8	mode 1 and 3
	Position	2	16	mode 2 and 4
	Time	4	32	all modes
	Charge	2	16	mode 1 and 2
	Signal samples	2	16	mode 3 and 4 - size per sample - n samples, with n selected in acquisition code
Hit structure absorber (17 bytes - mode 5, mode 6 with signal sampling) x number of involved blocks	Block number	1	8	both modes
	Time	4	32	both modes
	Charge PM 1-4	3	24	mode 5 - size per PM - 4 PMs per block
	Signal samples	2	16	mode 6 - size per sample per PM - n samples, with n selected in acquisition code, 4 PMs per block
Hit structure hodoscope (5 bytes - mode 7, 7 bytes - mode 8) x number of involved fibers	Fiber number	1	8	ranges from 0 to 128
	Time	4	32	in both modes 7 and 8
	Charge	2	16	only for mode 8
End of file (10 bytes)	File end ID	2	16	F1F1 (hex) fixed ID
	Number of events in file	4	32	for verification and debugging
	Number of octets in file	4	32	for verification and debugging

List of abbreviations

¹¹¹**In** Indium-111 179

¹²³**I** Iodine-123 66

¹³¹**I** Iodine-131 66, 67, 172, 178

¹³¹**In** Indium-131 4

¹⁷⁷**Lu** Lutetium-177 66

²²**Na** Sodium-22 xi, 108–115, 124, 126, 127

⁴²**K** Potassium-42 179

⁵⁷**Co** Cobalt-57 108

⁵⁹**Fe** Iron-59 179

⁶⁰**Co** Cobalt-60 x, xi, 109, 111, 112, 116, 118–123, 142

^{91m}**Y** Yttrium-91m 179

μ-TCA Micro Advanced Telecommunications Computing Architecture vi, x, xv, xvii, xviii, 48, 92, 100–104, 137–141, 196, 203–206, 211, 213–219, 221, 222, 224

A.D.A.M. Advanced Oncotherapy 23

ADC Analog-to-Digital Converter 86, 92, 97, 109–111, 115, 123, 130, 131

AMC Advanced Mezzanine Card x, 100–102, 137, 141

ART Algebraic Reconstruction Technique 39

ASIC Application-Specific Integrated Circuit 86, 87, 97, 98, 103, 108, 137, 207, 210

ASM Analog Sampling Module x, 90, 92, 93, 100, 138, 139, 204–207, 221, 222

ATCA Advanced Telecommunications Computing Architecture 100

AVIRM Application et Valorisation des Interactions Rayonnements-Matière 90, 92, 93, 130

BaF₂ Barium Fluoride xi, 44, 63, 113, 114, 126, 128

BGO Bismuth Germanium Oxide - $\text{Bi}_{12}\text{GeO}_{20}$ i, iv, ix–xi, xiv, xvii, xviii, 44, 45, 62–64, 81, 88–94, 100, 106, 107, 109–111, 113–115, 126, 128–130, 138, 142, 148–150, 175, 176, 186, 205, 207, 216, 220–222

BIC Binary Intra-nuclear Cascade 15

BME Boltzmann-Master-Equation 12

BNCT Boron Neutron Capture Therapy 20

BNL Brookhaven National Laboratory 61

CAL Centre Antoine Lacassagne, Nice, France 16, 48, 50, 103, 196

CCD Charge-Coupled Device 40

CdTe Cadmium Telluride xiv, 51, 177, 185

CdZnTe Cadmium Zinc Telluride 84

CeBr₃ Cerium Bromide 139

CERN Conseil Européen pour la Recherche Nucléaire, Geneva, Switzerland 23, 100

CLaRyS Contrôle en Ligne de l'hadronthérapie par Rayonnements Secondaires i, ii, 47, 48, 82, 84, 94, 100, 106, 107, 137, 141, 142, 148, 150, 165, 170, 172, 173, 184, 188, 191, 193, 196

CMOS Complementary Metal Oxide Semiconductor 49

CNAO Centro Nazionale di Adroterapia Oncologica, Italy vii, 22, 47

CPPM Centre de Physique des Particules de Marseille, France 82, 100, 141

CR-RC Capacitor Resistor - Resistor Capacitor 86

CREATIS Centre de Recherche en Acquisition et Traitement de l'Image pour la Santé, Lyon, France 82, 106, 176

CRT Coincidence Resolution Time 47

CSA Charge Sensitive Amplifier 86

CSDA Continuous Slowing Down Approach 8, 9

CsF Cesium Fluoride 44, 63

CsI Cesium Iodide 39

CT Computed Tomography i, viii, 27, 29, 34, 36–43, 46, 53, 146

CTV Clinical Target Volume 32

DLL Delay Locked Loop 97

DOI Depth Of Interaction 60–62

DPGA *Détecteur Pixélisé de Grande Acceptance* 48, 82, 90, 92

DRS Domino Ring Sampler 92

DSB Double-Strand Break 16, 17

DSSD Double-sided Silicon Strip Detector i, 84–86, 107, 108, 137, 138, 142, 148, 175, 177, 192

DWA Dielectric Wall Accelerator 23

EC Electron Capture 56

EM Electromagnetic 8, 10

ENC Equivalent Noise Charge 86, 175, 184, 185, 191

ESRF European Synchrotron Radiation Facility, Grenoble, France 140

FBP Filtered Back-Projection 39, 61

FDG Fluoro-Deoxy-Glucose 48, 59, 62

FE Front-End ix, x, xviii, 48, 85–88, 90, 92, 93, 95, 97–100, 102, 108, 109, 132, 136, 137, 139–142, 203–207, 210, 214, 215, 217–219, 221, 222, 224

FFAG Fixed Field Alternating Gradient 22

FNAL Fermi National Accelerator Laboratory 39

FOP Fall-Off Position 158

FOV Field Of View 65

FPGA Field Programmable Gate Array 86, 87, 92, 97, 98, 100, 210, 213, 217, 218

FWHM Full Width at Half Maximum vii, xi, xiv, 12, 44, 47, 60, 64, 86, 99, 108, 109, 114, 124–126, 128–130, 138, 149, 150, 175, 176, 186

- GANIL** Grand Accelerateur National d’Ions Lourds, Caen, France 15, 98, 99, 138, 140, 150, 175
- GATE** GEANT4 Application for Tomographic Emission 178
- GE** General Electric 62, 64
- GEANT4** GEometry And Tracking 4 173
- GEM** Gas Electron Multiplier 39
- GSI** GSI Helmholtz Centre for Heavy Ion Research, Germany vii, viii, 15, 27, 29–31, 41, 43, 45, 46
- Gsps** Giga Sample Per Second 92
- HEGP** High Energy General Purpose 65, 178, 192
- HIMAC** Heavy Ion Medical Accelerator in Chiba, Japan 5, 15, 28, 31, 41, 45, 46, 51
- HIT** Heidelberg Ion Therapy Center, Germany vii, viii, xvii, 5, 22, 28, 40, 46–49, 98, 99, 151, 152
- HSMC** High-Speed Mezzanine Card 92
- HU** Hounsfield Units 29, 34, 37
- IBA** Ion Beam Applications, Belgium vii, xvii, 22, 24, 152
- IC** Internal Conversion 57
- IC** Ionization Chamber 40, 50
- ICRP** International Commission on Radiological Protection 15
- IMPT** Intensity-Modulated Particle Therapy 26, 32
- IMRT** Intensity-Modulated RadioTherapy 27, 32
- INC** Intra-nuclear Cascade 12, 15
- INFN** Istituto Nazionale di Fisica Nucleare, Italy 23
- INSIDE** Innovative Solutions for Dosimetry in Hadrontherapy 47
- IPNL** Institut de Physique Nucléaire de Lyon, France 82, 85–87, 93, 95, 97, 102, 103, 107, 109, 110, 130, 137–139, 141–143, 175

- IPNO** Institut de Physique Nucléaire d'Orsay, France 99
- IRFU** Institut de Recherche sur les lois Fondamentales de l'Univers, Paris, France 110
- IVI** Interaction Vertex Imaging 49
- LaBr₃** Lanthanum Bromide 108
- LAL** Laboratoire de l'Accélérateur Linéaire, Paris, France 110
- LAPD** Large Area Pixelized Detector 48
- LBL** Lawrence Berkeley Laboratory 44
- LED** Light Emitting Diode xi, xii, 130–135
- LEGP** Low Energy General Purpose 65
- LEHR** Low Energy High Resolution 65
- LEM** Local Effect Model 31
- LET** Linear Energy Transfer vii, 17–19, 26, 29, 35
- LFS** Lutetium Fine Silicate 47
- LHCb** Large Hadron Collider beauty 100
- LIGHT** Linac for Image Guided HadronTherapy 23
- LLNL** Lawrence Livermore National Laboratory, USA 23
- LLU** Loma Linda University 39
- LM-MLEM** List Mode-Maximum Likelihood Expectation Maximization 106, 156–158, 164, 165, 170, 176, 184–186, 191, 192
- LOR** Line Of Response ix, 60, 61, 63
- LPC** Laboratoire de Physique de Clermont, France 48, 82, 90, 93, 100, 130, 142
- LPSC** Laboratoire de Physique Subatomique et Corpusculaire, Grenoble, France 82, 140
- LQ** Linear-Quadratic 17, 31
- LSO** Cerium-doped Lutetium Oxyorthosilicate - Lu_{2(1-x)}Ce_{2x}SiO₄ 62–64, 89
- LVDS** Low-Voltage Differential Signaling 86

List of abbreviations

- LYSO** Lutetium-Yttrium OxyorthoSilicate - Lu_{2(1-x)}Y_{2x}SiO₅ 46–48, 63, 64, 89, 90, 92, 139
- MCH** μ-TCA Carrier HUB 100
- MCS** Multiple Coulomb Scattering 11, 32–34, 38
- MEGAlib** Medium-Energy Gamma-ray Astronomy library 176
- MEGP** Medium Energy General Purpose 65
- MGH** Massachusetts General Hospital 46, 61
- MICRHau** Micro-électronique RHône AUvergne 97
- MIT** Massachusetts Institute of Technology 67
- MKM** Microdosimetric Kinetic Model 31
- MLEM** Maximum Likelihood Expectation Maximization 148, 170
- MLP** Most Likely Path 37
- MRI** Magnetic Resonance Imaging 4, 29, 42, 50, 64
- Msp**s Mega Sample Per Second 86
- MWPC** Multi Wire Proportional Chamber 39
- Nal** Sodium Iodide 39
- Nal(Tl)** Sodium Iodide doped with Thallium 61–63, 178, 179, 181
- NIM** Nuclear Instrumentation Module 107–111, 113, 115, 138, 142
- NIRS** National Institute of Radiological Sciences, Japan 27–29, 31, 40, 45
- NIST** National Institute of Standards and Technology 38, 78
- NIU** Northern Illinois University 39
- NURBS** Non-Uniform Rational Basis Splines xiii, 159, 164
- OAR** Organ At Risk 6, 27, 29, 32, 35, 146
- OER** Oxygen Enhancement Ratio 19
- pCT** proton Computed Tomography 29

- PET** Positron Emission Tomography i, viii, ix, 4, 15, 29, 40–48, 50–53, 56, 58–64, 67, 82, 88, 90, 93, 109, 138, 146, 172, 196
- PG** Prompt-Gamma i, iii, 24, 37, 47, 48, 50–52, 69, 78, 139, 146, 147, 159
- PIDE** Particle Radiation Data Ensemble 18
- PM** Photo-Multiplier iv, x–xii, 44, 46, 48, 62–64, 81, 89–91, 93, 95–99, 109–111, 115–117, 129–136, 138–140, 142, 207, 210, 221, 224
- PMMA** Poly Methyl Metacrylate viii, 15, 40, 42, 45–49, 93, 148, 157, 158, 220
- PRaVDA** Proton Radiotherapy Verification and Dosimetry Application 40
- PSF** Point-Spread Function 60
- PSI** Paul Scherrer Institut, Villigen, Switzerland 27–29, 39, 92
- PTCOG** Particle Therapy Co-Operative Group 48
- PTV** Planned Target Volume 24–26, 29, 32, 33, 78
- QMD** Quantum Molecular Dynamics 12, 15
- RAM** Random Access Memory 102
- RBE** Relative Biological Effectiveness vii, viii, 18, 19, 29–31, 35, 146
- RF** Radio-Frequency 24
- RMS** Root Mean Square 86, 97, 140, 141, 187
- ROI** Region Of Interest 159
- RPC** Resistive Plate Chamber 47
- RSP** Relative Stopping Power 29
- SHS** Slow Shaper 86
- SI** Internation System of units 54
- SiPM** Silicon Photo-Multiplier 47, 63, 64, 139
- SNR** Signal-to-Noise Ratio 50
- SOBP** Spread-Out Bragg Peak vii, 25, 26, 29, 31, 33, 35

SPECT Single Photon Emission Computed Tomography i, 48, 53, 59, 63–67, 139, 172, 173, 175, 178, 184, 186, 191, 192

SPTR Single Photon Time Resolution 139

TCP Tumor Control Probability 29

TCP Transmission Control Protocol 102, 104

TDC Time-to-Digital Converter 87, 97, 203

THOR Trigger et HORloge x, 92, 100, 101, 138, 205, 206, 217, 218

TOF Time-Of-Flight viii, ix, 41, 43, 44, 47, 63, 64, 83, 84, 94, 100, 107, 139, 140, 170

TOT Time-Over-Threshold 64

TPS Treatment-Planning System 29

UCSC University of California and Santa Cruz 39

UDP User Datagram Protocol 102, 103, 141

USB Universal Serial Bus 110

VME VERSABUS Module Eurocard 48, 90, 100, 108, 139

WEPL Water-Equivalent Path Length 29, 34

YAG:Ce Cerium-activated yttrium aluminum garnet 39

Bibliography

- Abe, S., K. Nishimura, H. Sato, H. Muraishi, T. Inada, T. Tomida, T. Fujisaki, Y. Futami, T. Kanai, K. Kawachi, and S. Tazawa (2002). “Heavy ion CT system based on measurement of residual range distribution.” In: *Igaku Butsuri* 22.1, pp. 39–47 (cit. on p. 40).
- Abellan, C., J.-P. Cachemiche, F. Réthoré, and C. Morel (June 2013). “A data acquisition system for medical imaging”. In: *2013 3rd International Conference on Advancements in Nuclear Instrumentation, Measurement Methods and their Applications (ANIMMA)*, pp. 1–7. DOI: 10.1109/ANIMMA.2013.6728028 (cit. on p. 100).
- Adam, L.-E., J. Zaers, H. Ostertag, H. Trojan, M. E. Bellemann, and G. Brix (June 1997). “Performance evaluation of the whole-body PET scanner ECAT EXACT HR + following the IEC standard”. In: *IEEE Transactions on Nuclear Science* 44.3, pp. 1172–1179. ISSN: 0018-9499. DOI: 10.1109/23.596983 (cit. on p. 88).
- Agodi, C., G. Battistoni, F. Bellini, G. A. P. Cirrone, F. Collamati, G. Cuttone, E. De Lucia, M. De Napoli, A. Di Domenico, R. Faccini, F. Ferroni, S. Fiore, P. Gauzzi, E. Iarocci, M. Marafini, I. Mattei, S. Muraro, A. Paoloni, V. Patera, L. Piersanti, F. Romano, A. Sarti, A. Sciubba, E. Vitale, and C. Voena (2012). “Charged particle’s flux measurement from PMMA irradiated by 80 MeV/u carbon ion beam”. In: *Physics in Medicine & Biology* 57.18, p. 5667. URL: <http://stacks.iop.org/0031-9155/57/i=18/a=5667> (cit. on p. 49).
- Ainsley, C. G. and C. M. Yeager (May 2014). “Practical considerations in the calibration of CT scanners for proton therapy”. In: *Journal of Applied Clinical Medical Physics* 15.3, pp. 202–220. DOI: 10.1120/jacmp.v15i3.4721. URL: <http://www.ncbi.nlm.nih.gov/pmc/articles/PMC5711046/> (cit. on p. 34).
- Albertini, F., A. Bolsi, A. J. Lomax, H. P. Rutz, B. Timmerman, and G. Goitein (Feb. 2008). “Sensitivity of intensity modulated proton therapy plans to changes in patient weight.” In: *Radiother Oncol* 86.2, pp. 187–194 (cit. on p. 34).
- Albertini, F., E. B. Hug, and A. J. Lomax (2011). “Is it necessary to plan with safety margins for actively scanned proton therapy?” In: *Physics in Medicine & Biology* 56.14, p. 4399. URL: <http://stacks.iop.org/0031-9155/56/i=14/a=011> (cit. on p. 32).
- Aldawood, S., P. G. Thirolf, A. Miani, M. Böhmer, G. Dedes, R. Gernhäuser, C. Lang, S. Liprandi, L. Maier, T. Marinsek, M. Mayerhofer, D. R. Schaart, I. Valencia Lozano, and K. Parodi (2017). “Development of a Compton camera for prompt-gamma medical imaging”. In: *Radiation Physics and Chemistry* 140. 2nd International Conference on Dosimetry and its Applications (ICDA-2) University of Surrey, Guildford, United Kingdom, 3-8 July 2016, pp. 190–197. ISSN: 0969-806X. DOI: <https://doi.org/10.1016/j.radphyschem.2017.01.024>. URL: <http://www.sciencedirect.com/science/article/pii/S0969806X17300981> (cit. on p. 147).
- Alharbi, T. (2018). “Energy resolution improvement of CdTe detectors by using the principal component analysis technique”. In: *Nuclear Instruments and Methods in Physics Research Section A: Accelerators, Spectrometers, Detectors and Associated Equipment* 882, pp. 114–

116. ISSN: 0168-9002. DOI: <https://doi.org/10.1016/j.nima.2017.11.027>. URL: <http://www.sciencedirect.com/science/article/pii/S0168900217312251> (cit. on p. 185).
- Altera (2009). *Stratix II GX Device Handbook*. Volume 1. Altera Corporation (cit. on pp. 87, 98).
- Altera (2012). *Cyclone III Device Handbook*. Volume 1. Altera Corporation (cit. on pp. 87, 97).
- Altera (2015). *Stratix V Device Handbook*. Volume 3. Altera Corporation (cit. on p. 92).
- Altera (2016). *Cyclone IV Device Handbook*. Volume 1. Altera Corporation (cit. on p. 100).
- Alzahrani, A. S., O. AlShaikh, M. Tuli, A. Al-Sugair, R. Alamawi, and M. M. Al-Rasheed (Mar. 2012). “Diagnostic value of recombinant human thyrotropin-stimulated ^{123}I whole-body scintigraphy in the follow-up of patients with differentiated thyroid cancer.” In: *Clin Nucl Med* 37.3, pp. 229–234 (cit. on p. 66).
- Amaldi, U. (2009). “Cyclinacs: Fast-Cycling Accelerators for Hadrontherapy”. In: *Nucl. Instrum. Meth. A*. arXiv: 0902.3533 [physics.med-ph] (cit. on p. 23).
- Amaldi, U., P. Berra, K. Crandall, D. Toet, M. Weiss, R. Zennaro, E. Rosso, B. Szeless, M. Vretenar, C. Cicardi, C. De Martinis, D. Giove, D. Davino, M. R. Masullo, and V. Vaccaro (2004). “LIBO-a linac-booster for protontherapy: construction and tests of a prototype”. In: *Nuclear Instruments and Methods in Physics Research Section A: Accelerators, Spectrometers, Detectors and Associated Equipment* 521.2, pp. 512–529. ISSN: 0168-9002. DOI: <https://doi.org/10.1016/j.nima.2003.07.062>. URL: <http://www.sciencedirect.com/science/article/pii/S0168900203023994> (cit. on p. 23).
- Amaldi, U., A. Bianchi, Y.-H. Chang, A. Go, W. Hajdas, N. Malakhov, J. Samarati, F. Sauli, and D. A. Watts (2011). “Construction, test and operation of a proton range radiography system”. In: *Nuclear Instruments and Methods in Physics Research Section A: Accelerators, Spectrometers, Detectors and Associated Equipment* 629.1, pp. 337–344. ISSN: 0168-9002. DOI: <https://doi.org/10.1016/j.nima.2010.11.096>. URL: <http://www.sciencedirect.com/science/article/pii/S0168900210026318> (cit. on p. 39).
- Amaldi, U., R. Bonomi, S. Braccini, M. Crescenti, A. Degiovanni, M. Garlasché, A. Garonna, G. Magrin, C. Mellace, P. Pearce, G. Pittà, P. Puggioni, E. Rosso, S. Verdú Andrés, R. Wegner, M. Weiss, and R. Zennaro (2010a). “Accelerators for hadrontherapy: From Lawrence cyclotrons to linacs”. In: *Nuclear Instruments and Methods in Physics Research Section A: Accelerators, Spectrometers, Detectors and Associated Equipment* 620.2, pp. 563–577. DOI: <https://doi.org/10.1016/j.nima.2010.03.130>. URL: <http://www.sciencedirect.com/science/article/pii/S0168900210007357> (cit. on p. 22).
- Amaldi, U., S. Braccini, and P. Puggioni (2009). “High Frequency Linacs for Hadrontherapy”. In: *Reviews of Accelerator Science and Technology* 02.01, pp. 111–131. DOI: 10.1142/S179362680900020X. eprint: <https://doi.org/10.1142/S179362680900020X>. URL: <https://doi.org/10.1142/S179362680900020X> (cit. on p. 23).
- Amaldi, U., W. Hajdas, S. Iliescu, N. Malakhov, J. Samarati, F. Sauli, and D. A. Watts (2010b). “Advanced Quality Assurance for CNAO”. In: *Nuclear Instruments and Methods in Physics*

- Research Section A: Accelerators, Spectrometers, Detectors and Associated Equipment* 617.1. 11th Pisa Meeting on Advanced Detectors, pp. 248–249. ISSN: 0168-9002. DOI: <https://doi.org/10.1016/j.nima.2009.06.087>. URL: <http://www.sciencedirect.com/science/article/pii/S0168900209013424> (cit. on pp. 39, 49).
- Anger, H. O. (1958). “Scintillation Camera”. In: *Review of Scientific Instruments* 29.1, pp. 27–33. DOI: 10.1063/1.1715998. eprint: <http://dx.doi.org/10.1063/1.1715998>. URL: <http://dx.doi.org/10.1063/1.1715998> (cit. on pp. 53, 64, 65, 172).
- Anger, H. O. (1964). “Scintillation Camera with Multichannel Collimators”. In: *Journal of Nuclear Medicine* 5.7, pp. 515–531. eprint: <http://jnm.snmjournals.org/content/5/7/515.full.pdf+html>. URL: <http://jnm.snmjournals.org/content/5/7/515.short> (cit. on pp. 65, 172).
- Anger, H. O. (1969). *Multiplane Tomographic Gamma-Ray Scanner*. International Atomic Energy Agency (IAEA): IAEA (cit. on p. 65).
- Antoine, S., B. Autin, W. Beeckman, J. Collot, M. Condat, F. Forest, J. Fourrier, E. Froidefond, J. L. Lancelot, J. Mandrillon, P. Mandrillon, F. Méot, Y. Mori, D. Neuvéglise, C. Ohmori, J. Pasternak, and T. Planche (2009). “Principle design of a protontherapy, rapid-cycling, variable energy spiral FFAG”. In: *Nuclear Instruments and Methods in Physics Research Section A: Accelerators, Spectrometers, Detectors and Associated Equipment* 602.2, pp. 293–305. DOI: <https://doi.org/10.1016/j.nima.2009.01.025>. URL: <http://www.sciencedirect.com/science/article/pii/S0168900209000059> (cit. on p. 23).
- Arena, C., V. Micco, E. Macaeva, and R. Quintens (Nov. 2014). “Space radiation effects on plant and mammalian cells”. In: 104, pp. 419–431 (cit. on p. 18).
- Aspen Aerogels (2011). *Spaceloft® - High performance Insulation for building envelopes. Data Sheet*. Aspen Aerogels Inc. (cit. on p. 87).
- Attanasi, F., N. Belcari, M. Camarda, G. Cirrone, G. Cuttone, A. Del Guerra, F. Di Rosa, N. Lanconelli, V. Rosso, G. Russo, and S. Vecchio (2008). “Preliminary results of an in-beam PET prototype for proton therapy”. In: *Nuclear Instruments and Methods in Physics Research Section A: Accelerators, Spectrometers, Detectors and Associated Equipment* 591.1. Radiation Imaging Detectors 2007, pp. 296–299. ISSN: 0168-9002. DOI: <https://doi.org/10.1016/j.nima.2008.03.076>. URL: <http://www.sciencedirect.com/science/article/pii/S0168900208004610> (cit. on p. 46).
- Attanasi, F., N. Belcari, A. Del Guerra, W. Enghardt, S. Moehrs, K. Parodi, V. Rosso, and S. Vecchio (2009). “Comparison of two dedicated ‘in beam’ PET systems via simultaneous imaging of 12 C-induced β + -activity”. In: *Physics in Medicine & Biology* 54.2, N29. URL: <http://stacks.iop.org/0031-9155/54/i=2/a=N01> (cit. on p. 46).
- Barth, R. F., J. A. Coderre, M. G. H. Vicente, and T. E. Blue (2005). “Boron Neutron Capture Therapy of Cancer: Current Status and Future Prospects”. In: *Clinical Cancer Research* 11.11, pp. 3987–4002. DOI: 10.1158/1078-0432.CCR-05-0035. eprint: <http://clincancerres.aacrjournals.org/content/11/11/3987.full.pdf>. URL: <http://clincancerres.aacrjournals.org/content/11/11/3987> (cit. on p. 20).

- Baskar, R., K. A. Lee, R. Yeo, and K.-W. Yeoh (2012). “Cancer and radiation therapy: current advances and future directions.” eng. In: *Int J Med Sci* 9.3, pp. 193–199. DOI: 10.7150/ijms.3635 (cit. on p. 5).
- Basko, R., G. L. Zeng, and G. T. Gullberg (1998). “Application of spherical harmonics to image reconstruction for the Compton camera”. In: *Physics in Medicine and Biology* 43.4, p. 887. URL: <http://stacks.iop.org/0031-9155/43/i=4/a=016> (cit. on p. 78).
- Bauer, J., D. Unholtz, F. Sommerer, C. Kurz, T. Haberer, K. Herfarth, T. Welzel, S. E. Combs, J. Debus, and K. Parodi (2013). “Implementation and initial clinical experience of offline PET/CT-based verification of scanned carbon ion treatment”. In: *Radiotherapy and Oncology* 107.2, pp. 218–226. ISSN: 0167-8140. DOI: <https://doi.org/10.1016/j.radonc.2013.02.018>. URL: <http://www.sciencedirect.com/science/article/pii/S0167814013001606> (cit. on pp. 43, 46).
- Baum, R. P. and H. R. Kulkarni (2012). “THERANOSTICS: From Molecular Imaging Using Ga-68 Labeled Tracers and PET/CT to Personalized Radionuclide Therapy - The Bad Berka Experience.” In: *Theranostics* 2.5, pp. 437–447 (cit. on p. 67).
- Bazalova, M., J.-F Carrier, L. Beaulieu, and F Verhaegen (2008). “Dual-energy CT-based material extraction for tissue segmentation in Monte Carlo dose calculations”. In: *Physics in Medicine & Biology* 53.9, p. 2439. URL: <http://stacks.iop.org/0031-9155/53/i=9/a=015> (cit. on p. 34).
- Bednarz, B., J. Daartz, and H. Paganetti (Dec. 2010). “Dosimetric accuracy of planning and delivering small proton therapy fields.” In: *Phys Med Biol* 55.24, pp. 7425–7438 (cit. on p. 36).
- Belkić, D. (May 2010). “Review of theories on ionization in fast ion-atom collisions with prospects for applications to hadron therapy”. In: *Journal of Mathematical Chemistry* 47.4, pp. 1366–1419. DOI: 10.1007/s10910-010-9662-x. URL: <https://doi.org/10.1007/s10910-010-9662-x> (cit. on p. 6).
- Belli, M., D. T. Goodhead, F. Ianzini, G. Simone, and M. A. Tabocchini (1992). “Direct Comparison of Biological Effectiveness of Protons and Alpha/particles of the Same LET. II. Mutation Induction at the HPRT Locus in V79 Cells”. In: *International Journal of Radiation Biology* 61.5, pp. 625–629. DOI: 10.1080/09553009214551431. eprint: <https://doi.org/10.1080/09553009214551431> (cit. on p. 17).
- Bennett, G. W., A. C. Goldberg, G. S. Levine, J. Guthy, J. Balsamo, and J. O. Archambeau (1975). “Beam localization via ^{15}O activation in proton-radiation therapy”. In: *Nuclear Instruments and Methods* 125.3, pp. 333–338. ISSN: 0029-554X. DOI: [https://doi.org/10.1016/0029-554X\(75\)90246-3](https://doi.org/10.1016/0029-554X(75)90246-3). URL: <http://www.sciencedirect.com/science/article/pii/0029554X75902463> (cit. on p. 44).
- Bentzen, S. M. (2006). “Preventing or reducing late side effects of radiation therapy: radiobiology meets molecular pathology.” eng. In: *Nat Rev Cancer* 6.9, pp. 702–713. DOI: 10.1038/nrc1950 (cit. on p. 5).

- Berger, M., J. Coursey, M. Zucker, and J. Chang (2018). *ESTAR, PSTAR, and ASTAR: Computer Programs for Calculating Stopping-Power and Range Tables for Electrons, Protons, and Helium Ions*. URL: <http://physics.nist.gov/Star> (visited on 08/23/2018) (cit. on p. 38).
- Bergstrom, P. M. and R. H. Pratt (1997). “An overview of the theories used in compton scattering calculations”. In: *Radiation Physics and Chemistry* 50.1. Inelastic Scattering of X-Rays and Gamma Rays, pp. 3–29. ISSN: 0969-806X. DOI: [https://doi.org/10.1016/S0969-806X\(97\)00022-4](https://doi.org/10.1016/S0969-806X(97)00022-4). URL: <http://www.sciencedirect.com/science/article/pii/S0969806X97000224> (cit. on p. 75).
- Bert, C., S. O. Grözinger, and E. Rietzel (2008). “Quantification of interplay effects of scanned particle beams and moving targets”. In: *Physics in Medicine & Biology* 53.9, p. 2253. URL: <http://stacks.iop.org/0031-9155/53/i=9/a=003> (cit. on p. 31).
- Bert, C. and K. Herfarth (2017). “Management of organ motion in scanned ion beam therapy”. In: *Radiation Oncology (London, England)* 12, p. 170. DOI: 10.1186/s13014-017-0911-z. URL: <http://www.ncbi.nlm.nih.gov/pmc/articles/PMC5674859/> (cit. on p. 32).
- Bertini, H. W., T. A. Gabriel, R. T. Santoro, O. W. Hermann, N. M. Larson, and J. M. Hunt (1974). “HIC-1: a first approach to the calculation of heavy-ion reactions at energies greater than or equal to 50 MeV/nucleon”. In: ORNL-TM-4134 (cit. on p. 12).
- Bethe, H. (1930). “Zur Theorie des Durchgangs schneller Korpuskularstrahlen durch Materie”. In: *Annalen der Physik* 397.3, pp. 325–400. DOI: 10.1002/andp.19303970303. eprint: <https://onlinelibrary.wiley.com/doi/pdf/10.1002/andp.19303970303>. URL: <https://onlinelibrary.wiley.com/doi/abs/10.1002/andp.19303970303> (cit. on p. 8).
- Bhat, M. R. (1992). *Evaluated Nuclear Structure Data File (ENSDF), Nuclear Data for Science and Technology, page 817*, edited by S. M. Qaim (SpringerVerlag, Berlin, Germany, 1992). URL: <https://www.nndc.bnl.gov/> (visited on 03/27/2017) (cit. on p. 174).
- Bichsel, H. (2013). “Chapter One - Stochastics of Energy Loss and Biological Effects of Heavy Ions in Radiation Therapy”. In: *Theory of Heavy Ion Collision Physics in Hadron Therapy*. Vol. 65. Advances in Quantum Chemistry. Academic Press, pp. 1–38. DOI: <https://doi.org/10.1016/B978-0-12-396455-7.00001-7>. URL: <http://www.sciencedirect.com/science/article/pii/B9780123964557000017> (cit. on p. 6).
- Bischel, H. and T. Hiraoka (1992). “Energy loss of 70 MeV protons in elements”. In: *Nuclear Instruments and Methods in Physics Research Section B: Beam Interactions with Materials and Atoms* 66.3, pp. 345–351. ISSN: 0168-583X. DOI: [https://doi.org/10.1016/0168-583X\(92\)95995-4](https://doi.org/10.1016/0168-583X(92)95995-4). URL: <http://www.sciencedirect.com/science/article/pii/0168583X92959954> (cit. on p. 36).
- Bisogni, M. G., A. Attili, G. Battistoni, N. Belcari, N. Camarlinghi, P. Cerello, S. Coli, A. Del Guerra, A. Ferrari, V. Ferrero, E. Fiorina, G. Giraudo, E. Kostara, M. Morrocchi, F. Pennazio, C. Peroni, M. A. Piliero, G. Pirrone, A. Rivetti, M. D. Rolo, V. Rosso, P. Sala, G. Sportelli, and R. Whealon (Jan. 2017). “INSIDE in-beam positron emission tomography system for particle range monitoring in hadrontherapy.” In: *J Med Imaging (Bellingham)* 4.1, p. 011005 (cit. on p. 47).

- Black, R. D., C. W. Scarantino, G. G. Mann, M. S. Anscher, R. D. Ornitz, and B. E. Nelms (Sept. 2005). “An analysis of an implantable dosimeter system for external beam therapy.” In: *Int J Radiat Oncol Biol Phys* 63.1, pp. 290–300 (cit. on p. 50).
- Blahd, W. H. (Aug. 1996). “Ben Cassen and the development of the rectilinear scanner.” In: *Semin Nucl Med* 26.3, pp. 165–170 (cit. on p. 53).
- Blakely, E. A. and P. Y. Chang (2009). “Biology of charged particles.” eng. In: *Cancer J* 15.4, pp. 271–284. DOI: 10.1097/PPO.0b013e3181b666c5 (cit. on p. 5).
- Blakely, E. A., F. Q. H. Ngo, S. B. Curtis, and C. A. Tobias (1984). “Heavy-Ion Radiobiology: Cellular Studies”. In: *Advances in Radiation Biology*. Ed. by J. T. Lett. Vol. 11. Advances in Radiation Biology. Elsevier, pp. 295–389. DOI: <https://doi.org/10.1016/B978-0-12-035411-5.50013-7>. URL: <http://www.sciencedirect.com/science/article/pii/B9780120354115500137> (cit. on pp. 17, 19).
- Bloch, F. (1933). “Zur Bremsung rasch bewegter Teilchen beim Durchgang durch Materie”. In: *Annalen der Physik* 408.3, pp. 285–320. DOI: 10.1002/andp.19334080303. eprint: <https://onlinelibrary.wiley.com/doi/pdf/10.1002/andp.19334080303>. URL: <https://onlinelibrary.wiley.com/doi/abs/10.1002/andp.19334080303> (cit. on p. 8).
- Bohr, N. (1915). “On the decrease of velocity of swiftly moving electrified particles in passing through matter”. In: *The London, Edinburgh, and Dublin Philosophical Magazine and Journal of Science* 30.178, pp. 581–612. DOI: 10.1080/14786441008635432. eprint: <https://doi.org/10.1080/14786441008635432>. URL: <https://doi.org/10.1080/14786441008635432> (cit. on p. 10).
- Boltwood, B. B. and E. Rutherford (1911). “LV. Production of helium by radium”. In: *The London, Edinburgh, and Dublin Philosophical Magazine and Journal of Science* 22.130, pp. 586–604. DOI: 10.1080/14786441008637154. eprint: <https://doi.org/10.1080/14786441008637154>. URL: <https://doi.org/10.1080/14786441008637154> (cit. on p. 55).
- Bothe, W. (Jan. 1921). “Das allgemeine Fehlergesetz, die Schwankungen der Feldstärke in einem Dielektrikum und die Zerstreuung dera α -Strahlen”. In: *Zeitschrift für Physik* 5.1, pp. 63–69. DOI: 10.1007/BF01349687. URL: <https://doi.org/10.1007/BF01349687> (cit. on p. 11).
- Braccini, S. (2010). “Scientific and technological development of hadrontherapy”. In: *Astroparticle, Particle and Space Physics, Detectors and Medical Physics Applications*, pp. 598–609. DOI: 10.1142/9789814307529_0099. eprint: https://www.worldscientific.com/doi/pdf/10.1142/9789814307529_0099. URL: https://www.worldscientific.com/doi/abs/10.1142/9789814307529_0099 (cit. on p. 20).
- Braccini, S., A. Ereditato, I. Kreslo, U. Moser, C. Pistillo, S. Studer, P. Scampoli, A. Coray, and E. Pedroni (2010). “First results on proton radiography with nuclear emulsion detectors”. In: *Journal of Instrumentation* 5.09, P09001. URL: <http://stacks.iop.org/1748-0221/5/i=09/a=P09001> (cit. on p. 40).
- Bragg, W. H. M. A. and R. Kleeman (1904). “On the ionization curves of radium”. In: *The London, Edinburgh, and Dublin Philosophical Magazine and Journal of Science* 8.48, pp. 726–738. DOI:

- 10.1080/14786440409463246. eprint: <https://doi.org/10.1080/14786440409463246>. URL: <https://doi.org/10.1080/14786440409463246> (cit. on pp. 6, 146).
- Bragg, W. H. M. A. and R. Kleeman (1905). “On the α particles of radium, and their loss of range in passing through various atoms and molecules”. In: *The London, Edinburgh, and Dublin Philosophical Magazine and Journal of Science* 10.57, pp. 318–340. DOI: 10.1080/14786440509463378. eprint: <https://doi.org/10.1080/14786440509463378>. URL: <https://doi.org/10.1080/14786440509463378> (cit. on pp. 6, 10).
- Brahme, A. (2004). “Recent advances in light ion radiation therapy”. In: *International Journal of Radiation Oncology Biology Physics* 58.2, pp. 603–616. DOI: 10.1016/j.ijrobp.2003.09.034. URL: <http://dx.doi.org/10.1016/j.ijrobp.2003.09.034> (cit. on p. 5).
- Braunn, B. (Nov. 2010). “ ^{12}C fragmentation at 95 MeV per nucleon for hadrontherapy. Experimental study and simulation with thick PMMA targets.” Theses. Université de Caen. URL: <https://tel.archives-ouvertes.fr/tel-00536121> (cit. on p. 15).
- Braunn, B., M. Labalme, G. Ban, M. Chevallier, J. Colin, D. Cussol, D. Dauvergne, J. M. Fontbonne, F. Haas, A. Guertin, D. Lebhertz, F. Le Foulher, C. Pautard, C. Ray, M. Rousseau, M. D. Salsac, L. Stuttge, É. Testa, and M. Testa (2011). “Nuclear reaction measurements of 95MeV/u ^{12}C interactions on PMMA for hadrontherapy”. In: *Nuclear Instruments and Methods in Physics Research Section B: Beam Interactions with Materials and Atoms* 269.22, pp. 2676–2684. ISSN: 0168-583X. DOI: <https://doi.org/10.1016/j.nimb.2011.08.010>. URL: <http://www.sciencedirect.com/science/article/pii/S0168583X11007865> (cit. on p. 15).
- Breton, D., E. Delagnes, J. Maalmi, and P. Rusquart (May 2014). “The WaveCatcher family of SCA-based 12-bit 3.2-GS/s fast digitizers”. In: *2014 19th IEEE-NPSS Real Time Conference*, pp. 1–8. DOI: 10.1109/RTC.2014.7097545 (cit. on p. 110).
- Brix, G., J. Zaers, L.-E. Adam, M. E. Bellemann, H. Ostertag, H. Trojan, U. Haberkorn, J. Doll, F. Oberdorfer, and W. Lorenz (1997). “Performance Evaluation of a Whole-Body PET Scanner Using the NEMA Protocol”. In: *Journal of Nuclear Medicine* 38.10, pp. 1614–1623. eprint: <http://jnm.snmjournals.org/content/38/10/1614.full.pdf+html>. URL: <http://jnm.snmjournals.org/content/38/10/1614.short> (cit. on p. 88).
- Brun, R. and F. Rademakers (1997). “ROOT: An object oriented data analysis framework”. In: *Nucl. Instrum. Meth.* A389, pp. 81–86. DOI: 10.1016/S0168-9002(97)00048-X (cit. on pp. 103, 106, 112).
- Brunner, S. E., L. Gruber, A. Hirtl, K. Suzuki, J. Marton, and D. R. Schaart (2016). “A comprehensive characterization of the time resolution of the Philips Digital Photon Counter”. In: *Journal of Instrumentation* 11.11, P11004. URL: <http://stacks.iop.org/1748-0221/11/i=11/a=P11004> (cit. on p. 139).
- Bucciantonio, M. (2015). “Development of an advanced Proton Range Radiography system for hadrontherapy”. PhD thesis. Albert Einstein Center for Fundamental Physics - Laboratorium für Hochenergiephysik - Physikalisches Institut - Universität Bern (cit. on pp. 39, 49).

- Bucciantonio, M.**, U. Amaldi, R. Kieffer, F. Sauli, and D. A. Watts (2013). “Development of a fast proton range radiography system for quality assurance in hadrontherapy”. In: *Nuclear Instruments and Methods in Physics Research Section A: Accelerators, Spectrometers, Detectors and Associated Equipment* 732. Vienna Conference on Instrumentation 2013, pp. 564–567. ISSN: 0168-9002. DOI: <https://doi.org/10.1016/j.nima.2013.05.110>. URL: <http://www.sciencedirect.com/science/article/pii/S0168900213007213> (cit. on p. 39).
- Bucciantonio, M.** and F. Sauli (2015). “Proton computed tomography”. In: *Mod. Phys. Lett.* A30.17, p. 1540024. DOI: 10.1142/S0217732315400246 (cit. on p. 37).
- Buitenhuis, H. J. T.**, F. Diblen, K. W. Brzezinski, S. Brandenburg, and P. Dendooven (June 2017). “Beam-on imaging of short-lived positron emitters during proton therapy.” In: *Phys Med Biol* 62.12, pp. 4654–4672 (cit. on p. 47).
- Cachemiche, J.-P.**, P. Y. Duval, F. Hachon, R. Le Gac, and F. Réthoré (Sept. 2012). “xTCA developments in Marseille for the LHCb Readout”. In: *TWEPP 2012 Topical Workshop on Electronics for Particle Physics*. Oxford, United Kingdom. URL: <http://hal.in2p3.fr/in2p3-00757616> (cit. on p. 100).
- Camarlinghi, N.**, G. Sportelli, G. Battistoni, N. Belcari, M. Cecchetti, G. A. P Cirrone, G. Cuttone, S. Ferretti, A. C. Kraan, A. Retico, F. Romano, P. Sala, K. Straub, A. Tramontana, A. Del Guerra, and V. Rosso (2014). “An in-beam PET system for monitoring ion-beam therapy: test on phantoms using clinical 62 MeV protons”. In: *Journal of Instrumentation* 9.04, p. C04005. URL: <http://stacks.iop.org/1748-0221/9/i=04/a=C04005> (cit. on p. 47).
- Cambraia Lopes, P.**, J. Bauer, A. Salomon, I. Rinaldi, V. Tabacchini, T. Tessonniere, P. Crespo, K. Parodi, and D. R. Schaart (Aug. 2016). “First in situ TOF-PET study using digital photon counters for proton range verification.” In: *Phys Med Biol* 61.16, pp. 6203–6230 (cit. on p. 47).
- Cantor, D.** (Apr. 1988). “Pioneers and early years. A history of British radiology”. In: *Medical History* 32.2, pp. 224–224. URL: <http://www.ncbi.nlm.nih.gov/pmc/articles/PMC1139872/> (cit. on p. 4).
- Caporaso, G. J.**, Y.-J. Chen, and S. E. Sampayan (2009). “The Dielectric Wall Accelerator”. In: *Reviews of Accelerator Science and Technology* 02.01, pp. 253–263. DOI: 10.1142/S1793626809000235. URL: <https://doi.org/10.1142/S1793626809000235> (cit. on p. 23).
- Carnicer, A.**, V. Letellier, G. Rucka, G. Angellier, W. Sauerwein, and J. Hérault (Oct. 2014). “An indirect in vivo dosimetry system for ocular proton therapy”. In: *Radiation protection dosimetry* 161.1-4, pp. 373–376. ISSN: 0144-8420. DOI: 10.1093/rpd/nct284. URL: <https://doi.org/10.1093/rpd/nct284> (cit. on p. 16).
- Castro, J. R.** (1995). “Results of heavy ion radiotherapy.” eng. In: *Radiat Environ Biophys* 34.1, pp. 45–48 (cit. on p. 19).
- Catterall, M.**, C. Rogers, R. H. Thomlinson, and S. B. Field (1971). “An investigation into the clinical effects of fast neutrons”. In: *The British Journal of Radiology* 44.524. PMID: 4997649,

- pp. 603–611. doi: 10.1259/0007-1285-44-524-603. eprint: <https://doi.org/10.1259/0007-1285-44-524-603>. URL: <https://doi.org/10.1259/0007-1285-44-524-603> (cit. on p. 20).
- Cecchin, D.**, D. Poggiali, L. Riccardin, P. Turco, F. Bui, and S. De Marchi (2015). “Analytical and experimental FWHM of a gamma camera: theoretical and practical issues.” In: *PeerJ* 3:e722 (cit. on p. 184).
- Chatterjee, A.**, E. L. Alpen, C. A. Tobias, J. Llacer, and J. Alonso (1981). “High energy beams of radioactive nuclei and their biomedical applications”. In: *International Journal of Radiation Oncology*Biology*Physics* 7.4, pp. 503–507. ISSN: 0360-3016. doi: [https://doi.org/10.1016/0360-3016\(81\)90137-1](https://doi.org/10.1016/0360-3016(81)90137-1). URL: <http://www.sciencedirect.com/science/article/pii/0360301681901371> (cit. on p. 44).
- Chen, X.** (2017). “Développement de cartes Front-End avec leur firmware associé pour un hodoscope de faisceau et un diffuseur silicium utilisées pour le contrôle de dose en ligne en hadronthérapie.” Mémoire for CNAM engineer degree in Electronic Systems (cit. on pp. 87, 98).
- Cherry, S. R.**, Y. Shao, R. W. Silverman, K. Meadors, S. Siegel, A. Chatzioannou, J. W. Young, W. Jones, J. C. Moyers, D. Newport, A. Boutefnouchet, T. H. Farquhar, M. Andreaco, M. J. Paulus, D. M. Binkley, R. Nutt, and M. E. Phelps (1997). “MicroPET: a high resolution PET scanner for imaging small animals”. In: *IEEE Transactions on Nuclear Science* 44.3, pp. 1161–1166. ISSN: 0018-9499. doi: 10.1109/23.596981 (cit. on p. 63).
- Chesler, D. A.** (1971). “Three-dimensional activity distribution from multiple positron scintigraphs”. In: *Journal of Nuclear Medicine* 12, pp. 347–348 (cit. on p. 61).
- Chu, W. T.**, B. A. Ludewigt, and T. R. Renner (1993). “Instrumentation for treatment of cancer using proton and light-ion beams”. In: *Review of Scientific Instruments* 64.8, pp. 2055–2122. doi: 10.1063/1.1143946. eprint: <https://doi.org/10.1063/1.1143946>. URL: <https://doi.org/10.1063/1.1143946> (cit. on p. 37).
- Chvetsov, A. V.** and S. L. Paige (Mar. 2010). “The influence of CT image noise on proton range calculation in radiotherapy planning.” In: *Phys Med Biol* 55.6, N141–9 (cit. on pp. 34, 36).
- Cirrone, G. P.**, G. Cuttone, R. A. Lojacono, S. Lo Nigro, V. Mongelli, I. V. Patti, G. Privitera, L. Raffaele, D. Rifuggiato, M. G. Sabini, V. Salamone, C. Spatola, and L. M. Valastro (Oct. 2003). “A 62 MeV proton beam for the treatment of ocular melanoma at Laboratori Nazionali del Sud-INFN (CATANIA)”. In: *2003 IEEE Nuclear Science Symposium. Conference Record (IEEE Cat. No.03CH37515)*. Vol. 5, 3658–3662 Vol.5. doi: 10.1109/NSSMIC.2003.1352701 (cit. on p. 46).
- Colléaux, C.** and É. Testa (2018). “Caractérisation d’un détecteur.” Bachelor internship report (cit. on p. 136).
- Compton, A. H.** (May 1923). “A Quantum Theory of the Scattering of X-rays by Light Elements”. In: *Phys. Rev.* 21 (5), pp. 483–502. doi: 10.1103/PhysRev.21.483. URL: <https://link.aps.org/doi/10.1103/PhysRev.21.483> (cit. on p. 72).

- Cookson, J. A. (May 1974). “Radiography with protons”. In: *Naturwissenschaften* 61.5, pp. 184–191. ISSN: 1432-1904. DOI: 10.1007/BF00599915. URL: <https://doi.org/10.1007/BF00599915> (cit. on p. 37).
- Cormack, A. M. (1963). “Representation of a Function by Its Line Integrals, with Some Radiological Applications”. In: *Journal of Applied Physics* 34.9, pp. 2722–2727. DOI: 10.1063/1.1729798. eprint: <https://doi.org/10.1063/1.1729798>. URL: <https://doi.org/10.1063/1.1729798> (cit. on p. 37).
- Cormack, A. M. and A. M. Koehler (1976). “Quantitative proton tomography: preliminary experiments”. In: *Physics in Medicine & Biology* 21.4, p. 560. URL: <http://stacks.iop.org/0031-9155/21/i=4/a=007> (cit. on p. 37).
- Coudurier, V. (2015). “Caractérisation d’un hodoscope de faisceau pour l’hadronthérapie”. Master internship report (cit. on pp. 132, 142).
- Crandall, P. H. and B. Cassen (Aug. 1966). “High speed section scanning of the brain.” In: *Arch Neurol* 15.2, pp. 163–171 (cit. on p. 65).
- Cree, M. J. and P. J. Bones (June 1994). “Towards direct reconstruction from a gamma camera based on Compton scattering”. In: *IEEE Transactions on Medical Imaging* 13.2, pp. 398–407. DOI: 10.1109/42.293932 (cit. on p. 78).
- Crespo, P., G. Shakirin, and W. Enghardt (2006). “On the detector arrangement for in-beam PET for hadron therapy monitoring”. In: *Physics in Medicine & Biology* 51.9, p. 2143. URL: <http://stacks.iop.org/0031-9155/51/i=9/a=002> (cit. on pp. 43, 44, 46).
- Crespo, P., G. Shakirin, F. Fiedler, W. Enghardt, and A. Wagner (Dec. 2007). “Direct time-of-flight for quantitative, real-time in-beam PET: a concept and feasibility study.” In: *Phys Med Biol* 52.23, pp. 6795–6811 (cit. on p. 43).
- Cunha, M., C. Monini, É. Testa, and M. Beuve (Feb. 2017). “NanOx, a new model to predict cell survival in the context of particle therapy.” In: *Phys Med Biol* 62.4, pp. 1248–1268 (cit. on p. 31).
- Curie, P. and S. Curie (1898). “Sur une substance nouvelle radio-active, contenue dans la pechblende”. In: *Comptes Rendus Hebdomadaires des Séances de l’Académie. des Sciences* 127, pp. 175–178 (cit. on p. 55).
- Dahiya, M. (Apr. 2016). “BRACHYTHERAPY: A REVIEW”. In: 3, pp. 6–10 (cit. on p. 55).
- Dahoumane, M., D. Dauvergne, J. Krimmer, J.-L. Ley, É. Testa, and Y. Zoccarato (Nov. 2014). “A low noise and high dynamic range CMOS integrated Electronics associated with double sided Silicon Strip Detectors for a Compton camera gamma-ray detecting system”. In: *2014 IEEE Nuclear Science Symposium and Medical Imaging Conference (NSS/MIC)*, pp. 1–6. DOI: 10.1109/NSSMIC.2014.7431122 (cit. on p. 86).
- Dahoumane, M., D. Dauvergne, J. Krimmer, H. Mathez, C. Ray, É. Testa, A. H. Walenta, and Y. Zoccarato (Oct. 2012). “A low noise and high dynamic charge sensitive amplifier-shaper

- associated with Silicon Strip Detector for compton camera in hadrontherapy". In: *2012 IEEE Nuclear Science Symposium and Medical Imaging Conference Record (NSS/MIC)*, pp. 1445–1451. DOI: 10.1109/NSSMIC.2012.6551351 (cit. on p. 87).
- Dauvergne, D., M. Battaglia, G. Montarou, and É. Testa (Mar. 2009). "New methods of real-time control imaging for ion therapy". In: (cit. on p. 49).
- Degenhardt, C., P. Rodrigues, A. Trindade, B. Zwaans, O. Mülhens, R. Dorscheid, A. Thon, A. Salomon, and T. Frach (Oct. 2012). "Performance evaluation of a prototype Positron Emission Tomography scanner using Digital Photon Counters (DPC)". In: *2012 IEEE Nuclear Science Symposium and Medical Imaging Conference Record (NSS/MIC)*, pp. 2820–2824. DOI: 10.1109/NSSMIC.2012.6551643 (cit. on p. 47).
- Degiovanni, A. and U. Amaldi (2015). "History of hadron therapy accelerators". In: *Physica Medica* 31.4, pp. 322–332. ISSN: 1120-1797. DOI: <https://doi.org/10.1016/j.ejmp.2015.03.002>. URL: <http://www.sciencedirect.com/science/article/pii/S1120179715000629> (cit. on p. 20).
- Dendooven, P., H. J. T. Buitenhuis, F. Diblen, P. N. Heeres, A. K. Biegun, F. Fiedler, M.-J. van Goethem, E. R. van der Graaf, and S. Brandenburg (Dec. 2015). "Short-lived positron emitters in beam-on PET imaging during proton therapy." In: *Phys Med Biol* 60.23, pp. 8923–8947 (cit. on p. 47).
- Deng, S.-M. (2012). "Etude de conception d'ASICs de lecture et d'étiquetage en temps associés à des photomultiplicateurs pour un hodoscope de faisceau en hadronthérapie". PhD thesis. École Doctorale EEA (Électronique, Électrotechnique et Automatique), Université Claude Bernard - Lyon 1 (cit. on p. 97).
- Deng, S.-M., H. Mathez, D. Dauvergne, G.-N. Lu, and Y. Zoccarato (2012). "Front-end multi-channel PMT-associated readout chip for hodoscope application". In: *Nuclear Instruments and Methods in Physics Research Section A: Accelerators, Spectrometers, Detectors and Associated Equipment* 695. New Developments in Photodetection NDIP11, pp. 390–393. ISSN: 0168-9002. DOI: <https://doi.org/10.1016/j.nima.2011.11.042>. URL: <http://www.sciencedirect.com/science/article/pii/S0168900211020845> (cit. on p. 97).
- Deng, S.-M., H. Mathez, D. Dauvergne, Y. Zoccarato, and G.-N. Lu (Jan. 2013). "Very fast front end ASIC associated with multi-anode PMTs for a scintillating-fibre beam hodoscope". In: *Journal of Instrumentation* 8, p. C01047. DOI: 10.1088/1748-0221/8/01/C01047. URL: <https://hal.archives-ouvertes.fr/hal-00990850> (cit. on p. 97).
- Despeignes, V. (1896). "Observations on a case of cancer of the stomach treated by Röntgen rays." In: *Lyon Medical Journal* 82, p. 428 (cit. on p. 4).
- Dowdell, S., C. Grassberger, G. C. Sharp, and H. Paganetti (2013). "Interplay effects in proton scanning for lung: a 4D Monte Carlo study assessing the impact of tumor and beam delivery parameters". In: *Physics in Medicine & Biology* 58.12, p. 4137. URL: <http://stacks.iop.org/0031-9155/58/i=12/a=4137> (cit. on p. 35).

- Draeger, E., S. Peterson, D. Mackin, H. Chen, S. Beddar, and J. C. Polf (2017). “Feasibility Studies of a New Event Selection Method to Improve Spatial Resolution of Compton Imaging for Medical Applications.” eng. In: *IEEE Trans Radiat Plasma Med Sci* 1.4, pp. 358–367. DOI: 10.1109/TRPMS.2017.2703095 (cit. on pp. 148, 155, 169).
- Duck, F. A. (June 2014). “The origins of medical physics”. In: *Physica Medica: European Journal of Medical Physics* 30.4, pp. 397–402. DOI: 10.1016/j.ejmp.2014.03.005. URL: <http://dx.doi.org/10.1016/j.ejmp.2014.03.005> (cit. on p. 4).
- DuMond, J. W. M. (1928). “The Structure of the Compton Shifted Line”. In: *Proceedings of the National Academy of Sciences of the United States of America* 14.11, pp. 875–878. URL: <http://www.jstor.org/stable/85639> (cit. on p. 75).
- DuMond, J. W. M. (May 1929). “Compton Modified Line Structure and its Relation to the Electron Theory of Solid Bodies”. In: *Phys. Rev.* 33 (5), pp. 643–658. DOI: 10.1103/PhysRev.33.643. URL: <https://link.aps.org/doi/10.1103/PhysRev.33.643> (cit. on p. 75).
- Durante, M. and J. S. Loeffler (Dec. 2009). “Charged particles in radiation oncology”. In: *Nature Reviews Clinical Oncology* 7, p. 37. URL: <http://dx.doi.org/10.1038/nrclinonc.2009.183> (cit. on pp. 5, 19).
- Durante, M. and H. Paganetti (2016). “Nuclear physics in particle therapy: a review”. In: *Reports on Progress in Physics* 79.9, p. 096702. URL: <http://stacks.iop.org/0034-4885/79/i=9/a=096702> (cit. on pp. 5–7, 10, 12, 13, 18, 20, 25, 35, 36).
- Elftmann, R., J. Tammen, S. R. Kulkarni, C. Martin, S. Böttcher, and R. Wimmer-Schweingruber (2015). “Characterization of an LSO scintillator for space applications”. In: *Journal of Physics: Conference Series* 632.1, p. 012006. URL: <http://stacks.iop.org/1742-6596/632/i=1/a=012006> (cit. on p. 88).
- Elsässer, T., W. K. Weyrather, T. Friedrich, M. Durante, G. Iancu, M. Krämer, G. Kragl, S. Brons, M. Winter, K.-J. Weber, and M. Scholz (2004). “Quantification of the Relative Biological Effectiveness for Ion Beam Radiotherapy: Direct Experimental Comparison of Proton and Carbon Ion Beams and a Novel Approach for Treatment Planning”. In: *International Journal of Radiation Oncology Biology Physics* 78.4, pp. 1177–1183. DOI: 10.1016/j.ijrobp.2010.05.014. URL: <http://dx.doi.org/10.1016/j.ijrobp.2010.05.014> (cit. on p. 146).
- Engelsman, M., M. Schwarz, and L. Dong (2013). “Physics Controversies in Proton Therapy”. In: *Seminars in Radiation Oncology* 23.2. Controversies in Proton Therapy, pp. 88–96. ISSN: 1053-4296. DOI: <https://doi.org/10.1016/j.semradonc.2012.11.003>. URL: <http://www.sciencedirect.com/science/article/pii/S1053429612001063> (cit. on p. 31).
- Enghardt, W., P. Crespo, F. Fiedler, R. Hinz, K. Parodi, J. Pawelke, and F. Pönisch (2004). “Charged hadron tumour therapy monitoring by means of PET”. In: *Nuclear Instruments and Methods in Physics Research Section A: Accelerators, Spectrometers, Detectors and Associated Equipment* 525.1. Proceedings of the International Conference on Imaging Techniques in Subatomic Physics, Astrophysics, Medicine, Biology and Industry, pp. 284–288. ISSN: 0168-9002. DOI: <https://doi.org/10.1016/j.nima.2004.03.128>. URL: <http://www.sciencedirect.com/science/article/pii/S0168900204004218> (cit. on pp. 44, 45, 48, 146).

- Enghardt, W., W. D. Fromm, H. Geissel, H. Heller, G. Kraft, A. Magel, P. Manfrass, G. Munzenberg, F. Nickel, J. Pawelke, D. Schardt, C. Scheidenberger, and M. Sobiella (1992). "The spatial distribution of positron-emitting nuclei generated by relativistic light ion beams in organic matter". In: *Physics in Medicine & Biology* 37.11, p. 2127. URL: <http://stacks.iop.org/0031-9155/37/i=11/a=009> (cit. on p. 45).
- España, S. and H. Paganetti (Dec. 2010). "The impact of uncertainties in the CT conversion algorithm when predicting proton beam ranges in patients from dose and PET-activity distributions." In: *Physics in Medicine & Biology* 55.24, pp. 7557–7571 (cit. on p. 36).
- España, S. and H. Paganetti (2011a). "Uncertainties in planned dose due to the limited voxel size of the planning CT when treating lung tumors with proton therapy". In: *Physics in Medicine & Biology* 56.13, p. 3843. URL: <http://stacks.iop.org/0031-9155/56/i=13/a=007> (cit. on p. 34).
- España, S., X. Zhu, J. Daartz, G. El Fakhri, T. Bortfeld, and H. Paganetti (May 2011b). "Reliability of proton-nuclear interaction cross section data to predict proton-induced PET images in proton therapy". In: *Physics in medicine and biology* 56.9, pp. 2687–2698 (cit. on p. 40).
- Essers, M. and B. Mijnheer (Feb. 1999). "In vivo dosimetry during external photon beam radiotherapy". In: 43, pp. 245–59 (cit. on p. 50).
- Evans, T. C. (1951). "X-Ray Treatment-Its Origin, Birth and Early History. Emil H. Grubbe". In: *The Quarterly Review of Biology* 26.2, pp. 223–223. DOI: 10.1086/398163. eprint: <https://doi.org/10.1086/398163>. URL: <https://doi.org/10.1086/398163> (cit. on p. 4).
- Everett, D. B., J. S. Fleming, R. W. Todd, and J. M. Nightingale (1977). "Gamma-radiation imaging system based on the Compton effect". In: *Proceedings of the Institution of Electrical Engineers* 124.11, p. 995. ISSN: 0020-3270. DOI: 10.1049/piee.1977.0203 (cit. on p. 172).
- Fattori, G., M. Riboldi, E. Scifoni, M. Krämer, A. Pella, M. Durante, S. Ronchi, M. Bonora, R. Orecchia, and G. Baroni (2014). "Dosimetric effects of residual uncertainties in carbon ion treatment of head chordoma". In: *Radiotherapy and Oncology* 113.1, pp. 66–71. ISSN: 0167-8140. DOI: <https://doi.org/10.1016/j.radonc.2014.08.001>. URL: <http://www.sciencedirect.com/science/article/pii/S0167814014003223> (cit. on p. 35).
- Fermi, E. (1950). "High Energy Nuclear Events". In: *Progress of Theoretical Physics* 5.4, pp. 570–583. DOI: 10.1143/ptp/5.4.570. eprint: [/oup/backfile/content_public/journal/ptp/5/4/10.1143/ptp/5.4.570/2/5-4-570.pdf](http://oup/backfile/content_public/journal/ptp/5/4/10.1143/ptp/5.4.570/2/5-4-570.pdf). URL: <http://dx.doi.org/10.1143/ptp/5.4.570> (cit. on p. 12).
- Ferrero, V., E. Fiorina, M. Morrocchi, F. Pennazio, G. Baroni, G. Battistoni, N. Belcari, N. Camarlinghi, M. Ciocca, A. Del Guerra, M. Donetti, S. Giordanengo, G. Giraudo, V. Patera, C. Peroni, A. Rivetti, M. D. R. Rolo, S. Rossi, V. Rosso, G. Sportelli, S. Tampellini, F. Valvo, R. Wheaton, P. Cerello, and M. G. Bisogni (2018). "Online proton therapy monitoring: clinical test of a Silicon-photodetector-based in-beam PET". In: *Scientific Reports* 8.1, p. 4100 (cit. on p. 47).
- Fiedler, F., D. Kunath, M. Priegnitz, and W. Enghardt (Jan. 2012). "Online Irradiation Control by means of PET". In: (cit. on p. 42).

- Fiedler, F., M. Priegnitz, R. Julich, J. Pawelke, P. Crespo, K. Parodi, F. Pönisch, and W. Enghardt (2008a). “In-beam PET measurements of biological half-lives of ^{12}C irradiation induced β^+ -activity.” In: *Acta Oncol* 47.6, pp. 1077–1086 (cit. on p. 41).
- Fiedler, F., M. Priegnitz, D. Möckel, J. Pawelke, K. Parodi, F. Pönisch, W. Enghardt, and G. Shakirin (2008b). “Results of a 20 minutes decay measurement of a patient irradiation by the in-beam PET scanner”. In: *GSI Scientific Report* 380 (cit. on p. 43).
- Fiedler, F., G. Shakirin, J. Skowron, H. Braess, P. Crespo, D. Kunath, J. Pawelke, F. Pönisch, and W. Enghardt (Apr. 2010). “On the effectiveness of ion range determination from in-beam PET data.” In: *Phys Med Biol* 55.7, pp. 1989–1998 (cit. on p. 41).
- Finck, C., Y. Karakaya, V. Reithinger, R. Rescigno, J. Baudot, J. Constanzo, D. Juliani, J. Krimmer, I. Rinaldi, M. Rousseau, É. Testa, M. Vanstalle, and C. Ray (Nov. 2017). “Study for online range monitoring with the interaction vertex imaging method.” In: *Phys Med Biol* 62.24, pp. 9220–9239 (cit. on p. 49).
- Fontana, M., D. Dauvergne, J. M. Létang, R. Della Negra, F. Mounier, L. Zanetti, Y. Zoccarato, and É. Testa (2018). “Large surface gamma cameras for medical imaging: characterization of the bismuth germanate blocks”. In: *Journal of Instrumentation* 13.08, P08018. URL: <http://stacks.iop.org/1748-0221/13/i=08/a=P08018> (cit. on pp. 81, 142, 148).
- Fontana, M., D. Dauvergne, J. M. Létang, J.-L. Ley, and É. Testa (2017a). “Compton camera study for high efficiency SPECT and benchmark with Anger system”. In: *Physics in Medicine and Biology* 62.23, p. 8794. URL: <http://stacks.iop.org/0031-9155/62/i=23/a=8794> (cit. on pp. 66, 171).
- Fontana, M., D. Dauvergne, J.-L. Ley, J. M. Létang, V. Maxim, and É. Testa (2017b). “Versatile Compton camera for high energy gamma rays: Monte Carlo comparison with Anger camera for medical imaging”. In: *2nd Jagiellonian Symposium on Fundamental and Applied Subatomic Physics*. Vol. 48. Krakow, Poland, pp. 1639–1645. doi: 10.5506/APhysPolB.48.1639. URL: <https://hal.archives-ouvertes.fr/hal-01609541> (cit. on pp. 66, 165, 171).
- Foray, N. (Nov. 2016). “Victor Despeignes, the Forgotten Pioneer of Radiation Oncology.” eng. In: *Int J Radiat Oncol Biol Phys* 96.4, pp. 717–721. doi: 10.1016/j.ijrobp.2016.07.019 (cit. on p. 4).
- Fossati, P., S. Molinelli, N. Matsufuji, M. Ciocca, A. Mirandola, A. Mairani, J. Mizoe, A. Hasegawa, R. Imai, T. Kamada, R. Orecchia, and H. Tsujii (2012). “Dose prescription in carbon ion radiotherapy: a planning study to compare NIRS and LEM approaches with a clinically-oriented strategy”. In: *Physics in Medicine & Biology* 57.22, p. 7543. URL: <http://stacks.iop.org/0031-9155/57/i=22/a=7543> (cit. on p. 31).
- Francis, Z., E. Seif, S. Incerti, C. Champion, M. Karamitros, M. A. Bernal, V. N. Ivanchenko, A. Mantero, H. N. Tran, and Z. El Bitar (Dec. 2014). “Carbon ion fragmentation effects on the nanometric level behind the Bragg peak depth.” In: *Phys Med Biol* 59.24, pp. 7691–7702 (cit. on p. 15).

- Frandes, M.**, A. Zoglauer, V. Maxim, and R. Prost (2010). “A Tracking Compton-Scattering Imaging System for Hadron Therapy Monitoring”. In: *IEEE Transactions on Nuclear Science* 57.1, pp. 144–150. ISSN: 0018-9499. DOI: 10.1109/TNS.2009.2031679 (cit. on p. 147).
- Friedländer, E. M.** and H. H. Heckman (Apr. 1982). “Relativistic heavy ion collisions: experiment”. In: (cit. on p. 15).
- Friedrich, T.**, U. Scholz, T. Elsässer, M. Durante, and M. Scholz (2012). “Calculation of the biological effects of ion beams based on the microscopic spatial damage distribution pattern”. In: *International Journal of Radiation Biology* 88.1-2, pp. 103–107. DOI: 10.3109/09553002.2011.611213. eprint: <https://doi.org/10.3109/09553002.2011.611213>. URL: <https://doi.org/10.3109/09553002.2011.611213> (cit. on p. 5).
- Gaglione, R.** (2013). “Electronique d’acquisition d’une gamma-caméra.” PhD thesis. École Doctorale Sciences pour l’ingénieur de Clermont-Ferrand (cit. on pp. 130, 142).
- Gallin-Martel, M.-L.**, Abbassi, L., Bes, A., Bosson, G., Collot, J., Crozes, T., Curtoni, S., Dauvergne, D., De Nolf, W., Fontana, M., Gallin-Martel, L., Hostachy, J.-Y., Krimmer, J., Lacoste, A., Marcatili, S., Morse, J., Motte, J.-F., Muraz, J.-F., Rarbi, F. E., Rossetto, O., Salomé, M., Testa, É., Vuïart, R., and Yamouni, M. (2018). “A large area diamond-based beam tagging hodoscope for ion therapy monitoring”. In: *EPJ Web Conf.* 170, p. 09005. DOI: 10.1051/epjconf/201817009005. URL: <https://doi.org/10.1051/epjconf/201817009005> (cit. on p. 141).
- Gallin-Martel, M.-L.**, A. Bes, A. Boukhémiri, G. Bosson, J. Collot, D. Dauvergne, M. Fontana, L. Gallin-Martel, A. Gorecki, J.-Y. Hostachy, J. Krimmer, A. Lacoste, S. Marcatili, J. Morse, J.-F. Muraz, F. E. Rarbi, O. Rossetto, M. Salomé, É. Testa, and M. Yamouni (2016). “Large area polycrystalline diamond detectors for online hadron therapy beam tagging applications”. In: *2016 IEEE Nuclear Science Symposium, Medical Imaging Conference and Room-Temperature Semiconductor Detector Workshop (NSS/MIC/RTSD)*, pp. 1–5. DOI: 10.1109/NSSMIC.2016.8069398 (cit. on p. 141).
- Gallo, G.**, D. Lo Presti, D. L. Bonanno, F. Longhitano, D. G. Bongiovanni, S. Reito, N. Randazzo, E. Leonora, V. Sipala, and F. Tommasino (2016). “QBeRT: an innovative instrument for qualification of particle beam in real-time”. In: *Journal of Instrumentation* 11.11, p. C11014. URL: <http://stacks.iop.org/1748-0221/11/i=11/a=C11014> (cit. on p. 39).
- Gariod, R.**, R. Allemand, E. Cormoreche, M. Laval, and M. Moszynski (1982). “The LETI positron tomograph architecture and time of flight improvements.” In: (cit. on p. 44).
- GE Healthcare** (June 2006). “Infinia”. In: Release 2.5 (cit. on pp. 172, 178).
- GeckoDrive** (2010). *G203V stepper drive - data sheet*. REV7. GeckoDrive Motor Controls Inc. (cit. on p. 130).
- Gensheimer, M. F.**, T. I. Yock, N. J. Liebsch, G. C. Sharp, H. Paganetti, N. Madan, P. E. Grant, and T. Bortfeld (Sept. 2010). “In vivo proton beam range verification using spine MRI changes.” In: *Int J Radiat Oncol Biol Phys* 78.1, pp. 268–275 (cit. on p. 50).

- Gerard, S. K. and R. R. Cavalieri (Jan. 2002). “I-123 diagnostic thyroid tumor whole-body scanning with imaging at 6, 24, and 48 hours.” In: *Clin Nucl Med* 27.1, pp. 1–8 (cit. on p. 66).
- Giantsoudi, D., C. Grassberger, D. Craft, A. Niemierko, A. Trofimov, and H. Paganetti (2013). “Linear energy transfer-guided optimization in intensity modulated proton therapy: feasibility study and clinical potential.” eng. In: *Int J Radiat Oncol Biol Phys* 87.1, pp. 216–222. DOI: 10.1016/j.ijrobp.2013.05.013 (cit. on p. 19).
- Gillam, J. E., C. Lacasta, I. Torres-Espallardo, C. Candela Juan, G. Llosá, P. Solevi, J. Barrio, and M. Rafecas (2011). “A Compton imaging algorithm for on-line monitoring in hadron therapy”. In: vol. 7961, pp. 7961–8. DOI: 10.1117/12.877678. URL: <https://doi.org/10.1117/12.877678> (cit. on pp. 78, 156).
- Giovannini, G., T. Bohlen, G. Cabal, J. Bauer, T. Tessonnier, K. Frey, J. Debus, A. Mairani, and K. Parodi (2016). “Variable RBE in proton therapy: comparison of different model predictions and their influence on clinical-like scenarios.” eng. In: *Radiat Oncol* 11, p. 68. DOI: 10.1186/s13014-016-0642-6 (cit. on p. 19).
- Golnik, C. (2015). “Treatment verification in proton therapy based on the detection of prompt gamma-rays.” PhD thesis. TU Dresden and Oncoray (cit. on pp. 109, 138).
- Golovkov, M. S., D. V. Aleksandrov, L. V. Chulkov, G. Kraus, and D. Schardt (Jan. 1997). “Fragmentation of 270 a MeV carbon ions in water”. In: GSI-97-08, 9 p. URL: <https://cds.cern.ch/record/328169> (cit. on p. 15).
- Goodman, G. B., G. K. Y. Lam, R. W. Harrison, M. Bergstrom, W. R. Martin, and B. D. Pate (1986). “The use of positron emission tomography in pion radiotherapy”. In: *International Journal of Radiation Oncology *Biology *Physics* 12.10, pp. 1867–1871 (cit. on p. 44).
- Gottschalk, B. (Dec. 2006). “Neutron dose in scattered and scanned proton beams: in regard to Eric J. Hall (Int J Radiat Oncol Biol Phys 2006;65:1-7).” eng. In: *Int J Radiat Oncol Biol Phys* 66.5, p. 1595. DOI: 10.1016/j.ijrobp.2006.08.014 (cit. on p. 16).
- Gottschalk, B. (Jan. 2010). “On the scattering power of radiotherapy protons.” In: *Med Phys* 37.1, pp. 352–367 (cit. on p. 11).
- Gottschalk, B., A. M. Koehler, R. J. Schneider, J. M. Sisterson, and M. S. Wagner (1993). “Multiple Coulomb scattering of 160 MeV protons”. In: *Nuclear Instruments and Methods in Physics Research Section B: Beam Interactions with Materials and Atoms* 74.4, pp. 467–490. ISSN: 0168-583X. DOI: [https://doi.org/10.1016/0168-583X\(93\)95944-Z](https://doi.org/10.1016/0168-583X(93)95944-Z). URL: <http://www.sciencedirect.com/science/article/pii/0168583X9395944Z> (cit. on p. 11).
- Gottschalk, B. and E. Pedroni (2008). “Treatment delivery systems”. In: *Proton and charged particle radiotherapy*. Vol. chap. 5. T. F. DeLaney, H. M. Kooy (Lippincott Williams, and Wilkins, Philadelphia), pp. 33–49 (cit. on p. 25).
- Graeff, C., R. Lüchtenborg, J. G. Eley, M. Durante, and C. Bert (2013). “A 4D-optimization concept for scanned ion beam therapy”. In: *Radiotherapy and Oncology* 109.3, pp. 419–424.

DOI: 10.1016/j.radonc.2013.09.018. URL: <https://doi.org/10.1016/j.radonc.2013.09.018> (cit. on p. 32).

Grassberger, C., S. Dowdell, G. C. Sharp, and H. Paganetti (May 2015). “Motion mitigation for lung cancer patients treated with active scanning proton therapy.” In: *Med Phys* 42.5, pp. 2462–2469 (cit. on p. 35).

Grassberger, C. and H. Paganetti (2011). “Elevated LET components in clinical proton beams”. In: *Physics in Medicine and Biology* 56.20, p. 6677. URL: <http://stacks.iop.org/0031-9155/56/i=20/a=011> (cit. on p. 15).

Grevillot, L., D. Bertrand, F. Dessy, N. Freud, and D. Sarrut (2011). “A Monte Carlo pencil beam scanning model for proton treatment plan simulation using GATE/GEANT4.” eng. In: *Phys Med Biol* 56.16. DOI: 10.1088/0031-9155/56/16/008 (cit. on p. 151).

Guan, F., L. Bronk, U. Titt, S. H. Lin, D. Mirkovic, M. D. Kerr, X. R. Zhu, J. Dinh, M. Sobieski, C. Stephan, C. R. Peeler, R. Taleei, R. Mohan, and D. R. Grosshans (May 2015). “Spatial mapping of the biologic effectiveness of scanned particle beams: towards biologically optimized particle therapy”. In: *Scientific Reports* 5. URL: <http://dx.doi.org/10.1038/srep09850> (cit. on p. 19).

Gunter, D. L. (2004). “CHAPTER 8 - Collimator Design for Nuclear Medicine”. In: *Emission Tomography*. Ed. by M. N. Wernick and J. N. Aarsvold. San Diego: Academic Press, pp. 153–168. ISBN: 978-0-12-744482-6. DOI: <https://doi.org/10.1016/B978-012744482-6.50011-9>. URL: <http://www.sciencedirect.com/science/article/pii/B9780127444826500119> (cit. on p. 65).

Gunzert-Marx, K., H. Iwase, D. Schardt, and R. S. Simon (2008). “Secondary beam fragments produced by 200 MeV/u ^{12}C ions in water and their dose contributions in carbon ion radiotherapy”. In: *New Journal of Physics* 10.7, p. 075003. URL: <http://stacks.iop.org/1367-2630/10/i=7/a=075003> (cit. on p. 49).

Gwosch, K., B. Hartmann, J. Jakubek, C. Granja, P. Soukup, O. Jäkel, and M. Martisikova (June 2013). “Non-invasive monitoring of therapeutic carbon ion beams in a homogeneous phantom by tracking of secondary ions.” In: *Phys Med Biol* 58.11, pp. 3755–3773 (cit. on p. 49).

Haberer, T., W. Becher, D. Schardt, and G. Kraft (1993). “Magnetic scanning system for heavy ion therapy”. In: *Nuclear Instruments and Methods in Physics Research Section A: Accelerators, Spectrometers, Detectors and Associated Equipment* 330.1, pp. 296–305. ISSN: 0168-9002. DOI: [https://doi.org/10.1016/0168-9002\(93\)91335-K](https://doi.org/10.1016/0168-9002(93)91335-K). URL: <http://www.sciencedirect.com/science/article/pii/016890029391335K> (cit. on p. 27).

Haettner, E., H. Iwase, M. Krämer, G. Kraft, and D. Schardt (2013). “Experimental study of nuclear fragmentation of 200 and 400 MeV/u C ions in water for applications in particle therapy”. In: *Physics in Medicine and Biology* 58.23, p. 8265. URL: <http://stacks.iop.org/0031-9155/58/i=23/a=8265> (cit. on p. 15).

Bibliography

- Haettner, E., H. Iwase, and D. Schardt (2006). “Experimental fragmentation studies with ^{12}C therapy beams”. In: *Radiation Protection Dosimetry* 122.1-4, pp. 485–487. DOI: 10.1093/rpd/ncl402. URL: <http://dx.doi.org/10.1093/rpd/ncl402> (cit. on pp. 14, 15).
- Hall, E. J. and A. J. Giaccia (2012). *Radiobiology for the radiologist*. URL: <http://public.eblib.com/choice/publicfullrecord.aspx?p=2031840> (cit. on p. 17).
- Halperin, E. C. (2006). “Particle therapy and treatment of cancer”. In: *The Lancet Oncology* 7.8, pp. 676–685. DOI: 10.1016/S1470-2045(06)70795-1. URL: [http://dx.doi.org/10.1016/S1470-2045\(06\)70795-1](http://dx.doi.org/10.1016/S1470-2045(06)70795-1) (cit. on p. 5).
- Hamamatsu (1995). *Metal Package Photomultiplier Tube R5600 Series*. TPMH1066E08. Hamamatsu Photonics K. K. (cit. on p. 130).
- Hamamatsu (2006). *Flat Panel Type Multianode Photomultiplier Tube Assembly H8500, H8500B*. TPMH1282E09. Hamamatsu Photonics K. K. (cit. on pp. 95, 130, 135).
- Hamm, R. W., K. R. Crandall, and J. M. Potter (1991). “Preliminary design of a dedicated proton therapy linac”. In: *Conference Record of the 1991 IEEE Particle Accelerator Conference*. DOI: 10.1109/PAC.1991.165037 (cit. on p. 23).
- Han, L., W. L. Rogers, S. S. Huh, and N. Clinthorne (2008). “Statistical performance evaluation and comparison of a Compton medical imaging system and a collimated Anger camera for higher energy photon imaging”. In: *Physics in Medicine and Biology* 53.24, p. 7029. URL: <http://stacks.iop.org/0031-9155/53/j=24/a=002> (cit. on pp. 172, 173, 175, 191).
- Hayakawa, Y., J. Tada, N. Arai, K. Hosono, M. Sato, T. Wagai, H. Tsuji, and H. Tsujii (n.d.). “Acoustic pulse generated in a patient during treatment by pulsed proton radiation beam”. In: *Radiation Oncology Investigations* 3.1 () , pp. 42–45. DOI: 10.1002/roi.2970030107. eprint: <https://onlinelibrary.wiley.com/doi/pdf/10.1002/roi.2970030107>. URL: <https://onlinelibrary.wiley.com/doi/abs/10.1002/roi.2970030107> (cit. on p. 50).
- Hendee, W. R. and R. Ritenour E (2002). *Medical Imaging Physics*. John Wiley & Sons (cit. on p. 55).
- Henriet, P., É. Testa, M. Chevallier, D. Dauvergne, G. Dedes, N. Freud, J. Krimmer, J. M. Létang, C. Ray, M.-H. Richard, and F. Sauli (July 2012). “Interaction vertex imaging (IVI) for carbon ion therapy monitoring: a feasibility study.” In: *Phys Med Biol* 57.14, pp. 4655–4669 (cit. on p. 49).
- Herault, J., N. Iborra, B. Serrano, and P. Chauvel (Apr. 2005). “Monte Carlo simulation of a protontherapy platform devoted to ocular melanoma.” In: *Med Phys* 32.4, pp. 910–919 (cit. on p. 196).
- Hermanns, C. F. (2013). “X-ray absorption studies of metalloporphyrin molecules on surfaces”. PhD thesis. Freie Universität Berlin (cit. on p. 76).
- Hertz, B. (2016). “Dr. Saul Hertz (1905-1950) Discovers the Medical Uses of Radioactive Iodine: The First Targeted Cancer Therapy”. In: *Thyroid Cancer*. Ed. by H. Ahmadzadehfar. Rijeka:

- IntechOpen. Chap. 1. DOI: 10.5772/64609. URL: <https://doi.org/10.5772/64609> (cit. on p. 67).
- Hertz, S. and A. Roberts (Jan. 1942). “RADIOACTIVE IODINE AS AN INDICATOR IN THYROID PHYSIOLOGY. V. THE USE OF RADIOACTIVE IODINE IN THE DIFFERENTIAL DIAGNOSIS OF TWO TYPES OF GRAVES’ DISEASE”. In: *Journal of Clinical Investigation* 21.1, pp. 31–32 (cit. on p. 67).
- Hettler, C., A. Zografos, Y. Parker, D. Pearson, V. Joshkin, C. Cohen-Jonathan, F. Huang, K. Leung, M. Rougieri, and T. Brown (June 2013). “Development of a dielectric wall accelerator proton therapy system”. In: *2013 Abstracts IEEE International Conference on Plasma Science (ICOPS)*, pp. 1–1. DOI: 10.1109/PLASMA.2013.6635175 (cit. on p. 23).
- Highland, V. L. (1975). “Some practical remarks on multiple scattering”. In: *Nuclear Instruments and Methods* 129.2, pp. 497–499. DOI: [https://doi.org/10.1016/0029-554X\(75\)90743-0](https://doi.org/10.1016/0029-554X(75)90743-0). URL: <http://www.sciencedirect.com/science/article/pii/0029554X75907430> (cit. on p. 11).
- Hilaire, E., C. Robert, X. Lojacono, D. Sarrut, I. Buvat, F. Peyrin, and V. Maxim (Feb. 2014). “Compton imaging in proton therapy: reconstructed image of the simulated prompt- γ distribution”. In: *ICTR-PHE 2014*. Genève, Switzerland, S43. URL: <https://hal.archives-ouvertes.fr/hal-01052717> (cit. on pp. 106, 157).
- Hilaire, E., D. Sarrut, F. Peyrin, and V. Maxim (2016). “Proton therapy monitoring by Compton imaging: influence of the large energy spectrum of the prompt-gamma radiation.” eng. In: *Phys Med Biol* 61.8, pp. 3127–3146. DOI: 10.1088/0031-9155/61/8/3127 (cit. on p. 148).
- Hirasawa, M. and T. Tomitani (Apr. 21, 2003). “An analytical image reconstruction algorithm to compensate for scattering angle broadening in Compton cameras.” eng. In: *Phys Med Biol* 48.8, pp. 1009–1026 (cit. on p. 78).
- Hishikawa, Y., K. Kagawa, M. Murakami, H. Sakai, T. Akagi, and M. Abe (2002). “Usefulness of positron-emission tomographic images after proton therapy”. In: *International Journal of Radiation Oncology *Biology *Physics* 53.5, pp. 1388–1391. DOI: 10.1016/S0360-3016(02)02887-0. URL: [http://dx.doi.org/10.1016/S0360-3016\(02\)02887-0](http://dx.doi.org/10.1016/S0360-3016(02)02887-0) (cit. on p. 46).
- Hoffmann, E. J., M. E. Phelps, N. A. Mullani, C. S. Higgins, and M. M. Ter-Pogossian (June 1976). “Design and performance characteristics of a whole-body positron transaxial tomograph.” In: *J Nucl Med* 17.6, pp. 493–502 (cit. on pp. 53, 61).
- Holley, W. R. and A. Chatterjee (1996). “Clusters of DNA induced by ionizing radiation: formation of short DNA fragments. I. Theoretical modeling.” eng. In: *Radiat Res* 145.2, pp. 188–199 (cit. on p. 17).
- Hong, L., M. Goitein, M. Bucciolini, R. Comiskey, B. Gottschalk, S. Rosenthal, C. Serago, and M. Urie (1996). “A pencil beam algorithm for proton dose calculations”. In: *Physics in Medicine & Biology* 41.8, p. 1305. URL: <http://stacks.iop.org/0031-9155/41/i=8/a=005> (cit. on p. 33).

- Hsi, W. C., D. J. Indelicato, C. Vargas, S. Duvvuri, Z. Li, and J. Palta (Sept. 2009). “In vivo verification of proton beam path by using post-treatment PET/CT imaging.” In: *Med Phys* 36.9, pp. 4136–4146 (cit. on p. 46).
- Huang, H.-M., C.-C. Liu, M.-L. Jan, and M.-W. Lee (2018). “A low-count reconstruction algorithm for Compton-based prompt gamma imaging”. In: *Physics in Medicine & Biology* 63.8, p. 085013. URL: <http://stacks.iop.org/0031-9155/63/i=8/a=085013> (cit. on p. 156).
- Hubbell, J. H. and M. J. Berger (1987). *XCOM: Photon Cross Sections on a Personal Computer, Report NBSIR 87-3597 (1987)*, National Institute for Standards and Technology, U.S.A. URL: <http://physics.nist.gov/PhysRefData/XrayMassCoef/> (visited on 02/21/2017) (cit. on pp. 179, 192).
- Hueso-González, F., A. K. Biegun, P. Dendooven, W. Enghardt, F. Fiedler, C. Golnik, K. Heidel, T. Kormoll, J. Petzoldt, K. E. Römer, R. Schwengner, A. Wagner, and G. Pausch (2015). “Comparison of LSO and BGO block detectors for prompt gamma imaging in ion beam therapy”. In: *Journal of Instrumentation* 10.09, P09015. URL: <http://stacks.iop.org/1748-0221/10/i=09/a=P09015> (cit. on pp. 89, 109, 138).
- Hüfner, J., K. Schäfer, and B. Schürmann (Dec. 1975). “Abrasion-ablation in reactions between relativistic heavy ions”. In: *Phys. Rev. C* 12 (6), pp. 1888–1898. DOI: 10.1103/PhysRevC.12.1888. URL: <https://link.aps.org/doi/10.1103/PhysRevC.12.1888> (cit. on p. 12).
- Hünemohr, N., H. Paganetti, S. Greilich, O. Jäkel, and J. Seco (June 2014). “Tissue decomposition from dual energy CT data for MC based dose calculation in particle therapy”. In: *Medical Physics* 41.6, p. 061714. DOI: 10.1118/1.4875976. URL: <http://www.ncbi.nlm.nih.gov/pmc/articles/PMC4032427/> (cit. on p. 34).
- ICRU (1980a). “ICRU Report 33 - Radiation Quantities and Units”. In: *Journal of the International Commission on Radiation Units and Measurements, Bethesda, MD* (cit. on p. 17).
- ICRU (1980b). “ICRU Report 49 - Stopping Powers and Ranges for Protons and Alpha Particles”. In: *Journal of the International Commission on Radiation Units and Measurements, Bethesda, MD* (cit. on p. 36).
- ICRU (1998). “ICRU Report 60 - Fundamental Quantities and Units for Ionising Radiation”. In: *Journal of the International Commission on Radiation Units and Measurements, Bethesda, MD* (cit. on p. 17).
- ICRU (2007). “ICRU Report 78 - Prescribing, recording, and reporting proton beam therapy”. In: *Journal of the International Commission on Radiation Units and Measurements, Bethesda, MD* (cit. on p. 29).
- Ido, T., C.-N. Wan, V. Casella, J. S. Fowler, A. P. Wolf, M. Reivich, and D. E. Kuhl (n.d.). “Labeled 2-deoxy-D-glucose analogs. 18F-labeled 2-deoxy-2-fluoro-D-glucose, 2-deoxy-2-fluoro-D-mannose and 14C-2-deoxy-2-fluoro-D-glucose”. In: *Journal of Labelled Compounds and Radiopharmaceuticals* 14.2 (), pp. 175–183. DOI: 10.1002/jlcr.2580140204. eprint: <https://onlinelibrary.wiley.com/doi/pdf/10.1002/jlcr.2580140204>. URL: <https://onlinelibrary.wiley.com/doi/abs/10.1002/jlcr.2580140204> (cit. on p. 62).

- Inaniwa, T., N. Kanematsu, N. Matsufuji, T. Kanai, T. Shirai, K. Noda, H. Tsuji, T. Kamada, and H. Tsujii (2015). “Reformulation of a clinical-dose system for carbon-ion radiotherapy treatment planning at the National Institute of Radiological Sciences, Japan”. In: *Physics in Medicine & Biology* 60.8, p. 3271. URL: <http://stacks.iop.org/0031-9155/60/i=8/a=3271> (cit. on p. 31).
- Inaniwa, T., H. Tashima, and N. Kanematsu (Mar. 2018). “Optimum size of a calibration phantom for x-ray CT to convert the Hounsfield units to stopping power ratios in charged particle therapy treatment planning”. In: *Journal of Radiation Research* 59.2, pp. 216–224. DOI: 10.1093/jrr/rrx059 (cit. on p. 29).
- Iseki, Y., T. Kanai, M. Kanazawa, A. Kitagawa, H. Mizuno, T. Tomitani, M. Suda, and E. Urakabe (July 2004). “Range verification system using positron emitting beams for heavy-ion radiotherapy.” In: *Phys Med Biol* 49.14, pp. 3179–3195 (cit. on p. 45).
- Iwata, Y., K. Noda, T. Murakami, T. Shirai, T. Furukawa, T. Fujita, S. Mori, K. Mizushima, K. Shouda, T. Fujimoto, T. Ogitsu, T. Obama, N. Amemiya, T. Orikasa, S. Takami, and S. Takayama (2013). “Development of a superconducting rotating-gantry for heavy-ion therapy”. In: *Nuclear Instruments and Methods in Physics Research Section B: Beam Interactions with Materials and Atoms* 317. XVIth International Conference on ElectroMagnetic Isotope Separators and Techniques Related to their Applications, December 2-7, 2012 at Matsue, Japan, pp. 793–797. DOI: <https://doi.org/10.1016/j.nimb.2013.03.050>. URL: <http://www.sciencedirect.com/science/article/pii/S0168583X13003856> (cit. on p. 28).
- Jäkel, O., C. Jacob, D. Schardt, C. P Karger, and G. H. Hartmann (2001a). “Relation between carbon ion ranges and x-ray CT numbers.” eng. In: *Med Phys* 28.4, pp. 701–703. DOI: 10.1118/1.1357455 (cit. on pp. 29, 30).
- Jäkel, O., M. Krämer, C. P Karger, and J. Debus (2001b). “Treatment planning for heavy ion radiotherapy: clinical implementation and application”. In: *Physics in Medicine & Biology* 46.4, p. 1101. URL: <http://stacks.iop.org/0031-9155/46/i=4/a=314> (cit. on p. 31).
- Jäkel, O. and P. Reiss (2007). “The influence of metal artefacts on the range of ion beams”. In: *Physics in Medicine & Biology* 52.3, p. 635. URL: <http://stacks.iop.org/0031-9155/52/i=3/a=007> (cit. on p. 34).
- Jaszczak, R. J., L.-T. Chang, N. A. Stein, and F. E. Moore (1979). “Whole-body single-photon emission computed tomography using dual, large-field-of-view scintillation cameras”. In: *Physics in Medicine & Biology* 24.6, p. 1123. URL: <http://stacks.iop.org/0031-9155/24/i=6/a=003> (cit. on p. 66).
- Jaszczak, R. J., P. H. Murphy, D. Huard, and J. A. Burdine (Apr. 1977). “Radionuclide emission computed tomography of the head with 99mCc and a scintillation camera.” In: *J Nucl Med* 18.4, pp. 373–380 (cit. on p. 66).
- Jemal, A., M. M. Center, C. DeSantis, and E. M. Ward (2010). “Global Patterns of Cancer Incidence and Mortality Rates and Trends”. In: *Cancer Epidemiology and Prevention Biomarkers* 19.8, pp. 1893–1907. ISSN: 1055-9965. DOI: 10.1158/1055-9965.EPI-10-0437. eprint: <http://cancen.acrphub.org/1055-9965.EPI-10-0437>

- //cebp.aacrjournals.org/content/19/8/1893.full.pdf. URL: <http://cebp.aacrjournals.org/content/19/8/1893> (cit. on p. 4).
- Johnson, R. P.** (2017). “Review of medical radiography and tomography with proton beams”. In: *Reports on Progress in Physics* 81.1, p. 016701. URL: <http://stacks.iop.org/0034-4885/81/i=1/a=016701> (cit. on p. 38).
- Johnson, R. P.**, V. Bashkirov, L. DeWitt, V. Giacometti, R. F. Hurley, P. Piersimoni, T. E. Plautz, H. F-W. Sadrozinski, K. Schubert, R. Schulte, B. Schultze, and A. Zatserklyaniy (Feb. 2016). “A Fast Experimental Scanner for Proton CT: Technical Performance and First Experience with Phantom Scans.” In: *IEEE Trans Nucl Sci* 63.1, pp. 52–60 (cit. on p. 39).
- Jones, B.** (2015). “Towards Achieving the Full Clinical Potential of Proton Therapy by Inclusion of LET and RBE Models.” eng. In: *Cancers (Basel)* 7.1, pp. 460–480. DOI: 10.3390/cancers7010460 (cit. on p. 19).
- Kabuki, S.**, K. Hattori, R. Kohara, E. Kunieda, A. Kubo, H. Kubo, K. Miuchi, T. Nakahara, T. Nagayoshi, H. Nishimura, Y. Okada, R. Orito, H. Sekiya, T. Shirahata, A. Takada, T. Tanimori, and K. Ueno (2007). “Development of Electron Tracking Compton Camera using micro pixel gas chamber for medical imaging”. In: *Nuclear Instruments and Methods in Physics Research Section A: Accelerators, Spectrometers, Detectors and Associated Equipment* 580.2. Imaging 2006, pp. 1031–1035. ISSN: 0168-9002. DOI: <https://doi.org/10.1016/j.nima.2007.06.098>. URL: <http://www.sciencedirect.com/science/article/pii/S0168900207013186> (cit. on p. 193).
- Kanai, T., K. Kawachi, H. Matsuzawa, and T. Inada (1983). “Three-dimensional beam scanning for proton therapy”. In: *Nuclear Instruments and Methods in Physics Research* 214.2, pp. 491–496. ISSN: 0167-5087. DOI: [https://doi.org/10.1016/0167-5087\(83\)90621-X](https://doi.org/10.1016/0167-5087(83)90621-X). URL: <http://www.sciencedirect.com/science/article/pii/016750878390621X> (cit. on p. 27).
- Kanazawa, M.**, A. Kitagawa, S. Kouda, T. Nishio, M. Torikoshi, K. Noda, T. Murakami, M. Suda, T. Tomitani, T. Kanai, Y. Futami, M. Shinbo, E. Urakabe, and Y. Iseki (2002). “Application of an RI-beam for cancer therapy: In-vivo verification of the ion-beam range by means of positron imaging”. In: *Nuclear Physics A* 701.1. 5th International Conference on Radioactive Nuclear Beams, pp. 244–252. ISSN: 0375-9474. DOI: [https://doi.org/10.1016/S0375-9474\(01\)01592-5](https://doi.org/10.1016/S0375-9474(01)01592-5). URL: <http://www.sciencedirect.com/science/article/pii/S0375947401015925> (cit. on p. 45).
- Kanematsu, N.**, N. Matsufuji, R. Kohno, S. Minohara, and T. Kanai (2003). “A CT calibration method based on the polybinary tissue model for radiotherapy treatment planning”. In: *Physics in Medicine and Biology* 48.8, p. 1053. URL: <http://stacks.iop.org/0031-9155/48/i=8/a=307> (cit. on p. 29).
- Karp, J. S.** and M. E. Daube-Witherspoon (1987). “Depth-of-interaction determination in NaI(Tl) and BGO scintillation crystals using a temperature gradient”. In: *Nuclear Instruments and Methods in Physics Research Section A: Accelerators, Spectrometers, Detectors and Associated Equipment* 260.2, pp. 509–517. ISSN: 0168-9002. DOI: [https://doi.org/10.1016/0168-9002\(87\)90124-0](https://doi.org/10.1016/0168-9002(87)90124-0). URL: <http://www.sciencedirect.com/science/article/pii/0168900287901240> (cit. on p. 62).

- Karp, J. S., S. Surti, M. E. Daube-Witherspoon, and G. Muehllehner (Mar. 2008). “Benefit of time-of-flight in PET: experimental and clinical results.” In: *J Nucl Med* 49.3, pp. 462–470 (cit. on p. 63).
- Keevil, S. F. (2012). “Physics and medicine: a historical perspective”. In: *The Lancet* 379.9825, pp. 1517–1524. ISSN: 0140-6736. DOI: [https://doi.org/10.1016/S0140-6736\(11\)60282-1](https://doi.org/10.1016/S0140-6736(11)60282-1). URL: <http://www.sciencedirect.com/science/article/pii/S0140673611602821> (cit. on p. 4).
- Kereiakes, J. G. (1987). “The history and development of medical physics instrumentation: Nuclear medicine”. In: *Medical Physics* 14.1, pp. 146–155. DOI: 10.1118/1.596105. eprint: <https://aapm.onlinelibrary.wiley.com/doi/pdf/10.1118/1.596105>. URL: <https://aapm.onlinelibrary.wiley.com/doi/abs/10.1118/1.596105> (cit. on p. 4).
- Keyes, J. W. J., N. Orlandea, W. J. Heetderks, P. F. Leonard, and W. L. Rogers (Apr. 1977). “The Humongotron—a scintillation-camera transaxial tomograph.” In: *J Nucl Med* 18.4, pp. 381–387 (cit. on p. 66).
- Kitagawa, A., Y. Furusawa, T. Kanai, M. Kanazawa, H. Mizuno, M. Muramatsu, S. Sato, M. Suda, T. Tomitani, E. Urakabe, M. Yoshimoto, Q. Li, Z. Wei, K. Hanawa, Y. Iseki, and K. Sato (2006). “Medical application of radioactive nuclear beams at HIMAC”. In: *Review of Scientific Instruments* 77.3, p. 03C105. DOI: 10.1063/1.2149309. eprint: <https://doi.org/10.1063/1.2149309>. URL: <https://doi.org/10.1063/1.2149309> (cit. on p. 45).
- Klein, O. and Y. Nishina (Nov. 1929). “Über die Streuung von Strahlung durch freie Elektronen nach der neuen relativistischen Quantendynamik von Dirac”. In: *Zeitschrift für Physik* 52.11, pp. 853–868. DOI: 10.1007/BF01366453. URL: <https://doi.org/10.1007/BF01366453> (cit. on p. 73).
- Knoll, G. F. (2000). *Radiation Detection and Measurement*. Third Edition. John Wiley & Sons Inc. (cit. on pp. 72, 74, 77, 84).
- Knopf, A.-C. and A. J. Lomax (2013). “In vivo proton range verification: a review”. In: *Physics in Medicine & Biology* 58.15, R131. URL: <http://stacks.iop.org/0031-9155/58/i=15/a=R131> (cit. on pp. 33, 146).
- Knopf, A.-C., K. Parodi, H. Paganetti, T. Bortfeld, J. Daartz, M. Engelsman, N. Liebsch, and H. Shih (Jan. 2011). “Accuracy of proton beam range verification using post-treatment positron emission tomography/computed tomography as function of treatment site.” In: *Int J Radiat Oncol Biol Phys* 79.1, pp. 297–304 (cit. on p. 46).
- Koehler, A. M. (1968). “Proton Radiography”. In: *Science* 160.3825, pp. 303–304. ISSN: 0036-8075. DOI: 10.1126/science.160.3825.303. eprint: <http://science.sciencemag.org/content/160/3825/303.full.pdf>. URL: <http://science.sciencemag.org/content/160/3825/303> (cit. on pp. 34, 37, 38).
- Komori, M., E. Sekihara, T. Yabe, R. Horita, T. Toshito, and S. Yamamoto (May 2018). “Luminescence imaging of water during uniform-field irradiation by spot scanning proton beams.” In: *Phys Med Biol* 63.11, 11NT01 (cit. on p. 51).

- Kraan, A. C. (2015). “Range Verification Methods in Particle Therapy: Underlying Physics and Monte Carlo Modeling.” In: *Front Oncol* 5, p. 150 (cit. on p. 48).
- Kraan, A. C., G. Battistoni, N. Belcari, N. Camarlinghi, F. Cappucci, M. Ciocca, A. Ferrari, S. Ferretti, A. Mairani, S. Molinelli, M. Pullia, A. Retico, P. Sala, G. Sportelli, A. Del Guerra, and V. Rosso (Nov. 2015). “First tests for an online treatment monitoring system with in-beam PET for proton therapy”. In: 10 (cit. on p. 47).
- Kraan, A. C., G. Battistoni, N. Belcari, N. Camarlinghi, G. A. . Cirrone, G. Cuttone, S. Ferretti, A. Ferrari, G. Pirrone, F. Romano, P. Sala, G. Sportelli, K. Straub, A. Tramontana, A. Del Guerra, and V. Rosso (July 2014). “Proton range monitoring with in-beam PET: Monte Carlo activity predictions and comparison with cyclotron data.” In: *Phys Med* 30.5, pp. 559–569 (cit. on p. 42).
- Krämer, M., O. Jäkel, T. Haberer, G. Kraft, D. Schardt, and U. Weber (2000). “Treatment planning for heavy-ion radiotherapy: physical beam model and dose optimization.” eng. In: *Phys Med Biol* 45.11, pp. 3299–3317 (cit. on pp. 31, 152).
- Kramer, S. L., R. L. Martin, D. R. Moffett, and E. Colton (1977). *Application of proton radiography to medical imaging*. Tech. rep. United States (cit. on p. 37).
- Krimmer, J., L. Caponetto, X. Chen, M. Chevallier, D. Dauvergne, M. De Rydt, S.-M. Deng, J.-L. Ley, H. Mathez, C. Ray, V. Reithinger, É. Testa, and Y. Zoccarato (Feb. 1, 2014). “111: Real-time monitoring of the ion range during hadrontherapy: An update on the beam tagging hodoscope”. In: *Radiotherapy and Oncology* 110, S54–S55. DOI: 10.1016/S0167-8140(15)34132-3. URL: [http://dx.doi.org/10.1016/S0167-8140\(15\)34132-3](http://dx.doi.org/10.1016/S0167-8140(15)34132-3) (cit. on p. 97).
- Krimmer, J., D. Dauvergne, J. M. Létang, and É. Testa (2017). “Prompt-gamma monitoring in hadrontherapy: A review”. In: *Nuclear Instruments and Methods in Physics Research Section A: Accelerators, Spectrometers, Detectors and Associated Equipment* 878. Radiation Imaging Techniques and Applications, pp. 58–73. ISSN: 0168-9002. DOI: <https://doi.org/10.1016/j.nima.2017.07.063>. URL: <http://www.sciencedirect.com/science/article/pii/S0168900217308380> (cit. on pp. 24, 79).
- Krimmer, J., J.-L. Ley, C. Abellan, J.-P. Cachemiche, L. Caponetto, X. Chen, M. Dahoumane, D. Dauvergne, N. Freud, B. Joly, D. Lambert, L. Lestand, M. Magne, H. Mathez, V. Maxim, G. Montarou, C. Morel, M. Pinto, C. Ray, V. Reithinger, E. Testa, and Y. Zoccarato (2015). “Development of a Compton camera for medical applications based on silicon strip and scintillation detectors”. In: *Nuclear Instruments and Methods in Physics Research Section A: Accelerators, Spectrometers, Detectors and Associated Equipment* 787, pp. 98–101. DOI: 10.1016/j.nima.2014.11.042. URL: <https://hal.archives-ouvertes.fr/hal-01101334> (cit. on p. 148).
- Kubiak, T. (Oct. 2016). “Particle therapy of moving targets—the strategies for tumour motion monitoring and moving targets irradiation”. In: *The British Journal of Radiology* 89.1066, p. 20150275. doi: 10.1259/bjr.20150275. URL: <http://www.ncbi.nlm.nih.gov/pmc/articles/PMC5124789/> (cit. on p. 32).

- Kuchment, P and F. Terzioglu (2016). “3D Image Reconstruction from Compton camera data”. In: arXiv: 1604.03805 [physics.data-an] (cit. on pp. 147, 192).
- Kuhl, D. E. and R. Q. Edwards (1963). “Image Separation Radioisotope Scanning”. In: *Radiology* 80.4, pp. 653–662. DOI: 10.1148/80.4.653. eprint: <https://doi.org/10.1148/80.4.653>. URL: <https://doi.org/10.1148/80.4.653> (cit. on p. 61).
- Kuhl, D. E., R. Q. Edwards, A. R. Ricci, R. J. Yacob, T. J. Mich, and A. Alavi (Nov. 1976). “The Mark IV system for radionuclide computed tomography of the brain.” In: *Radiology* 121.2, pp. 405–413 (cit. on p. 66).
- Kumazaki, Y., T. Akagi, T. Yanou, D. Suga, Y. Hishikawa, and T. Teshima (2007). “Determination of the mean excitation energy of water from proton beam ranges”. In: *Radiation Measurements* 42.10, pp. 1683–1691. ISSN: 1350-4487. DOI: <https://doi.org/10.1016/j.radmeas.2007.10.019>. URL: <http://www.sciencedirect.com/science/article/pii/S135044870700409X> (cit. on p. 36).
- Kwekkeboom, D. J., W. W. de Herder, B. L. Kam, C. H. van Eijck, M. van Essen, P. P. Kooij, R. A. Feelders, M. O. van Aken, and E. P. Krenning (May 2008). “Treatment with the radiolabeled somatostatin analog [¹⁷⁷Lu-DOTA 0,Tyr₃]octreotate: toxicity, efficacy, and survival.” In: *J Clin Oncol* 26.13, pp. 2124–2130 (cit. on p. 67).
- Landau, L. (1944). “On the energy loss of fast particles by ionization”. In: *J. Phys.(USSR)* 8, pp. 201–205 (cit. on p. 10).
- Landry, G., K. Parodi, J. E. Wildberger, and F. Verhaegen (2013). “Deriving concentrations of oxygen and carbon in human tissues using single- and dual-energy CT for ion therapy applications”. In: *Physics in Medicine & Biology* 58.15, p. 5029. URL: <http://stacks.iop.org/0031-9155/58/i=15/a=5029> (cit. on p. 42).
- Lang, C., D. Habs, K. Parodi, and P. G. Thirolf (2014). “Sub-millimeter nuclear medical imaging with high sensitivity in positron emission tomography using $\beta + \gamma$ coincidences”. In: *Journal of Instrumentation* 9.01, P01008. URL: <http://stacks.iop.org/1748-0221/9/i=01/a=P01008> (cit. on pp. 51, 52).
- Larsson, B. (1962). “On the application of a 185 MeV proton beam to experimental cancer therapy and neurosurgery: A biophysical study.” PhD thesis. Acta Universitatis Upsaliensis (cit. on p. 21).
- Larsson, S. A. (1980). “Gamma camera emission tomography. Development and properties of a multi-sectional emission computed tomography system.” In: *Acta Radiol Suppl* 363, pp. 1–75 (cit. on p. 66).
- Lawrence, E. O. and M. S. Livingston (Apr. 1932). “The Production of High Speed Light Ions Without the Use of High Voltages”. In: *Phys. Rev.* 40 (1), pp. 19–35. DOI: 10.1103/PhysRev.40.19. URL: <https://link.aps.org/doi/10.1103/PhysRev.40.19> (cit. on p. 20).

- Lecoq, P. (2017). “Pushing the Limits in Time-of-Flight PET Imaging”. In: *IEEE Transactions on Radiation and Plasma Medical Sciences* 1.6, pp. 473–485. ISSN: 2469-7311. DOI: 10.1109/TRPMS.2017.2756674 (cit. on p. 64).
- Lee, C. Y., H. Song, C. W. Park, Y. H. Chung, J. S. Kim, and J. C. Park (May 2016). “Optimization of Proton CT Detector System and Image Reconstruction Algorithm for On-Line Proton Therapy”. In: *PLOS ONE* 11.5, pp. 1–12. DOI: 10.1371/journal.pone.0156226. URL: <https://doi.org/10.1371/journal.pone.0156226> (cit. on p. 40).
- Lehrack, S., W. Assmann, D. Bertrand, S. Henrotin, J. Herault, V. Heymans, F. V. Stappen, P. G. Thirolf, M. Vidal, J. Van de Walle, and K. Parodi (2017). “Submillimeter ionoacoustic range determination for protons in water at a clinical synchrocyclotron”. In: *Physics in Medicine & Biology* 62.17, p. L20. URL: <http://stacks.iop.org/0031-9155/62/i=17/a=L20> (cit. on p. 50).
- Lennox, A. J. (1991). “Hospital-based proton linear accelerator for particle therapy and radioisotope production”. In: *Nuclear Instruments and Methods in Physics Research Section B: Beam Interactions with Materials and Atoms* 56-57, pp. 1197–1200. ISSN: 0168-583X. DOI: [https://doi.org/10.1016/0168-583X\(91\)95130-6](https://doi.org/10.1016/0168-583X(91)95130-6). URL: <http://www.sciencedirect.com/science/article/pii/0168583X91951306> (cit. on p. 23).
- Leone, M. and N. Robotti (2010). “Frédéric Joliot, Irène Curie and the early history of the positron (1932-33)”. In: *European Journal of Physics* 31.4, p. 975. URL: <http://stacks.iop.org/0143-0807/31/i=4/a=027> (cit. on pp. 56, 57).
- Levin, C., G. Glover, T. Deller, D. McDaniel, W. Peterson, and S. H. Maramraju (2013). “Prototype time-of-flight PET ring integrated with a 3T MRI system for simultaneous whole-body PET/MR imaging”. In: *Journal of Nuclear Medicine* 54.supplement 2, p. 148. URL: http://jnm.snmjournals.org/content/54/supplement_2/148.abstract (cit. on p. 64).
- Levy, R. P. (2007). “PET-CT: Evolving role in hadron therapy”. In: *Nuclear Instruments and Methods in Physics Research Section B: Beam Interactions with Materials and Atoms* 261.1. The Application of Accelerators in Research and Industry, pp. 782–785. ISSN: 0168-583X. DOI: <https://doi.org/10.1016/j.nimb.2007.04.039>. URL: <http://www.sciencedirect.com/science/article/pii/S0168583X07007975> (cit. on p. 29).
- Lewellen, T. K., A. N. Bice, R. L. Harrison, M. D. Pencke, and J. M. Link (1988). “Performance measurements of the SP3000/UW time-of-flight positron emission tomograph”. In: *IEEE Transactions on Nuclear Science* 35.1, pp. 665–669. ISSN: 0018-9499. DOI: 10.1109/23.12808 (cit. on p. 63).
- Lewellen, T. and J. Karp (2004). “CHAPTER 10 - PET Systems”. In: *Emission Tomography*. Ed. by M. N. Wernick and J. N. Aarsvold. San Diego: Academic Press, pp. 179–194. ISBN: 978-0-12-744482-6. DOI: <https://doi.org/10.1016/B978-012744482-6.50013-2>. URL: <http://www.sciencedirect.com/science/article/pii/B9780127444826500132> (cit. on p. 61).
- Lewis, H. W. (June 1950). “Multiple Scattering in an Infinite Medium”. In: *Phys. Rev.* 78 (5), pp. 526–529. DOI: 10.1103/PhysRev.78.526. URL: <https://link.aps.org/doi/10.1103/PhysRev.78.526> (cit. on p. 11).

- Ley, J.-L. (2015). "Mise en oeuvre d'un démonstrateur de caméra Compton pour l'imagerie en médecine nucléaire et pour le contrôle en temps réel de l'hadronthérapie à l'aide des rayonnements gamma prompts." PhD thesis. École Doctorale de Physique et d'Astrophysique de Lyon (cit. on pp. 85, 87, 107, 138, 175).
- Litzenberg, D. W., J. F. Bajema, F. D. Becchetti, J. A. Brown, R. S. Raymond, D. A. Roberts, J. Caraher, G. Hutchins, R. Ronningen, R. Smith, and M. Abbott (1992). "On-line monitoring and PET imaging of proton radiotherapy beams". In: *IEEE Conference on Nuclear Science Symposium and Medical Imaging*, pp. 954–956. doi: 10.1109/NSSMIC.1992.301095 (cit. on p. 45).
- Litzenberg, D. W., D. A. Roberts, M. Y. Lee, K. Pham, A. M. Vander Molen, R. Ronningen, and F. D. Becchetti (June 1999). "On-line monitoring of radiotherapy beams: experimental results with proton beams." In: *Med Phys* 26.6, pp. 992–1006 (cit. on p. 45).
- Liu, H., T. Omura, M. Watanabe, and T. Yamashita (2001). "Development of a depth of interaction detector for γ -rays". In: *Nuclear Instruments and Methods in Physics Research Section A: Accelerators, Spectrometers, Detectors and Associated Equipment* 459.1, pp. 182–190. ISSN: 0168-9002. doi: [https://doi.org/10.1016/S0168-9002\(00\)00939-6](https://doi.org/10.1016/S0168-9002(00)00939-6). URL: <http://www.sciencedirect.com/science/article/pii/S0168900200009396> (cit. on p. 62).
- Llacer, J., A. Chatterjee, E. L. Alpen, W. Saunders, S. Andreea, and H. C. Jackson (1984a). "Imaging by Injection of Accelerated Radioactive Particle Beams". In: *IEEE Transactions on Medical Imaging* 3.2, pp. 80–90. ISSN: 0278-0062. doi: 10.1109/TMI.1984.4307660 (cit. on p. 44).
- Llacer, J., A. Chatterjee, H. C. Jackson, J. C. Lin, and M. V. Zunzunegui (Feb. 1979). "An Imaging Instrument for Positron Emitting Heavy Ion Beam Injection". In: *IEEE Transactions on Nuclear Science* 26.1, pp. 634–647. ISSN: 0018-9499. doi: 10.1109/TNS.1979.4329701 (cit. on p. 44).
- Llacer, J., J. B. Schmidt, and C. A. Tobias (Mar. 1990). "Characterization of fragmented heavy-ion beams using a three-stage telescope detector: measurements of 670-MeV/amu 20Ne beams." In: *Med Phys* 17.2, pp. 151–157 (cit. on p. 15).
- Llacer, J., C. A. Tobias, W. R. Holley, and T. Kanai (May 1984b). "On-line characterization of heavy-ion beams with semiconductor detectors." In: *Med Phys* 11.3, pp. 266–278 (cit. on p. 15).
- Lo Presti, D., S. Aiello, D. L. Bonanno, G. A. P. Cirrone, E. Leonora, F. Longhitano, C. Pugliatti, N. Randazzo, F. Romano, G. V. Russo, M. Russo, C. Stancampiano, and V. Sipala (2014). "OFFSET: Optical Fiber Folded Scintillating Extended Tracker". In: *Nuclear Instruments and Methods in Physics Research Section A: Accelerators, Spectrometers, Detectors and Associated Equipment* 737, pp. 195–202. ISSN: 0168-9002. doi: <https://doi.org/10.1016/j.nima.2013.11.049>. URL: <http://www.sciencedirect.com/science/article/pii/S0168900213015908> (cit. on p. 39).
- Lo Presti, D., D. L. Bonanno, F. Longhitano, D. G. Bongiovanni, G. V. Russo, E. Leonora, N. Randazzo, S. Reito, V. Sipala, and G. Gallo (Sept. 2016). "Design and characterisation of a real time proton and carbon ion radiography system based on scintillating optical fibres." In: *Phys Med* 32.9, pp. 1124–1134 (cit. on p. 39).

- Lobrich, M.**, P. K. Cooper, and B. Rydberg (1996). “Non-random distribution of DNA double-strand breaks induced by particle irradiation”. In: *International Journal of Radiation Biology* 70.5, pp. 493–503. DOI: 10.1080/095530096144680. eprint: <https://doi.org/10.1080/095530096144680>. URL: <https://doi.org/10.1080/095530096144680> (cit. on p. 17).
- Locher, G. L.** (1936). “Biological effects and therapeutic possibilities of neutrons”. In: *Am. J. Roentgenol. Radium Ther.* 36.1, pp. 1–13 (cit. on p. 20).
- Lojacono, X.**, M.-H. Richard, J.-L. Ley, É. Testa, C. Ray, N. Freud, J. M. Létang, D. Dauvergne, V. Maxim, and R. Prost (2013). “Low Statistics Reconstruction of the Compton Camera Point Spread Function in 3D Prompt-gamma Imaging of Ion Beam Therapy”. In: *IEEE Transactions on Nuclear Science* 60.5, pp. 3355–3363. ISSN: 0018-9499. DOI: 10.1109/TNS.2013.2275200 (cit. on pp. 78, 106, 176).
- Lomax, A. J.** (2009). “Charged Particle Therapy: The Physics of Interaction”. In: *The Cancer Journal* 15.4. URL: https://journals.lww.com/journalppo/Fulltext/2009/08000/Charged_Particle_Therapy__The_Physics_of.4.aspx (cit. on p. 6).
- Lomax, A. J.**, T. Boehringer, A. Coray, E. Egger, G. Goitein, M. Grossmann, P. Juelke, S. Lin, E. Pedroni, B. Rohrer, W. Roser, B. Rossi, B. Siegenthaler, O. Stadelmann, H. Stauble, C. Vetter, and L. Wisser (Mar. 2001). “Intensity modulated proton therapy: a clinical example.” In: *Med Phys* 28.3, pp. 317–324 (cit. on p. 35).
- Lu, H.-M.** (Dec. 2008a). “A point dose method for in vivo range verification in proton therapy.” In: *Phys Med Biol* 53.23, N415–22 (cit. on p. 50).
- Lu, H.-M.** (Mar. 2008b). “A potential method for in vivo range verification in proton therapy treatment.” In: *Phys Med Biol* 53.5, pp. 1413–1424 (cit. on p. 50).
- Lu, H.-M.**, G. Mann, and E. Cascio (Nov. 2010). “Investigation of an implantable dosimeter for single-point water equivalent path length verification in proton therapy.” In: *Med Phys* 37.11, pp. 5858–5866 (cit. on p. 50).
- Lühr, A.**, C. von Neubeck, M. Krause, and E. G. C. Troost (Feb. 2018). “Relative biological effectiveness in proton beam therapy –Current knowledge and future challenges”. In: *Clinical and Translational Radiation Oncology* 9, pp. 35–41. DOI: 10.1016/j.ctro.2018.01.006. URL: <http://www.ncbi.nlm.nih.gov/pmc/articles/PMC5862688/> (cit. on p. 31).
- MacCabee, H. D.** and M. A. Ritter (1974). “Fragmentation of High-Energy Oxygen-Ion Beams in Water”. In: *Radiation Research* 60.3, pp. 409–421. DOI: 10.2307/3574021. eprint: <http://www.rrjournal.org/doi/pdf/10.2307/3574021>. URL: <http://www.rrjournal.org/doi/abs/10.2307/3574021> (cit. on p. 15).
- Mackin, D.**, S. Peterson, S. Beddar, and J. Polf (June 7, 2012). “Evaluation of a stochastic reconstruction algorithm for use in Compton camera imaging and beam range verification from secondary gamma emission during proton therapy.” eng. In: *Phys Med Biol* 57.11, pp. 3537–3553. DOI: 10.1088/0031-9155/57/11/3537 (cit. on pp. 78, 156).

- Mandrillon, P.**, F. Farley, N. Brassart, J. Herault, A. Courdi, P. Chauvel, N. Fietier, and J. Y. Tang (1992). “Recent activities of the cyclotron laboratory in Nice”. In: *Proceedings of the 13th International Conference on Cyclotrons and their Applications, Vancouver, Canada* (cit. on p. 196).
- Mandrillon, P.**, F. Farley, N. Brassart, J. Herault, A. Susini, and R. Ostojic (1989). “Commissioning and implementation of the MEDiCYC cyclotron programme”. In: *Proceedings of the 12th International Conference on Cyclotrons and their Applications, Berlin, Germany* (cit. on p. 196).
- Manescu, P.**, H. Ladjal, J. Azencot, M. Beuve, and B. Shariat (June 2013). “Biomechanical-based respiratory motion-compensation for 4D dose calculation during hadron therapy”. In: *27th International Congress and Exhibition, Computer Assisted Radiology*. Vol. 8. 1. Heidelberg, Germany, pp. 39–44. doi: 10.1007/s11548-013-0849-z. URL: <https://hal.archives-ouvertes.fr/hal-00850636> (cit. on p. 32).
- Marafini, M.**, A. Attili, G. Battistoni, N. Belcari, M. Bisogni, N. Camarlinghi, F. Cappucci, M. Cecchetti, P. Cerello, F. Ciciriello, G. Cirrone, S. Coli, F. Corsi, G. Cuttone, E. De Lucia, S. Ferretti, R. Faccini, E. Fiorina, P. Frallicciardi, G. Giraudo, E. Kostara, A. Kraan, F. Licciulli, B. Liu, N. Marino, C. Marzocca, G. Matarrese, C. Morone, M. Morrocchi, S. Muraro, V. Patera, F. Pennazio, C. Peroni, L. Piersanti, M. Piliero, G. Pirrone, A. Rivetti, F. Romano, V. Rosso, P. Sala, A. Sarti, A. Sciubba, G. Sportelli, C. Voena, R. Wheardon, and A. Del Guerra (May 2015). “The INSIDE Project: Innovative Solutions for In-Beam Dosimetry in Hadrontherapy”. English. In: *Acta Physica Polonica A* 127.5, pp. 1465–1467. doi: 10.12693/APhysPolA.127.1465 (cit. on p. 47).
- Matsufuji, N.**, A. Fukumura, M. Komori, T. Kanai, and T. Kohno (2003). “Influence of fragment reaction of relativistic heavy charged particles on heavy-ion radiotherapy”. In: *Physics in Medicine and Biology* 48.11, p. 1605. URL: <http://stacks.iop.org/0031-9155/48/i=11/a=309> (cit. on p. 15).
- Matsufuji, N.**, T. Kanai, N. Kanematsu, T. Miyamoto, M. Baba, T. Kamada, H. Kato, S. Yamada, J.-E. Mizoe, and H. Tsujii (2007). “Specification of Carbon Ion Dose at the National Institute of Radiological Sciences (NIRS).” eng. In: *J Radiat Res* 48 Suppl A, A81–6 (cit. on p. 31).
- Matsufuji, N.**, M. Komori, H. Sasaki, K. Akiu, M. Ogawa, A. Fukumura, E. Urakabe, T. Inaniwa, T. Nishio, T. Kohno, and T. Kanai (July 2005). “Spatial fragment distribution from a therapeutic pencil-like carbon beam in water.” In: *Phys Med Biol* 50.14, pp. 3393–3403 (cit. on p. 15).
- Matsufuji, N.**, H. Tomura, Y. Futami, H. Yamashita, A. Higashi, S. Minohara, M. Endo, and T. Kanai (1998). “Relationship between CT number and electron density, scatter angle and nuclear reaction for hadron-therapy treatment planning.” eng. In: *Phys Med Biol* 43.11, pp. 3261–3275 (cit. on pp. 29, 36).
- Mattiazzo, S.**, D. Bisello, P. Giubilato, D. Pantano, N. Pozzobon, W. Snoeys, and J. Wyss (2015). “Advanced proton imaging in computed tomography”. In: *Radiation Protection Dosimetry* 166.1-4, pp. 388–392 (cit. on p. 38).

- Maxim, V. (Jan. 2014). “Filtered Backprojection Reconstruction and Redundancy in Compton Camera Imaging”. In: *IEEE Transactions on Image Processing* 23.1, pp. 332–341. ISSN: 1057-7149. DOI: 10.1109/TIP.2013.2288143 (cit. on p. 106).
- Maxim, V., M. Frandes, and R. Prost (2009). “Analytical inversion of the Compton transform using the full set of available projections”. In: *Inverse Problems* 25.9, p. 095001. URL: <http://stacks.iop.org/0266-5611/25/i=9/a=095001> (cit. on p. 78).
- McKenzie, A. L., M. van Herk, and B. Mijnheer (2000). “The width of margins in radiotherapy treatment plans”. In: *Physics in Medicine & Biology* 45.11, p. 3331. URL: <http://stacks.iop.org/0031-9155/45/i=11/a=315> (cit. on p. 32).
- McKisson, J. E., P. S. Haskins, G. W. Phillips, S. E. King, R. A. August, R. B. Piercy, and R. C. Mania (1994). “Demonstration of three-dimensional imaging with a germanium Compton camera”. In: *IEEE Transactions on Nuclear Science* 41.4, pp. 1221–1224. ISSN: 0018-9499. DOI: 10.1109/23.322888 (cit. on p. 147).
- McMillan, E. M. (1945). “The synchrotron - a proposed high energy accelerator.” In: *Phys. Rev.* 68.143 (cit. on p. 22).
- McNamara, A. L., J. P. Schuemann, and H. Paganetti (2015). “A phenomenological relative biological effectiveness (RBE) model for proton therapy based on all published in vitro cell survival data”. In: *Physics in Medicine & Biology* 60.21, p. 8399. URL: <http://stacks.iop.org/0031-9155/60/i=21/a=8399> (cit. on p. 19).
- Melcher, C. L. and J. S. Schweitzer (1992). “A promising new scintillator: cerium-doped lutetium oxyorthosilicate”. In: *Nuclear Instruments and Methods in Physics Research Section A: Accelerators, Spectrometers, Detectors and Associated Equipment* 314.1, pp. 212–214. ISSN: 0168-9002. DOI: [https://doi.org/10.1016/0168-9002\(92\)90517-8](https://doi.org/10.1016/0168-9002(92)90517-8). URL: <http://www.sciencedirect.com/science/article/pii/0168900292905178> (cit. on p. 62).
- Miller, M., J. Zhang, K. Binzel, J. Griesmer, T. Laurence, M. Narayanan, D. Natarajamani, S. Wang, and M. Knopp (2015). “Characterization of the Vereos Digital Photon Counting PET System”. In: *Journal of Nuclear Medicine* 56.supplement 3, p. 434. URL: http://jnm.snmjournals.org/content/56/supplement_3/434.abstract (cit. on p. 64).
- Min, C.-H., C. H. Kim, M.-Y. Youn, and J.-W. Kim (2006). “Prompt-gamma measurements for locating the dose falloff region in the proton therapy”. In: *Applied Physics Letters* 89.18, p. 183517. DOI: 10.1063/1.2378561. eprint: <https://doi.org/10.1063/1.2378561>. URL: <https://doi.org/10.1063/1.2378561> (cit. on pp. 48, 146).
- Mizuno, H., T. Tomitani, M. Kanazawa, A. Kitagawa, J. Pawelke, Y. Iseki, E. Urakabe, M. Suda, A. Kawano, R. Iritani, S. Matsushita, T. Inaniwa, T. Nishio, S. Furukawa, K. Ando, Y. K. Nakamura, T. Kanai, and K. Ishii (Aug. 2003). “Washout measurement of radioisotope implanted by radioactive beams in the rabbit.” In: *Phys Med Biol* 48.15, pp. 2269–2281 (cit. on p. 41).
- Moding, E. J., M. B. Kastan, and D. G. Kirsch (2013). “Strategies for optimizing the response of cancer and normal tissues to radiation.” eng. In: *Nat Rev Drug Discov* 12.7, pp. 526–542. DOI: 10.1038/nrd4003 (cit. on p. 5).

- Moffett, D. R.**, E. P. Colton, G. A. Concaaldi, E. W. Hoffman, R. D. Klem, M. J. Knott, S. L. Kramer, R. L. Martin, E. F. Parker, A. R. Passi, P. F. Schultz, R. L. Stockley, R. E. Timm, L. S. Skaggs, and V. W. Steward (June 1975). "Initial Test of a Proton Radiographic System". In: *IEEE Transactions on Nuclear Science* 22.3, pp. 1749–1751. ISSN: 0018-9499. DOI: 10.1109/TNS.1975.4327982 (cit. on p. 38).
- Molière, G.** (Feb. 1948). "Theorie der Streuung schneller geladener Teilchen II. Mehrfach- und Vielfachstreuung". In: *Zeitschrift Naturforschung Teil A* 3, pp. 78–97. DOI: 10.1515/zna-1948-0203 (cit. on p. 11).
- Monini, C.**, M. Cunha, É. Testa, and M. Beuve (Apr. 2018). "Study of the Influence of NanOx Parameters". In: *Cancers* 10.4, p. 87 (cit. on p. 31).
- Montarou, G.**, M. Bony, E. Busato, R. Chadelas, D. Donnarieix, P. Force, C. Guicheney, C. Insa, D. Lambert, L. Lestand, M. Magne, F. Martin, C. Millardet, M. Nivoix, F. Podlyski, and A. Rozes (Jan. 2016). "Construction and tests of an in-beam PET-like demonstrator for hadrontherapy beam ballistic control". In: 845 (cit. on p. 48).
- Morrocchi, M.**, S. Marcatili, N. Belcari, M. G. Bisogni, G. Collazuol, G. Ambrosi, F. Corsi, M. Foresta, C. Marzocca, G. Matarrese, G. Sportelli, P. Guerra, A. Santos, and A. Del Guerra (2012). "Timing performances of a data acquisition system for Time of Flight PET". In: *Nuclear Instruments and Methods in Physics Research Section A: Accelerators, Spectrometers, Detectors and Associated Equipment* 695. New Developments in Photodetection NDIP11, pp. 210–212. ISSN: 0168-9002. DOI: <https://doi.org/10.1016/j.nima.2011.11.073>. URL: <http://www.sciencedirect.com/science/article/pii/S0168900211021413> (cit. on p. 47).
- Moses, W. W.** and S. E. Derenzo (1999). "Prospects for time-of-flight PET using LSO scintillator". In: *IEEE Transactions on Nuclear Science* 46.3, pp. 474–478. ISSN: 0018-9499. DOI: 10.1109/23.775565 (cit. on p. 63).
- Moyers, M. F.**, D. W. Miller, D. A. Bush, and J. D. Slater (2001). "Methodologies and tools for proton beam design for lung tumors". In: *International Journal of Radiation Oncology *Biology *Physics* 49.5, pp. 1429–1438. DOI: 10.1016/S0360-3016(00)01555-8. URL: [https://doi.org/10.1016/S0360-3016\(00\)01555-8](https://doi.org/10.1016/S0360-3016(00)01555-8) (cit. on p. 34).
- Muehllehner, G.** and R. A. Wetzel (1971). "Section imaging by computer calculation". In: *Journal of Nuclear Medicine* 12, pp. 76–84 (cit. on p. 66).
- Muller, C.**, K. Zhernosekov, U. Koster, K. Johnston, H. Dorrer, A. Hohn, N. T. van der Walt, A. Turler, and R. Schibli (Dec. 2012). "A unique matched quadruplet of terbium radioisotopes for PET and SPECT and for alpha- and beta- radionuclide therapy: an in vivo proof-of-concept study with a new receptor-targeted folate derivative." In: *J Nucl Med* 53.12, pp. 1951–1959 (cit. on p. 66).
- Mumot, M.**, C. Algranati, M. Hartmann, J. M. Schippers, E. Hug, and A. J. Lomax (Aug. 2010). "Proton range verification using a range probe: definition of concept and initial analysis." In: *Phys Med Biol* 55.16, pp. 4771–4782 (cit. on p. 50).

- Murayama, H., I. Ishibashi, H. Uchida, T. Omura, and T. Yamashita (1998). “Depth encoding multicrystal detectors for PET”. In: *IEEE Transactions on Nuclear Science* 45.3, pp. 1152–1157. ISSN: 0018-9499. DOI: 10.1109/23.681994 (cit. on p. 62).
- Nadaraya, E. A. (1964). “On Estimating Regression”. In: *Theory of Probability & Its Applications* 9.1, pp. 141–142. DOI: 10.1137/1109020. URL: <https://doi.org/10.1137/1109020> (cit. on p. 159).
- Naimuddin, M., G. Coutrakon, G. Blazey, S. Boi, A. Dyshkant, B. Erdelyi, D. Hedin, E. Johnson, J. Krider, V. Rukalin, S. A. Uzunyan, V. Zutshi, R. Fordt, G. Sellberg, J. E. Rauch, M. Roman, P. Rubinov, and P. Wilson (2016). “Development of a proton Computed Tomography detector system”. In: *Journal of Instrumentation* 11.02, p. C02012. URL: <http://stacks.iop.org/1748-0221/11/i=02/a=C02012> (cit. on p. 39).
- National Instruments (2010). *PXI Express - NI PXIe-1082 User Manual*. 372752B-01. National Instruments (cit. on p. 130).
- Nedunchezian, K., N. Aswath, M. Thiruppatti, and S. Thirugnanamurthy (Dec. 2016). “Boron Neutron Capture Therapy - A Literature Review”. In: *Journal of Clinical and Diagnostic Research : JCDR* 10.12, ZE01–ZE04. DOI: 10.7860/JCDR/2016/19890.9024 (cit. on p. 20).
- Nestor, O. H. and C. Y. Huang (1975). “Bismuth Germanate: A High-Z Gamma-Ray and Charged Particle Detector”. In: *IEEE Transactions on Nuclear Science* 22.1, pp. 68–71. ISSN: 0018-9499. DOI: 10.1109/TNS.1975.4327617 (cit. on p. 62).
- Newhauser, W. D. and M. Durante (May 2011). “Assessing the risk of second malignancies after modern radiotherapy”. In: *Nature Reviews Cancer* 11, p. 438. URL: <http://dx.doi.org/10.1038/nrc3069> (cit. on p. 16).
- Newhauser, W. D., J. Fontenot, N. Koch, L. Dong, K. A. Lee, Y. Zheng, L. Waters, and R. Mohan (2007). “Monte Carlo simulations of the dosimetric impact of radiopaque fiducial markers for proton radiotherapy of the prostate”. In: *Physics in Medicine & Biology* 52.11, p. 2937. URL: <http://stacks.iop.org/0031-9155/52/i=11/a=001> (cit. on p. 34).
- Newhauser, W. D., U. Titt, D. Dexheimer, X. Yan, and S. Nill (2002). “Neutron shielding verification measurements and simulations for a 235-MeV proton therapy center”. In: *Nuclear Instruments and Methods in Physics Research Section A: Accelerators, Spectrometers, Detectors and Associated Equipment* 476.1. Int. Workshop on Neutron Field Spectrometry in Science, Technology and Radiation Protection, pp. 80–84. ISSN: 0168-9002. DOI: [https://doi.org/10.1016/S0168-9002\(01\)01400-0](https://doi.org/10.1016/S0168-9002(01)01400-0). URL: <http://www.sciencedirect.com/science/article/pii/S0168900201014000> (cit. on p. 16).
- Newhauser, W. D. and R. Zhang (2015). “The physics of proton therapy”. In: *Physics in Medicine and Biology* 60.8, R155. URL: <http://stacks.iop.org/0031-9155/60/i=8/a=R155> (cit. on pp. 6, 8, 14).
- Newport (2017). *XPS-Q8 Universal High-Performance Motion Controller/Driver*. v.1.4.x. Newport Corporation (cit. on p. 98).

- Niedźwiecki, S., P. Bialas, C. Curceanu, E. Czerwiński, K. Dulski, A. Gajos, B. Glowacz, M. Gorgol, B. Hiesmayr, B. Jasińska, L. Kaplon, D. Kisielewska-Kamińska, G. Korcyl, P. Kowalski, T. Kozik, N. Krawczyk, W. Krzemień, E. Kubicz, M. Mohammed, M. Pawlik-Niedźwiecka, M. Packa, L. Raczyński, Z. Rudy, N. Sharma, S. Sharma, R. Y. Shopa, M. Silarski, M. Skurzok, A. Wieczorek, W. Wiślicki, B. Zgardzińska, M. Zieliński, and P. Moskal (2017). “J-PET: a new technology for the whole-body PET imaging”. In: *Acta Phys. Polon.* B48, p. 1567. DOI: 10.5506/APhysPolB.48.1567. arXiv: 1710.11369 [physics.ins-det] (cit. on p. 64).
- Nishio, T., A. Miyatake, T. Ogino, K. Nakagawa, N. Saijo, and H. Esumi (Jan. 2010). “The development and clinical use of a beam ON-LINE PET system mounted on a rotating gantry port in proton therapy.” In: *Int J Radiat Oncol Biol Phys* 76.1, pp. 277–286 (cit. on p. 46).
- Nishio, T., T. Ogino, K. Nomura, and H. Uchida (Nov. 2006). “Dose-volume delivery guided proton therapy using beam on-line PET system.” In: *Med Phys* 33.11, pp. 4190–4197 (cit. on p. 45).
- NuPECC (2014). “Nuclear Physics for Medicine”. In: *Strasbourg: European Science Foundation*. URL: <http://www.nupecc.org> (cit. on p. 6).
- Nurdan, T. C., K. Nurdan, A. B. Brill, and A. H. Walenta (2015). “Design criteria for a high energy Compton Camera and possible application to targeted cancer therapy”. In: *Journal of Instrumentation* 10.07, p. C07018. URL: <http://stacks.iop.org/1748-0221/10/i=07/a=C07018> (cit. on p. 173).
- Oelfke, U., G. K. Y. Lam, and M. S. Atkins (1996). “Proton dose monitoring with PET: quantitative studies in Lucite”. In: *Physics in Medicine & Biology* 41.1, p. 177. URL: <http://stacks.iop.org/0031-9155/41/i=1/a=013> (cit. on pp. 40, 45).
- Oger, T., W.-T. Chen, J.-P. Cussonneau, J. Donnard, S. Duval, J. Lamblin, O. Lemaire, A. F. M. Hadi, P. Leray, E. Morteau, L. L. Scotto, J.-S. Stutzmann, and D. Thers (2012). “A liquid xenon TPC for a medical imaging Compton telescope”. In: *Nuclear Instruments and Methods in Physics Research Section A: Accelerators, Spectrometers, Detectors and Associated Equipment* 695. New Developments in Photodetection NDIP11, pp. 125–128. ISSN: 0168-9002. DOI: <https://doi.org/10.1016/j.nima.2011.12.004>. URL: <http://www.sciencedirect.com/science/article/pii/S0168900211021632> (cit. on p. 52).
- Oliphant, M. O. (1943). “The acceleration of particles to very high energies”. In: *Classified memo submitted to DSIR, United Kingdom, Sept. 1943* (cit. on p. 22).
- Ordonez, C. E., A. Bolozdynya, and W. Chang (1997). “Doppler broadening and energy uncertainties in Compton cameras”. In: *IEEE Nucl. Sci. Symp. Conf. Rec.* 2 1361–65 (cit. on p. 147).
- Ortega, P. G., I. Torres-Espallardo, F. Cerutti, A. Ferrari, J. E. Gillam, C. Lacasta, G. Llosá, J. F. Oliver, P. R. Sala, P. Solevi, and M. Rafecas (Mar. 7, 2015). “Noise evaluation of Compton camera imaging for proton therapy”. eng. In: *Phys Med Biol* 60.5, pp. 1845–1863. DOI: 10.1088/0031-9155/60/5/1845 (cit. on pp. 89, 148, 157).

- Owen, H. L., D. Holder, J. Alonso, and R. MacKay (2014). “Technologies for Delivery of Proton and Ion Beams for Radiotherapy”. In: *Int. J. Mod. Phys. A*29, p. 1441002. DOI: 10.1142/S0217751X14410024. arXiv: 1310.0237 [physics.acc-ph] (cit. on p. 28).
- Paans, A. M. J. and J. M. Schippers (1993). “Proton therapy in combination with PET as monitor: a feasibility study”. In: *IEEE Transactions on Nuclear Science* 40.4, pp. 1041–1044. ISSN: 0018-9499. DOI: 10.1109/23.256709 (cit. on p. 45).
- Paganetti, H. (2012a). *Proton Therapy Physics*. Boca Raton: CRC Press (cit. on pp. 7, 21).
- Paganetti, H. (June 2012b). “Range uncertainties in proton therapy and the role of Monte Carlo simulations”. In: *Physics in Medicine and Biology* 57.11, R99–R117. DOI: 10.1088/0031-9155/57/11/R99. URL: <http://www.ncbi.nlm.nih.gov/pmc/articles/PMC3374500/> (cit. on pp. 32, 35, 146).
- Paganetti, H. (2014). “Relative biological effectiveness (RBE) values for proton beam therapy. Variations as a function of biological endpoint, dose, and linear energy transfer.” eng. In: *Phys Med Biol* 59.22, R419–72. DOI: 10.1088/0031-9155/59/22/R419 (cit. on p. 31).
- Paganetti, H. and M. Goitein (May 2000). “Radiobiological significance of beamline dependent proton energy distributions in a spread-out Bragg peak.” In: *Med Phys* 27.5, pp. 1119–1126 (cit. on pp. 35, 36).
- Paganetti, H., A. Niemierko, M. Ancukiewicz, L. E. Gerweck, M. Goitein, J. S. Loeffler, and H. D. Suit (2002). “Relative biological effectiveness (RBE) values for proton beam therapy.” eng. In: *Int J Radiat Oncol Biol Phys* 53.2, pp. 407–421 (cit. on p. 29).
- Paganetti, H. and P. Van Luijk (2013). “Biological Considerations When Comparing Proton Therapy With Photon Therapy”. In: *Seminars in Radiation Oncology* 23.2, pp. 77–87. DOI: 10.1016/j.semradonc.2012.11.002. URL: <http://dx.doi.org/10.1016/j.semradonc.2012.11.002> (cit. on pp. 16, 31).
- Parodi, K. (2014). “Heavy ion radiography and tomography”. In: *Physica Medica* 30.5. Particle Radiosurgery Conference, pp. 539–543. ISSN: 1120-1797. DOI: <https://doi.org/10.1016/j.ejmp.2014.02.004>. URL: <http://www.sciencedirect.com/science/article/pii/S1120179714000271> (cit. on pp. 39, 40).
- Parodi, K. (2015). “On- and off-line monitoring of ion beam treatment”. In: *Nuclear Instruments and Methods in Physics Research Section A: Accelerators, Spectrometers, Detectors and Associated Equipment* 809. Advances in detectors and applications for medicine, pp. 113–119. DOI: <https://doi.org/10.1016/j.nima.2015.06.056>. URL: <http://www.sciencedirect.com/science/article/pii/S0168900215008062> (cit. on pp. 35, 43, 146).
- Parodi, K. (Aug. 2018). “On the feasibility of dose quantification with in-beam PET data in radiotherapy with ¹²C and proton beams”. PhD thesis (cit. on p. 41).
- Parodi, K. and W. Assmann (2015). “Ionoacoustics: A new direct method for range verification”. In: *Modern Physics Letters A* 30.17, p. 1540025. DOI: 10.1142/S0217732315400258.

- eprint: <https://doi.org/10.1142/S0217732315400258>. URL: <https://doi.org/10.1142/S0217732315400258> (cit. on pp. 50, 51).
- Parodi, K. and T. Bortfeld (Apr. 2006). “A filtering approach based on Gaussian-powerlaw convolutions for local PET verification of proton radiotherapy.” In: *Phys Med Biol* 51.8, pp. 1991–2009 (cit. on p. 41).
- Parodi, K., T. Bortfeld, and T. Haberer (July 2008). “Comparison between in-beam and offline positron emission tomography imaging of proton and carbon ion therapeutic irradiation at synchrotron- and cyclotron-based facilities.” In: *Int J Radiat Oncol Biol Phys* 71.3, pp. 945–956 (cit. on p. 46).
- Parodi, K., S. Brons, F. Cerutti, A. Ferrari, A. Mairani, H. Paganetti, and F. Sommerer (2010). “The FLUKA code for application of Monte Carlo methods to promote high precision ion beam therapy”. In: URL: <https://cds.cern.ch/record/1238366> (cit. on p. 41).
- Parodi, K., P. Crespo, H. Eickhoff, T. Haberer, J. Pawelke, D. Schardt, and W. Enghardt (2005). “Random coincidences during in-beam PET measurements at microbunched therapeutic ion beams”. In: *Nuclear Instruments and Methods in Physics Research Section A: Accelerators, Spectrometers, Detectors and Associated Equipment* 545.1, pp. 446–458. ISSN: 0168-9002. DOI: <https://doi.org/10.1016/j.nima.2005.02.002>. URL: <http://www.sciencedirect.com/science/article/pii/S0168900205005759> (cit. on p. 48).
- Parodi, K., H. Paganetti, H. A. Shih, S. Michaud, J. S. Loeffler, T. F. DeLaney, N. J. Liebsch, J. E. Munzenrider, A. J. Fischman, A.-C. Knopf, and T. Bortfeld (2007). “Patient Study of In Vivo Verification of Beam Delivery and Range, Using Positron Emission Tomography and Computed Tomography Imaging After Proton Therapy”. In: *International Journal of Radiation Oncology Biology Physics* 68.3, pp. 920–934. DOI: [10.1016/j.ijrobp.2007.01.063](https://doi.org/10.1016/j.ijrobp.2007.01.063). URL: <http://dx.doi.org/10.1016/j.ijrobp.2007.01.063> (cit. on pp. 41, 46).
- Parra, L. C. (Aug. 2000). “Reconstruction of cone-beam projections from Compton scattered data”. In: *IEEE Transactions on Nuclear Science* 47.4, pp. 1543–1550. DOI: [10.1109/23.873014](https://doi.org/10.1109/23.873014) (cit. on p. 78).
- Particle Therapy Cooperative Group, P (2017). “PTCOG stats”. In: www.ptcog.ch (cit. on p. 146).
- Pawelke, J., L. Byars, W. Enghardt, W. D. Fromm, H. Geissel, B. G. Hasch, K. Lauckner, P. Manfrass, D. Schardt, and M. Sobiella (Feb. 1996). “The investigation of different cameras for in-beam PET imaging.” In: *Phys Med Biol* 41.2, pp. 279–296 (cit. on p. 45).
- Peach, K. J., J. H. Cobb, S. L. Sheehy, H. Witte, T. Yokoi, M. Aslaninejad, M. J. Easton, J. Pasternak, R. Barlow, H. L. Owen, S. C. Tygier, C. D. Beard, P. A. McIntosh, S. M. Pattalwar, S. L. Smith, S. I. Tzenov, N. Bliss, T. J. Jones, J. Strachan, R. Edgecock, J. K. Pozimski, R. J. L. Fenning, A. Khan, I. S. K. Gardner, D. J. Kelliher, S. Machida, M. A. Hill, C. Johnstone, B. Jones, B. Vojnovic, and R. Seviour (2010). “PAMELA : overview and status”. In: *Proceedings of the 1st International Particle Accelerator Conference IPAC 2010*. Kyoto, Japan: JACoW, pp. 112–114. URL: <http://eprints.hud.ac.uk/id/eprint/15286/> (cit. on p. 23).

- Pedroni, E., R. Bacher, H. Blattmann, T. Bohringer, A. Coray, A. J. Lomax, S. Lin, G. Munkel, S. Scheib, and U. Schneider (1995). “The 200-MeV proton therapy project at the Paul Scherrer Institute: conceptual design and practical realization.” In: *Med Phys* 22.1, pp. 37–53 (cit. on pp. 27, 28).
- Pedroni, E., S. Scheib, T. Bohringer, A. Coray, M. Grossmann, S. Lin, and A. J. Lomax (Feb. 2005). “Experimental characterization and physical modelling of the dose distribution of scanned proton pencil beams.” eng. In: *Phys Med Biol* 50.3, pp. 541–561 (cit. on pp. 11, 14).
- Pemler, P., J. Besserer, J. de Boer, M. Dellert, C. Gahn, M. Moosburger, U. Schneider, E. Pedroni, and H. Stäuble (1999). “A detector system for proton radiography on the gantry of the Paul-Scherrer-Institute”. In: *Nuclear Instruments and Methods in Physics Research Section A: Accelerators, Spectrometers, Detectors and Associated Equipment* 432.2, pp. 483–495. ISSN: 0168-9002. doi: [https://doi.org/10.1016/S0168-9002\(99\)00284-3](https://doi.org/10.1016/S0168-9002(99)00284-3). URL: <http://www.sciencedirect.com/science/article/pii/S0168900299002843> (cit. on p. 39).
- Penfold, S. N., A. B. Rosenfeld, R. W. Schulte, and K. E. Schubert (Oct. 2009). “A more accurate reconstruction system matrix for quantitative proton computed tomography.” In: *Med Phys* 36.10, pp. 4511–4518 (cit. on p. 38).
- Pennazio, F., G. Battistoni, M. G. Bisogni, N. Camarlinghi, A. Ferrari, V. Ferrero, E. Fiorina, M. Morrocchi, P. Sala, G. Sportelli, R. Wheaton, and P. Cerello (2018). “Carbon ions beam therapy monitoring with the INSIDE in-beam PET”. In: *Physics in Medicine & Biology* 63.14, p. 145018. URL: <http://stacks.iop.org/0031-9155/63/i=14/a=145018> (cit. on p. 47).
- Peters, A., R. Cee, T. Hoffmann, A. Reiter, M. Schwickert, and T. Winkelmann (Jan. 2008). “Spill structure measurements at the Heidelberg Ion Therapy center”. In: *Proceedings of EPAC08, Genoa, Italy* (cit. on p. 151).
- Phillips, M. H., E. Pedroni, H. Blattmann, T. Boehringer, A. Coray, and S. Scheib (1992). “Effects of respiratory motion on dose uniformity with a charged particle scanning method.” eng. In: *Phys Med Biol* 37.1, pp. 223–234 (cit. on p. 31).
- Piersanti, L., F. Bellini, F. Bini, F. Collamati, E. De Lucia, M. Durante, R. Faccini, F. Ferroni, S. Fiore, E. Iarocci, C. La Tessa, M. Marafini, I. Mattei, V. Patera, P. G. Ortega, A. Sarti, C. Schuy, A. Sciubba, M. Vanstalle, and C. Voena (Apr. 2014). “Measurement of charged particle yields from PMMA irradiated by a 220 MeV/u (12)C beam.” In: *Phys Med Biol* 59.7, pp. 1857–1872 (cit. on p. 49).
- Pinto, M., D. Dauvergne, N. Freud, J. Krimmer, J. M. Létang, C. Ray, F. Roellinghoff, and É. Testa (2014). “Design optimisation of a TOF-based collimated camera prototype for online hadrontherapy monitoring”. In: *Physics in Medicine and Biology* 59.24, p. 7653. URL: <http://stacks.iop.org/0031-9155/59/i=24/a=7653> (cit. on p. 88).
- Plautz, T., V. Bashkirov, V. Feng, F. Hurley, R. P. Johnson, C. Leary, S. Macafee, A. Plumb, V. Rykalin, H. F-W. Sadrozinski, K. Schubert, R. Schulte, B. Schultze, D. Steinberg, M. Witt, and A. Zatserklyaniy (Apr. 2014). “200 MeV Proton Radiography Studies with a Hand Phantom Using a Prototype Proton CT Scanner”. In: *IEEE transactions on medical imaging* 33.4, pp. 875–881 (cit. on p. 38).

- Podgorsak, E. B. (2010). *Radiation Physics for Medical Physicists*. Springer (cit. on pp. 71, 74).
- Polf, J. C., S. Avery, D. S. Mackin, and S. Beddar (2015). “Imaging of prompt-gamma rays emitted during delivery of clinical proton beams with a Compton camera: feasibility studies for range verification”. In: *Physics in Medicine and Biology* 60.18, p. 7085. URL: <http://stacks.iop.org/0031-9155/60/i=18/a=7085> (cit. on p. 147).
- Polf, J. C., S. Peterson, G. Ciangaru, M. Gillin, and S. Beddar (2009). “Prompt-gamma-ray emission from biological tissues during proton irradiation: a preliminary study.” eng. In: *Phys Med Biol* 54.3, pp. 731–743. DOI: 10.1088/0031-9155/54/3/017 (cit. on p. 148).
- Poludniowski, G., N. M. Allinson, and P. M. Evans (Sept. 2015). “Proton radiography and tomography with application to proton therapy.” In: *Br J Radiol* 88.1053, p. 20150134 (cit. on p. 37).
- Pönisch, F., K. Parodi, B. G. Hasch, and W. Enghardt (Dec. 2004). “The modelling of positron emitter production and PET imaging during carbon ion therapy.” In: *Phys Med Biol* 49.23, pp. 5217–5232 (cit. on p. 41).
- Powsner, R. A., R. P. Matthew, and E. R. Powsner (2013). *Essentials of Nuclear Medicine Physics and Instrumentation*. John Wiley & Sons (cit. on p. 55).
- Radon, J. (1917). “Über die Bestimmung von Funktionen durch ihre Integralwerte längs gewisser Mannigfaltigkeiten”. In: *Akad. Wiss.* 69, pp. 262–277 (cit. on p. 53).
- Richard, M.-H. (2012). “Design study of a Compton camera for prompt-gamma imaging during ion beam therapy”. PhD thesis. Université Claude Bernard - Lyon I (cit. on p. 84).
- Rietzel, E., D. Schardt, and T. Haberer (2007). “Range accuracy in carbon ion treatment planning based on CT-calibration with real tissue samples”. In: *Radiation Oncology (London, England)* 2, pp. 14–14. DOI: 10.1186/1748-717X-2-14. URL: <http://www.ncbi.nlm.nih.gov/pmc/articles/PMC1858700/> (cit. on pp. 29, 30, 34).
- Rinaldi, I., S. Brons, J. Gordon, R. Panse, B. Voss, O. Jäkel, and K. Parodi (Feb. 2013). “Experimental characterization of a prototype detector system for carbon ion radiography and tomography.” In: *Phys Med Biol* 58.3, pp. 413–427 (cit. on p. 40).
- Ritt, S. (2009). *9 Channel, 5 GSPS Switched Capacitor Array DRS4*. Revision 0.9. Paul Scherrer Institut (cit. on p. 92).
- Robert, C., G. Dedes, G. Battistoni, T. T. Böhlen, I. Buvat, F. Cerutti, M. P. W. Chin, A. Ferrari, P. Gueth, C. Kurz, L. Lestand, A. Mairani, G. Montarou, R. Nicolini, P. G. Ortega, K. Parodi, Y. Prezado, P. R. Sala, D. Sarrut, and E. Testa (2013). “Distributions of secondary particles in proton and carbon-ion therapy: a comparison between GATE/Geant4 and FLUKA Monte Carlo codes”. In: *Physics in Medicine and Biology* 58.9, p. 2879. URL: <http://stacks.iop.org/0031-9155/58/i=9/a=2879> (cit. on p. 146).

- Robertson, J. B., J. R. Williams, R. A. Schmidt, J. B. Little, D. F. Flynn, and H. D. Suit (June 1975). “Radiobiological studies of a high-energy modulated proton beam utilizing cultured mammalian cells.” In: *Cancer* 35.6, pp. 1664–1677 (cit. on pp. 35, 36).
- Robertson, J. S., R. B. Marr, M. Rosenblum, V. Radeka, and Y. L. Yamamoto (1972). *32-crystal positron transverse section detector*. Tech. rep. United States (cit. on p. 61).
- Roellinghoff, F., A. Benilov, D. Dauvergne, G. Dedes, N. Freud, G. Janssens, J. Krimmer, J. M. Létang, M. Pinto, D. Prieels, C. Ray, J. Smeets, F. Stichelbaut, and E. Testa (2014). “Real-time proton beam range monitoring by means of prompt-gamma detection with a collimated camera”. In: *Physics in Medicine and Biology* 59.5, p. 1327. URL: <http://stacks.iop.org/0031-9155/59/i=5/a=1327> (cit. on p. 152).
- Rogers, D. F. (2001). *An Introduction to NURBS: With Historical Perspective*. San Francisco, CA, USA: Morgan Kaufmann Publishers Inc. ISBN: 1-55860-669-6 (cit. on p. 159).
- Rogers, J. G., R. Nutt, M. Andreaco, and C. W. Williams (Aug. 1994). “Testing 144- and 256-crystal BGO block detectors”. In: *IEEE Transactions on Nuclear Science* 41.4, pp. 1423–1429. DOI: 10.1109/23.322926 (cit. on pp. 109, 138).
- Rogers, W. L., N. H. Clinthorne, L. Shao, P. Chiao, Y. Ding, J. A. Stamos, and K. F. Koral (1988). “SPRINT II: a second generation single photon ring tomograph.” In: *IEEE Trans Med Imaging* 7.4, pp. 291–297 (cit. on p. 66).
- Rolo, M. D., R. Bugalho, F. Goncalves, G. Mazza, A. Rivetti, J. C. Silva, R. Silva, and J. Varela (2013). “TOFPET ASIC for PET applications”. In: *Journal of Instrumentation* 8.02, p. C02050. URL: <http://stacks.iop.org/1748-0221/8/i=02/a=C02050> (cit. on p. 47).
- Ronsivalle, C., M. Carpanese, C. Marino, G. Messina, L. Picardi, S. Sandri, E. Basile, B. Caccia, D. M. Castelluccio, E. Cisbani, S. Frullani, F. Ghio, V. Macellari, M. Benassi, M. D’Andrea, and L. Strigari (2011). “The TOP-IMPLART project”. In: *The European Physical Journal Plus* 126.7, p. 68. DOI: 10.1140/epjp/i2011-11068-x. URL: <https://doi.org/10.1140/epjp/i2011-11068-x> (cit. on p. 23).
- Rossi, B. B. (1952). *High-energy particles*. Prentice-Hall physics. New York, NY: Prentice-Hall. URL: <https://cds.cern.ch/record/99081> (cit. on p. 10).
- Rosso, V., G. Battistoni, N. Belcari, N. Camarlinghi, A. Ferrari, S. Ferretti, A. C. Kraan, A. Mairani, N. Marino, J. E. Ortuño, M. Pullia, P. Sala, A. Santos, G. Sportelli, K. Straub, and A. Del Guerra (2013). “A new PET prototype for proton therapy: comparison of data and Monte Carlo simulations”. In: *Journal of Instrumentation* 8.03, p. C03021. URL: <http://stacks.iop.org/1748-0221/8/i=03/a=C03021> (cit. on p. 47).
- Ruth, T. J. (2009). “The Production of Radionuclides for Radiotracers in Nuclear Medicine”. In: *Reviews of Accelerator Science and Technology* 02.01, pp. 17–33. DOI: 10.1142/S1793626809000314. eprint: <https://doi.org/10.1142/S1793626809000314>. URL: <https://doi.org/10.1142/S1793626809000314> (cit. on p. 58).

- Rutherford, E. (1899). "Uranium radiation and the electrical conduction produced by it". In: *Philos. Mag.* 47, p. 109. URL: <http://cds.cern.ch/record/261896> (cit. on p. 55).
- Rutherford, E. (1911). "The scattering of α and β particles by matter and the structure of the atom". In: *Phil. Mag. Ser.6* 21, pp. 669–688. DOI: 10.1080/14786440508637080 (cit. on p. 11).
- Rydberg, B. (1996). "Clusters of DNA damage induced by ionizing radiation: formation of short DNA fragments. II. Experimental detection." eng. In: *Radiat Res* 145.2, pp. 200–209 (cit. on p. 17).
- Sadrozinski, H. F., V. Bashkirov, B. Colby, G. Coutrakon, B. Erdelyi, D. Fusi, F. Hurley, R. P. Johnson, S. Kashigune, S. McAllister, F. Martinez-McKinney, J. Missaghian, M. Scaringella, S. Penfold, V. Rykalin, R. Schulte, K. Schubert, D. Steinberg, and A. Zatserklniy (Oct. 2011). "Detector development for Proton Computed Tomography (pCT)". In: *2011 IEEE Nuclear Science Symposium Conference Record*, pp. 4457–4461. DOI: 10.1109/NSSMIC.2011.6152494 (cit. on p. 39).
- Saint Gobain (2016). *BGO Bismuth Germanate Scintillation material - Datasheet*. Saint Gobain Ceramics & Plastics (cit. on p. 126).
- Saint Gobain (2017). *Plastic Scintillating Fibers - Product brochure*. Saint Gobain Ceramics & Plastics (cit. on pp. 94, 99).
- Sandjong, S., M. Fontana, and É. Testa (2017). "Compton camera prototype for ion beam therapy monitoring: characterization of the BGO scintillators and simulation of the scintillating fiber beam hodoscope". Master internship report (cit. on pp. 90, 142).
- Saraya, Y., T. Izumikawa, J. Goto, T. Kawasaki, and T. Kimura (2014). "Study of spatial resolution of proton computed tomography using a silicon strip detector". In: *Nuclear Instruments and Methods in Physics Research Section A: Accelerators, Spectrometers, Detectors and Associated Equipment* 735, pp. 485–489. ISSN: 0168-9002. DOI: <https://doi.org/10.1016/j.nima.2013.09.051>. URL: <http://www.sciencedirect.com/science/article/pii/S0168900213012850> (cit. on p. 40).
- Sauli, F. (1997). "GEM: A new concept for electron amplification in gas detectors". In: *Nuclear Instruments and Methods in Physics Research Section A: Accelerators, Spectrometers, Detectors and Associated Equipment* 386.2, pp. 531–534. ISSN: 0168-9002. DOI: [https://doi.org/10.1016/S0168-9002\(96\)01172-2](https://doi.org/10.1016/S0168-9002(96)01172-2). URL: <http://www.sciencedirect.com/science/article/pii/S0168900296011722> (cit. on p. 39).
- Sawakuchi, G. O., U. Titt, D. Mirkovic, and R. Mohan (Sept. 2008). "Density heterogeneities and the influence of multiple Coulomb and nuclear scatterings on the Bragg peak distal edge of proton therapy beams." In: *Phys Med Biol* 53.17, pp. 4605–4619 (cit. on p. 36).
- Scarantino, C. W., B. R. Prestidge, M. S. Anscher, C. R. Ferree, W. T. Kearns, R. D. Black, N. G. Bolick, and G. P. Beyer (Oct. 2008). "The observed variance between predicted and measured radiation dose in breast and prostate patients utilizing an in vivo dosimeter." In: *Int J Radiat Oncol Biol Phys* 72.2, pp. 597–604 (cit. on p. 50).

- Scaringella, M., M. Brianzi, M. Bruzzi, M. Bucciolini, M. Carpinelli, G. A. P. Cirrone, C. Civinini, G. Cuttone, D. Lo Presti, S. Pallotta, C. Pugliatti, N. Randazzo, F. Romano, V. Sipala, C. Stancampiano, C. Talamonti, M. Tesi, E. Vanzi, and M. Zani (2013). “The PRIMA (PRoton IMAGING) collaboration: Development of a proton Computed Tomography apparatus”. In: *Nuclear Instruments and Methods in Physics Research Section A: Accelerators, Spectrometers, Detectors and Associated Equipment* 730. Proceedings of the 9th International Conference on Radiation Effects on Semiconductor Materials Detectors and Devices, pp. 178–183. ISSN: 0168-9002. DOI: <https://doi.org/10.1016/j.nima.2013.05.181>. URL: <http://www.sciencedirect.com/science/article/pii/S0168900213008036> (cit. on p. 39).
- Schaffner, B. (1998). “Range precision of therapeutic proton beams”. In: *Medical Physics* 25.8, pp. 1555–1555. DOI: 10.1118/1.598334. eprint: <https://aapm.onlinelibrary.wiley.com/doi/pdf/10.1118/1.598334>. URL: <https://aapm.onlinelibrary.wiley.com/doi/abs/10.1118/1.598334> (cit. on p. 34).
- Schaffner, B. and E. Pedroni (1998). “The precision of proton range calculations in proton radiotherapy treatment planning: experimental verification of the relation between CT-HU and proton stopping power”. In: *Physics in Medicine and Biology* 43.6, p. 1579. URL: <http://stacks.iop.org/0031-9155/43/i=6/a=016> (cit. on pp. 29, 36).
- Schall, I., D. Schardt, H. Geissel, H. Irnich, E. Kankeleit, G. Kraft, A. Magel, M. F. Mohar, G. Münenberg, F. Nickel, C. Scheidenberger, and W. Schwab (1996). “Charge-changing nuclear reactions of relativistic light-ion beams ($5 \leq Z \leq 10$) passing through thick absorbers”. In: *Nuclear Instruments and Methods in Physics Research Section B: Beam Interactions with Materials and Atoms* 117.3, pp. 221–234. ISSN: 0168-583X. DOI: [https://doi.org/10.1016/0168-583X\(96\)00325-4](https://doi.org/10.1016/0168-583X(96)00325-4). URL: <http://www.sciencedirect.com/science/article/pii/0168583X96003254> (cit. on pp. 13, 15).
- Schardt, D., T. Elsässer, and D. Schulz-Ertner (Feb. 2010). “Heavy-ion tumor therapy: Physical and radiobiological benefits”. In: *Rev. Mod. Phys.* 82 (1), pp. 383–425. DOI: 10.1103/RevModPhys.82.383. URL: <https://link.aps.org/doi/10.1103/RevModPhys.82.383> (cit. on pp. 5, 6, 19, 26, 28, 32).
- Schardt, D., P. Steidl, M. Krämer, U. Weber, K. Parodi, and S. Brons (2008). “Precision Bragg-curve measurements for light-ion beams in water” (cit. on pp. 13, 14).
- Schimmerling, W., J. Miller, M. Wong, M. Rapkin, J. Howard, G. H. Spieler, and V. B. Jarret (Nov. 1989). “The Fragmentation of 670A MeV Neon-20 as a Function of Depth in Water: I. Experiment”. In: 120, pp. 36–71 (cit. on p. 15).
- Schimmerling, W., T. S. Subramanian, W. J. McDonald, S. N. Kaplan, A. Sadoff, and G. Gabor (1983). “Beam analysis spectrometer for relativistic heavy ions”. In: *Nuclear Instruments and Methods in Physics Research* 205.3, pp. 531–543. ISSN: 0167-5087. DOI: [https://doi.org/10.1016/0167-5087\(83\)90021-2](https://doi.org/10.1016/0167-5087(83)90021-2). URL: <http://www.sciencedirect.com/science/article/pii/0167508783900212> (cit. on p. 15).
- Schlegel, W., T. Bortfeld, A. Grosu, T. Pan, and D. Luo (Mar. 2008). “New Technologies in Radiation Oncology”. In: 49, pp. 683–684 (cit. on p. 33).

- Schneider, U.**, J. Besserer, P. Pemler, M. Dellert, M. Moosburger, E. S. Pedroni, and B. Kaser-Hotz (2004). "First proton radiography of an animal patient." In: *Medical physics* 31 5, pp. 1046–51 (cit. on p. 38).
- Schneider, U.** and R. Hälg (2015). "The Impact of Neutrons in Clinical Proton Therapy". In: *Frontiers in Oncology* 5, p. 235. DOI: 10.3389/fonc.2015.00235. URL: <http://www.ncbi.nlm.nih.gov/pmc/articles/PMC4617104/> (cit. on p. 16).
- Schneider, U.** and E. Pedroni (n.d.). "Proton radiography as a tool for quality control in proton therapy". In: *Medical Physics* 22.4 (), pp. 353–363. DOI: 10.1118/1.597470. eprint: <https://aapm.onlinelibrary.wiley.com/doi/pdf/10.1118/1.597470>. URL: <https://aapm.onlinelibrary.wiley.com/doi/abs/10.1118/1.597470> (cit. on pp. 34, 38, 39).
- Schneider, U.**, E. Pedroni, and A. J. Lomax (1996). "The calibration of CT Hounsfield units for radiotherapy treatment planning". In: *Physics in Medicine and Biology* 41.1, p. 111. URL: <http://stacks.iop.org/0031-9155/41/i=1/a=009> (cit. on pp. 29, 34).
- Schneider, W.**, T. Bortfeld, and W. Schlegel (2000). "Correlation between CT numbers and tissue parameters needed for Monte Carlo simulations of clinical dose distributions". In: *Physics in Medicine & Biology* 45.2, p. 459. URL: <http://stacks.iop.org/0031-9155/45/i=2/a=314> (cit. on p. 34).
- Schöne, S.**, W. Enghardt, F. Fiedler, C. Golnik, G. Pausch, H. Rohling, and T. Kormoll (2017). "An Image Reconstruction Framework and Camera Prototype Aimed for Compton Imaging for In-vivo Dosimetry of Therapeutic Ion Beams". In: *IEEE Transactions on Radiation and Plasma Medical Sciences* 1.1, pp. 96–107. ISSN: 2469-7311. DOI: 10.1109/TRNS.2016.2623220 (cit. on p. 156).
- Schöne, S.**, G. Shakirin, T. Kormoll, C. M. Herbach, G. Pausch, and W. Enghardt (Oct. 2010). "A common approach to image reconstruction for different applications of Compton cameras". In: *IEEE Nuclear Science Symposium Medical Imaging Conference*, pp. 2292–2293. DOI: 10.1109/NSSMIC.2010.5874192 (cit. on pp. 78, 156).
- Schuemann, J. P.**, S. Dowdell, C. Grassberger, C. Min, and H. Paganetti (2014). "Site-Specific Range Uncertainties Due to by Dose Calculation Algorithms for Proton Therapy". In: *International Journal of Radiation Oncology *Biology *Physics* 90.1, S26. DOI: 10.1016/j.ijrobp.2014.05.125. URL: <https://doi.org/10.1016/j.ijrobp.2014.05.125> (cit. on p. 34).
- Schulz-Ertner, D.**, O. Jäkel, and W. Schlegel (2006). "Radiation therapy with charged particles." In: *Semin Radiat Oncol* 16.4, pp. 249–259. DOI: 10.1016/j.semradonc.2006.04.008 (cit. on p. 27).
- Seltzer, S. M.** (1993). "Calculation of Photon Mass Energy-Transfer and Mass Energy-Absorption Coefficients". In: *Radiation Research* 136.2, pp. 147–170. DOI: 10.2307/3578607. eprint: <http://www.rrjournal.org/doi/pdf/10.2307/3578607>. URL: <http://www.rrjournal.org/doi/abs/10.2307/3578607> (cit. on p. 78).

- Serber, R. (Dec. 1947). “Nuclear Reactions at High Energies”. In: *Phys. Rev.* 72 (11), pp. 1114–1115. DOI: 10.1103/PhysRev.72.1114. URL: <https://link.aps.org/doi/10.1103/PhysRev.72.1114> (cit. on p. 12).
- Sethi, R. V., D. Giantsoudi, M. Raiford, I. Malhi, A. Niemierko, O. Rapalino, P. Caruso, T. I. Yock, N. J. Tarbell, H. Paganetti, and S. M. MacDonald (2014). “Patterns of Failure After Proton Therapy in Medulloblastoma; Linear Energy Transfer Distributions and Relative Biological Effectiveness Associations for Relapses”. In: *International Journal of Radiation Oncology *Biology *Physics* 88.3, pp. 655–663. DOI: 10.1016/j.ijrobp.2013.11.239. URL: <https://doi.org/10.1016/j.ijrobp.2013.11.239> (cit. on p. 19).
- Shakirin, G., H. Braess, F. Fiedler, D. Kunath, K. Laube, K. Parodi, M. Priegnitz, and W. Enghardt (Mar. 2011). “Implementation and workflow for PET monitoring of therapeutic ion irradiation: a comparison of in-beam, in-room, and off-line techniques.” In: *Phys Med Biol* 56.5, pp. 1281–1298 (cit. on pp. 43, 45).
- Sheehy, S. L. (2017). “Fixed-Field Alternating-Gradient Accelerators”. In: *Proceedings, CERN Accelerator School: Accelerators for Medical Applications: Vösendorf, Austria, May 26 - June 5, 2015*, pp. 321–336. arXiv: 1604.05221 [physics.acc-ph]. URL: <https://inspirehep.net/record/1448340/files/arXiv:1604.05221.pdf> (cit. on p. 22).
- Shinoda, H., T. Kanai, and T. Kohno (Aug. 2006). “Application of heavy-ion CT.” In: *Phys Med Biol* 51.16, pp. 4073–4081 (cit. on p. 40).
- Shirato, H., R. Harrison, R. O. Kornelsen, G. K. Y. Lam, C. C. Gaffney, G. B. Goodman, E. Grochowski, and B. Pate (n.d.). “Detection of pion-induced radioactivity by autoradiography and positron emission tomography (PET)”. In: *Medical Physics* 16.3 (), pp. 338–345. DOI: 10.1118/1.596426. eprint: <https://aapm.onlinelibrary.wiley.com/doi/pdf/10.1118/1.596426>. URL: <https://aapm.onlinelibrary.wiley.com/doi/abs/10.1118/1.596426> (cit. on p. 44).
- Singh, M. (1983). “An electronically collimated gamma camera for single photon emission computed tomography. Part I: theoretical considerations and design criteria”. In: *Medical Physics* 10.4, pp. 421–427. ISSN: 2473-4209. DOI: 10.1118/1.595313. URL: <http://dx.doi.org/10.1118/1.595313> (cit. on pp. 66, 172).
- Singh, M. and D. Doria (1981). “Computer Simulation Of Image Reconstruction With A New Electronically Collimated Gamma Tomography System”. In: vol. 0273, pp. 273–279. DOI: 10.1117/12.931803. URL: <https://doi.org/10.1117/12.931803> (cit. on p. 66).
- Singh, M. and D. Doria (Aug. 1983). “An electronically collimated gamma camera for single photon emission computed tomography. Part II: Image reconstruction and preliminary experimental measurements.” In: *Med Phys* 10.4, pp. 428–435 (cit. on p. 66).
- Smeets, J., F. Roellinghoff, D. Prieels, F. Stichelbaut, A. Benilov, P. Busca, C. Fiorini, R. Peloso, M. Basilavecchia, T. Frizzi, J. C. Dehaes, and A. Dubus (May 2012). “Prompt gamma imaging with a slit camera for real-time range control in proton therapy”. In: 57, pp. 3371–405 (cit. on p. 152).

- Solevi, P., E. Munoz, C. Solaz, M. Trovato, P. Dendooven, J. E. Gillam, C. Lacasta, J. F. Oliver, M. Rafecas, I. Torres-Espallardo, and G. Llosá (2016). “Performance of MACACO Compton telescope for ion-beam therapy monitoring: first test with proton beams.” eng. In: *Phys Med Biol* 61.14, pp. 5149–5165. doi: 10.1088/0031-9155/61/14/5149 (cit. on p. 147).
- Sommerer, F., F. Cerutti, K. Parodi, A. Ferrari, W. Enghardt, and H. Aigner (July 2009). “In-beam PET monitoring of mono-energetic (^{16}O) and (^{12}C) beams: experiments and FLUKA simulations for homogeneous targets.” In: *Phys Med Biol* 54.13, pp. 3979–3996 (cit. on p. 46).
- Sonoda, S., Y. Ichimura, H. Kimura, S. Kabuki, A. Takada, T. Mizmoto, H. Kubo, S. Miyamoto, S. Komura, T. Takemura, T. Sawano, T. Kishimoto, Y. Matsuoka, Y. Mizumura, and T. Tanimori (2015). “Application of Electron Tracking Compton Camera (ETCC) in medical imaging”. In: *2015 IEEE Nuclear Science Symposium and Medical Imaging Conference (NSS/MIC)*, pp. 1–3. doi: 10.1109/NSSMIC.2015.7582015 (cit. on p. 193).
- Spieler, H. (1998). “Semiconductor Detectors Part 2”. Lectures on Detector Techniques, Stanford Linear Accelerator Center , September 1998 - February, 1999 (cit. on p. 108).
- Sportelli, G., N. Belcari, N. Camarlinghi, G. A. P. Cirrone, G. Cuttone, S. Ferretti, A. C. Kraan, J. E. Ortúñoz, F. Romano, A. Santos, K. Straub, A. Tramontana, A. Del Guerra, and V. Rosso (2014). “First full-beam PET acquisitions in proton therapy with a modular dual-head dedicated system”. In: *Physics in Medicine & Biology* 59.1, p. 43. URL: <http://stacks.iop.org/0031-9155/59/i=1/a=43> (cit. on p. 47).
- Srivastava, R., B. Jyoti, M. Gupta, and N. Singh (2015). “CyberKnife: The cutting edge technology in precision surgery”. In: *SRM Journal of Research in Dental Sciences* 6.2, pp. 106–115. doi: 10.4103/0976-433X.155469. eprint: <http://www.srmjrds.in/article.asp?issn=0976-433X;year=2015;volume=6;issue=2;spage=106;epage=115;aulast=Srivastava;t=6>. URL: <http://www.srmjrds.in/article.asp?issn=0976-433X;year=2015;volume=6;issue=2;spage=106;epage=115;aulast=Srivastava;t=6> (cit. on p. 27).
- Steinsträter, O., R. Grün, U. Scholz, T. Friedrich, M. Durante, and M. Scholz (2012). “Mapping of RBE-Weighted Doses Between HIMAC- and LEM-Based Treatment Planning Systems for Carbon IonTherapy”. In: *International Journal of Radiation Oncology *Biology *Physics* 84.3, pp. 854–860. doi: 10.1016/j.ijrobp.2012.01.038. URL: <https://doi.org/10.1016/j.ijrobp.2012.01.038> (cit. on p. 31).
- Steward, V. W. and A. M. Koehler (1973). “Proton Beam radiography in tumor detection”. In: *Science* 179, p. 913 (cit. on p. 37).
- Stichelbaut, F. and Y. Jongen (2003). “Verification of the proton beam position in the patient by the detection of prompt gamma-ray emission”. In: *Proceedings of the 39th Meeting of the Particle Therapy Co-Operative Group* (cit. on pp. 48, 146).
- Stone, R. S. (June 1948). “Neutron therapy and specific ionization.” eng. In: *Am J Roentgenol Radium Ther* 59.6, pp. 771–785 (cit. on p. 20).
- Stone, R. S., J. H. Lawrence, and P. C. Aebersold (1940). “A Preliminary Report on the Use of Fast Neutrons in the Treatment of Malignant Disease”. In: *Radiology* 35.3, pp. 322–

327. DOI: 10.1148/35.3.322. eprint: <https://doi.org/10.1148/35.3.322>. URL: <https://doi.org/10.1148/35.3.322> (cit. on p. 20).
- Strosberg, J., G. El-Haddad, E. Wolin, A. Hendifar, J. Yao, B. Chasen, E. Mittra, P. L. Kunz, M. H. Kulke, H. Jacene, D. Bushnell, T. M. O'Dorisio, R. P. Baum, H. R. Kulkarni, M. Caplin, R. Lebtahi, T. Hobday, E. Delpassand, E. Van Cutsem, A. Benson, R. Srirajaskanthan, M. Pavel, J. Mora, J. Berlin, E. Grande, N. Reed, E. Seregni, K. Oberg, M. Lopera Sierra, P. Santoro, T. Thevenet, J. L. Erion, P. Ruszniewski, D. Kwekkeboom, and E. Krenning (Jan. 2017). "Phase 3 Trial of (177)Lu-Dotatate for Midgut Neuroendocrine Tumors." In: *N Engl J Med* 376.2, pp. 125–135 (cit. on p. 67).
- Suit, H., T. DeLaney, S. Goldberg, H. Paganetti, B. Clasie, L. Gerweck, A. Niemierko, E. Hall, J. Flanz, J. Hallman, and A. Trofimov (Apr. 2010). "Proton vs carbon ion beams in the definitive radiation treatment of cancer patients." In: *Radiother Oncol* 95.1, pp. 3–22 (cit. on p. 30).
- Suntharalingam, N., B. E. Podgorsak, and H. Tölli (Jan. 2005). "Brachytherapy: Physical and clinical aspects". In: (cit. on p. 55).
- Surti, S. and J. S. Karp (Jan. 2016). "Advances in time-of-flight PET." In: *Phys Med* 32.1, pp. 12–22 (cit. on p. 64).
- Surti, S., A. Kuhn, M. E. Werner, A. E. Perkins, J. Kolthammer, and J. S. Karp (Mar. 2007). "Performance of Philips Gemini TF PET/CT scanner with special consideration for its time-of-flight imaging capabilities." In: *J Nucl Med* 48.3, pp. 471–480 (cit. on p. 44).
- Surti, S., W. Zou, M. E. Daube-Witherspoon, J. McDonough, and J. S. Karp (May 2011). "Design Study of an In-Situ PET Scanner for Use in Proton Beam Therapy". In: *Physics in medicine and biology* 56.9, pp. 2667–2685 (cit. on p. 43).
- Sweet, W. H. (1951). "The Uses of Nuclear Disintegration in the Diagnosis and Treatment of Brain Tumor". In: *New England Journal of Medicine* 245.23. PMID: 14882442, pp. 875–878. DOI: 10.1056/NEJM195112062452301. eprint: <https://doi.org/10.1056/NEJM195112062452301>. URL: <https://doi.org/10.1056/NEJM195112062452301> (cit. on p. 61).
- Tada, J., Y. Hayakawa, K. Hosono, and T. Inada (Nov. 1991). "Time resolved properties of acoustic pulses generated in water and in soft tissue by pulsed proton beam irradiation—a possibility of doses distribution monitoring in proton radiation therapy." In: *Med Phys* 18.6, pp. 1100–1104 (cit. on p. 50).
- Tajima, T., D. Habs, and X. Yan (2009). "Laser Acceleration of Ions for Radiation Therapy". In: *Reviews of Accelerator Science and Technology* 02.01, pp. 201–228. DOI: 10.1142/S1793626809000296. URL: <https://doi.org/10.1142/S1793626809000296> (cit. on p. 23).
- Takeda, S., T. Takahashi, S. Watanabe, H. Tajima, T. Tanaka, K. Nakazawa, and Y. Fukazawa (Jan. 2008). "Double-sided silicon strip detector for x-ray imaging". In: (cit. on p. 85).
- Tashima, H., T. Yamaya, E. Yoshida, S. Kinouchi, M. Watanabe, and E. Tanaka (2012). "A single-ring OpenPET enabling PET imaging during radiotherapy". In: *Physics in Medicine &*

Biology 57.14, p. 4705. URL: <http://stacks.iop.org/0031-9155/57/i=14/a=4705> (cit. on pp. 44, 46).

Tashima, H., E. Yoshida, N. Inadama, F. Nishikido, Y. Nakajima, H. Wakizaka, T. Shinaji, M. Nitta, S. Kinouchi, M. Suga, H. Haneishi, T. Inaniwa, and T. Yamaya (Feb. 2016). “Development of a small single-ring OpenPET prototype with a novel transformable architecture.” In: *Phys Med Biol* 61.4, pp. 1795–1809 (cit. on p. 46).

Taya, T., J. Kataoka, A. Kishimoto, L. Tagawa, S. Mochizuki, T. Toshito, M. Kimura, Y. Nagao, K. Kurita, M. Yamaguchi, and N. Kawachi (2017). “Optimization and verification of image reconstruction for a Compton camera towards application as an on-line monitor for particle therapy”. In: *Journal of Instrumentation* 12.07, P07015. URL: <http://stacks.iop.org/1748-0221/12/i=07/a=P07015> (cit. on p. 156).

Taylor, J. T., P. P. Allport, G. L. Casse, N. A. Smith, I. Tsurin, N. M. Allinson, M. Esposito, A. Kacperek, J. Nieto-Camero, T. Price, and C. Waltham (Feb. 2015). “Proton tracking for medical imaging and dosimetry.” In: *J Instrum* 10 (cit. on p. 40).

Taylor, J. T., G. Poludniowski, T. Price, C. Waltham, P. P. Allport, G. L. Casse, M. Esposito, P. M. Evans, S. Green, S. Manger, S. Manolopoulos, J. Nieto-Camero, D. J. Parker, J. Symons, and N. M. Allinson (Nov. 2016). “An experimental demonstration of a new type of proton computed tomography using a novel silicon tracking detector.” In: *Med Phys* 43.11, p. 6129 (cit. on p. 40).

Telsemeyer, J., O. Jäkel, and M. Martisikova (Dec. 2012). “Quantitative carbon ion beam radiography and tomography with a flat-panel detector.” In: *Phys Med Biol* 57.23, pp. 7957–7971 (cit. on p. 40).

Ter-Pogossian, M. M. (1983). “Positron Emission Tomography (PET)”. In: *Diagnostic Imaging in Medicine*. Ed. by R. C. Reba, D. J. Goodenough, and H. F. Davidson. Dordrecht: Springer Netherlands, pp. 273–277. ISBN: 978-94-009-6810-3. DOI: 10.1007/978-94-009-6810-3_12. URL: https://doi.org/10.1007/978-94-009-6810-3_12 (cit. on p. 53).

Ter-Pogossian, M. M., D. C. Ficke, M. Yamamoto, and J. T. Hood (1982). “Super PETT I: A Positron Emission Tomograph Utilizing Photon Time-of-Flight Information”. In: *IEEE Transactions on Medical Imaging* 1.3, pp. 179–187 (cit. on p. 63).

Ter-Pogossian, M. M., M. E. Phelps, E. J. Hoffman, and N. A. Mullani (Jan. 1975). “A positron-emission transaxial tomograph for nuclear imaging (PETT).” In: *Radiology* 114.1, pp. 89–98 (cit. on p. 53).

Terasic (2009). *SFP HSMC Terasic Board User Manual*. Revision 1. Terasic Technologies Inc. (cit. on p. 92).

Terasic (2015). *SoCKit User Manual*. Revision F. Terasic Technologies Inc. (cit. on p. 92).

Testa, É., M. Bajard, M. Chevallier, D. Dauvergne, F. Le Foulher, N. Freud, J.-M. Létang, J.-C. Poizat, C. Ray, and M. Testa (2008). “Monitoring the Bragg peak location of 73 MeV/u carbon ions by means of prompt γ -ray measurements”. In: *Applied Physics Letters* 93.9,

p. 093506. DOI: 10.1063/1.2975841. eprint: <https://doi.org/10.1063/1.2975841>. URL: <https://doi.org/10.1063/1.2975841> (cit. on pp. 48, 146).

Testa, M., M. Bajard, M. Chevallier, D. Dauvergne, N. Freud, P. Henriet, S. Karkar, F. Le Foulher, J. M. Létang, R. Plescak, C. Ray, M.-H. Richard, D. Schardt, and É. Testa (2010). “Real-time monitoring of the Bragg-peak position in ion therapy by means of single photon detection.” eng. In: *Radiat Environ Biophys* 49.3, pp. 337–343. DOI: 10.1007/s00411-010-0276-2 (cit. on pp. 16, 148, 154).

Thörnqvist, S., L. P. Muren, L. Bentzen, L. B. Hysing, M. Hoyer, C. Grau, and J. B. B. Petersen (2013). “Degradation of target coverage due to inter-fraction motion during intensity-modulated proton therapy of prostate and elective targets”. In: *Acta Oncologica* 52.3, pp. 521–527. DOI: 10.3109/0284186X.2012.752860. URL: <https://doi.org/10.3109/0284186X.2012.752860> (cit. on p. 31).

Thun, M. J., J. O. DeLancey, M. M. Center, A. Jemal, and E. M. Ward (Jan. 2010). “The global burden of cancer: priorities for prevention”. In: *Carcinogenesis* 31.1, pp. 100–110. DOI: 10.1093/carcin/bgp263. URL: <http://www.ncbi.nlm.nih.gov/pmc/articles/PMC2802672/> (cit. on p. 4).

Tobias, C. A., E. V. Benton, M. P. Capp, A. Chatterjee, M. R. Cruty, and R. P. Henke (1977). “Particle radiography and autoactivation”. In: *International Journal of Radiation Oncology*Biology*Physics* 3. Particles and Radiation Therapy Second International Conference, pp. 35–44. ISSN: 0360-3016. DOI: [https://doi.org/10.1016/0360-3016\(77\)90224-3](https://doi.org/10.1016/0360-3016(77)90224-3). URL: <http://www.sciencedirect.com/science/article/pii/0360301677902243> (cit. on p. 37).

Tobias, C. A., E. A. Blakely, E. L. Alpen, J. R. Castro, E. J. Ainsworth, S. B. Curtis, F. Q. H. Ngo, A. Rodriguez, R. J. Roots, T. Tenfordf, and T. C. H. Yang (1982). “Molecular and cellular radiobiology of heavy ions”. In: *International Journal of Radiation Oncology*Biology*Physics* 8.12. Particle Accelerators in Radiation Therapy, pp. 2109–2120. ISSN: 0360-3016. DOI: [https://doi.org/10.1016/0360-3016\(82\)90554-5](https://doi.org/10.1016/0360-3016(82)90554-5). URL: <http://www.sciencedirect.com/science/article/pii/0360301682905545> (cit. on pp. 5, 17).

Tobias, C. A., A. Chatterjee, and A. R. Smith (1971). “Radioactive fragmentation of N7+ ion beam observed in a beryllium target”. In: *Physics Letters A* 37.2, pp. 119–120. ISSN: 0375-9601. DOI: [https://doi.org/10.1016/0375-9601\(71\)90086-7](https://doi.org/10.1016/0375-9601(71)90086-7). URL: <http://www.sciencedirect.com/science/article/pii/0375960171900867> (cit. on p. 45).

Tobias, C. A., J. H. Lawrence, J. L. Born, R. K. McCombs, J. E. Roberts, H. O. Anger, B. V. A. Low-Beer, and C. B. Huggins (1958). “Pituitary Irradiation with High-Energy Proton Beams. A Preliminary Report”. In: *Cancer Research* 18.2, pp. 121–134. eprint: <http://cancerres.aacrjournals.org/content/18/2/121.full.pdf>. URL: <http://cancerres.aacrjournals.org/content/18/2/121> (cit. on pp. 5, 20).

Tobias, C. A., J. E. Roberts, J. H. Lawrence, B. V. A. Low-Beer, H. O. Anger, and J. L. Born (1955). “Irradiation Hypophysectomy and related studies using 340 MeV protons an 190 MeV deuterons”. In: *Lawrence Berkeley National Laboratory. LBNL Report UCRL-2907* (cit. on pp. 5, 20).

- Todd, R. W., J. M. Nightingale, and D. B. Everett (Sept. 1974). "A proposed γ camera". In: *Nature* 251, 132 EP (cit. on pp. 66, 147).
- Toltz, A., M. Hoesl, J. Schuemann, J. Seuntjens, H.-M. Lu, and H. Paganetti (Nov. 2017). "Time-resolved diode dosimetry calibration through Monte Carlo modeling for in vivo passive scattered proton therapy range verification." In: *J Appl Clin Med Phys* 18.6, pp. 200–205 (cit. on p. 50).
- Tomitani, T., J. Pawelke, M. Kanazawa, K. Yoshikawa, K. Yoshida, M. Sato, A. Takami, M. Koga, Y. Futami, A. Kitagawa, E. Urakabe, M. Suda, H. Mizuno, T. Kanai, H. Matsuura, I. Shinoda, and S. Takizawa (Apr. 2003). "Washout studies of ^{11}C in rabbit thigh muscle implanted by secondary beams of HIMAC." In: *Phys Med Biol* 48.7, pp. 875–889 (cit. on p. 41).
- Tornai, M. P., G. Germano, and E. J. Hoffman (Aug. 1994). "Positioning and energy response of PET block detectors with different light sharing schemes". In: *IEEE Transactions on Nuclear Science* 41.4, pp. 1458–1463. ISSN: 0018-9499. DOI: 10.1109/23.322931 (cit. on pp. 109, 138).
- Tsai, Y.-S. (1974). "Pair Production and Bremsstrahlung of Charged Leptons". In: *Rev. Mod. Phys.* 46. [Erratum: *Rev. Mod. Phys.* 49, 521(1977)], p. 815. DOI: 10.1103/RevModPhys.46.815, 10.1103/RevModPhys.49.421 (cit. on p. 11).
- Unkelbach, J. and H. Paganetti (2018). "Robust Proton Treatment Planning: Physical and Biological Optimization". In: *Seminars in Radiation Oncology* 28.2. Proton Radiation Therapy, pp. 88–96. ISSN: 1053-4296. DOI: <https://doi.org/10.1016/j.semradonc.2017.11.005>. URL: <http://www.sciencedirect.com/science/article/pii/S1053429617301078> (cit. on p. 31).
- Urakabe, E., T. Kanai, M. Kanazawa, A. Kitagawa, K. Noda, T. Tomitani, M. Suda, Y. Iseki, K. Hanawa, K. Sato, M. Shimbo, H. Mizuno, Y. Hirata, Y. Futami, Y. Iwashita, and A. Noda (2001). "Spot Scanning Using Radioactive ^{11}C Beams for Heavy-Ion Radiotherapy". In: *Japanese Journal of Applied Physics* 40.4R, p. 2540. URL: <http://stacks.iop.org/1347-4065/40/i=4R/a=2540> (cit. on p. 45).
- Uribe, J., H. Li, T. Xing, Y. Liu, H. Baghaei, Y. Wang, M. Aykac, R. Ramirez, and W.-H. Wong (June 2003). "Signal characteristics of individual crystals in high resolution BGO detector designs using PMT-quadrant sharing". In: *IEEE Transactions on Nuclear Science* 50.3, pp. 355–361. DOI: 10.1109/TNS.2003.812478 (cit. on p. 126).
- Urie, M., M. Goitein, W. R. Holley, and G. T. Y. Chen (1986). "Degradation of the Bragg peak due to inhomogeneities". In: *Physics in Medicine & Biology* 31.1, p. 1. URL: <http://stacks.iop.org/0031-9155/31/i=1/a=001> (cit. on pp. 34, 36).
- Uzawa, A., K. Ando, S. Koike, Y. Furusawa, Y. Matsumoto, N. Takai, R. Hirayama, M. Watanabe, M. Scholz, T. Elsässer, and P. Peschke (2009). "Comparison of Biological Effectiveness of Carbon-Ion Beams in Japan and Germany". In: *International Journal of Radiation Oncology*Biology*Physics* 73.5, pp. 1545–1551. ISSN: 0360-3016. DOI: <https://doi.org/10.1016/j.ijrobp.2008.12.021>. URL: <http://www.sciencedirect.com/science/article/pii/S0360301608039175> (cit. on p. 31).

- Vallois, Y. (2016). "Test d'un hodoscope de faisceau à fibres scintillantes". Master internship report (cit. on pp. 133, 142).
- Vandenberghé, S., E. Mikhaylova, E. D'Hoe, P. Mollet, and J. S. Karp (Dec. 2016). "Recent developments in time-of-flight PET". In: *EJNMMI Physics* 3, p. 3 (cit. on p. 41).
- Vaquero, J. J. and P. Kinahan (2015). "Positron Emission Tomography: Current Challenges and Opportunities for Technological Advances in Clinical and Preclinical Imaging Systems." In: *Annu Rev Biomed Eng* 17, pp. 385–414 (cit. on pp. 60, 63).
- Vavilov, P. V. (1957). "Ionization losses of high-energy heavy particles". In: *Sov. Phys. JETP* 5. [Zh. Eksp. Teor. Fiz. 32, 920 (1957)], pp. 749–751 (cit. on p. 10).
- Vecchio, S., F. Attanasi, N. Belcari, M. Camarda, G. A. P. Cirrone, G. Cuttone, F. Di Rosa, N. Lanconelli, S. Moehrs, V. Rosso, G. Russo, and A. Del Guerra (Feb. 2009). "A PET Prototype for "In-Beam" Monitoring of Proton Therapy". In: *IEEE Transactions on Nuclear Science* 56.1, pp. 51–56. ISSN: 0018-9499. DOI: 10.1109/TNS.2008.2008306 (cit. on p. 46).
- Veksler, V. I. (1944). "A new method of accelerating relativistic particles." In: *Comptes Rendus (Dokal'dy) de l'Academie Sciences de l'URSS* 43.8, pp. 329–331 (cit. on p. 21).
- Vynckier, S., F. Vanneste, F. Richard, A. Bol, C. Michel, and A. Wambersie (Nov. 1989). "Control of patient positioning for fast neutron therapy using positron emission tomography." In: *Br J Radiol* 62.743, pp. 1031–1032 (cit. on p. 44).
- Watson, G. S. (1964). "Smooth Regression Analysis". In: *Sankhyā: The Indian Journal of Statistics, Series A* (1961-2002) 26.4, pp. 359–372. URL: <http://www.jstor.org/stable/25049340> (cit. on p. 159).
- Watts, D. A., U. Amaldi, A. Go, Y. H. Chang, W. Hajdas, S. Iliescu, N. Malakhov, J. Samarati, and F. Sauli (Oct. 2009). "A proton range telescope for quality assurance in hadrontherapy". In: *2009 IEEE Nuclear Science Symposium Conference Record (NSS/MIC)*, pp. 4163–4166. DOI: 10.1109/NSSMIC.2009.5402303 (cit. on p. 50).
- Watts, D. A., F. Borghi G. and Sauli, and U. Amaldi (July 2013). "The use of multi-gap resistive plate chambers for in-beam PET in proton and carbon ion therapy". In: *Journal of Radiation Research* 54. Suppl 1, pp. i136–i142 (cit. on p. 47).
- Webb, S. (2009). "The contribution, history, impact and future of physics in medicine". In: *Acta Oncologica* 48, pp. 169–177. DOI: 10.1080/02841860802244158 (cit. on p. 4).
- Weber, M. J. and R. R. Monchamp (1973). "Luminescence of Bi₄Ge₃O₁₂: Spectral and decay properties". In: *Journal of Applied Physics* 44.12, pp. 5495–5499. DOI: 10.1063/1.1662183. eprint: <https://doi.org/10.1063/1.1662183>. URL: <https://doi.org/10.1063/1.1662183> (cit. on p. 62).
- Weisskopf, V. (Aug. 1937). "Statistics and Nuclear Reactions". In: *Phys. Rev.* 52 (4), pp. 295–303. DOI: 10.1103/PhysRev.52.295. URL: <https://link.aps.org/doi/10.1103/PhysRev.52.295> (cit. on p. 12).

- WeissTechnik (2017). *Products brochure*. rev. Jan 2017. Weiss Technik North America, Inc. (cit. on p. 107).
- Weyrather, W. K., S. Ritter, M. Scholz, and G. Kraft (1999). “RBE for carbon track-segment irradiation in cell lines of differing repair capacity”. eng. In: *Int J Radiat Biol* 75.11, pp. 1357–1364 (cit. on p. 146).
- Wideröe, R. (July 1928). “Über ein neues Prinzip zur Herstellung hoher Spannungen”. In: *Archiv für Elektrotechnik* 21.4, pp. 387–406. ISSN: 1432-0487. DOI: 10.1007/BF01656341. URL: <https://doi.org/10.1007/BF01656341> (cit. on p. 20).
- Wilkens, J. J. and U. Oelfke (Jan. 2008). “Direct comparison of biologically optimized spread-out bragg peaks for protons and carbon ions.” In: *Int J Radiat Oncol Biol Phys* 70.1, pp. 262–266 (cit. on p. 19).
- Willers, H., A. Allen, D. R. Grosshans, S. J. McMahon, C. von Neubeck, C. Wiese, and B. Vikram (2018). “Toward A variable RBE for proton beam therapy”. In: *Radiotherapy and Oncology* 128.1, pp. 68–75. ISSN: 0167-8140. DOI: <https://doi.org/10.1016/j.radonc.2018.05.019>. URL: <http://www.sciencedirect.com/science/article/pii/S0167814018302780> (cit. on p. 31).
- Wilson, R. (2004). *A brief history of the Harvard cyclotrons*. Harvard University Press (cit. on p. 21).
- Wilson, R. R. (1946). “Radiological Use of Fast Protons”. In: *Radiology* 47.5. PMID: 20274616, pp. 487–491. DOI: 10.1148/47.5.487. eprint: <https://doi.org/10.1148/47.5.487>. URL: <https://doi.org/10.1148/47.5.487> (cit. on pp. 5, 20).
- Wohlfahrt, P., C. Möhler, C. Richter, and S. Greilich (2018). “Evaluation of Stopping-Power Prediction by Dual- and Single-Energy Computed Tomography in an Anthropomorphic Ground-Truth Phantom”. In: *International Journal of Radiation Oncology*Biology*Physics* 100.1, pp. 244–253. ISSN: 0360-3016. DOI: <https://doi.org/10.1016/j.ijrobp.2017.09.025>. URL: <http://www.sciencedirect.com/science/article/pii/S0360301617338920> (cit. on p. 34).
- Wouters, B. G., G. K. Lam, U. Oelfke, K. Gardey, R. E. Durand, and L. D. Skarsgard (Aug. 1996). “Measurements of relative biological effectiveness of the 70 MeV proton beam at TRIUMF using Chinese hamster V79 cells and the high-precision cell sorter assay.” In: *Radiat Res* 146.2, pp. 159–170 (cit. on pp. 35, 36).
- Wrenn, F. R., M. L. Good, and P. Handler (1951). “The Use of Positron-emitting Radioisotopes for the Localization of Brain Tumors”. In: *Science* 113.2940, pp. 525–527. ISSN: 0036-8075. DOI: 10.1126/science.113.2940.525. eprint: <http://science.sciencemag.org/content/113/2940/525.full.pdf>. URL: <http://science.sciencemag.org/content/113/2940/525> (cit. on p. 61).
- Wroe, A. J., I. M. Cornelius, and A. B. Rosenfeld (2005). “The role of nonelastic reactions in absorbed dose distributions from therapeutic proton beams in different medium”. In: *Medical Physics* 32.1, pp. 37–41. DOI: 10.1118/1.1824194. eprint: <https://aapm.onlinelibrary.wiley.com/doi/pdf/10.1118/1.1824194>. URL: <https://aapm.onlinelibrary.wiley.com/doi/abs/10.1118/1.1824194> (cit. on p. 15).

- Yamaguchi, M.**, Y. Nagao, K. Ando, S. Yamamoto, M. Sakai, R. K. Parajuli, K. Arakawa, and N. Kawachi (2018). "Imaging of monochromatic beams by measuring secondary electron bremsstrahlung for carbon-ion therapy using a pinhole x-ray camera". In: *Physics in Medicine & Biology* 63.4, p. 045016. URL: <http://stacks.iop.org/0031-9155/63/i=4/a=045016> (cit. on p. 51).
- Yamaguchi, M.**, K. Torikai, N. Kawachi, H. Shimada, T. Satoh, Y. Nagao, S. Fujimaki, M. Kokubun, S. Watanabe, T. Takahashi, K. Arakawa, T. Kamiya, and T. Nakano (2012). "Beam range estimation by measuring bremsstrahlung". In: *Physics in Medicine & Biology* 57.10, p. 2843. URL: <http://stacks.iop.org/0031-9155/57/i=10/a=2843> (cit. on p. 51).
- Yamaya, T.** (2017). "OpenPET: a novel open-type PET system for 3D dose verification in particle therapy". In: *Journal of Physics: Conference Series* 777.1, p. 012023. URL: <http://stacks.iop.org/1742-6596/777/i=1/a=012023> (cit. on pp. 44, 46).
- Yamaya, T.** (2018). "Development of the OpenPET for in-beam carbon ion therapy imaging" (cit. on p. 146).
- Yamaya, T.**, T. Inaniwa, S. Minohara, E. Yoshida, N. Inadama, F. Nishikido, K. Shibuya, C. F. Lam, and H. Murayama (2008). "A proposal of an open PET geometry". In: *Physics in Medicine & Biology* 53.3, p. 757. URL: <http://stacks.iop.org/0031-9155/53/i=3/a=015> (cit. on pp. 44, 46).
- Yamaya, T.**, T. Inaniwa, S. Mori, T. Furukawa, S. Minohara, E. Yoshida, F. Nishikido, K. Shibuya, N. Inadama, and H. Murayama (Jan. 2009). "Imaging simulations of an "OpenPET" geometry with shifting detector rings." In: *Radiol Phys Technol* 2.1, pp. 62–69 (cit. on p. 46).
- Yamaya, T.**, E. Yoshida, H. Tashima, A. Tsuji, K. Nagatsu, M. Yamaguchi, N. Kawachi, Y. Okumura, M. Suga, and K. Parodi (2017). "Whole gamma imaging (WGI) concept: simulation study of triple-gamma imaging". In: *Journal of Nuclear Medicine* 58.supplement 1, p. 152. URL: http://jnm.snmjournals.org/content/58/supplement_1/152.abstract (cit. on p. 52).
- Yan, X.**, U. Titt, A. M. Koehler, and W. D. Newhauser (2002). "Measurement of neutron dose equivalent to proton therapy patients outside of the proton radiation field". In: *Nuclear Instruments and Methods in Physics Research Section A: Accelerators, Spectrometers, Detectors and Associated Equipment* 476.1. Int. Workshop on Neutron Field Spectrometry in Science, Technology and Radiation Protection, pp. 429–434. ISSN: 0168-9002. DOI: [https://doi.org/10.1016/S0168-9002\(01\)01483-8](https://doi.org/10.1016/S0168-9002(01)01483-8). URL: <http://www.sciencedirect.com/science/article/pii/S0168900201014838> (cit. on p. 16).
- Yang, M.**, G. Virshup, J. Clayton, X. R. Zhu, R. Mohan, and L. Dong (2010). "Theoretical variance analysis of single- and dual-energy computed tomography methods for calculating proton stopping power ratios of biological tissues". In: *Physics in Medicine & Biology* 55.5, p. 1343. URL: <http://stacks.iop.org/0031-9155/55/i=5/a=006> (cit. on pp. 29, 34).
- Yordanova, A.**, E. Eppard, S. Kürpig, R. A. Bundschuh, M. Schönberger S.and Gonzalez-Carmona, G. Feldmann, H. Ahmadzadehfari, and M. Essler (2017). "Theranostics in nuclear medicine practice". In: *OncoTargets and therapy* 10, pp. 4821–4828 (cit. on pp. 59, 67).

- Yoshihara, Y.**, K. Shimazoe, Y. Mizumachi, H. Takahashi, K. Kamada, A. Takeda, T. Tsuru, and Y. Arai (2017). “Development of electron-tracking Compton imaging system with 30- μm SOI pixel sensor”. In: *Journal of Instrumentation* 12.01, p. C01045. URL: <http://stacks.iop.org/1748-0221/12/i=01/a=C01045> (cit. on p. 147).
- Zeng, G. L.**, J. R. Galt, M. N. Wernick, R. A. Mintzer, and J. N. Aarsvold (2004). “CHAPTER 7 - Single-Photon Emission Computed Tomography”. In: *Emission Tomography*. Ed. by M. N. Wernick and J. N. Aarsvold. San Diego: Academic Press, pp. 127–152. ISBN: 978-0-12-744482-6. DOI: <https://doi.org/10.1016/B978-012744482-6.50010-7>. URL: <http://www.sciencedirect.com/science/article/pii/B9780127444826500107> (cit. on p. 65).
- Zhu, X.**, S. España, J. Daartz, N. Liebsch, J. Ouyang, H. Paganetti, T. R. Bortfeld, and G. El Fakhri (July 2011). “Monitoring proton radiation therapy with in-room PET imaging”. In: *Physics in medicine and biology* 56.13, pp. 4041–4057 (cit. on p. 46).
- Zhu, X.** and G. E. Fakhri (2013). “Proton Therapy Verification with PET Imaging”. In: *Theranostics* 3.10, pp. 731–740 (cit. on p. 45).
- Zoglauer, A.**, R. Andritschke, and F. Schopper (2006). “MEGAlib The Medium Energy Gamma-ray Astronomy Library”. In: *New Astronomy Reviews* 50, pp. 629–632. DOI: 10.1016/j.newar.2006.06.049 (cit. on p. 176).
- Zoglauer, A.**, E. S. Boggs, M. Galloway, M. Amman, N. P. Luke, and R. Kippen (Oct. 2011). “Design, implementation, and optimization of MEGAlib’s image reconstruction tool Mimrec”. In: 652, pp. 568–571 (cit. on pp. 78, 156).
- Zografos, A.**, T. Brown, C. Cohen-Jonathan, C. Hettler, F. Huang, V. Joshkin, K. Leung, M. F. Moyers, Y. Parker, D. Pearson, M. Rougieri, and R. W. Hamm (2013). “Development of the Dielectric Wall Accelerator”. In: *Proceedings, 4th International Particle Accelerator Conference (IPAC 2013): Shanghai, China, May 12-17, 2013*, THOAB201. URL: <http://JACoW.org/IPAC2013/papers/thoab201.pdf> (cit. on p. 23).

Index

- Aarsvold, J. N., 274
Abbassi, L., 240
Abbott, M., 251
Abe, M., 244
Abe, S., 40, 227
Abellan, C., 100, 227, 249
Adam, L.-E., 88, 227, 233
Aebersold, P. C., 267
Agodi, C., 49, 227
Ahmadzadehfar, H., 274
Aiello, S., 252
Aiginger, H., 267
Ainsley, C. G., 34, 227
Ainsworth, E. J., 270
Akagi, T., 244, 250
Aken, M. O. van, 250
Akiu, K., 254
Al-Rasheed, M. M., 228
Al-Sugair, A., 228
Alamawi, R., 228
Alavi, A., 250
Albertini, F., 32, 34, 227
Aldawood, S., 147, 227
Aleksandrov, D. V., 241
Algranati, C., 256
Alharbi, T., 185, 227
Allemand, R., 241
Allen, A., 273
Allinson, N. M., 261, 269
Allport, P. P., 269
Alonso, J., 234, 258
Alpen, E. L., 234, 252, 270
AlShaikh, O., 228
Altera, 87, 92, 97, 98, 100, 228
Alzahrani, A. S., 66, 228
Amaldi, U., vii, 22, 23, 39, 49, 228, 233,
 236, 272
Ambrosi, G., 255
Amemiya, N., 246
Amman, M., 275
Ancukiewicz, M., 258
Ando, K., 255, 271, 273
Andreaco, M., 235, 262
Andreae, S., 252
Andritschke, R., 275
Angellier, G., 234
Anger, H. O., 53, 64, 65, 172, 229, 270
Anscher, M. S., 231, 264
Antoine, S., 23, 229
Arai, N., 243
Arai, Y., 274
Arakawa, K., 273
Archambeau, J. O., 230
Arena, C., 18, 229
Aslaninejad, M., 260
Aspen Aerogels, 87, 229
Assmann, W., 251, 259
Aswath, N., 256
Atkins, M. S., 258
Attanasi, F., 46, 229, 272
Attili, A., 231, 254
August, R. A., 254
Autin, B., 229
Avery, S., 261
Aykac, M., 271
Azencot, J., 253
Böhlen, T. T., 262
Böttcher, S., 238
Baba, M., 254
Bacher, R., 260
Baghaei, H., 271
Bajard, M., 269
Bajema, J. F., 251
Balsamo, J., 230
Ban, G., 233
Barlow, R., 260
Baroni, G., 239
Barrio, J., 241
Barth, R. F., 20, 229
Bashkirov, V., 247, 261, 263
Basilavecchia, M., 266
Basile, E., 262
Baskar, R., 5, 230
Basko, R., 78, 230
Battaglia, M., 236
Battistoni, G., 227, 231, 234, 239, 249,
 254, 260, 262, 263
Baudot, J., 239
Bauer, J., 43, 46, 230, 234, 241
Baum, R. P., 67, 230, 268
Bazalova, M., 34, 230
Beard, C. D., 260
Beaulieu, L., 230
Becchetti, F. D., 251, 252

- Becher, W., 243
Beddar, S., 237, 253, 261
Bednarz, B., xvii, 36, 230
Beeckman, W., 229
Belcari, N., 229, 231, 234, 239, 249, 254,
 255, 263, 267, 272
Belkić, D., 6, 230
Bellemann, M. E., 227, 233
Belli, M., 17, 230
Bellini, F., 227, 261
Benassi, M., 262
Benilov, A., 262, 266
Bennett, G. W., 44, 230
Benson, A., 268
Benton, E. V., 270
Bentzen, L., 270
Bentzen, S. M., 5, 230
Berger, M. J., 245
Berger, M.J., 38, 230
Bergstrom, M., 241
Bergstrom, P. M., 75, 231
Berlin, J., 268
Bernal, M. A., 240
Berra, P., 228
Bert, C., 31, 32, 231, 242
Bertini, H. W., 12, 231
Bertrand, D., 242, 251
Bes, A., 240
Besserer, J., 260, 265
Bethe, H., 8, 231
Beuve, M., 236, 253, 255
Beyer, G. P., 264
Bhat, M. R., xvii, 174, 231
Bialas, P., 257
Bianchi, A., 228
Bice, A. N., 251
Bichsel, H., 6, 231
Biegun, A. K., 237, 245
Bini, F., 261
Binkley, D. M., 235
Binzel, K., 255
Bischel, H., xvii, 36, 231
Bisello, D., 254
Bisogni, M., 254
Bisogni, M. G., 47, 231, 239, 255, 260
Black, R. D., 50, 231, 264
Blahd, W. H., 53, 231
Blakely, E. A., 5, 17, 19, 232, 270
Blattmann, H., 260
Blazey, G., 256
Bliss, N., 260
Bloch, F., 8, 232
Blue, T. E., 229
Boehringer, T., 253, 260
Boer, J. de, 260
Boggs, E. S., 275
Bohlen, T., 241
Bohr, N., 10, 232
Bohringer, T., 260
Boi, S., 256
Bol, A., 272
Bolick, N. G., 264
Bolozdynya, A., 258
Bolsi, A., 227
Boltwood, B. B., 55, 232
Bonanno, D. L., 252
Bonanno, D. L., 241, 252
Bones, P. J., 236
Bongiovanni, D. G., 241, 252
Bonomi, R., 228
Bonora, M., 239
Bony, M., 255
Borghi G. and Sauli, F., 272
Born, J. L., 270
Bortfeld, T., 238, 241, 248, 259, 265
Bortfeld, T. R., 274
Bosson, G., 240
Bothe, W., 11, 232
Boukhémiri, A., 240
Boutefnouchet, A., 235
Braccini, S., 20, 40, 228, 232
Braess, H., 239, 266
Bragg, W. H. M. A., 6, 10, 146, 232
Brahme, A., 5, 233
Brandenburg, S., 234, 237
Brassart, N., 253
Braunn, B., 15, 233
Breton, D., 110, 233
Brianzi, M., 264
Brill, A. B., 257
Brix, G., 88, 227, 233
Bronk, L., 242
Brons, S., 238, 259, 262, 264
Brown, J. A., 251
Brown, T., 244, 275
Brun, R., x, 103, 106, 112, 233
Brunner, S. E., 139, 233
Bruzzi, M., 264

- Brzezinski, K. W., 234
 Bucciantonio, M., 37, 39, 49, 233
 Bucciolini, M., 245, 264
 Bugalho, R., 262
 Bui, F., 234
 Buitenhuis, H. J. T., 47, 234, 237
 Bundschuh, R. A., 274
 Burdine, J. A., 247
 Busato, E., 255
 Busca, P., 266
 Bush, D. A., 256
 Bushnell, D., 268
 Buvat, I., 244, 262
 Byars, L., 260
 Böhmer, M., 227
 Cabal, G., 241
 Caccia, B., 262
 Cachemiche, J.-P., 100, 227, 234, 249
 Camarda, M., 229, 272
 Camarlinghi, N., 47, 231, 234, 239, 249,
 254, 260, 263, 267
 Cambraia Lopes, P., 47, 234
 Candela Juan, C., 241
 Cantor, D., 4, 234
 Caplin, M., 268
 Caponetto, L., 249
 Caporaso, G. J., 23, 234
 Capp, M. P., 270
 Cappucci, F., 249, 254
 Caraher, J., 251
 Carnicer, A., 16, 234
 Carpanese, M., 262
 Carpinelli, M., 264
 Carrier, J.-F., 230
 Caruso, P., 266
 Cascio, E., 253
 Casella, V., 246
 Casse, G. L., 269
 Cassen, B., 236
 Castelluccio, D. M., 262
 Castro, J. R., 19, 234, 270
 Catterall, M., 20, 234
 Cavalieri, R. R., 241
 Cecchetti, M., 234, 254
 Cecchin, D., 184, 234
 Cee, R., 260
 Center, M. M., 247, 270
 Cerello, P., 231, 239, 254, 260
 Cerutti, F., 258, 259, 262, 267
 Chadelas, R., 255
 Champion, C., 240
 Chang, J., 230
 Chang, L.-T., 246
 Chang, P. Y., 232
 Chang, W., 258
 Chang, Y. H., 272
 Chang, Y.-H., 228
 Chasen, B., 268
 Chatterjee, A., 44, 234, 245, 252, 270
 Chatziioannou, A., 235
 Chauvel, P., 244, 253
 Chen, G. T. Y., 271
 Chen, H., 237
 Chen, W.-T., 258
 Chen, X., 87, 98, 235, 249
 Chen, Y.-J., 234
 Cherry, S. R., 63, 235
 Chesler, D. A., 61, 235
 Chevallier, M., 233, 244, 249, 269
 Chiao, P., 262
 Chin, M. P. W., 262
 Chu, W. T., 37, 235
 Chulkov, L. V., 241
 Chung, Y. H., 250
 Chvetsov, A. V., xvii, 34, 36, 235
 Ciangaru, G., 261
 Cicardi, C., 228
 Ciciriello, F., 254
 Ciocca, M., 239, 240, 249
 Cirrone, G., 254
 Cirrone, G. A. P., 249
 Cirrone, G. A. P., 227, 234, 252, 264, 267,
 272
 Cirrone, G. A. P., 46, 235
 Cirrone, G. A. P., 229
 Cisbani, E., 262
 Civinini, C., 264
 Clasie, B., 268
 Clayton, J., 274
 Clinthorne, N., 243
 Clinthorne, N. H., 262
 Cobb, J. H., 260
 Coderre, J. A., 229
 Cohen-Jonathan, C., 244, 275
 Colby, B., 263
 Coli, S., 231, 254
 Colin, J., 233
 Colléaux, C., 136, 235

- Collamati, F., 227, 261
Collazuol, G., 255
Collot, J., 229, 240
Colton, E., 249
Colton, E. P., 255
Combs, S. E., 230
Comiskey, R., 245
Compton, A. H., 72, 235
Concaildi, G. A., 255
Conjat, M., 229
Constanzo, J., 239
Cookson, J. A., 37, 235
Cooper, P. K., 252
Coray, A., 232, 253, 260
Cormack, A. M., 37, 235
Cormoreche, E., 241
Cornelius, I. M., 273
Corsi, F., 254, 255
Coudurier, V., 132, 142, 235
Courdi, A., 253
Coursey, J.S., 230
Coutrakon, G., 256, 263
Craft, D., 241
Crandall, K., 228
Crandall, K. R., 243
Crandall, P. H., 65, 236
Cree, M. J., 78, 236
Crescenti, M., 228
Crespo, P., 43, 44, 46, 234, 236, 238, 239, 259
Crozes, T., 240
Cruty, M. R., 270
Cunha, M., 31, 236, 255
Curceanu, C., 257
Curie, P., 55, 236
Curie, S., 236
Curtis, S. B., 232, 270
Curtoni, S., 240
Cussol, D., 233
Cussonneau, J.-P., 258
Cuttone, G., 227, 229, 234, 235, 249, 254, 264, 267, 272
Czerwiński, E., 257
D'Andrea, M., 262
D'Hoe, E., 271
Daartz, J., 230, 238, 248, 274
Dahiya, M., 55, 236
Dahoumane, M., 86, 87, 236, 249
Daube-Witherspoon, M. E., 247, 248, 268
Dauvergne, D., 49, 233, 236, 237, 239, 240, 244, 249, 252, 261, 262, 269
Davino, D., 228
De Lucia, E., 227, 254, 261
De Marchi, S., 234
De Martinis, C., 228
De Napoli, M., 227
De Nolf, W., 240
De Rydt, M., 249
Debus, J., 230, 241, 246
Dedes, G., 227, 244, 262
Degenhardt, C., 47, 236
Degiovanni, A., 20, 228, 236
Dehaes, J. C., 266
Del Guerra, A., 229, 231, 234, 239, 249, 254, 255, 263, 267, 272
Delagnes, E., 233
DeLancey, J. O., 270
DeLaney, T., 268
DeLaney, T. F., 259
Della Negra, R., 239
Deller, T., 251
Dellert, M., 260, 265
Delpassand, E., 268
Dendooven, P., 47, 234, 237, 245, 267
Deng, S.-M., 97, 237, 249
Derenzio, S. E., 256
DeSantis, C., 247
Despeignes, V., 4, 237
Dessy, F., 242
DeWitt, L., 247
Dexheimer, D., 257
Di Domenico, A., 227
Di Rosa, F., 229, 272
Diblen, F., 234, 237
Ding, Y., 262
Dinh, J., 242
Doll, J., 233
Donetti, M., 239
Dong, L., 238, 257, 274
Donnard, J., 258
Donnarieix, D., 255
Doria, D., 266
Dorrer, H., 256
Dorscheid, R., 236
Dowdell, S., 35, 237, 242, 265
Draeger, E., 148, 155, 169, 237
Dubus, A., 266
Duck, F. A., 4, 237

- Dulski, K., 257
 DuMond, J. W. M., 75, 237
 Durand, R. E., 273
 Durante, M., vii, xvii, 5–7, 10, 12, 13, 18–
 20, 25, 35, 36, 237–240, 242, 257,
 261, 267
 Duval, P. Y., 234
 Duval, S., 258
 Duvvuri, S., 245
 Dyshkant, A., 256
 Easton, M. J., 260
 Edgecock, R., 260
 Edwards, R. Q., 250
 Egger, E., 253
 Eickhoff, H., 259
 Eijck, C. H. van, 250
 El Bitar, Z., 240
 El Fakhri, G., 238, 274
 El-Haddad, G., 268
 Eley, J. G., 242
 Elftmann, R., 88, 238
 Elsässer, T., 146, 238, 240, 271
 Elsässer, T., 264
 Endo, M., 254
 Engelsman, M., 31, 238, 248
 Enghardt, W., 44, 45, 48, 146, 229, 236,
 238, 239, 245, 259–261, 265–267
 Eppard, E., 274
 Erdelyi, B., 256, 263
 Ereditato, A., 232
 Erion, J. L., 268
 España, S., xvii, 34, 36, 40, 238, 274
 Esposito, M., 269
 Essen, M. van, 250
 Essers, M., 50, 238
 Essler, M., 274
 Esumi, H., 257
 Evans, P. M., 261, 269
 Evans, T. C., 4, 239
 Everett, D. B., 172, 239, 270
 Faccini, R., 227, 254, 261
 Fakhri, G. E., 274
 Farley, F., 253
 Farquhar, T. H., 235
 Fattori, G., 35, 239
 Feelders, R. A., 250
 Feldmann, G., 274
 Feng, V., 261
 Fenning, R. J. L., 260
 Fermi, E., 12, 239
 Ferrari, A., 231, 249, 258–260, 262, 263,
 267
 Ferree, C. R., 264
 Ferrero, V., 47, 231, 239, 260
 Ferretti, S., 234, 249, 254, 263, 267
 Ferroni, F., 227, 261
 Ficke, D. C., 269
 Fiedler, F., viii, 41–43, 236–239, 245, 265,
 266
 Field, S. B., 234
 Fietier, N., 253
 Finck, C., 49, 239
 Fiore, S., 227, 261
 Fiorina, E., 231, 239, 254, 260
 Fiorini, C., 266
 Fischman, A. J., 259
 Flanz, J., 268
 Fleming, J. S., 239
 Flynn, D. F., 262
 Fontana, M., 66, 81, 142, 148, 165, 171,
 239, 240, 263
 Fontbonne, J. M., 233
 Fontenot, J., 257
 Foray, N., 4, 240
 Force, P., 255
 Fordt, R., 256
 Forest, F., 229
 Foresta, M., 255
 Fossati, P., 31, 240
 Fourrier, J., 229
 Fowler, J. S., 246
 Frach, T., 236
 Frallicciardi, P., 254
 Francis, Z., 15, 240
 Frandes, M., 147, 240, 254
 Freud, N., 242, 244, 249, 252, 261, 262,
 269
 Frey, K., 241
 Friedländer, E. M., 15, 240
 Friedrich, T., 5, 238, 240, 267
 Frizzi, T., 266
 Froidefond, E., 229
 Fromm, W. D., 238, 260
 Frullani, S., 262
 Fujimaki, S., 273
 Fujimoto, T., 246
 Fujisaki, T., 227

- Fujita, T., 246
Fukazawa, Y., 268
Fukumura, A., 254
Furukawa, S., 255
Furukawa, T., 246, 274
Furusawa, Y., 248, 271
Fusi, D., 263
Futami, Y., 227, 247, 254, 271

Gabor, G., 265
Gabriel, T. A., 231
Gaffney, C. C., 266
Gaglione, R., 130, 142, 240
Gahn, C., 260
Gajos, A., 257
Gallin-Martel, L., 240
Gallin-Martel, M.-L., 141, 240
Gallo, G., 39, 241, 252
Galloway, M., 275
Galt, J. R., 274
Gardey, K., 273
Gardner, I. S. K., 260
Gariod, R., 44, 241
Garlasché, M., 228
Garonna, A., 228
Gauzzi, P., 227
GE Healthcare, 172, 178, 241
GeckoDrive, 130, 241
Geissel, H., 238, 260, 264
Gensheimer, M. F., 50, 241
Gerard, S. K., 66, 241
Germano, G., 271
Gernhäuser, R., 227
Gerweck, L., 268
Gerweck, L. E., 258
Ghio, F., 262
Giaccia, A. J., 243
Giacometti, V., 247
Giantsoudi, D., 19, 241, 266
Gillam, J. E., 78, 156, 241, 258, 267
Gillin, M., 261
Giordanengo, S., 239
Giovannini, G., 19, 241
Giove, D., 228
Giraudo, G., 231, 239, 254
Giubilato, P., 254
Glover, G., 251
Glowacz, B., 257
Go, A., 228, 272
Goethem, M.-J. van, 237

Goitein, G., 227, 253
Goitein, M., 245, 258, 271
Goldberg, A. C., 230
Goldberg, S., 268
Golnik, C., 109, 138, 241, 245, 265
Golovkov, M. S., 15, 241
Goncalves, F., 262
Good, M. L., 273
Goodhead, D. T., 230
Goodman, G. B., 44, 241, 266
Gordon, J., 262
Gorecki, A., 240
Gorgol, M., 257
Goto, J., 263
Gottschalk, B., 11, 16, 25, 242, 245
Grözinger, S. O., 231
Graaf, E. R. van der, 237
Graeff, C., 32, 242
Grande, E., 268
Granja, C., 243
Grant, P. E., 241
Grassberger, C., 15, 35, 237, 241, 242, 265
Grau, C., 270
Green, S., 269
Greilich, S., 245, 273
Grevillot, L., 151, 242
Griesmer, J., 255
Grochowski, E., 266
Grosshans, D. R., 242, 273
Grossmann, M., 253, 260
Grosu, A., 265
Gruber, L., 233
Grün, R., 267
Guan, F., 19, 242
Guerra, P., 255
Guertin, A., 233
Gueth, P., 262
Guicheney, C., 255
Gullberg, G. T., 230
Gunter, D. L., 65, 242
Gunzert-Marx, K., 49, 242
Gupta, M., 267
Guthy, J., 230
Gwosch, K., 49, 243

Hüfner, J., 12, 245
Hérault, J., 234
Haas, F., 233
Haberer, T., 27, 230, 243, 249, 259, 261
Haberkorn, U., 233

- Habs, D., 250, 268
Hachon, F., 234
Hadi, A. F. M., 258
Haettner, E., 14, 15, 243
Hajdas, W., 228, 272
Hall, E., 268
Hall, E. J., 17, 243
Hallman, J., 268
Halperin, E. C., 5, 243
Hamamatsu, 95, 130, 135, 243
Hamm, R. W., 23, 243, 275
Han, L., 172, 173, 175, 191, 243
Hanawa, K., 248, 271
Handler, P., 273
Haneishi, H., 269
Harrison, R., 266
Harrison, R. L., 251
Harrison, R. W., 241
Hartmann, B., 243
Hartmann, G. H., 246
Hartmann, M., 256
Hasch, B. G., 260, 261
Hasegawa, A., 240
Haskins, P. S., 254
Hattori, K., 247
Hayakawa, Y., 50, 243, 268
Heckman, H. H., 240
Hedin, D., 256
Heeres, P. N., 237
Heetderks, W. J., 248
Heidel, K., 245
Heller, H., 238
Hendee, W. R., 55, 243
Hendifar, A., 268
Henke, R. P., 270
Henriquet, P., 49, 244, 269
Henrotin, S., 251
Herault, J., 196, 244, 251, 253
Herbach, C. M., 265
Herder, W. W. de, 250
Herfarth, K., 230, 231
Herk, M. van, 254
Hermann, O. W., 231
Hermanss, C. F., ix, 76, 244
Hertz, B., 67, 244
Hertz, S., 67, 244
Hettler, C., 23, 244, 275
Heymans, V., 251
Hiesmayr, B.C., 257
Higashi, A., 254
Higgins, C. S., 244
Highland, V. L., 11, 244
Hilaire, E., 106, 148, 157, 244
Hill, M. A., 260
Hinz, R., 238
Hiraoka, T., 231
Hirasawa, M., 78, 244
Hirata, Y., 271
Hirayama, R., 271
Hirtl, A., 233
Hishikawa, Y., 46, 244, 250
Hobday, T., 268
Hoesl, M., 270
Hoffman, E. J., 269, 271
Hoffman, E. W., 255
Hoffmann, E. J., 53, 61, 244
Hoffmann, T., 260
Hohn, A., 256
Holder, D., 258
Holley, W. R., 17, 245, 252, 271
Hong, L., 33, 245
Hood, J. T., 269
Horita, R., 248
Hosono, K., 243, 268
Hostachy, J.-Y., 240
Howard, J., 264
Hoyer, M., 270
Hsi, W. C., 46, 245
Huang, C. Y., 257
Huang, F., 244, 275
Huang, H.-M., 156, 245
Huard, D., 247
Hubbell, J. H., 179, 192, 245
Hueso-González, F., 89, 109, 138, 245
Hug, E., 256
Hug, E. B., 227
Huggins, C. B., 270
Huh, S. S., 243
Hunt, J. M., 231
Hurley, F., 261, 263
Hurley, R. F., 247
Hutchins, G., 251
Hysing, L. B., 270
Hälg, R., 265
Hünemohr, N., 34, 245
Iancu, G., 238
Ianzini, F., 230
Iarocci, E., 227, 261

- Iborra, N., 244
Ichimura, Y., 267
ICRU, xvii, 17, 29, 36, 245
Ido, T., 62, 246
Iliescu, S., 228, 272
Imai, R., 240
Inada, T., 227, 247, 268
Inadama, N., 269, 274
Inaniwa, T., 29, 31, 246, 254, 255, 269, 274
Incerti, S., 240
Indelicato, D. J., 245
Insa, C., 255
Iritani, R., 255
Irnich, H., 264
Iseki, Y., 45, 246–248, 255, 271
Ishibashi, I., 256
Ishii, K., 255
Ivanchenko, V. N., 240
Iwase, H., 242, 243
Iwashita, Y., 271
Iwata, Y., 28, 246
Izumikawa, T., 263

Jäkel, O., viii, 29–31, 34, 243, 246, 249, 262, 265, 269
Jacene, H., 268
Jackson, H. C., 252
Jacob, C., 246
Jakubek, J., 243
Jan, M.-L., 245
Janssens, G., 262
Jarret, V. B., 264
Jasińska, B., 257
Jaszczak, R. J., 66, 246, 247
Jemal, A., 4, 247, 270
Johnson, E., 256
Johnson, R. P., 38, 39, 247, 261, 263
Johnston, K., 256
Johnstone, C., 260
Joly, B., 249
Jones, B., 19, 247, 260
Jones, T. J., 260
Jones, W., 235
Jongen, Y., 267
Joshkin, V., 244, 275
Juelke, P., 253
Juliani, D., 239
Julich, R., 239
Jyoti, B., 267

Jäkel, O., 245
Kabuki, S., 193, 247, 267
Kacperek, A., 269
Kagawa, K., 244
Kam, B. L., 250
Kamada, K., 274
Kamada, T., 240, 246, 254
Kamiya, T., 273
Kanai, T., 27, 227, 246–248, 252, 254, 255, 266, 271
Kanazawa, M., 45, 246–248, 255, 271
Kanematsu, N., 29, 246, 247, 254
Kankeleit, E., 264
Kaplan, S. N., 265
Kaplon, L., 257
Karakaya, Y., 239
Karamitros, M., 240
Karger, C. P., 246
Karkar, S., 269
Karp, J., 251
Karp, J. S., 62, 63, 247, 248, 268, 271
Kaser-Hotz, B., 265
Kashiguine, S., 263
Kastan, M. B., 255
Kataoka, J., 269
Kato, H., 254
Kawachi, K., 227, 247
Kawachi, N., 269, 273, 274
Kawano, A., 255
Kawasaki, T., 263
Kearns, W. T., 264
Keevil, S. F., 4, 248
Kelliher, D. J., 260
Kereiakes, J. G., 4, 248
Kerr, M. D., 242
Keyes, J. W. Jr., 66, 248
Khan, A., 260
Kieffer, R., 233
Kim, C. H., 255
Kim, J. S., 250
Kim, J.-W., 255
Kimura, H., 267
Kimura, M., 269
Kimura, T., 263
Kinahan, P., 271
King, S. E., 254
Kinouchi, S., 268, 269
Kippen, R., 275
Kirsch, D. G., 255

- Kishimoto, A., 269
 Kishimoto, T., 267
 Kisielewska-Kamińska, D., 257
 Kitagawa, A., 45, 246–248, 255, 271
 Kleeman, R., 232
 Klein, O., 73, 248
 Klem, R. D., 255
 Knoll, G. F., ix, 72, 74, 77, 84, 248
 Knopf, A.-C., viii, 33, 46, 146, 248, 259
 Knopp, M., 255
 Knott, M. J., 255
 Koch, N., 257
 Koehler, A. M., 34, 37, 38, 235, 242, 248, 267, 274
 Koga, M., 271
 Kohara, R., 247
 Kohno, R., 247
 Kohno, T., 254, 266
 Koike, S., 271
 Kokubun, M., 273
 Kolthammer, J., 268
 Komori, M., 51, 248, 254
 Komura, S., 267
 Kooij, P. P., 250
 Koral, K. E., 262
 Korcyl, G., 257
 Kormoll, T., 245, 265
 Kornelsen, R. O., 266
 Kostara, E., 231, 254
 Koster, U., 256
 Kouda, S., 247
 Kowalski, P., 257
 Kozik, T., 257
 Krämer, M., 31, 152, 239, 243, 246, 249, 264
 Kraan, A., 254
 Kraan, A. C., 42, 47, 48, 234, 249, 263, 267
 Kraft, G., 238, 243, 249, 264, 272
 Kragl, G., 238
 Kramer, S. L., 37, 249, 255
 Kraus, G., 241
 Krause, M., 253
 Krawczyk, N., 257
 Krenning, E., 268
 Krenning, E. P., 250
 Kreslo, I., 232
 Krider, J., 256
 Krimmer, J., ix, xvii, 24, 79, 97, 148, 236, 239, 240, 244, 249, 261, 262
 Krzemień, W., 257
 Krämer, M., 238
 Kubiak, T., 32, 249
 Kubicz, E., 257
 Kubo, A., 247
 Kubo, H., 247, 267
 Kuchment, P., 147, 192, 249
 Kuhl, D. E., 61, 66, 246, 250
 Kuhn, A., 268
 Kulkarni, H. R., 230, 268
 Kulkarni, S. R., 238
 Kulke, M. H., 268
 Kumazaki, Y., xvii, 36, 250
 Kunath, D., 239, 266
 Kunieda, E., 247
 Kunz, P. L., 268
 Kurita, K., 269
 Kurz, C., 230, 262
 Kwekkeboom, D., 268
 Kwekkeboom, D. J., 67, 250
 Kürpig, S., 274
 Létang, J. M., 239, 240, 244, 249, 252, 261, 262, 269
 Létang, J.-M., 269
 La Tessa, C., 261
 Labalme, M., 233
 Lacasta, C., 241, 258, 267
 Lacoste, A., 240
 Ladjal, H., 253
 Lam, C. F., 274
 Lam, G. K., 273
 Lam, G. K. Y., 241, 258, 266
 Lambert, D., 249, 255
 Lamblin, J., 258
 Lancelot, J. L., 229
 Lanconelli, N., 229, 272
 Landau, L., 10, 250
 Landry, G., 42, 250
 Lang, C., 51, 52, 227, 250
 Larson, N. M., 231
 Larsson, B., 21, 250
 Larsson, S. A., 66, 250
 Laube, K., 266
 Lauckner, K., 260
 Laurence, T., 255
 Laval, M., 241
 Lawrence, E. O., 20, 250
 Lawrence, J. H., 267, 270
 Le Foulher, F., 233, 269

- Le Gac, R., 234
Leary, C., 261
Lebhertz, D., 233
Lebtahi, R., 268
Lecoq, P., 64, 250
Lee, C. Y., 40, 250
Lee, K. A., 230, 257
Lee, M. Y., 252
Lee, M.-W., 245
Lehrack, S., 50, 251
Lemaire, O., 258
Lennox, A. J., 23, 251
Leonard, P. F., 248
Leone, M., 56, 57, 251
Leonora, E., 241, 252
Leray, P., 258
Lestand, L., 249, 255, 262
Letellier, V., 234
Leung, K., 244, 275
Levin, C., 64, 251
Levine, G. S., 230
Levy, R. P., 29, 251
Lewellen, T., viii, 61, 251
Lewellen, T. K., 63, 251
Lewis, H. W., 11, 251
Ley, J.-L., 85, 87, 107, 138, 175, 236, 240, 249, 251, 252
Li, H., 271
Li, Q., 248
Li, Z., 245
Licciulli, F., 254
Liebsch, N., 248, 274
Liebsch, N. J., 241, 259
Lin, J. C., 252
Lin, S., 253, 260
Lin, S. H., 242
Link, J. M., 251
Liprandi, S., 227
Little, J. B., 262
Litzenberg, D. W., 45, 251, 252
Liu, B., 254
Liu, C.-C., 245
Liu, H., 62, 252
Liu, Y., 271
Livingston, M. S., 250
Llacer, J., 15, 44, 234, 252
Llosá, G., 241, 258, 267
Lo Nigro, S., 235
Lo Presti, D., 39, 241, 252, 264
Lobrich, M., 17, 252
Locher, G. L., 20, 252
Loeffler, J. S., 237, 258, 259
Lojacono, R. A., 235
Lojacono, X., 78, 106, 176, 244, 252
Lomax, A. J., 6, 35, 227, 248, 253, 256, 260, 265
Longhitano, F., 241, 252
Lopera Sierra, M., 268
Lorenz, W., 233
Low-Beer, B. V. A., 270
Lu, G.-N., 237
Lu, H.-M., 50, 253, 270
Ludewigt, B. A., 235
Luke, N. P., 275
Luo, D., 265
Lüchtenborg, R., 242
Lühr, A., 31, 253
Möckel, D., 239
Möhlerm, C., 273
Mühlens, O., 236
Méot, F., 229
Maalmi, J., 233
Macaeva, E., 229
Macafee, S., 261
Macabee, H. D., 15, 253
MacDonald, S. M., 266
Macellari, V., 262
Machida, S., 260
MacKay, R., 258
Mackin, D., 78, 156, 237, 253
Mackin, D. S., 261
Madan, N., 241
Magel, A., 238, 264
Magne, M., 249, 255
Magrin, G., 228
Maier, L., 227
Mairani, A., 240, 241, 249, 259, 262, 263
Malakhov, N., 228, 272
Malhi, I., 266
Mandrillon, J., 229
Mandrillon, P., xiv, 196, 229, 253
Manescu, P., 32, 253
Manfrass, P., 238, 260
Manger, S., 269
Mania, R. C., 254
Mann, G., 253
Mann, G. G., 231
Manolopoulos, S., 269

- Mantero, A., 240
Marafini, M., 47, 227, 254, 261
Maramraju, S. H., 251
Marcatili, S., 240, 255
Marino, C., 262
Marino, N., 254, 263
Marinsek, T., 227
Marr, R. B., 262
Martin, C., 238
Martin, F., 255
Martin, R. L., 249, 255
Martin, W. R., 241
Martinez-McKinney, F., 263
Martisikova, M., 243, 269
Marton, J., 233
Marzocca, C., 254, 255
Masullo, M. R., 228
Matarrese, G., 254, 255
Mathez, H., 236, 237, 249
Matsufuji, N., xvii, 15, 29, 31, 36, 240, 246, 247, 254
Matsumoto, Y., 271
Matsuoka, Y., 267
Matsushita, S., 255
Matsuura, H., 271
Matsuzawa, H., 247
Mattei, I., 227, 261
Matthew, R. P., 261
Mattiazzo, S., 38, 254
Maxim, V., 78, 106, 240, 244, 249, 252, 254
Mayerhofer, M., 227
Mazza, G., 262
McAllister, S., 263
McCombs, R. K., 270
McDaniel, D., 251
McDonald, W. J., 265
McDonough, J., 268
McIntosh, P. A., 260
McKenzie, A. L., 32, 254
McKisson, J. E., 147, 254
McMahon, S. J., 273
McMillan, E. M., 22, 254
McNamara, A. L., 19, 255
Meadors, K., 235
Melcher, C. L., 62, 255
Mellace, C., 228
Messina, G., 262
Miani, A., 227
Micco, V., 229
Mich, T. J., 250
Michaud, S., 259
Michel, C., 272
Mijnheer, B., 238, 254
Mikhaylova, E., 271
Millardet, C., 255
Miller, D. W., 256
Miller, J., 264
Miller, M., 64, 255
Min, C., 265
Min, C.-H., 48, 146, 255
Minohara, S., 247, 254, 274
Mintzer, R. A., 274
Mirandola, A., 240
Mirkovic, D., 242, 264
Missaghian, J., 263
Mittra, E., 268
Miuchi, K., 247
Miyamoto, S., 267
Miyamoto, T., 254
Miyatake, A., 257
Mizmoto, T., 267
Mizoe, J., 240
Mizoe, J.-E., 254
Mizumachi, Y., 274
Mizumura, Y., 267
Mizuno, H., 41, 246, 248, 255, 271
Mizushima, K., 246
Mochizuki, S., 269
Moding, E. J., 5, 255
Moehrs, S., 229, 272
Moffett, D. R., 38, 249, 255
Mohammed, M., 257
Mohan, R., 242, 257, 264, 274
Mohar, M. F., 264
Molinelli, S., 240, 249
Molière, G., 11, 255
Mollet, P., 271
Monchamp, R. R., 272
Mongelli, V., 235
Monini, C., 31, 236, 255
Montarou, G., 48, 236, 249, 255, 262
Moore, F. E., 246
Moosburger, M., 260, 265
Mora, J., 268
Morel, C., 227, 249
Mori, S., 246, 274
Mori, Y., 229

- Morone, C., 254
Morrocchi, M., 47, 231, 239, 254, 255, 260
Morse, J., 240
Morteau, E., 258
Moser, U., 232
Moses, W. W., 63, 256
Moskal, P., 257
Moszynski, M., 241
Motte, J.-F., 240
Mounier, F., 239
Moyers, J. C., 235
Moyers, M. F., 34, 256, 275
Muehllehner, G., 66, 248, 256
Mullani, N. A., 244, 269
Muller, C., 66, 256
Mumot, M., 50, 256
Munkel, G., 260
Munoz, E., 267
Munzenberg, G., 238
Munzenrider, J. E., 259
Muraishi, H., 227
Murakami, M., 244
Murakami, T., 246, 247
Muramatsu, M., 248
Muraro, S., 227, 254
Murayama, H., 62, 256, 274
Muraz, J.-F., 240
Muren, L. P., 270
Murphy, P. H., 247
Münzenberg, G., 264
Nadaraya, E. A., 159, 256
Nagao, Y., 269, 273
Nagatsu, K., 274
Nagayoshi, T., 247
Naimuddin, M., 39, 256
Nakagawa, K., 257
Nakahara, T., 247
Nakajima, Y., 269
Nakamura, Y. K., 255
Nakano, T., 273
Nakazawa, K., 268
Narayanan, M., 255
Natarajamani, D., 255
National Instruments, 130, 256
Nedunchezhian, K., 20, 256
Nelms, B. E., 231
Nestor, O. H., 62, 257
Neubeck, C. von, 253, 273
Neuvéglise, D., 229
Newhauser, W. D., vii, 6, 8, 14, 16, 34, 257, 274
Newport, 98, 257
Newport, D., 235
Ngo, F. Q. H., 232, 270
Nickel, F., 238, 264
Nicolini, R., 262
Niedźwiecki, S., 64, 257
Niemierko, A., 241, 258, 266, 268
Nieto-Camero, J., 269
Nightingale, J. M., 239, 270
Nill, S., 257
Nishikido, F., 269, 274
Nishimura, H., 247
Nishimura, K., 227
Nishina, Y., 248
Nishio, T., 45, 46, 247, 254, 255, 257
Nitta, M., 269
Nivoix, M., 255
Noda, A., 271
Noda, K., 246, 247, 271
Nomura, K., 257
NuPECC, 6, 257
Nurdan, K., 257
Nurdan, T. C., 173, 257
Nutt, R., 235, 262
O'Dorisio, T. M., 268
Obana, T., 246
Oberdorfer, F., 233
Oberg, K., 268
Oelfke, U., 40, 45, 258, 272, 273
Ogawa, M., 254
Oger, T., 52, 258
Ogino, T., 257
Ogitsu, T., 246
Ohmori, C., 229
Okada, Y., 247
Okumura, Y., 274
Oliphant, M. O., 22, 258
Oliver, J. F., 258, 267
Omura, T., 252, 256
Ordonez, C. E., 147, 258
Orecchia, R., 239, 240
Orikasa, T., 246
Orito, R., 247
Orlandea, N., 248
Ornitz, R. D., 231
Ortega, P. G., 89, 148, 157, 258, 261, 262
Ortuño, J. E., 263, 267

- Ostertag, H., 227, 233
Ostojic, R., 253
Ouyang, J., 274
Owen, H. L., 28, 258, 260

Pönisch, F., 41, 239, 261
Paans, A. M. J., 45, 258
Packa, M., 257
Paganetti, H., vii, xvii, 7, 16, 21, 29, 31, 32, 35, 36, 146, 230, 237, 238, 241, 242, 245, 248, 255, 258, 259, 265, 266, 268, 270, 271, 274
Paige, S. L., 235
Pallotta, S., 264
Palta, J., 245
Pan, T., 265
Panse, R., 262
Pantano, D., 254
Paoloni, A., 227
Parajuli, R. K., 273
Park, C. W., 250
Park, J. C., 250
Parker, D. J., 269
Parker, E. F., 255
Parker, Y., 244, 275
Parodi, K., 35, 39–41, 43, 46, 48, 50, 51, 146, 227, 229, 230, 234, 238, 239, 241, 248, 250, 251, 259, 261, 262, 264, 266, 267, 274
Parra, L. C., 78, 260
Particle Therapy Cooperative Group, PTCOG, 146, 260
Passi, A. R., 255
Pasternak, J., 229, 260
Pate, B., 266
Pate, B. D., 241
Patera, V., 227, 239, 254, 261
Pattalwar, S. M., 260
Patti, I. V., 235
Paulus, M. J., 235
Pausch, G., 245, 265
Pautard, C., 233
Pavel, M., 268
Pawelke, J., 45, 238, 239, 255, 259, 260, 271
Pawlak-Niedźwiecka, M., 257
Peach, K. J., 23, 260
Pearce, P., 228
Pearson, D., 244, 275

Pedroni, E., 11, 14, 27, 28, 232, 242, 253, 260, 264, 265
Pedroni, E. S., 265
Peeler, C. R., 242
Pella, A., 239
Peloso, R., 266
Pemler, P., 39, 260, 265
Pencke, M. D., 251
Penfold, S., 263
Penfold, S. N., 38, 260
Pennazio, F., 47, 231, 239, 254, 260
Perkins, A. E., 268
Peroni, C., 231, 239, 254
Peschke, P., 271
Peters, A., 151, 260
Petersen, J. B. B., 270
Peterson, S., 237, 253, 261
Peterson, W., 251
Petzoldt, J., 245
Peyrin, F., 244
Pham, K., 252
Phelps, M. E., 235, 244, 269
Phillips, G. W., 254
Phillips, M. H., 31, 260
Picardi, L., 262
Piercey, R. B., 254
Piersanti, L., 49, 227, 254, 261
Piersimoni, P., 247
Piliero, M., 254
Piliero, M. A., 231
Pinto, M., 88, 249, 261, 262
Pirrone, G., 231, 249, 254
Pistillo, C., 232
Pittà, G., 228
Planche, T., 229
Plautz, T., 38, 261
Plautz, T. E., 247
Plescak, R., 269
Plumb, A., 261
Podgorsak, B. E., 268
Podgorsak, E. B., ix, 71, 74, 261
Podlyski, F., 255
Poggiali, D., 234
Poizat, J.-C., 269
Polf, J., 253
Polf, J. C., 147, 148, 237, 261
Poludniowski, G., 37, 261, 269
Potter, J. M., 243
Powsner, E. R., 261

- Powsner, R. A., 55, 261
Pozimski, J. K., 260
Pozzobon, N., 254
Pratt, R. H., 231
Prestidge, B. R., 264
Prezado, Y., 262
Price, T., 269
Prieels, D., 262, 266
Priegnitz, M., 239, 266
Privitera, G., 235
Prost, R., 240, 252, 254
Puggioni, P., 228
Pugliatti, C., 252, 264
Pullia, M., 249, 263
Pönisch, F., 238

Quintens, R., 229

Römer, K. E., 245
Réthoré, F., 227
Raczyński, L., 257
Radeka, V., 262
Rademakers, F., 233
Radon, J., 53, 261
Rafecas, M., 241, 258, 267
Raffaele, L., 235
Raiford, M., 266
Ramirez, R., 271
Randazzo, N., 241, 252, 264
Rapalino, O., 266
Rapkin, M., 264
Rarbi, F. E., 240
Rauch, J. E., 256
Ray, C., 233, 236, 239, 244, 249, 252, 261, 262, 269
Raymond, R. S., 251
Reed, N., 268
Reiss, P., 246
Reiter, A., 260
Reithinger, V., 239, 249
Reito, S., 241, 252
Reivich, M., 246
Renner, T. R., 235
Rescigno, R., 239
Retico, A., 234, 249
Riboldi, M., 239
Riccardin, L., 234
Ricci, A. R., 250
Richard, F., 272
Richard, M.-H., 84, 244, 252, 261, 269

Richter, C., 273
Rietzel, E., viii, 29, 30, 34, 231, 261
Rifuggiato, D., 235
Rinaldi, I., 40, 234, 239, 262
Ritenour E, R., 243
Ritt, S., 92, 262
Ritter, M. A., 253
Ritter, S., 272
Rivetti, A., 231, 239, 254, 262
Robert, C., 146, 244, 262
Roberts, A., 244
Roberts, D. A., 251, 252
Roberts, J. E., 270
Robertson, J. B., xvii, 35, 36, 262
Robertson, J. S., 61, 262
Robotti, N., 251
Rodrigues, P., 236
Rodriguez, A., 270
Roellinghoff, F., 152, 261, 262, 266
Rogers, C., 234
Rogers, D. F., 159, 262
Rogers, J. G., 109, 138, 262
Rogers, W. L., 66, 243, 248, 262
Rohling, H., 265
Rohrer, B., 253
Rolo, M. D., 47, 231, 262
Rolo, M. D. R., 239
Roman, M., 256
Romano, F., 227, 234, 249, 252, 254, 264, 267
Ronchi, S., 239
Ronningen, R., 251, 252
Ronsivalle, C., 23, 262
Roots, R. J., 270
Rosenblum, M., 262
Rosenfeld, A. B., 260, 273
Rosenthal, S., 245
Roser, W., 253
Rossetto, O., 240
Rossi, B., 253
Rossi, B. B., 10, 262
Rossi, S., 239
Rosso, E., 228
Rosso, V., 47, 229, 231, 234, 239, 249, 254, 263, 267, 272
Rougieri, M., 244, 275
Rousseau, M., 233, 239
Rozes, A., 255
Rubinov, P., 256

- Rucka, G., 234
 Rudy, Z., 257
 Rukalin, V., 256
 Rusquart, P., 233
 Russo, G., 229, 272
 Russo, G. V., 252
 Russo, M., 252
 Ruszniewski, P., 268
 Ruth, T. J., xvii, 58, 263
 Rutherford, E., 11, 55, 232, 263
 Rutz, H. P., 227
 Rydberg, B., 17, 252, 263
 Rykalin, V., 261, 263
 Réthoré, F., 234
 Sabini, M. G., 235
 Sadoff, A., 265
 Sadrozinski, H. F., 39, 263
 Sadrozinski, H. F.-W., 247, 261
 Sajio, N., 257
 Saint Gobain, 94, 99, 126, 263
 Sakai, H., 244
 Sakai, M., 273
 Sala, P., 231, 234, 249, 254, 260, 263
 Sala, P. R., 258, 262
 Salamone, V., 235
 Salomon, A., 234, 236
 Salomé, M., 240
 Salsac, M. D., 233
 Samarati, J., 228, 272
 Sampayan, S. E., 234
 Sandjong, S., 90, 142, 263
 Sandri, S., 262
 Santoro, P., 268
 Santoro, R. T., 231
 Santos, A., 255, 263, 267
 Saraya, Y., 40, 263
 Sarrut, D., 242, 244, 262
 Sarti, A., 227, 254, 261
 Sasaki, H., 254
 Sato, H., 227
 Sato, K., 248, 271
 Sato, M., 243, 271
 Sato, S., 248
 Satoh, T., 273
 Sauerwein, W., 234
 Sauli, F., 39, 228, 233, 244, 263, 272
 Saunders, W., 252
 Sawakuchi, G. O., xvii, 36, 264
 Sawano, T., 267
 Scampoli, P., 232
 Scarantino, C. W., 50, 231, 264
 Scaringella, M., 39, 263, 264
 Schäfer, K., 245
 Schöne, S., 78, 156, 265
 Schürmann, B., 245
 Schaart, D. R., 227, 233, 234
 Schaffner, B., xvii, 29, 34, 36, 264
 Schall, I., 13, 15, 264
 Schardt, D., vii, 5, 6, 13, 14, 19, 26, 28, 32,
 238, 241–243, 246, 249, 259–261,
 264, 269
 Scheib, S., 260
 Scheidenberger, C., 238, 264
 Schibli, R., 256
 Schimmerling, W., 15, 264, 265
 Schippers, J. M., 256, 258
 Schlegel, W., 33, 265
 Schmidt, J. B., 252
 Schmidt, R. A., 262
 Schneider, R. J., 242
 Schneider, U., 16, 29, 34, 38, 39, 260, 265
 Schneider, W., 34, 265
 Scholz, M., 238, 240, 267, 271, 272
 Scholz, U., 240, 267
 Schopper, F., 275
 Schubert, K., 247, 261, 263
 Schubert, K. E., 260
 Schuemann, J., 270
 Schuemann, J. P., 34, 255, 265
 Schulte, R., 247, 261, 263
 Schulte, R. W., 260
 Schultz, P. F., 255
 Schultze, B., 247, 261
 Schulz-Ertner, D., vii, 27, 264, 265
 Schuy, C., 261
 Schwab, W., 264
 Schwarz, M., 238
 Schweitzer, J. S., 255
 Schwengner, R., 245
 Schwickert, M., 260
 Schönberger S. and Gonzalez-Carmona, M.,
 274
 Scifoni, E., 239
 Sciubba, A., 227, 254, 261
 Scotto, L. L., 258
 Seco, J., 245
 Seif, E., 240
 Sekihara, E., 248

- Sekiya, H., 247
Sellberg, G., 256
Seltzer, S. M., 78, 265
Serago, C., 245
Serber, R., 12, 266
Seregni, E., 268
Serrano, B., 244
Sethi, R. V., 19, 266
Seuntjens, J., 270
Seviour, R., 260
Shakirin, G., 43, 45, 236, 239, 265, 266
Shao, L., 262
Shao, Y., 235
Shariat, B., 253
Sharma, N.G., 257
Sharma, S., 257
Sharp, G. C., 237, 241, 242
Sheehy, S. L., 22, 260, 266
Shibuya, K., 274
Shih, H., 248
Shih, H. A., 259
Shimada, H., 273
Shimazoe, K., 274
Shimbo, M., 271
Shinaji, T., 269
Shinbo, M., 247
Shinoda, H., 40, 266
Shinoda, I., 271
Shirahata, T., 247
Shirai, T., 246
Shirato, H., 44, 266
Shopa, R. Y., 257
Shouda, K., 246
Siegel, S., 235
Siegenthaler, B., 253
Silarski, M., 257
Silva, J. C., 262
Silva, R., 262
Silverman, R. W., 235
Simon, R. S., 242
Simone, G., 230
Singh, M., 66, 172, 266
Singh, N., 267
Sipala, V., 241, 252, 264
Sisterson, J. M., 242
Skaggs, L. S., 255
Skarsgard, L. D., 273
Skowron, J., 239
Skurzok, M., 257
Slater, J. D., 256
Smeets, J., 152, 262, 266
Smith, A. R., 270
Smith, N. A., 269
Smith, R., 251
Smith, S. L., 260
Snoeys, W., 254
Sobiella, M., 238, 260
Sobieski, M., 242
Solaz, C., 267
Solevi, P., 147, 241, 258, 267
Sommerer, F., 46, 230, 259, 267
Song, H., 250
Sonoda, S., 193, 267
Soukup, P., 243
Spatola, C., 235
Spieler, G. H., 264
Spieler, H., 108, 267
Sportelli, G., 47, 231, 234, 239, 249, 254,
 255, 260, 263, 267
Srirajaskanthan, R., 268
Srivastava, R., 27, 267
Stäuble, H., 260
Stadelmann, O., 253
Stamos, J. A., 262
Stancampiano, C., 252, 264
Stappen, F. V., 251
Stauble, H., 253
Steidl, P., 264
Stein, N. A., 246
Steinberg, D., 261, 263
Steinsträter, O., 31, 267
Stephan, C., 242
Steward, V. W., 37, 255, 267
Stichelbaut, F., 48, 146, 262, 266, 267
Stockley, R. L., 255
Stone, R. S., 20, 267
Strachan, J., 260
Straub, K., 234, 249, 263, 267
Strigari, L., 262
Strosberg, J., 67, 268
Studer, S., 232
Stuttge, L., 233
Stutzmann, J.-S., 258
Subramanian, T. S., 265
Suda, M., 246–248, 255, 271
Suga, D., 250
Suga, M., 269, 274
Suit, H., viii, 30, 268

- Suit, H. D., 258, 262
 Suntharalingam, N., 55, 268
 Surti, S., 43, 44, 64, 248, 268
 Susini, A., 253
 Suzuki, K., 233
 Sweet, W. H., 61, 268
 Symons, J., 269
 Szeless, B., 228
 Tölli, H., 268
 Tabacchini, V., 234
 Tabocchini, M. A., 230
 Tada, J., 50, 243, 268
 Tagawa, L., 269
 Tajima, H., 268
 Tajima, T., 23, 268
 Takada, A., 247, 267
 Takahashi, H., 274
 Takahashi, T., 268, 273
 Takai, N., 271
 Takami, A., 271
 Takami, S., 246
 Takayama, S., 246
 Takeda, A., 274
 Takeda, S., 85, 268
 Takemura, T., 267
 Takizawa, S., 271
 Talamonti, C., 264
 Taleei, R., 242
 Tammen, J., 238
 Tampellini, S., 239
 Tanaka, E., 268
 Tanaka, T., 268
 Tang, J. Y., 253
 Tanimori, T., 247, 267
 Tarbell, N. J., 266
 Tashima, H., 44, 46, 246, 268, 269, 274
 Taya, T., 156, 269
 Taylor, J. T., 40, 269
 Tazawa, S., 227
 Telsemeyer, J., 40, 269
 Tenfordf, T., 270
 Ter-Pogossian, M. M., 53, 63, 244, 269
 Terasic, 92, 269
 Terzioglu, F., 249
 Teshima, T., 250
 Tesi, M., 264
 Tessonniere, T., 234, 241
 Testa, É, 244
 Testa, É., 48, 146, 233, 235, 236, 239, 240, 249, 252, 255, 261, 263, 269
 Testa, E., 249, 262
 Testa, M., 16, 148, 154, 233, 269
 Thörnqvist, S., 31, 270
 Thers, D., 258
 Thevenet, T., 268
 Thirolf, P. G., 227, 250, 251
 Thirugnanamurthy, S., 256
 Thiruppathy, M., 256
 Thomlinson, R. H., 234
 Thon, A., 236
 Thun, M. J., 4, 270
 Timm, R. E., 255
 Timmerman, B., 227
 Titt, U., 242, 257, 264, 274
 Tobias, C. A., 5, 17, 20, 37, 45, 232, 234, 252, 270
 Todd, R. W., 66, 147, 239, 270
 Toet, D., 228
 Toltz, A., 50, 270
 Tomida, T., 227
 Tomitani, T., 41, 244, 246–248, 255, 271
 Tommasino, F., 241
 Tomura, H., 254
 Torikai, K., 273
 Torikoshi, M., 247
 Tornai, M. P., 109, 138, 271
 Torres-Espallardo, I., 241, 258, 267
 Toshito, T., 248, 269
 Tramontana, A., 234, 249, 267
 Tran, H. N., 240
 Trindade, A., 236
 Trofimov, A., 241, 268
 Trojan, H., 227, 233
 Troost, E. G. C., 253
 Trovato, M., 267
 Tsai, Y.-S., 11, 271
 Tsuji, A., 274
 Tsuji, H., 243, 246
 Tsujii, H., 240, 243, 246, 254
 Tsurin, I., 269
 Tsuru, T., 274
 Tuli, M., 228
 Turco, P., 234
 Turler, A., 256
 Tygier, S. C., 260
 Tzenov, S. I., 260
 Uchida, H., 256, 257

- Ueno, K., 247
Unholtz, D., 230
Unkelbach, J., 31, 271
Urakabe, E., 45, 246–248, 254, 255, 271
Uribe, J., 126, 271
Urie, M., xvii, 34, 36, 245, 271
Uzawa, A., 31, 271
Uzunyan, S. A., 256

Vaccaro, V., 228
Valastro, L. M., 235
Valencia Lozano, I., 227
Vallois, Y., 133, 142, 271
Valvo, F., 239
Van Cutsem, E., 268
Van de Walle, J., 251
Van Luijk, P., 259
Vandenberghé, S., viii, 41, 271
Vander Molen, A. M., 252
Vanneste, F., 272
Vanstalle, M., 239, 261
Vanzi, E., 264
Vaquero, J. J., viii, ix, 60, 63, 271
Varela, J., 262
Vargas, C., 245
Vavilov, P. V., 10, 272
Vecchio, S., 46, 229, 272
Veksler, V. I., 21, 272
Verdú Andrés, S., 228
Verhaegen, F., 230, 250
Vetter, C., 253
Vicente, M. G. H., 229
Vidal, M., 251
Vikram, B., 273
Virshup, G., 274
Vitale, E., 227
Voena, C., 227, 254, 261
Vojnovic, B., 260
Voss, B., 262
Vretenar, M., 228
Vuiart, R., 240
Vynckier, S., 44, 272

Wagai, T., 243
Wagner, A., 236, 245
Wagner, M. S., 242
Wakizaka, H., 269
Walenta, A. H., 236, 257
Walt, N. T. van der, 256
Waltham, C., 269

Wambersie, A., 272
Wan, C-N., 246
Wang, S., 255
Wang, Y., 271
Ward, E. M., 247, 270
Watanabe, M., 252, 268, 271
Watanabe, S., 268, 273
Waters, L., 257
Watson, G. S., 159, 272
Watts, D. A., 47, 50, 228, 233, 272
Webb, S., 4, 272
Weber, K.-J., 238
Weber, M. J., 62, 272
Weber, U., 249, 264
Wegner, R., 228
Wei, Z., 248
Weiss, M., 228
Weisskopf, V., 12, 272
WeissTechnik, 107, 272
Welzel, T., 230
Werner, M. E., 268
Wernick, M. N., 274
Wetzel, R. A., 256
Weyrather, W. K., 146, 238, 272
Wheadon, R., 231, 239, 254, 260
Wiślicki, W., 257
Wideröe, R., 20, 272
Wieczorek, A., 257
Wiese, C., 273
Wildberger, J. E., 250
Wilkens, J. J., 19, 272
Willers, H., 31, 273
Williams, C. W., 262
Williams, J. R., 262
Wilson, P., 256
Wilson, R., 21, 273
Wilson, R. R., 5, 20, 273
Wimmer-Schweingruber, R., 238
Winkelmann, T., 260
Winter, M., 238
Wisser, L., 253
Witt, M., 261
Witte, H., 260
Wohlfahrt, P., 34, 273
Wolf, A. P., 246
Wolin, E., 268
Wong, M., 264
Wong, W.-H., 271
Wouters, B. G., xvii, 35, 36, 273

- Wrenn, F. R., 61, 273
Wroe, A. J., 15, 273
Wyss, J., 254
Xing, T., 271
Yabe, T., 248
Yacob, R. J., 250
Yamada, S., 254
Yamaguchi, M., 51, 269, 273, 274
Yamamoto, M., 269
Yamamoto, S., 248, 273
Yamamoto, Y. L., 262
Yamashita, H., 254
Yamashita, T., 252, 256
Yamaya, T., 44, 46, 52, 146, 268, 269, 273, 274
Yamouni, M., 240
Yan, X., 16, 257, 268, 274
Yang, M., 29, 34, 274
Yang, T. C. H., 270
Yanou, T., 250
Yao, J., 268
Yeager, C. M., 227
Yeo, R., 230
Yeoh, K.-W., 230
Yock, T. I., 241, 266
Yokoi, T., 260
Yordanova, A., 59, 67, 274
Yoshida, E., 268, 269, 274
Yoshida, K., 271
Yoshihara, Y., 147, 274
Yoshikawa, K., 271
Yoshimoto, M., 248
Youn, M.-Y., 255
Young, J. W., 235
- Zaers, J., 227, 233
Zanetti, L., 239
Zani, M., 264
Zatserklyaniy, A., 263
Zatserklyaniy, A., 247, 261
Zeng, G. L., ix, 65, 230, 274
Zennaro, R., 228
Zgardzińska, B., 257
Zhang, J., 255
Zhang, R., 257
Zheng, Y., 257
Zhernosekov, K., 256
Zhu, X., 45, 46, 238, 274
- Zhu, X. R., 242, 274
Zieliński, M., 257
Zoccarato, Y., 236, 237, 239, 249
Zoglauer, A., 78, 156, 176, 240, 275
Zografos, A., 23, 244, 275
Zou, W., 268
Zucker, M.A., 230
Zunzunegui, M. V., 252
Zutshi, V., 256
Zwaans, B., 236

Acknowledgements